THE UNIVERSITY OF
WARWICK

LIBRARY DECLARATION

Candidate's name: ……..

Date of birth: …… ID Number: …….

I agree that this thesis shall be made available by the University Library in accordance with the regulations governing University of Warwick theses.

I agree that the summary of this thesis may be submitted for publication.

I agree that the thesis may be photocopied (single copies for study purposes only) **YES / NO**
(please delete as appropriate)

Theses with no restriction on photocopying will also be made available to the British Library for microfilming. The British Library may supply copies to individuals or libraries, subject to a statement from them that the copy is supplied for non-publishing purposes. All copies supplied by the British Library will carry the following statement: "Attention is drawn to the fact that the copyright of this thesis rests with its author. This copy of the thesis has been supplied on condition that anyone who consults it is understood to recognise that its copyright rests with its author and that no quotation from the thesis and no information derived from it may be published without the author's written consent."

Author's Signature: ……. Date: ……...

……

USER'S DECLARATION

1. I undertake not to quote or make use of any information from this thesis without making acknowledgement to the author.

2. I further undertake to allow no-one else to use this thesis while it is in my care.

DATE	**SIGNATURE**	**ADDRESS**

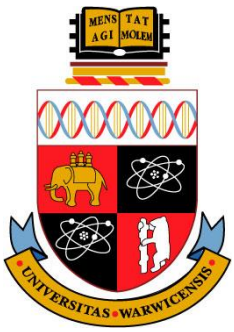

Investigation of the relationship between iron and high field MRI in healthy and Alzheimer's Disease tissue

by

Mary Elizabeth Finnegan

Submitted for the degree:

Doctor of Philosophy

School of Engineering

The University of Warwick

November 2013

THE UNIVERSITY OF WARWICK

Contents

List of figures

Chapter 4: Methodology

Chapter 5: Bulk tissue iron analysis

Chapter 6: Synchrotron X-ray fluorescence mapping

Chapter 7: MRI relaxometry

Chapter 8: The relationship between iron and MRI

List of tables

Chapter 5: Bulk tissue iron analysis

Chapter 6: Synchrotron X-ray fluorescence mapping

Chapter 7: MRI Relaxometry

Chapter 8: The relationship between iron and MRI

Chapter 9: Discussion

List of abbreviations

AD	Alzheimer's Disease
Amyg	Amygdala
A_β	Amyloid beta peptide
CAR	Ratio of the iron concentration in control tissue to AD tissue
CN	Caudate nucleus
DLS	Diamond Light Source
emu	Electromagnetic unit
FDRI	Field dependent R_2 increase
FID	Free induction decay
FLASH	Fast low-angle shot
FOV	Field of view
GFAAS	Graphite furnace atomic absorption spectrometry
GP	Globus pallidus
HD	Huntington's Disease
ICP-MS	Inductively coupled plasma mass spectrometry
INAA	Instrumental neuron activation analysis
IRM	Isothermal remanent magnetisation
LA-ICP-MS	Laser ablation inductively coupled plasma mass spectrometry
MCI	Mild cognitive impairment
MGE	Multiple gradient-echo
MRI	Magnetic resonance imaging
MSA	Multiple System Atrophy
MSME	Multi-slice mutli-echo
NBIA	Neurodegeneration with brain iron accumulation

NMV	Net magnetisation vector
NTF	Neurofibrillary tangles
Oe	Oersted
PD	Parkinson's Disease
PIXE	Particle induced X-ray emission
Pu	Putamen
RF	Radio frequency
ROI	Region of interest
SN	Substantia nigra
SP	Senile plaques
SQUID	Superconducting quantum interference device
SXRF	Synchrotron X-ray fluorescence
T	Tesla
T_e	Echo time
T_R	Repetition time
XANES	X-ray absorption near edge spectroscopy
XRF	X-ray fluorescence

Acknowledgments

First of all I would like to thank my supervisor Joanna Collingwood, for all of her support and encouragement and for always pushing me to achieve more than I thought I could. I think that the last four years have been an adventure for both of us! Thanks also to my two second supervisors: Michael Chappell who gave advice on statistics and Jon Dobson who was always enthusiastic and encouraging.

I would also really like to thank all of the excellent scientists with whom I have worked during this project. In particular: Naomi Visaji and Lili-Naz Hazrati who provided the samples for this project, and gave continual neuroanatomical advice; the past and present beamline scientists for beamline I18 at the Diamond Light Source: Fred Mosselmans, Tina Geraki and Paul Quinn, who helped with data collection and processing and generally made sure the experiments happened at all! At the University of Florida: JP Bullivant, Dan Plant, Vijay Antharam, Mark Davidson and Albina Mikhailova who gave me my first MRI and sectioning experience, before we had the facilities at Warwick. The Exley group at Keele University, in particular Emily House who carried out the GFAAS measurements. Also to Joe Gallagher who provided advice on histology.

At The University of Warwick I would like to thank: Martin Davis who helped multiple times with practicalities in the lab; Martin Lees and his student Michael Smidman, who gave advice on SQUID measurements; everyone who helped me as an interloper with an MRI probe at the NMR facility, particularly John Hanna and Thomas Kemp; The Sadler group in the department of Chemistry, especially Isolda Romero who made the ICP-MS measurements happen and Kevin Ray, a summer project student who tested ImageJ protocols.

Thanks to my parents, Helen Sang and David Finnegan, for all their support and encouragement - particularly for putting me up over the last four and a half months! I'd also like to wish good luck to my brother John who is just one year into his PhD. Thanks also go to

my extended family on both the Finnegan and Sang side, in particular Dave and Jan Sang and my Grandmother, Elizabeth Finnegan. A special thank you should go to my proof readers: my parents and my lovely friends Lisa Campbell, Grace Huxford and Sophie Rees. Sophie deserves an extra mention for being a brilliant housemate and keeping me sane, even from holiday in Canada!

I would like to thank all my friends from Warwick and further afield who have supported and encouraged me with words like “You can do it!” and “Keep going!”, which have made all the difference over the last few months in particular. A special mention to: Jenny Crane, Alex Sinclair, Becky Vanderkar, Sarah Cawley, Andrew Denty, Adam Wollman, Rachel Thwaites, Abi Jaitman, Nefeli Chatzstefani, Jen Dring, Claire Sewell, Jane Hand, Marcus Ong, Matt Jackson and David Doddington. I’d also like to mention members of Warwick Anti Sexism Society who really helped to make my time at Warwick special and provided my extra-curricular education: Kate Arnold, Joe Doherty-Bailey, Fi Grieg, Clare Stone, Anjeli Shah and Daniel Woodhouse.

Synchrotron measurements were supported by the Diamond Light Source and the MRI work was supported by the Milburn House NMR suit at the University of Warwick. The Bruker micro-imaging MicWB40 probe used in this research was obtained through the Science City Translational Medicine: Experimental Medicine Network of Excellence project and the SQUID magnetometer was bought through the Science City Advanced Materials: Creating and Characterising Next Generation Advanced Materials project. Both had support from Advantage West Midlands (AWM) and the SQUID magnetometer was part funded by the European Regional Development Fund (ERDF).

A portion of this work was performed at the National High Magnetic Field Laboratory, which is supported by National Science Foundation Cooperative Agreement No. DMR-1157490, the State of Florida, and the U.S. Department of Energy.

This research was made possible by a PhD studentship grant from the Alzheimer's Society. Thank you to the society and to the Research Network Volunteers: Jean Dutton, Sue Harris, Sue Boex and Chris West. I very much enjoyed meeting with them and have really appreciated their support.

I must also thank Julian and Kim Piercey for their kind donation to fund the purchase of the cryomicrotome at which I have spent many hours. Also, thank you to the staff at DARO Capitals for finding support for my work.

Finally, thank you to the Canadian Brain Tissue Bank for providing the samples used in this thesis and to all those who donated tissue used in this project. Also thank you to anyone who has ever donated their tissue to medical research.

Declaration

This thesis is submitted to the University of Warwick in support of my application for the degree of Doctor of Philosophy. It has been composed by myself and has not been submitted in any previous application for any degree to this, or any other university.

The work presented (including data generated and data analysis) was carried out by the author except in the cases outlined below:

- Initial preparation and measurement of the pons samples was carried out before this project began. The samples were prepared for SQUID magnetometry by Dr Joanna Collingwood, who also measured one sample from each disease (control, AD, PD and MSA) with MRI at the McKnight Brain Institute, University of Florida. Each of these samples were sectioned by Albina Mikhailova and the control and MSA example mapped at the Diamond Light Source by Dr Joanna Collingwood.
- Graphite furnace atomic absorption spectroscopy (GFAAS) measurements of the pons and substantia nigra samples were carried out by Dr Emily House at Keele University.

Parts of this thesis have been published by the author:

Visanji NP, Collingwood JF, Finnegan ME, Tandon A, House E, Hazrati LN. (2013) *'Iron Deficiency in Parkinsonism: Region-Specific Iron Dysregulation in Parkinson's Disease and Multiple System Atrophy*'. J Parkinsons Dis. 2013 PMID: 24113558

Abstract

It has been proposed that increased tissue iron concentration, which has been observed in certain regions of the brain in individuals with Alzheimer's Disease (AD), could provide a marker for diagnosis through detection with MRI. This is investigated in this thesis using high field MRI to examine *post mortem* human brain tissue. It is shown here that by using data from multiple brain regions discriminant analysis can successfully differentiate between AD and control samples, even when no statistically significant differences are observed in individual brain regions.

A unique set of complementary techniques was used to investigate iron content, R_2 and R_2* of tissue samples from the caudate nucleus, putamen, globus pallidus substantia nigra, amygdala and pons, from a set of three control and AD cases. The particulate iron content of the samples was investigated by SQUID magnetometry and was followed by iron quantification. A trend of increased particulate and total iron concentration was observed in the AD tissue compared to control, however this did not reach statistical significance in any brain region. High resolution MRI relaxometry at 9.4 T was carried out on tissue from the caudate nucleus, putamen, globus pallidus and substantia nigra using a custom design Bruker micro-imaging MicWB40 probe. As part of the work towards this PhD the probe was tested, and MRI relaxometry protocols optimised for high resolution (86 x 86 μm in plane, 150 μm slice thickness) mapping of tissue samples with high iron concentration. Again, no statistically significant differences were observed between AD and control tissue.

However, discriminant analysis of these data (particulate or total iron or R_2 or R_2*) from multiple brain regions achieved differentiation between control and AD cases with 100% sensitivity and specificity for this small sample set. This demonstrates the potential clinical usefulness of MRI of measurements of non-haem brain iron to aid in disease diagnosis.

Synchrotron X-ray fluorescence (SXRF) mapping of 30 μm thick sections, cut from the MRI samples, showed the relative concentration distribution of iron, copper and zinc in one AD and control sample from each brain region. Each metal was shown to have a distinct distribution. In particular, the inhomogeneity of iron concentration within individual brain regions, such as the putamen, was demonstrated. This may explain the wide variation in iron concentration reported in the literature for the same brain regions, and highlights the importance of close anatomical matching of samples when making comparisons. The ability of high resolution SXRF mapping to investigate the metal content within individual cells was demonstrated and used to show an increase in iron in individual AD neurons, in addition to the surrounding grey and white matter tissue.

Spatially matched SXRF and MRI maps were used to demonstrate a strong, statistically significant linear relationship between tissue iron concentration and R_2, R_2* and R_2' at 9.4 T. The gradient of the linear relationship between iron and R_2, agrees extremely well with the predicted gradient at this field, where the prediction was made by Vymazal *et al.* (1996) using MRI relaxometry at 0.05 to 1.5 T. To the best of my knowledge, this is the first time that this relationship has been quantified at 9.4 T, or at any field above 7 T.

MRI at 14.1 T was carried out on low iron concentration regions (the pons and amygdala). Matched SXRF and R_2* maps did not show a strong linear relationship between iron and R_2*. The iron concentration in these regions is less than 50 μg/g and it was concluded that in tissue with low iron content, other tissue properties - such as water content - are dominating the value of R_2*. This result was replicated with data measured at 9.4 T, when only tissue with an iron concentration of less than 50 μg/g was considered.

Publications

The following publications have arisen from work related to this thesis:

Visanji NP, Collingwood JF, Finnegan ME, Tandon A, House E, Hazrati LN. (2013) '*Iron Deficiency in Parkinsonism: Region-Specific Iron Dysregulation in Parkinson's Disease and Multiple System Atrophy*'. J Parkinsons Dis. 2013 PMID: 24113558

Antharam V, Collingwood JF, Bullivant JP, Davidson MR, Chandra S, Mikhaylova A, Finnegan ME, Batich C, Forder JR, Dobson J (2012). *High field magnetic resonance microscopy of the human hippocampus in Alzheimer's disease: Quantitative imaging and correlation with iron.* Neuroimage 59(2): 1249-1260.

Gallagher JJ, Finnegan ME, Grehan B, Dobson J, Collingwood JF, Lynch MA (2012). '*Modest Amyloid Deposition is Associated with Iron Dysregulation, Microglial Activation, and Oxidative Stress*.' Journal of Alzheimers Disease 28(1): 147-161.

Ugarte M, Grime GW, Lord G, Geraki K, Collingwood JF, Finnegan ME, Farnfield H, Merchant M, Bailey MJ, Ward NI, Foster PJ, Bishop PN, Osborne NN (2012). '*Concentration of various trace elements in the rat retina and their distribution in different structures.*' Metallomics 4(12): 1245-1254.

The following posters, presented at international conferences, have included work related to this thesis:

At the 10th International Conference on Alzheimer's & Parkinson's Diseases (March 2011, Barcelona):

M. Finnegan, J.F. Collingwood, N Visanji, E. House, M. R. Lees, V. Antharam, A. Mikhailova, J. Dobson, L.-N. Hazrati (2011) *Determining the source of elevated iron concentrations: The human pons in neurodegenerative disorders, published in 'Neurodegenerative Diseases',* ISBN 978-3-8055-9738-8

At the 15th International Congress of Parkinson's Disease and Movement Disorders (June 2011, Toronto):

Visanji NP, Collingwood JF, Finnegan M, House E, Tandon A, Hazrati LN (2011). '*Disregulation of iron storage in multiple system atrophy*.' Movement Disorders 26: S30-S30.

The 11th International Conference on Alzheimer's & Parkinson's Diseases (March 2013, Florence):

Mary E. Finnegan, Naomi Visanji, Emily House, Vijay Antharam, John-Paul Bullivant, Martin R. Lees, Albina Mikhailova, Jon Dobson, Lili-Naz Hazrati, Joanna F. Collingwood (2013) *Tissue iron accumulation in Alzheimer's disease parallels increased grey/white matter contrast in MRI of the human pons*

The 5th meeting of the International Bioiron Society (April 2013, London):

Joanna Collingwood, Mary E. Finnegan, Naomi P. Visanji, Emily House, Lili−Naz Hazrati, Vijay Antharam, John−Paul Bullivant, Lees MR, Mikhailova A, Batich C, Davidson MR, Dobson J (2013) *Brain iron and MRI in Alzheimer's Disease, Parkinson's Disease, and Multiple System Atrophy*

Chapter 1:
Introduction and Background

1.1 Introduction

1.1.1 Motivation

Alzheimer's disease (AD) is a very common neurodegenerative disease, which affects almost half a million people in the UK [1]. The global and national cost of dementia is huge. The estimated total cost for informal (family), social and medical care was reported as $604 billion in the *World Alzheimer Report 2010 - The Global Economic Impact of Dementia* [2].

Only a small proportion of AD cases have been identified as autosomal dominant and these cases are known as familial Alzheimer's disease (FAD) [3]. The vast majority of cases are sporadic AD for which the aetiology is unclear. Determining the pathogenesis of AD is a major area of interest in AD research with conflicting opinions on whether the disease is triggered by the accumulation of amyloid [4] or whether this is in response to another initial cause of oxidative stress [5, 6], such as the accumulation of iron [7, 8] or breakdown of myelin [9, 10].

Currently there is no proven diagnosis of the disease until *post mortem* when the underlying disease pathology can be examined and during life only a diagnosis of probable AD can be made based on the assessment of clinical symptoms [11, 12]. Although AD is the most common cause of dementia, there are a number of different neurodegenerative diseases which present with similar symptoms, such as vascular dementia and dementia with Lewy bodies. Current diagnosis criteria are based on the reported progression of disease symptoms by the patient and their carers and the cognitive assessment by tests, such as the mini metal state examination [11].

A more definitive test, or series of tests, which enable a sensitive and specific diagnosis of AD is highly desirable. Recent developments in PET (positron emission tomography) imaging of amyloid deposition, volumetric MRI (magnetic resonance imaging) of brain atrophy and measurement of amyloid in the cerebral spinal fluid have led to proposals for potential new AD diagnosis criteria [13, 14].

MRI is a particularly attractive option as it is non-invasive and does not involve exposure to ionising radiation. However, volumetric changes in the AD brain due to atrophy have shown significant overlap with atrophy in normal aging [15] and rely on a change that has occurred due to cell death.

Increased iron concentration has been observed in particular regions of the AD brain [16-22] and a number of other neurodegenerative diseases [23]. Tissue iron concentration shows a positive linear correlation with MRI transverse relaxation rate (R_2) and the susceptibility related relaxation (R_2*). Therefore it may be possible for the iron changes observed in AD to be detected by quantitative MRI mapping (MRI relaxometry) and iron disregulation has been suggested as a possible marker for Alzhiemer's Disease via its effect on MRI [24].

The effect of iron on MRI is field dependent and increases linearly with field, therefore high field MRI provides a more sensitive investigative tool. However, it has been suggested that the effect will saturate at higher fields [25]. The linear relationship of the field dependence has been shown at fields of up to 4.7 T [26] and 7 T [27] respectively. However, this area warrants further investigation as the relationship at fields above 7 T is under-studied.

Additionally, the number of studies which have investigated the relationship between iron concentration and R_2 and R_2* using *post mortem* tissue is small. These studies are important as they allow direct comparison of MRI, followed by tissue iron quantification, rather than relying on general iron values in the existing literature, which *in vivo* studies necessarily do.

1.1.2 Aims

The aim of this thesis is to investigate whether iron changes in Alzheimer's disease could aid diagnosis via the measurable effect it has on the MRI relaxation rate R_2 and the susceptibility related R_2*. This question will be addressed by measuring iron content and carrying out high field MRI relaxometry on a set of control and AD human *post mortem* tissue samples from multiple regions of the brain. Three questions will be investigated: i) are there changes to the iron content of the samples which can be used to differentiate between disease and control? ii) are corresponding changes observed in MRI relaxometry measurements which also allow differentiation between AD and control? iii) what is the relationship between tissue iron content at high field (9.4 T and 14.1 T) and is this the same for control and AD tissue?

The measurements made in this project contribute to further understanding the nature of the changes to iron (and copper and zinc) in AD, however the main focus of the project is to examine the potential role of iron in AD diagnosis.

1.1.3 Thesis structure

A brief background to Alzheimer's disease and its diagnosis is given in Section 1.2 as well as an introduction to non-haem brain iron and its measurement by MRI. This is followed by a detailed review of the literature showing comparative studies of iron content in control and AD tissue in Section 1.3 and summarised in Figure 1.3. In Chapter 2: *Theory*, the magnetic properties of tissue iron and its interaction with MRI are described in addition to introducing synchrotron X-ray fluorescence (SXRF), which will be used to map iron distribution in tissue samples.

The literature review demonstrates that there is evidence of increased iron concentration and a change in the form of iron in certain regions of the brain. However, a wide variety of measurement techniques have been used in these previous studies, and there are conflicting results from the different studies. Due to the conflicting results it is hypothesised that a

multiregional approach may be necessary to differentiate between control and AD tissues. Therefore six regions of the brain are investigated: the caudate nucleus, putamen, globus pallidus, substantia nigra, amygdala and pons. The rationale behind the choice of regions and the preparation of the samples for each measurement technique is detailed in Chapter 3: *Samples*.

Three Parkinson's Disease (PD) and Multiple System Atrophy (MSA) cases are also examined from a subset of the regions, in order to begin to investigate how AD may be differentiated from other neurodegenerative diseases as well as from normal aging. Some of the data from these regions form part of a collaborative study with the University of Toronto and are included in the paper *Iron Deficiency in Parkinsonism: Region-Specific Iron Dysregulation in Parkinson's Disease and Multiple System Atrophy* by Visanji *et al.* [28], attached in Appendix H.

A unique set of complementary measurement techniques was used to examine the form, concentration and distribution of iron in the samples set. The methodology used, including newly developed and improved laboratory protocols, is described in Chapter 4. This included testing and setting up MRI protocols with the new custom design Bruker micro-imaging MicWB40 probe funded through the Birmingham Science City Translational Medicine project. The probe was purchased in early 2010 and became the first MRI probe in the Milburn House NMR suit at the University of Warwick. This work and the final MRI relaxometry protocols are described in Section 4.3.1.3.

Additionally, a histochemical staining protocol was developed to stain tissue sections which had been mapped with SXRF. This was challenging due to the fragile nature of the tissue, which had been exposed to high intensity X-rays, but important to enable identification of tissue structures, including individual cells. The protocol and its development are described in Section 4.5.2.

In Chapter 5: *Bulk tissue iron analysis* the particulate and iron content of tissue samples is investigated. This provides information about the quantity and form of iron in the samples. In Chapter 6 SXRF mapping is used to produce high resolution, high sensitivity maps of the iron, copper and zinc distribution in a control and AD example from each brain region. The results of high resolution MRI mapping are presented in Chapter 7, with some brain regions mapped at 14.1 T, and the majority mapped at 9.4 T. T_1 data were also collected for each sample, however these were not analysed due to time constraints. The analysis of T_2 and T_2* data was prioritised due to their higher sensitivity to iron concentration. In each of these chapters a comparison is made between the control and AD samples and discriminant analysis is used to combine data from multiple brains to predict the disease state of each sample.

Finally, in Chapter 8 the relationship between iron and MRI is examined by comparing the iron measurements (Chapters 5 and 6) with the results of MRI relaxometry (Chapter 7). In particular, matching of high resolution SXRF iron maps with MRI maps is used to test the linear relationship between iron concentration and R_2 and R_2* at high field.

1.2 Background

1.2.1 Alzheimer's Disease

Alzheimer's disease (AD) is the most common form of dementia, accounting for 62 % of dementia and affecting almost half a million people in the UK alone [1]. Worldwide the number of people living with dementia is set to rise from 35.6 million people in 2010 to 65.7 million people in 2030 [2], mainly due to the aging population. The rate of dementia increases with age: for people aged 65-69 years the rate is 1 in 100, whereas for those over 80 the rate is 1 in 6 [29].

Memory impairment is usually the first symptom of AD followed by degeneration of communication, learning, movement and changes to personality such as increased irritability and depression. As the disease progresses patients become less able to perform the basic tasks of daily life and rely more on care from the state and family. The nature of the memory loss and altered personality with progressing AD is often very distressing not only for the patient, but has been shown to increase the rate of depression in carers [30].

1.2.1.1 Disease pathology

The development of AD pathology is thought to begin up to decades before presentation of the first clinical symptoms. Individuals who show some AD pathology, but no clinical symptoms can be termed as having pre-symptomatic AD. However, when this assessment is made of *post mortem* tissue this categorisation assumes that they would have developed symptoms if they had lived long enough, which cannot be proven. The second phase in the disease is Mild Cognitive Impairment (MCI) which is shown by individuals who also display cognitive symptoms, such as some memory loss, but who do not meet the criteria for dementia. Again these individuals may die before developing dementia [4].

At a cellular level AD pathology is characterised by the presence of senile plaques (SPs) and neurofibrillary tangles (NFTs). The main constituent of SPs is the peptide beta amyloid (A_β)

[31]. A_β is one product of the amyloid precursor protein (APP) and is deposited extracellularly. Senile plaques can range in size from 2 – 500 μm and can be diffuse or neuritic and contain neuropeptides, ubiquitin, APP and a number of other enzymes in addition to A_β. SPs are visualised in pathology sections using histochemical stains such as Congo red or antibodies that bind to A_β.

NFTs are bundles of filaments that form in neuronal bodies and are made from tau protein. Tau is an abnormally phosphorylated component of paired helical filaments [32]. NFTs correlate more strongly with dementia than SPs and their numbers increase throughout the disease [33]. Loss of grey matter throughout the progression of AD has been shown to follow the accumulation of NFTs [34].

Non-haem brain iron is altered from the norm in many neuropathological diseases [35]. It is thought to contribute to oxidative stress and neuronal degeneration in AD through the production of hydroxyl radicals [5, 36]. Redox-active iron has been shown to be associated with senile plaques and NFTs *in vivo* [37] and with A_β *in vitro* [38]. Changes in the concentration, form and distribution of iron in AD are discussed in depth in the literature review in Section 1.3.

There is also evidence for changes in concentration of other metals, such as copper and zinc, in the AD brain. For example, Deibel *et al.* measured a statistically significant increase in iron and zinc and a decrease in copper in the hippocampus and amygdala of the AD brain [39]. A number of other studies have also found a decrease in the concentration of copper in AD [40], although copper has also been associated with senile plaques [41].

Cell death in AD causes a physical shrinking of the brain. General atrophy of the cerebral hemispheres [42] is observed in AD as well as specifically in the hippocampus [43] and amygdala [15]. Atrophy is observed to some extent in the normal aging brain and AD atrophy overlaps with the normal range [42].

1.2.1.2 AD pathogenesis

The amyloid cascade hypothesis is that A_β accumulation and subsequent deposition into SPs is the first stage in AD pathology which is followed by a series of events leading to neuronal cell death and onset of dementia. Evidence in support of this hypothesis includes the presence of genetic mutations that increase the processing of APP into A_β in FAD [44]. There is also evidence for NFT formation later in disease progression, after initial amyloid plaque deposition [45]. However, there are also findings which refute the amyloid cascade hypothesis. This includes the fact that the degree of amyloid deposition does not correlate well with disease severity [45] and some normal aging patients show SPs in autopsy tissue. Additionally clinical trials of drugs targeting A_β have proved inconclusive [46].

Oxidative stress has been proposed as an alternative mechanism of AD pathogenesis, with increased production of APP and tau in response to the initial redox imbalance [6, 44]. Disregulation or disrupted homeostasis of non-haem brain iron is one possible [7, 8, 36] cause of oxidative stress.

1.2.2 Diagnosis of AD

Currently there is no proven diagnosis of AD until *post mortem* tissue can be examined and the pathology of AD identified. This is a major problem as AD is only one of a number of dementias including: vascular dementia, dementia with Lewy bodies and frontotemporal dementia [33]. These all have differing underlying disease pathology, but often similar or overlapping symptoms. For clinicians it is important to have a confident diagnosis for a patient in order to administer the right treatment and in drug trials it is vital to be able to have a cohort of subjects with the underlying disease the drug is targeting. Therefore there is huge interest in finding a biomarker of Alzheimer's disease that can be measured *pre mortem* and ideally before significant disease pathology develops.

The traditional route to AD diagnosis (the NINCDS-ADRDA criteria for clinical diagnosis of AD) and some of potential biomarkers that are being investigated are described below.

1.2.2.1 The NINCDS-ADRDA criteria for clinical diagnosis of AD

Before a probable diagnosis of AD is given, a patient must first be diagnosed with dementia. This diagnosis is often considered after they present with symptoms such as short-term memory loss, inability to remember names of people or objects, depression, problems with dressing or eating. Tests such as the Cambridge Examination for Mental Disorders of the Elderly (CAMDEX) can be used to gain a clinical diagnosis of dementia [11]. Scaled tests for dementia such as the mini-mental state examination or the Blessed scale are often used on the road to a diagnosis of AD and can be repeated over time to assess symptomatic progression.

The combination of symptoms and the manner in which they present can be indicative of the underlying cause of dementia, for example vascular dementia often has a more rapid onset than AD [47].

The NINCDS-ADRDA criteria for clinical diagnosis of AD is widely used. It provides criteria for possible and probable AD based on clinical examination of dementia and the assessment of symptoms, but requires additional histopathological evidence for a diagnosis of definite AD [12].

1.2.2.2 Developments in AD diagnosis

The International Working Group for New Research Criteria [13, 48] for the Diagnosis of AD and National Institute on Aging–Alzheimer's Association (NIA-AA) [14] have proposed revised criteria for the diagnosis of AD. The proposals consider the use of *in vivo* biological markers of AD pathology in addition to the clinical symptoms as outlined above.

The markers can be divided into two groups. The first being pathophysiological markers which are directly linked to the pathology of AD. Samples of the cerebral spinal fluid (CSF) can be taken and the reduced concentration of A_{β}, and increased tau and phospho-tau have been

shown to be associated with AD [49]. Additionally Positron Emission Tomography (PET), with a tracer that binds to amyloid, has been used to predict the development of AD in healthy adults [50]. The second category is topographical markers which covers measurement of atrophy as measured by structural MRI (see next section) and reduced glucose metabolism which can be observed using fluorodeoxyglucose PET [51].

Although studies using the markers described above have shown promising results, the general consensus is that they are not yet ready to be used clinically [52, 53]. In particular the difficulty in standardising the assessment of these markers is highlighted [14].

Another hurdle is determining the order and rate of progression of AD pathology and monitoring this through measurement of biomarkers [4]. This would not only enable improved diagnosis of AD, but also identify the stage of the disease. Understanding the state of the underlying disease pathology is particularly important when considering clinical trials of disease-modifying treatments.

There is still plenty of room for further investigation of potential biomarkers to improve diagnosis and monitoring of AD.

1.2.2.3 Magnetic Resonance Imaging

Magnetic resonance imaging (MRI) is a commonly used clinical imaging technique. Structural MRI is used to image soft tissue, such as the brain, and aid diagnosis of tumours, internal bleeding and more. MRI (without the use of tracers) has an advantage over some of the other biomarker detection methods, as unlike CSF measurement it is non-invasive and does not involve the exposure to the ionising radiation that PET does.

MRI and the different relaxation processes are described in more detail in Chapter 2 along with details of how relaxation rates can be measured and how tissue iron content affects their value. At a basic level MRI works by imputing a pulse of energy into the hydrogen nuclei of the tissue. This energy then dissipates at different rates (relaxation rates) depending on the

composition of the tissue: it is this difference in relaxation rate that provides image contrast. Clinical MRI does not usually measure the relaxation rates in the tissue, it merely takes a snapshot of the energy distribution sometime shortly after the energy pulse. However, it is possible to use clinical scanners to quantitatively map the relaxation rates of tissue which is called MRI relaxometry.

There are two different mechanisms of MR relaxation: i) the longitudinal relaxation which is described by a time T_1 and a rate of $R_1=1/T_1$ and ii) the transverse relaxation which is described by T_2 and has a rate of $R_2=1/T_2$. Transverse relaxation is readily affected by MRI field inhomogeneities and therefore MRI scans usually correct for this. When these effects are not corrected for, the relaxation time is T_2* which is always shorter than T_2.

Structural MRI has been used to observe the atrophy of the brain during ageing and with neurodegenerative diseases [42, 43, 54] and has had mixed success in separating AD and normal ageing brains. For example, Laakso *et al.* demonstrated statistically significant atrophy in the AD amygdala compared to control. However, there was a significant overlap between the size of the amygdala in AD and normal aging individuals, reducing the clinical usefulness of this measurement [15]. A major disadvantage of measuring brain atrophy to diagnose AD is that by the time atrophy is measurable, significant cell death will have occurred. However, in a study of subjects with familial AD, atrophy was shown to begin before symptomatic onset [55].

More recently, MRI mapping has been considered as a technique to examine the changing properties of the brain on a cellular level [26, 56]. There are many factors which can contribute to changes in transverse relaxation time T_2 and longitudinal relaxation time T_1 in the ageing and demented brain. For example, demyelination of the frontal lobe white matter in AD [56, 57], water concentration [19] and the form and concentration of non-haem brain iron. The linear relationship between T_2 shortening and iron concentration has been demonstrated in the human liver [58] and in *post mortem* human AD brain tissue [26].

MRI has also been used to directly examine AD pathology, with the imaging of SPs achieved in histological sections of *post mortem* human tissue [59, 60] and *in vivo* in mouse models of AD [61].

1.2.2.4 Iron as a potential marker in MRI

Non-haem brain iron homeostasis is altered in AD and this has been considered a possible biomarker for AD diagnosis. However, in order to achieve this, the concentration, form and clustering of iron in the normal and AD brain must be understood and suitably sensitive and specific detection methods developed.

Tissue iron concentration plays a major role in determining the contrast in MRI (see Section 2.2 for more details) and therefore it is possible that iron changes in AD and other neurodegenerative diseases could be observed with MRI and thus aid diagnosis. An extreme example of this is seen in the disease Neurodegeneration with Brain Iron Accumulation (NBIA, formerly known as Hallervorden-Spatz disease) where accumulation of iron causes an 'eye-of-the-tiger' pattern in the region of the globus pallidus [62] (see Figure 1.1).

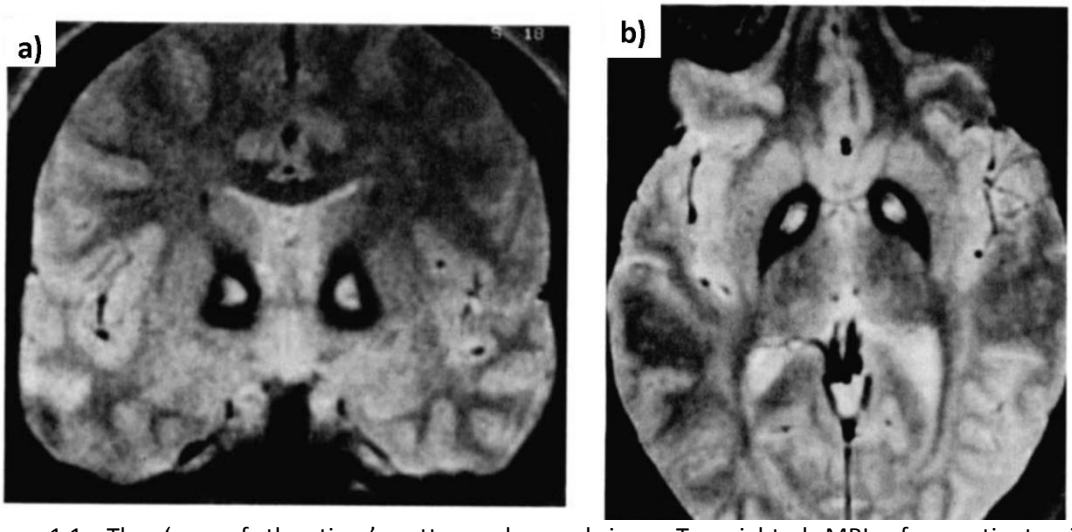

Figure 1.1: The 'eye of the tiger' pattern observed in a T_2-weighted MRI of a patient with neurodegeneration with brain iron accumulation (NBIA). In a) the coronal and b) the axial view there is a hypo-intense region in the vicinity of the globus pallidus, which produces an eye-of-the-tiger pattern and is caused by a large accumulation of iron. This figure was adapted from Sethi *et al.* 1988 [62].

The iron changes observed in AD are much more subtle than in NBIA and therefore more sensitive MRI techniques must be utilised. These are discussed in more detail later in the chapter.

1.2.3 Non-haem brain iron

Non-haem iron refers to iron that is not bound in haemoglobin (and some other enzymes). Iron is the most abundant metal in the in the body and is involved in a very large number of cell functions including myelination and synthesis of neurotransmitters [63, 64]. Therefore the body has a sophisticated iron regulatory system involving a number of storage and transport proteins. Genetic mutations which affect these proteins have been demonstrated in some neurodegenerative diseases, for example neuroferritinopathy [65] and acaeruloplasminemia [66]. There is also evidence for disruption of iron homeostasis in AD and Parkinson's disease (PD), but the underlying cause of this is currently unknown [67].

The regulation and function of trace metals in the brain are interdependent. For example, caeruloplasmin is a multi-copper oxidase which oxidizes Fe^{2+} to Fe^{3+} and is the major plasma anti-oxidant. It has been shown to be decreased in the PD substantia nigra where there is increased iron [68]. Conversely, caeruloplasmin has been shown to be increased in other regions of the PD and AD brain [69].

1.2.3.1 Forms of non-haem iron in the brain

Iron can be present in the brain as ferric (Fe^{3+}) or ferrous (Fe^{2+}) ions. Ferric iron is relatively unreactive, whereas ferrous iron is very redox active. It is this ability to switch between redox states that makes iron such a useful element in the body. However, ferrous iron can react with hydrogen peroxide and produce hydroxyl radicals (·OH) by the Fenton reaction [70, 71]:

$$\mathrm{Fe^{2+} + H_2O_2 \rightarrow Fe^{3+} + \cdot OH + OH^-} \qquad (1.1)$$

The hydroxyl radicals are highly reactive and cause cellular damage. It has been hypothesised that iron could play a major role in cell death in AD and other neurodegenerative diseases through the oxidative stress caused by free radical production [72, 73].

1.2.3.1.1 Ferritin

The majority of non-haem iron in the brain (up to 90% [74]) is found in a storage protein called ferritin. Ferritin consists of a 12 nm outer diameter protein shell which sequesters iron in a mineral core of up to about 8 nm in diameter [75] (Figure 1.2). This iron is often referred to as 'ferritin iron' or just 'ferritin' and is in the non-toxic ferric form.

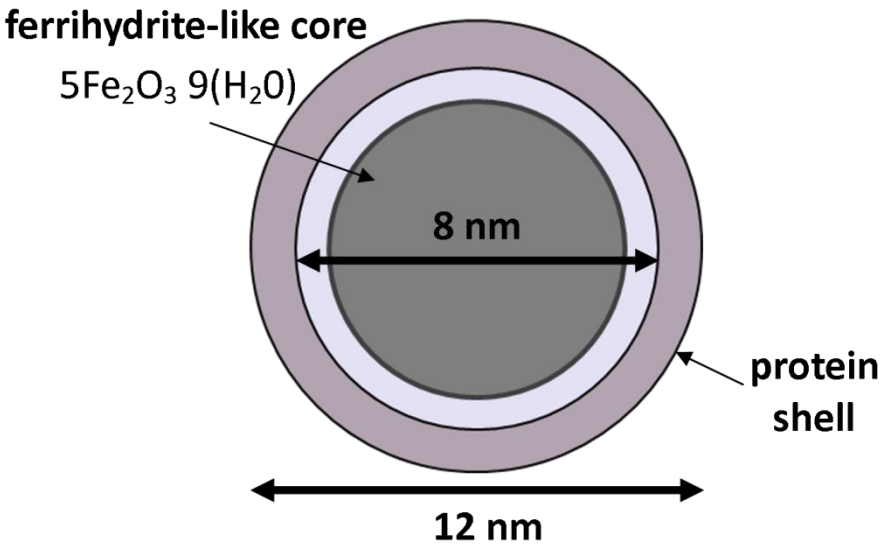

Figure 1.2: A simplified diagram of ferritin. The spherical protein shell has a 12 nm outer diameter and an 8 nm inner diameter. Iron is sequestered inside the protein to form a ferrihydrite-like mineral core of up to 4500 iron atoms and approaching 8 nm in diameter.

Ferritin cores are typically a single nanocrystal with a ferrihydrite-like structure, which has the approximate chemical formula $5Fe_2O_3$ $9(H_2O)$. However, other phases such as hematite and magnetite are also observed within the nanocrystal [76, 77].

The controlled mineralisation of iron occurs in such a way as to minimise the Fenton chemistry [76]. The size of the cores is controlled by ferritin and the soluble protein shell ensures that no insoluble aggregates are deposited.

Up to 4500 iron atoms can be stored in the core of one ferritin protein and the number of iron atoms in the core is known as the loading factor. Dedman *et al.* reported an average of around 1500 iron atoms per ferritin in the cerebral cortex of healthy controls with no statistically significant difference in AD [21].

Ferritin is found throughout the human body and across the animal kingdom. It is both an iron store and an iron reserve. The substructure protein shell varies based on the iron requirements of the tissue [70].

1.2.3.1.2 Haemosiderin

Haemosiderin is another form of stored non-haem iron in the brain. It is thought to be a degradation product of ferritin [75] and has a less easily characterised structure, although studies have shown a ferritin-like core [76]. Additional iron phases have also been identified in haemosiderin (and in some pathological ferritin), such as magnetite, goethite and wustite [76-78], but examination of these phases is beyond the scope of this PhD.

Haemosiderin is associated with an excess of iron [70]. The iron in its core may be more easily released than in ferritin [78], but it has also been suggested that haemosiderin may play a protective role where there is an overload of iron [79].

1.2.3.1.3 Transferrin

Transferrin is the most prolific iron transport protein and its concentration has been shown to be altered in AD. Conner *et al.* found decreased transferrin throughout the AD brain [22] in contrast to increased ferritin and iron in some regions.

1.2.3.1.4 Magnetic iron oxides

Magnetite has a ferrimagnetic structure and the chemical formula Fe_3O_4. It is present in many organisms and in 1992 was identified in the human brain using magnetometry by Kirschvink *et al.* [80]. It has since been extracted from tissue and identified using TEM and electron diffraction [81] and *in situ* in autopsy tissue by X-ray spectroscopy [82].

As magnetite has been associated particularly with brain regions with a high iron content, such as the hippocampus [81], there is interest in its role and prevalence in neurodegenerative diseases. A small study of neuroferritinopathy (an iron overload disorder) patients indicated an increase in magnetite concentration [83]. In men, but not women, an increase in magnetite concentration with age has been observed [84], which is interesting in light of the fact that men have an increased risk of developing AD at a younger age.

1.2.3.1.5 Neuromelanin

Non-haem brain iron is also found in the neurons of the substantia nigra and locus coeruleus as part of the complex molecule neuromelanin. Iron in neuromelanin (NM) is also in the Fe^{3+} state and makes up 10-20% of iron total in the SN [85] (with the majority of the remainder in ferritin in glial cells).

NM has been shown to have similar properties to ferritin [86]. A study of substantia nigra tissue from control and PD cases showed only ferritin-like iron [87]. However, unlike ferritin NM contains different magnetic domains which vary in size [88].

1.2.3.2 Iron in fixed and frozen tissue

Fixed tissues have been used in some imaging and iron quantification studies [89, 90]. Fixed tissues are easier to work with than fresh-frozen tissue as they remain stable over long periods of time at room temperature. However, the process of fixing tissue in formalin has been shown to leach metals, including iron, from the tissue into the fixing solution. The degree of leaching depends on the duration of storage of the tissue in the solution and also on the element [91]. Furthermore, metals that are known to be strongly bound to proteins, such as gold, do not leach into formalin as much as other elements. This suggests that the degree of leaching depends on how the metal is bound within the tissue [91].

Additionally, a study of iron in the SN in control and PD tissue showed the presence of non-ferritin iron in formalin-fixed tissue only [87], suggesting that the formalin had altered the form

of iron in the tissue. Furthermore reduced Perls' staining intensity has been associated with exposure to fixatives [92].

1.2.3.3 Iron concentration and age

In 1958 Hallgren and Sourander reported a study of iron concentration from 11 regions (frontal white matter, globus pallidus, cerebellar cortex, prefrontal cortex, temporal cortex, sensory cortex, parietal cortex, occipital cortex, motor cortex, caudate nucleus and putamen) of 81 brains. They plotted iron concentration in the brain with age from 0 to 100 years [93] and produced a set of empirical exponential equations for iron with age in each of the 11 regions. In general iron was shown to increase at an approximately linear rate in each region until the age of around 20 to 30 years, after which iron concentration begins to plateau.

More recently Bartzokis *et al.* [94] calculated ferritin iron concentration in the brain and showed a linear increase of iron with age in the hippocampus, putamen, caudate nucleus and globus pallidus, but a linear reduction of iron in the frontal lobe white matter. The iron concentration was also compared between male and female patients and women were found to have a lower iron concentration than men in multiple grey and white matter brain regions. This is significant as men have a high risk of developing AD at an earlier age than women.

Loeffler *et al.* [18] reported iron concentration in the caudate nucleus, putamen, globus pallidus, substantia nigra and frontal cortex for young (n=8; average age = 45.4 ± 13.8 years) and aged (n=8; average age = 74.6 ± 7.6) controls. No comparisons reached statistical significance, but the trend was that iron was increased in the elderly controls. The exception to this being the globus pallidus which showed reduced iron concentration.

Laakso *et al.* [15] also showed an increase in iron concentration with age. The spread of data in both this and the above paper is fairly large, meaning that any attempt to estimate the iron concentration of a sample based on age has a wide margin of error.

1.2.4 Measuring iron in the brain

Since Goodman first reported positive staining for iron in AD cerebral cortex tissue in 1953 [95], various measurement techniques have been used to examine the changes in iron in AD and other neurodegenerative diseases. Each technique examines different properties of the tissue iron. Some measure total iron quantification from dissected tissue samples, others give a spatial distribution of iron within a section of tissue and some can provide information about the form of iron in the tissue. A selection of some iron analysis techniques which have been used to examine iron in the brain are described below.

1.2.4.1 Histology

Intensity and distribution of Perls' stain has been used to compare control and AD tissue. Increased staining in AD tissue has been reported as well as positive staining in cells associated with senile plaques [96, 97]. Multiple slices can be stained and imaged to build a 3D image of iron distribution in an area of brain [98].

Perls' stain is a histochemical stain for non-haem iron based on the ferrocyanide-Prussian blue reaction. The Prussian blue colour is produced when ferric ions, which are released from the sample using a hydrochloric acid solution, react with potassium ferrocyanide [99]. Therefore this is a stain for ferric iron. Modifications to the Perls' staining technique have increased staining intensity and enable staining of less 'accessible' iron, in particular in white matter [100].

Although staining provides information about iron distribution with high spatial resolution it has a number of disadvantages when considering its use for concentration comparison, including the fact that it can only stain ferric iron. This was demonstrated in the first published work quantifying iron in AD brain tissue: in 1960 Hallgren and Sourander positively stained for iron in the frontal temporal cortex of AD tissue, but not of control. However, when the total iron was measured no significant increase was observed in AD compared to control [97].

Despite the fact that Perls' staining cannot provide a good estimate of total iron concentration or show a true distribution of all tissue iron, changes in staining pattern do indicate a change in the form of iron in the tissue and therefore altered iron homeostasis.

Morris *et al.* showed that exposure of tissue sections to common fixatives reduced the intensity of Perls' staining [92]. This could be due to fixatives leaching iron from the tissue or reducing the concentration of stainable ferric iron. Any comparative study must use very consistent protocols.

Relevant literature reports that oligodendrocytes are the cell which most strongly stains positively for iron, with occasional staining in astrocytes and microglia [101, 102]. Neurons do not generally stain strongly with Perls' despite the fact that other measurement techniques have shown that they do contain iron.

Immunochemistry and immunofluorescence are used to stain for iron-associated proteins such as ferritin and transferrin [40, 103].

1.2.4.2 Iron quantification in bulk tissue samples

The iron concentration of dissected tissue can be measured using a number of different techniques. Ion Coupled Plasma Mass Spectrometry (ICP-MS) [23, 104] and Atomic Absorption Spectroscopy (AAS) [105, 106] both require tissue digestion in acid before iron quantification.

Instrumental Neutron Activation Analysis (INAA) has also been used to quantify brain iron content [17, 39]. Brain tissue is dissected and freeze dried before irradiation with neutrons and analysis of iron content based on nuclear decays.

Hallgren and Sourander used colorimetry by the orthophenalthroline method to determine iron concentration in their 1958 landmark study *The effect of age on the non-haemin iron in the human brain* [93]. Hydrochloric acid is used to extract iron from tissue homogenate, which is reacted with orthophenalthroline to produce a dark red colour. A spectrophotometer is then

used to measure the absorption of the solution from which the iron concentration can be calculated using Beer's Law.

All of the iron quantification methods mentioned above can be carried out on specific regions of the brain when they are dissected from the surrounding tissue. High resolution spatial information about the distribution of iron in the tissue is not obtained and total iron is measured with no information about the form of iron. Blood vessels need to be removed from dissected samples to give a measurement of non-haem iron only.

The result of bulk tissue analysis is also dependent on how precisely a particular brain region is dissected. This may be a source of experimental error which contributes to the spread in reported iron concentration for the same brain regions, which can be seen in the data collated by Haacke *et al.* [107].

1.2.4.3 Magnetometry

The magnetic properties of iron are determined by its form and therefore the hypothesis that there are changes in the form of non-haem iron in AD can be tested using Superconducting QUantum Interference Device magnetometry (SQUID). SQUID magnetomety of freeze dried brain tissue samples has been used to examine the magnetic properties of brain iron [108, 109] and has shown an increase in magnetite or maghemite in AD tissue when compared to control [110].

Magnetite has a greater effect on local field inhomogeneities than ferritin and it is therefore useful to consider the magnetic properties of the tissue samples when trying to identify regions which may provide useful targets for MRI identification of AD.

1.2.4.4 Synchrotron X-ray analysis

Synchrotron X-ray fluorescent mapping of biological tissues can be used to produce highly sensitive and specific maps of iron (and other metals) concentration, and relative distribution, at high resolution [82, 111].

As SXRF mapping is a non-destructive technique, the tissue sections can be mapped at multiple resolutions. Gallagher *et al.* (in collaboration with our group) mapped a large area of tissue from a mouse model of AD at 60 µm resolution and then selected areas which showed high iron concentration for further high resolution mapping at 5 µm [112]. Tissue can also be stained post mapping in order examine the cell distribution and disease pathology.

Popescue *et al.* have developed rapid scanning SXRF to a speed which allows large areas of the brain to be mapped in short periods of time. For example, they mapped the basal ganglia [89] in less than one hour. This technique uses thick fixed tissues of around 1 cm which is problematic because the full depth of the tissue is not penetrated equally by the X-rays and the escape/penetration thickness is different for the different metals being compared. Consequently the depth resolution is different for the different elements. Also fixatives have been shown to leach metals from tissues and therefore the results may not accurately represent the concentration of metals *in vivo*.

X-ray Absorption Near Edge Spectroscopy (XANES) using synchrotron radiation has been used to investigate the form of iron present by collecting absorption spectra from regions of interest first identified using SXRF mapping [111-113].

1.2.4.5 Other

Electron and X-ray analysis techniques such as Particle Induced X-Ray Emission (PIXE) [114] and Energy Dispersive X-ray (EDX) spectroscopy [115] have been used to examine iron in and around senile plaques. Transmission electron microscopy (TEM) can be used to examine the crystalline structure of ferritin cores [77, 80, 116], and together with electron energy-loss spectroscopy (EELS) and electron tomography has been used to characterise the iron content of AD plaques [115]. However, these techniques have a number of disadvantages compared to SXRF. They are less sensitive, require working within an ultra-high vacuum and cause more damage to the sample [117].

Laser Ablation Inductively Coupled Plasma Mass Spectroscopy (LA-ICP-MS) can produce a quantitative map of metal distribution in thin slices of brain tissue [118, 119] at a similar resolution and sensitivity to SXRF. The quantitative nature of LA-ICP-MS gives an advantage over SXRF mapping, which only provides a relative concentration distribution unless careful calibration can be carried out. However, unlike SXRF mapping, LA-ICP-MS is a destructive technique and therefore can only be mapped once and does not allow multiple maps, XANES or staining to be carried out on the same section.

1.2.5 MRI of non-haem brain iron

Tissue non-haem iron content has been shown to have a significant effect on MRI relaxation in phantoms [120], animals [121] and human post mortem tissue [19]. Since this was first demonstrated a number of different techniques have been developed to calculate tissue iron content in the brain (and the liver [58]) of living patients using data obtained by MRI.

Some of the methods used for imaging brain iron are described below. In 2005 Haacke *et al.* published a detailed review on this subject [107]. The magnetic properties of non-haem iron and its interaction with MRI relaxation is described in detail in Chapter 2, Section 2.2.

1.2.5.1 R_1, R_2 and R_2* mapping

MRI imaging techniques which quantitatively map the relaxation rates R_1, R_2 and R_2* (known as MRI relaxometry) have been shown to reveal subtle differences in brain tissue. For example, enabling differentiation between anatomical features in the brain that cannot be achieved with relaxation-weighted imaging [122].

Both the transverse relaxation rate R_2, and to a lesser extent the longitudinal relaxation rate R_1, have been shown to be linearly proportional to the iron content of tissue at field strengths similar to that of a clinical scanner [121]. A linear correlation has also been shown between R_2* and iron concentration [27], with a steeper gradient (and therefore greater sensitivity) than R_2 [123].

1.2.5.2 Field Dependent R_2 Increase imaging

The field dependent R_2 increase (FDRI) is the degree to which the value of R_2 depends on the external magnetic field. Bartzokis *et al.* have used this property to develop a means of examining iron content from R_2 MRI scans [124]. R_2 is measured at two different field strengths and the difference calculated to give the FDRI. They showed that FDRI of the frontal white matter, caudate nucleus, putamen, and globus pallidus correlated strongly with published iron concentration values in healthy adults and with phantoms of ferritin containing agarose gels [124]. FDRI has since been used to study ferritin iron concentration in AD compared to control [125] and also in other neurodegenerative diseases such as PD and HD [126, 127].

A disadvantage of FDRI is that it requires MRI mapping with two different instruments. This increases the cost and time of the imaging and also requires careful matching of anatomical features across the two data sets.

1.2.5.3 R_2', phase and Susceptibility Weighted Imaging

Tissue degeneration in AD causes increased water concentration in the tissue. This has the opposite effect to increased iron concentration and reduces R_2 [125, 128]. Therefore a number of groups have been developing new imaging techniques which separate the effect of iron from that of tissue water concentration.

R_2' is the portion of R_2* that is caused by the dephasing of spins due to local field inhomogeneities. Ordidge *et al.* developed a method for mapping R_2' that reduces the influence of background field variations (which can inflate changes in R_2*). Using this technique, they measured an increase in iron in the SN of PD patients that agrees with post mortem studies, but had not been observed in R_2 mapping [129].

In susceptibility weighted imaging (SWI) a mask of phase information is applied to a magnitude MRI image to enhance the contrast. The mask can be chosen to highlight particular phases (features) and has been used to enhance contrast between grey and white matter [130],

resolve structures not observable with T_2 or T_1 weighted imaging [131] and examine the iron concentration distribution of brain tissue [27].

1.2.5.4 High field MRI

Although most clinical scanners typically have a magnetic field strength of around 1.5 T, higher field research instruments have become more common. The field dependent R_2 increase described above means that the contrast caused by variation in tissue iron content should increase at higher field. It has been suggested that the effect will reach saturation due to the saturation of magnetisation of ferritin iron. This was reported in a study of monkey brain by Bizzi *et al.* at field of up to 4.7 T [25]. However, in a study of human *post mortem* tissue House *et al.* report a strong linear relationship between iron and R_2 at 4.7 T [26].

7 T MRI measurements of human brains *in vivo* and *post mortem* (Yao *et al.*) have been used to quantitatively described the linear relationship between iron and R_2*. In the same study they demonstrated that R_2* is linearly dependent on field by imaging at fields of 1.5, 3 and 7 T [27].

In a study published by our group the linear relationship between relative iron concentration and R_2 and R_2* was shown in tissue from the hippocampus at 14.1 T [132]. However, as iron was not quantified in that preliminary study it is not possible to check whether the field dependent R_2 and R_2* increase follows the same trend as predicted at lower fields.

1.2.5.5 Comparing MRI and tissue iron concentration

When MRI is used to make an estimation of brain iron without using direct tissue iron measurement to corroborate the results, for example when estimating iron in the brain of living patients, the values published by Hallgren and Sourander in 1958 [93] are often still used for calibration [133, 134]. The age range of the subjects was 30 to 100 years and iron concentration was measured by the orthophenalthroline method. Table 1.1 reproduces the iron concentration in micrograms per gram of fresh tissue.

Brain Region	Number of Samples	Fe µg/g fresh mass	SD µg/g
Globus Pallidus	55	213	34.9
Red Nucleus	44	194.8	68.6
Substantia Nigra	52	184.6	65.2
Putamen	56	133.2	34.3
Dentate Nucleus	45	103.5	48.6
Caudate Nucleus	58	92.8	21.4
Thalamus	52	47.6	11.6
Cerebellar Cortex	53	33.5	8.7
Motor Cortex	46	50.3	8.8
Occipital Cortex	38	45.5	6.7
Sensory Cortex	45	43.2	5.8
Parietal Cortex	37	38.1	6.7
Temporal Cortex	47	31.3	5.7
Prefontal Cortex	58	29.2	4.1
Frontal White Matter	59	42.4	8.8
Medulla Oblongata	41	14.0	11.6
Meninges	10	10.2	2.9

Table 1.1: Iron concentration in regions of the brain as reported by Hallgren and Sourander. Concentrations were determined by colorimetry from healthy adults aged 30 to 100 years [93].

Other studies have used *post mortem* samples to directly compare iron concentration with the measured R_2 and R_2* of the samples. These included studies by Vymazal *et al.* (human and monkey brain) at fields from 0.5 to 1.5 T [135]; House *et al.* at 1.4 T [19] and 4.7 T [26] and Langkammer *et al.* at 3 T [123].

The number of studies of *post mortem* tissue is fairly small, due to the difficulty in obtaining samples. These studies are important as they do not rely on the assumption that the iron concentration quoted in the literature accurately reflects the iron concentration in the individual involved in the study. Reported iron concentration values vary considerably as is shown in a review by Haacke *et al.* [107], which likely reflects some natural variation as well as measurement errors within and between studies.

However, there are also a number of disadvantages in studying *post mortem* tissue, in particular the changes in MRI relaxation rates which occur over time. Vymazal *et al.* have reported a decrease of 6-9% in R_2 over the first 12 hours *post mortem* and of 13-22% in samples which had been frozen [135].

1.2.5.6 MRI and SXRF

Recently MRI maps of *post mortem* tissue have been compared to SXRF fluorescence maps of sections cut from the imaged sample. This allows direct spatial comparison of iron distribution and MRI, using the highly sensitive and specific X-ray fluorescence maps.

McCrea *et al.* used rapid scanning SXRF to compare iron distribution with MRI maps and conclude that susceptibility weight imaging (SWI) was the best MRI indicator of iron concentration [136]. The same group carried out SWI on fixed brains at a clinical resolution, using a 1.5 T scanner. They then mapped 1 mm thick sections of these samples using rapid scanning SXRF and matched these sections to the MRI maps [90]. Metal foils were used to calibrate the SXRF signal and to produce quantitative iron maps, showing a linear relationship between iron concentration and phase.

Antharam *et al.* mapped fresh hippocampal tissue at very high resolution at a field of 14.1 T [132]. Tissues were then sectioned at 30 μm and air dried onto quartz slides before mapping (a very similar protocol is used in this thesis and described in detail Chapter 4). Fresh tissue was used to avoid metal leaching by fixatives and the thin sections used ensure the full depth of the sample contributes to the map.

1.3 Literature review: iron in the AD brain

In AD (and other neurodegenerative diseases) there is evidence of iron disregulation with increased concentration in some regions of the brain, as well as changes in the distribution and concentration of some of the associated regulatory proteins.

One aim of this project is to investigate the potential for MRI to aid diagnosis of AD by detecting iron changes in the brain. This question was investigated using high resolution, pre-clinical MRI of human *post mortem* tissue. The bore size of the high resolution MRI probe means that only a small volume of tissue can be imaged at a time. The careful analysis required, instrument time and the availability of samples limited the number of brain regions which could be investigated. A careful literature review was carried out to assess which six regions of the brain may be most useful in aiding diagnosis.

1.3.1 Iron concentration in AD and control tissue

A summary of literature reporting comparisons between tissue iron concentration in specific brain regions of AD cases compared to control is shown in Figure 1.3. Each row represents data published for a different region of the brain and these regions have been grouped approximately according to their neuroanatomy. Red cells indicate a study in which a decrease in iron was observed in AD, blue cells show no change and yellow cells indicate a statistically significant increase. The reported statistical significance is indicated with one asterisk for $p<0.05$ and two asterisks for $p<0.01$. Where a change approached significance this is indicated in a blue cell with an arrow showing the direction of change and the p value stated. Each cell also contains the iron measurement method used in that study and a letter in bold that relates to Table 1.2 which gives the details of the paper in which the data were published.

Letter	Lead Author (year)	Method	Number of samples (control, AD)	Reference
A	Bartzokis (1994)	FDRI	8, 5	[125]
B	Bartzokis (2000)	FDRI	68, 31	[133]
C	Bartzokis (2004)	FDRI	36, 10	[126]
D	Connor (1992)	Ferrochem II serum	11, 13	[22]
E	Cornett (1998)	INAA	21, 58	[17]
F	Dedman (1992)	Ferrozine reagent	11, 11	[21]
G	Deibel (1996)	INAA	11, 10	[39]
H	Ding (2009)	Phase shift MRI	24, 26	[137]
I	House (2008)	ICP-AES	3 to 5	[19]
J	Laakso (1996)	T_2 mapping	18, 54	[138]
K	Loeffler (1995)	Ferrochem II serum	8, 14	[18]
L	Lovell (1998)	micro PIXE	5, 9	[114]
M	Magaki (2007)	GFAAS	6, 8	[40]
N	Samudralwar (1995)	INAA	56, 98	[16]
O	Thompson (1988)	INAA	15, 14	[20]
P	Zhu (2009)	Phase shift MRI	15, 15	[139]

Table 1.2: Papers referenced in the literature review in Figure 1.3. The lead author, year of publication, methodology and number of control and AD samples are given. FDRI = field dependent R_2 increase; INAA = instrumental neutron activation analysis; ICP-AES = inductively coupled plasma atomic emission spectroscopy; PIXE = particle induced X-ray emission; GFAAS = graphite furnace atomic absorption spectroscopy.

Comparing between studies is difficult due to the large variety of iron quantification techniques used (these were described in more detail in Section 1.2.4). Studies also vary in their use of fixed or fresh tissue; however only studies of fresh tissue are included in this review. Papers mostly reported concentrations per gram of fresh tissue, but others gave values per gram of freeze dried tissue. Both are included in the literature summary.

Some published data are from small sample size studies, which is unsurprising due to the limited availability of donated human brain tissue for research. This means assessing statistical significance is non-trivial and in some reports $n<3$ and no statistical comparisons are made. Where no statistical comparison can be made data was not included in Figure 1.3, for example in a number of regions in the paper by House *et al.* [19]. Any data from studies that compared iron concentration through Perls' staining are also excluded from the summary, as this technique has been shown not to accurately reflect total iron concentration.

	Region							
Basal ganglia & mid brain	Putamen	**A** (↑p=0.07) FDRI	**K** Fe Serum	**B** ** FDRI	**C** ** FDRI	**H** * ϕ MRI	**P** * ϕ MRI	
	Caudate Nucleus	**K** Fe Serum	**C** * FDRI	**B** * FDRI	**P** * ϕ MRI	**A** * FDRI		
	Globus Pallidus	**C** (↑p=0.13) FDRI	**K** * Fe Serum	**B** ** FDRI	**H** * ϕ MRI	**A** * FDRI		
	Thalamus	**P** ϕ MRI	**J** T_2 mapping	ICP-AES				
	Nuclear Basalis of Meynert	**O** INAA						
	Substantia Nigra	**K** (↓ 25%) Fe Serum	**P** ϕ MRI					
	Red Nucleus	**P** ϕ MRI						
Limbic system	Hippocampus	**O** (↑p<0.10) INAA	**M** GFAAS	**H** * ϕ MRI	**P** * ϕ MRI	**J** * T_2 mapping	**G** * INAA	**E** * INAA
	Amygdala	**L** (↑p<0.08) mPIXE	**J** T_2 mapping	**G** (↑p=0.07) INAA	**E** * INAA	**O** * INAA	**N** * INAA	
Cerebellar	Cerebellum	**G** INAA	**E** INAA					
	Dentate Nucleus	**P** * ϕ MRI						
Olfactory	Olfactory Bulb	**E** INAA	**N** * INAA					
Cortex, lobes & gyri	Motor Cortex GM	**D** Fe Serum						
	Motor Cortex WM	**D** Fe Serum						
	Occipital Cortex GM	**D** * Fe Serum						
	Occipital Cortex WM	**D** * Fe Serum						
	Frontal Cortex	**M** GFAAS	**I** ICP-AES	**K** * Fe Serum	**E** * INAA			
	Parietal Cortex	**P** * ϕ MRI	**F** ** Ferrozine					
	Inferior Parietal Lobe	**G** INAA	**E** ** INAA					
	Piriform Cortex	**N** * INAA						
	Temporal Lobe	**E** * INAA	**I** * ICP-AES					
	Superior Temporal Gyrus	**G** INAA	**D** Fe Serum					
WM structures	Subcortical WM	**I** ICP-AES						
	Corpus Callosum	**I** ICP-AES						
	Frontal lobe WM	**B** FDRI	**C** (↓ p=0.14) FDRI	**P** ϕ MRI	**A** FDRI			
	Temporal WM	**J** T_2 mapping	**I** ICP-AES					
	Parietal WM	**J** T_2 mapping						

Key: Measurement techniques

FDRI = Field dependent R_2 increase

ϕ MRI = phase corrected MRI

ICP-AES = inductively coupled plasma atomic emission spectroscopy

GFAAS = graphite furnace atomic absorption spectroscopy

INAA = instrumental neutron activation analysis

mPIXE = micro particle induced X-ray emission

Figure 1.3: Summary of literature review. Each cell represents one study and the colour indicates whether a statistical significant change in iron in AD was observed: blue = no change; yellow = increase; red = decrease. The letter at the start of the cell indicates the study and corresponds to Table 1.2, which gives the full reference and further details from the paper. The letter is followed by an indication of the statistical significance observed where: * p<0.05; ** p<0.01. Where a change approached, but did not reach statistical significance, this information is given in brackets. Finally the measurement technique used is indicated and corresponds to the key in the figure.

Some of the data included in Figure 1.3 are from living patients where MRI has been used to estimate the iron content of the tissue and no secondary direct iron measurements could be made. Zhu *et al.* used phase corrected MRI to show increased iron in multiple brain regions and also to show an increase in iron with disease severity that was particularly strong in the parietal cortex [139]. Bartzokis has published a number of studies showing increased iron in AD in regions of the basal ganglia [125, 126, 133] as measured by FDRI.

Magaki *et al.* looked at loosely bound, as well as total, iron in the grey and white matter of the hippocampus and frontal cortex [40]. They found a decrease in loosely bound iron in the frontal cortex white matter; hippocampal grey matter and a statistically significant decrease in the hippocampal white matter. However, when the total non-haem iron was considered the differences between groups disappeared.

In Figure 1.3 it can be seen that different studies of the same brain regions sometimes show different results. For example, in the parietal cortex some MRI and direct measures of iron have found no increase of iron in AD, whereas other studies have shown an increase.

Certain nuclei in the brain have reported increased iron in a number of studies, for example the caudate nucleus and putamen. Nuclei are made up of a relatively dense cluster of neurons: they are grey matter structures. Conversely, none of the white matter structures or isolated cortical white matter tissues have shown a statistically significant increase in iron.

The literature review only uncovered one region for which a statistically significant decrease in iron concentration with AD was reported. Connor *et al.* reported decreased iron in both the grey and white matter of the occipital cortex [22]. On the other hand, some regions of the brain, such as the amygdala and the caudate nucleus, have widely been reported to show significant increases of iron in AD.

The hippocampus has shown increased iron concentration in the greatest number of studies. However, this region was studied in depth in a recent publication by our group (Antharam *et*

al. [132]). We showed a statistically significant decrease in R_2* in two of nine sub-fields of the hippocampus, but no statistically significant change in R_2. Increased R_2 and R_2* variance was observed two sub-fields in AD compared to control with a high statistical significance of $p<0.001$.

It is possible that underreporting of negative (no change) results means that the review is skewed towards positive findings. However, many studies examine multiple brain regions where not all regions show a statistically significant increase. These studies help to identify regions where there is likely no change in iron in AD, such as white matter structures and the thalamus.

1.3.1.1 Recent publications

Tissues samples for analysis were requested in late 2010 and therefore studies published since that time were not included in the initial literature review shown in Figure 1.3. A search using Web of Science for papers published from 2010-2013 uncovered just one study measuring tissue iron concentration with AD in individual brain regions. In a *post mortem* study using ICP-MS Akatsu *et al.* found a statistically significant increase in iron in the amygdala in AD compared to control, but no change in the hippocampus [140].

1.3.2 Altered iron form in AD

Ferritin has been shown to increase in some regions of the brain in AD, following a similar trend to iron concentration [22]. Dedman *et al.* also reported a similar increase in iron and ferritin in the AD parietal cortex [21].

Conversely, some studies have shown that although overall levels of iron increase in AD tissue, this is not paralleled by an increase in ferritin molecules [133], which may mean an increase in iron loading in ferritin or an increase in other forms of iron. For example, Quintana *et al.* have shown differences in the structure of ferritin cores in AD compared to control [77, 116].

SQUID magnetometry has been used to demonstrate increased magnetite concentration in AD tissue from the superior temporal gyrus [110, 141]. This is significant not only because of the increased magnetisation of magnetite compared to ferritin, but also because magnetite is the only stable iron oxide containing the redox active Fe^{2+} ion.

1.3.3 Iron associated with AD pathology

A number of studies have shown altered iron and its regulatory proteins associated with AD pathology, but as with reports of iron concentration and form there are some apparently conflicting results. For example, in the amygdala Lovell *et al.* showed that in addition to an increase in iron in AD neuropil compared to control, the iron concentration in the AD senile plaques was statistically significantly higher in than in the surrounding neuropil [114]. However, a study by House *et al.* found no correlation between plaque burden and iron concentration [19].

Collingwood *et al.* showed magnetite *in situ* in sections taken from the superior frontal gyrus of a confirmed AD patient [82]. Conner *et al.* [96] observed transferrin surrounding senile plaques in AD tissue as well as ferritin-containing cells around the plaque cores. Positive iron staining was also observed in cells surrounding plaques and diffusely around the area. Quintana *et al.* used TEM to demonstrate ferritin and haemosiderin around senile plaques [78].

Iron specifically in a redox active form has been shown to be associated with senile plaques and neurofibrillary tangles in hippocampal tissue [37]. *In vitro* experiments have shown that chelation of iron from A_β solutions prevents plaque formation [142].

Samudralwar *et al.* investigated iron concentration in the olfactory system as deficits in olfactory function had been observed even in mild cases of AD [16]. They found a statistically significant increase in iron in the olfactory system of 98 AD cases compared to 56 controls.

1.3.4 Assessment of iron in AD by MRI

As described in Section 1.2.3 MRI techniques to investigate brain iron concentration have been developed and these have been used to investigate iron in the AD brain.

1.3.4.1 R_1 R_2 and R_2* mapping

Laakso *et al.* showed decreased T_2 with statistical significance in some regions of the AD brain [15], but they concluded that the overlap between AD and control values would prevent T_2 from being a useful diagnostic tool for AD. However, the effect of iron is proportional to field strength and therefore T_2 may provide more useful information at higher field strengths.

House *et al.* looked at the correlation between iron concentration and R_1 and R_2 in a small sample set of post mortem tissues across 14 brain regions at 1.4 T [19]. Although they observed a linear correlation between R_1 and R_2 in some brain regions, they showed that tissue water content was a more significant factor in determining R_1 and R_2 at 1.4 T. However, in the AD samples iron contributed more to the value of R_1 and R_2 than it did in the control samples.

In the same paper House *et al.* showed no linear correlation between plaque density and R_2, despite the widely reported association between AD pathology and iron. A 7 T post mortem imaging study of the hippocampus by Huesgen *et al.* also showed no correlation between T_2 and the number of SPs or NFTs [143].

Brar *et al.* mapped T_2 in the substantia nigra of patients with AD and with AD and parkinsonism [144]. Instead of comparing the average T_2 values they considered the number of voxels with T_2 values below 30 ms, which correspond to tissue with high iron content (note that this cut off is field dependent). This approach may help to separate the effect of T_2 shortening by iron and T_2 lengthening due to increased water concentration in degrading tissues, but only if the effect is non-uniform across all the pixels in a region.

1.3.4.2 FDRI

The results of a number of FDRI studies by Bartzokis *et al.* are included in Figure 1.3. Additionally they have used FDRI to calculate brain iron concentration in a sample set that was split into AD patients with an age of onset was before and after 70 years. The results showed an increase in the iron in multiple brain regions of the early onset group [126].

1.3.5 Iron in other neurodegenerative diseases

Iron has also been shown to increase in other neurodegenerative diseases and importantly this appears to occur in different regions than with AD. For example, increased iron has been observed in the substantia nigra (SN) in PD [23, 145, 146] with iron increases directly observed in the dopaminergic neurons [147]. In contrast no change or a decrease in iron is observed in the SN in AD [18, 106], although increases have been observed in patients who developed PD alongside AD [144].

1.3.6 Conclusion

Although a number of studies have found an increase in iron concentration in AD in certain brain regions, other studies contradict these results showing no change in the same region. As the changes seem to affect a number of different brain regions a multiregional approach may be interesting. In addition to direct measurements of tissue, increased iron content has also been observed indirectly through MRI measurements. This ultimately supports the hypothesis that changes in brain iron could aid diagnosis.

Chapter 2:
Theory

This Chapter introduces magnetic resonance imaging (MRI) and the nuclear relaxation rates R_1, R_2 and the susceptibility related R_2*. The magnetic properties of non-haem brain iron are also described and the effect it has on R_2 and R_2* discussed. Synchrotron X-ray radiation and X-ray fluorescence mapping are also introduced.

2.1 Magnetic Resonance Imaging

^{1}H MRI was carried out on two different nuclear magnetic resonance (NMR) systems: a 600 MHz system (14.1 T) and a 400 MHz (9.4 T) system. MRI scan sequences were used which facilitate measurement of R_2, R_2* and R_1, rather than merely producing contrast images. Here the basic principles of MRI are outlined and the scan sequences which were used to measure R_2 and R_2* introduced.

The reference materials used for writing this section were two text books: *MRI In Practice* by Westbrook, Kaut Roth and Talbot [148] and *Magnetic Resonance Imaging: Physical Principles and Sequence Design* by Haacke *et al.* [149].

2.1.1 Nuclear magnetic resonance

Odd mass numbered nuclei possess a property called spin which creates magnetic moment (μ) due to the positive electrical charge all nuclei possess. This moment causes the nuclei to interact with external magnetic fields, such as that of an MRI scanner B_0. The nuclei will precess about the external field at a frequency, called the Larmor frequency (ω_0), which depends on the size of the external field and a constant property for that type of nucleus called the gyromagnetic ratio (λ). Equation 2.1 gives the Larmor frequency [149]:

$$\omega_0 = B_0\lambda \qquad (2.1)$$

Hydrogen (^{1}H) nuclei are by far the most common spin-possessing nuclei in the human body, in particular due to the abundance of water. It is therefore the nucleus used in clinical MRI and the MRI in this thesis. The frequency of an NMR system refers to the Larmor frequency of the hydrogen nuclei in that magnetic field.

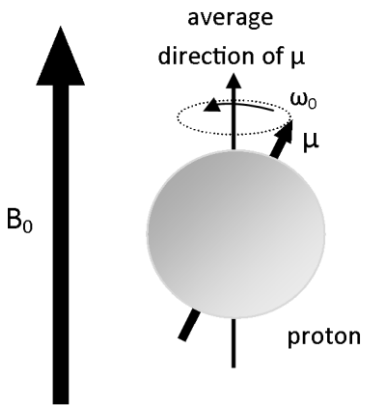

Figure 2.1: Precession about a magnetic field. The hydrogen nucleus (a proton) has a magnetic moment μ which precesses about the external magnetic field B_0 at the Larmor frequency ω_0.

The precession about the magnetic field creates an average magnetic moment for each nucleus (Figure 2.1), which can be aligned parallel (low energy) or antiparallel (high energy) to the external field. At equilibrium the majority of the nuclei will be in the low energy state. Therefore the total hydrogen nuclei in a volume of tissue (or in MRI, a voxel) have an average magnetic moment in the direction of B_0, known as the net magnetisation vector (NMV) – see Figure 2.2.

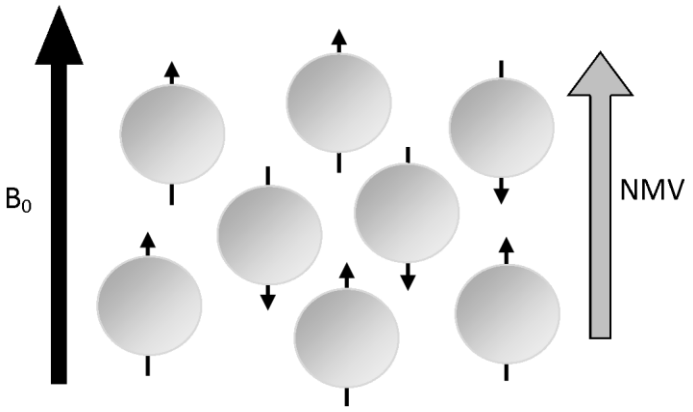

Figure 2.2: Arrangement of the magnetic moments of protons in the presence of an external field. At equilibrium the majority of the nuclei will align parallel to B_0 and create a net magnetic vector (NMV) in this direction.

Application of a pulse of energy with a frequency equal to the Larmor frequency (the resonant frequency) increases the energy of the system by exciting nuclei into the high energy state. The result of this is to change the direction of the NMV so that it is at an angle to B_0. The duration and amplitude of the resonant radio frequency (RF) pulse, applied to the system by a set of coils, determines the size of the angle of the NMV to B_0. In an MRI system B_0 is in the z direction, or longitudinal plane, parallel to the bore of the magnet.

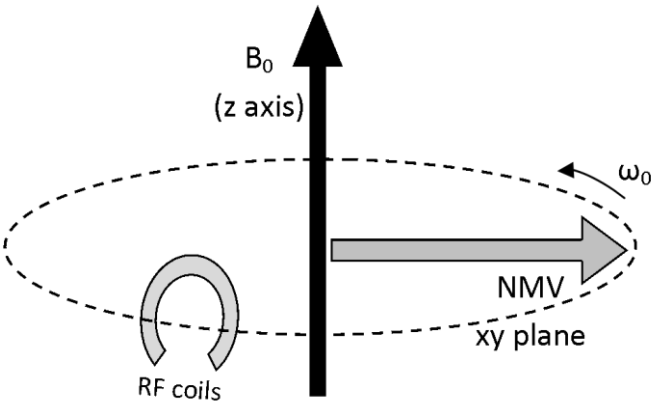

Figure 2.3: A 90° RF pulse flips the NMV into the xy plane. The NMV rotates about the z axis at the Larmor frequency and induces a current in the RF coils.

A 90° RF pulse will flip the NMV from lying parallel to z into the xy, or transverse, plane. Resonance also brings all of the nuclear spins into phase with one another and so the NMV is also rotating in the transverse plane at the Larmor frequency (Figure 2.3). This induces a voltage and alternating current in the RF coil, which is perpendicular to the transverse plane. Once the RF pulse is switched off the nuclei will i) begin to dephase and ii) to flip back into their equilibrium state meaning the NMV will move back in line with z. As this happens the induced voltage in the RF coils will decrease: this is the Free Induction Decay (FID) signal.

2.1.2 R_1, R_2 and R_2*

The process of spin dephasing and the returning of the NMV to the longitudinal plane is called relaxation and the two independent processes require dispersion of energy.

2.1.2.1 Longitudinal recovery

The return of the NMV into the longitudinal plane is called T_1 recovery (Figure 2.4a), where T_1 is the time take for 63% of the NMV to return to the longitudinal plane. The energy released during T_1 recovery is transferred from the nuclei to the surrounding lattice and is therefore known as spin-lattice relaxation. The spin-lattice relaxation rate, R_1, is equal to the reciprocal of T_1:

$$R_1 = \frac{1}{T_1} \qquad (2.2)$$

Where T_1 is in usually given in milliseconds and R_1 in s^{-1}.

Equation 2.3 describes the recovery of the magnetisation into the longitudinal plane (M_z) over time, after a 90° excitation pulse is applied [149]:

$$M_z(t) = M_0(1 - e^{-\frac{t}{T_1}}) \qquad (2.3)$$

where M_0 is the size of the magnetisation in the longitudinal plane at equilibrium.

T_1 data were collected for all samples, however the focus of this thesis is examining the effect of iron changes in the brain on T_2 and T_2*. Therefore T_1 data and in-depth detail of T_1 measurement are not included.

2.1.2.2 Transverse decay

The decay of the NMV from the transverse plane (Figure 2.4b) is called T_2 decay and can be described by Equation 2.4 [149]:

$$M_{xy}(t) = M_{xy}(0)e^{-t/T_2} \qquad (2.4)$$

Where $M_{xy}(0)$ is the magnetisation in the transverse plane when the NMV has been fully excited into the transverse plane.

This is caused by energy exchange through magnetic moment interactions between neighbouring nuclei and is termed spin-spin relaxation. T_2 is the time taken for 63% of the transverse relaxation to be lost and the transverse relaxation rate (R_2) is equal to the reciprocal of T_2.

$$R_2 = \frac{1}{T_2} \qquad (2.5)$$

Where T_2 is usually given in milliseconds and R_2 in s^{-1}.

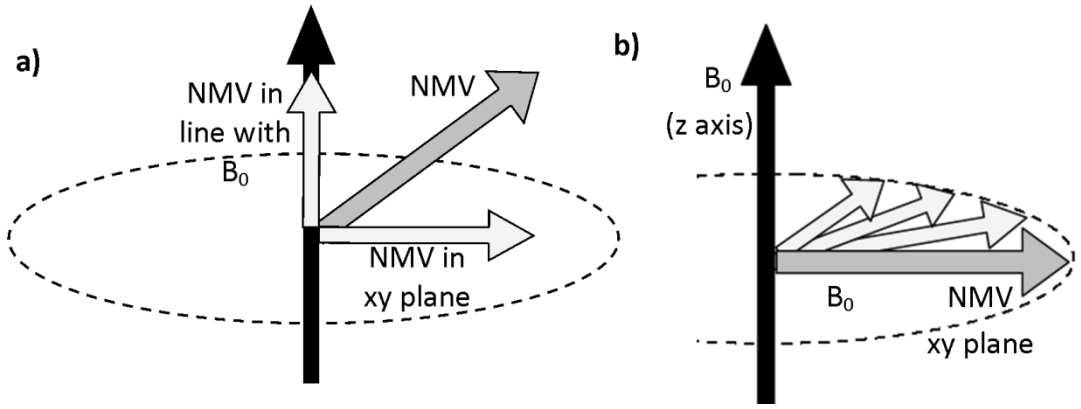

Figure 2.4: T_1 and T_2 decay. a) Individual spins flip back into the low energy state giving rise to T_1 recovery as the NMV moves back in line with B_0. b) The precessing nuclei lose phase causing T_2 relaxation and reducing the size of NMV in the xy plane.

2.1.2.3 R_2* and R_2'

The dephasing of magnetic moments can be greatly accelerated by localised field inhomogeneities. Areas of altered magnetic field cause rapid dephasing by changing the local Larmor frequency. Measurements of T_2 correct for this effect, but measurements of T_2* do not. Therefore T_2* is the spin-spin decay plus the dephasing due to local field inhomogeneities, which is described by T_2'. R_2* can therefore be represented by the following equation [149]:

$$R_2^* = \frac{1}{T_2^*} = \frac{1}{T_2} + \frac{1}{T_{2'}} \qquad (2.6)$$

The value of T_2' is both sample and machine dependent.

2.1.3 MRI hardware

The main magnetic field of the MRI systems used in this investigation is provided by superconducting magnets which are cooled by liquid nitrogen and liquid helium. These produce a close to homogeneous field, B_0, through the bore of the magnet (the z axis/longitudinal plane).

Clinical imaging systems generally have a field strength of 0.5 to 1.5 T, and image at a resolution of around 1 mm^3. Pre-clinical imaging systems can use much higher magnetic fields, which increases the size of the NMV. This produces higher signal from the same volume of sample and allows higher resolution imaging whilst still achieving good a signal to noise ratio. Most high field research instruments have a vertical bore, which is smaller than that found in clinical scanners. The bore is smaller due to the difficultly in creating strong, uniform magnetic fields.

Within the cooled system there is also a set of shim coils. The current through these coils can be manually or automatically adjusted to compensate for field inhomogeneities. Field inhomogeneities will be introduced whenever a sample is positioned within the bore of the magnet due to its magnetic properties interacting with B_0. Therefore the shim must be adjusted for every sample. The quality of the shim is assessed by examining the size and shape of the FID. As field inhomogeneities cause rapid dephasing of nuclear spins, a small FID is produced. To reduce field inhomogeneities the current to the shim coils is adjusted until the area under the FID is maximised and the shape is that of an exponential decay.

Inside the bore of the magnet the gradient coils are positioned. They apply gradient fields to the imaging space to provide the spatial encoding of the MR signal (see the following section). Gradient coils are cooled by a cool water supply to prevent over heating due to the currents which are ramped up and down in the coils as the gradients are switched on and off. The MRI

probe contains the RF coils which transmit RF pulses to the sample and pick up the signal from the proportion of the NMV in the transverse plane (as shown in Figure 2.3).

2.1.4 Spatial information

The gradient coils in an MR imaging system provide the means of spatially encoding the signal for the sample. They alter the magnetic field in the x, y, or z direction, by producing a magnetic field which either adds to or subtracts from the static magnetic field to produce a linear gradient. The steepness of this gradient can be controlled by the coils and coils can be used in combination to alter the gradient in any direction within the bore of the magnet. As the Larmor frequency is directly proportional to the external magnetic field (see Equation 2.1), applying a gradient to the sample space means that the frequency of the nuclear precession varies with position. The size gradient is controlled and the resulting field with position is known, and therefore the Larmor frequencies of the nuclei at a particular position can be calculated.

As the Larmor frequency changes the resonant frequency for nuclear excitation also changes. This allows the nuclei to be selectively excited by an RF pulse at the correct frequency. Slice selection is achieved by applying an RF pulse with a band of frequencies that match the Larmor frequencies of hydrogen nuclei within a particular physical slice of tissue, so that only these nuclei are excited. The gradient for slice selection is switched on during RF excitation pulses.

Gradients also facilitate frequency encoding and phase encoding to spatially locate signal along the other two axes. For example, if a slice is selected along the z axis, frequency and phase encoding locate the position of pixels along the x and y axis. The frequency encoding gradient is switched on to alter the frequency along one axis as the signal is collected. The phase encoding gradient is used to alter the phase of the nuclear spins, so that their position within a slice is linked to their phase. It is usually applied just before the 180° refocusing pulse. High resolution imaging requires steep gradients and increased power to the gradient coils.

2.1.5 Pulse sequences

In order to measure T_1, T_2 and T_2* different sequences of RF pulses, 'pulse sequences', are used. In general the sequence starts with an excitation RF pulse: usually a 90 ° pulse for T_2 measurements and 180 ° for T_1. The RF receiver only measures signal in the transverse plane (Figure 2.3). T_R is the repetition time of the entire sequence. To ensure that the system has reached equilibrium between measurements, T_R should be at least four times the value of T_1.

To fit the exponential recovery curve or decay curves the FID must be measured at several different times after the excitation pulse. The most time efficient way to do this is by measuring the FID multiple times within one T_R, using a multi-echo sequence.

2.1.5.1 Spin-echo sequences

A spin-echo sequence is used to correct for the rapid spin dephasing seen in T_2*. A 90 ° pulse is applied, which is followed by rapid dephasing caused by local field inhomogeneities. After a short time interval (τ) a 180° pulse is applied. This reverses the order of the dephasing, so that at the time 2τ the spins will have regained phase. At this point the signal produced is called a spin echo and this occurs at echo time T_E after the initial excitation pulse. The signal decay at this time is due to the spin-spin relaxation, rather than the dephasing due to local field inhomogeneities.

2.1.5.2 Gradient-echo sequences

To produce a gradient-echo two successive, but opposite gradients are applied to the sample. The first gradient causes the nuclei to dephase and the second reverses the direction of dephasing creating a gradient-echo at a time T_E, similar to a spin-echo. The gradient-echo sequence does not compensate for field inhomogeneities and therefore is used to measure T_2*. Gradient-echo sequences can use a variable flip angle of less than 90° and therefore the T_R is reduced.

2.2 Magnetic properties of non-haem brain iron and its effect on MRI

The main forms of non-haem brain iron were introduced in Section 1.3.1. In this section their magnetic properties and influence on MRI are discussed.

2.2.1 Ferritin and haemosiderin

Non-haem iron in the brain is primarily found in the spherical iron storage protein ferritin, in the form of a nanoparticle with a ferrihydrite-like structure (approximate formula $5Fe_2O_3$ $9(H_2O)$) up to 8 nm in diameter.

2.2.1.1 Magnetic properties of ferrihydrite in ferritin

Ferrihydrite has an antiferromagnetic structure. Classically antiferromagnetic materials have zero magnetic moment due to the antiparallel arrangement of the magnetic moments of the atoms in the material (Figure 2.5 a). However, nanoparticles of ferrihydrite (for example in ferritin) have uncompensated iron spins and therefore ferritin iron has a magnetic moment. It also means that fully iron loaded ferritin can act as an ideal monodispersed superparamagnetic system [150].

Superparamagnetic nanoparticles are individual magnetic domains with a magnetic moment that flips rapidly at a speed dependent (in addition to particle size and material) on the temperature [151]. Above the blocking temperature of the material it is superparamagnetic and in the absence of an applied field the net magnetisation of the sample will be zero, due to average direction of the flipping magnetic moment. However, below the blocking temperature the magnetisation of each nanoparticle will be non-zero. The blocking temperature of a superparamagnet depends on the material and size of the nanoparticles as described in Equation 2.6 [152]:

$$T_B = \frac{KV}{k_B} \qquad (2.7)$$

where k_B is the Boltzmann constant; K is the nanoparticle's magnetic anisotropy energy density and V the volume of the nanoparticle.

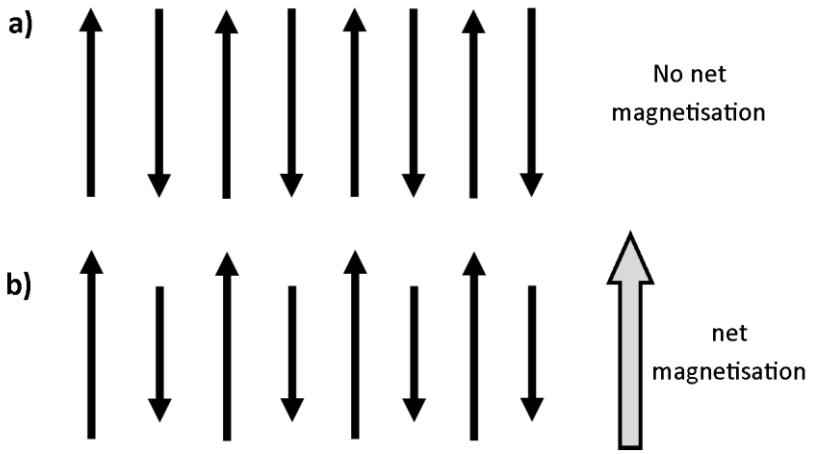

Figure 2.5: The alignment of magnetic moments in antiferromagnetic and ferrimagnetic materials. a) In antiferromagnetic materials the magnetic moments of the atoms or molecules align in an antiparallel formation and the net magnetisation is zero. b) In ferrimagnetic materials the magnetic moments are also antiparallel, but the magnitude of the moments in one direction is greater than those in the other and therefore there is a non-zero net magnetisation.

In the presence of an external magnetic field the magnetic moment of a superparamagnetic material will align with the field and create a net magnetisation. This means that individual ferritins in tissue create local field inhomogeneities in the external MRI field B_0. This effect is increased for clusters of ferritin [153]. The superparamagnetic properties of ferrihydrite in ferritin at body temperature mean that the net magnetisation will immediately disappear once the applied field is removed [152].

Below the blocking temperature, and in the absence of an applied field, the magnetisation of a sample containing ferritin will remain zero as the magnetic moments of individual ferrihydrite nanoparticles point in random directions. However, under an applied magnetic field the magnetic moments will align with the field, as described above. If the temperature is below T_B a remanent magnetisation will remain [83] once the field is switched off. The remanent magnetisation at a constant temperature is called isothermal remanent magnetisation (IRM). An IRM curve is produced by measuring the IRM of a sample after a series of applied fields with increasing magnitude.

As blocking temperature depends on the size of the nanoparticle (Equation 2.7) ferritin in the brain will have a range of blocking temperatures, depending on the iron loading of each ferritin molecule. However, ferritin is typically blocked below around 15 K [154]. Bell *et al.* showed that haemosiderin (isolated from iron-overload human spleens) also displays superparamagnetic properties and likely has a similar chemical form to that of ferritin. However, they also showed that the cores are markedly smaller [150] and therefore the blocking temperature will be lower.

2.2.1.2 The effect of ferritin on MRI relaxation

The superparamagnetic properties of the ferrihydrite-like core of ferritin mean that in the magnetic field of an MRI scanner ferritin creates local field inhomogeneities in the tissue. As hydrogen nuclei of water molecules diffuse through field inhomogeneities, these cause spin dephasing and therefore R_2 shortening [24]. The mechanism of dephasing is called the outer sphere mechanism because it applies to magnetic nanoparticles separated from water: in this case by a protein shell [155].

Ferritin in the human brain has been shown to shorten T_2 relaxation and to a lesser extent T_1 [153] and a linear relationship has been demonstrated between tissue iron concentration and the transverse relaxation rate, R_2, at a number of different field strengths [19, 26, 135]. As R_2* is more sensitive than R_2 to local field inhomogeneities, it is more sensitive to tissue iron concentration. Linear relationships between iron and R_2* [123] and R_2' [134] have also been measured.

At increased MRI fields, the magnetization of the ferrihydrite-like ferritin cores is increased and therefore the effect on R_2 is also increased [155]. This has been shown to be linear with imaging field strength [153, 156]. This property has been harnessed by Bartzokis *et al.* to develop a protocol for evaluating iron concentration from R_2 maps at two different field strengths [124]. It has been suggested that this effect will saturate higher imaging fields due to the saturation of ferritin magnetisation [25].

Vymazal *et al.* measured the relaxation rate of solutions of ferritin with different loading factors at typical clinical MRI field strengths. They found that the linear relationship between R_2 and iron concentration was independent of the loading factor of ferritin [157]. This supports the hypothesis that MRI could be used to measure total ferritin iron and without the need to make assumptions about the loading factor of ferritin.

The time taken for water molecules to diffuse through the local field inhomogeneities associated with ferritin is comparable to the inter-echo time of spin-echo of MRI sequences. In spin-echo sequences (see Section 2.1.5.1) with short τ times, the refocusing pulse occurs before the water molecule has had time to fully diffuse through the field and therefore it does not experience the maximum dephasing. Vymazal *et al.* showed that short τ times, less than about 25 ms, reduced the effect of iron concentration on T_2 [135]. The effect is τ dependent and reduces towards zero as τ increased towards 25 ms.

2.2.2 Magnetite

Magnetite is a ferrimagnetic iron oxide made of alternating lattices of Fe^{2+} and Fe^{3+}. The arrangement of a ferrimagnet is similar to that of an antiferromagnet, with magnetic moments antiparallel. However, the magnetic moment in one direction is greater than the other, resulting in a net magnetisation (Figure 2.5 b).

Magnetite has a magnetisation more than 100 times larger than that of ferrihydrite iron [110]. The same concentration of magnetite in solution has an affect approximately 200 times greater on T_1 and T_2 than the same concentration of ferritin and therefore synthetic magnetic nanoparticles are currently used as MRI contrast agents [158]. However, there is evidence that not all of the 'magnetite-like' iron in tissue has such a great effect on relaxation rates suggesting it does not have the same magnetic moment as true magnetite [159].

Nanoparticles of magnetite with a diameter of more than approximately 13 nm, which have been observed in human brain tissue [83], are magnetically blocked at 50 K. The IRM curve for

magnetite at 50 K typically saturates above an applied field of around 3000 Oe. Note that in a sample containing both ferrihydrite and magnetite, a 5 K IRM measurement will contain a contribution from both minerals, including smaller magnetite particles that have become magnetically blocked between 50 and 5 K. However, the fraction of iron in the form of magnetite will likely be very small and therefore the majority of the signal will be due to ferrihydrite.

2.2.3 Other tissue properties which affect MRI relaxation

In pure water and aqueous solutions the values of T_1 and T_2 are approximately equal, but in tissue T_1 is usually 10 to 20 times greater than T_2. Physically T_2 must always be equal to or less than T_1 [156]. Tissue, including brain tissue, is a complex system and there are a number of factors contributing to the rate of longitudinal recovery and transverse decay.

One of the major factors is the water and fat content of the tissue [148]. More fatty tissue (white matter) has a low inherent energy compared to water and therefore can more readily absorb energy into its lattice allowing rapid spin-lattice relaxation and a short T_1. T_2 is also short in fat as the molecular tumbling rate in fat is similar to the Larmor frequency and the molecules are closely packed together, allowing efficient spin-spin exchange. Water molecules are more spread out and the tumbling rate is faster than the Larmor frequency.

The amount of 'free water' (water not constrained by other molecules) affects the relaxation properties of the tissue. Increased free water causes T_2 lengthening and the effect of this can be seen where there is damage to the tissue with neurodegeneration [125, 160], for example due to demyelination [161].

Paramagnetic metals such as copper, manganese, nickel and iron, cause shortening of T_1 and to a greater extent T_2 and T_2* and have therefore been used as contrast agents in MRI imaging [156, 162]. Iron has by far the highest concentration in tissue, and a large proportion of it is in the form of superparamagnetic nanoparticles, and therefore it contributes the most to MRI

relaxation (as described in Section 2.2.2). The contribution of iron to the speed of relaxation in tissue becomes larger and begins to dominate over other tissue properties, with increased iron concentration or imaging field [26].

In this study fresh frozen, rather than fixed, tissue is used primarily because fixatives have been shown to leach metals from tissues [91]. However, fixing also causes protein cross-linking and therefore affects the mobility of water within the tissue. Kamman *et al.* showed a reduction in T_1 and an increase in T_2, over 24 hours, in rat brain tissue which had been perfused with formaldehyde [163].

The samples in is this study were frozen at -80 °C for several years before measurement, when they were defrosted and imaged just above freezing. Vymazal *et al.* showed that freezing of tissue decreased T_2 by 13-22% [135]. This could be due to cell membrane damage increasing the diffusion of water within the sample. A 6-9% decrease of T_2 with time was also observed over the first 12 hours *post mortem* (in tissue which had not been frozen) and it is proposed that this is due to changes in diffusion effects due to membrane damage.

In most *ex vivo* studies the measurement of human tissue directly *post mortem* is not practical and therefore a compromise must be made between preserving the longevity of the samples and changing their physical properties compared to *in vivo* measurements. In this study frozen samples are used, which were then warmed to just above freezing for measurement. Although T_2 is slower at low temperatures [164], the further degradation of the tissue (in addition to damage from freezing) is reduced.

2.3 Synchrotron X-ray fluorescence

Synchrotrons provide a very high intensity source of light, primarily in the X-ray region of the electromagnetic spectrum. The synchrotron X-rays can be used to produce maps of relative metal distribution through a technique called Synchrotron X-ray Fluorescence (SXRF) mapping.

2.3.1 Synchrotron X-ray radiation

In general synchrotrons are composed of: an electron source; accelerators to bring the electrons to relativistic speeds; a storage ring under vacuum into which the electrons are fed and maintained at relativistic speed; insertion devices and bending magnets which produce light tangentially to the storage ring. Typically light is produced at a number of different positions (beamlines) around the storage ring with the wavelength of light determined by the bending magnets and insertion devices. At each beamline the light can be further focused and tuned to achieve the desired properties for specific experiments.

A diagram of the UK's synchrotron, the Diamond Light Source (DLS), is shown in Figure 2.6. The electrons are produced by an electron gun and accelerated to 100 MeV by the linear accelerator. The booster synchrotron accelerates the electrons to the full beam energy of 3GeV, before they are injected into the storage ring. The 'ring' has 22 straight sections where insertion devices produce synchrotron light at the beamlines.

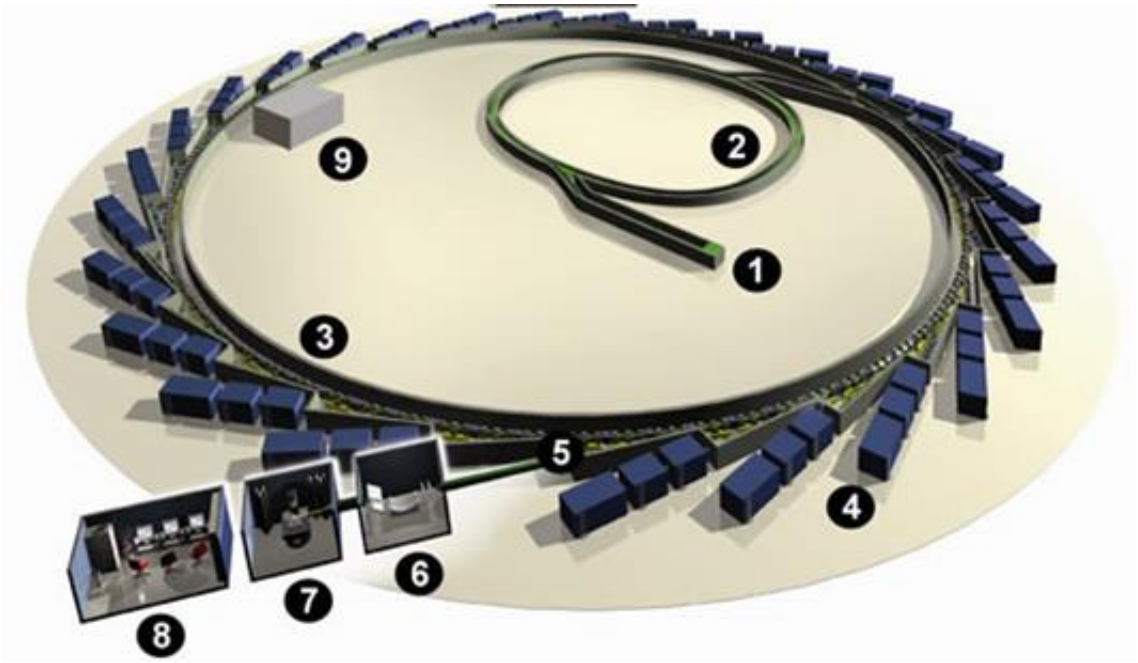

Figure 2.6: The Diamond Light Source synchrotron. The synchrotron is formed of 1: the electron gun and linear accelerator; 2: the booster synchrotron; 3: the storage ring; 9: the radiofrequency cavity and 4: the beamlines. Once a beam of synchrotron light is produced (5) it travels into the optics hutch (6) and then in to experimental hutch (7). The experiment is control from the control cabin (8). This image is reproduced from diamond.ac.uk/Home/Technology/Components.html.

2.3.2 X-ray fluorescence

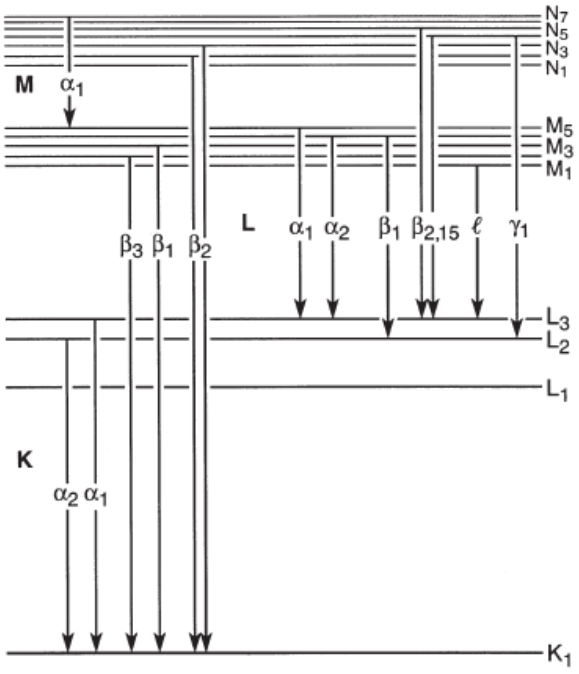

Figure 2.7: The electron transitions that give rise to X-ray fluorescence. The allowed transitions and their nomenclature are shown. Figure reproduced from the X-Ray Data Booklet by Thompson *et al.* [165].

When an X-ray photon is absorbed by an atom a core electron is expelled. The hole left behind is filled by an outer shell electron, which releases an X-ray in the process. The energy of the emitted X-ray is equal to the difference between the two energy levels. Possible energy transitions are well defined and produce narrow fluorescence lines. Fluorescence lines are named first according to which shell the electron falls into (see Figure 2.7): for example, K lines are produced by electrons relaxing into the K shell. Secondly, they are named for the electron shell from which the electron is relaxing: α, β, γ starting with the lowest energy transition. The lines are further split due to the spin-interactions and labelled with the suffix 1, 2, 3 and so on. The ratio between the intensity of different fluorescence lines for a particular element is constant. When a sample is irradiated X-ray fluorescence (XRF) will occur at energies below the incident X-rays and so the incident X-ray energy can be chosen to examine particular elements of interest. As each element has its own characteristic fluorescence spectrum, the combined XRF spectrum of a sample can be used to investigate its composition.

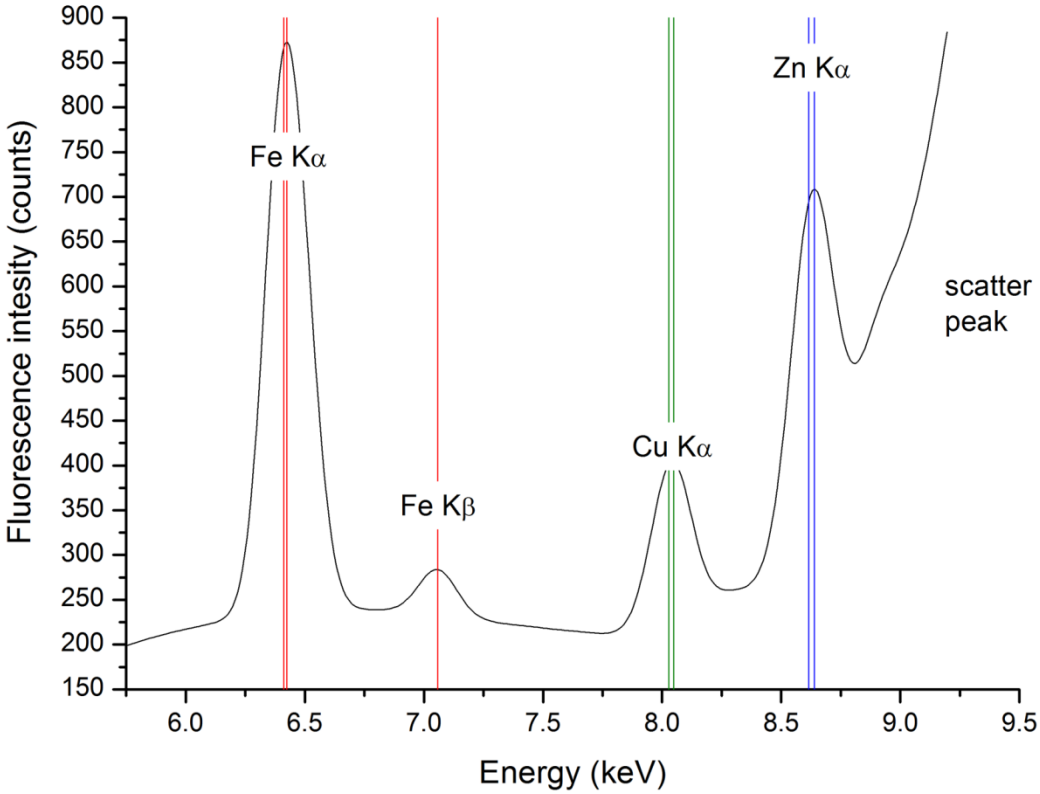

Figure 2.8: A typical biological fluorescence spectrum from a human brain tissue sample. The fluorescence lines Kα1 (6403.8 eV) and Kα2 (6390.8 eV) for iron are shown. These produce the fluorescence peak Kα. As the iron concentration is high, the Kβ peak is also seen. The Kα peaks of copper and zinc, which include the Kα1 and Kα2 fluorescence, are also present. The edge of the large scatter peak for the 10 keV incident beam is included.

For biological samples an incident X-ray beam of 10 keV will cause iron, copper and zinc to fluoresce. Figure 2.8 shows a typical florescence spectrum from an incident beam of 10 keV, averaged over an area of approximately 0.5 mm^2 of a 30 µm thick section of brain tissue. Table 2.1 gives the fluorescence energy for some of the typical metals and potential contaminants which could be found in a tissue section.

The main fluorescence lines of iron are $K\alpha_1$ at 6403.8 eV, with $K\alpha_2$ at 6390.8 eV and these combine to form a broader fluorescence peak as indicated by Fe Kα, as shown in Figure 2.8. Tissue iron content is relatively high and therefore the Kβ peak is also usually observed. Typically concentrations of copper and zinc are high enough for the Kα peaks to be observed; however, the Kβ peaks (at 8.9 and 9.6 keV respectively) tend to be masked by the large 10 keV scatter peak from the incident beam.

Metal	Fluorescence Peak (keV)		
	$K\alpha_1$	$K\alpha_2$	$K\beta_2$
Fe	6.404	6.391	7.058
Cu	8.048	8.028	8.905
Zn	8.639	8.027	9.572
Ni	7.478	7.461	8.264
Cr	5.415	5.406	5.947
Mn	5.899	5.888	6.490

Table 2.1: Energy of fluorescence lines for iron, copper, zinc, nickel, chromium and manganese. These fluorescence lines could all be excited by an incident beam of 10 keV.

The finely tuned, extremely high brilliance X-ray radiation of third generation synchrotrons enables a detection limit of less than 100 ng/g for many elements, and a spatial resolution of up to around 1 μm [117]. XRF carried out using synchrotron radiation is known as Synchrotron X-ray Fluorescence (SXRF).

2.3.3 Creating SXRF metal maps

A map of metal concentration distribution can be produced by collecting a fluorescence spectrum at consecutive points on a sample using a focused X-ray beam. If the flux of the incident beam remains constant then the changing area under an SXRF peak is directly proportional to the changing concentration of the metal to which the peak belongs. Therefore, the relative iron concentration of a section of brain tissue can be mapped by calculating the area under Kα peak at each point on the map.

The beamline I18, at the Diamond Light Source, can be tuned to a specific, stable energy of between 2 and 20 keV. When the X-ray beam is tuned to 10 keV the flux at the sample is very high: 4×10^{12} photons per second (ph/s). This very high flux allows iron, copper and zinc to be

mapped with high sensitivity. Iron concentrations of parts per billion can be measured with a collection time of around 1 s. The fact that the beam can also be focussed to just a few microns means that high spatial resolution mapping can also be achieved. The flux of the X-ray beam is not completely constant due to beam top-up, but this can be corrected for by normalisation to I_0, as described in Section 4.4, along with the full methodology used for SXRF mapping in this project.

Chapter 3:
Samples

The literature review in Chapter 1 showed that increased iron concentration and corresponding changes to MRI relaxation parameters have been measured in a number of different brain regions in Alzheimer's Disease (AD). However, for most regions there is also at least one conflicting study which reported no statistically significant change. It was hypothesised that a combining data from multiple regions may provide a way of differentiating between AD and control cases.

Six different regions of the brain were chosen for investigation, based on the literature review. Tissue from all six regions was obtained from a set of three healthy controls and three AD cases. In order to begin to compare AD to other neurodegenerative diseases, some of the measurements were also carried out on three Parkinson's Disease (PD) and three Multiple System Atrophy (MSA) cases for a subset of regions.

The iron and MRI properties of the samples were investigated using a unique set of complementary techniques which are detailed in Chapter 4. This chapter deals with the selection and preparation of the samples. In Section 3.1 the protocols used to minimise the possibility of metal contamination whilst handling tissue are described. The rationale behind the selection of the six brain regions and how each sample was dissected is given in Section 3.2 and in Section 3.3 the tissue preparation for each measurement technique is detailed.

Figure 3.1 gives an overview of the experimental model used. Two adjacent samples of tissue, of approximately 1 cm^3, are taken from a brain region. Sample A is taken for high resolution MRI mapping, followed by sectioning and histological staining to show cell distribution and look for amyloid plaques. A sub-selection of these samples had sections taken for high resolution Synchrotron X-ray Fluorescence (SXRF) mapping of the iron distribution. Part B was

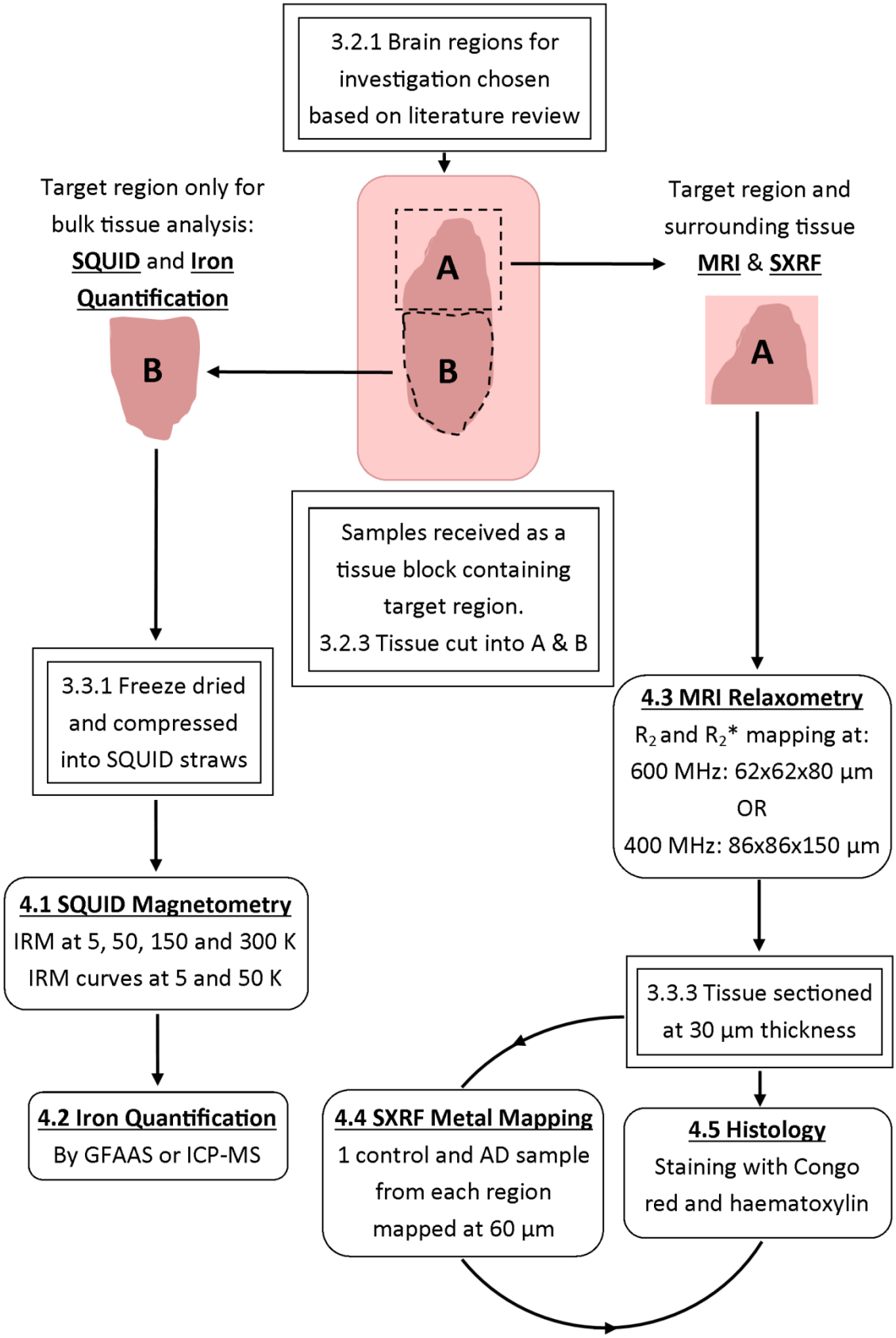

Figure 3.1: Experimental path for tissue samples. Tissue sample A is mapped with high field MRI and then it is sectioned and stained. For a sub-set of cases a section is taken for SXRF (Synchrotron X-ray Fluorescence) mapping before it is subsequently stained. Tissue sample B is freeze dried for SQUID (Superconducting Quantum Interference Device) magnetometry and then the total iron content is measured by GFAAS (Graphite Furnace Atomic Absorption Spectrometry) or ICP-MS (Inductively Coupled Plasma Mass Spectrometry). Numbers represent the sections of the chapter in which the techniques are described in detail.

Region	Case ID	SQUID	Iron Quantification		MRI		SXRF
			ICP-MS	GFAAS	600 MHz	400 MHz	
Pons	C1	✓	X	✓	✓	X	X
Pons	C2	✓	X	✓	✓	X	✓
Pons	C3	✓	X	✓	✓	X	X
Pons	AD1	✓	X	✓	✓	X	X
Pons	AD2	✓	X	✓	✓	X	✓
Pons	AD3	✓	X	✓	✓	X	X
Pons	PD1	✓	X	✓	✓	X	✓
Pons	PD2	✓	X	✓	✓	X	X
Pons	PD3	✓	X	✓	X	X	X
Pons	PD4	X	X	X	✓	X	X
Pons	MSA1	✓	X	✓	✓	X	✓
Pons	MSA2	✓	X	✓	✓	X	X
Pons	MSA3	✓	X	✓	X	X	X
Amyg	C1	X	X	X	✓	X	X
Amyg	C2	X	X	X	✓	X	X
Amyg	C3	X	X	X	✓	X	✓
Amyg	AD1	X	X	X	✓	X	X
Amyg	AD2	X	X	X	✓	X	✓
Amyg	AD3	X	X	X	✓	X	X
CN	C1	✓	✓	X	✓	X	X
CN	C2	✓	✓	X	✓	X	✓
CN	C3	✓	✓	X	✓	X	X
CN	AD1	✓	✓	X	✓	X	✓
CN	AD2	✓	✓	X	✓	X	X
CN	AD3	✓	✓	X	✓	X	X
GP	C1	✓	X	X	✓	X	X
GP	C2	✓	X	X	✓	X	✓
GP	C3	✓	X	X	✓	X	X
GP	AD1	✓	X	X	✓	X	X
GP	AD2	✓	X	X	✓	X	X
GP	AD3	✓	X	X	✓	X	✓
Pu	C1	✓	✓	X	✓	X	X
Pu	C2	✓	✓	X	✓	X	X
Pu	C3	✓	✓	X	✓	X	✓
Pu	AD1	✓	✓	X	✓	X	X
Pu	AD2	✓	✓	X	✓	X	X
Pu	AD3	✓	✓	X	✓	X	✓
Pu	PD1	✓	✓	X	X	X	X
Pu	PD2	✓	✓	X	X	X	X
Pu	PD4	✓	✓	X	X	X	X
Pu	MSA1	✓	✓	X	X	X	X
Pu	MSA2	✓	✓	X	X	X	X
Pu	MSA3	✓	✓	X	X	X	X
SN	C1	✓	X	✓	✓	X	X
SN	C2	✓	X	✓	✓	X	✓
SN	C3	✓	X	✓	X	X	X
SN	AD1	✓	X	✓	✓	X	X
SN	AD2	✓	X	✓	✓	X	✓
SN	AD3	✓	X	✓	X	X	X
SN	PD1	✓	X	✓	✓	X	X
SN	PD2	✓	X	✓	X	X	X
SN	PD4	✓	X	✓	✓	X	X
SN	MSA1	✓	X	✓	X	X	X
SN	MSA2	✓	X	✓	X	X	X
SN	MSA3	✓	✓	X	X	X	X

Table 3.1: A summary of the measurements that were made on each case. The case ID represents the specific control (C), Alzheimer's Disease (AD), Parkinson's Disease (PD) or Multiple System Atrophy (MSA) case, the full details for which are given in Table. 3.4. Samples were taken from the pons, amygdala (Amyg), caudate nucleus (CN), globus pallidus (GP), putamen (Pu) and substantia nigra (SN). Depending on tissue and instrument availability, the following measurement techniques were used: SQUID (Superconducting Quantum Interference Device) magnetometry, iron quantification by GFAAS (Graphite Furnace Atomic Absorption Spectrometry) or ICP-MS (Inductively Coupled Plasma Mass Spectrometry), MRI relaxometry at 400 MHz (9.4 T) or 600 MHz (14.1) and SXRF (Synchrotron X-ray Fluorescence) metal mapping.

taken for bulk tissue analysis: SQUID (Superconducting QUantum Interference Device) magnetometry followed by iron quantification by GFAAS (Graphite Furnace Atomic Absorption Spectrometry) or ICP-MS (Inductively Coupled Plasma Mass Spectrometry).

Not every technique was applied to each case from every brain region due to limited tissue in some regions and limited access to experimental facilities (in particular for SXRF mapping at the Diamond Light Source). Table 3.1 provides a record of the measurements made on each sample, with the reason for making each measurement on each sample explained in greater detail throughout the following chapters.

3.1 Preventing iron contamination

The study of iron, both directly through iron quantification and SXRF mapping and indirectly through SQUID magnetometry and MRI, is the main focus of this project. Therefore minimising contamination of the samples with iron is paramount. This was achieved through careful acid washing of tools and by cutting samples using non-metal blades.

3.1.1 Acid washing

The protocol for washing plastic and other acid resistant tools is: 30 minutes in a 3% HCl solution; 10 mins in ultra-pure, 18 MΩ water and a final wash in 18 MΩ water. Tools were then left to air dry in the biohazard hood which provides a relatively dust-free environment. Plastic tools were acid washed between every sample, with a few of sets of tweezers washed and ready to prepare a number of samples in a row.

Materials that were susceptible to damage or etching from exposure to acid (for example the sapphire sectioning blade and quartz slides) were washed for 10 minutes in a solution of 0.1% HCl in ethanol. They were then rinsed with at least two changes of ultra-pure water. After every sample preparation blades were wiped down with dust free Whatman lens cleaning tissue and analytical grade ethanol to remove any tissue fragments and after every third

sample they were again acid washed. Washing was not carried out between every sample so as to minimise degradation of tools.

3.1.2 A clean lab environment

To reduce the potential for metal contamination, tissue handling environments were kept as free from metal particulates as possible. This meant avoiding the use of even weak acids around metal surfaces and checking the fume hood, biohazard cabinet and the cryomicrotome for any signs of corrosion.

Tools and slides were left to air dry in the biohazard cabinet as the air flow is designed to minimise transfer of particulates in and out of the cabinet. Therefore, in addition to providing a safe environment for working with the human tissue samples, it reduced the chance of contamination compared to fume hood or lab bench.

3.2 Brain region selection and sample excision

3.2.1 Brain region selection

The brain regions studied in this project were chosen based on the literature review of iron in the AD brain that is given in full in Chapter 1. The main criterion for selection was whether increased iron with AD had been observed in published studies. However, other factors were considered including whether iron changes have been observed in the region in other neurodegenerative diseases.

The six regions chosen for investigation include four of the five nuclei of the basal ganglia [166], shown in Figure 3.2. From the basal ganglia the caudate nucleus (CN), putamen (Pu), globus pallidus (GP) and substantia nigra (SN) were included in the study, but the subthalamic nucleus was not. These regions all work closely together and are involved in motor control, learning and emotion. The other two regions chosen were the amygdala (Amyg) and pons.

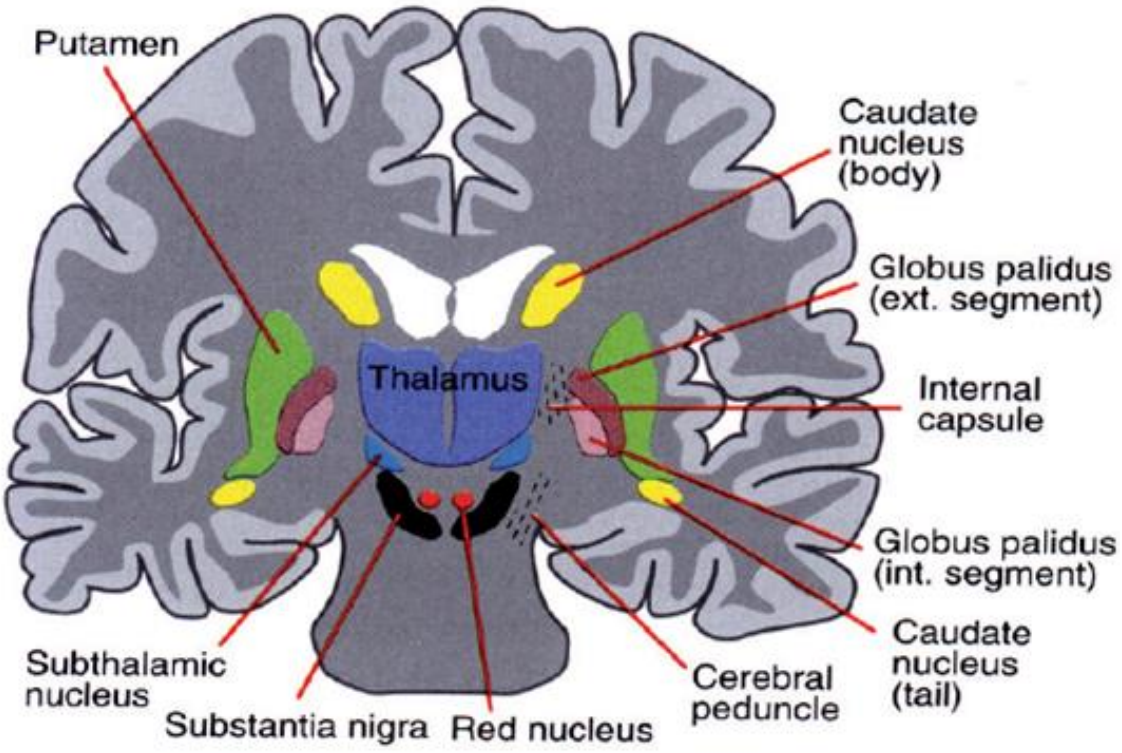

Figure 3.2: A coronal view of the basal ganglia. The nuclei of the basal ganglia are the caudate nucleus, putamen, globus pallidus, substantia nigra and subthalmic nucleus. This figure is reproduced from *Basal Ganglia—An Integrative View,* edited by Barrios and Bauer [166].

The rationale behind choosing each of these regions is outlined below along with a brief introduction to the anatomy, function and AD pathology in each region. Appendix A contains a more expansive anatomical reference for the regions, with the main anatomical reference material used being Atlas of the Human Brain by J.K. Mai, G, Paxinos and T. Voss [167] and the accompanying website (thehumanbrain.info) from which the images are reproduced.

The tables below provide iron concentration information for each of the regions gathered from a number of sources. Table 3.2 shows iron concentration values for the regions to be studied as taken from a literature review by Haacke *et al.* [107]. Only the data from whole tissue samples (rather than supernatant) is reproduced here, with the number of samples in the study and quantification method given in brackets. The table shows the fairly large range of reported values for each region, with sub regions of the substantia nigra and globus pallidus also included. No data for iron concentration in the pons was included by Haacke *et al.* or could be found in a separate literature search.

Region	Reported Iron Concentrations µg/g fresh tissue (no of samples, technique)
Amygdala	49.0 (21, INAA); 48.6 (11, INAA); 48.9 (15, INAA);
Caudate Nucleus	79 (58, Col); 115.6 (4, INAA); 92.5 (10, AAS); 117.4 (59, ICP); 99.6 (6, AAS);
Globus Pallidus - GP lateral - GP medial - GP total	213 (55, Col); 175.3 (10, AAS); 182.0 (6, AAS) 159.4 (24, ICP); 207.0 (6, AAS) 141.2 (23, ICP); 163.8 (6, AAS) 300.6 (23, ICP); 370.8 (6, AAS)
Pons	Not available
Putamen	130.0 (56, Col); 120.8 (10, AAS); 110 (6, AAS); 163.8 (31, ICP); 119.8 (6, AAS)
Substantia Nigra - Substantia Nigra ZC	185.0 (52, Col); 139.9 (6, AAS) 159.4 (59, ICP)

Table 3.2: Iron concentration in brain regions of healthy adults. A large range of iron concentrations have been reported in each region and a large number of different measurement techniques used. Data reproduced from the review table in Haacke *et al.* [107]. INAA = instrumental neutron activation analysis; Col=colorimetry; ICP = inductively couple plasma spectrometry; AAS = atomic absorption spectrometry. Substantia nigra ZC = zona compacta.

Table 3.3 shows the iron concentration, as reported in the literature, for AD and control tissue from the six brain regions studied. It reveals a similar spread of values as for those shown in Table 3.2. These data were collected during the literature review in Section 1.3 and the table includes data from all papers which published numerical values, or for which values could be interpreted from graphs. The number of samples, method of iron quantification and reference to paper are given in brackets. Statistical significance between disease and control is indicated where it was reported. Only studies in which the iron concentration is directly measured are included and not those which made calculations from MRI data. (For a summary of the full result of the literature review refer to Figure 1.3). Likewise, data are only included from fresh not fixed tissue due to the potential iron leaching caused by fixatives. Data are quoted in micrograms of iron per gram (µg/g) of fresh tissue (wet mass) where possible, but in some publications iron is given per gram of freeze dried tissue (dry mass).

Region	Wet or dry mass (wm/dm)	Iron Concentration: Control µg/g (no of samples, technique, ref)	Iron Concentration: AD µg/g (no of samples, technique, ref)
Amygdala	wm	48.3 ± 3.0 (14, RAC, [20]) 49 ± 4 (21, INAA, [17]) 50.8 ± 3.7 (56, INAA, [16]) 34 (2, ICP-AES, [19])	60.6 ± 4.9 (15, INAA, [20])* 64 ± 3 (58, INAA, [17])** 70.8 ± 4 (98, INAA, [16])* 40 (2, ICP-AES, [19])
	dm	243 ± 11 (11, INAA, [39])	322 ± 29 (10, INAA, [39])
Caudate Nucleus	wm	100 (2, ICP-AES, [19]) 93.1 (1, GFAAS, [26])	137 (2, ICP-AES, [19]) 95.1 ± 21.1 (5, GFAAS, [26])
Globus Pallidus	wm	250 (2, ICP-AES, [19]) 132.7 (1, GFAAS, [26])	252 (2, ICP-AES, [19]) 160.0 ± 49.4 (8, GFAAS, [26])
Pons	wm	Not available	Not available
Putamen	wm	102 (2, ICP-AES, [19]) 85.8 ± 24.0 (2, GFAAS, [26])	131 (2, ICP-AES, [19]) 157.5 ± 48.6 (8, GFAAS, [26])
Substantia Nigra	wm	145.6 (1, GFAAS, [26])	136.1 ± 36.8 (2, GFAAS, [26])

Table 3.3: Iron concentration in control and AD tissue. The iron concentration in the 6 brain regions chosen for investigation from studies of AD and healthy aged matched control tissue. Only studies using fresh not fixed tissue are included. The number of samples, quantification method; reference to the study and level of statistical significance reported is included is given in curved brackets after the iron concentration. ICP-AES = ion coupled plasma atomic emission spectroscopy; INAA = instrumental neutron activation analysis; GFAAS = graphite furnace atomic absorption spectroscopy. Where statistically significant differences were observed this is indicated as: * $p < 0.05$; ** $p < 0.01$.

3.2.1.1 Caudate Nucleus

Together with the putamen the caudate nucleus makes up the striatum and these are the input nuclei of the basal ganglia [168]. The caudate nucleus is C shaped and is made up of a head, body and tail. Figure 3.3 shows a coronal section of the brain which includes the head portion of the caudate nucleus. The white matter separating the caudate nucleus from the putamen is the anterior portion of the internal capsule (AIC). The caudate nucleus is involved in emotion, language comprehension, memory and learning. The head of the CN has been specifically linked to processing feedback and the body and tail linked to successful learning [169].

Hallgren and Sourander [93] found an iron concentration of 93 ± 21 µg/g of tissue in the CN and described the relationship between iron concentration and age as:

$$y = 9.66(1 - e^{-0.05x}) + 0.33 \qquad (3.1)$$

Where y = iron concentration in mg/100g of tissue and x = age in years.

This region was chosen for investigation because several studies have inferred an increase in iron in AD based on MRI experiments [126, 127, 133, 139]. This suggests that iron in this region could be of use as an indicator of AD. House *et al.* [19] measured a direct increase in iron in AD CN compared to control and a corresponding increase in R_2. However, with a sample size of 2 no statistical significance was reached.

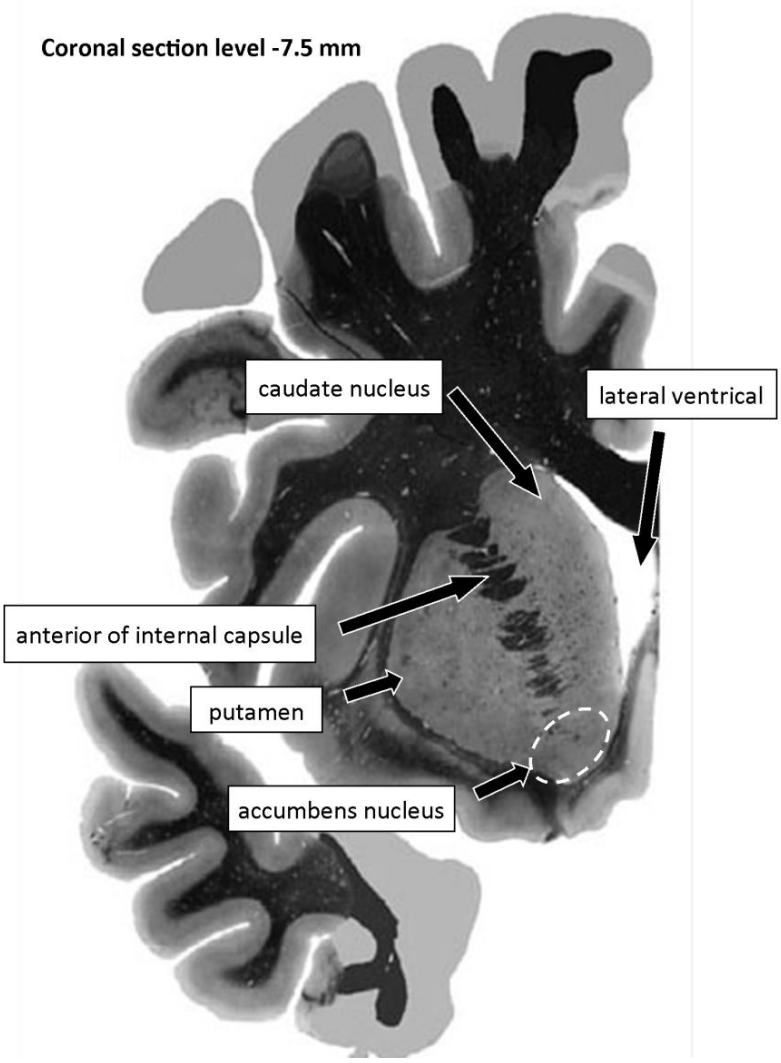

Figure 3.3: A coronal section of the brain showing the caudate nucleus and putamen of the basal ganglia. This image is at level coronal section level -7.5 mm and reproduced from thehumanbrain.info [167].

3.2.1.2 Putamen

The putamen is another structure of the basal ganglia. It is rostrally continuous with the head of the caudate nucleus. Figure 3.3 shows a coronal section of the putamen at a level at which it is separated from the head of the caudate nucleus by the anterior part of the internal capsule. Figure 3.4 is a more posterior section, which shows the putamen neighbouring the globus pallidus. The putamen is interconnected with the other structures of the basal ganglia and like them is involved in movement and learning. Like the body of the CN the putamen is associated with successful learning [169].

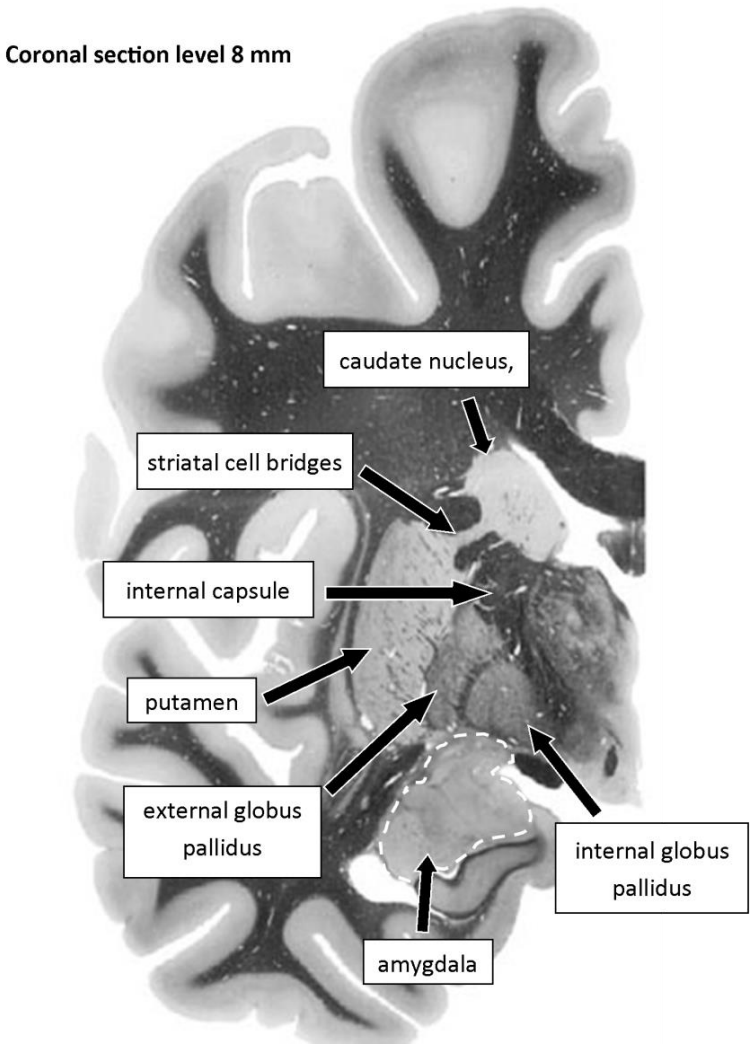

Figure 3.4: Coronal section of the brain showing the caudate nucleus, putamen, globus pallidus and amygdala. This image is at coronal section level 8 mm and is reproduced from thehumanbrain.info [167].

The putamen (Pu) is another iron rich region of the brain with an iron concentration of 130-200 μg/g [93, 102]. Hallgren and Sourander's [93] empirical equation for iron concentration (y, in mg/100g) with age (x, in years) is:

$$y = 14.62(1 - e^{-0.04x}) + 0.46 \qquad (3.2)$$

In the putamen the concentration of iron has been shown, through MRI measurement techniques [126, 127, 139], to increase with AD and so it was selected for inclusion in this study. As with the CN, House *et al.* [19] showed an increase in iron with AD through ICP-AES measurements, but this did not reach statistical significance.

3.2.1.3 Globus Pallidus

The globus pallidus is found medial to the putamen as shown in Figure 3.4. It is divided into two parts: the globus pallidus external and internal (GPe and GPi respectively), which are separated by a thin lamina of white matter [170]. The GP works in conjunction with the rest of the basal ganglia and is involved in regulating voluntary movement.

The globus pallidus (GP) is the region of the brain where the highest concentration of iron can be expected. Hallgren and Sourander [93] measured an average value of 213 ± 34.9 μg/g in a healthy adult and show a variation of iron concentration (y, in mg/100g) with age (x, in years) of:

$$y = 21.41(1 - e^{-0.09x}) + 0.37 \qquad (3.2.1.3)$$

Although there is a study showing reduced iron in the medial section of the GP [106] with AD and another showing no change [19], direct iron measurements published by Loeffler *et al.* showed a statistically significant increase in iron for both AD and PD compared to control [18]. There is evidence for increased iron with AD in a number of MRI studies of the globus pallidus [125, 126, 133, 139] and therefore it is included in this study.

The literature shows evidence of both increased and decreased iron in the globus pallidus with AD, possibly depending on whether the GPe or GPi is measured. Therefore this could be an interesting area to study with high resolution MRI mapping and SXRF metal maps as the sub-regions of the GP can be examined in detail.

3.2.1.4 Substantia nigra

The substantia nigra is also part of the basal ganglia. It is situated in the midbrain, towards the top of the brain stem, inferior to the rest of the basal ganglia. An axial view of the substantia nigra is shown in Figure 3.5. The SN can be divided into the pars compacta (SNc) and pars reticulata (SNr) [171]. A striking feature of the SNc is the strongly pigmented dopaminergic neurons [172], which cause the dark band in the tissue and can be seen under a microscope without additional staining. On the other hand, the neurons of the SNr are smaller and more dispersed. The SNr and the internal globus pallidus have a similar structure and function and can be considered part of the same structure separated by the internal capsule. Together they form the major output of the basal ganglia [168].

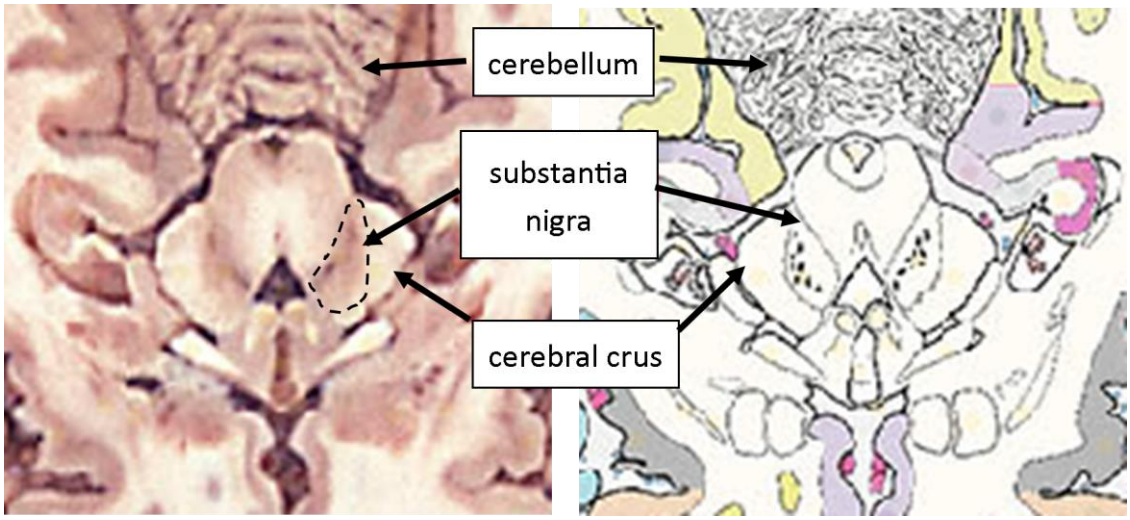

Figure 3.5: An axial view of the substantia nigra and surrounding structures. Note: the cerebral crus is sometimes known as the cerebral peduncle. This figure is adapted from the horizontal *in situ* atlas from thehumanbrain.info [167].

The SN is important in movement and emotion. It is not generally affected by AD pathology, but experiences huge neuronal loss in PD, which leads to the characteristic resting tremor [171].

This region was included in the study despite the fact that no literature was found describing increased iron in this region in AD. Studies either showed no change by bulk iron [106] or MRI [139] measurements or showed a decrease [18] in iron in AD compared to control. However, iron in the substantia nigra (SN) has been shown to increase in Parkinson's disease (PD) [147] and Brar *et al.* showed that patients with AD who also had Parkinsonism had a statistically significantly higher iron concentration than those who had only AD [144]. The SN could therefore be an interesting region for comparing AD and PD and may be a useful area to target in differentiating between the diseases.

3.2.1.5 Amygdala

The amygdala is part of the limbic system and is made from a collection of nuclei found within the medial temporal lobe (Figure 3.4). The amygdala is involved in fear, anger and emotional memory [173].

The amygdala is significantly and consistently affected by AD pathology causing neuropsychiatric symptoms which begin to present early in the disease [174]. Senile plaques are formed and the pyramidal neurons are susceptible to neurofibrillary tangle formation [175] leading to cell death and atrophy [15, 34].

Direct measurements of iron in the amygdala have shown an increase of iron in AD compared to control with statistical significance of $p<0.05$ [16, 17, 20] or $p<0.10$ [39]. Additionally iron was shown to be increased in the neurophil of the amygdala in AD compared to control [114]. However, no studies were found that looked at the effects of iron on MRI of the amygdala in AD and so it was included in this study.

3.2.1.6 Pons

The pons is a fibrous structure in the brain stem. An axial view of the pons is given in Figure 3.6. It is important in motor function, and lesions in the pons are associated with a variety of motor syndromes [176].

The literature review did not reveal any studies of iron in the pons in AD. However, iron was measured in a singular AD pons sample during a collaborative study with Dr Naomi Visanji and Dr Lili-Naz Hazrati (from the University of Toronto). The focus of the collaboration was to investigate iron dysregulation in the pons in MSA and PD [28]. The singular AD sample showed increased iron compared to control and PD tissue and therefore two additional AD samples were requested from this region. A benefit of studying this region was that tissue and data from MSA, PD and control data were already available for comparison to the AD samples.

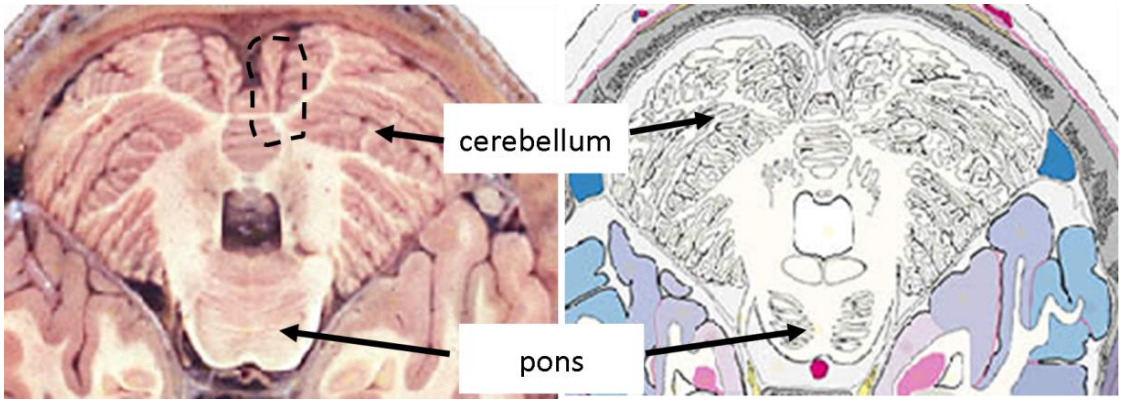

Figure 3.6: An axial view of the pons. This figure is adapted from the horizontal *in situ* atlas from thehumanbrain.info [167].

3.2.2 Sample details

Tissue samples were requested from the Canadian Brain Tissue Bank, which provided three disease and control samples from each of the regions that were requested. The work in this project was done under multi regional ethics committee (MREC) approval for the project 'Metal-ion accumulation in neurodegenerative disease' (REC ref: 07/MRE08/12) held by Dr Joanna Collingwood at University of Warwick, current until 2015.

For the putamen, substantia nigra and pons three PD and MSA cases were also provided as these regions and diseases were being investigated as part of a collaborative study recently published in the Journal of Parkinson's Disease: *Iron Deficiency in Parkinsonism: Region-Specific Iron Dysregulation in Parkinson's Disease and Multiple System Atrophy* by Visanji *et al.* (2013) [28]. Note that for PD a total of 4 cases were used, as the pons from one case was missing and therefore a different brain was used.

Each region was dissected, including some surrounding tissue, by the group in Toronto and the resulting tissue blocks shipped to the University of Warwick in dry ice. Dr Naomi Visanji (PhD) and neuropathologist Dr Lili-Naz Hazrati (MD, PhD) at the University of Toronto provided support in identifying the anatomy, structures and regions of interest in the tissue throughout the project.

Fresh frozen, rather than fixed, tissue was used as fixing has been shown to leach metals from tissue [91], potentially changing the concentration and distribution of metal within the sample. Once received at the University of Warwick, all tissues used in the study were stored at -80 °C.

The samples were received with assigned case numbers. To ensure anonymity and for ease of data presentation the samples were renamed with a number from 1 to 3 (and 4 for PD cases) and the letters C, AD, PD or MSA to indicate their disease state.

Table 3.4 gives the details of the tissue received for each case, including the age, sex and pathology information. For the AD cases the Braak stage of the disease pathology is given as either V or VI which describes the pathology of fully developed AD [177]. All Parkinson's Disease cases present as akinetic-rigid and all multiple system atrophy (MSA) cases as MSA-P.

Table 3.4 shows that the control and AD samples are not perfectly age-matched: the mean ages are 67 and 82 respectively. The potential consequence of this can be estimated using the empirical equations for iron concentration with age that were produced by Hallgren and Sourander [93] and were given above: Equation 3.1 for the CN, 3.2 for the putamen and 3.3 for

the globus pallidus.

Case Number	Brain regions	Sex	Age	Pathology information
C1	Amyg, CN, GP, Pu, Pons, SN	F	47	Pulmonary embolism
C2	Amyg, CN, GP, Pu, Pons, SN	M	78	Lung cancer
C3	Amyg, CN, GP, Pu, Pons, SN	M	76	Cardiac infarction
AD1	Amyg, CN, GP, Pu, Pons, SN	M	73	Braak vi
AD2	Amyg, CN, GP, Pu, Pons, SN	F	75	Braak vi
AD3	Amyg, CN, GP, Pu, Pons, SN	F	98	Braak v
PD1	Pu, Pons, SN	M	73	Akinetic-rigid
PD2	Pu, Pons, SN	M	56	Akinetic-rigid
PD3	Pons	F	79	Akinetic-rigid
PD4	Pu, Pons, SN	M	76	Akinetic-rigid
MSA1	Pu, Pons, SN	M	76	MSA-P
MSA2	Pu, Pons, SN	M	66	MSA-P
MSA3	Pu, Pons, SN	F	46	MSA-P

Table 3.4: Case details for the samples used in this project. The regions studied from each case are given, where: Amyg = amygdala; CN = caudate nucleus; Pu = putamen; GP = globus pallidus; SN = substantia nigra. The sex and age of each individual at death is given. For the control cases the cause of death is stated. For the Alzheimer's Disease (AD) cases the Braak stage of the disease pathology is given. All Parkinson's Disease cases present as akinetic-rigid and all multiple system atrophy (MSA) cases as MSA-P.

Region	Predicted control concentration (μg/g)	Predicted AD concentration(μg/g)	Percentage increase for iron in AD samples due to age
Caudate Nucleus	96.5	98.3	1.9%
Putamen	140.8	145.3	3.2%
Globus Pallidus	217.3	217.7	0.2%

Table 3.5: Predicted iron concentration for the control and AD sample set. The mean age of the three control and AD cases was used to predict the mean iron concentration in caudate nucleus, putamen and globus pallidus. As the AD cases had a greater mean age they are predicted to have slightly higher iron concentrations. The largest predicted change of 3.2% is in the putamen.

Table 3.5 gives the mean predicted iron concentration for the control and AD samples and the difference between them due to the difference in mean age of the sample set. The largest predicted difference is for the putamen, which shows a predicted 3.2% increase in the AD

sample set. No empirical equations were available for the pons, substantia nigra or amygdala.

3.2.3 Sample excision

The blocks of tissue received from the University of Toronto were much larger than the imaging space in either of the high resolution imaging probes. Additionally the blocks contained tissue from surrounding structures that were not intended for inclusion in bulk tissue analysis. Therefore, smaller samples appropriate to the different measurement techniques were cut from the original blocks.

Before cutting, tissue was placed overnight in a -25 °C freezer. It was then allowed to warm to just below freezing so that it was just soft enough to cut without fracturing the block. To prevent uncontrolled defrosting and to keep the tissue just frozen, cutting was carried out in the cool environment of either a cryostat or biohazard hood cooled with dry ice. Tissue was cut with a ceramic blade and stored in clean cryotubs or weigh boats sealed in double layered zip-lock bags to prevent the tissue drying.

For the pons, SN, Pu and CN two adjacent tissue samples were cut: one for MRI and one for SQUID magnetometry and iron quantification as shown in Figure 3.1. This was not done for the GP as there was not enough tissue available and MRI was prioritised. For the amygdala, region identification was particularly tricky and confidence about anatomical identification was not great enough to cut a second block for SQUID magnetometry.

For the samples to be imaged with the 400 MHz probe, which has the larger internal diameter, some surrounding tissue was purposefully included in the tissue block taken for MRI. This context can help to identify the structure in the resulting data. It also provides information about the contrast between the structure and its surroundings, which may be relevant when comparing cases and could be useful in considering how the MRI data collected in the lab would compare to clinical MRI imaging of living subjects.

Each case was shipped with accompanying photos identifying the brain region within the block. Tissue was further photographed and a cutting plan made and sent to Dr Lili-Naz Hazrati for confirmation that each region had been identified correctly and that the samples cut from each region would produce a comparable set. After confirmation was received tissue was cut as described below.

Accompanying the description of the cutting protocols for each brain region is a Figure showing the cutting of an example case. A photographical record of the cutting of each sample can be found in Appendix B. In each case part A is taken for MRI and part B for bulk tissue analysis.

For the same brain regions from different cases, care was taken to cut from approximately the same part of each region so as to provide a good match between control and AD and more comparable imaging and iron concentration data.

Photos show how the surface of each MRI block is scored with the ceramic blade before cutting, in order to help keep track of tissue orientation throughout preparation and imaging. Tissues were cut to either fit the 8 mm diameter NMR tubes for imaging at 600 MHz or the 20 mm tubes for imaging at 400 MHz. Samples had to be small enough to be slipped easily in and out of the tubes, but large enough to best utilise the imaging volume. The thickness of the original tissue blocks was around 1 to 2 cm and the full thickness of each sample was retained for imaging.

3.2.3.1 Caudate nucleus and putamen

For each case the caudate nucleus and putamen samples were cut from the same block of tissue. Using the coronal sections in *The Atlas of the Human Brain* [167] and the associated website (thehumanbrain.info) as a reference, each sample's position in the brain was identified as being between -7.5 and -15 mm. See Appendix A for a more extensive reference.

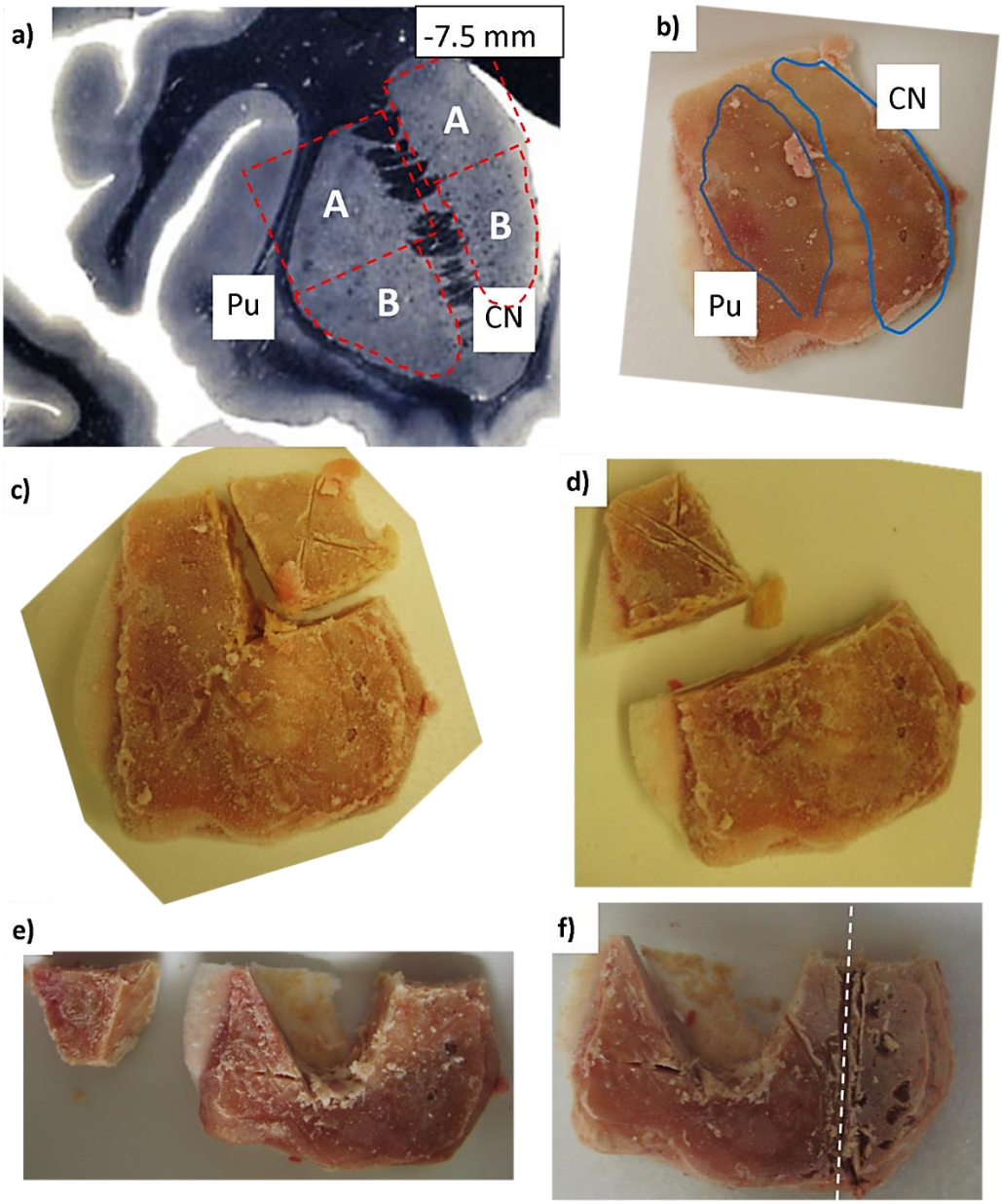

Figure 3.7: Preparation of putamen and caudate nucleus sample C1 for MRI and bulk tissue analysis. a) The approximate level of the tissue (image adapted from thehumanbrain.info), with the planned cutting of tissue for MRI (A) and bulk tissue analysis (B) outlined. b) Tissue from case C1 with the caudate nucleus and putamen outlined. First the caudate nucleus MRI sample is cut c) and then the putamen sample d). Then the putamen bulk tissue sample e) is cut, followed by the caudate nucleus sample which is shown on the right hand side of the dashed line in f).

Figure 3.7 shows how the CN and Pu tissue was cut from the main block of sample C1. MRI tissue (A) was cut to fit inside the 20 mm diameter NMR tubes of the 400 MHz probe. Tissue from the surrounding structures was included in these samples. Samples that were for bulk tissue analysis (B) were carefully cut to keep within the specific brain region. In some cases the white matter surrounding the grey matter was trimmed off after the initial cuts. For example,

tissue often needed to be removed at the back of the sample where the region of interest did not run through the full depth of the block.

Bulk tissue MSA and PD putamen samples were cut following the same principle. However, no tissue was cut for MRI as there was not sufficient time to image these samples and priority was given to the control and AD tissue. Appendix B-1 shows the cutting of all CN and Pu samples.

3.2.3.2 Globus pallidus

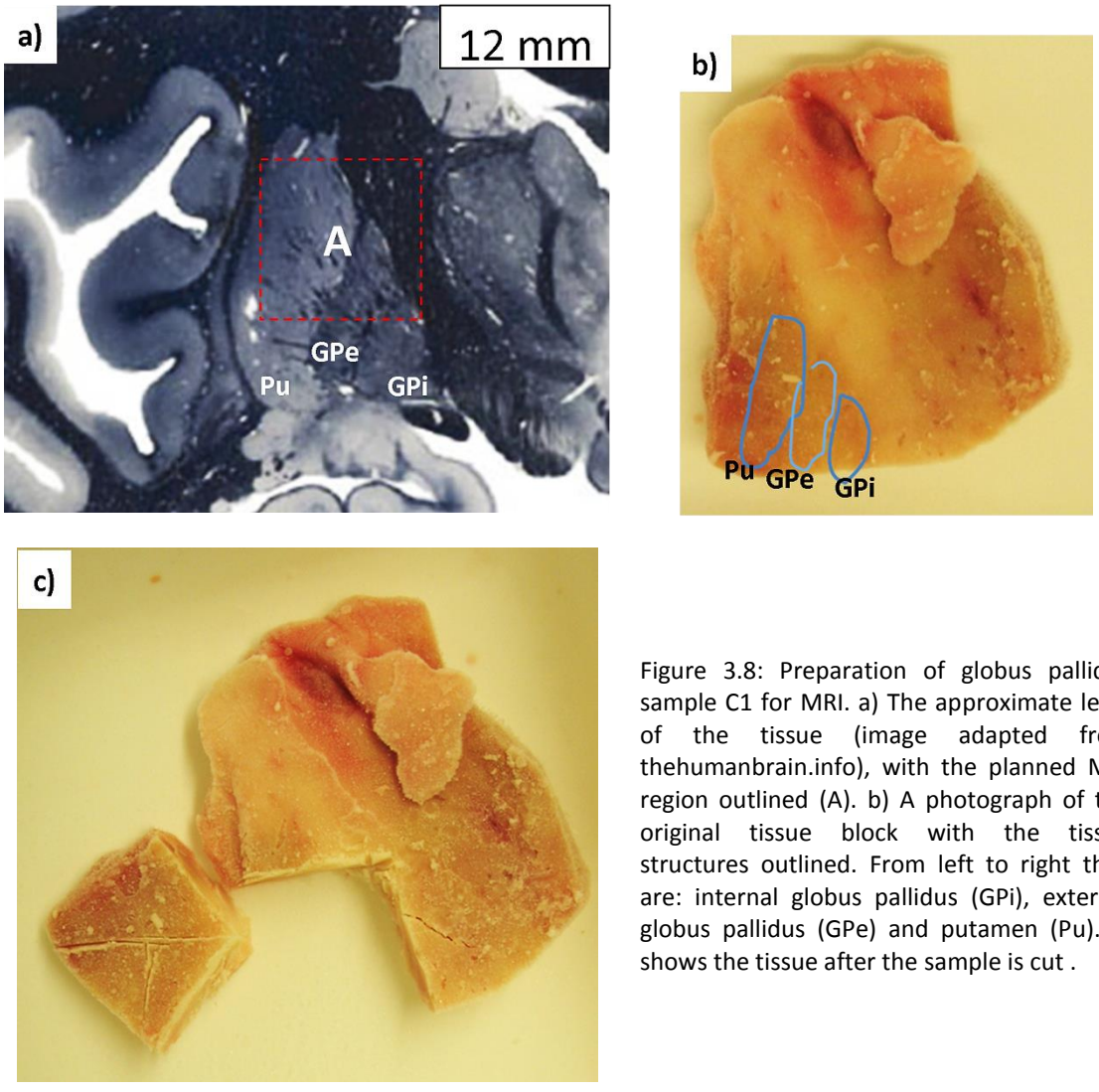

Figure 3.8: Preparation of globus pallidus sample C1 for MRI. a) The approximate level of the tissue (image adapted from thehumanbrain.info), with the planned MRI region outlined (A). b) A photograph of the original tissue block with the tissue structures outlined. From left to right they are: internal globus pallidus (GPi), external globus pallidus (GPe) and putamen (Pu). c) shows the tissue after the sample is cut .

Samples for the globus pallidus ranged from coronal level 4 to 12 mm as identified by referencing coronal sections from *The Atlas of the Human Brain* [167]. MRI samples were all cut to try and include tissue from the internal and external globus pallidus as well as the

neighbouring part of the putamen. Not enough tissue from the regions of interest was present in the blocks to allow for samples to also be cut for bulk tissue analysis. An example of globus pallidus preparation is shown for case C1 in Figure 3.8. The globus pallidus was imaged at 400 MHz and was cut to fit inside the 20 mm diameter NMR tube. Appendix B-2 shows the cutting of all of the other GP samples.

3.2.3.3 Substantia nigra

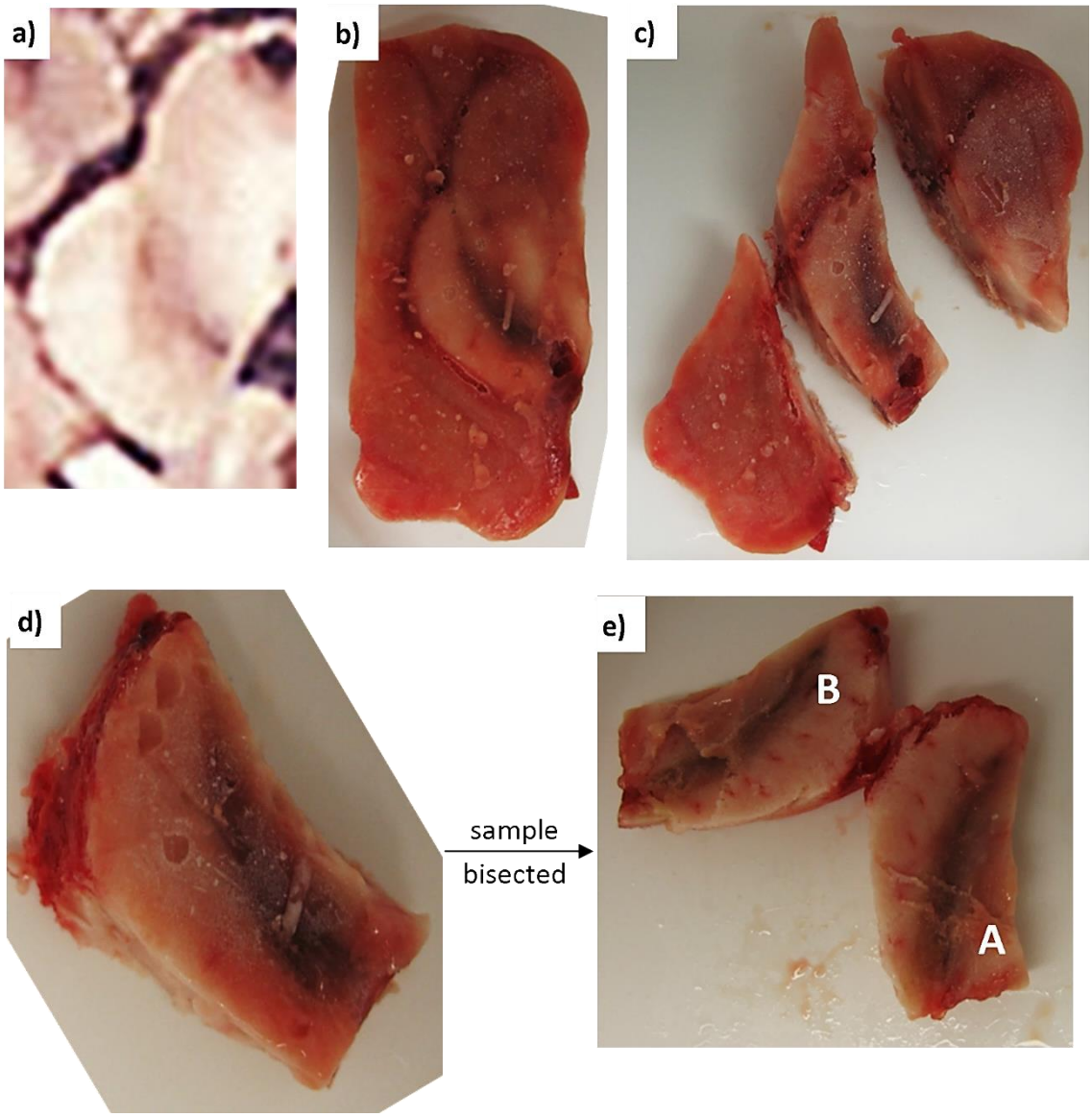

Figure 3.9: Preparation of substantia nigra sample C2 for MRI and bulk tissue analysis. a) An *in situ* view of the SN as shown in the axial atlas from thehumanbrain.info. The original tissue block is shown in b). The substantia nigra was cut from the surrounding tissue c) & d) and then bisected axially e) into block A (for MRI) and B (for bulk tissue analysis).

The tissue block from the SN was cut axially, rather than coronally. The whole substantia nigra was cut out of the larger block and cut in half along its length as shown in Figure 3.9. Block B is the top half and was prepared for bulk tissue analysis.

The preparation of all other SN samples is shown in Appendix B-3 and this includes tissue from the three PD and MSA cases. SQUID and iron quantification were prioritised over MRI for the SN in order to complete the MSA study [28]. This meant that for a few cases the whole SN was taken for bulk tissue analysis. This was the case for samples C3 and AD3, where only a small amount of SN tissue was available and bisecting the sample would have resulted in samples too small for either MRI or SQUID magnetometry to be carried out. Note, limited experimental time meant that no MRI mapping was carried out on MSA samples.

The bottom half of the bisected sample is part A and was reserved for MRI where enough tissue was present. The SN was imaged using the 400 MHz system which was large enough to image almost the entire sample in each case. Where necessary a small portion (maximum 2 mm) of the sample was trimmed at either end in order for the sample to sit horizontally in the NMR tube.

3.2.3.4 Amygdala

The amygdala was a challenging area to dissect. Therefore extra care was taken to obtain advice before tissue was cut for MRI. Figure 3.10 shows the MRI sample cut from amygdala case C3. Part a) shows the feedback from Dr Hazrati and Dr Visanji who draw the blue oval over photos of the tissue block to indicate the position of the amygdala. The amygdala was imaged at 600 MHz and the pieces were cut from the block to fit the 8 mm diameter NMR tube. Appendix B-4 shows the cutting of all other amygdala samples.

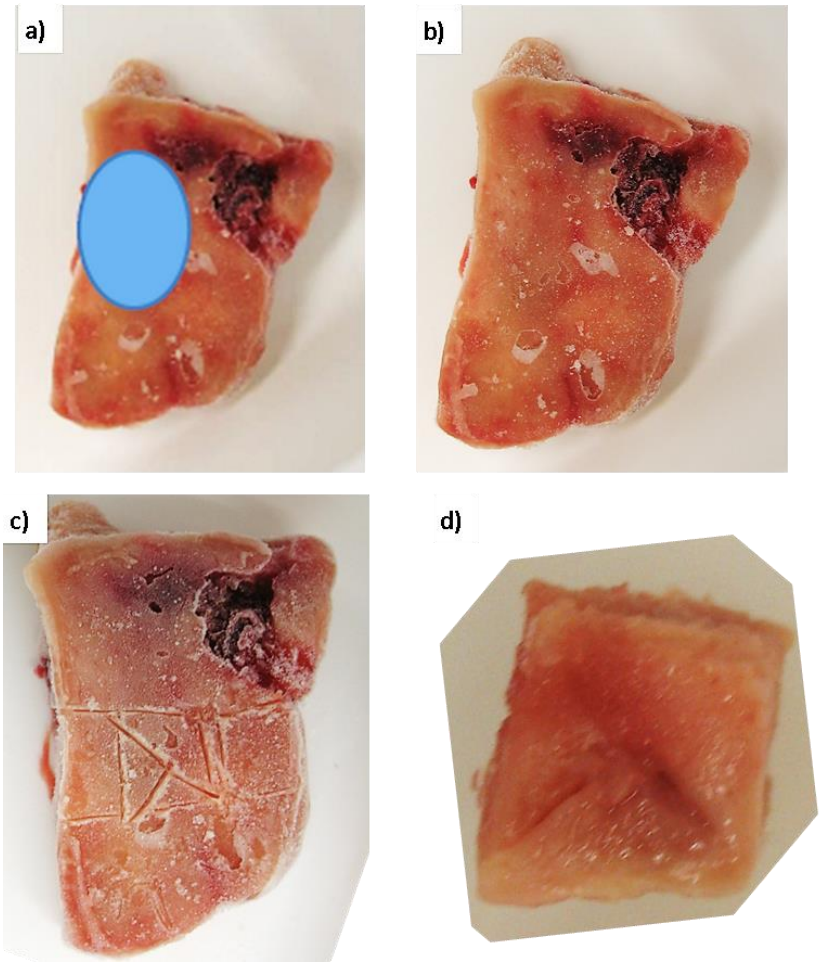

Figure 3.10: Preparation of amygdala sample C3 for MRI. a) The sample with a blue oval drawn over the position of the amygdala. b) The sample before cutting; c) score marks indicating where cuts will be made and d) the sample for MRI.

3.2.3.5 Pons

As part of the collaborative study with The University of Toronto, tissue for bulk iron analysis was cut from the pons for all samples (apart from AD1 and AD3) before the commencement of this project. Figure 3.11 shows how tissue was cut for MRI imaging from the pons using sample C1 as an example. Part a) shows the cutting reference used for the pons. Tissue for the bulk iron analysis was cut by Dr Joanna Collingwood, University of Warwick, before the beginning of this PhD. The same guide as shown in a) was used, but tissue was cut from the adjacent block of tissue. Pons samples were imaged using the 600 MHz system at the University of Florida and so tissue was cut to fit inside the 8 mm diameter NMR tubes.

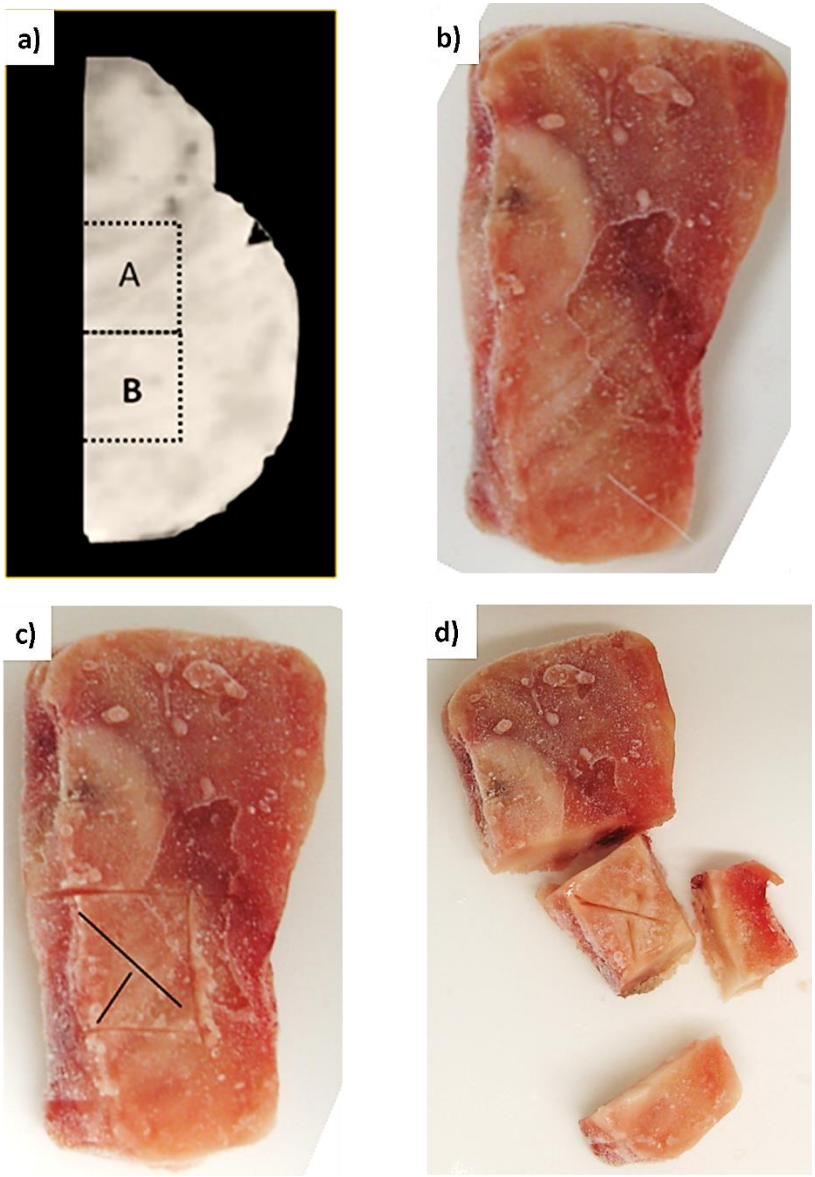

Figure 3.11: Preparation of pons sample C1 for MRI. The reference for the planned cutting is shown in a), and the original tissue block is shown in b). The cuts are first marked out by scoring the surface of the tissue as shown in c). Finally the sample for MRI is cut from the main block d).

3.3 Sample preparation

Figure 3.1 showed the experimental path for each sample. Section 3.3.1 describes how block B was freeze-dried for SQUID magnetometry and iron quantification and Sections 3.3.2 and 3.3.3 detail how block A was prepared for MRI relaxometry and then sectioned for histology and metal mapping.

3.3.1 Preparation for bulk tissue analysis

Tissue was prepared for SQUID measurement as described by Hautot *et al.*, 2005 [108]. The excised tissue was freeze dried for at least 8 hours until the sample mass stabilised. After drying, the mass of the sample had typically reduced by a factor of 3 to 4. Freeze dried tissue was cut into small pieces using an acid washed, non-metallic knife and fed into a SQUID straw. It was then compressed into a pellet using non-metallic rods as shown in Figure 3.12. The SQUID straw was supported with a strong tube during this process to prevent bending or buckling around the tissue.

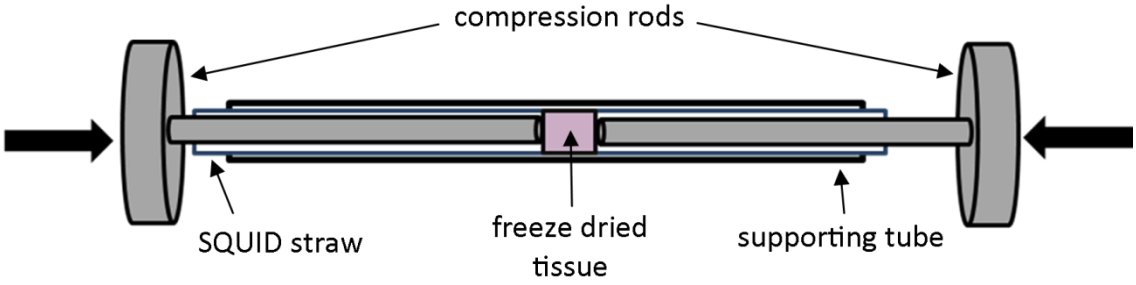

Figure 3.12: Tissue compression for SQUID magnetometry. The freeze dried tissue was compressed inside a SQUID straw using two non-metallic compression rods which were pushed towards each other by hand. The SQUID straw was positioned inside a non-metallic, strong supporting tube during the compression to prevent bulging or splitting of the SQUID straw.

As the SQUID straw is held vertically during measurement the pellet was supported inside the straw using a second straw that was cut in two, folded along its length and fed into either end of the straw containing the sample.

3.3.2 Preparation for MRI

MRI of the pons and amygdala was carried out at the McKnight Brain Institute at the University of Florida using a probe with a 10 mm bore that held an 8 mm diameter NMR tube. At the University of Warwick a 30 mm bore probe containing a 20 mm diameter NMR tube was used to image the putamen, globus pallidus, caudate nucleus and substantia nigra.

For both probes the tissue was suspended in Fluorinert (3M, Belgium NV), which gives zero MRI signal, in Wilmad-Labglass NMR tubes. Both the NMR tubes and Fluorinert were cooled to

-20 °C before being brought into contact with the frozen tissue. In both set-ups, care was taken to minimise the number of bubbles present in the vicinity of the sample as they cause artefacts in the MRI, particularly in T_2* measurements. Although the sample environment for MRI was similar, the different sized systems required two slightly different mechanisms to support the tissue samples during measurement.

3.3.2.1 600 MHz MRI sample set-up

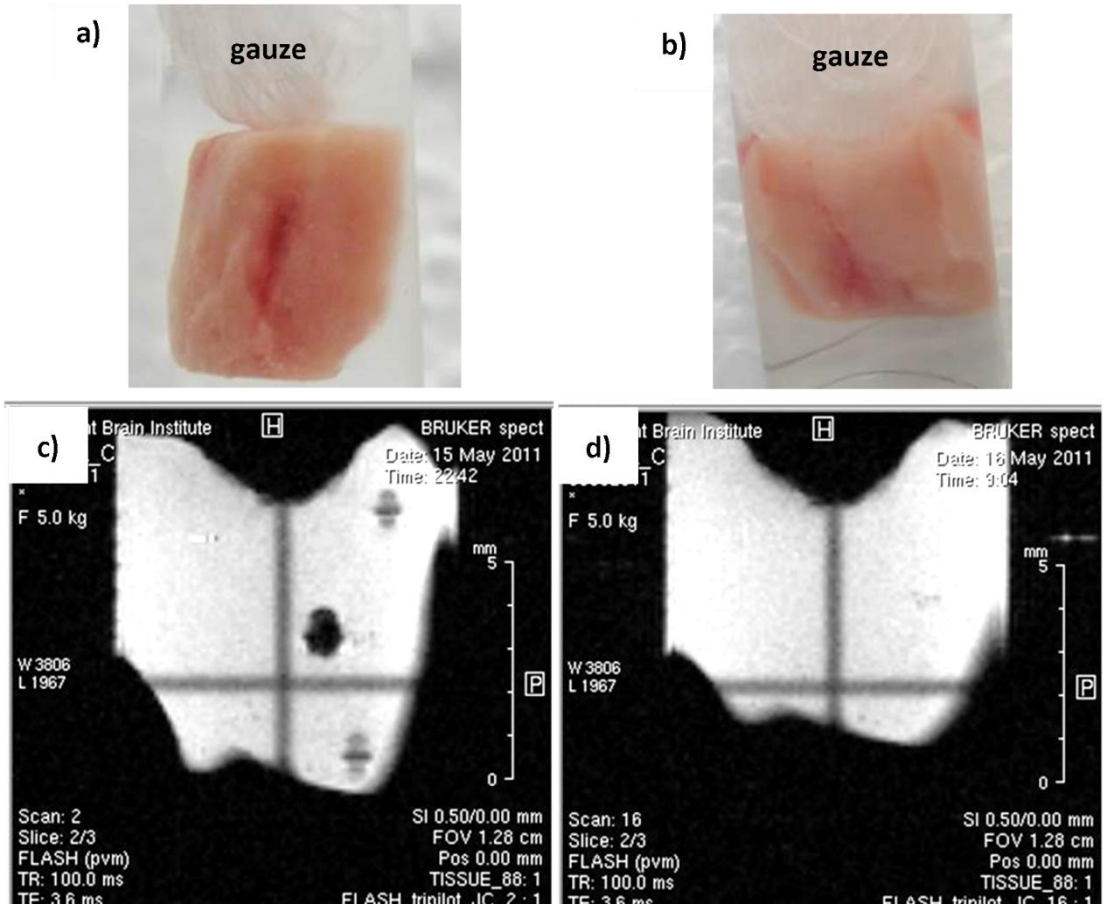

Figure 3.13: The effect of 12 hours of imaging on the shape of a tissue sample. a) The still frozen tissue block submerged in Fluorinert by a gauze plug. b) The defrosted sample immediately after imaging. c) A FLASH image shows the tissue after around 30 minutes in the scanner—the period of time taken for the sample to defrost and for initial imaging set-up to be carried out. The top of the tissue has already begun to mould around the gauze plug and the side of the NMR tube. d) After 12 hours imaging the FLASH image shows the tissue has further moulded around the gauze and to the shape of the NMR tube. However the gauze has remained in place.

For the smaller bore magnet, where the inner diameter of the NMR tube is around 8 mm, the tissue was held just below the surface of the Fluorinert using a plug of cotton gauze as described by Antharam *et al.* 2012 [132] and shown in Figure 3.13 a) and b). Approximately 1.5

ml of Fluorinert was poured into the NMR tube before the tissue was dropped carefully into place. Gauze, which had been soaked in cold Fluorinert, was then pushed into the tube using a plastic stick. The stick was also used to manipulate the gauze and free any trapped air bubbles.

Although the gauze plug remained firmly in place inside the narrow tubes, it did not provide a flat support surface. This allowed tissue samples sit an angle within the tube and for the tissue to deform around the curved bottom of the plug. This deformation was due to the upwards pressure of the relatively dense Fluorinert on the soft, defrosted tissue. Figure 3.13 shows a particularly bad example of tissue deforming during imaging.

3.3.2.2 400 MHz MRI sample set-up

As the 400 MHz magnet has a larger bore and the NMR tubes used to hold the samples had an inner diameter of 20 mm, a new method of holding the tissue below the surface of the Fluorinert was devised. Figure 3.14 shows the new support and the resulting tissue shape over the course of the MRI scan.

A small three-part insert was designed, in collaboration with Peter Kimber (School of Engineering, University of Warwick). As shown in Figure 3.13, the device was made of two pieces of plastic which clip together and hold a disk of nylon stocking. This creates a firm, but gentle support for the tissue. The diameter of the device is just below 20 mm and therefore drops easily down into the NMR tube. Tapping and gently tipping the NMR tube was enough to encourage most bubbles to pass through the nylon or around the sides of the support. The weight of the support was enough to hold the tissue block just below the surface of the Fluorinert and the stretched nylon was firm enough to provide a flat support for the tissue samples. The design includes a lip which allows a specially designed plastic rod to hook the support from the tube after imaging. All of the plastic parts of the support are reusable and were acid washed between uses. The nylon was thrown out and replaced after each use.

Figure 3.14 e) and f) show that the new design, with much more even tissue support, is an improvement to the gauze plug design and results in greatly reduced deformation of the tissue during imaging.

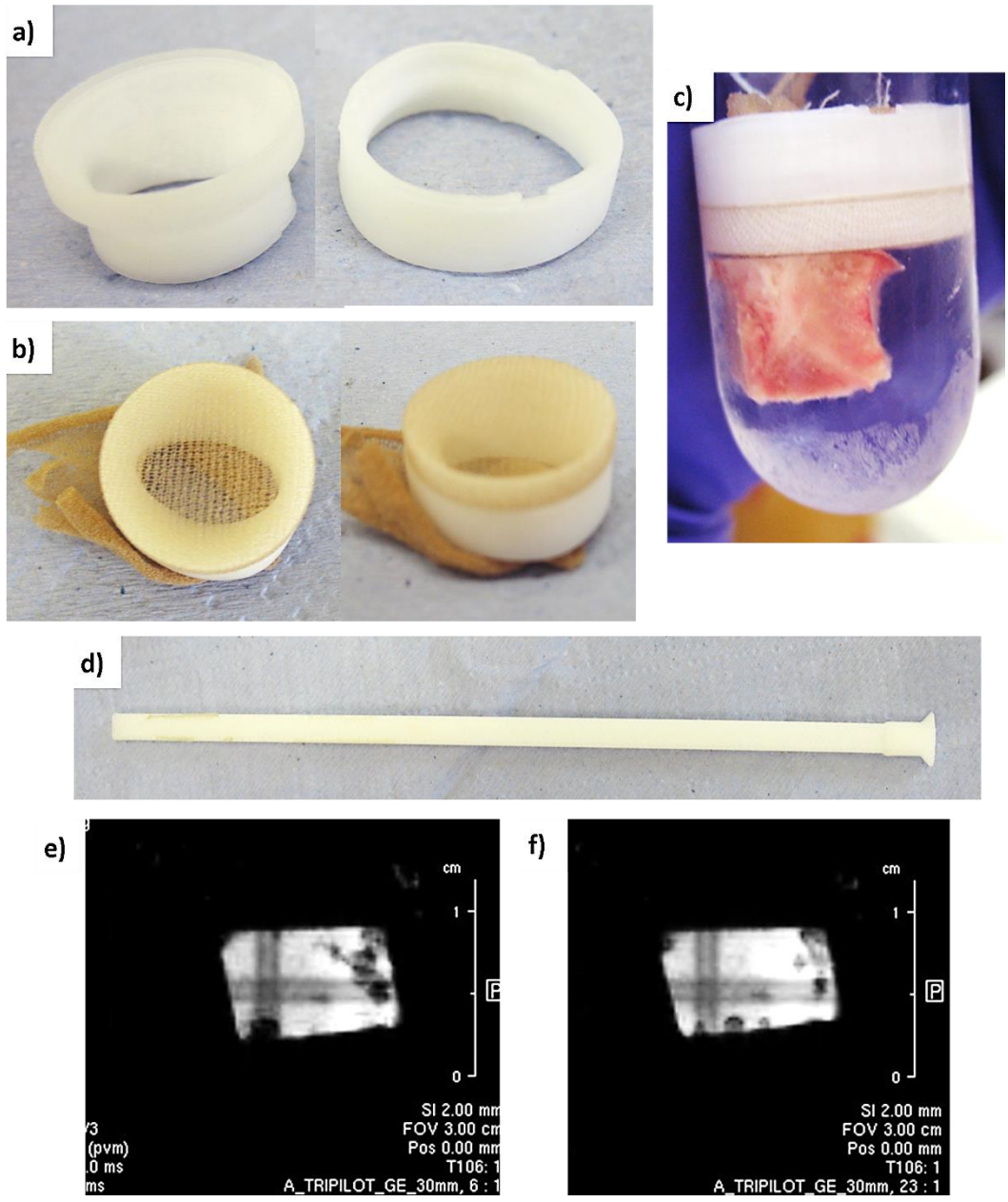

Figure 3.14: The tissue support for imaging at 400 MHz and the result of 12 hours imaging on the shape of the tissue. a) The plastic parts of the tissue support clip together to hold a piece of nylon tights b). c) This creates a firm, flat surface which held the tissue just below the surface of Fluorinert in a 20 mm NMR tube. d) A plastic was rod designed to hook into the plastic support and remove it from the NMR tube after imaging was complete. e) and f) show the typical effect of 12 hours of imaging on the shape of the sample, where e) was taken at the beginning of the session and f) at the end.

3.3.2.3 Sample temperature

In both protocols tissue was positioned in the NMR in the cold environment of a -20 °C cryomicrotome to prevent any defrosting. After preparation the samples were kept at -25 °C until just before imaging, with minimal temperature cycling and storage at temperature of -25 °C for no longer than 24 hours before imaging to minimise tissue degradation. Initially samples were refrozen to -80 °C before imaging, which froze the Fluorinert. However, this meant a longer time was required before measurement temperature was reached and more importantly air bubbles formed as the Fluorinert melted, increasing the incidence of artefacts in the imaging.

During imaging at the University of Florida the samples were warmed to 3.0 ± 0.1 °C and during imaging at the University of Warwick the temperature was kept to 2.0 ± 0.1 °C. Once imaging was completed, the imaged tissue was thoroughly refrozen before being removed from the NMR tube. The gauze or the plastic support was pulled from the tube using a plastic hook and this usually brought the tissue with it. If the tissue remained in the tube it was encouraged out using the plastic hook. The gauze or nylon was then carefully pulled from the tissue using plastic, acid washed tweezers, again working inside the cryomicrotome. Tissue was then stored in cryotubs at -80 °C until required for sectioning.

3.3.3 Sectioning MRI tissue blocks

MRI mapped tissue blocks were sectioned using a Leica cyromicrotome (model: Jung CM3000) so that the tissue sections could be histochemically stained to aid with anatomical identification (Section 4.5 *Histology*).

Samples were carefully mounted onto the sectioning block at the same orientation that they were in during MRI. For samples imaged at 400 MHz, the flat surface of the tissue blocks, where they had rested against the nylon support, made this alignment straightforward. For samples measured at 600 MHz, where the top of the sample had slightly moulded around the

gauze plug, alignment was judged by eye using the MRI FLASH images as a guide. Tissue-Tek mounting medium was used to stick the samples to the chuck using just enough to firmly attach the sample. As shown in Figure 3.15, the samples were not embedded in the mounting medium.

Sectioning was carried out with the blade at an angle of 10 degrees and a thickness of 30 µm. The object temperature was set to around -17 °C and adjusted to suit the sample. Covered samples were left in the cryotome for at least 1 hour before sectioning to allow the temperature to equilibrate from -80 °C. The fresh-frozen, not embedded tissue required very careful sectioning. The tip of a paint brush (Figure 3.15) was used to control the sections as they were cut, to prevent curling and manipulate the sample onto the slide. Sections for histology were captured on glass slides, kept cold in the sample chamber, and the heat from a finger was used to melt the sample onto the slide.

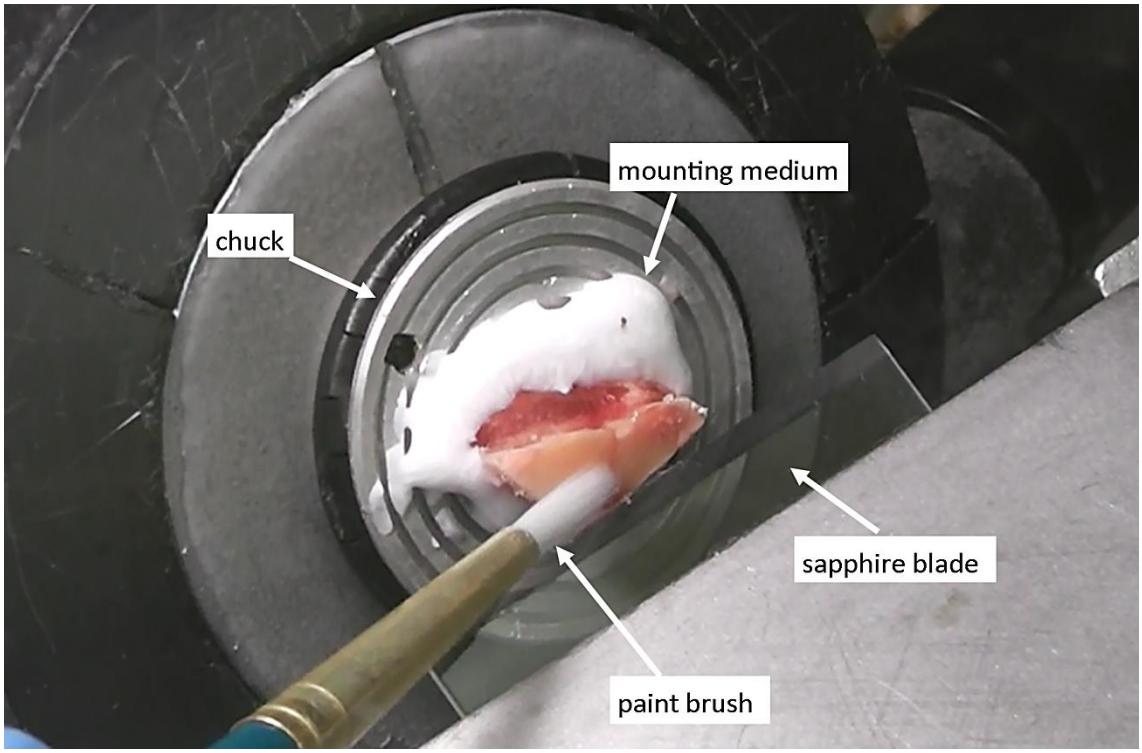

Figure 3.15 Tissue sectioning. Just enough mounting medium was used to anchor the sample to the chuck, without embedding the sample. As the tissue was cut with the sapphire blade, the paintbrush was used to control the section and prevent it from curling.

Some samples were particularly difficult to section, especially those made largely of grey matter which was more likely to splinter during sectioning. Careful temperature control allowed good sections to be captured for most of the samples.

Not every section was collected, but particular care was taken to sample heavily from the high resolution MRI region of each sample. In addition to visual comparison of the surface of the sectioning block and the MRI maps, the MRI records and the cyromicrotome's section counter were used to calculate the approximate position within the tissue block and determine when the high resolution MRI region had been entered. Detailed notes were made of the sections collected on each slide including the section number, where counting was started at first contact between the blade and the tissue block.

3.3.3.1 Tissue sections for SXRF mapping

Features of the sectioning protocol described above, such as non-embedded samples, use of a sapphire blade and the 30 µm sectioning thickness, have been used as part of a protocol designed to provide sections suitable for SXRF mapping in addition to histochemical staining. This is a similar protocol as previously described by Antharam *et al.* [132].

The SXRF metal mapping technique is highly sensitive, and any contamination can lead to false results or could provide such a strong signal so as to overshadow the neighbouring area. Therefore it is imperative to avoid metal particulate contamination in the preparation of the sample. As iron is the main focus of this study, elimination of potential iron contamination was a priority.

The sapphire blade was used to avoid the potential for metal contamination that would arise if using a metal blade, which would necessarily come into contact with the whole of the surface of the section as it was cut. The sapphire blade was held in a metal blade holder within the cryomicrotome in such a way that approximately 15 mm of blade protrudes from the clamp (Figure 3.15). Therefore, as sections were cut they fell onto the blade rather than the metal

surface. With sections that were to be mapped, particular care was taken to avoid them coming into contact with any metal surface in the cryomicrotome. This was not important for sections cut for immediate staining.

Mounting medium was not used to embed the samples for two reasons. Firstly, it would provide a possible route for contamination as mounting medium may contain traces of iron and other metals. Secondly, although the sapphire blade cuts the brain tissue cleanly and effectively, it struggled to cut the mounting medium and if used to do so it rapidly deteriorated.

Sections were cut at 30 µm thickness as experience from previous SXRF mapping experiments by our group has shown that at this thickness a strong, above background SXRF signal can be achieved with a measurement time of 1 second per point. Comparatively, the MRI slice thicknesses are 80 µm for imaging at the University of Florida and 150 µm at the University of Warwick and therefore one MRI slice represents several sections.

Once the high resolution MRI region of the sample was entered sections were collected for SXRF mapping. At least four sections spaced throughout the high resolution region were collected onto high quality quartz slides for each sample. Quartz slides have a low iron content and produce a much more homogeneous fluorescence signal than normal glass slides, providing a reasonably consistent background that can be subtracted from SXRF metal maps.

Sections for SXRF were collected for every MRI sample, however due to limited beam time at the Diamond Light Source, only one control and one AD sample from each brain region was mapped, with an additional PD and MSA pons case. The specific cases to be mapped were chosen based on the quality of the MRI images and whether they were judged to show a good example of the regions of interest. SXRF mapping is described in detail in Section 4.4. All unmapped samples have been stored for future use if desired.

The sections on quartz slides were prepared for mapping by air-drying for at least 4 hours. The samples were left to dry inside a biohazard hood to minimise the chance of iron particulate containing dust landing on them. The slides were then sealed with a layer of X-ray transparent kapton film, fixed around the edge of the slide with PAP pen and sealed with epoxy resin. This procedure both protected the samples from damage or contamination and sealed in the human tissue in order to comply with the health and safety requirements of the Diamond Light Source.

Finally, the sections to be mapped were selected based on section quality and matching to the high resolution MRI maps. Where good matching was not achieved, for example due to sectioning in a slightly different plane to MRI imaging, a section was chosen that contained the same structural features as were visible in the high resolution MRI scans. Using the same protocol to cut sections for histology and for SXRF mapping (rather than switching to a metal blade, or reducing section thickness) meant that sectioning was continuous. Therefore, sections immediately adjacent to the SXRF sections were captured on glass and could be stained with haematoxylin. These were then taken to experiments at the Diamond Light Source and used as a guide when choosing the positioning of SXRF maps.

Chapter 4: Methodology

This chapter describes the different methods used to investigate iron content and MRI relaxation rates in the samples that were described in Chapter 3, where Figure 3.1 showed the experimental model and Table 3.1 gave a summary of the measurements made on each sample. Bulk tissue analysis is described in Sections 4.1 *Superconducting quantum interference device magnetometry* and 4.2 *Iron quantification*. The high resolution MRI mapping is described in Section 4.3 and the synchrotron X-ray Fluorescence (SXRF) mapping in 4.4. Section 4.5 describes the basic histology used to stain tissue sections cut from the samples analysed by MRI and the protocol developed to stain tissue sections after SXRF mapping. Finally Section 4.6 details the statistical methods that are used to examine the data from the above experiments.

4.1 Superconducting quantum interference device magnetometry

Super Conducting QUantum Interference Device (SQUID) magnetometers are capable of measuring very small magnetic moments as well as accurately controlling the temperature of the sample and applied field. The SQUID sits inside a superconducting magnet which is used to apply fields to the sample. Liquid nitrogen and helium cool the superconducting magnet and are used to control the temperature of the sample. The sample is moved through a superconducting ring containing two Josephson junctions in parallel, inducing a current and voltage proportional to the magnetic moment of the sample. The SQUID is shielded from the surrounding superconducting magnet so that it only detects signal from the sample.

Magnetisation measurements were made using a Quantum Design MPMS-5S SQUID capable of measuring over a temperature range of 1.8 to 400 K and with an applied field of ± 50 000 Oersted (Oe). It can measure down to a magnetic moment of around 5×10^{-8} electromagnetic

units (emu). The sample is moved through a distance of 4 cm in a series of 32 steps and the resulting signal is fitted to giving the magnetic moment of the sample.

The SQUID was used to examine magnetic properties of the freeze-dried, bulk tissue from control, Alzheimer's Disease (AD), Parkinson's Disease (PD) and Multiple System Atrophy (MSA) samples from the pons, substantia nigra and putamen and from the control and AD caudate nucleus.

4.1.1 Isothermal remanent magnetisation

The magnetic properties of the non-haem iron in the brain have been described in Section 2.2. However, the dominating signal from biological samples under an applied field is diamagnetic. The diamagnetic signal can be subtracted from the magnetic hysteresis of a biological sample in order to examine non-diamagnetic components in the sample, including contributions from particulate iron [108]. One simple way to avoid the diamagnetic contributions and examine only the material that can retain a net magnetisation after exposure to an applied field (primarily particulate iron in tissue) is to measure the isothermal remanent magnetisation.

Isothermal remanent magnetisation (IRM) is the magnetic moment of a sample, at a fixed temperature, after a magnetic field is applied and then abruptly removed. After the field is switched off the diamagnetic contribution will be lost and only material that is magnetically blocked will retain a magnetic moment. Typically, ferrihydrite-like iron oxide nanoparticles in ferritin are still blocked at temperatures below 15 K [154], whereas nanoparticles of magnetite of greater than ~ 13 nm in diameter will be blocked at 50 K [83].

4.1.2 Methodology for measuring IRM

Before measuring the magnetic moment of a sample it is important that it be centred in the SQUID. This was achieved for each sample by applying a small field to the sample and running the built in direct current centring scan. The position of the sample was adjusted automatically and the dipole position checked by eye. The centring was repeated until the dipole was

properly centred. Slight shifts in the position of the sample are possible due to the wide range of temperatures at which IRM was measured. Therefore auto-centring, under the IRM applied field, was included in the scan sequences after any change in temperature.

The magnetic history of the sample can affect the IRM. Therefore it was important to 'demagnetise' the samples by applying a field and cycling it slowly to zero in the 'No Overshoot' mode, before beginning measurements. This ensured that all samples began the IRM measurements with the same magnetic history. For the same reason the order of subsequent IRM measurements, at the different temperatures, is the same for all samples.

In order to measure IRM the field of the superconducting magnet must be switched off abruptly, which is achieved by using the 'Magnet Reset' function of the SQUID to quench the magnet. The energy released during the controlled quench causes a large amount of liquid helium to boil off when compared to other typical magnetometry measurements. This helium use restricted the number of IRM measurements that could be made on each sample.

After switching off the magnetic field the IRM of each sample was measured 8 times over a period of about 10 minutes, where each of the 8 measurements given by the magnetometer was the average of 5 measurements. The final IRM quoted was the average of the last 4 values.

The linear regression fit mode was selected for all data above 5 K. In this mode the software fits the magnetisation data with the centre of the dipole fixed, unlike the iterative regression mode which allows for sample movement. As the sample is centred under an applied field before scanning at a new temperature, the centre position is reliable. The benefit of using linear regression mode for samples with very small magnetic moments is that iterative regression mode is more likely to falsely report a non-zero magnetic moment.

A full record of the IRM measurements made on each sample is given at the beginning of Chapter 5 *Bulk tissue iron analysis* and Appendix C contains the full scan protocols.

4.1.2.1 IRM curves at 5 and 50 K

IRM curves are made by measuring the IRM of a sample at a fixed temperature, after a series of applied fields with increasing magnitude. IRM curves were made at 5 and 50 K for a selection of putamen and caudate nucleus samples and for one substantia nigra sample.

Before each curve was obtained, the temperature of the sample was raised to 300 K and the demagnetising sequence run. The sample temperature was then reduced to the measurement temperature and a 250 Oe field was applied to centre the sample. This field was abruptly switched off and the IRM measured to give the first point on the IRM curve. The curve was completed with IRM measurements from applied fields of 500, 750, 1000, 1500, 2000, 3000, 4000, 5000, 7500 and 10000 Oe. The full scan sequence is given in Appendix C-1.

4.1.2.2 IRM at 5, 50 150 and 300 K

IRM from an applied field of 10 kOe was measured at 300, 150, 50 and 5K in that order. The same order was used for each sample to ensure that all samples had the same magnetic history. Ideally the demagnetising sequence would have been run in between each measurement, but the time and helium used in raising the temperature to 300 K to run the 'demag' sequence was prohibitive. As the temperature of the IRM measurements decreases more nanoparticles will become magnetically blocked, therefore the IRM measurements were made in order of decreasing temperature. As the magnetic history of the samples was the same, and the measurements were made in the same order, the results between samples are comparable.

The data reported in the literature [83] and the IRM curves show that IRM at 5 K, which is dominated by ferrihydrite, will very likely not have reached saturation from an applied field of 1 T. Therefore it is important that the same field is applied for each sample and the SQUID magnetometer's no-overshoot mode was used. The full SQUID sequence used to measure IRM at 300, 150, 50 and 5 K is given in Appendix C-2.

4.1.3 Correcting SQUID data for sample length

The SQUID magnetometer assumes a point-like sample and consequently there is a loss of signal for samples over 3 mm long. All data were corrected for sample length using the empirical formula described by Hautot *et al.* [108]:

$$V(z) = \frac{R}{[R^2+(z-A)^2]^{3/2}} + \frac{R}{[R^2+(z+A)^2]^{3/2}} - \frac{2R}{(R^2+z^2)^{3/2}} \qquad (4.1)$$

$$f = \frac{\int_{-b/2}^{b/2} V(z)dz}{bV(0)} \qquad (4.2)$$

Where: A is the distance between coils of the SQUID; R is the radius of pickup coils; z is the on-axis coordinate and b is the sample length. For the Quantum Design MPMS-5 A = 1.519 cm and R = 0.97 cm.

The length of each compressed sample, to the nearest 0.5 mm, was measured by holding a vernier calliper to the side of the transparent SQUID straw. The mathematical software Maple 14 was then used to substitute the length of each sample into Equation 4.2 and find the loss of signal due to length. Maximum sample length was 13.5 mm and this resulted in f = 0.75. IRM values were then corrected by a factor of 1/f and are given as emu per gram of freeze dried or fresh frozen tissue.

4.1.4 Quality of data

Above, the assumption is made that the IRM data obtained at 5 K are not significantly affected by the fact that the sample has previously been subjected to 10 kOe at 300, 150 and 50 K. This assumption can be tested to some extent by comparing the IRM at 5 K measurement to the value of the last point in the IRM curves for the same sample. The demagnetisation sequence was run before each IRM curve was measured, and therefore the last point on the curve represents the first time that the sample was exposed to a field of 10 kOe (all other points on the curve are from smaller fields). If the data from the two measurements agree well it suggests that the IRM measurement at 5 K is not significantly affected by the measurements at

300, 150 and 50 K. The comparison of these two measurements is shown in Figure 4.1 a) for the 5 K data and similarly for the 50 K data in 4.1 b). Note that IRM measurements were not made for all samples, however for all samples measured with both protocols the agreement is good.

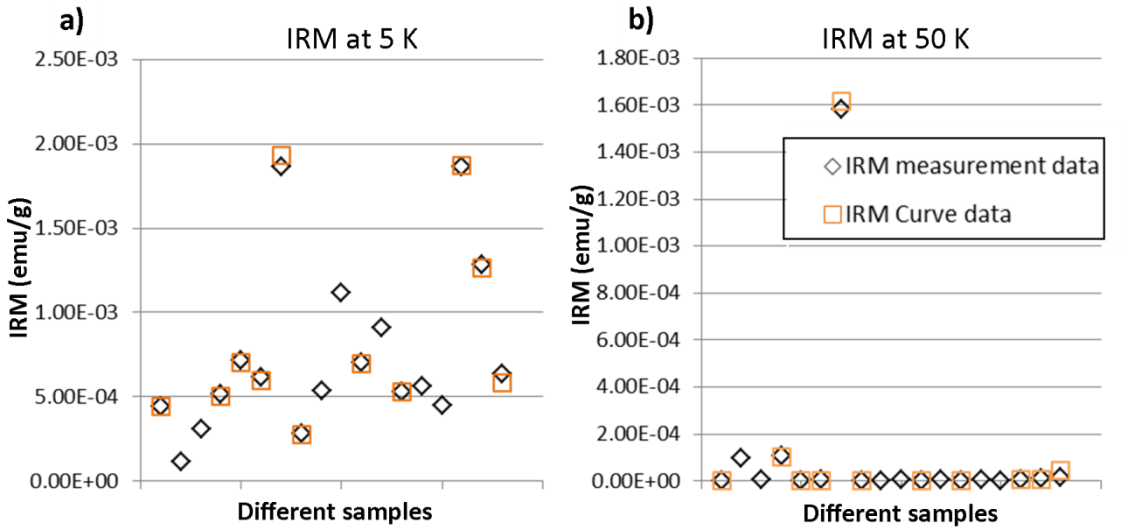

Figure 4.1: Comparison of IRM data from individual IRM measurements and IRM curves. The IRM after an applied field of 10 kOe at 5 K, a), and 50 K, b), for each putamen and caudate nucleus sample is shown with a grey diamond. Overlaid as a brown square is the last point of the IRM curve of the same sample, which was also made after an applied field of 10 kOe. Note IRM curves were only collected for a sub-set of samples. The data agree well.

Typically the first few points on the IRM curves have an extremely small magnitude, often below the reliable detection limit of the instrument of 5 x 10^{-8} emu. However, quantitative comparisons are only being made with data from an applied field of 10 kOe. All 5 K IRM values are well above the detection limit and only a couple of 50 K values are below it. These data are indicated in the data set in Chapter 5 as appropriate.

The error given for each IRM measurement is the combined error from: the standard deviation of the averaged IRM measurements, the measurement error in weighing the sample and the measurement error in measuring sample length.

4.2 Iron quantification

The concentration of iron in each of the SQUID samples was subsequently measured using either Graphite Furnace Atomic Absorption Spectroscopy (GFAAS) or Inductively Coupled Plasma Mass Spectrometry (ICP-MS). The method used for each sample is shown in Table 5.2 at the beginning of Chapter 5 *Bulk tissue iron analysis*.

4.2.1 Graphite furnace atomic absorption spectroscopy

GFAAS was carried out by Dr Emily House in the Birchall Centre at Keele University and was used to measure the iron concentration of the pons and substantia nigra samples (with the exception of SN, MSA3). A Mars Xpress microwave was used to digest the tissue samples in 1 ml HNO_3 and 1 ml H_2O_2 using a CEM-provided Tissue Xpress program. Ultrapure water (3 ml) was added and the digest volume corrected for venting. The iron concentration was determined from 800-fold dilutions using a hollow-cathode lamp at 30 mA and atomic absorption measured at 248.3 nm.

4.2.2 Inductively coupled plasma mass spectroscopy

Inductively coupled plasma mass spectroscopy (ICP-MS) was carried out in collaboration with Dr Isolda Romero using the ICP-MS Agilent Technologies 7500 series from the Mass Spectrometry Facility of the University of Warwick. The compressed, freeze dried SQUID samples were transferred into acid washed 3 ml capacity glass Wheaton v-vials for digestion in 72 % double distilled nitric acid. To transfer the sample with minimum opportunity for sample contamination, the SQUID straw was cut a little above and below the sample with a cleanroom-standard blade and the inner supporting straw used to push the sample directly from the straw into the vial. A test sample, T, taken from near the SN was also digested.

A total of 1.5 ml of nitric acid was added to the vials in aliquots of 0.5 ml. Vials were placed in the oven at 55 °C for 5 hours, after which the tissue had visibly dissolved. Samples were then left in the oven at 55 °C overnight, for approximately 16 hours. After this time a very small

amount of fat was visibly floating on the top of the acid, however this was tiny compared to the original sample volume and it was judged that the iron in the tissue would be dissolved in the acid solution.

A sample of the acid and tissue solution, pipetted from below the fat deposit, was dissolved to 1:10 to achieve a safe acid concentration for ICP-MS. All water used for dilution was milliQ grade (18.2 MΩ).

Before measuring the samples, the spectrometer was calibrated using a 1000 part per million (ppm) iron standard that was diluted in a 5% nitric acid solution to give a range from 5 to $2x10^5$ parts per trillion (ppt). Good curves were produced, with the best calibration curve achieved for the ^{57}Fe isotope in the 'no gas' mode, therefore the values from this measurement were used.

The 'test' sample was measured first and showed an iron concentration of 1.8×10^6 ppt. This is much more concentrated than the standards that were used for calibration. Ideally the sample would be in the $x10^4$ ppt range and therefore all samples were diluted by 1:10 and 1:100. The 1:100 dilution test sample produced the best results, so the 1:100 dilutions of all the samples were measured. Two samples (MSA1 and MSA2) had to be further diluted by a factor of 10 to 1:1000 in order to achieve an appropriate iron concentration.

To ensure that there was no build-up of sample within the instrument, 'blanks' consisting of a 1:100 dilution of the 72% nitric acid were run after every 4 samples. These consistently produced an iron concentration below the detection limit of the spectrometer, giving a reading of zero.

4.3 Magnetic resonance imaging

MRI relaxometry was carried out at high fields (9.4 and 14.1 T). At high field the MRI signal is increased and this allows very high resolution mapping, whilst retaining a good signal to noise ratio. The effect of iron on the transverse relaxation rate R_2, and the susceptibility related parameter R_2*, increases with imaging field and therefore high field MRI relaxometry is more sensitive to tissue iron content [124].

The MRI protocols used to measure T_2 and T_2*, and to produce the corresponding R_2 and R_2* maps, at the two different fields are described below. The full MRI protocols for the measurement of T_1 are also included, however this not the focus of this study and therefore is not discussed in detail here and the data are not included in the results chapter.

4.3.1 MRI data collection

The MRI relaxometry in this project was carried out at two different field strengths, at two different research facilities. Mapping of the pons and amygdala was carried out using an established 600 MHz (14.1 T) probe at the Advanced Magnetic Resonance Imaging and Spectroscopy (AMRIS) facility in the McKnight Brain Institute at the University of Florida. A brand new 400 MHz (9.4 T) imaging probe at the Magnetic Resonance facility at the University of Warwick was used to map the caudate nucleus, putamen, globus pallidus and substantia nigra. Parameters specific to the 600 MHz probes are described in Section 4.3.1.2 and Section 4.3.1.3 gives details of how the standard Bruker imaging sequences were optimised for mapping with the 400 MHz probe.

4.3.1.1 Common features of measurement protocol at 600 and 400 MHz

4.3.1.1.1 Sample temperature

The temperature of the samples during imaging was kept at 3 °C in the 600 MHz probe and at 2 °C in the 400 MHz probe. In both systems the temperature was maintained throughout the

measurement by a cooler blowing air around the sample. This was controlled by Topspin through feedback from a calibrated thermocouple in the sample space.

Before using the new 400 MHz probe the temperature of the sample space was calibrated using an NMR tube filled with methanol. The NMR spectrum of methanol has distinct peaks for CH_3 and OH. The distance between these peaks in ppm (Δ) can be related to the temperature of the methanol in Kelvin, by the following equation [178]:

$$T = -23.832\Delta^2 - 29.46\Delta + 403.0 \qquad (4.3)$$

The desired temperature of the sample is just above freezing. Through trial and error a methanol temperature of 275 K was achieved by setting a target temperature of 270 K and an air flow of 800 litres per hour.

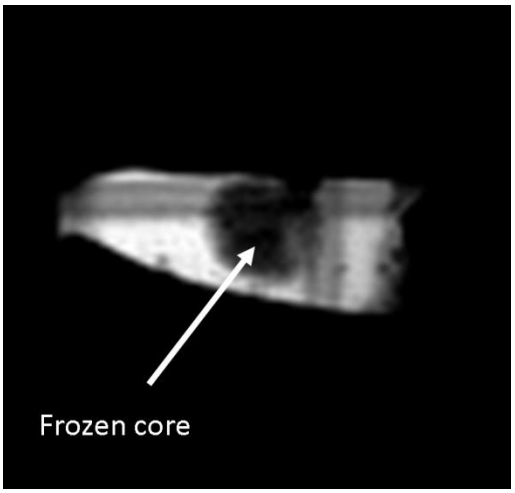

Figure 4.2: FLASH image of a partially frozen tissue sample. As the core of the sample is still frozen, it shows little signal.

Before carrying out MRI relaxometry it was important to wait for the samples to defrost, as in frozen tissue the water molecules are immobilised. Therefore, Fast Angle Low SHot (FLASH) images were used to monitor defrosting of the sample. In practice, a partially frozen sample is easily observed by the black core (absence of signal) at the centre of the block (Figure 4.2).

4.3.1.1.2 Tune and match and shimming

Before imaging the probes were tuned and matched to the ^{1}H channel. TopSpin was used to manually shim the gradients until a smooth free induction decay (FID) of maximum size, and a symmetrical, as narrow as possible water peak with a full-width-half-maximum (FWHM) of below 60 Hz was achieved. Shimming increases the field homogeneity within the sample space and is therefore necessary to produce good quality, reliable, reproducible data for high resolution imaging.

4.3.1.1.3 Pulse sequences

At both fields T_2 was measured using a Carr-Purcell-Meiboom-Gill sequence (CPMG). This sequence is a multi-echo, spin echo sequence. After the initial 90° excitation pulse, a 180° pulse is repeated to produce a series of echoes at times T_E, $2T_E$, $3T_E$ *etc.* The decreasing magnitude of the echoe train follows the transverse decay.

The shape of the transverse decay is described by Equation 2.4. With the addition of a constant (A) representing a finite background, this can be expressed as [132]:

$$y = A + Ce^{-t/T_2} \qquad (4.3)$$

Where y is equal to the signal in the transverse plane at a time, t, after the initial excitation pulse and C is the signal in the transverse plane at t = 0.

The sequence to measure T_2 was also a multi-slice sequence, i.e. many slices were measured within T_R. Slice-selective RF pulses were used to create a stack of consecutive images for each slice, where each image is the RF signal measured at that time after the initial excitation pulse.

The multi-slice multi-echo (MSME) sequence was chosen as it minimised the imaging time compared to single echo, or single slice imaging. The number of slices that can be measured is limited to T_R divided by the longest echo time.

T_2* was measured using a multiple gradient-echo (MGE) sequence. Selective slice excitation was followed by successive reversals of the readout gradient to produce a train of echoes. The echo train produces a decay with the same shape as described by Equation 4.3.

4.3.1.1.4 Scan order and geometry

A common approach was taken to arranging scan slices and scan order in both systems, as developed in prior work by the group [132, 179]. Low resolution scans were used first to measure the majority of the tissue sample volume. Data from these scans were then used to choose the volume of tissue to image at high resolution. The effect of any bubble artefacts, as well as the structure visible in the tissue, was taken into account before choosing the high resolution region.

First, a FLASH pulse sequence was used to create tri-pilot images: a contrast image in each of the x, y and z planes (Figure 4.3 a). These were used as a reference for choosing the position of the mapping scans. A FLASH tri-pilot was carried out at the start of imaging, after the low resolution scans and again after the high resolution scans. This allowed any change in sample shape or position to be monitored.

Low resolution data were collected by three sets of scans with interleaving geometry (Figure 4.3 b). It is good practice to leave some space between slices when using multi-slice scan sequences in order to avoid interference between the slices. The Bruker option of 'interlaced' collection order of the slices within a scan was used, further reducing the likelihood of crosstalk. The multi-slice sequences can only measure a limited number of slices per scan and therefore three sets of scans were required to cover the entire tissue volume. A smaller volume of tissue was mapped at high resolution and two sets of interleaving scans were used (Figure 4.3 c).

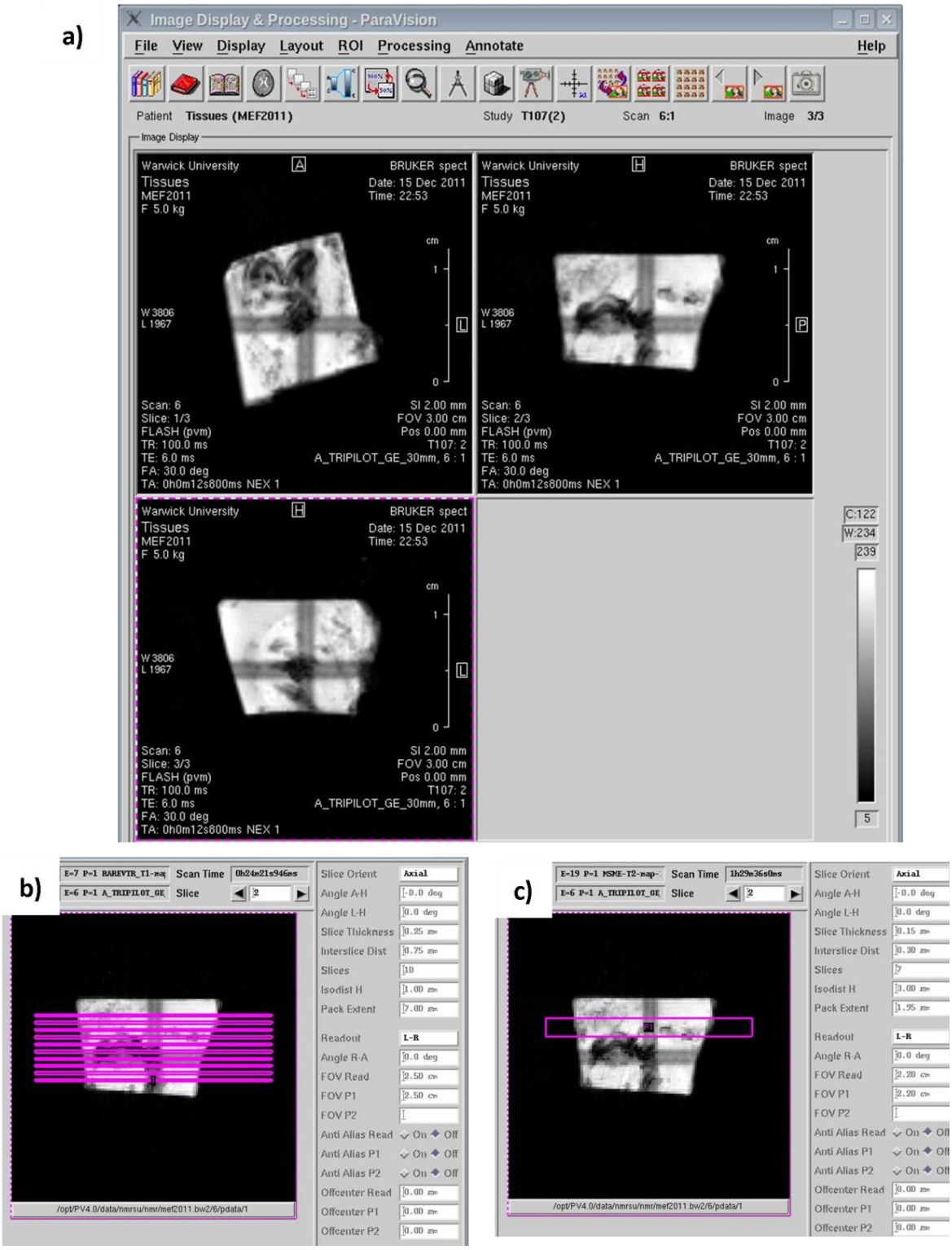

Figure 4.3: Setting up slice geometry for MRI mapping. This is an example from the scan set up on the 400 MHz probe. a) A FLASH scan shows the tissue in the x, y and z direction and this was used to set up the position of b) the low resolution scans which covered most of the tissue and c) the high resolution scans which covered only a small portion of the tissue. Note that the low resolution scans in c) had a gap of 150 µm between each slice which is not shown in the image.

4.3.1.1.5 Amplifiers and receiver gain

During the set up for a scan Paravision has an option to run the pulse sequence and display the signal without recording data, allowing attenuation of the maximum amplifier power to the RF pulses to be optimised. Changing the power to the pulse affects its flip angle. If it is not optimised the pulses may not produce exactly 90° and 180° pulses and therefore a true T_2 decay or T_1 recovery would not be produced.

This is controlled through Paravision by setting the value of A0 (attenuation of power to the excitation pulse) and A1 (attenuation of power to the refocusing pulse). The values were optimised for each scan by adjusting the values until a maximum signal was detected (shown by the level of digitizer filling). The shape of the decay is also displayed in the Paravision set-up window and shows a smooth decay when the attenuation is optimised. Once optimised for each scan, on each system, these values were used as the default settings for each experiment. As the decay shape is displayed by Paravision during set-up, this was also checked by eye at the beginning of each experiment.

The receiver gain was adjusted for each measurement so that for each scan type the digitiser filling reached approximately 70% (an arbitrary limit appropriate to the version of Paravision used) to ensure saturation did not occur.

4.3.1.2 Imaging at the McKnight Brain Institute, University of Florida

Quantitative MRI mapping was carried out on control, AD, PD and MSA samples from the pons and control and AD tissue from the amygdala. The protocol used is as described by Antharam *et al.* [132]. Each sample was imaged with a 10 mm TXI radiofrequency probe in the bore of a 600 MHz (14.1 T) Bruker Advance spectrometer. Paravision version 3.0 was used to run the spectrometer and drive pulse sequences.

The samples were prepared in NMR tubes as described in Section 3.3.2.1. The high and low resolution scans were set up as described in Section 4.3.1.1.4. Table 4.1 gives a summary of

the scan parameters used for mapping at 600 MHz. The low resolution scans had an in-plane resolution of 200 x 200 µm and a slice thickness of 250 µm. The in-plane resolution of the high resolution scans was 62 x 62 µm, with a slice thickness of 80 µm. Each high resolution scan had 15 slices and was used to map a volume of tissue 2.4 mm high (in the z direction),

Measurement: / Parameter:	T_2 (low res)	T_2 (high res)	T_2* (low res)	T_2* (high res)	T_1 (low res)	T_1 (high res)
Resolution (µm)	200x200	62x62	200x200	62x62	200x200	62x62
Slice thickness (µm)	250	80	250	80	250	80
Scan sequence	MSME	MSME	MGE	MGE	MSMEVTR	MSMEVTR
Attenuators: A0, A1	16, 8.5	16, 8.5	21, -	21, -	18, 12	18, 12
T_R (ms)	4000	4000	3500	3500	*	*
T_E [T first echo] (ms)	8.62	8.62	6.66 [3.70]	6.66 [3.70]	9.62	9.62
No. echoes	20	15	18	18	1	1
No. of averages	6	12	6	12	3	6
Scan time	16m00s	1h42m24s	14m00s	1h29m36s	20m40s	2h9m58s

Table 4.1: Scan parameters for MRI relaxometry at 600 MHz. MSME = multi-slice multi-echo; MGE = multi-gradient-echo; MSMEVTR = MSME variable repetition time. *T_1 repetition times = 3500, 2250, 1500, 1000, 750, 500, 350 and 250 ms.

Although high resolution scans with interleaving geometry were set up for each sample, both scans were not collected in every case in order to reduce imaging time. For all samples only one high resolution T_1 scan was run. Both sets of high resolution T_2 and T_2* scans were only run for one tissue from each disease group. The measurement time, including set up, was approximately 11 hours for the lesser number of scans and 14 hours for the full set of scans.

The excitation and refocusing pulses of the MSME sequence were Sinc3 RF pulses and the T_2 decay was measured using 15 echoes at 8.62 ms intervals with the first echo at 8.62 ms. The repetition time (T_R) was 4000 ms and the number of averages (N_A) was 12. Twelve dummy

scans were also run at the beginning of the sequence to achieve a steady state before measurement was begun.

The excitation pulse of the MGE sequence was a Gaussian pulse and was followed by a gradient-echo train created by reversals of the readout gradient. Eighteen echoes were used to measure the T_2* decay with a spacing of 6.66 ms after an initial echo time of 3.7 ms. The number of averages was 12, the number of repetitions was 12 and the number of dummy scans was 16.

High resolution T_1 measurement was carried out using an MSME, variable repetition time (MSMEVTR) scan. One echo time of 9.62 ms was used, with variable repetition times of 3500, 2250, 1500, 1000, 750, 500, 350 and 250 ms. Twelve dummy scans were run before beginning data collection and the data for each echo was averaged from nine scans.

4.3.1.3 Imaging at the University of Warwick

A custom design Bruker micro-imaging MicWB40 probe (Figure 4.4), funded through the Birmingham Science City Translational Medicine project, was purchased in early 2010 and became the first MRI probe in the Milburn House NMR suit at the University of Warwick. The scans and data collection were controlled using Paravison version 4.0.

The new probe was set up and tested as described below. The imaging parameters of the Bruker scan sequences were optimised to carry out high resolution MRI relaxometry on control and AD tissue from the caudate nucleus, putamen, globus pallidus and substantia nigra.

4.3.1.3.1 Hardware

The high resolution imaging probe gradients were designed to work with the existing 400 MHz spectrometer. A set of gradients (Figure 4.4 b) fit from the bottom into the vertical bore of the magnetic (Figure 4.4 a). They are maintained at approximately room temperature using cooled water, which is continuously pumped around the gradients and the temperature is monitored using an internal thermocouple. The imaging probe with RF coil (Figure 4.4 c and d) is then

inserted inside the gradient coils and the thermocouple inside the probe. The inner diameter of the probe is 3 cm and can hold a 2 cm diameter NMR tube, allowing space for air to circulate around the tube. The sample is loaded into the probe before both are positioned within the bore of the magnet.

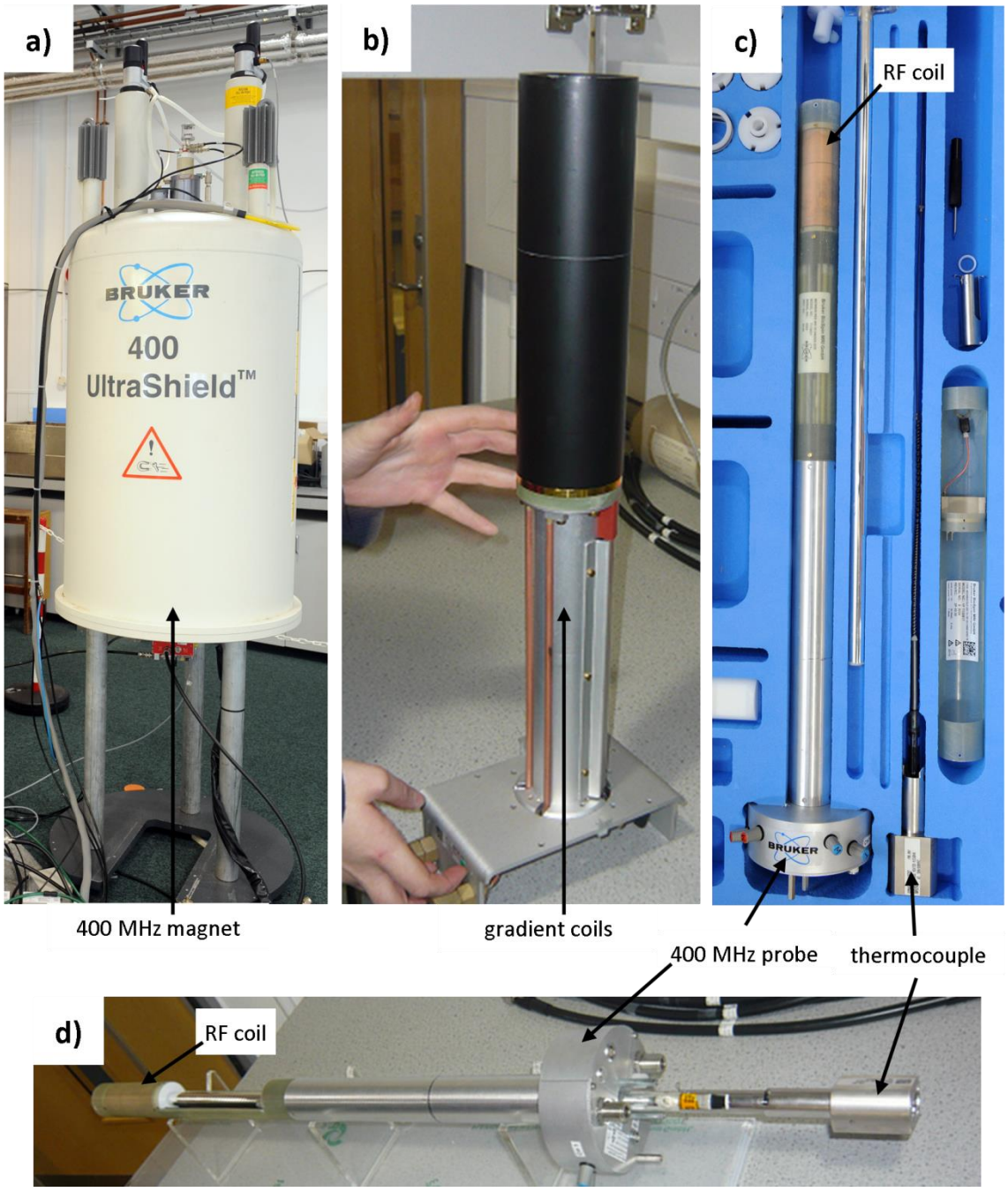

Figure 4.4: MRI hardware at the University of Warwick. a) The existing vertical bore 400 MHz magnet was fitted with b) gradient coils and c), d) an MRI probe. During the experiment the gradient coils are loaded into the bore of the magnet and the probe inserted inside the gradient. The temperature of the experiment can be monitored using the thermocouple shown in the box in c) and inside the probe in d).

4.3.1.3.2 Testing the new probe

During initial scanning inconsistent data were produced. Agarose gel samples (2% by weight) were used to trial scans as they should have reasonably uniform relaxation properties throughout the imaging volume. When only one slice was mapped the T_2, T_2* and T_1 values were approximately as expected and showed reasonable uniformity across the slice. However, when multiple slices were imaged in a single sequence the relaxation values were inconsistent and 'rings' appeared in the image.

A number of different parameters were altered in an attempt to achieve good quality high resolution mapping. This included: lengthening repetition time T_R to ensure complete relaxation of spins; increasing the distance between slices in case crosstalk was causing artefacts and changing the order in which the slices were measured to further reduce the risk of interference.

No improvement in the multi-slice imaging was observed and Bruker were asked to service the probe. Eventually a Bruker engineer discovered a problem in the way the hardware from the new probe had been connected to the old probe, which was quickly rectified.

4.3.1.3.3 Adjusting Bruker scans

Once the probe was working correctly, default Bruker scan sequences were adjusted to produce low and high resolution scans for mapping T_1, T_2 and T_2* using agarose gel phantoms and finally testing the scans on a piece of chicken breast.

Relaxometry sequences were chosen using advice from the Paravision help file and then adjusted for mapping the fresh-frozen, iron-rich tissues at high and low resolution. The aim of scan optimisation was to achieve i) high quality maps; ii) the ability to map rapid decays and iii) keeping imaging time to under 12 hours. A time limit of 12 hours was set in order to minimise the tissue degradation over time and to maximise the use of limited instrument time.

In order to produce high quality maps, a good signal to noise ratio (SNR) was required in enough echoes in order to fit Equation 4.3. The SNR was found by dividing the difference between the tissue signal and background signal, by the standard deviation of the background signal. The scan protocols were designed to maintain a SNR of approximately ≥ 10 in the third echo. A number of competing factors had to be balanced in order to achieve high resolution mapping, with good SNR, with a total imaging time of less than 12 hours.

A major challenge in the imaging was capturing very rapid T_2 and T_2* decays in regions of the samples with very high tissue iron concentration. The minimum T_E values possible were used for both the MSME (for measuring T_2) and MGE (for measuring T_2*) sequences. The results of rapid decay fitting and the limit to what can be measured using these sequences is discussed in Section 4.3.3.3.

As imaging resolution is increased, the voxel size is reduced, the number of spins contributing to the signal decreased, and therefore the SNR decreases. Increasing the number of averages for each scan can compensate for this, but this increases scan time. Additionally, the lower magnet strength of 400 MHz (compared to 600 MHz at the University of Florida), and the lower current gradients on the 400 MHz system, means less signal is obtained from the same sized voxel, resulting in a lower signal to noise ratio. Therefore the high resolution scans on the 400 MHz system had larger voxels than the 600 MHz system in order to maintain signal quality.

The in-plane resolution is defined by dividing the field of view (FOV) by a matrix of 128, 256, 512, 1024 or 2048. Ultra-high resolution was selected by setting the matrix size to 2048. The FOV was set to 22 mm, to ensure the whole diameter of the NMR tube would be captured. The resulting in-plane resolution is 86 x 86 µm. A slice thickness of 150 µm was chosen after trial and error testing in order to achieve a good signal to noise ratio.

A further practical consideration in pushing the resolution of imaging is that it increases the workload for the gradient coils. Steeper gradients are required to achieve high resolution,

which means a larger current is passed thought the gradients. This could cause them to overheat and become damaged. The problem is increased for scan sequences in which gradients are switched on and off very rapidly, without any periods of rest. Throughout scan set-up the temperature of the gradients was monitored using the readout of their internal thermocouple.

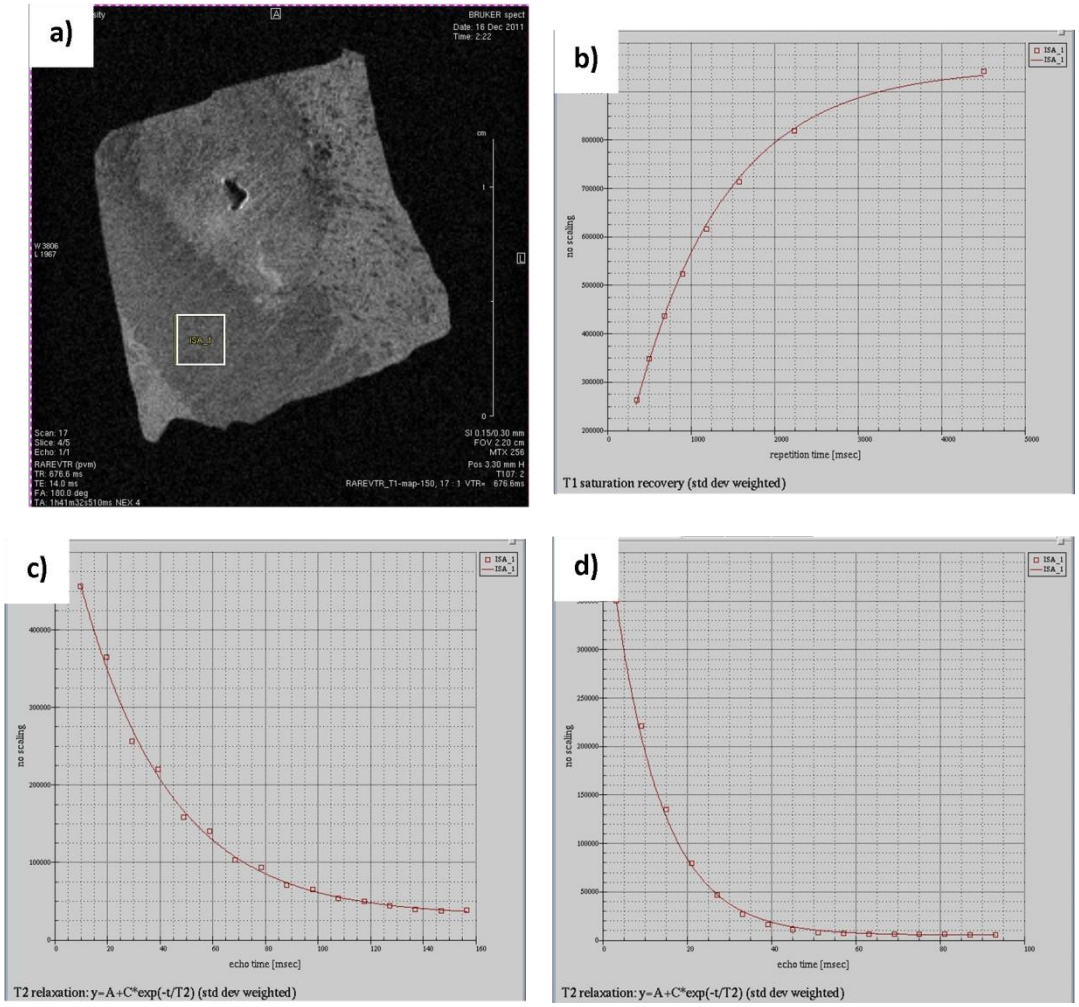

Figure 4.5: Example data collected using the 400 MHz probe at the University of Warwick. a) A 25x25 voxel area was selected for one slice of sample C3, globus pallidus. The average signal from this area is shown from the T_1 b), T_2 c) and T_2* d) scans, where the points on the graph show the signal intensity for the series of echoes. The data shown was plotted and fitted in Paravision.

The final scan parameters for the high and low resolution mapping are given in Table 4.2 and an example of the data produced by each scan is shown in Figure 4.5. Details of how each scan was optimised are given below.

Measurement: / Parameter:	T_2 (low res)	T_2 (high res)	T_2* (low res)	T_2* (high res)	T_1 (low res)	T_1 (high res)
Resolution (μm)	195x195	86x86	195x195	86x86	195x195	86x86
Slice thickness (μm)	250	150	250	150	250	150
Scan sequence	MSME	MSME	MGE	MGE	RAREVTR	RAREVTR
Attenuators: A0, A1	16, 3	16, 3	22.5, -	22.5, -	21, 8	22, 8
T_R (ms)	7000	7000	3500	4000	*	**
T_E [T first echo] (ms)	7.248	9.783	6.0 [3.08]	6.0 [3.90]	14	14
No. echoes	16	16	16	16	1	1
No. of averages	2	4	2	4	2	4
Scan time	22m24s	1h29m36s	11m12s	51m12s	24m19s	1h41m32s

Table 4.2: Scan parameters for MRI relaxometry at 400 MHz. MSME = multi-slice multi-echo; MGE = multi-gradient-echo; RAREVTR = rapid acquisition with relaxation enhancement, variable repetition time.* Low resolution T_1 repetition times (ms) = 347, 481, 643, 841, 1095, 1449, 2043, 4500. ** High resolution T_1 repetition times (ms) = 344, 496, 677, 896, 1179, 1573, 2234, 4500.

Longitudinal recovery, T_1

For each sample T_1 was mapped using a Rapid Acquisition with Relaxation Enhancement scan with Variable T_R (RARE-VTR). This is the recommended scan for ultra-high resolution T_1 measurement given in the Paravision 4.0 Biospin manual. Hermite pulses are used for both excitation and refocusing and these were not altered from the automatic setting.

The repetition times were calculated automatically by Paravision, which determines them based on the estimated approximate value of T_1. By trial and error, using different T_1 values, the approximate value of T_1 was found to be 1100 ms. The only alteration made to the values of T_R was extending the final repetition time to 4500 ms for both the high and low resolution scans. This was to ensure full T_1 recovery between successive scans.

During high resolution T_1 mapping the gradients began to overheat. This was due to the way the RARE-VTR scan sequence measures all short T_R values back-to-back, meaning the gradients

are working almost continuously during this period. The number of slices collected in the scan was reduced to from 7 to 5 which allowed enough rest time for the gradients to prevent overheating.

Transverse decay, T_2

The MSME sequence was used to map T_2 as suggested in the Paravision manual. This sequence uses CPMG pulse sequence with slice-selective RF pulses. The Bruker sequence uses a Hermite excitation pulse and Mao refocusing pulse. The time taken to apply the excitation and refocusing pulses determines the minimum T_E. Different pulse combinations (Sinc3, Gauss) were tested to try and reduce minimum T_E in order achieve better fits of rapid decays in the high iron tissue. However, changing the pulse shape compromised the measured T_2 decay produced at high resolution and therefore the Bruker original scan sequences were used, with the minimum echo times.

A long T_R was used as it is important for the NMV to have completely returned to the longitudinal plane between successive excitation pulses. The minimum appropriate T_R is considered to be at least four times T_1, which is approximately 1100 ms in the tissue. This gives a minimum T_R of 4400 ms. However, during scan testing a more consistent T_2 was achieved using a longer T_R of 7000 ms.

Susceptibility related T_2*

A multiple gradient-echo (MGE) sequence was used to measure T_2* in accordance with the Bruker manual recommendation. A Gauss excitation pulse is used and T_E is short due to the fact that there is no refocusing pulse (refocusing is achieved by applying readout gradients). Shorter T_R values (3500 ms at low resolution and 4000 ms at high resolution) could be used for the MGE measurements as the sequence is less susceptible to T_1 not being fully recovered and as excitation angles of below 90 ° were used.

4.3.1.3.4 Final scanning protocol

The samples were prepared for imaging as described in Section 3.3.2.2 before being taken on ice to the imaging facility. The scan parameters shown in Table 4.2 were used for imaging all of the tissues at 400 MHz. Table 4.3 shows a list of the scans in the order in which they were collected, which follows the same general principles that were described in section 4.3.1.1.4. A Paravision macro was used to run scans 3 to 18 automatically over approximately 11 hours.

	Scan	Slices	Centre Position
1	FLASH	-	-
2	T_1 (low res)	Up to 10	a
3	T_1 (low res)	Up to 10	a + 250
4	T_1 (low res)	Up to 10	a + 500
5	T_2 (low res)	Up to 10	a
6	T_2 (low res)	Up to 10	a + 250
7	T_2 (low res)	Up to 10	a + 500
8	T_2* (low res)	Up to 10	a
9	T_2* (low res)	Up to 10	a + 250
10	T_2* (low res)	Up to 10	a + 500
11	FLASH	-	-
12	T_1 (high res)	5	b
13	T_1 (high res)	5	b + 150
14	T_2 (high res)	7	b
15	T_2 (high res)	7	b + 150
16	T_2* (high res)	7	b
17	T_2* (high res)	7	b + 150
18	FLASH	-	-

Table 4.3: The order of scans for MRI at 400 MHz. A FLASH (fast low angle shot) scan examines the overall shape and position of the tissue at the beginning, middle and end of the imaging process. Three sets of up to 10 interleaving scans were used to map T_1, T_2 and T_2* at low resolution. Two sets of 5 (for T_1) or 7 (for T_2 and T_2*) slices mapped the tissue at high resolution.

4.3.2 Data Processing

4.3.2.1 Paravision

In addition to driving the hardware, Paravision can be used to fit the MRI data using the 'Image Sequence Analysis' tool. The contrast image of the first or second echo is used to select a region of interest (ROI) and then T_2 (or T_2*) is fitted to the decay produced from the average signal of the ROI in each echo. The 'absolute bias' is set to 'varied' in order to allow the software to take into account the finite background signal and ensure a better fit. Paravision uses a Levenberg-Marquardt nonlinear least squares fitting algorithm to fit the relaxation decays using Equation 4.3.

Paravision does not provide very easy control of ROIs and was mainly used to visualise decays and examine data during imaging.

4.3.2.2 ImageJ

ImageJ [180] is a free, open-source, image processing software written in Java and available for download. It allows careful drawing and management of ROIs as well as image manipulation. In addition to the main software package a number of plugins are available, including plugins to process MRI data. Two plugins were used to process the MRI data. The 'Bruker Opener' plugin (available from the ImageJ website [181]) and the 'MRI Processor' plugin (available from the ImageJ wiki [182]).

The Bruker Opener plugin allows ImageJ to open the '2dseq' data file produced by Paravision to produce a stack of images made up from the consecutive echoes for each consecutive slice in the scan. These stacks were divided into separate stacks for each slice using the Substack Maker tool.

The MRI Processor plugin was then used to produce a T_2 or T_2* map by fitting the signal decay in each pixel as produced by the sequence of echoes. The map type option 'T2 Exponential'

was used with the Levenberg-Marquardt fit algorithm. The echo times for the sequence were input and then the T_2 (or T_2*) map generated.

Work carried out in 2011 by a summer project student (Kevin Ray, Department of Physics, University of Warwick) showed that fitting using the MRI Processor plugin produced the same numerical results as fitting using Paravision. The decay properties of individual pixels and the average over an ROI were also examined in OriginPro 8.5 (Origin). This showed that the best fit was obtained with a mono-exponential decay.

Once the set of maps was produced for each sample, the 'Math' tool in ImageJ was used to find the reciprocal value for each pixel and therefore create an R_2 or R_2* map. The maps from consecutive slices could then be stacked to create a 3D volume of the sample.

Initially only the high resolution MRI data were fitted, but for some samples, where further information was required, lower resolution data were also fitted.

4.3.3 Artefacts and data quality

4.3.3.1 Variation across the sample space

Imaging at the AMRIS facility at the University of Florida was carried out early on in the project using established scan sequences. Upon examination of the T_2 data it was found that the data were not consistent throughout the sample volume. A typical example of the variation observed is given in Figure 4.6, which shows T_2 and T_2* for an ROI of 2000 pixels overlaid onto the maps of amygdala AD3. The T_2* data remains fairly constant for each slice, whereas the T_2 data increases to a maximum at slice 4 and then decreases.

Although T_2 data from other samples showed a similar trend, the exact shape and position of the peak was not consistent from sample to sample, even when corrected for relative slice position within the sample space. Therefore there was no reliable way of correcting the data and measuring true T_2 and only T_2* data for the amygdala and pons samples were analysed.

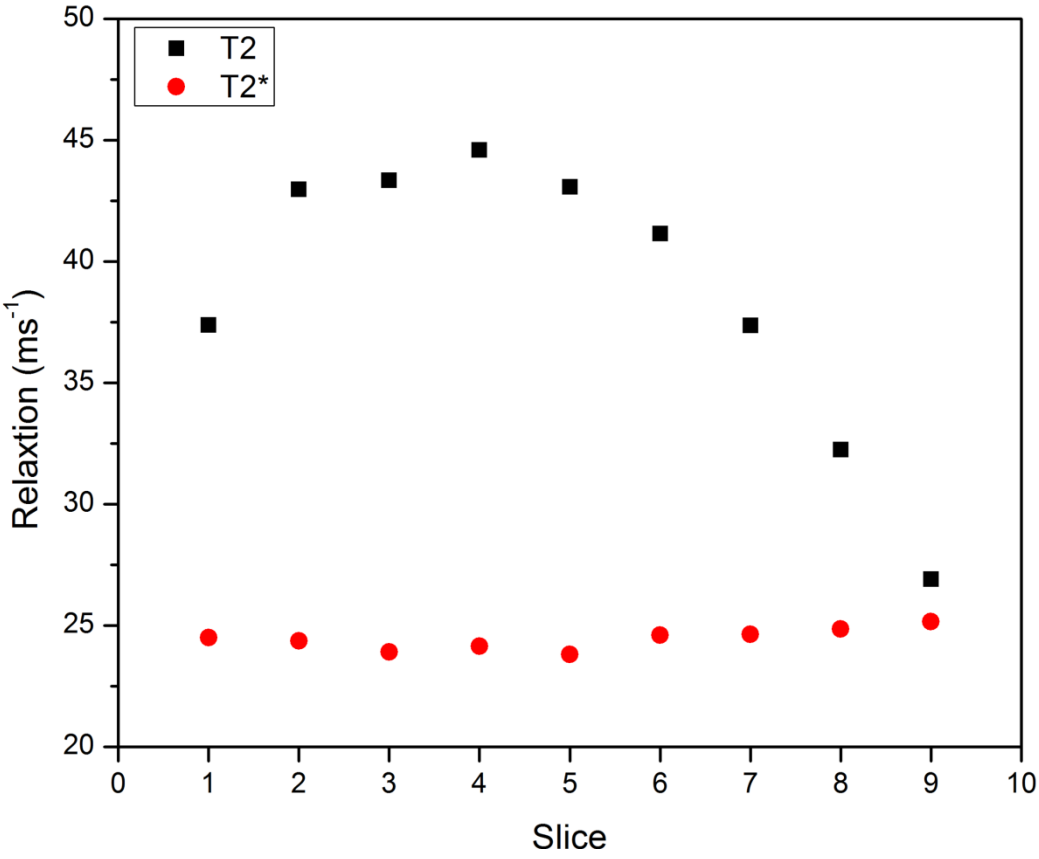

Figure 4.6: Typical T_2 and T_2* data collected at AMRIS, University of Florida. T_2 data show significant inconsistency with slice number, despite T_2* data being consistent.

It is likely that the unusable T_2 data is due to a step in the scan set-up where the power to the gradient coils was limited for the MSME sequence. This was done to prevent overheating when driving the coils hard to image at such high resolution. As the power to the gradient coils was not as large for the MGE sequence, the same problem with the data is not observed for the T_2* data.

4.3.3.2 Artefacts

Figure 4.7 shows some artefacts encountered during imaging. Part a) uses data from amygdala sample C1 to demonstrate an artefact that appeared in all T_2* MRI maps made at the AMRIS facility. There is a vertical line of pixels which is visibly altered from the surrounding image. As the artefact is limited to a single line of pixels, and do not have a large difference in value from the surrounding map, it is unlikely to cause any significant difference to the average value of any ROIs which include some of the pixels. However, the artefact is excluded from analysis.

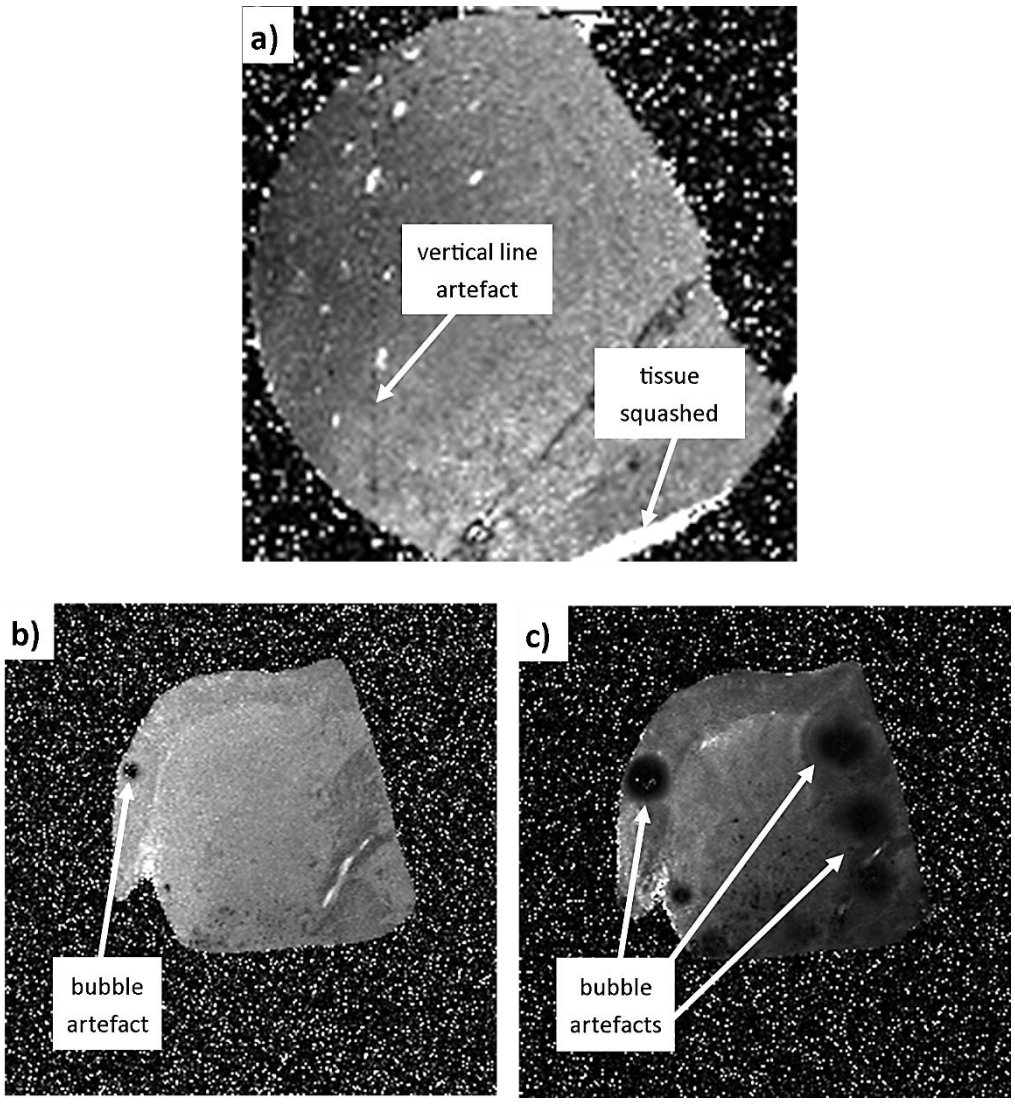

Figure 4.7: Typical artefacts in MRI maps. The vertical line artefact in a) appears in all T_2* maps made at AMRIS. Squashed tissue at the edge of the NMR tube also provides an unusual signal. b) An artefact in a T_2 map caused by an air bubble. c) The same slice of the corresponding T_2* map, showing much larger artefacts caused by air bubbles.

Also worth noting in this picture is the bright signal at one edge of the sample, where the tissue was particularly compressed against the NMR tube. Unusual signal at sample edges is always excluded from analysis.

The main source of artefacts was from bubbles of air trapped around the sample. The air-sample interface creates an artefact that can affect a large area of the map, as shown for caudate nucleus sample C2 in Figure 4.7 b) for a T_2 map and part c) for a T_2* map. As can be seen here, bubbles affect T_2* maps much more significantly than T_2 maps, with a relatively small bubble potentially causing large distortion of the image. When segmenting the maps of

R_2 or R_2*, ROIs were drawn to exclude these artefacts. In the case of c) no measurements would be made from this slice.

4.3.3.3 Rapid decays

When optimising the Bruker scans to measure T_2 and T_2* short T_E values were used in order to try and capture the rapid decays expected in the tissue with a high iron content. However, some decays observed were still too rapid to be reliably measured. An estimation of the minimum echo decay that can be measured using the optimised scan sequences for the 400 MHz probe at the University of Warwick was made.

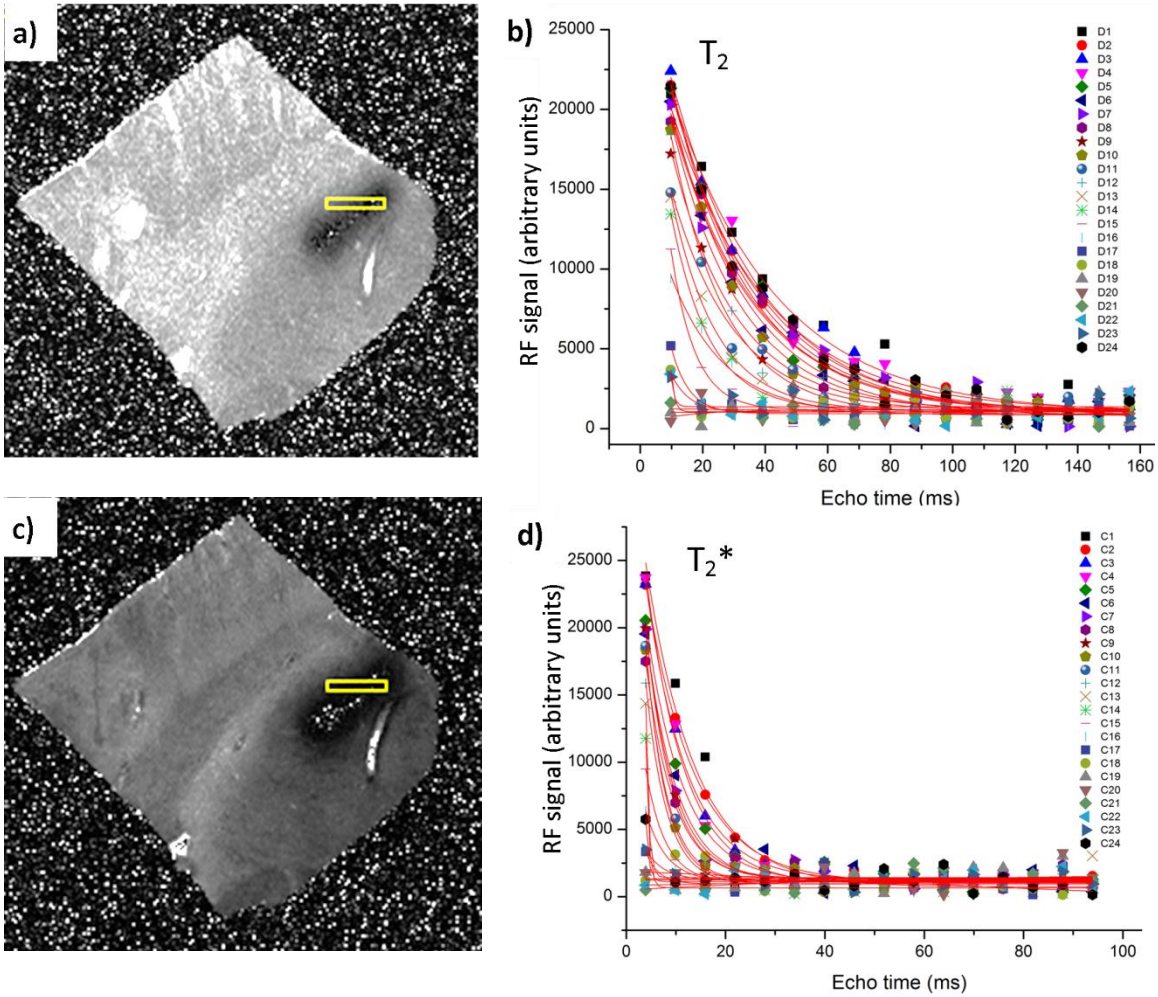

Figure 4.8: ImageJ maps and Origin fitting of the same MRI data. a) A T_2 map of putamen sample AD3 with an ROI drawn over a region of signal drop-out. b) The pixel values from one row of the ROI are plotted for the 16 original echoes and fitted in OriginPro 8.5. c) and d) show the same principle for the corresponding T_2* map.

a)

	Origin			ImageJ		Origin			ImageJ
Pixel	T_2 (ms)	Error (%)	r^2	T_2 (ms)	Pixel	T_2 (ms)	Error (%)	r^2	T_2 (ms)
D1	33.287	9.5	0.9785	33.287	D13	14.405	6.4	0.9877	14.405
D2	26.089	4.9	0.9933	26.089	D14	12.173	11.9	0.9598	12.173
D3	29.134	7.5	0.9851	29.134	D15	7.610	15.1	0.9524	7.610
D4	30.301	11.9	0.9645	30.301	D16	17.045	19.1	0.8975	17.045
D5	24.992	7.2	0.9853	24.992	D17	5.596	33.0	0.8604	5.596
D6	24.415	8.3	0.9805	24.415	D18	1.007	37494.7	0.5611	1.699
D7	26.078	10.1	0.9719	26.078	D19	14.420	334.5	-0.1161	14.417
D8	26.603	8.7	0.9791	26.603	D20	-477.831	-2945.9	-0.0983	1.200
D9	20.391	11.1	0.9633	20.391	D21	-60.039	-910.3	-0.1410	1.614
D10	22.056	8.5	0.9790	22.056	D22	5.872	69.1	0.5433	5.872
D11	20.153	10.1	0.9698	20.153	D23	1.022	51499.3	0.3080	1.748
D12	17.493	7.0	0.9849	17.493	D24	28.298	7.3	0.9859	28.298

b)

	Origin			ImageJ		Origin			ImageJ
Pixel	T_2^* (ms)	Error (%)	r^2	T_2^* (ms)	Pixel	T_2^* (ms)	Error (%)	r^2	T_2^* (ms)
C1	10.005	13.3	0.9481	10.005	C13	0.579	17232.2	0.9546	1.158
C2	9.709	6.3	0.9880	9.709	C14	0.609	5878.5	0.9863	1.212
C3	8.209	3.3	0.9967	8.209	C15	3.917	22.0	0.9196	3.917
C4	7.782	6.1	0.9890	7.782	C16	4.122	33.7	0.8176	4.122
C5	7.455	7.2	0.9849	7.455	C17	2.548	121.7	0.4310	2.548
C6	6.328	11.9	0.9624	6.328	C18	--	--	--	28.784
C7	5.657	7.9	0.9843	5.657	C19	--	--	--	0.656
C8	5.537	10.3	0.9738	5.537	C20	--	--	--	0.700
C9	5.223	12.4	0.9643	5.223	C21	55.434	242.8	0.1156	0.712
C10	4.294	9.8	0.9812	4.294	C22	--	--	--	0.486
C11	3.999	10.9	0.9785	3.999	C23	3.726	56.4	0.6367	3.726
C12	4.187	11.0	0.9768	4.187	C24	0.624	22762.1	0.7509	1.229

Table 4.4: Comparing ImageJ calculations of T_2 and T_2* by ImageJ and Origin in a region of high signal drop out. a) Shows the value of T_2 calculated by ImageJ and the results of fitting to the same points with OriginPro 8.5, which gives an error and r^2 value for each fit. b) Shows the results for a set of T_2* data.

T_2 (or T_2*) is the time taken after the excitation pulse is switched off for the signal to decay by 63% (37% remaining). Therefore a T_2 of less than T_E can be measured, as long as the signal is still sufficient above noise and T_E cannot simply be taken as the minimum measureable relaxation.

As detailed fitting information (error, r-squared) is not attached to each pixel in a fitted T_2 map in ImageJ, a sample of pixels was selected and the decays for each pixel fitted in the software OriginPro 8.5 (Origin). Putamen sample AD3 was chosen as this contains a very high iron

inclusion that ImageJ struggles to fit. This is later shown to coincide with a region of very high iron due a blood vessel. An ROI was drawn so as to include some of this signal drop out as shown in Figure 4.8 a). Each ROI is 4 rows (labelled A-D) and 24 columns (numbered 1-24). The ROI can be saved as a text image providing the value of T_2 for each pixel.

The same ROI was overlaid onto the original 16 echoes and Origin was used to plot the decays of the all the pixels from row D of the ROI. These data were then fitted in Origin to the same exponential decay function used by ImageJ and Paravision: Equation 4.3. Figure 4.8 b) shows the fit to each pixel and the Table 4.4 a) shows the calculated value of T_2 for each pixel calculated in Origin and the result from the ImageJ MRI processor plugin. The table shows that there is very good agreement between the T_2 values calculated in ImageJ and by fitting in Origin. This holds for all T_2 values from 5.9 ms (pixel D22) and above, but not so well for any of the pixels where T_2 is less than 2 ms (D23, D21, D20, D18).

The error in T_2 is typically around 10% until the decay is faster than around 20 ms. At approximately this value the r-squared (r^2) value of the fit begins to decrease. However, there are exceptions such as point D13 where a T_2 of 14.405 is calculated by both Origin and ImageJ and the fit is good and r^2=0.99.

The ImageJ T_2* map is shown in Figure 4.8 c) and the Origin fits in d). Table 4.4 b) provides T_2* values as calculated in Origin and in ImageJ for pixels in row C. There is extremely good agreement between the results until T_2* falls below ~ 2 ms. However, the fit quality drops and the error increases for values below ~ 5 ms.

The minimum measureable decay is dependent to the size of the signal as well as the value of T_E. Where there is higher initial signal, signal remains above background for long enough to fit a decay, even when it is very rapid. Therefore it is difficult to determine a precise value for the minimum measurable decay. However, after examining the sample data above T_2 decays of

less than 20 ms and T_2* decays of less than 5 ms will be treated with caution. This corresponds to $R_2 > 50\ s^{-1}$ and $R_2^* > 200\ s^{-1}$.

It is worth noting that in most instances the values of individual pixels are not examined, but instead the average over a particular region. If the majority of the pixels in the region have a decay that can be well fitted this reduces the impact of any individual pixels with very rapid decays which may be poorly fitted.

4.4 Synchrotron X-ray fluorescence mapping

Tissue sections cut from the MRI imaged tissue blocks and matched to the high resolution MRI maps (as described in Section 3.3.3) were taken for synchrotron X-ray fluorescence (SXRF) mapping at the Diamond Light Source where data were collected.

Region	Case Number	Map Resolution	Experiment Number	Date	Collection Mode	Attenuators	Software
Pons	C2	60 µm	DLS2	Sept 2009	Step	none	GDA
		3 µm	DLS4	July 2011			
	AD2	60 µm	DLS3	Aug2010			
		10 µm					
		3 µm	DLS4	July 2011			
	PD1	60 µm	DLS3	Aug 2010			
		10 µm					
		3 µm	DLS4	July 2011			
	MSA1	60 µm	DLS1	Sept 2009			
		3 µm	DLS4	July 2011			
CN	C2	60 µm	DLS5	March 2012	Continuous	0.15 mm Al	RCP
CN	AD1						
Pu	C3						
Pu	AD3						
GP	C3						
GP	AD2						
SN	C2						
SN	AD2						
Amyg	C3						
Amyg	AD2						

Table 4.5: Summary of SXRF experimental details for all SXRF mapping experiments. The pons samples were mapped over a number of experiments. All other regions were mapped during experiment DLS5. These samples were from the caudate nucleus (CN); putamen (Pu); globus pallidus (GP); substantia nigra (SN) and amygdala (Amyg). The details for each case are given in Table 3.4.

Data were collected during five visits to the Diamond Light Source (DLS). The experiments have been labelled in chronological order DLS1, DLS2 and so on. Table 4.5 lists all of the samples mapped, during which visit they were mapped and what the experimental set up was on that occasion. After mapping the data were processed to create iron, copper and zinc maps which show the relative metal concentration distribution across an individual map and between different samples. Note, experiments DLS1 and DLS2 were carried out by Dr Joanna Collingwood before the beginning of this PhD.

4.4.1 Data collection at the Diamond Light Source

The iron distribution in the tissue sections was mapped at the microfocus spectroscopy beamline, I18, at the DLS in a similar way to that described by Collingwood *et al.* 2005 [82].

4.4.1.1 Hardware

The X-ray beam at I18 can be tuned to a specific energy and focused with silicon KB mirrors and slits to square spot sizes from approximately 100 x 100 to 3 x 3 μm. Focussing is carried out by Diamond beamline scientists at the beginning of each experiment and the hardware settings for a number of spot sizes is stored so that they can be recalled to focus the beam to the desired size during the experiment.

The beam energy at I18 can be tuned to between 2 and 20 keV (core energy 5 to 17 keV) and was tuned at the beginning of each visit to 10 keV. The energy of the beam at the sample is very stable with a variation of only ± 0.05 eV per day.

When the beam is tuned to 10 keV, the flux at the sample is 4 x 10^{12} photons per second (ph/s). However, before the beam impacts the sample there is the option of reducing the signal intensity by inserting attenuators into the path of the beam. It may be prudent to reduce beam intensity in order to protect a delicate sample or to reduce the intensity of scattered X-rays and to prevent detector saturation. The final X-ray beam that impacts the sample is named I_0 and is monitored immediately upstream of the sample.

Figure 4.9 shows the experimental set-up of the sample and detector for SXRF mapping at beamline I18. The quartz slide containing the tissue sample is mounted onto a slide holder, which sits on the sample stage, and held in the path of I_0 at an angle of 45°. The detector is a 9 element Ge detector with an energy range of 4 – 20 keV and is positioned at 90° to I_0.

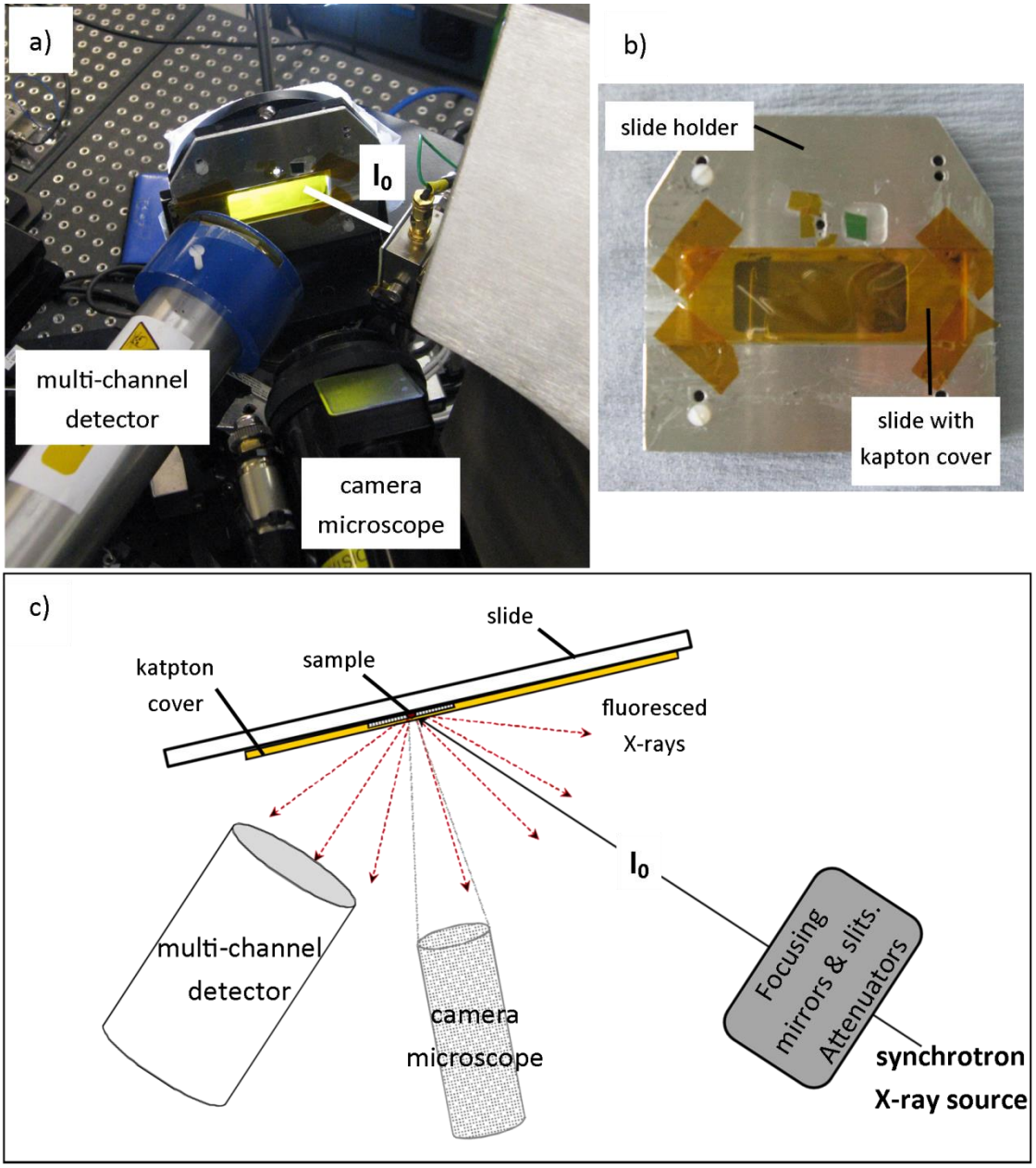

Figure 4.9: Experimental set-up for SXRF mapping at beamline I18. a) A photograph taken at I18 showing the configuration of the sample, detector, camera and the approximate position of I_0. b) A slide, covered in a katpton film, mounted onto the sample holder. c) A schematic of the experimental set-up.

The microscope camera allows the sample position to be viewed from the experiment control station. The microscope focus is locked to the focal point of the beam. To bring the sample into the focal point of the microscope (and hence of the beam) it can be moved back and forth (z-

direction) by moving the sample stage which is controlled by a piezoelectric motor. The sample stage can also be moved left and right (x-direction) and up and down (y-direction) in steps of one micron to create the SXRF map. When the sample is in focus the X-ray beam is at or near the centre of the image from the microscope.

4.4.1.2 Software

General Data Acquisition (GDA) software, co-developed by DLS and STFC (Science and Technologies Facilities Council) staff, is used to control the data acquisition at the beamline. Two different versions of the software were used over the duration of this project (see Table 4.5 for details of which software was used for each map). All of the pons data were collected using the old GDA software, which produced a large number of data files, in multiple formats, for each map.

At the last experimental visit to Diamond, when the majority of the samples were measured, the software had been updated to the RCP version of GDA, which exports all of the SXRF data for each map in one NeXus file. The data output from the different software requires slightly different processing – see 4.4.2 SXRF *data processing*.

4.4.1.3 Mapping protocol

4.4.1.3.1 Set up

Once the slide was mounted on the sample stage the first step was to set up the coordinates for the map. The microscope camera was used to confirm that the sample was in the focal plane, after which z was kept constant throughout mapping. Then the x and y coordinates were chosen. The microscope camera allowed a reasonable amount of detail to be seen on the tissue section, in particular grey and white matter could be differentiated. Photographs of the slide and stained adjacent or neighbouring slides were used to help select the area. It is important to carefully select the map area as mapping at high resolution is time consuming

and experimental time at the facility was limited. A region of slide with no tissue was included in the map of each sample so that slide signal could later be subtracted.

Whilst the map coordinates were being selected, the X-ray beam was prevented from reaching the samples by one of two shutters. This prevented unnecessary exposure of the tissue to the very high intensity X-rays, which can damage the sample over time. Keeping this shutter closed when not measuring is good practice at all times.

The spot size used to make the large, main map for each sample was 60 x 60 μm. Therefore each point on the map was effectively measuring a volume of 60 x 60 x 30 μm of wet tissue. Maps with smaller area and higher resolution were also collected for the pons samples (see Table 4.5).

Before mapping was initiated, the signal intensity to the detector from an area of tissue was assessed to see if the detector filling fell within the minimum and maximum ideal filling range defined in the software. If the signal was too high an attenuator was inserted into the beam to reduce the flux on the sample. For low detector filling the collection time could be increased, however this was not necessary for any of the experiments. To reduce variability between measurements the collection time and attenuation was kept the same where possible during each experimental visit (see Table 4.5 for details).

4.4.1.3.2 Making a map

There are two modes of mapping i) Step Mode and ii) Continuous Mode. In the first mode the sample is moved by one step (where step size is matched to beam spot size) and then the detector collects for a set time (one second per point for these samples), before the sample is moved to the next point in the map. In this mode approximately 0.5 seconds is lost between each point as the sample stage is moved. Therefore, with a collection time of 1 second per point, the actual mapping time is approximately equal to the number of points multiplied by

1.5 seconds. An overhead of 50% is significant when mapping 1 cm^2 at 60 x 60 µm resolution (equating to 11.5 hours to map 28 000 pixels).

In the second mode the detector collects continuously and the sample is moved continuously through the beam. The time to scan an entire row and the number of points in the row is set by the user. This information determines the collection time per point and the data are divided accordingly as the detector collects. In this mode the effective collection time per point is set by the user and there is no 'lost' time between points. Therefore up to 50% of mapping time is saved compared to stepwise mapping. However, there are some limitations to the time saving in this mode. Most significantly, the detector collection and mapping on I18 is set up so as to pause during electron beam top-up which happens every 10 minutes. This wait cannot occur during a row collection in continuous mode and therefore the software will not begin a row if it cannot complete it before the top up is due. Therefore, depending on row length, there could be regular long waits when no mapping is occurring. This wasted time can be minimised by calculating the optimum row lengths to fit between top-ups. This forces rows of certain lengths, reducing the flexibility of map dimensions.

4.4.2 SXRF data processing

The raw data files for each SXRF map contain the fluorescence spectrum for each pixel. In order to produce comparable maps of relative iron, copper and zinc concentration, the fluorescence peaks in these spectra need to be fitted and the area under the peaks calculated. Maps must also be normalised to correct for variation due to fluctuating beam intensity and minimise experimental error. The open source software packages PyMCA [183] and ImageJ [180] were used to process the data.

4.4.2.1 Output data files

Software updates at DLS beamline I18 mean that the data were exported in two formats. Data collected using the old GDA software (all of the pons maps) were exported in a number of

separate files: MCA (Multi-Channel Analyser), DAT and RGB files. The fluorescence spectra are exported in a large number of MCA files, one for each point on the map. DAT files contain the information needed to spatially arrange the MCA files into one SXRF map.

In order to process the data in PyMCA the MCA files need to be converted into a set of EDF (ESRF (European Synchrotron Radiation Facility) Data File) files, one for each map row. A macro called 'dls_writeedf2.exe' written by DLS staff was used to convert MCA files into EDF files.

The RGB files contain an initial estimate of the SXRF signal intensity for key metals expected in biological tissue. They are produced without fitting the fluorescence peaks but by assigning all fluoresced x-rays over a set range to a particular metal. This does not correct for any overlapping peaks or correct properly for background and therefore does not provide the accurate measurement of relative metal concentration that fitting the peaks does. However, the RGB files produce an instant estimation of metal distribution that is useful during mapping. They also contain the intensity of I_0 for each point on the map.

The majority of the data were collected using the RCP software. This exports the data in the form of NeXus files which can be read directly into PyMCA. A NeXus RGB file is also produced for each of these maps.

4.4.2.2 Fitting SXRF spectra

PyMCA was used to fit the fluorescence spectra that make up the SXRF maps. Firstly a master fitting configuration file was created by fitting the average fluorescence spectrum of the whole map and then this file was used to fit the individual spectra collected for each pixel on the map. Figure 4.10 shows the result of careful fitting to a typical fluorescence spectrum.

The process of creating the configuration file is described in full in Appendix D. In summary: firstly, the energy of the detector channels was calibrated using the characteristic peaks in a fluorescence spectrum of brain tissue (as shown in Figure 2.8 in section 2.3.2) and secondly, the 'Advanced Fit' tool was used to fit the peaks and the background signal, including the edge

of the scatter peak. One master configuration file was saved and reused, however for each new map the fitting was checked and the fitting parameters adjusted if necessary.

The output of batch fitting is a single DAT file for each map. When opened using the PyMCA 'RGB Correlator' tool the file contains a map for each metal fitted. Each point on the map represents the area under the fluorescence peak for that particular metal: the map shows the relative metal concentration distribution for that sample.

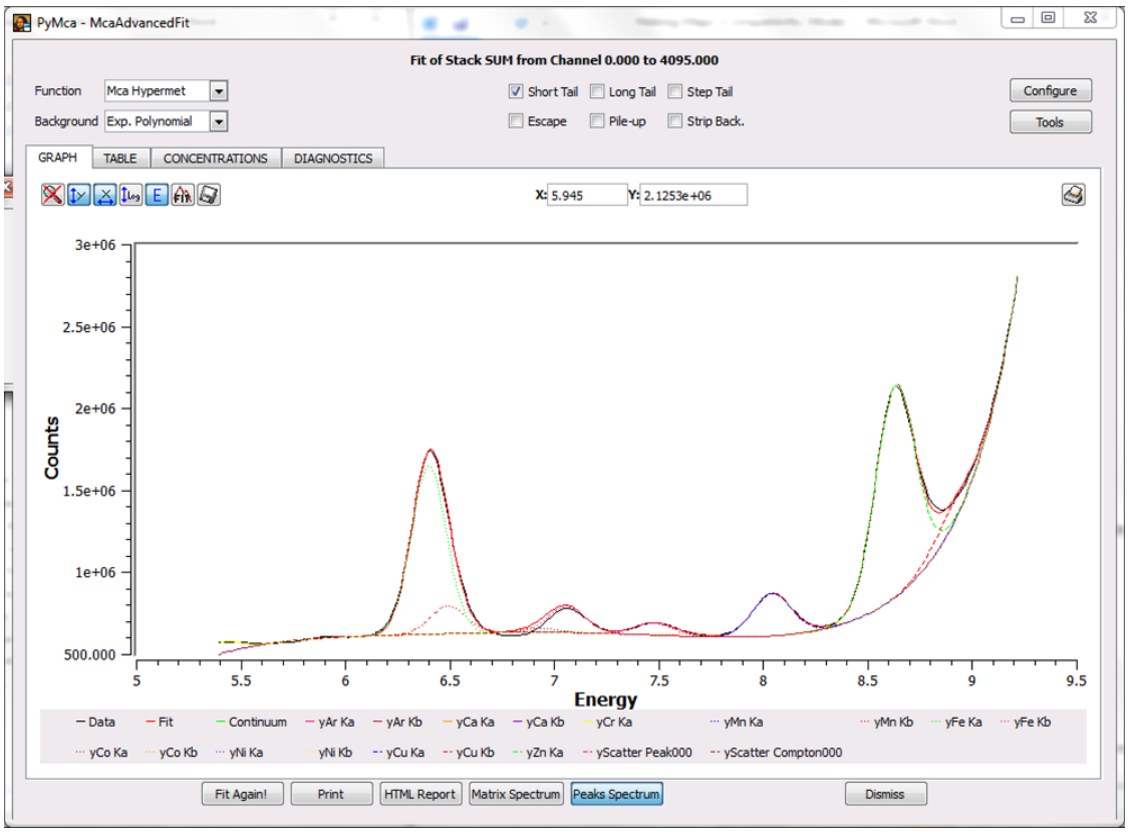

Figure 4.10: A typical fitted fluorescence spectrum in PyMCA. The spectrum is the average of a whole map. Each metal peak and the background, including the edge of the scatter peak, has been fitted.

4.4.2.3 Normalising data and subtracting background signal

Fitting the SXRF spectra provides very sensitive and specific maps of iron (and copper and zinc) distribution across individual tissue samples. In order for the maps to show relative concentration across the section and between different samples they must be carefully normalised to correct for a number of experimental variables. Table 4.6 lists the possible sources of experimental error and the normalising step which was taken in order to correct for

that factor. Note: these variables have been kept constant where possible, but some variation is unavoidable, particularly between visits to the DLS.

Source of Experimental Error	Correct by normalising to:
Changing electron beam intensity	I_0
Attenuator used	I_0
Detector position	Fe signal of quartz slide

Table 4.6: Normalisations made to SXRF maps. The sources of experimental error are corrected for by normalisation to I_0 or the iron signal from the slide.

Although the tuned energy of I_0 is very stable the intensity can vary: between experiments, over the course of one visit and also during the time taken for a map to be made. The intensity of I_0 is determined by the electron beam in the synchrotron and this has a step profile as the beam decays over time and is periodically topped up. Figure 4.11 shows the typical variation of I_0 for each pixel of a map. Changes to the intensity of I_0 (and therefore to the flux of X-rays on the sample) proportionately change the number of fluoresced X-rays. Normalising each pixel in a metal map to I_0 for that pixel will correct for this variation.

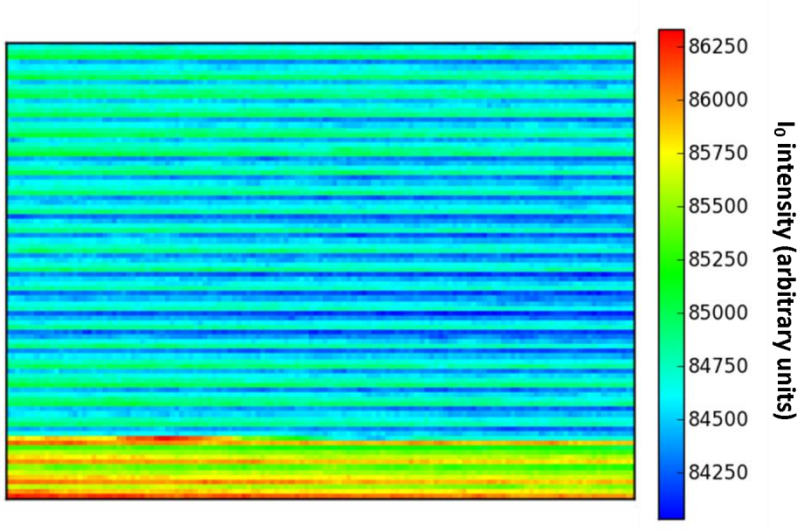

Figure 4.11: Variation of I_0 over the course of SXRF map data acquisition. I_0 varies over time and therefore for each pixel of an SXRF map, as shown above using a temperature scale.

Normalisation to I_0 was done using the RGB Correlator tool in PyMCA. Both the fitted metal maps (in the DAT file produced by batch fitting) and the I_0 map (from the RGB file) were opened in RGB Correlator and the Image Calculator Tool used to divide each metal map by the I_0 map. The normalised maps were saved together into a new DAT file. The insertion of attenuators into the X-ray beam also affects the intensity of I_0 and was therefore corrected for by this process.

A potentially major source of experimental error was the detector position. The distance and angle of the detector relative to the sample affects the amount of fluoresced X-rays received. The position of the detector varied considerably between visits to the DLS as changes were made to the experimental set-up. During some visits the detector could remain untouched during the whole experiment, but in others it was moved in and out of position during sample changes. This was the case for DLS5 and although the position of the detector was set with marker to minimise error, small variation in position is possible.

As all samples were mounted on the same type of quartz slide, and each map included an area of slide, the average signal from the slide can be used to normalise for changes in detector position. For each of the metal maps (iron, copper and zinc) the average slide signal for that metal was subtracted from the each pixel on the map. Then each pixel was normalised to the average iron signal of the slide. Details of the slide background signal and how the normalisation affected each sample are given in Chapter 6 Section 6.1.2 *Normalising to slide background.*

4.4.2.4 Exporting maps for further analysis in ImageJ

The normalised metal distribution maps were analysed using the open access, image processing software ImageJ. Before this was possible the maps had to be converted from the DAT format into an image format, TIFF, with one file produced for each metal map. This conversion was done using a macro written in Python by DLS beamline scientist Paul Quinn

called ‘rgb_to_manyimages2.py’. The resulting TIFFs are maps for which the value of each pixel is the fitted area under the fluorescence peak for that metal, normalised to incoming beam.

As is the case for the MRI maps, ImageJ was used to create ROIs around different tissue structures and measure their mean normalised SXRF signal intensity. How maps were segmented will be further described in Chapter 6: *Synchrotron X-Ray fluorescence mapping*.

4.5 Histology

4.5.1 Staining sections on glass with Congo red and haematoxylin

Tissue sections cut from the MRI blocks were sectioned at 30 μm (as described in Section 3.3.3) and were stained with Congo red and haematoxylin using the solutions and staining protocols below, that were based on protocols from *Histological and Histochemical Methods: Theory and Practice* by Kiernan [99].

The haematoxylin solution used is an alum haematoxylin, or haemalum solution [99]. This is commonly referred to as haematoxylin and will be known as such throughout this thesis. Haematoxylin stains cell nuclei and therefore reveals the cell distribution in tissue sections. Congo red stains a number of substances including amyloid, however the amyloid staining can be confirmed by the apple green birefringence displayed under crossed polarised light.

Two baths of xylene were used: the ‘dirty’ bath was used first and the ‘clean’ one second. This was to try and minimise any dust and dirt appearing on the slides after staining.

Protocol for making Congo red stain:

- 100 ml ethanol
- 100ml water
- 1 g congo red
- Stir

Protocol for making haematoxylin stain:

- Boil 0.2 g haematoxylin in 100 ml ultrapure water
- Add 100 ml ultrapure water
- Add 10 g aluminium potassium sulphate
- Add 0.04 g sodium iodate
- Cool and filter

Congo red and haematoxylin staining Protocol:

i) Hydrate to 30%:
   a. 100% ethanol, 7 minutes
   b. 70% ethanol, 3 minutes
ii) Congo Red, 5 minutes
iii) Rinse in distilled water
iv) KOH in ethanol to differentiate stain , about 2 minutes 30 seconds
v) Tap water wash, 3 minutes
vi) Haematoxylin: 4 minutes
vii) Tap water wash in large beaker
viii) Tap water and 6 drops NaOH 10 M: 1 minute
ix) Tap water wash
x) Dehydrate:
   a. 70% ethanol, 3 minutes
   b. 100% ethanol, 3 minutes
xi) Clear in xylene
   a. 'Dirty', 3 minutes
   b. 'Clean', 3 minutes
xii) DPX mountant and cover slip

4.5.2 Staining post-SXRF

In past SXRF studies in our group, problems have been encountered with staining SXRF mapped tissue. Sections tended to float off slides, breaking apart and crumpling when staining solutions were applied. As part of the work towards this thesis, a protocol was developed to provide reasonable quality staining of sections post-SXRF mapping.

The difficulty in staining SXRF mapped sections is caused by tissue fragility due to exposure to extremely intense X-rays during mapping. Additionally, the very clean quartz slides the sections are mounted on do not have the adhesive coating that standard histology slides do.

It was noted that the sections began to float off the quartz slides as soon as the slides were placed in 70 % ethanol to begin section hydration and that detaching was aggravated by the motion of moving the slide in and out of staining baths. Therefore the protocol was designed to include gradual hydration and minimal turbulence. The protocol was tested using thoroughly dried tissue sections on quartz slides. Although these sections were not as fragile as the post-SXRF samples, they allowed protocol development without risking valuable mapped samples.

The final protocol does not include staining with Congo red as at the stage of differentiating the staining intensity with KOH in ethanol the section lifted completely from the slide and crumpled. Therefore SXRF mapped samples were only stained with haematoxylin. Adjacent samples, which were also stained with Congo red, were used to look for signs of amyloid deposition.

The preparation for staining began with removing the kapton film from the slide and carefully scraping off any epoxy glue on the front of the slide using a razor blade. This is an important step as any glue on the surface of the slide will create an uneven texture and prevent good contact between the cover slip and the slide at the end of staining.

PAP pen is then used to draw a ring around each sample which is then left to dry for at least 10 minutes. This creates a water-proof ring into which solutions can be carefully pipetted, using a 200 µl pipette, making a droplet which covers the surface of the section. The reduced turbulence and volume of solution stopped the sections from detaching from the slide. The solutions were removed from the slide by carefully absorbing the droplet with a cotton bud.

Once the PAP pen had dried, the tissue was stained following the protocol below.

i) Fix in ice cold 100% ethanol for 10 minutes
ii) Gradually bring to water, 2 minutes 30 seconds in each of the following:
    a. 95% ethanol
    b. 90% ethanol
    c. 80% ethanol
    d. 70% ethanol

e. 50% ethanol
f. 30% ethanol

iii) Ultra-pure water, 3 minutes
iv) Haematoxylin, 1 minute 30 seconds
v) Tap water wash, several changes
vi) Tap water and NaOH, 1 minute
vii) Dehydrate:
a. 70% ethanol, 2 changes of 2 minutes 30 seconds each
b. 100% ethanol, 3 changes of 1 minute 30 seconds
viii) Clear in Xylene
a. 'Dirty' xylene, 5 minutes
b. 'Clean' xylene, 3 minutes
ix) Cover slip with DPX mountant.

To carry out step i) 'fixing in ice cold ethanol' the slide was placed in a petri dish on top of an ice pack and 100 % ethanol at -25 °C was pipetted onto the tissue. The petri dish was then covered and left for 10 minutes. Covering the dish is important in order to reduce both ethanol evaporation and water condensation onto the cold slide. Condensation across the surface of the slide reduced the efficacy of the PAP pen barrier and could lead to the droplets of liquid spilling out and running all over the slide, which reduced the control over staining. After 10 minutes the petri dish was removed from the ice pack and the ethanol removed. Step ii) was carried out using chilled ethanol, but no ice pack.

Note that sufficient dehydrating in step vii) required multiple changes of ethanol to make up for the small volume of ethanol that is in contact with the section in this droplet technique.

It was not possible to carry out xylene clearing (step viii) using the droplet method for a number of reasons, including the fact that xylene dissolves PAP pen and also evaporates very quickly. Therefore the PAP pen was wiped off using a cotton bud dipped in xylene and then the slide was very carefully lowered into the two xylene baths, one after another. Occasionally the sections could be seen to begin to detach from the slide, but with careful handling all samples were retained.

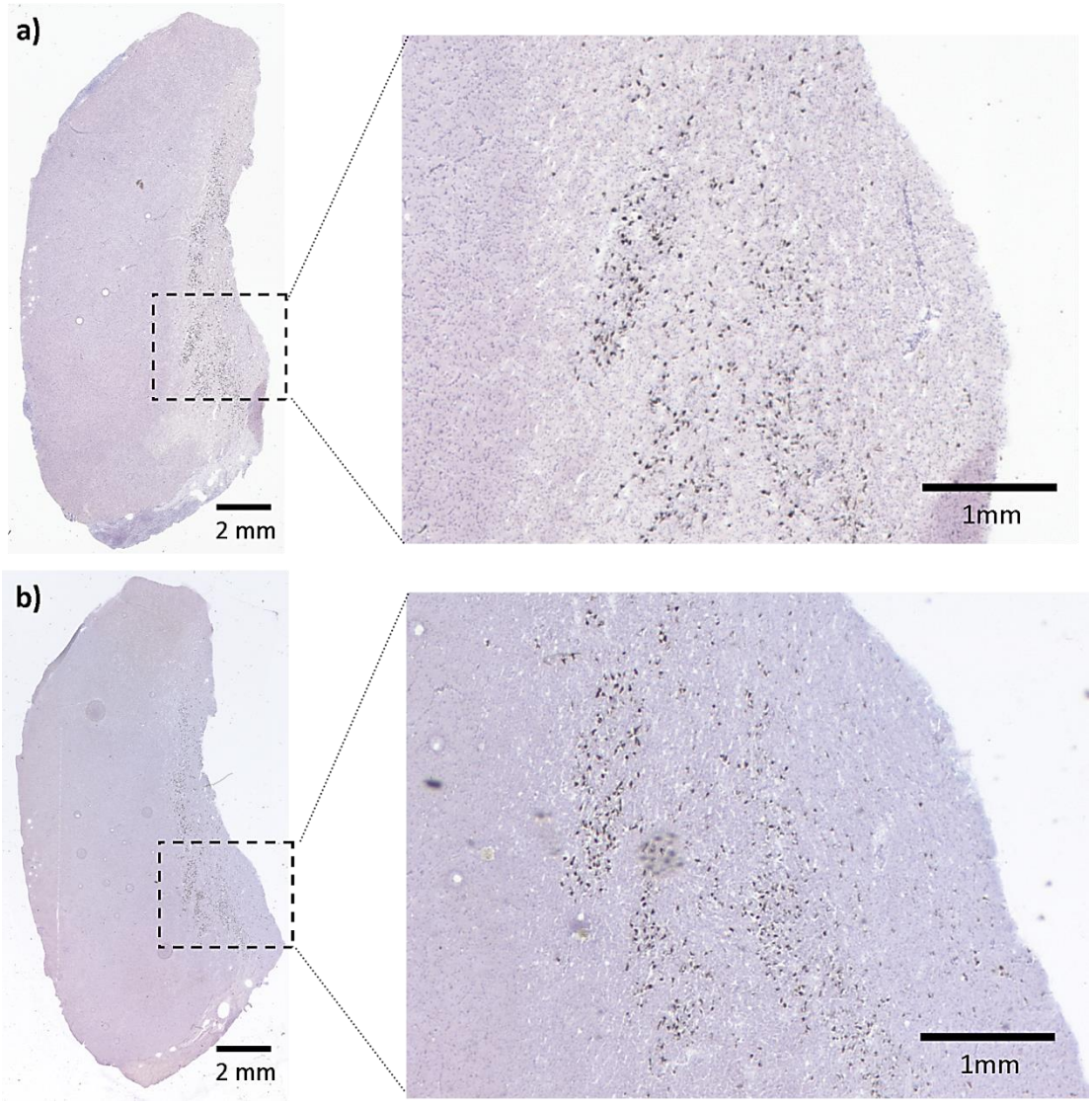

Figure 4.12: Staining of SXRF mapped tissue compared to non-mapped tissue. Slide scan images of haematoxylin stained sections from substantia nigra sample AD2. a) The stained section on glass shows good contrast between tissue types in addition to nuclear staining. b) The section on quartz, stained after SXRF mapping, still shows nuclear staining, but a predominantly uniform background stain.

The result of staining post-SXRF sections using the above protocol, as compared to staining the fresh-frozen tissue on glass, is shown in Figure 4.12 for substantia nigra sample AD2. The staining for the tissue on glass (a) shows clearer differentiation between tissue types and is much sharper than the staining of the tissue post-SXRF mapping (b). The difference in staining quality is due both to the damaged tissue and to the protocol: the protocol does not allow for rapid changing between solutions or thorough soaking in each solution.

As the staining is better for un-mapped tissues, and includes Congo red stain, in general an adjacent or near section is used for comparison to the SXRF maps to identify structures.

However, where this staining is particularly useful is for high resolution maps (as were made of the pons) where staining information at cellular level is required. Figure 4.13 shows the staining of pons sample AD2 after SXRF mapping. Part a) is a slide scan image of the entire sample and areas of high resolution mapping can clearly be observed. The higher resolution SXRF mapped areas are shown as microscope composite images in b), mapped at 10 µm, and c), mapped at 3 µm. The staining quality reduced as the resolution of the mapping increased. However, some individual cells can be identified in the area of the 3 µm map. This image is examined further in Chapter 6, Section 6.5.2 and is used to help compare the relative metal concentrations in the neurons of the pons.

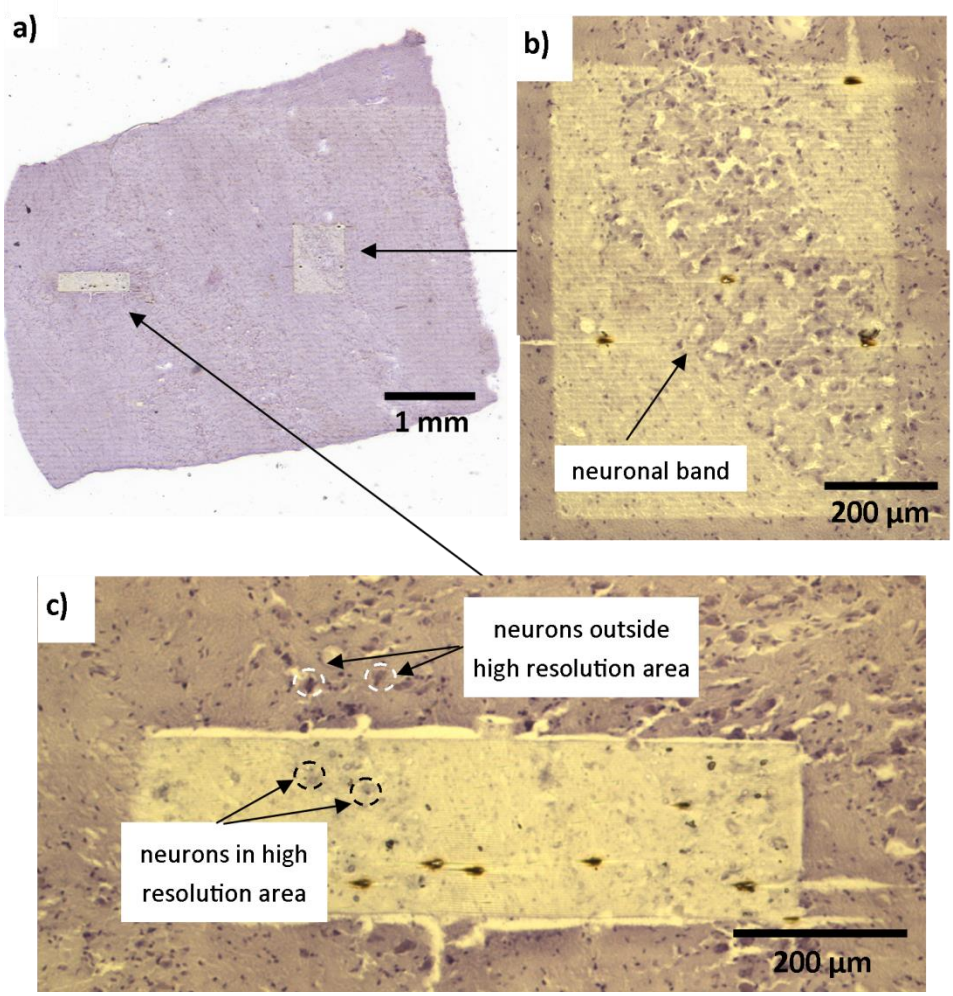

Figure 4.13: Staining of high resolution SXRF-mapped tissue. a) A slide scanned image of the section from pons sample PD1, which contains areas mapped at high resolution. Microscope images are shown of these areas: b) mapped at 10 µm and c) mapped at 3 µm. A band of neurons runs from top left to bottom right through b). Staining is very light in the mapped area in c), but some individual neurons can still be identified, with two examples circled inside and outside of the high resolution area.

4.6 Statistical analysis techniques

The data sets in this thesis are very small with n=3 for each disease group, therefore statistical analysis is non-trivial. A property of statistical testing is that it is hard to reach statistical significance with a low number of samples. However, in order to correctly describe the significance the test used must be suitable for the data. Where possible the tests used are those recommended for small sample sizes and all assumptions made about the data are tested as far as possible.

Statistical analysis was carried out using SSPS Statistics Version 21 and Laerd Statistics tutorials (2013) [184] for reference. Unless otherwise stated statistical significance will be indicated as follows: * $p<0.05$; ** $p<0.01$; *** $p<0.001$.

4.6.1 Analysis of variance

One-way ANalysis Of VAriance (ANOVA) tests for statistically significant differences between group means of two or more groups of independent samples using an F-test. The data must be grouped by an independent, categorical variable (in this project this is always disease state) and the dependent variable data in each group must be continuous (for example, tissue iron concentration).

The main principle of AVONA is to compare the within-group variance to the between-group variance, which is the total variance minus total within-group variance [185]. Here variance is the sum of squares. If the sum of the variance within the groups is approximately the same as the total variance, then any difference in means can be explained as being due to random sampling effects. If the between group variability is larger than the total within-group variability, then there may be a statistically significant difference between the means. One-way ANOVA uses F-test to calculate the p-value.

The null hypothesis for one-way ANOVA is that there is no difference between the group means. Therefore when this is violated there is at least one group mean that is different.

However, one-way ANOVA does not compare between individual pairs of means and a *post-hoc* test is required to find the p-value between each possible pairing.

One-way ANOVA makes a number of assumptions about the data: i) there are no outliers; ii) the data follow an approximately normal distribution and iii) the data in each group have equal variance. It is important to assess whether the data fit these assumption. However, ANOVA is robust enough to provide valid results even if this assumption is a little violated.

4.6.1.1 One-way ANOVA using SSPS

First the data were tested for outliers and for normality. The 'Explore' option was selected from the 'Descriptive Statistics' menu and the options 'Outliers' and 'Normality plots with tests' selected. The results of the Shapiro-Wilk test for normality were used, which is the recommend test for small sample sizes. The null hypothesis, which is that the data follow a normal distribution, is violated if $p<0.05$. Provided the null hypothesis is not violated parametric statistical tests are suitable for analysing the data.

SSPS can be used to test for the equal variances assumption using Levene's Test for Homogeneity of Variance at the same time as carrying out one-way ANOVA. Both one-way ANOVA assuming homogeneity of variance, and a second robust ANOVA (Welch's ANOVA) in case this assumption is violated, were performed simultaneously. The data were then interpreted based on the result of Levene's Test.

The 'One-way ANOVA' option was selected from the 'Compare Means' menu. Then the options 'Descriptives', 'Homogeneity of variance' and 'Welch' were selected. *Post-hoc* tests were also selected to examine the difference between individual group means when there are more than two groups. Tucky's *post-hoc* test is valid if the data shows equal variance and the Games-Howell test in the case of unequal variance. These tests were selected before the analysis was run.

The result of Levene's test are given in the output file. The null hypothesis is that homogeneity of variance is equal and this is considered violated if $p<0.05$. For a data set for which $p>0.05$ the results of one-way ANOVA and Tucky's test were recorded. Where $p<0.05$ the result of Welch's ANOVA and the Games-Howell test are shown. When results are presented the result of the tests for normality and homogeneity of variance will not be stated in each case, but the type of AVONA and *post-hoc* test will be stated.

4.6.2 Non parametric statistics

ANOVA is only valid when the data follow a normal distribution. If the data were shown to violate the Shapiro-Wilk test for normality a non-parametric test, which does not make assumptions about the shape of the distribution, was used.

The 'Two or more independent samples option' was selected from the 'Nonparametric' menu. The 'Kruskal-Wallis' test was chosen on the settings tab. This is a nonparametric equivalent to one-way ANOVA. The pairwise comparison option was selected so that the output will include comparison between pairs of groups.

4.6.3 Linear regression analysis

Linear regression analysis is used to create a linear model to describe the relationship between a dependent variable and one or more independent variables or predictors. When the model contains only one predictor the analysis is called simple linear regression and the model takes the form of the familiar equation for a straight line:

$$y = mx + c \qquad (4.5)$$

Where y is the dependent variable; x is the predictor; m is the gradient of the line and c is the intercept where x is equal to zero.

Where there is more than one predictor (multiple linear regression) the straight line relationship can be described by Equation 4.6, as given in SSPS:

$$y_i = b_0 + b_1 x_{i1} + \cdots + b_p x_{ip} + e_i \qquad (4.6)$$

where y_i is the value of i^{th} dependent variable; p is the total number of predictors; b_j is the j^{th} coefficient and j=0 … p; x_{ij} is the value of the i^{th} case of the j^{th} predictor and e_i is the error in the observed value for the i^{th} case. The intercept, b_0, occurs when the value of all predictors is zero.

The 'Linear' option was selected from the 'Regression' menu and the dependent and independent data entered. The statistics option 'Collinearity diagnostics' and 'Covariance matrix' were selected and the analysis run.

The output for each model includes the value of the constant (b_0) and the regression coefficient (b) for each predictor. The standardised coefficients (B), which can have values of between 0 and 1, allow a comparison of the strength of the relationship of each predictor to the dependent variable where a larger B indicates a stronger relationship. The sign of the regression coefficient gives the direction of the relationship.

The correlation coefficient, r, describes the degree to which the total model is related to the dependent variable. For simple linear regression r is equal to the absolute value of the standardised correlation coefficient B. The goodness of fit can be described by r-squared (r^2) which represents the percentage of the variation of the dependent data which is explained by the fit.

SSPS calculates a p-value for the whole model and for each predictor. When the p-value for the model reaches significance ($p<0.05$) the prediction of the model is better than chance. The p-value for each predictor tests the null hypothesis that the coefficient is zero (that the value of the predictor has no effect of the value of the dependent). When $p<0.05$ the null hypothesis is rejected and the predictor can be considered a significant addition to the model.

4.6.4 Discriminant analysis

Discriminant analysis creates a predictive model to group observations based on the information provided by observations from known groups. Data should be from mutually exclusive groups and each case must belong to only one group. Discriminant analysis also makes the following assumptions about the data: i) predictors are not highly correlated with one another; ii) there is no correlation between the mean and variance of a predictor; iii) correlation between two predictors is constant across groups and iv) the data follow a normal distribution.

In this project the groups are the disease state and the independent variables, also known as 'predictors', could be iron concentration, IRM at 5 K, R_2 or R_2* in a particular brain region, i.e. iron in the pons is a different predictor from iron in the SN. Therefore discriminant analysis can be carried out to investigate how a discriminating model could be built using information from multiple brain regions, rather than looking for statistically significant differences between disease and control for one region at a time.

As described in the previous section assumption iv) can be tested using the Shapiro-Wilk test for normality in the 'Explore' tool from the 'Descriptive Statistics' menu. Some of the other assumptions can be tested in SSPS at the same time as running discriminant analysis. The 'Box M' test (included in the discriminant analysis output file) examines the homogeneity of variance of the data.

The statistical analysis software SSPS was used to carry out discriminant analysis, to test some of the assumptions made and to examine the quality of the model. The 'Discriminant Analysis' option was selected from the 'Classify' menu and the grouping variables (the disease state) and independent variable entered. Then the 'Summary Table' 'Leave-one-out Classification options were selected.

4.6.4.1 Assessing contribution of variables to the model

Another output of discriminant analysis generated by SSPS is a one-way ANOVA test. As described in Section 4.6.1 above, one-way ANOVA tests for any differences between means of each group for each variable. P-values are produced for each variable and low value suggests that the predictor contributes more to the model.

The 'standardized canonical discriminant function coefficients' table shows the order of how important each variable is in discriminating between groups. A large absolute coefficient indicates more discriminating ability.

4.6.4.2 Validating the model

The model is used to classify each of the cases into one disease group. How well the model fits the data can be assessed by checking what proportion of samples were correctly grouped. Information for each individual sample is given by SSPS, meaning the cases which are incorrectly grouped can be identified.

As only the data used to create the model are being assessed the successful classification rate for the model is inflated. In order to partially validate the model SSPS can cross validate each sample by leaving it out of the data used to calculate the model and then classifying it with the resulting model. This is what the 'Leave-one-out Classification' option was selected for.

If a large sample set were available, a randomly selected sub-set of the data would have been excluded from the model. The model calculated using the rest of the data would then be used to classify this set of data and give the percentage of correctly classified samples. This is known as sub-set validation. However, with the small number of samples available for this study sub-set validation was not possible.

Chapter 5:
Bulk tissue iron analysis

In this chapter the total and particulate iron content is investigated in samples from four brain regions: the pons, substantia nigra (SN), putamen (Pu) and caudate nucleus (CN). These measurements are referred to as 'bulk tissue' measurements as they do not have the spatial resolution that is achieved with MRI or SXRF mapping techniques, which are used to examine samples in later chapters.

The literature review in Section 1.3 revealed a number of studies which report increased iron concentration in Alzheimer's Disease (AD) in specific regions of the brain. However, there is disagreement in the literature with some studies showing no statistically significant change. The results of the literature review for the SN, Pu and CN regions are reproduced in Figure 5.1. No data for iron concentration in the pons were found during the literature search.

Putamen	**A** (↑p=0.07) FDIR	**K** Fe Serum	**B** ** FDIR	**C** ** FDIR	**H** * ϕ MRI	**P** * ϕ MRI
Caudate Nucleus	**K** Fe Serum	**C** * FDIR	**B** * FDIR	**P** * ϕ MRI	**A** * FDIR	
Substantia Nigra	**K** (↓ 25%) Fe Serum	**P** ϕ MRI				

Figure 5.1: Literature review of publications comparing iron in control and AD tissue. Blue boxes indicate a study which showed no statistically significant change in iron in AD (where changes were large, or approached significance this information is given in brackets and the direction of change indicated by an arrow). Yellow boxes indicate a study which showed a statistically significant increase, where * $p<0.05$ and ** $p<0.01$. No studies showed a statistically significant decrease in iron with AD. The methods of iron measurement are: FDRI= field dependent R_2 increase; Fe Serum = Ferrochem II serum analysis; ϕ MRI = phase shift MRI. The first letter in each box indicates the reference: A = Bartzokis (1994) [125]; B = Bartzokis (2000) [133]; C = Bartzokis (2004) [126]; H = Ding (2009) [137]; K = Loeffler (1995) [18]; P = Zhu (2009) [139].

For both the Pu and CN the literature review showed that an increase in iron concentration in AD has been indirectly measured using MRI [126, 133, 139], but that in direct measurements of iron concentration in *post mortem* tissue no increase was observed [18]. No statistically significant change in iron concentration with AD was observed by direct [18] or MRI

measurements [139] of the substantia nigra, however increased iron has been reported in this region with Parkinson's Disease (PD) [145]. The literature search did not reveal any reports of iron concentration in control or AD pons tissue.

In this study, iron concentration is measured by acid digestion of freeze-dried tissue samples, followed by GFAAS or ICP-MS. Table 5.1 details the age and sex of each case and Table 5.2 summarises the measurements made on each sample. Three control and AD samples from the pons, substantia nigra, putamen and caudate nucleus are examined. Three PD and Multiple System Atrophy (MSA) samples from the pons, substantia nigra and putamen provide a comparison to other neurodegenerative diseases.

Case Number	Sex	Age	Case Number	Sex	Age
C1	F	47	PD1	M	73
C2	M	78	PD2	M	56
C3	M	76	PD3	F	79
AD1	M	73	PD4	M	76
AD2	F	75	MSA1	M	76
AD3	F	98	MSA2	M	66
			MSA3	F	46

Table 5.1: Age and sex of each case measured by bulk tissue analysis. C = control; AD = Alzheimer's Disease; PD = Parkinson's Disease; MSA = Multiple System Atrophy.

Quantifying the differences in the total iron concentration between control, AD and other neurodegenerative diseases is interesting in terms of increasing our understanding of homeostasis in neurodegenerative diseases. However, it is particulate iron which most affects MRI and is therefore of particular interest in this study. Furthermore, the form of the particulate iron determines the magnitude of the effect on MRI: magnetite, which has been shown to be increased in AD [110], has an approximately 200 times greater effect on R_2 than ferritin [159].

Region	Disease Group	Case	IRM Curves	IRM	ICP-MS	GFAAS
Pons	Control	C1	X	5, 50 and 150 K	X	✓
Pons	Control	C2	X	5, 50 and 150 K	X	✓
Pons	Control	C3	X	5, 50 and 150 K	X	✓
Pons	AD	AD1	X	5, 50, 150 and 300 K	X	✓
Pons	AD	AD2	X	5, 50, 150 and 300 K	X	✓
Pons	AD	AD3	X	5, 50 and 150 K	X	✓
Pons	PD	PD2	X	5, 50 and 150 K	X	✓
Pons	PD	PD1	X	5, 50, 150 and 300 K	X	✓
Pons	PD	PD3	X	5, 50 and 150 K	X	✓
Pons	MSA	MSA1	X	5, 50 and 150 K	X	✓
Pons	MSA	MSA3	X	5, 50 and 150 K	X	✓
Pons	MSA	MSA2	X	5, 50 and 150 K	X	✓
SN	Control	C1	X	5, 50, 150 and 300 K	X	✓
SN	Control	C3	X	5, 50, 150 and 300 K	X	✓
SN	Control	C2	X	5, 50, 150 and 300 K	X	✓
SN	AD	AD3	X	5, 50, 150 and 300 K	X	✓
SN	AD	AD1	X	5, 50, 150 and 300 K	X	✓
SN	AD	AD2	X	5, 50, 150 and 300 K	X	✓
SN	PD	PD2	X	5, 50, 150 and 300 K	X	✓
SN	PD	PD1	X	5, 50, 150 and 300 K	X	✓
SN	PD	PD4	X	5, 50, 150 and 300 K	X	✓
SN	MSA	MSA1	X	5, 50, 150 and 300 K	X	✓
SN	MSA	MSA3	✓	5, 50, 150 and 300 K	✓	X
SN	MSA	MSA2	X	5, 50, 150 and 300 K	X	✓
Pu	Control	C1	✓	5, 50, 150 and 300 K	✓	X
Pu	Control	C3	X	5, 50, 150 and 300 K	✓	X
Pu	Control	C2	X	5, 50, 150 and 300 K	✓	X
Pu	AD	AD1	✓	5, 50, 150 and 300 K	✓	X
Pu	AD	AD2	✓	5, 50, 150 and 300 K	✓	X
Pu	AD	AD3	X	5, 50, 150 and 300 K	✓	X
Pu	PD	PD4	✓	5, 50, 150 and 300 K	✓	X
Pu	PD	PD1	X	5, 50, 150 and 300 K	✓	X
Pu	PD	PD2	X	5, 50, 150 and 300 K	✓	X
Pu	MSA	MSA1	✓	5, 50, 150 and 300 K	✓	X
Pu	MSA	MSA2	✓	5, 50, 150 and 300 K	✓	X
Pu	MSA	MSA3	✓	5, 50, 150 and 300 K	✓	X
CN	Control	C1	✓	5, 50, 150 and 300 K	✓	X
CN	Control	C3	✓	5, 50, 150 and 300 K	✓	X
CN	Control	C2	✓	5, 50, 150 and 300 K	✓	X
CN	AD	AD1	X	5, 50, 150 and 300 K	✓	X
CN	AD	AD2	X	5, 50, 150 and 300 K	✓	X
CN	AD	AD3	✓	5, 50, 150 and 300 K	✓	X

Table 5.2: A summary of the bulk tissue iron and magnetometry measurements. Isothermal remanent magnetisation (IRM) measurements at 5, 50, 150 and 300 K. The iron concentration of the pons and substantia nigra samples was measured by Dr Emily House at the University of Keele, using graphite furnace atomic absorption spectrometry (GFAAS). The putamen and caudate nucleus samples (and SN sample MSA3) were measured at the University of Warwick using inductively coupled plasma mass spectrometry (ICP-MS). IRM curves at 5 and 50 K were measured for a subset of samples from the putamen and caudate nucleus with at least one curve measured for each disease group in each region. IRM curves were also made of SN sample MSA2. SN = substantia nigra, Pu = putamen; CN = caudate nucleus.

In order to investigate the concentration and form of particulate iron, Superconducting QUantum Interference Device (SQUID) magnetometry measurements were made (Section 5.2) of the samples before they were digested for iron quantification. Particulate iron content is evaluated in terms of ferrihydrite-like iron in ferritin and magnetite. Examination of other iron oxide phases that have been observed in ferritin and haemosiderin, such as hematite, wustite and goethite [76-78], is beyond the scope of this thesis.

In addition to making statistical comparisons between disease groups for each region, discriminant analysis is used to combine the data from multiple regions and create a model to predict the disease state of each sample (Section 5.4).

The result of iron quantification and IRM at 5 K for the control, PD and MSA samples has been published in the paper *Iron Deficiency in Parkinsonism: Region-Specific Iron Dysregulation in Parkinson's Disease and Multiple System Atrophy* (Appendix H) [28]. This paper does not include data from the AD samples.

5.1 Iron concentration

Iron concentration in the pons and substantia nigra samples was measured by GFAAS, by Dr Emily House at Keele University. The exception being SN samples MSA3 which was measured with the putamen and caudate nucleus samples, by ICP-MS, at the University of Warwick. Figure 5.2 shows the iron concentration in micrograms of iron per gram of fresh-frozen tissue for each sample from each region. The mean and standard deviation for each group are given and statistically significant differences between groups indicated on the graph. Note that for the substantia nigra case MSA1 the fresh-frozen sample mass was not recorded and therefore this sample is not included in wet mass analysis.

Table 5.3 shows the mean iron concentration for each disease group in each region and the change in iron relative to control. Iron concentration is given per gram of freeze-dried and fresh-frozen tissue. All data sets, apart from the AD pons wet mass data, followed a normal

distribution as examined by the Shapiro-Wilk test. Therefore statistical analysis in the pons was carried out by i) one-way ANOVA when excluding the AD data and ii) by the nonparametric Kruskal-Wallis test when including the AD data.

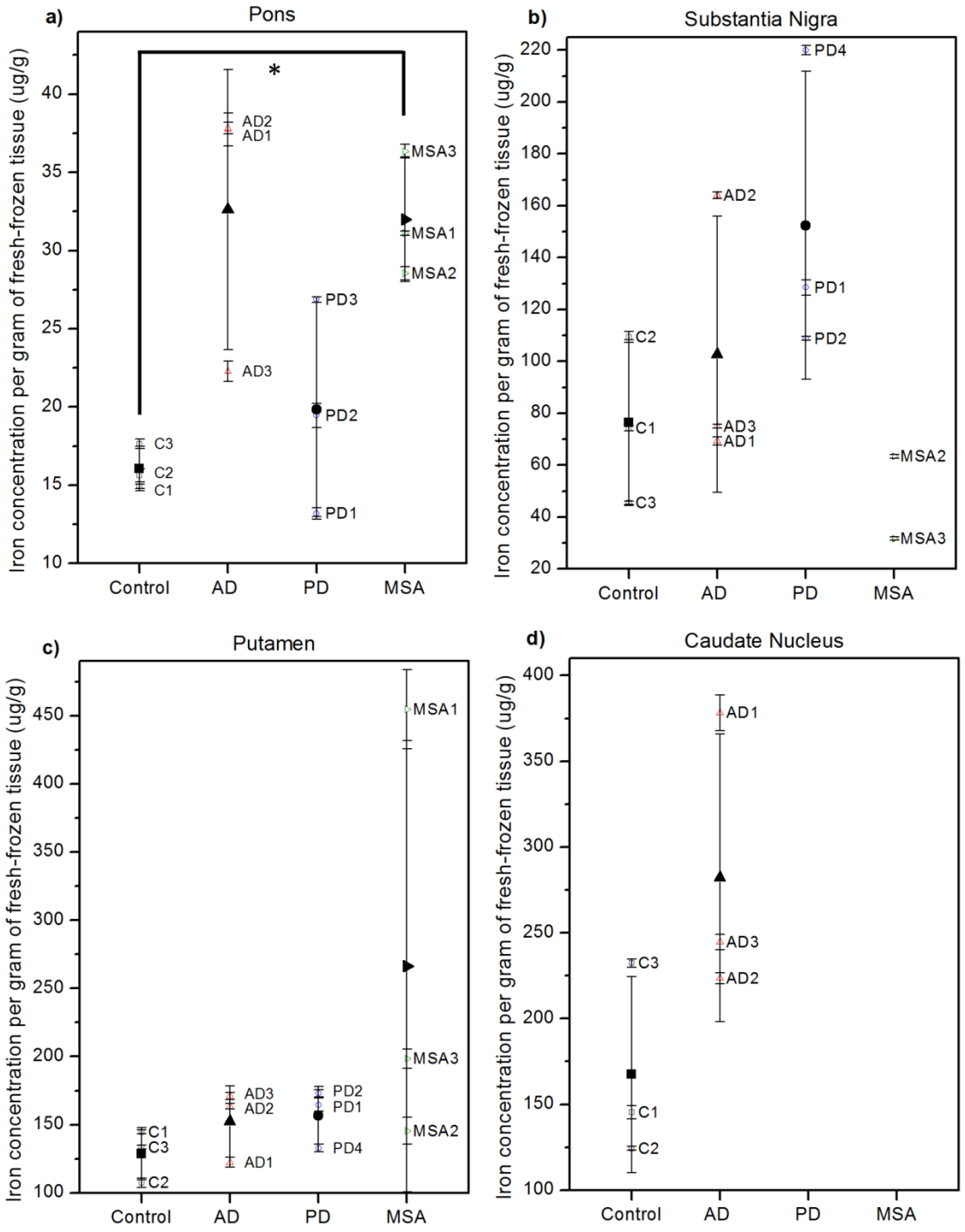

Figure 5.2: Iron concentration per gram of fresh-frozen tissue. Measured by GFAAS in a) the pons and b) the substantia nigra; and by ICP-MS in c) the putamen and d) the caudate nucleus. (Note the exception: SN sample MSA3 was measured by ICP-MS.) A statistically significant increase in iron concentration is shown in MSA compared to control pons. Open symbol = individual sample with measurement error; closed symbol = mean for disease group with standard deviation; * = statistically significant difference between means, where $p<0.05$ by one-way ANOVA.

Region (technique)	Disease	Iron concentration (µg/g freeze-dried tissue)		Iron concentration (µg/g fresh-frozen tissue)	
		Mean (µg/g)	Normalised to control	Mean (µg/g)	Normalised to control
Pons (GFAAS)	Control	55.0 ± 8.4	1	16.1 ± 1.4	1
	AD	102.0 ± 14.8	*1.9 ± 0.2	32.6 ± 8.9	2.0 ± 0.3
	PD	55.6 ± 22.4	1.0 ± 0.4	19.8 ± 6.8	1.2 ± 0.4
	MSA	129.0 ± 17.9	*2.4 ± 0.2	32.0 ± 4.0	*2.0 ± 0.2
Substantia nigra (GFAAS)	Control	295.2 ± 124.0	1	76.3 ± 32.0	1
	AD	397.0 ± 165.7	1.3 ± 0.6	102.7 ± 53.2	1.3 ± 0.7
	PD	542.4 ± 234.8	1.8 ± 0.6	152.4 ± 59.3	2.0 ± 0.6
	MSA	196.1 ± 78.9	0.7 ± 0.6	47.5 ± 22.4	♦0.6 ± 0.6
Putamen (ICP-MS)	Control	571.3 ± 115.5	1	128.6 ± 19.1	1
	AD	786.6 ± 174.7	1.4 ± 0.3	152.3 ± 26.2	1.2 ± 0.2
	PD	783.9 ± 84.7	1.4 ± 0.2	156.8 ± 21.1	1.2 ± 0.2
	MSA	1452.8 ± 970.0	2.5 ± 0.7	266.2 ± 165.4	2.1 ± 0.6
Caudate nucleus	Control	746.5 ± 251.5	1	167.3 ± 57.2	1
	AD	1535.1 ± 393.2	*2.1 ± 0.4	282.1 ± 83.9	1.7 ± 0.5

Table 5.3: Mean iron concentration in each brain region. The average iron concentration of each disease group in each brain region is given in micrograms per gram of freeze-dried and fresh-frozen tissue. For each region the mean of each disease group is normalised to control and any statistically significant change compared to control indicated by: * = $p<0.05$ by one-way ANOVA. Iron quantification method is indicated for each brain region, where: GFAAS = graphite furnace atomic absorption spectrometry, ICP-MS = inductively coupled mass spectrometry. Note: one substantia nigra MSA sample was measured with ICP-MS). ♦ = one missing sample from the group.

Iron concentration is doubled in the MSA and AD pons compared to control. This change is statistically significant for MSA in the fresh and dried mass comparison and for AD in the dried mass comparison only.

In the substantia nigra there is no statistical significance between disease groups, however there is an increase in iron in the PD tissue compared to AD and control which agrees with what has been reported in the literature [23]. There is a marked decrease in the average iron

concentration in the MSA samples compared to the PD samples, however this does not reach statistical significance (p=0.11).

For both freeze-dried and fresh-frozen putamen tissue the average iron concentration increases in all diseases compared to control, however this does not reach statistical significance. A particularly large difference in MSA compared to control was observed, but this was largely due to the extremely high iron concentration in sample MSA1, which has an iron concentration more than double that of any other sample.

A statistically significant doubling of iron with AD is found in freeze-dried CN (p=0.04). However, when corrected for fresh tissue mass the difference decreases and loses significance.

5.1.1 Comparison with the literature

Table 5.4 shows the mean iron concentration in the control and AD samples of the putamen and caudate nucleus reported in two papers by House *et al.* [19, 26]. These were the only papers found which reported mean concentration in control and AD tissue for these regions.

Region	Reference	Iron concentration control (µg/g fresh mass)	Iron concentration AD (µg/g fresh mass)	AD normalised to control
Putamen	House 2007 [26]	85.8 ± 24.0	157.5 ± 48.6	1.8
	House 2008 [19]	102	131	1.3
Caudate nucleus	House 2007 [26]	93.1	95.1 ± 21.1	1.0
	House 2008 [19]	100	137	1.4

Table 5.4: Literature iron concentrations in control and AD putamen and caudate nucleus. Quantification was carried out by GFAAS (2007 paper) and ICP-AES (2008 paper). The ratio of iron concentration in AD tissue compared to control is given and varies considerably between the two studies. No statistical comparison between AD and control was made in either study due to the small sample size.

The ratio of AD to control iron concentration is given for each paper. In the 2008 paper the ratios agree within error with the ratio reported in Table 5.3. However, a very different AD to control ratio is found in the 2007 paper.

The absolute iron concentrations measured in this study are higher than reported by House *et al.*, in particular in the caudate nucleus. In their 2005 paper Haacke *et al.* included a review of iron concentration data for healthy brain tissue [107]. This showed that there is a large variation in the reported values within brain regions: 45 to 185 μg/g in the substantia nigra; 76 to 164.8 μg/g in the putamen and 56 to 117.4 μg/g in the caudate nucleus. The measurements reported here for the putamen and substantia nigra fall within the range in the literature, however the caudate nucleus results do not.

The standard deviation of the mean iron concentration for the control (and diseased) samples in each region is fairly large (Table 5.3), however this is also reflected in the literature. In Hallgren and Sourander's landmark study of iron concentration in the brain [93], which is still widely used for reference today, the size of the standard deviation is also large. Their reported iron concentrations are: SN = 183.6 ± 65.2 μg/g; Pu = 133.2 ± 34.3 μg/g and CN = 92.8 ± 21.4 μg/g.

5.2 SQUID magnetometry measurements

The majority of non-haem brain iron is stored as a nanoparticle in the core of the storage protein ferritin. Some studies have shown that ferritin concentration increases with iron concentration [22], whereas other papers report that iron increases are not accompanied by an increase in ferritin [133]. Normal ferritin iron has a ferrihydrite-like, antiferromagnetic structure, but changes in the structure of ferritin cores have been reported in AD [77]. Additionally, an increase in the ferrimagnetic material magnetite has been reported [141].

An MPMS-5S SQUID magnetometer was used to examine particulate iron in the tissue samples through isothermal remanent magnetisation (IRM) measurements. IRM is the remanent magnetisation of a sample at a fixed temperature after a magnetic field is applied and then abruptly switched off. As the measurement is made with no applied field it is free from diamagnetic effects which usually dominate the magnetic properties of biological samples

[108]. IRM signal is only present for materials which are magnetically blocked at the measurement temperature. Ferritin is typically blocked at temperatures below about 15 K [154] and any blocked magnetic material above this temperature is likely to be the ferrimagnetic iron oxide phases magnetite and/or maghemite which have been observed in *post mortem* human brain tissue [80].

In the substantia nigra, antiferromagnetic grains with superparamagnetic properties are also present in neuromelanin, which stores 10-20% of the total iron in that region [85]. These grains have a range of blocking temperatures from 5 K to room temperature [88]. However, the majority of iron in the SN is still stored in ferritin.

IRM measurements were made of each sample at temperatures 5, 50, 150 and 300 K, after an applied field of 10 000 Oe. IRM curves at 5 and 50 K were made for a sub-set of samples to check for characteristic properties of ferritin and magnetite. All SQUID measurements were corrected for sample length using the empirical formula described by Hautot *et al.* [108], which was given in detail in Section 4.1.3. The error given for each IRM measurement is the combined error from: the standard deviation of the averaged SQUID measurement; the measurement error in the weighing the sample and the measurement error in measuring sample length.

Note that samples were freeze dried before SQUID magnetometry measurements were made, however in most instances the data are given per gram of fresh tissue.

5.2.1 IRM at 5 K

Figure 5.3 shows the IRM at 5 K, after an applied field of 10 kOe, in emu per gram of fresh-frozen tissue. Each individual sample is shown in addition to the mean and standard deviation for each disease group in each region. Table 5.5 shows the mean IRM at 5 K of each neurodegenerative disease normalised to mean control for that region. All data sets passed

the Shapiro-Wilk test for normality and therefore ANOVA was used to test for differences between group means.

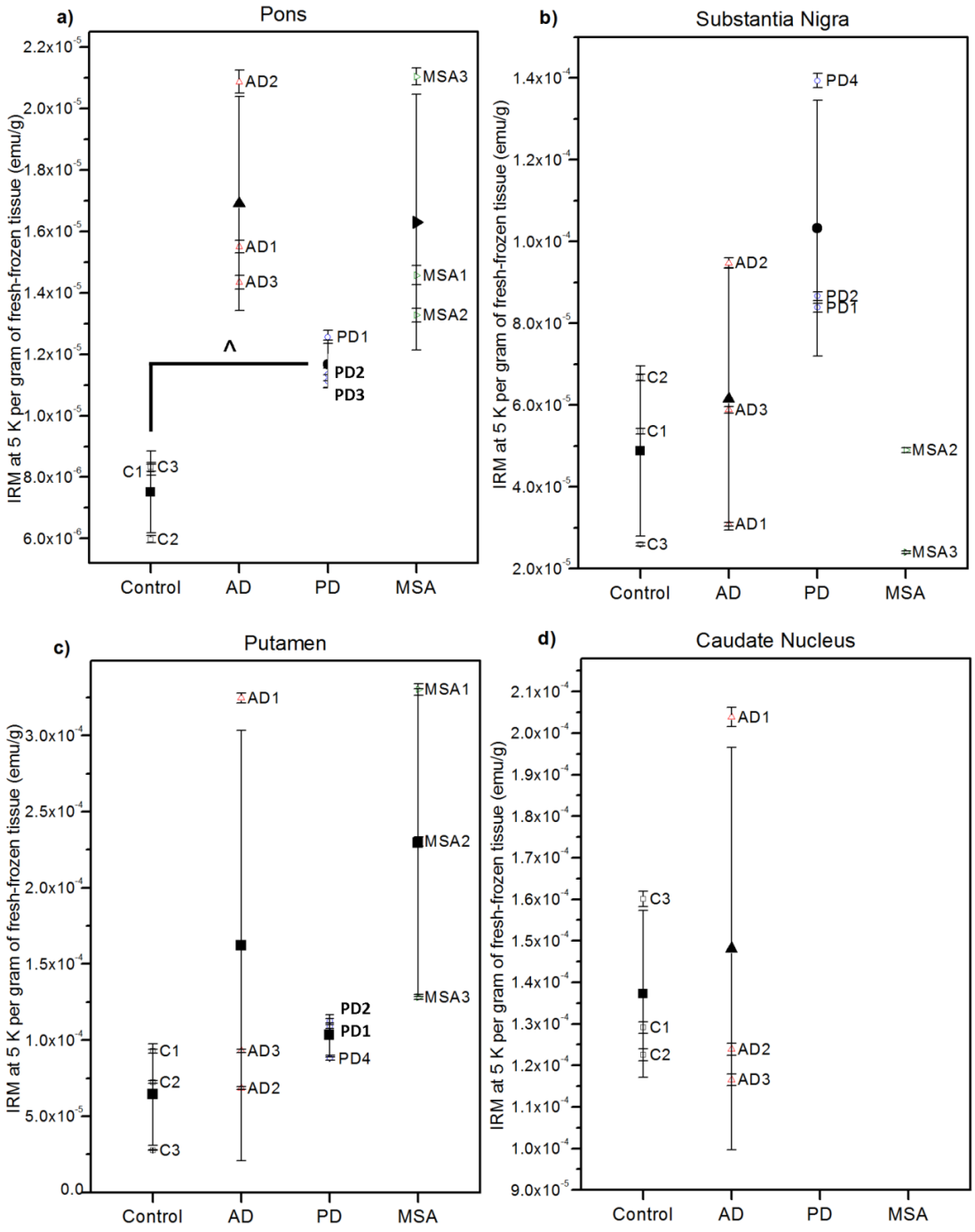

Figure 5.3: Isothermal remanent magnetisation at 5 K, after an applied field of 10 kOe, per gram of fresh-frozen tissue in a) the pons, b) the substantia nigra, c) the putamen and d) the caudate nucleus. The pons is the only region for which a statistically significant difference is observed. IRM at 5 K is increased in PD compared to control. Case MSA1 is missing from the SN data set as this sample was not weighed before freeze drying. Open symbol = individual sample measurement with measurement error; closed symbol = mean for disease group with standard deviation; ^ = statistically significant difference between means, where $p<0.05$ by Welch's ANOVA.

Region	Disease State	IRM at 5 K (normalised to Control) Freeze dried tissue	IRM at 5 K (normalised to control) Fresh tissue
Pons	Control	1	1
	AD	^2.1 ± 0.3	2.2 ± 0.3
	PD	1.3 ± 0.2	^1.6 ± 0.2
	MSA	2.6 ± 0.2	2.2 ± 0.3
Substantia Nigra	Control	1	1
	AD	1.3 ± 0.6	1.3 ± 0.7
	PD	1.9 ± 0.6	2.1 ± 0.5
	MSA	0.8 ± 0.6	♦0.7 ± 0.6
Putamen	Control	1	1
	AD	3.1 ± 1.1	2.5 ± 1.0
	PD	1.8 ± 0.6	1.6 ± 0.5
	MSA	4.3 ± 0.7	3.6 ± 0.7
Caudate Nucleus	Control	1	1
	AD	1.3 ± 0.3	1.1 ± 0.4

Table 5.5: Average IRM at 5 K normalised to control. The average IRM at 5 K of each disease group in each brain region as normalised to the average control value in that region. Data per gram of freeze dried and fresh-frozen tissue is shown. ^ = statistically significant difference between means, where $p<0.05$ by Welch's ANOVA; ♦ = average of only two samples.

Comparison of Figure 5.3 with Figure 5.2 shows that IRM at 5 K follows a similar trend to the iron concentration data for each sample across the four brain regions. IRM at 5 K is sensitive to particulate iron and therefore the preserved trend is consistent with a similar proportion of total iron being bound in ferritin for each of the samples. The relationship between iron and IRM at 5 K is examined further in Section 5.3.

Similarly to the results of the iron concentration analysis, mean IRM at 5 K is approximately double in AD and MSA pons samples compared to control. However, in this case the difference does not reach statistical significance. For fresh-frozen tissue the only statistically significant difference between any disease groups is the small but statistically significant ($p=0.048$, by Welch's ANOVA) increase in IRM in the PD pons compared to control.

The trend in the iron concentration data is preserved in the IRM at 5 K data for all disease groups in the substantia nigra: there is a slight increase in IRM in AD compared to control, with a doubling in PD and decrease in MSA. Although the mean IRM at 5 K of the PD is 2.8 times greater than for MSA (2.5 times larger for the freeze-dried tissue) the difference does not reach statistical significance.

In the putamen the average IRM at 5 K is increased compared to control to a much larger degree for AD and MSA than would be predicted from the iron concentration measurements. This can be explained by the samples AD1 and MSA2 which have a much higher than expected IRM at 5 K.

In the caudate nucleus the difference between control and AD is reduced to nearly nothing, in particular for the wet mass data.

5.2.2 IRM at 50, 150 and 300 K

Figure 5.4 shows the IRM at 50, 150 and 300 K, after an applied field of 10 kOe, for each sample in each brain region. Data are plotted on a log scale in order to show outliers.

The blocking temperature for ferritin is around 15 K and therefore ferritin will not contribute to IRM at these higher temperatures. For most samples the majority of the IRM signal is lost at the 50, 150 and 300 K, which is consistent with the majority of IRM at 5 K being due to ferritin. However, the small, but non-zero, IRM at 50 K (and decreasing slightly at 150 and 300 K) shown for most samples is consistent with a small amount of magnetite.

There are a small number of samples which show elevated IRM at 50, 150 and 300 K. Pons samples PD1 and MSA3 show elevated IRM at 50 and 150 K. In the data set from the putamen AD1 has very high IRM at 50, 150 and 300 K; approximately 1000 times greater than average. IRM is also elevated, to a lesser extent, in C3. In the caudate nucleus C1 has high IRM at 50, 150 and 300 K.

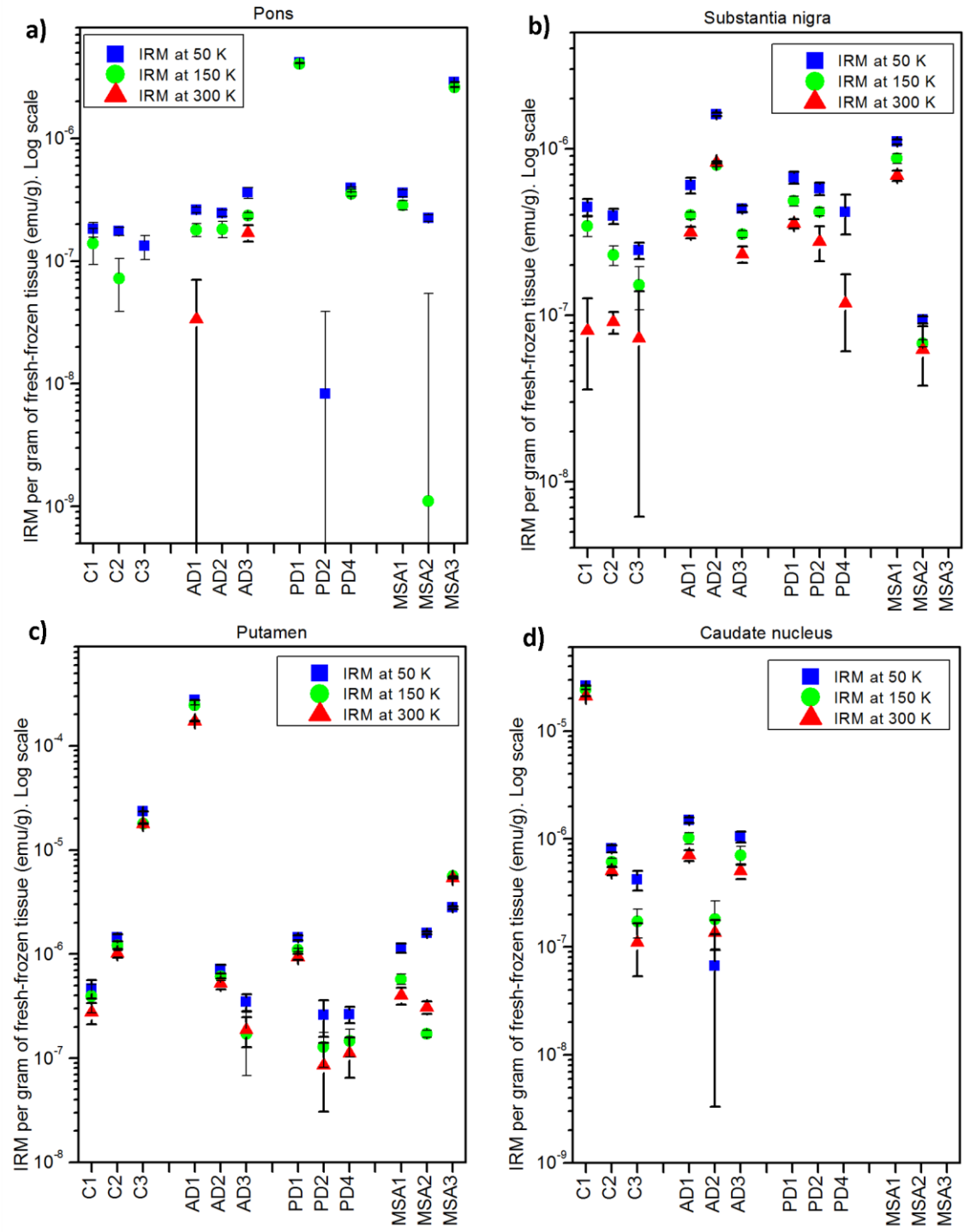

Figure 5.4: Isothermal remanent magnetisation (IRM) at 50, 150 and 300 K per gram of fresh tissue. All data are plotted on a log scale. a) All pons samples were measured at 50 and 150 K, with additional measurements at 300 K for AD1 and AD3. Samples PD1 and MSA3 have increased IRM at 50 and 150 K. Note: Samples PD2 and C3 had a measured IRM of below zero at 150 K and are not shown on the graph. b) All substantia nigra samples show similar IRMs. Data from MSA3 was not available. c) Putamen samples AD1 and C3 have higher than average IRMs at all three temperatures with approximately 1000 and 100 times greater signal, respectively. MSA3 is unusual in that the IRM at 150K and 300K is increased compared to at 50 K. d) Caudate nucleus sample C1 has increased IRM at all temperatures compared to the average for this region. Sample AD2 is atypical as the IRM is increased at 150 K and 300 K compared to 50 K.

Figure 5.5 shows the ratio of IRM at 50K to IRM at 5K. This shows the magnitude of the signal at 5K compared to at 50 K. For the majority of samples the ratio is less than 0.05, showing that the size of the IRM signal at 50 K is less than 5% of the signal at 5 K. This is consistent with the majority of the particulate iron being in the form of ferrihydrite and the large majority of the 5 K IRM being due to magnetically blocked ferrihydrite-like ferritin cores.

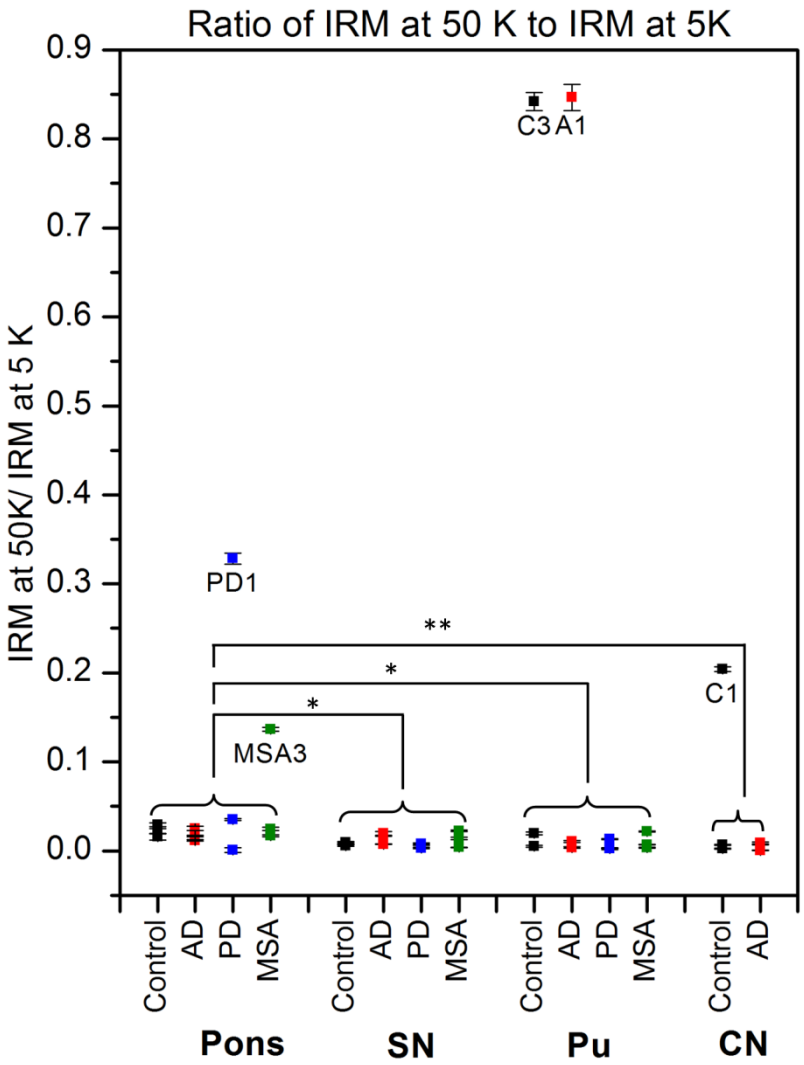

Figure 5.5: Ratio of IRM at 50 K to IRM at 5 K. The majority of samples show a ratio below 0.05, showing that the IRM at 50 K is less than 5% of the IRM at 5 K. Pons samples PD1 and MSA3; putamen samples C3 and AD1 and caudate nucleus sample C1 have increased ratios. This suggests a greater proportion of iron in magnetite or a measurement error or contamination of the samples. Statistical analysis was carried out on the data, excluding the outliers. No statistically significant differences between disease groups within each region were observed. When data from each region were pooled (excluding outliers) the pons showed a statistically significantly (*p<0.05, **p<0.01) higher ratio than the other regions, suggesting that in the pons there is an elevated proportion of magnetite.

A handful of samples have an increased 50 K to 5 K IRM ratio. These are the same samples which, in Figure 5.4, were identified as having elevated IRM at 50 K and are not grouped by

brain region or disease. Statistical analysis (excluding the outlying samples) revealed no significant difference in the 50 K to 5 K IRM ratio between disease groups in each region. However, when data from all diseases in each region was pooled a statistically significant increase in the ratio of IRM at 50 to 5 K was seen in the pons compared to the other three brain regions. This suggests that despite the lower total iron concentration, there is a higher proportion of particulate iron in the form of magnetite in the pons.

As the superparamagnetic grains in neuromelanin in the SN have blocking temperatures ranging from 5 K to room temperature, an increase in the 50 K to 5 K IRM ratio may have been expected. However, this was not observed, perhaps because the fraction of iron in the neuromelanin is only 10 to 20% [85], and a smaller fraction again will remain blocked at 50K.

5.2.3 IRM curves at 5 and 50 K

IRM curves are produced by taking IRM measurements, at a fixed temperature, after a series of applied fields of increasing magnitude. In this section IRM curves at 5 and 50 K with applied fields ranging from 250 Oe to 10 kOe are presented for a sub-set of samples. The 5 K IRM curve of a biological sample would typically be expected to be dominated by ferrihydrite-like iron in ferritin, with a small component due to magnetite. A smooth curve that is not saturated at 10 kOe is typical for the antiferromagnetic ferrihydrite-like core of ferritin [83, 186]. The 50 K IRM curve can confirm the presence of magnetite, which typically saturates at around 3000 Oe for particles with a diameter larger than about 13 nm [80, 83, 187].

IRM curves were not made for all samples, due to limited instrument time. They were made for substantia nigra samples MSA3 (Figure 5.6); putamen samples C1, AD1, AD2, PD4, MSA1, MSA2 and MSA3 (Figures 5.7 to 5.10); and for caudate nucleus samples C1, C2, C3 and AD2 (Figures 5.11 and 5.12). Error bars indicate the combined measurement error. The IRM curves at 5 K for all samples are typical for ferritin. The only exception is the 5 K IRM curve for AD1 putamen, which is shown in Figure 5.8 a). The curve has a ‘kink’ at around 3000 Oe, which is

around the saturation point of magnetite: recall that this sample showed a high 50 K IRM to 5 K IRM ratio. This sample also shows a relatively large measurement error compared to the other samples.

The 50 K IRM curves of most samples are consistent with the presence of a small amount of magnetite or maghemite. For some samples the raw IRM measurements at 50 K (before correction for sample mass and length) are pushing the detection limitations of the instrument and therefore there are large error bars on the curves for these samples.

The 50 K IRM curve for CN sample C3 (Figure 5.11 f) does not appear to reach saturation, with the trend of the curve still rising at 10 000 Oe. There is very low signal for this sample (and therefore large error bars) which indicates little or no magnetite content. The iron concentration and IRM at 5 K measurements for this sample were as expected.

The 50 K IRM curve for putamen sample AD1 (Figure 5.8 b) does not resemble a typical IRM curve. The IRM drops and then rises as the applied field is increased. This sample also showed a very high IRM at 5 K compared to its iron concentration and an atypical 5 K IRM curve. This sample was particularly small (only 0.0284 g, freeze-dried) and therefore the IRM signal from the sample was very small. This could have compromised the quality of the data, however examining the raw data shows good dipoles centred correctly at the 2 cm position.

In the 50 K IRM curves of samples MSA3 putamen (Figure 5.10 f) and C1 caudate nucleus (Figure 5.11 b) the first point, measured after an applied field of 250 Oe, is significantly above zero compared to the other samples. This is may be due to the SQUID not reaching a perfect zero-field after quenching, which may not show the same effect on each sample due to the varying samples sizes. However, this small effect should not affect the overall results of the analysis and the IRM curves are otherwise typical of magnetite.

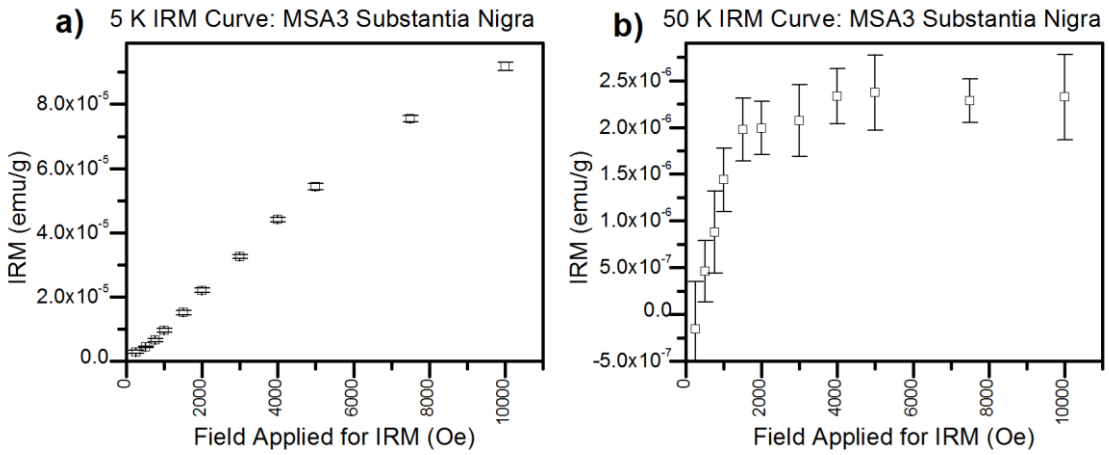

Figure 5.6 IRM curves at 5 K and 50 K for substantia nigra sample MSA3. a) The 5 K IRM curve does not saturate, which is consistent with the magnetic properties of ferritin. b) The 50 K IRM curve, which saturates at approximately 3000 Oe, is consistent with nanoparticles of magnetite larger than about 13 nm in diameter.

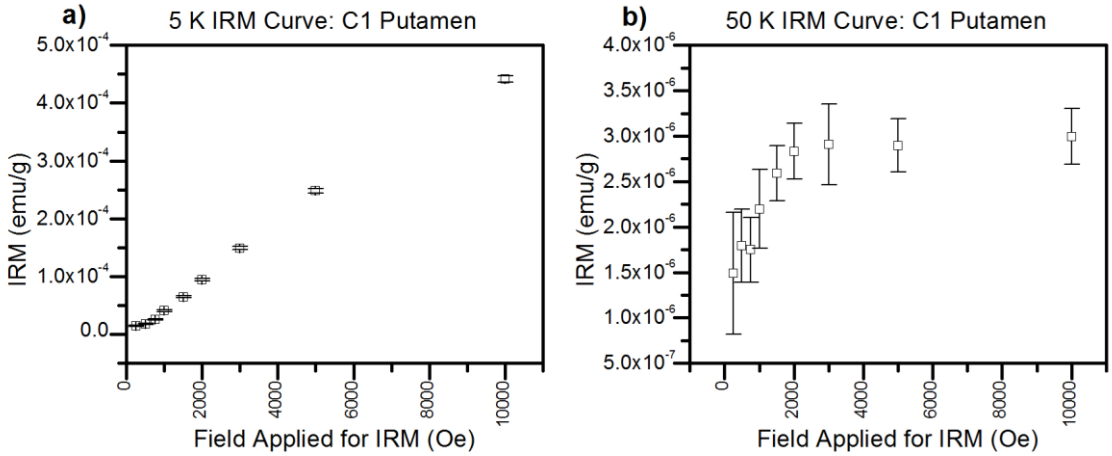

Figure 5.7: IRM curves at 5 K and 50 K for putamen sample C1. a) The 5 K IRM curve does not saturate, which is consistent with the magnetic properties of ferritin. b) The 50 K IRM curve, which saturates at approximately 3000 Oe, is consistent with nanoparticles of magnetite larger than about 13 nm in diameter.

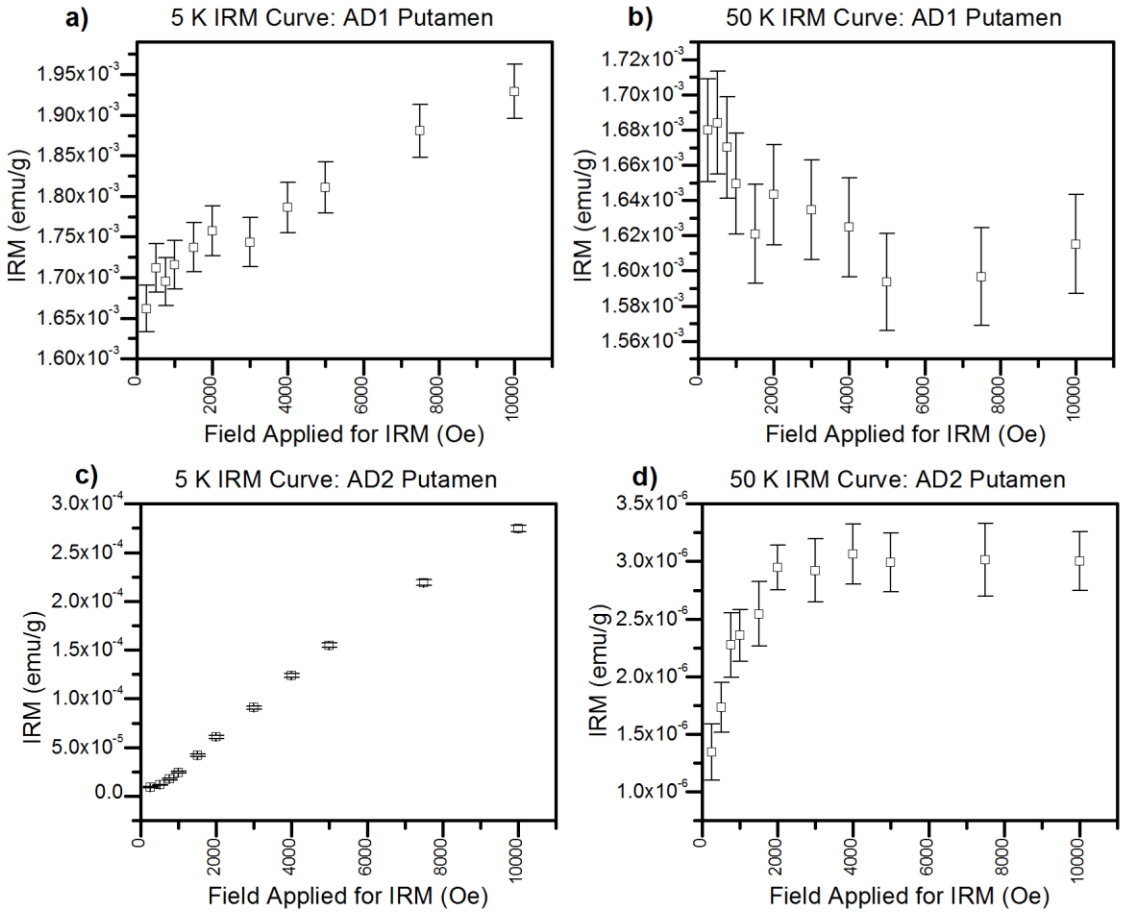

Figure 5.8: IRM curves at 5 K and 50 K for putamen samples AD1 and AD2. The 5 K curve for AD1 a) is not consistent with the typical curve for ferritin iron, unlike for AD2 c) which shows a smooth non-saturating curve. The AD1 50 K curve b) is also not as expected for magnetite, unlike the curve for AD2 d) which shows a curve saturating around 3000 Oe.

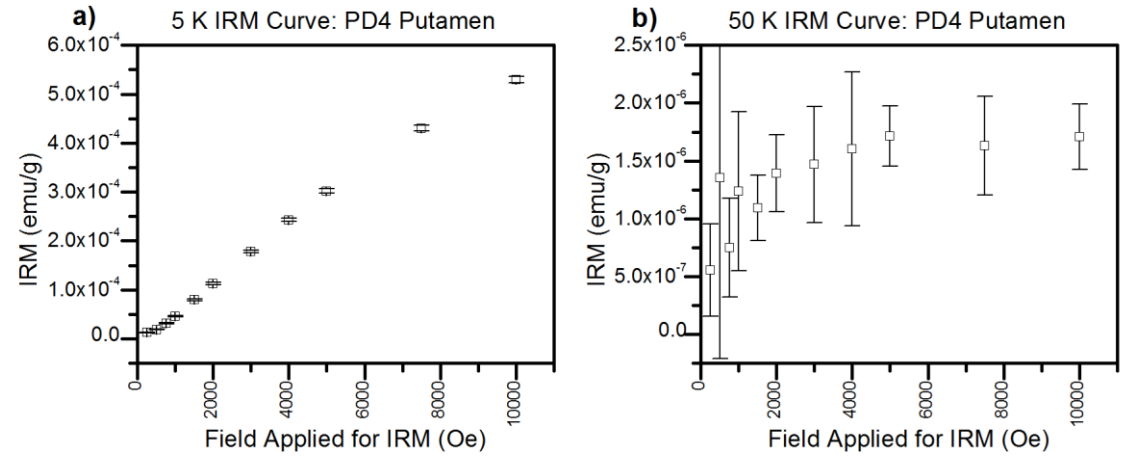

Figure 5.9: IRM curves at 5 K and 50 K for putamen sample PD4. a) The 5 K IRM curve does not saturate, which is consistent with the magnetic properties of ferritin. b) The 50 K IRM curve, which saturates at approximately 3000 Oe, is consistent with nanoparticles of magnetite larger than about 13 nm in diameter.

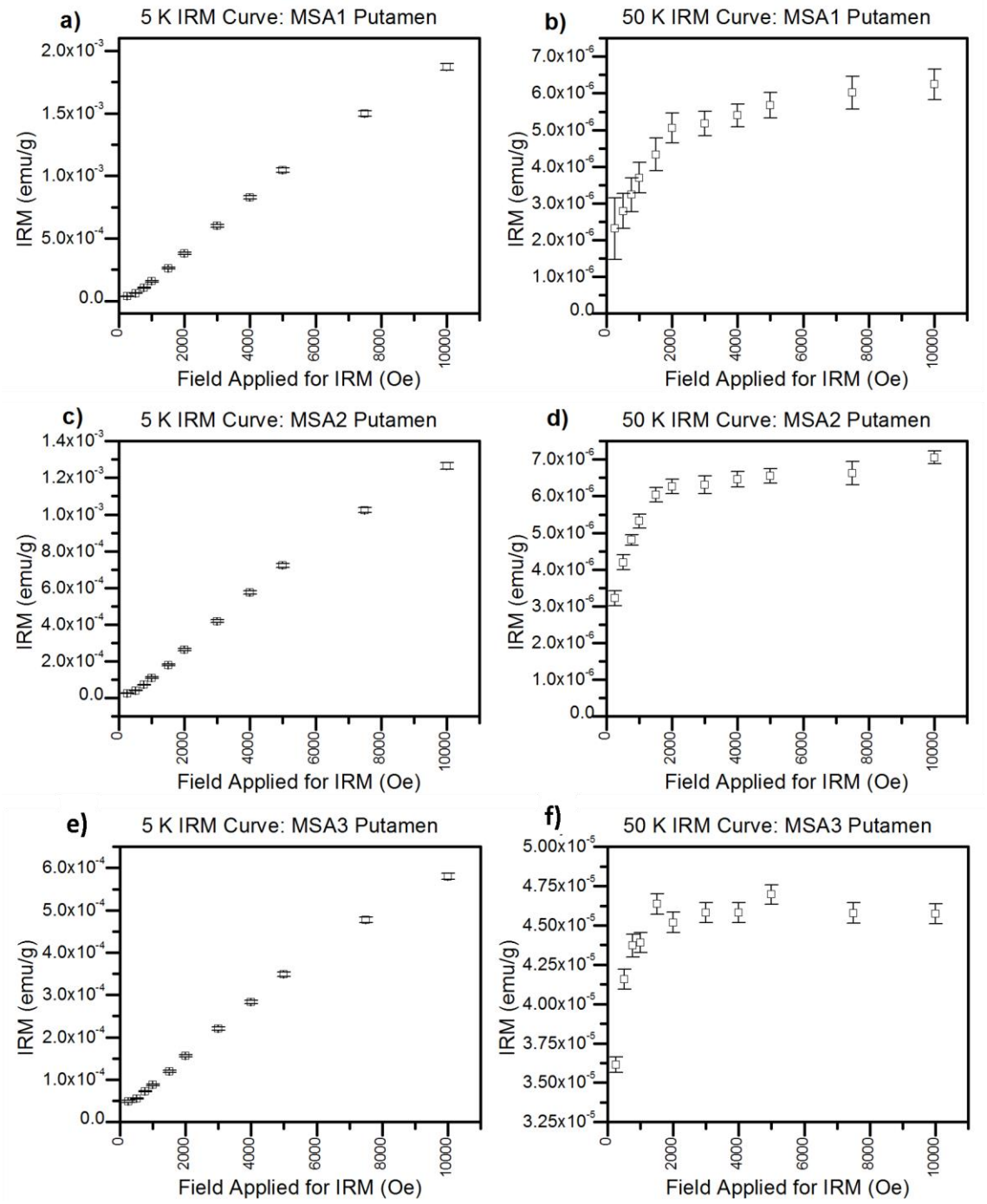

Figure 5.10: IRM curves at 5 K and 50 K for putamen samples MSA1, MSA2 and MSA3. 5 K IRM curves a), c) and e) show a curve which does not saturate at 10 000 Oe and is typical for ferritin. The 50 K IRM curves in b), d) and f) saturate at around 3000 Oe, which is typical for magnetite.

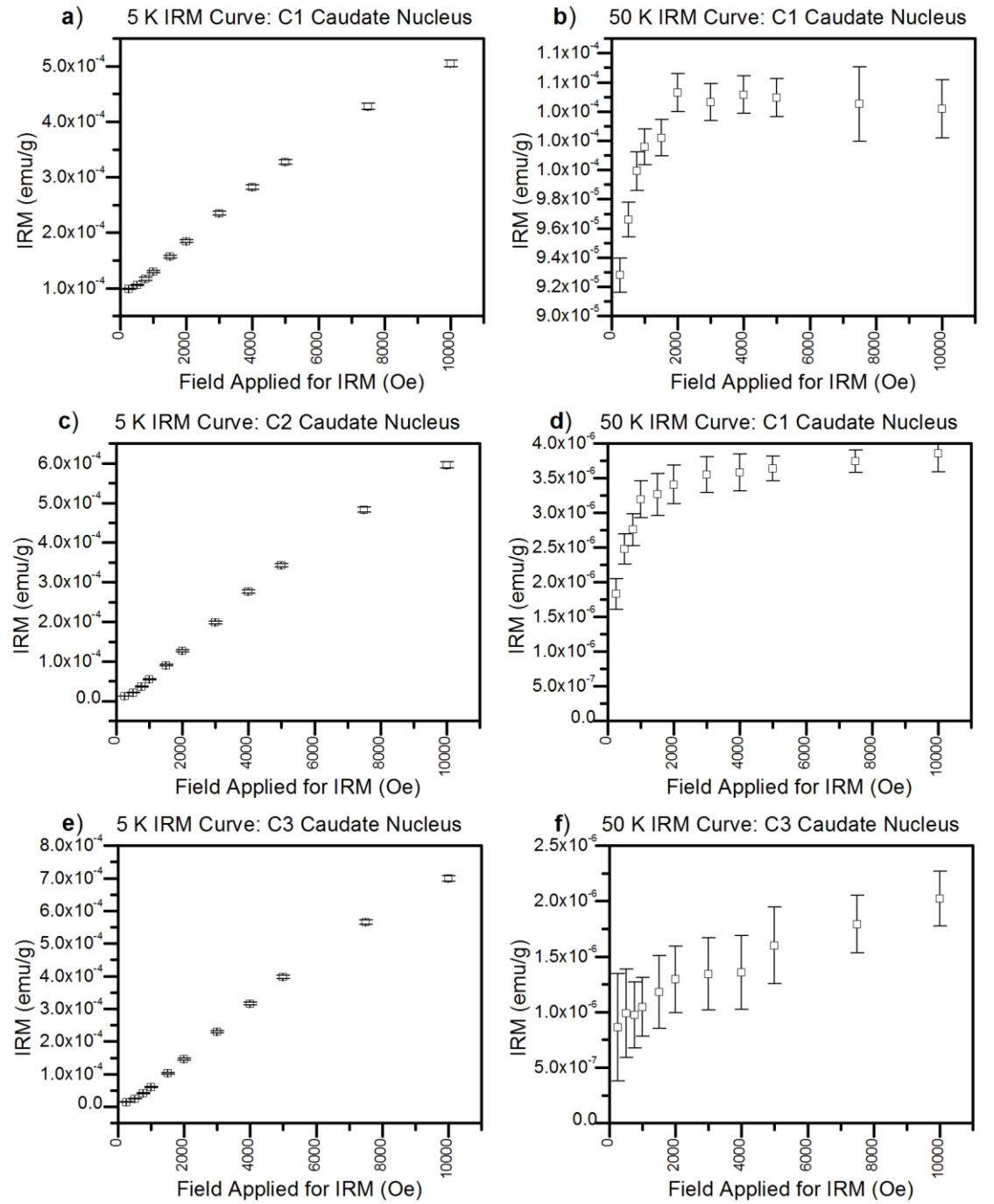

Figure 5.11: IRM curves at 5 K and 50 K for caudate nucleus samples C1, C2 and C3. 5 K IRM curves a), c) and e) show a curve which does not saturate at 10 000 Oe and is typical for ferritin. The 50 K IRM curves in b) and d) saturate at around 3000 Oe which is typical for magnetite. f) The 50 K IRM curve for caudate nucleus sample C3 does not saturate at 3000 Oe as would be expected for magnetite. The large error bars on the data points on this curve indicate that this may be due to a measurement error.

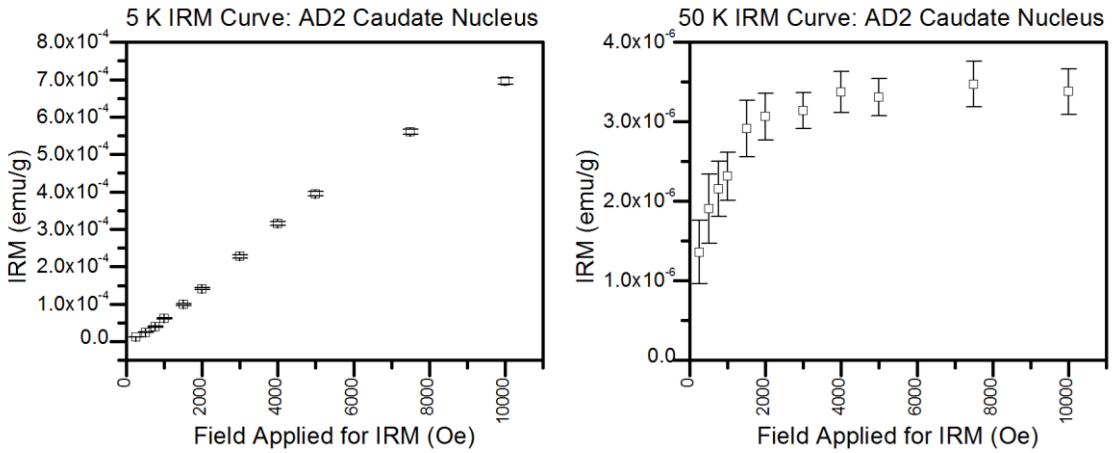

Figure 5.12: IRM curves at 5 K and 50 K for caudate nucleus sample AD2. a) The 5 K IRM curve does not saturate, which is consistent with the magnetic properties of ferritin. b) The 50 K IRM curve, which saturates at approximately 3000 Oe, is consistent with nanoparticles of magnetite larger than about 13 nm in diameter.

5.2.4 Relative proportion of iron as ferritin and magnetite

The 50 K IRM curves in the previous section confirm the presence of magnetite in the majority of the samples measured. Hautot *et al.* [83] showed that by fitting the 5 K and 50 K IRM curves an estimation of ferritin and magnetite concentration in each sample can be made. However, this could not be achieved with this data set as limited experimental time meant IRM curves were not measured for all samples and for those samples for which IRM curves were measured, not enough data points on each curve were collected to allow accurate fitting.

Instead, an estimation of the relative proportion (between samples) of iron in ferritin is made by dividing the IRM at 5 K by the total iron concentration in the sample. The same is done for IRM at 50 K to estimate the relative proportion of iron in magnetite. For the 5 K comparison an assumption is made that the contribution of the magnetite particles to IRM at 5 K is negligible compared to the contribution from ferritin. For most samples this assumption is reasonable, as was demonstrated by the ratio of 50 K IRM to 5 K IRM in Figure 5.5.

The outlying samples in Figure 5.5 are excluded from the estimation as they show elevated signal at 50 K and violate the assumption that the magnetite signal at 5 K is negligible. The elevated IRM at 50 K could be indicative of contamination, measurement error or a

concentration of magnetite that is much larger than normal. The data collected from these samples and the conclusions that can be made about the sample are summarised in Table 5.6.

Blocking temperature is dependent on particle size and at 50 K magnetite particles with a diameter larger than about 13 nm are blocked [83]. The tissue may contain nanoparticles of magnetite which become magnetically ordered at lower temperatures. Therefore the estimation of relative proportion of iron in magnetite does not include nanoparticles smaller than around 13 nm in diameter.

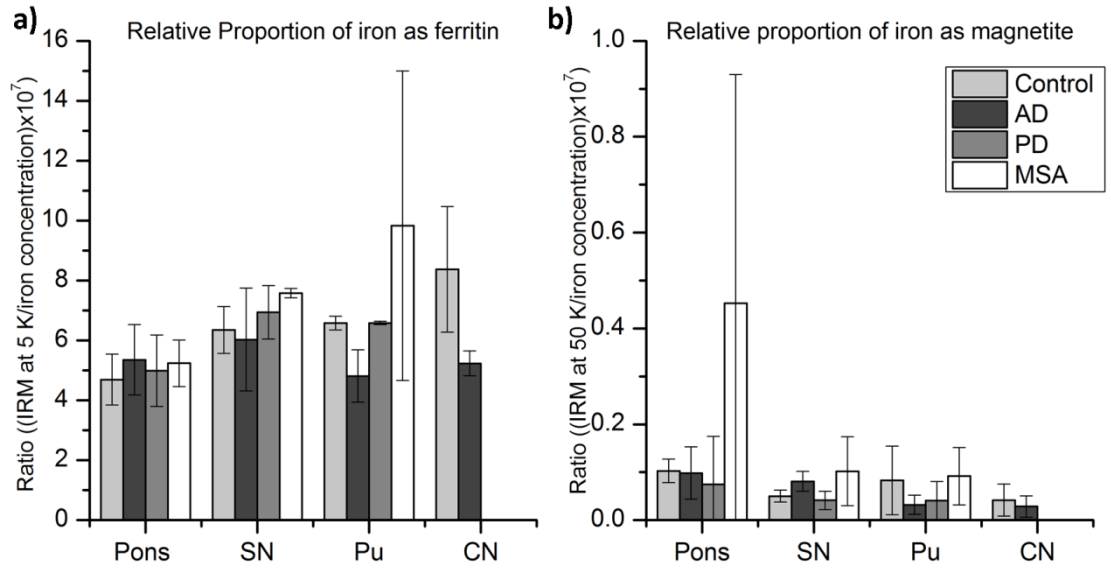

Figure 5.13: Estimation of the relative proportion of iron in ferritin and magnetite. a) An estimation of the relative proportion of iron in ferritin was made by dividing IRM at 5 K (emu/g) by total iron concentration (µg/g). The mean is shown for each disease group in each region. b) An estimation of the relative proportion of iron in magnetite was made by dividing IRM at 50 K (emu/g) by total iron concentration (µg/g). The mean is shown for each disease group in each region. The ratios are scaled by 10^7 for ease of comparison. No statistically significant difference was found between disease groups within each region or between the mean of each region.

Figure 5.13 a) shows the mean relative proportion of iron in ferritin for each disease group in each brain region and part b) shows the mean relative proportion of iron in magnetite for each disease group in each brain region. For ease of comparison the ratios (IRM in emu per g/ iron concentration in µg per g) are scaled by 10^7. The data passed the Shapiro Wilk test for normality and therefore one-way ANOVA was used to test for differences between means, but no statistically significant differences between means were observed. There was also no statistically significant difference between brain regions, when disease groups were pooled.

Table 5.6 shows that there is no reason to suspect contamination in the samples which have elevated IRM at 50 K. Sample AD1 from the putamen was very small and therefore may have been difficult for the SQUID to centre on. However, sample C1 from the caudate nucleus showed typical IRM curves at 5 and 50 K and therefore there is no reason to suspect the high IRM at 50 K is not real.

Outlier	IRM (emu) 5K 50K	IRM (emu/g) 5K 50K	Mass (g)	IRM curve information	Conclusions
Pons PD1	7.75E-6 2.18E-6	2.91E-5 0.95E-5	0.2322	n/a	Inconclusive, but no reason to suspect contamination
Pons MSA3	8.81E-6 1.20E-6	8.28E-5 1.13E-5	0.1064	n/a	Inconclusive, but no reason to suspect contamination
Pu C3	9.03E-6 7.61E-6	11.70E-5 9.82E-5	0.0842	n/a	Inconclusive, but no reason to suspect contamination
Pu AD1	52.48E-6 46.89E-6	186.65E-5 166.78E-5	0.0240	Large error bars. 50 K curve may be inverted.	Sample is very small and error bars are large. May be a measurement error.
CN C1	34.31E-6 7.00E-6	51.63E-5 10.53E-5	0.0650	Typical IRM curves at 5 and 50 K	No reason to suspect signal is not real

Table 5.6: Summary of samples which showed an elevated IRM at 50 K. These five samples showed elevated IRM at 50 K, when compared to IRM at 5 K. The IRM measurements at 5 and 50 K for each sample are above the detection limit for the SQUID magnetometer. Sample Pu AD1 was very small in size, and although the signal was large it showed large error bars which may indicate a measurement error. On the other hand the IRM curves at 5 and 50 K for sample CN C1 were typical of ferritin and magnetite and therefore support the conclusion that this sample contains an elevated concentration of magnetite.

In conclusion there is evidence for increased magnetite in a number of individual tissue samples, but not for any particular disease group.

5.3 The linear relationship between iron concentration and IRM at 5 K

The analysis thus far has suggested that a similar proportion of total non-haem iron is stored in ferritin for each disease group and across each brain region. This was shown by the ratios of IRM at 5 K to total iron concentration in Figure 5.13 and the preserved trend in the iron

concentration and IRM at 5 K in Figures 5.2 and 5.3. In this section the relationship between total tissue iron concentration and IRM at 5 K is further examined using simple linear regression analysis. Firstly simple linear regression analysis is used to fit a straight line to all data from all regions, then to the data from each disease group and finally for all samples within each region.

5.3.1 All samples and individual disease groups

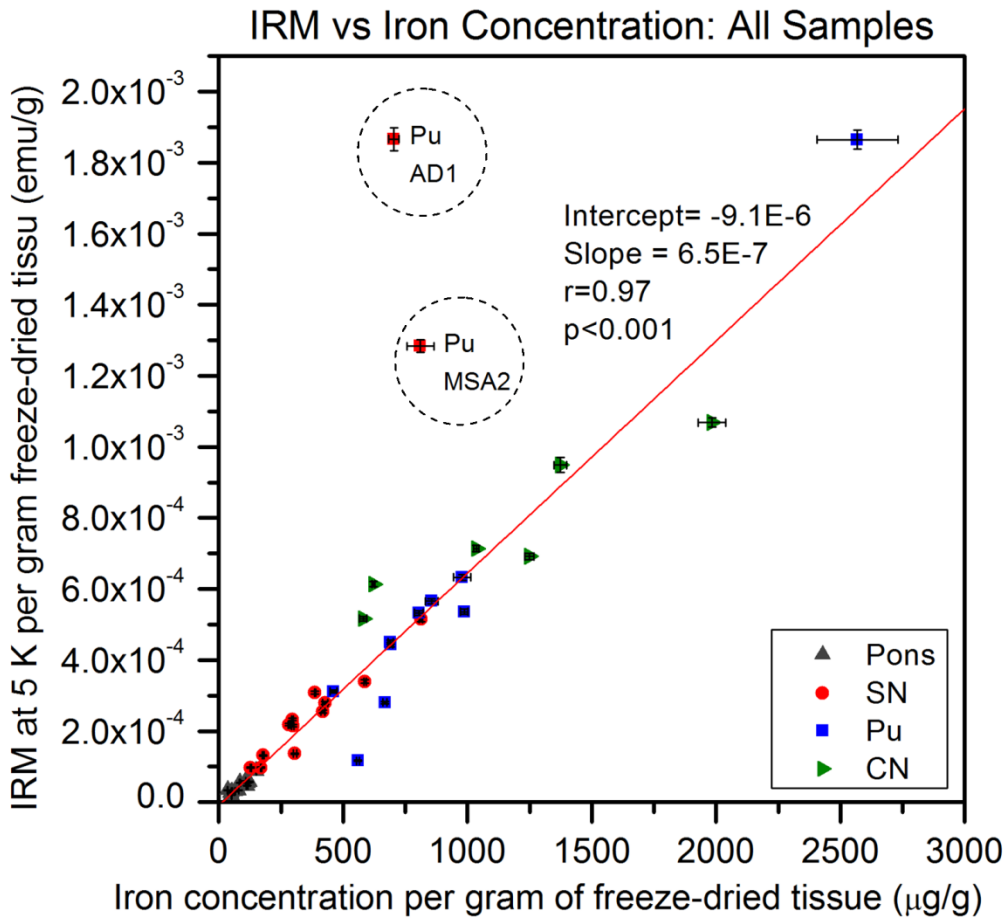

Figure 5.14: IRM at 5 K versus iron concentration for all samples. Data from the pons are in dark grey, the substantia nigra are in red, the putamen are in blue and the caudate nucleus are in green. A straight line is fitted to the data, excluding the outlying data point from the putamen samples MSA2 and AD1, and shows a strong (r=0.97), statistically significant (p<0.001) linear relationship.

Figure 5.14 shows a plot of the IRM at 5 K against iron concentration of all samples measured. The straight line represents the result of linear regression analysis, excluding two outlying samples from the putamen: MSA2 and AD1. There is a strong, positive linear correlation (r=0.97), which is statistically significant (p<0.001), between iron concentration and IRM. The r-

squared value shows that over 90% of the variation in the data is explained by the linear fit. As the variation in the pooled data is so well explained by the model, it suggests that there is a similar relationship between iron concentration and IRM at 5K in each of the diseases and brain regions.

Disease	n	Slope (emu/g)/(μg Fe/g)	Intercept (emu/g)	r	r^2	p
All [with outliers]	40 [42]	(6.5 ± 0.3) E-7 [(6.7 ± 0.7) E-7]	(-9.1 ± 19.1) E-6 [(2.7 ± 5.9) E-5]	0.97 [0.80]	0.94 [0.65]	<0.001 [<0.001]
Control	12	(4.71 ± 0.5) E-7	(-1.8 ± 5.6) E-5	0.90	0.81	<0.001
AD [with outlier]	11 [12]	(5.2 ± 0.4)E-7 [(5.2 ± 1.1) E-7]	(3.8 ± 22) E-6 [(1.3 ± 2.1) E-4]	0.99 [0.58]	0.98 [0.34]	<0.001 [0.047]
PD	9	(6.5 ± 0.4) E-7	(4.8 ± 13) E-6	0.995	0.991	<0.001
MSA [with outlier]	8 [9]	(7.2 ± 0.2) E-7 [7.5 ± 0.5) E-7]	(-1.7 ± 1.4) E-5 [(4.4 ± 10.7) E-5]	0.999 [0.93]	0.998 [0.87]	<0.001 [<0.001]

Table 5.7: Results of simple linear regression analysis of iron concentration versus IRM at 5 K, with data grouped by disease state. A strong, statistically significant linear relationship is shown between iron concentration and IRM at 5 K for each disease state and for all of the data combined. The r-squared values show that the majority of the variation in data is explained by the linear relationship in each case. The AD and MSA data are analysed without the outliers AD1 and MSA2. When these points are included (result in square brackets) the r-squared value is reduced, in particular for the AD data.

The intercept of the fit is very close to zero, which is consistent with the majority of iron in the tissue being stored as ferrihydrite-like iron in ferritin. An intercept much above zero could indicate a significant IRM contribution at 5 K from non-ferritin iron, such as magnetite, whereas an intercept below zero may indicate a significant amount of non-particulate iron.

The two outlying points, both from the putamen, are indicated on the graph: AD1 and MSA2. The point that lies furthest from the fitted line is AD1. This sample has already been observed to show abnormal IRM measurement (Table 5.6), which may be due to the sample's small size. In Section 5.2.1 it was noted that both AD1 and MSA2 had higher than expected IRM at 5K than would be expected for their iron content, but otherwise MSA2 has not shown any out of the ordinary characteristics.

In addition to pooling the data from all samples measured, Table 5.7 shows the results of simple linear regression analysis for each disease group individually. When the outlier AD1 is excluded, the linear relationship is highly statistically significant ($p<0.001$) for each disease group. The r-squared values show that over 90% of the variation in the data for the AD, PD and MSA samples and over 80% for control samples is explained by the fit.

The gradient of the fit of the control and AD data agree within error, however a steeper gradient is given for the PD data and steeper again for the MSA data. This suggests that relationship between total iron and ferritin iron may be slightly different in PD and MSA compared to control and AD. However, as 94% of the variation in the pooled data was explained by the linear fit, the difference is not very large.

5.3.2 Individual regions

Iron versus IRM was also plotted for each region and the results are shown in Figure 5.15. In each figure the fit to the data from all regions is shown in red and the fit to the data from that particular brain region is shown in black. Table 5.8 summarises the results of the linear regression analysis for each region and for the combined data from all regions. The r-squared values show that at least 80% of the variation in the data in each region is explained by the linear model. The gradients and intercept of each region do not agree within error, suggesting that the relationship between iron and IRM also varies slightly in the different brain regions.

In Figure 5.15 the different disease groups are labelled and this reveals clustering of data points by disease group, particularly in the pons and CN. In the pons the data seem to be clustered into two groups: one containing the AD and MSA data and the other containing the control and PD data. Within each of these two groups, the data are arguably clustered further into each disease group. In the CN graph there is a clear separation of the AD and control data. This clustering of samples in the IRM vs. iron data is investigated further using discriminant analysis in the following section.

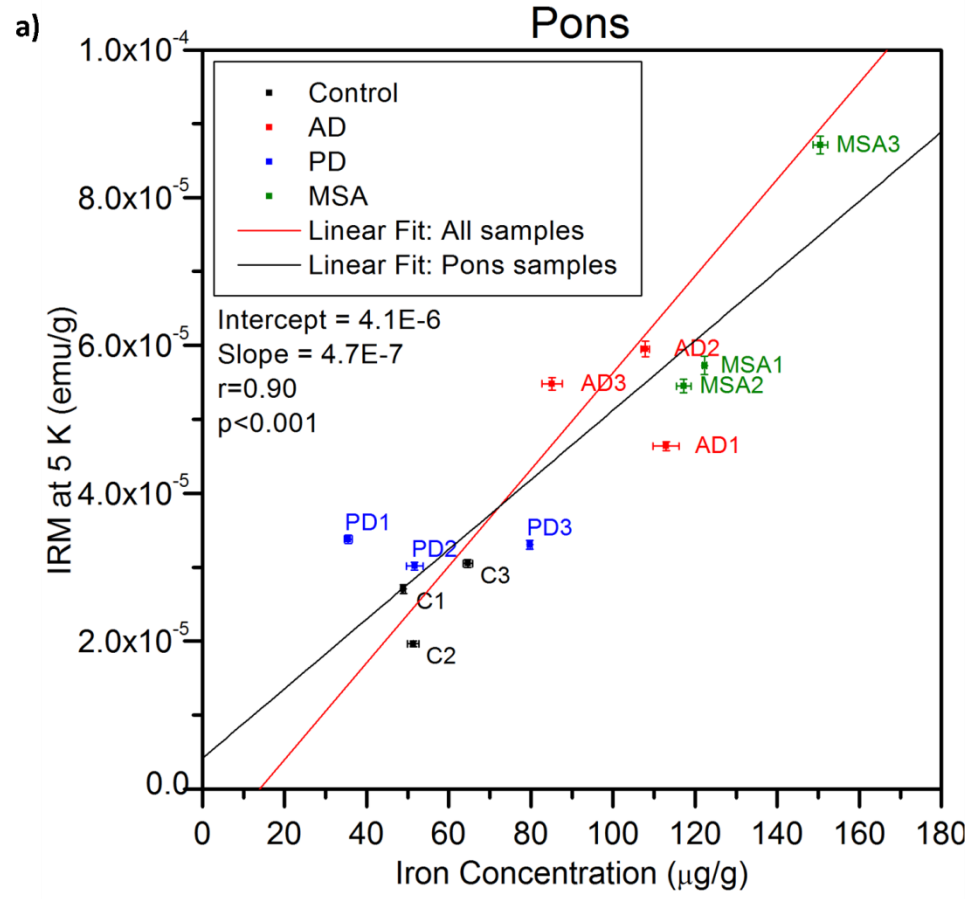
a)
Pons
Control
AD
PD
MSA
Linear Fit: All samples
Linear Fit: Pons samples
Intercept = 4.1E-6
Slope = 4.7E-7
r=0.90
p<0.001
IRM at 5 K (emu/g)
Iron Concentration (μg/g)
MSA3
AD2
MSA1
AD3
MSA2
AD1
PD1
PD2
PD3
C3
C1
C2

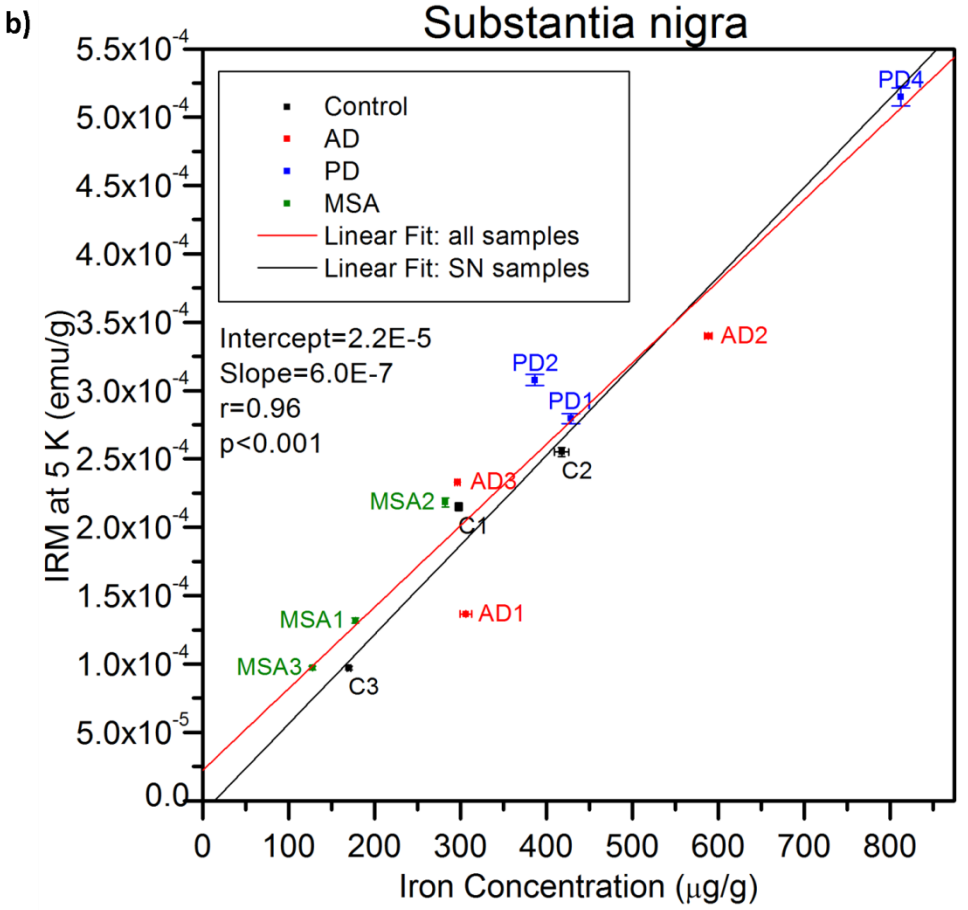
b)
Substantia nigra
Control
AD
PD
MSA
Linear Fit: all samples
Linear Fit: SN samples
Intercept=2.2E-5
Slope=6.0E-7
r=0.96
p<0.001
IRM at 5 K (emu/g)
Iron Concentration (μg/g)
PD4
AD2
PD2
PD1
C2
AD3
MSA2
C1
MSA1
AD1
MSA3
C3

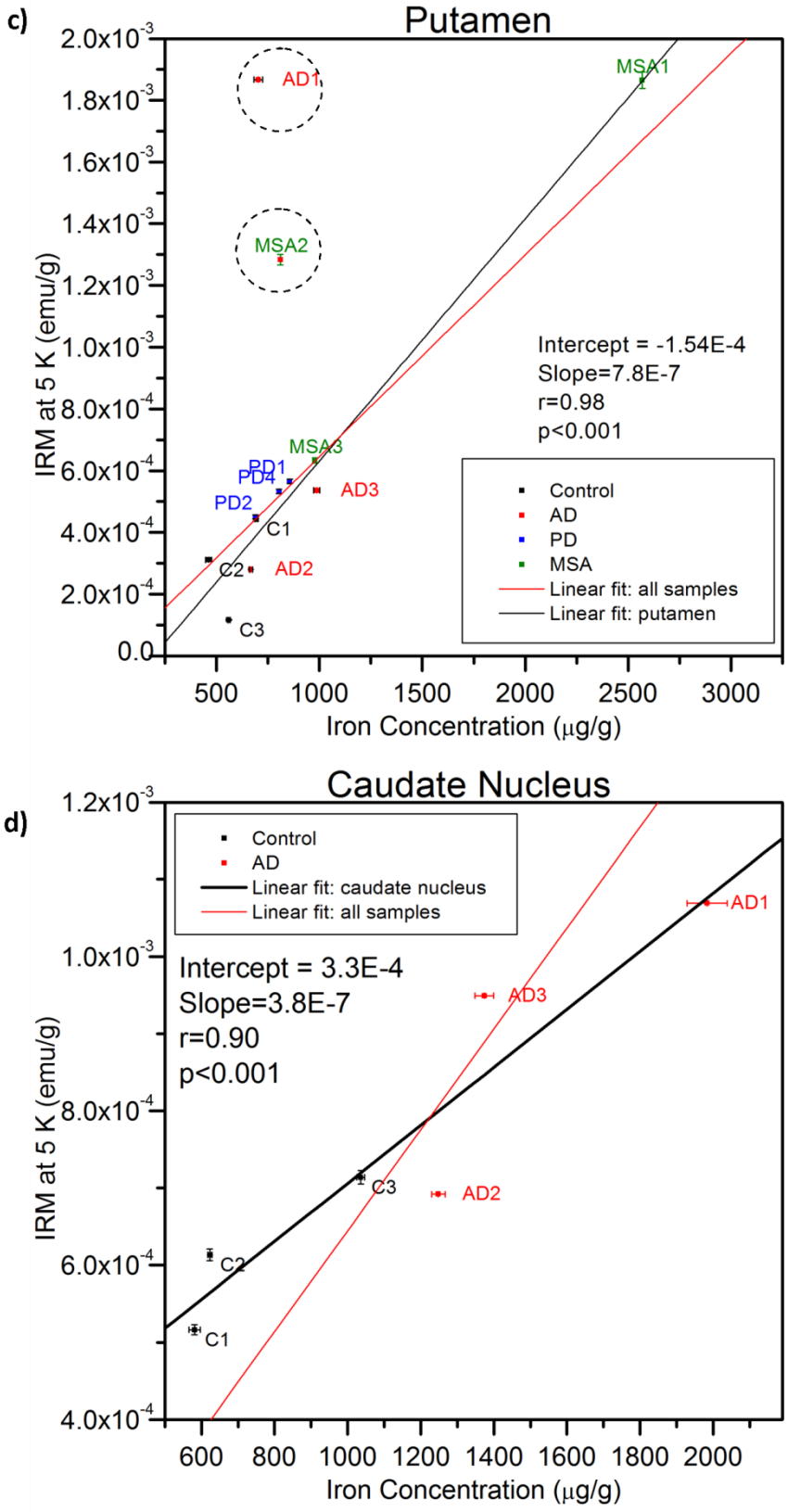

Figure 5.15: IRM at 5 K versus iron concentration in each brain region. The linear fit to data from all regions (from figure 5.14) is shown in red and the black line in each graph shows the fit to data from a) the pons, b) the substantia nigra, c) the putamen and d) caudate nucleus. In the putamen two outlying samples were excluded from the fit and are circled. The data in each region show a strong linear relationship between iron and IRM at 5 K with $r \geq 0.9$. In some regions the data seem to be clustered by disease group, in particular in a) the pons and d) the caudate nucleus.

Region	n	Slope (emu/g)/(μg Fe/g)	Intercept (emu/g)	r	r^2	p
All Regions [with outliers]	42 [40]	(6.5 ± 0.3) E-7 [(6.7 ± 0.7) E-7]	(-9.1 ± 19.1) E-6 [(2.7 ± 5.9) E-5	0.97 [0.80]	0.94 [0.65]	<0.001 [<0.001]
Pons	12	(4.7 ± 0.7) E-7	(4.1 ± 6.8) E-6	0.90	0.80	<0.001
SN	12	(6.0 ± 0.5) E-7	(2.2 ± 2.2) E-5	0.96	0.93	<0.001
Pu [with outliers]	10 [12]	(7.8 ± 0.5) E-7 [(6.7 ± 0.5)] E-7	(-1.5 ± 0.6) E-4 [(1.3 ± 2.8) E-4]	0.98 [0.62]	0.97 [0.39]	<0.001 [0.031]
CN	6	(3.8 ± 0.7) E-7	(3.3 ± 0.8) E-4	0.90	0.81	0.014

Table 5.8: Properties of the linear fits to IRM at 5 K versus iron concentration. A statistically significant linear relationship between IRM at 5 K and iron is observed in all regions. When the outliers are excluded the minimum r value is 0.9, which shows a strong linear correlation.

5.4 Discriminant analysis

In Sections 5.1 and 5.2 one-way ANOVA was used to look for differences between the means of each disease group for one variable (iron concentration or IRM at 5 K) in one brain region at a time. In Section 5.3 the relationship between these two variables was examined using linear regression analysis.

In this section discriminant analysis, a multivariate statistical analysis technique is used to combine the data from multiple brain regions or multiple variables (i.e. iron concentration and IRM). Discriminant analysis creates a model using the data from samples (e.g. pons C1, pons C2, pons C3 *etc*.) from known groups (i.e. control, AD, PD, MSA), and then groups the cases (e.g. C1, C2, C3 *etc.*) based on the model. The proportion of cases correctly grouped by the model shows how successful the model is at distinguishing between disease groups. Cross-validation of the model excludes each case from the model calculation and then uses the resulting model to classify the excluded case. Analysis was carried out using the statistical software SSPS and protocols described in Section 4.6.4.

5.4.1 Iron concentration or IRM at 5 K in multiple brain regions

Iron concentration or IRM at 5 K, per gram of fresh frozen tissue was not very successful in distinguishing between disease groups in most of the regions examined. The pons was the only region which showed statistically significant differences between groups. Discriminant analysis was carried out on all different combinations of brain regions to examine how using data from multiple regions as predictors can improve the potential of these measurements to distinguish between disease states. Discriminant analysis excludes a sample from analysis when there is not a complete data set for it, i.e. data for each variable. Therefore, in some models not every sample is included and the total number of samples involved in the model is given in the results tables.

For three brain regions (pons, SN and Pu) tissue samples from four diseases (control, AD, PD and MSA) were measured and the results of discriminant analysis of these data are shown in Table 5.9 a). Additional control and AD samples were measured from the CN and the result of discriminant analysis for these two disease states, across all four regions, is shown in Table 5.9 b).

Table 5.9 a) shows that no combination of data from the three brain regions can group the cases from all four diseases with 100% accuracy, using either the iron concentration or IRM data. The best iron concentration model, which correctly grouped 80% of the cases, was achieved using data from all three brain regions. The best IRM model also achieved 80% correct classification and used data from the pons and the SN. However, cross-validation showed a significant reduction in the success of the model. Cross-validation involves removing one sample at a time from the model and with such small data set, this is a significant proportion of the information and it is therefore unsurprising that it has such a large effect on the success of the model.

a) Brain Region Combination	Total samples	Control, AD, PD and MSA Proportion assigned to correct group by:			
		Iron concentration		IRM at 5 K	
		Model	Cross-validated	Model	Cross-validated
Pons	12	66.7%	33.3%	66.7%	50.0%
SN	11	36.4%	27.3%	54.5%	36.4%
Pu	12	41.7%	33.3%	58.3%	58.3%
Pons, SN	10	70.0%	50.0%	80.0%	60.0%
Pons, Pu	11	72.7%	27.3%	72.7%	54.5%
SN, Pu	11	54.5%	36.4%	63.6%	36.4%
Pons, SN, Pu	10	80.0%	50.0%	70.0%	50.0%

b) Brain Region Combination	Total samples	Control & AD Proportion assigned to correct group by:			
		Iron Concentration		IRM at 5 K	
		Model	Cross-validated	Model	Cross-validated
Pons	6	83.3%	83.3%	100%	100%
SN	6	50.0%	33.3%	66.7%	50.0%
Pu	6	66.7%	66.7%	66.7%	66.7%
CN	6	66.7%	66.7%	50.0%	33.3%
Pons, SN	6	83.3%	83.3%	100%	100%
Pons, Pu	6	100%	83.3%	100%	100%
Pons, CN	6	83.3%	83.3%	100%	66.7%
SN, Pu	6	66.7%	50.0%	83.3%	33.3%
SN, CN	6	83.3%	83.3%	83.3%	50.0%
Pu, CN	6	100%	66.7%	66.7%	16.7%
Pons, SN, Pu	6	100%	66.7%	100%	83.3%
Pons, SN, CN	6	100%	66.7%	100%	66.7%
Pons, Pu, CN	6	100%	83.3%	100%	83.3%
SN, Pu, CN	6	100%	83.3%	83.3%	16.7%
Pons, SN, Pu, CN	6	100%	66.7%	100%	50.0%

Table 5.9: Proportion of cases correctly classified by discriminant analysis of iron concentration (microgram of iron per gram fresh-frozen tissue) or IRM at 5 K (emu per gram of fresh-frozen tissue). Every possible combination of brain regions was analysed. Table a) shows the result of analysis of control, AD, PD and MSA samples from the pons, SN and Pu and Table b) shows the results of analysis of control and AD samples for the pons, SN, Pu and CN. The table gives the proportion of correctly classified cases for the model and for cross-validation. The best results for each parameter are highlighted in grey.

Table 5.9 b) shows the results of discriminant analysis of control and AD cases from the different combinations of measurements of the pons, SN, Pu and CN samples. Classification is achieved with 100% accuracy in more than one model. For the iron concentration data this always drops to 83.3% with cross-validation, however for the IRM at 5K data 100% correct classification is maintained in three combinations.

In Table 5.9 b) regional combinations which include the pons samples show at worst 83.3% successful grouping with iron data and 100% success with IRM data. All of the top IRM models included data from the pons, however with the iron data one of the most successful models used data from the SN, Pu and CN.

In both tables the iron concentration data in particular support the hypothesis that considering data from multiple regions of the brain may allow differentiation between disease and control, which was not possible when comparing measurements in just one region. Although with this data set differentiating between multiple neurodegenerative diseases is more difficult than between just control and AD, 80% success could still be achieved by combining data from more than one region. Consequently, this also supports the hypothesis that the iron changes across different regions of the brain are different for different neurodegenerative diseases. It is important to note that some combinations of regions reduced the accuracy of the model. For example, for the IRM data in Table 9 a) the combination of all three regions produced a model that was less good at grouping the cases than the one using pons and SN data only.

Something common to both tables is that the best IRM model is better than the best iron concentration model, when cross-validation is taken into account. This is a positive finding in terms of clinical usefulness as IRM at 5 K is a measure of particulate iron, which is the iron content of the tissue which most affects MRI.

5.4.2 Iron concentration and IRM at 5 K

In some of the IRM at 5 K versus iron graphs for individual brain regions in Section 5.3 it was noted that the data points seemed to cluster by disease group: for example for the pons data in Figure 5.15 a). Discriminant analysis of IRM at 5 K and iron concentration (per gram of fresh-frozen tissue) was carried out to examine this clustering and the results are described in Table 5.10. The table shows how the data from known groups was assigned to new groups, the proportion of correctly placed samples for each disease group and the total correct proportion for each region.

Region	Known / Put Into	Control	AD	PD	MSA	Total proportion correct
Pons	Control	3 (3)	0 (0)	0 (0)	0 (0)	
	AD	0 (0)	1 (0)	1 (1)	1 (2)	
	PD	0 (1)	0 (0)	3 (1)	0 (1)	
	MSA	0 (0)	1 (3)	0 (0)	2 (0)	
	Proportion correct	100% (100%)	33.3% (0%)	100% (33.3%)	66.7% (0%)	75.0% (33.3%)
SN	Control	1 (0)	1 (1)	0 (0)	1 (2)	
	AD	0 (1)	2 (0)	0 (1)	1 (1)	
	PD	0 (0)	0 (1)	3 (1)	0 (1)	
	MSA	0 (2)	0 (0)	0 (0)	2 (0)	
	Proportion Correct	33.3% (0%)	66.7% (0%)	100% (33.3%)	100% (0%)	72.7% (9.1%)
Pu	Control	2 (2)	0 (0)	1 (1)	0 (0)	
	AD	1 (1)	1 (0)	1 (1)	0 (1)	
	PD	1 (1)	0 (0)	2 (2)	0 (0)	
	MSA	0 (0)	1 (1)	1 (1)	1 (1)	
	Proportion Correct	66.7% (66.7%)	33.3% (0%)	66.7% (66.7%)	33.3% (33.3%)	50.0% (41.7%)
CN	Control	3 (3)	0 (1)	n/a	n/a	
	AD	0 (1)	3 (2)	n/a	n/a	
	Proportion Correct	100% (100%)	100% (66.7%)	n/a	n/a	100% (83.3%)

Table 5.10: Results of discriminant analysis of iron concentration and IRM at 5 K. The table shows how cases were grouped, compared to their known group. The total proportion of correctly grouped cases for each region is given as well as the proportion correctly grouped for each disease. The numbers in brackets refer to the cross-validation results. The highest proportion of correctly grouped cases was achieved using samples from the pons. For the caudate nucleus only control and AD data were measured, these cases were grouped with 100% accuracy.

In the caudate nucleus, for which only control and AD samples were available, cases were grouped with 100% accuracy. However, this is unsurprising as 100% accuracy was also achieved using just the IRM at 5 K data (Table 5.9 b). The classification of cases using data from the putamen was worse using the combined IRM and iron data, than using the IRM data alone (Table 5.9 a). On the other hand, the classification using pons or SN data was improved by combining the iron and IRM data, giving a success rate of 75% and 72.7% compared to 66.7% and 54.5% respectively. However, in both cases poor results were shown with cross-validation.

5.5 Water content of the tissue samples

The water content of tissue also has a significant influence on the MRI relaxation properties of the tissue. It has been hypothesised that increased water content in degenerating tissue causes a decrease in R_2 and R_2* which may counteract the increase in R_2 that is caused by increased iron concentration [125, 128].

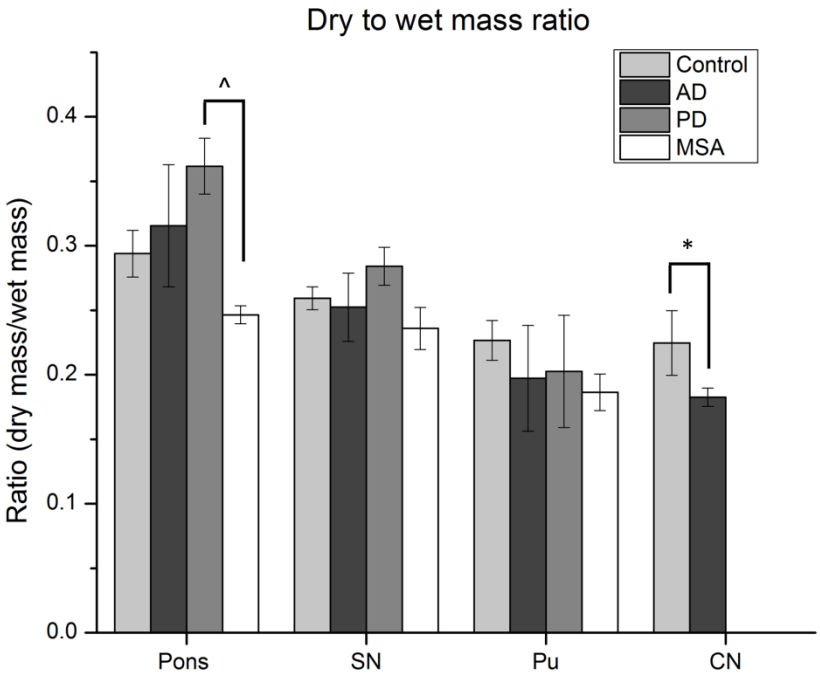

Figure 5.16: Dry to wet mass ratio of tissue samples. A statistically significant decrease in DWR is found in MSA compared to PD pons and in the AD compared to control caudate nucleus. A decrease in DWR indicates an increase in water content of the tissue. ^ = $p<0.05$ by Welch's ANOVA and Kruskal-Wallis test; * = $p<0.05$ by one-way ANOVA and Kruskal-Wallis test.

Figure 5.16 shows the average dry to wet mass ratio (DWR) for each disease group in each region. DWR is equivalent to one minus the water mass fraction of the tissue and therefore a decrease in DWR indicates an increase in water content of the tissue. Data from the control pons and AD putamen violated the Shapiro-Wilk test for a normal distribution ($p<0.05$), but all other groups passed this test. Therefore both parametric (ANOVA) and nonparametric (Kruskal-Wallis) statistical analysis was carried out in SSPS, with both tests giving agreement.

A statistically significant decrease in DWR was found in the pons for MSA compared to PD tissue and in the caudate nucleus for AD compared to control tissue. This shows an increase in tissue water content which may cause decreased R_2 and R_2* in these regions.

5.6 Discussion

5.6.1 Total and particulate iron concentration can differentiate between control and AD cases

The tissue iron concentration measurements in the pons, substantia nigra, putamen and caudate nucleus showed no statistically significant differences between AD and control tissue samples. Despite this, discriminant analysis was used to create a model which successfully grouped all of the cases into AD or control, when the iron concentration data from more than one brain region was used. The ability of information from multiple brain regions to differentiate between AD and other neurodegenerative diseases (PD and MSA) was also demonstrated with 80% success rate.

The SQUID magnetometry measurements of IRM at 5 K provided an estimate of the relative concentration of particulate (mainly ferrihydrite-like iron in ferritin) iron in each sample. Again, no statistically significant differences were observed between control and AD, but correct classification could be achieved with discriminant analysis. This result is particularly relevant for disease diagnosis as it is particulate iron which most influences MRI.

5.6.2 Iron concentration measurements are mostly in agreement with the literature

The mean iron concentrations measured in control substantia nigra and putamen samples fell within the range reported in the literature for healthy tissue in a review compiled by Haacke *et al.* [107]. The measured iron concentration in the caudate nucleus was higher than reported in the literature and no studies could be found of iron concentration in the pons. In this study, only a fairly small sample of tissue was taken from each region for iron quantification as other tissue was preserved for MRI. If the iron concentration throughout the region is non-homogeneous this could explain the increased iron observed in the control CN compared to the literature. For this reason, the position of the samples within the region was matched for each case as closely as possible in order to obtain comparable data. However, perfect matching was not achieved in every case and the consequences of this are discussed further in Section 9.3.

A small number of samples was measured and there was a relatively large variation across the different cases within each region and disease group, however this compared favourably to the size of standard deviations reported in the literature [93].

Although the only statistically significant difference in iron concentration was observed between control and MSA pons, the trend of other changes agrees with findings in the literature. Increased iron in the AD putamen and caudate nucleus is similar in size to a result reported by House *et al.* [19]. There was also evidence for increased iron concentrations in the PD substantia nigra, which again did not reach statistical significance, but is in agreement with the literature [23, 146].

5.6.3 There is no evidence for increased iron with age

Control and disease samples were not perfectly aged matched (Table 5.1), however there is no evidence of age being a dominant factor in the iron concentration measured for any disease

group. The order of samples from highest to lowest iron concentration changes in each brain region studied for the control samples and for each disease group (Figure 5.2).

In Table 3.5, Chapter 3 the empirical equations for iron concentration with age, produced by Hallgren and Sourander [93], were used to predict the consequence of the difference in mean age of the control and AD sample set. A predicted increase in iron concentration of 3.2% in the putamen and 1.9% in the caudate nucleus was made. These changes are much smaller than the standard deviations in mean iron concentration in each region.

5.6.4 There is no evidence for increased magnetite concentration in AD

In general the individual IRM measurements and IRM curves at 5 and 50K were consistent with the majority of particulate iron being in the form of ferritin with ferrihydrite-like core and a small amount of iron in being in the form of magnetite.

Without ferritin extraction or further magnetometry measurements, it is not possible to fully characterise the magnetic structure of the particulate iron. However, a ratio of IRM at 50 K to IRM at 5 K provided an estimation of the relative proportional of particulate iron in the form of magnetite. This showed an increase in magnetite concentration in the pons compared to in other regions. However, there was no evidence for an increase in proportion or total concentration in any particular disease group. Additionally, there was evidence of an increasde proportion of iron being in the form of magnetite in some individual samples (Table 5.6).

5.6.5 What is the potential clinical significance of these results in terms of detecting AD with MRI?

The ability of discriminant analysis to differentiate between control and AD supports the hypothesis that iron homeostasis is altered in the AD brain. Additionally, samples from Parkinson's Disease and Multiple System Atrophy cases have also been examined and provide evidence of iron changes in the brain that are disease specific. For example, a statistically

significant increase in iron was observed in the MSA pons where there was a trend for a decrease in iron in the substantia nigra.

If the changes in iron (more specifically in particulate iron) seen here can be detected with enough sensitivity by MRI, it should be possible to distinguish between AD and control by discriminant analysis of R_2 or R_2* measurements.

The results of discriminant analysis of IRM at 5 K (Table 5.9) show that the pons is a strong candidate both for aiding in the differentiation between AD and control and between AD and other neurodegenerative diseases. However, the total iron concentration in the pons is much lower than in the other brain regions studied and therefore the absolute differences in iron may be too small to be detected with MRI.

5.7 Summary

I. No statistically significant difference in total or ferritin iron (as estimated by measurement of IRM at 5 K) was observed between AD and control tissue in any of the four brain regions studied.

II. However, discriminant analysis was used to successfully differentiate between AD and control samples using iron concentration, or IRM at 5 K data, from multiple brain regions.

III. There was no evidence of increased magnetite in the AD samples compared to control, but there was evidence for at least some magnetite in most samples.

IV. From these results it is hypothesised that R_2 and/or R_2* measurements of multiple brain regions may allow differentiation between control and AD samples, even if no statistically significant differences are observed for individual regions.

Chapter 6:
Synchrotron X-ray fluorescence mapping

In Chapter 5 the iron concentration of 0.1 to 0.5 g blocks of tissue, which were cut from the caudate nucleus, putamen, substantia nigra and pons, was measured using GFAAS (Graphite Furnace Atomic Absorption Spectrometry) or ICP-MS (Inductively Coupled Plasma Mass Spectrometry). This achieved accurate quantification of total tissue iron concentration for the carefully dissected samples and allowed a comparison to be made between Alzheimer's Disease (AD) and control tissue. However, this technique does not provide comparable spatial resolution to the high resolution MRI mapping at 600 MHz (in plane resolution = 62 μm) or 400 MHz (in plane resolution = 86 μm) that will be presented in Chapter 7.

Synchrotron X-ray fluorescence (SXRF) mapping is a technique which allows highly sensitive and specific mapping of iron and other elements in biological samples, with a spatial resolution of down to approximately 1 μm^2. Alternative elemental mapping techniques such as electron microprobe and particle induced X-ray emission (PIXE) can provide similar or enhanced spatial resolution, but have lower detection limits and can cause beam damage to the sample [117]. Laser Ablation Inductively Coupled Plasma Mass Spectroscopy (LA-ICP-MS) can produce metal maps of tissue sections with a similar sensitivity and resolution to SXRF [119]. However, as it is a destructive technique there is no opportunity to create multiple maps at different resolutions for the same sample.

30 μm thick tissue sections that had been cut from the MRI mapped blocks were mapped at beamline I18 at the Diamond Light Source (DLS) to produce 60 μm resolution maps of relative iron, copper and zinc concentration. The samples were prepared using a protocol developed by our group that minimised the chance of contamination with metal particulates [132]: sections are cut using a non-metal blade from the un-embedded tissue and mounted on high

quality quartz slides. Samples were not fixed before sectioning as fixatives have been shown to leach metals from tissue [91].

The SXRF maps collected at the beamline I18 at the Diamond Light Source show the relative concentration distribution of metals, and not the absolute concentration. With careful control of variables and normalisation of each map, comparisons of relative concentration can also be made between different samples. The absolute iron concentration of adjacent blocks of tissue for some of the samples was measured and presented in Chapter 5. This information is used to approximately calibrate the SXRF iron maps as described in Section 6.4. This then allows estimation of iron concentration in regions for which SXRF maps were made, but bulk tissue measurements were not.

The SXRF metal maps show the inhomogeneity of metal distribution within and between brain regions. Each map is segmented into distinct anatomical structures and the mean and variance of each structure compared for the control and AD example. In Chapter 8 the SXRF maps will be spatially matched to the corresponding MRI maps to investigate the relationship between R_2 and R_2* and iron concentration in control and AD tissue.

6.1 SXRF metal maps

The details of each SXRF mapping experiment are given in Table 4.5 in Section 4.4 and the details of each case are given in Table 3.4 in Section 3.2.2. SXRF mapping of the caudate nucleus (CN), putamen (Pu), globus pallidus (GP), substantia nigra (SN) and amygdala (Amyg) was carried out over one 5 day experiment at the Diamond Light Source: experiment DLS5. The pons tissue samples were mapped over 4 experiments numbered DLS1 to DLS4. Collecting data over multiple visits increases the potential sources of experimental error and therefore the pons data are examined separately in Section 6.5.

Due to the time required to collect each map and the limited time available at the experimental facility, only one control and one AD sample were imaged for each brain region.

The samples to be mapped were chosen based on the results of MRI mapping (Chapter 7). Sections for mapping were collected on quartz slides and prepared as described in Section 3.3.3.1. No samples from control C1 were mapped as this sample was not well age-matched to the other controls or to the AD samples.

Section 4.4.2 describes fitting the SXRF spectra, using the software PyMCA, to produce metal maps and the normalisation of each pixel to the incident X-ray beam, I_0. The conversion of the data files into individual metal maps compatible with the image processing software ImageJ was also described. However, normalisation to I_0 does not correct for variation in the distance between the sample and the X-ray detector, which changes the intensity of the X-rays at the sample. Therefore each map is normalised to the chemically constant 'background' provided by the quartz slide. The slide contribution to each map is also subtracted from the map in order to leave only signal from the tissue section in the final SXRF iron, copper and zinc maps.

6.1.1 Subtracting slide background

Figure 6.1 shows a typical fluorescence spectrum for an area of quartz slide, where the fluorescence intensity is averaged over the number of pixels sampled. The iron and copper peaks are clearly present, but the zinc peak is only just visible on the edge of the scatter peak, showing that there is a very low concentration of zinc present in the slide. There is also a small concentration of nickel present in the slide.

Comparison of the zinc signal of the quartz slide to the typical signal on a tissue section shows that the background signal is around 1% of the total signal and therefore is considered negligible and not subtracted from the tissue map. In contrast, the copper signal of the slide is relatively high and is typically 50% of the on-tissue fluorescence signal. The iron signal in the quartz is well above background and so can be fitted in PyMCA and is subtracted from the map, although it is only around 5 % of the typical on-tissue signal. When each SXRF map was collected an area of quartz slide was included. ImageJ was used to find the mean and standard

deviation of the area of slide in the metal maps (which had been fitted in PyMCA and normalised to I_0). The average copper and iron signal, shown in Figure 6.2, was then subtracted from the whole map.

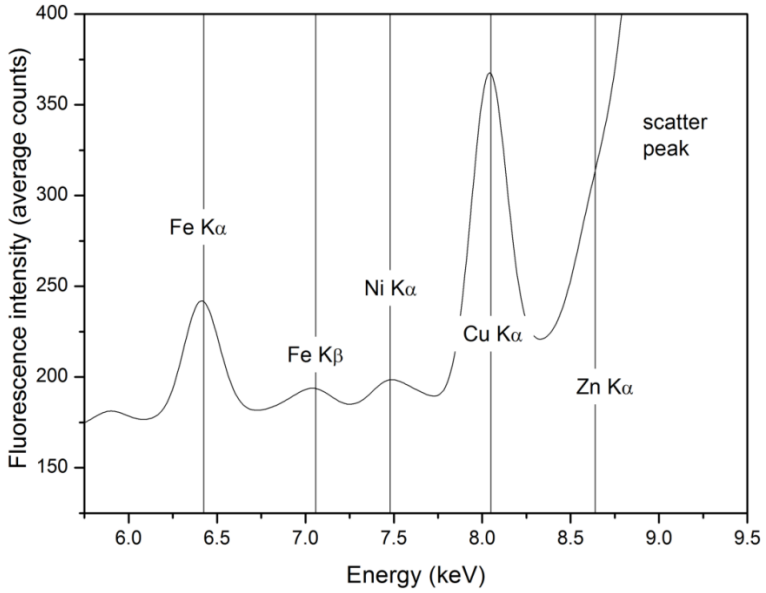

Figure 6.1: Typical fluorescence spectrum of an area of quartz slide, with the signal intensity averaged over the number of pixels sampled. The iron Kα and Kβ peaks can be seen above background, as can the nickel and copper Kα peaks. The Zn Kα is only just visible on the edge of the scatter peak from the incident beam I_0.

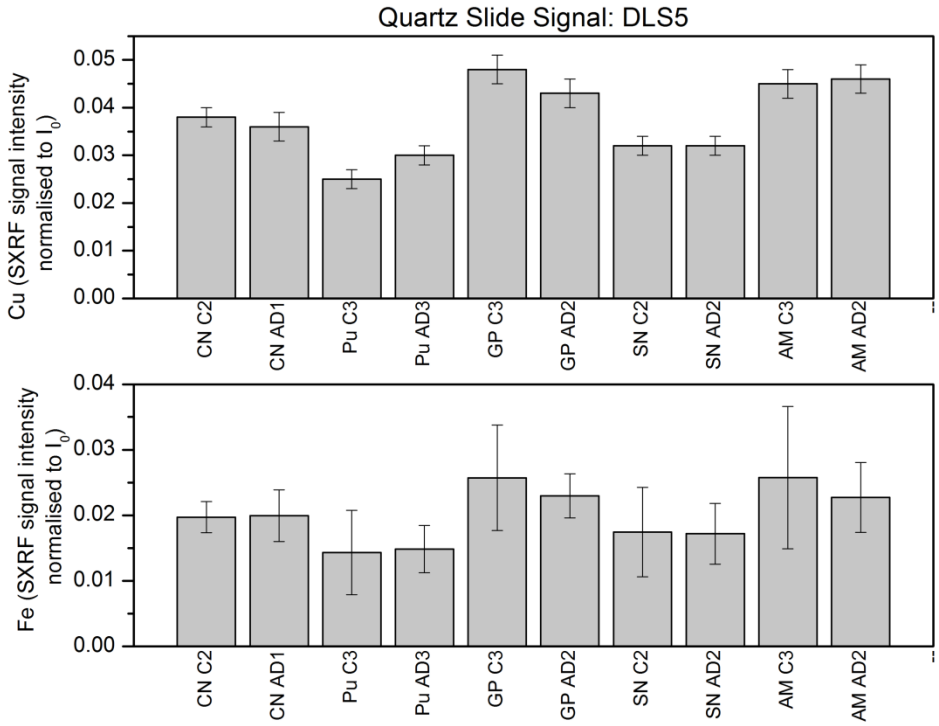

Figure 6.2: Quartz slide SXRF signal intensity. The mean and standard deviation of the a) copper and b) iron SXRF signal intensity (normalised to I_0) for the quartz slide for each sample mapped in experiment DLS5.

6.1.2 Normalising to slide background

In experiment DLS5 the detector was moved in and out of position between samples and although the position of the detector was marked with a gauge, slight variation between samples' position is possible. Figure 6.2 shows the mean and standard deviation of the iron and copper SXRF signal intensity of the area of the quartz slide included in each map. The trend of signal intensity is very similar for copper and iron, which is as expected as the same brand of high quality quartz slides was used in each case. As iron is the main focus of this study all three metal maps were normalised to the average background iron fluorescence intensity.

Table 6.1 gives the percentage difference in the iron SXRF signal from the slide background of the AD sample compared to the control sample for each of the brain regions measured during DLS5, calculated using the formula:

$$\left(\frac{Slide_C - Slide_{AD}}{Slide_C}\right) \times 100 \qquad (6.1)$$

This calculation shows the proportional change that normalising to the slide background has on the whole map.

Brain Region	Difference in slide Fe signal for AD compared to control
Caudate nucleus	1.2 %
Putamen	3.8 %
Globus pallidus	-10.7 %
Substantia nigra	-1.5 %
Amygdala	-11.9 %

Table 6.1: Percentage difference of the measured iron fluorescence intensity of the quartz slides for AD samples compared to the control. Data were normalised to slide background to correct for this variation.

6.1.3 Final adjustments and error estimation

6.1.3.1 Estimation of measurement error

Estimating the measurement error is important in order to compare relative metal concentrations within and between maps. As no standards with known metal concentration were available, estimating the measurement error is not trivial. A number of factors may contribute to the error in the maps including fitting the spectra in PyMCA and normalising to background.

The quartz slides provided a constant background and were used for normalising the data (as described above) and also to estimate the measurement error. As can be seen in Figure 6.2 there is a large standard deviation in the mean iron SXRF signal of each slide. However, the copper signal provides a second point of reference, where the ratio between the iron and copper in the slide should be the same across all maps. The ratio of iron to copper of the quartz slide in each map was calculated and the mean and standard deviation found. The standard deviation is ± 5% and this provides an estimation of the error in the normalisation of each map. As this error estimation is made from fitted SXRF maps it includes the effect of the error in fitting the SXRF spectra. Furthermore, as the quartz slide has the minimum SXRF signal intensity of any area of the map it is likely to have the greatest fitting error. Therefore ± 5% is used as a standard measurement error in the relative metal concentration measured by SXRF.

The other major potential source of error in comparing metal concentration between maps is variation in section thickness. Sections were cut at 30 μm using a recently serviced and calibrated cryomicrotome and therefore should be consistent.

6.1.3.2 Setting the threshold

Once the average slide background had been subtracted, individual pixels values for the slide were approximately zero. The ‘adjust threshold’ function in ImageJ was then used to set the slide pixels to ‘NaN’ meaning that they have no value and are therefore not included in any

measurements made on the maps. This is particularly useful for sections with tears or cracks, as it means there is no need to manually draw around the gaps in the tissue.

The upper threshold limit was set to remove very high signal due to any specks of contamination, for example from dust landing on the slide, or to remove areas where the tissue had folded or curled during sectioning. The threshold limits were set very carefully so as not to exclude the real variation in metal concentration in the tissue. Therefore in some cases areas of folded tissue were manually deleted from the map.

6.1.3.3 Colouring conventions

The individual iron, copper and zinc maps shown in Section 6.3 were assigned to a temperature colour scale, as this provides good contrast for the relative metal concentration distribution within each map. The normalisation to I_0 and slide background means that, in conjunction with the calibration bar, these maps can be used to visually compare relative metal concentrations between samples.

The different metal maps can also be overlaid in ImageJ, with each map assigned to a different colour channel. The convention in our group is to assign iron to red, copper to green and zinc to blue. These maps show the variation in distribution in the different metals across the section and also often highlight the boundaries between anatomical features more clearly than individual metal maps do.

After the final metal maps were produced (as described above) segmentation of the maps into regions of interest (ROI) and measurement of the average SXRF signal in each ROI were used to quantitatively compare between disease and control. Note that due to differences in fluorescence efficiency between different metals, comparisons of concentration between different metals are not simply reflected by signal intensity.

6.2 Segmenting SXRF maps

The brain regions studied in this thesis are introduced in Section 3.2.1 and Appendix A. In Section 3.2.3 and Appendix B the way in which each sample was cut from a larger tissue block is shown. This information, together with the contrast in the combined metal SXRF maps, haematoxylin stained tissue sections and a selection of reference materials [167, 171, 188], was used to identify the different neuroanatomical structures present in each map. As some contrast between tissue type was lost in the stained post-SXRF sections, adjacent sections were also used to aid in segmentation.

Each structure was manually drawn around using the region of interest (ROI) tool in ImageJ. The analysis is not limited to the six brain regions which were the main target of this study, but includes the surrounding structures present in the SXRF maps. This is important as the surrounding tissues may show changes in metal concentration and distribution with AD. Therefore examining these structures will help to answer the question: are changes in iron concentration localised to specific structures? Figures 6.3 to 6.12 show the segmentation of the combined iron, copper and zinc maps for each sample. The colour range in each map is set to give the best contrast between structures and is not the same for different samples.

Caudate Nucleus

Both the control (Figure 6.3) and AD (Figure 6.4) caudate nucleus samples contain the same structures: a portion of the head of the caudate nucleus (CN), tissue from the anterior limb of the internal capsule (AIC) and white matter medial to the CN (WM-CN).

Putamen

In addition to putamen tissue (Pu) both samples (control Figure 6.5 and AD Figure 6.6) contain white matter lateral to the putamen (Pu-WM). The control sample C3 also has tissue from the anterior limb of the internal capsule (AIC). The AD sample seems to be from a slightly more inferior level than the control and does not contain the top of the putamen.

In terms of iron concentration the putamen is observed as two distinct regions. The majority of the putamen had a high concentration of iron (Pu_high), whereas along the lateral edge there was a band of relatively low iron concentration (Pu_low).

The AD sample contains a very high inclusion of iron which surrounds a blood vessel and this was excluded from the segmentation of the regions Pu and Pu_high.

Globus Pallidus

In both the control (Figure 6.7) and AD (Figure 6.8) sample of the globus pallidus a region of the external globus pallidus (GPe) and high iron putamen (Pu_high-GP) are segmented. The thin lamina of white matter (WM-GP) separating the external globus pallidus and putamen is also segmented in both maps.

Additionally, in the control map tissue from the internal capsule (IC) is present and in the AD map the internal globus pallidus (GPi) and low iron region of the putamen (Pu_low-GP) are segmented.

Substantia Nigra

From the section stained with haematoxylin and the metal maps it is not straight forward to divide the substantia nigra into the pars reticulata and (SNr) and pars compacta (SNc). Therefore the image was segmented into the substantia nigra (SN) and cerebral crus (CC). The segmentation is shown for sample C2 in Figure 6.9 and AD2 in Figure 6.10.

In both maps a ‘gap’ in the high iron band is observed towards the LHS of the image. This is excluded from the SN segmentation and assigned its own ROI. Finally the SXRF section was stained after mapping and used to draw an ROI around the approximate distribution of the dopaminergic neurons.

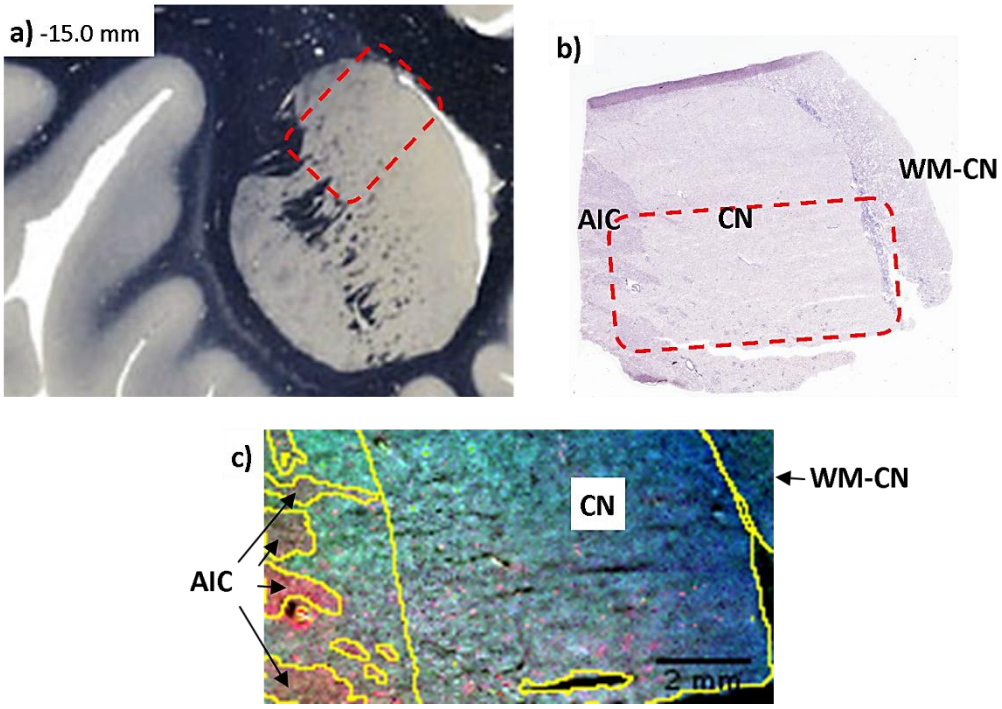

Figure 6.3: Segmentation of the SXRF map of caudate nucleus sample C2. a) Anatomical reference of the caudate nucleus at level –15 mm, with the approximate position of the SXRF map outlined in red. b) An adjacent section to the SXRF mapped section, stained with haematoxylin and with the approximate area of the map outlined in red. c) The SXRF map of iron, copper and zinc, showing the segmentation of the caudate nucleus (CN), anterior limb of the internal capsule (AIC) and white matter medial to the CN (WM-CN).

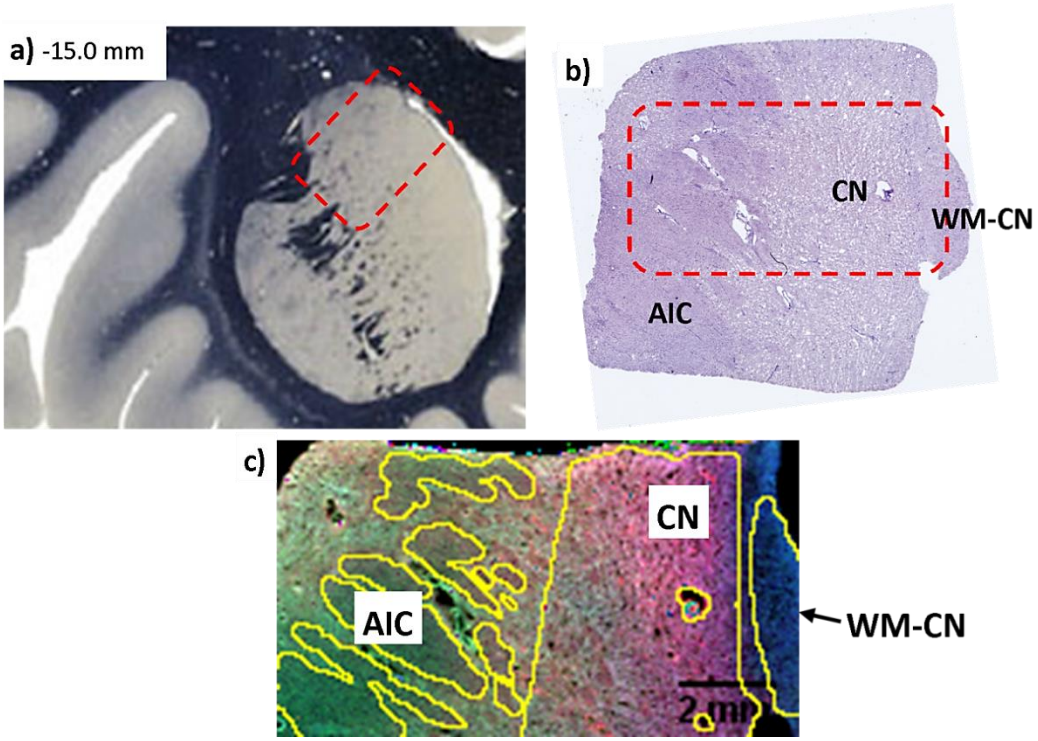

Figure 6.4: Segmentation of the SXRF map of caudate nucleus sample AD1. a) Anatomical reference of the caudate nucleus at level –15 mm, with the approximate position of the SXRF map outlined in red. b) An adjacent section to the SXRF mapped section, stained with haematoxylin and with the approximate area of the map outlined in red. c) The SXRF map of iron, copper and zinc, showing the segmentation of the caudate nucleus (CN), anterior limb of the internal capsule (AIC) and white matter medial to the CN (WM-CN).

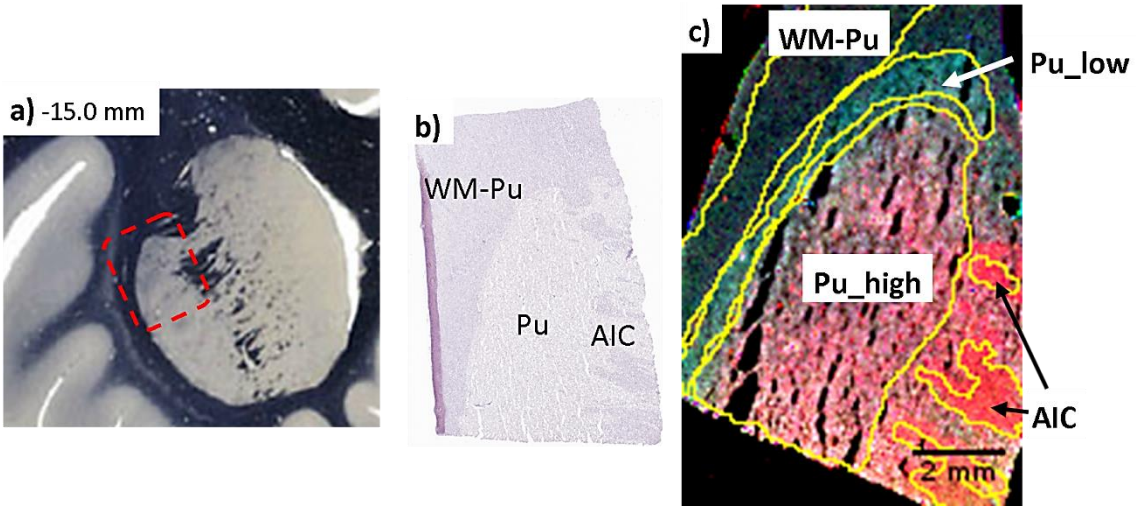

Figure 6.5: Segmentation of the SXRF map of putamen sample C3. a) Anatomical reference of the putamen at level –15 mm, with the approximate position of the SXRF map outlined in red. b) A haematoxylin stained section, adjacent to the SXRF mapped section. c) The SXRF map has been subdivided into three main regions: the putamen (Pu), the anterior limb of the internal capsule (AIC) and white matter adjacent to the putamen (WM-Pu). The putamen was further subdivided into two distinct areas: high iron (Pu_high) and low iron (Pu_low). This division between high and low iron is not visible in the stained section.

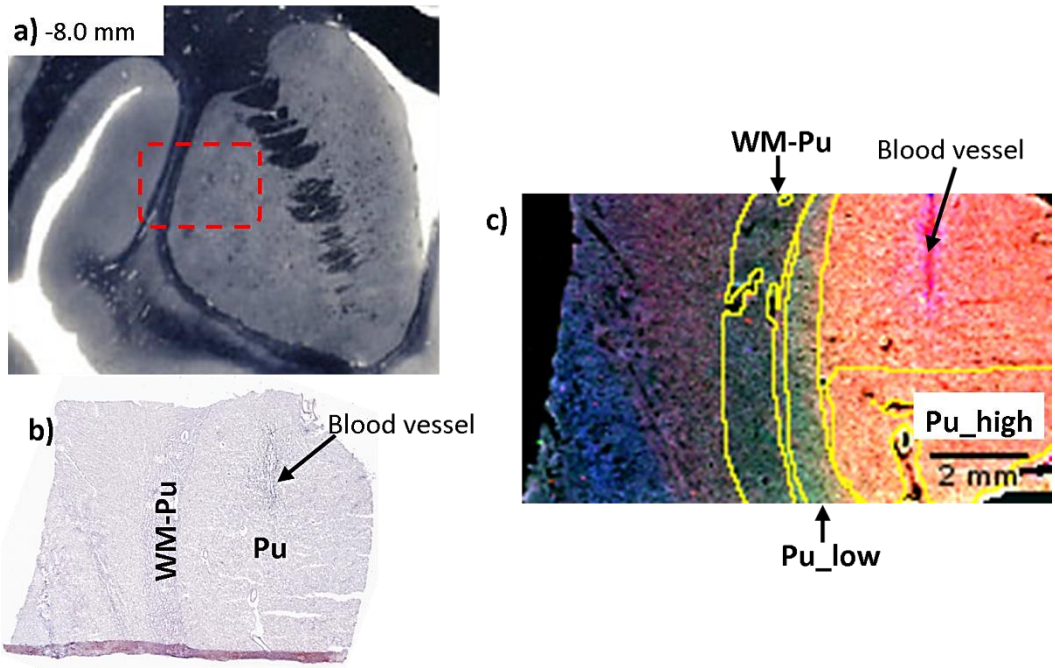

Figure 6.6: Segmentation of the SXRF map of putamen sample AD3. a) Anatomical reference of the putamen at level –8 mm, with the approximate position of the SXRF map outlined in red. b) A haematoxylin stained section of the putamen, adjacent to the SXRF mapped section. c) The SXRF map has been subdivided into three main regions: the putamen (Pu), the anterior limb of the internal capsule (AIC) and the white matter adjacent to the putamen (WM-Pu). The putamen was further subdivided into two distinct areas: high iron (Pu_high) and low iron (Pu_low). This division between high and low iron is not visible in the stained section. This sample contained a blood vessel which was surrounded by a very high concentration of iron. The blood vessel and the surrounding tissue was excluded from the segmentation.

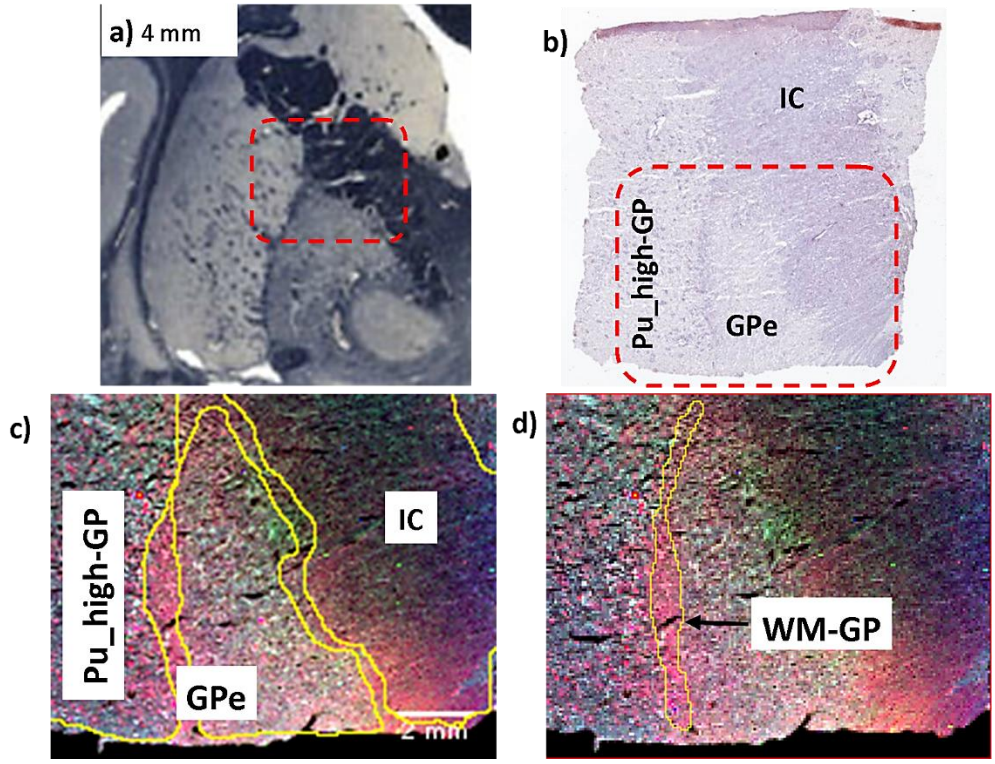

Figure 6.7: Segmentation of the SXRF map of globus pallidus sample C3. a) Anatomical reference of the globus pallidus at level 4 mm, with the approximate position of the SXRF map outlined in red. b) An adjacent section stained with haematoxylin. c) The combined metal SXRF map is segmented into the external globus pallidus (GPe), internal capsule (IC) and high iron region of the putamen (Pu_high-GP). d) The lamina of white matter separating the putamen and globus pallidus is also segmented (WM-GP).

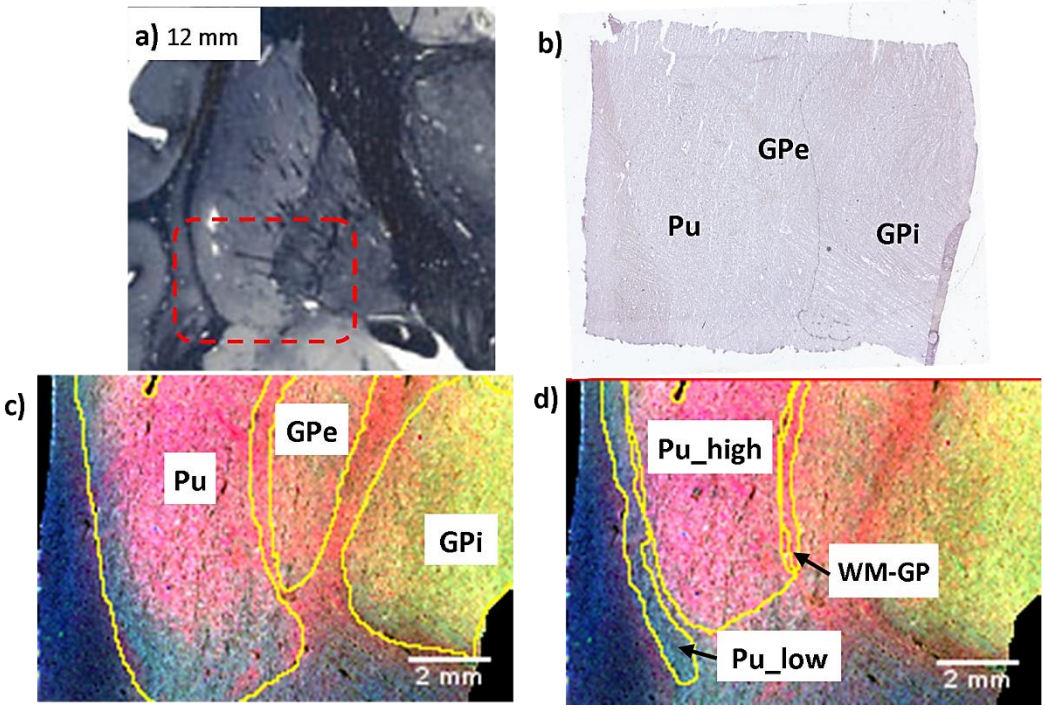

Figure 6.8 Segmentation of the SXRF map of globus pallidus sample AD2. a) Anatomical reference of the globus pallidus at level 12 mm, with the approximate position of the SXRF map outlined in red. b) The mapped section stained with haematoxylin. c) The combined metal SXRF map is segmented into the putamen (Pu), external globus pallidus (GPe) and internal globus pallidus (GPi). d) The putamen was further segmented into: the high and low iron regions (Pu_high and Pu_low) and the lamina of white matter separating the Pu and GPe (WM-GP).

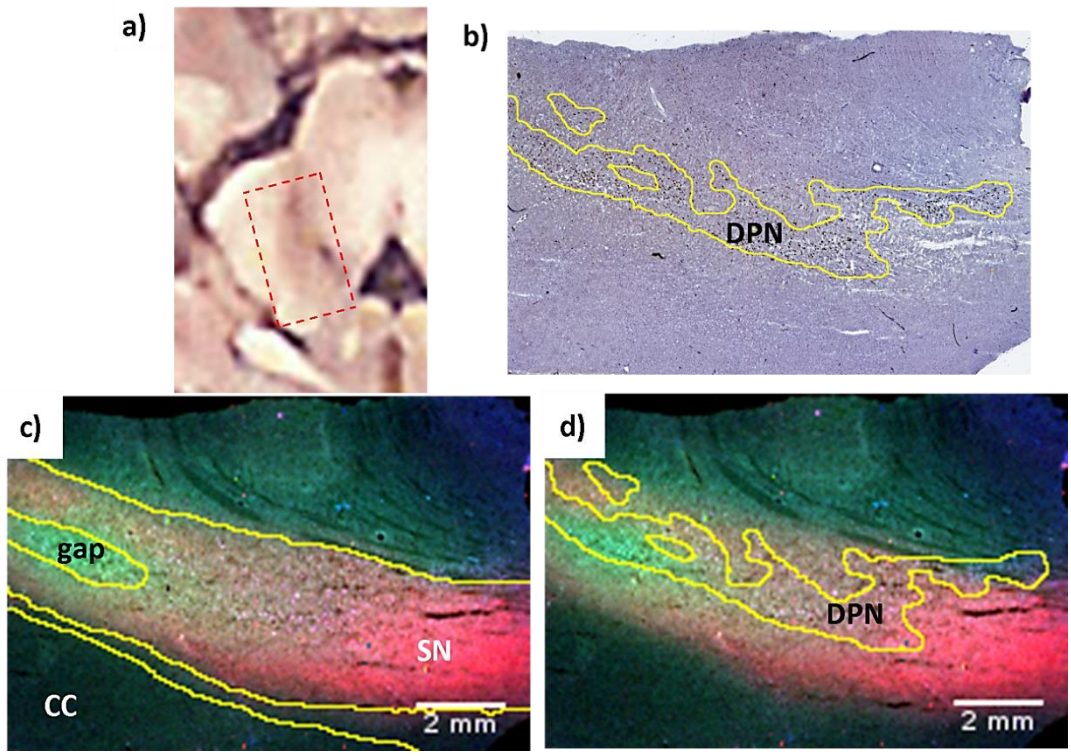

Figure 6.9: Segmentation of the SXRF map of substantia nigra sample C2. a) Anatomical reference of the substantia nigra with the approximate area of the mapped section outlined in red. b) The haematoxylin stained mapped section, with the dopaminergic neuron (DPN) dense region outlined in yellow. c) SXRF map with the cerebral crus (CC) and substantia nigra (SN) and 'gap' segmented. d) The SXRF map showing the approximate distribution of the DPNs.

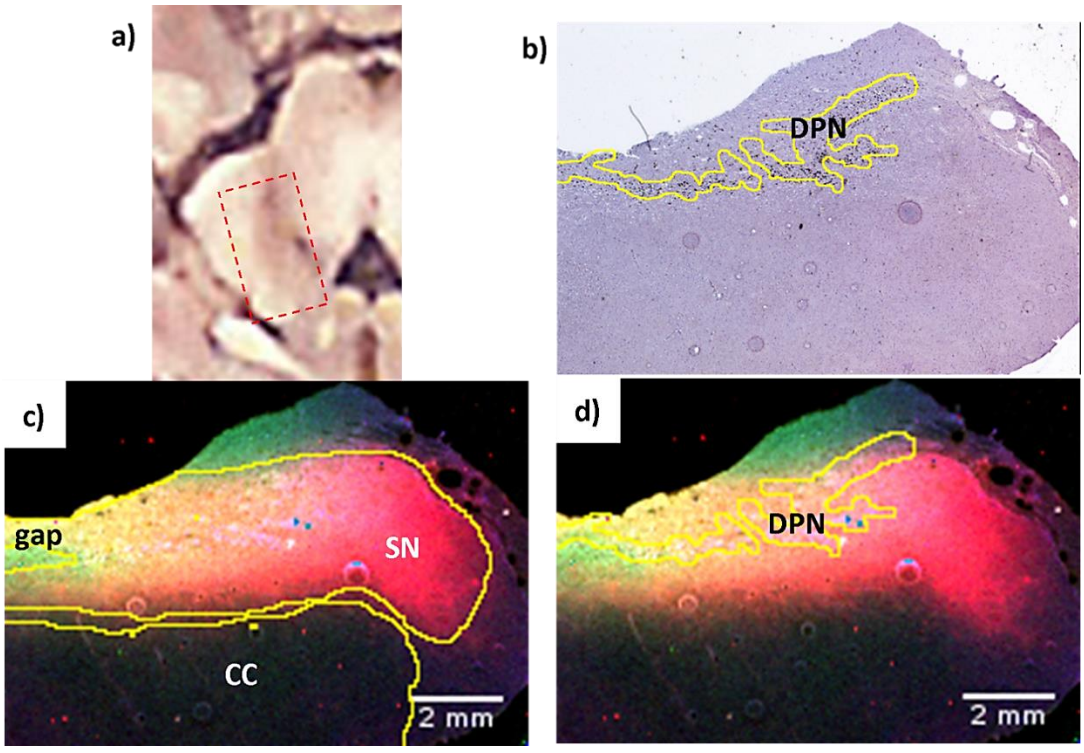

Figure 6.10: Segmentation of the SXRF map of the substantia nigra sample AD2. a) Anatomical reference of the substantia nigra with the approximate area of the mapped section outlined in red. b) The haematoxylin stained mapped section, with the dopaminergic neuron (DPN) dense region outlined in yellow. c) SXRF map with the cerebral crus (CC) and substantia nigra (SN) and 'gap' segmented. d) The SXRF map showing the approximate distribution of the DPNs.

Amygdala

The amygdala control sample C3 and Alzheimer's Disease sample AD2 are shown in Figures 6.11 and 6.12 respectively. It was not possible to segment the amygdala maps into any of the amygdala sub-nuclei due to the small sample which included no surrounding structures to aid identification. However, the feedback from neuropathologist Dr Lili-Naz Hazrati is that the tissue is from inside the amygdala and from a similar position in both samples.

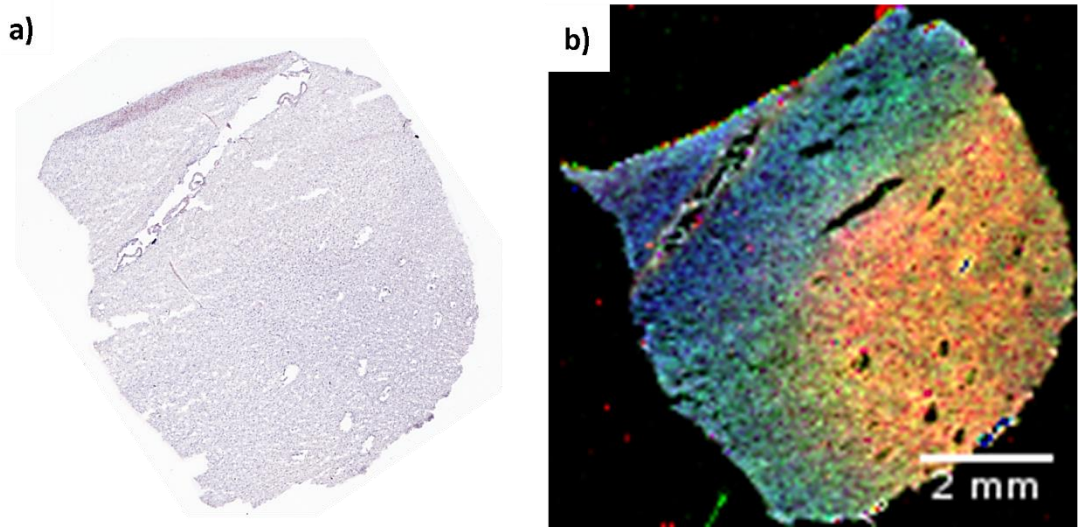

Figure 6.11: SXRF map of amygdala sample C3. a) A section cut from adjacent to the mapped section and stained with haematoxylin and Congo red. b) The iron, copper and zinc SXRF map.

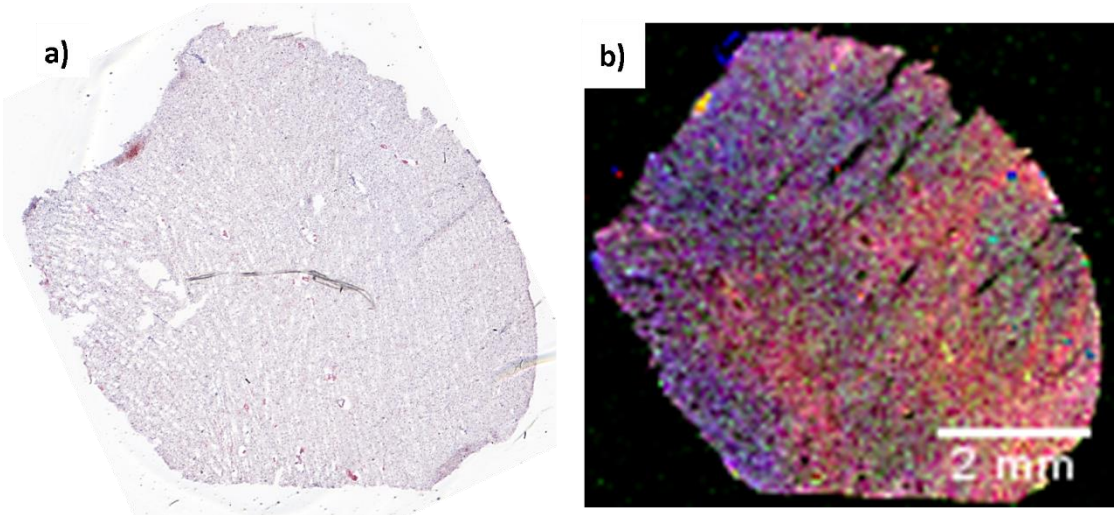

Figure 6.12: SXRF map of amygdala sample AD2. a) A section cut from adjacent to the mapped section and stained with haematoxylin and Congo red. b) The iron, copper and zinc SXRF map.

6.3 SXRF maps: qualitative and quantitative analysis

With the anatomical features in the SXRF maps identified, it is possible to examine the iron, copper and zinc distribution within each region and between the AD and control samples.

6.3.1 Qualitative observations

Figures 6.13 to 6.17 show the maps of relative concentration distribution of iron, copper and zinc in the control and AD example from the caudate nucleus, putamen, globus pallidus, substantia nigra and amygdala respectively. Due to the careful normalisation and subtraction of slide background, the concentrations can be directly compared between each map (of the same metal). A calibration bar is shown for each map, with units of 'normalised SXRF signal intensity'.

The maps are displayed using a temperature colour scheme for maximum contrast. The segmented, multi-metal maps are also included to show the main neuroanatomical features, with the intensity of each metal distribution within these maps set to produce the best contrast. In order to aid comparison of metal concentration distribution between pairs of AD and control maps the same intensity range was used where possible. However, in many cases this was not sensible as detail was lost in one or both of the maps if the same range was used and priority was given to showing the detail of metal distribution within the individual maps.

Caudate Nucleus

Figure 6.13 shows the metal distribution in the caudate nucleus samples C2 and AD1. In the CN the concentration of all three metals is higher in the AD sample compared to the control. There is also evidence for altered iron distribution within the CN and between the CN and surrounding structures. In the control CN the iron concentration decreases from the AIC towards the WM, whereas it remains high in this direction in the AD sample. In the control sample the concentration of iron in the AIC is higher than in the CN, whereas in the AD map the CN has a higher concentration.

Putamen

Figure 6.14 shows the SXRF maps of iron, copper and zinc in putamen samples C3 and AD3. A region of very high iron concentration in the AD putamen coincides with the location of a blood vessel. The distribution of copper and zinc is similar in the AD and control samples, but the overall concentration of zinc is increased.

A region of decreased iron concentration, Pu_low, was defined in the combined metal maps as a band of reduced iron concentration, which runs along the lateral edge of the putamen. The individual maps reveal that copper and zinc concentration are unchanged in this area compared to the rest of the putamen, whereas the iron concentration is reduced. The same feature is observed in the AD map of the globus pallidus in Figure 6.15, which includes tissue from the putamen.

Globus Pallidus

The iron, copper and zinc SXRF maps of the globus pallidus for samples C3 and AD2 are shown in Figure 6.15. In the control sample iron is elevated in the external globus pallidus, compared to the putamen, whereas the opposite is true in the AD map. The SXRF maps of the CN and Pu (Figures 6.13 and 6.14) show a close relationship between the distribution of copper and zinc. This is the case for most structures in the Figure 6.15, apart from the GPi where an elevation in copper is not matched by an elevation in zinc.

The putamen is a large structure and the tissue in these sections is approximately 10 to 20 mm away from the tissue in Figure 6.14. The iron concentration in Pu_high is higher in Figure 6.15 than in Figure 6.14. This shows that iron concentration changes throughout this nucleus, over distances that would be resolvable with clinical MRI.

Substantia Nigra

The normalised SXRF metal maps of C2 and AD2 substantia nigra are shown in Figure 6.16. Each metal shows a distinct distribution within the SN, which is seen in both the control and

AD sample. Iron is highest at the medial end of the substantia nigra. Conversely, copper is highest toward the lateral side of the SN and is particularly high in the region of the 'gap' in the high iron signal. This is particularly clear in the maps of sample C2. Zinc concentration remains more consistent across the SN with a slight increase at the medial end. The concentration of iron and zinc is higher in the SN of the AD sample compared to the control.

The 'gap' in iron seems to correspond approximately to nigrosome 1, which is an area defined by Damier *et al.* based on its poor staining for calbindin [189].

Amygdala

Figure 6.17 shows the SXRF metal maps for the amygdala from cases C3 and AD2. No structures could be positively identified within the map. The pattern of iron distribution is different in the AD sample compared to control, which could be due to the inclusion of different sub-nuclei of the amygdala in each map. However, this could not be confirmed by examination of the metal maps or haematoxylin stained sections.

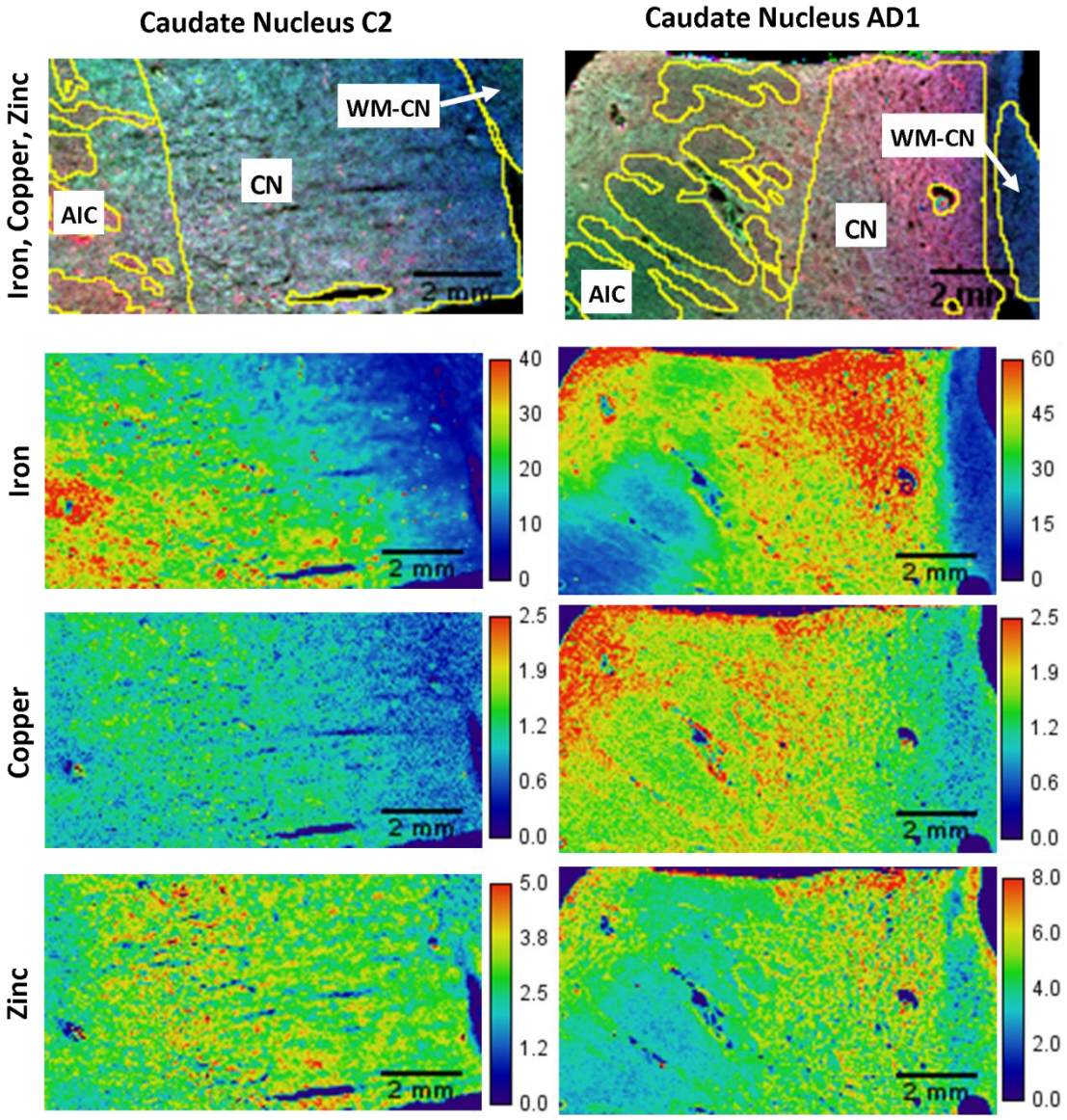

Figure 6.13: Iron, copper and zinc distribution in the caudate nucleus. The anatomical features present are the: caudate nucleus (CN), anterior limb of the internal capsule (AIC) and the white matter medial to the caudate nucleus (WM-CN). Individual metal maps show the relative concentration distribution of iron, copper and zinc, plotted on a temperature scale, where the calibration bars show the normalised SXRF signal intensity. In the CN tissue the concentration of each metal is higher in the AD sample compared to control. The distribution of Cu and Zn is similar in AD and control. The iron concentration in the control CN reduces gradually from the AIC towards the WM-CN, whereas it remains high throughout the CN in the AD map. The concentration of iron in the AIC is higher than in the CN in the control map, however in the AD sample it is lower than in the CN.

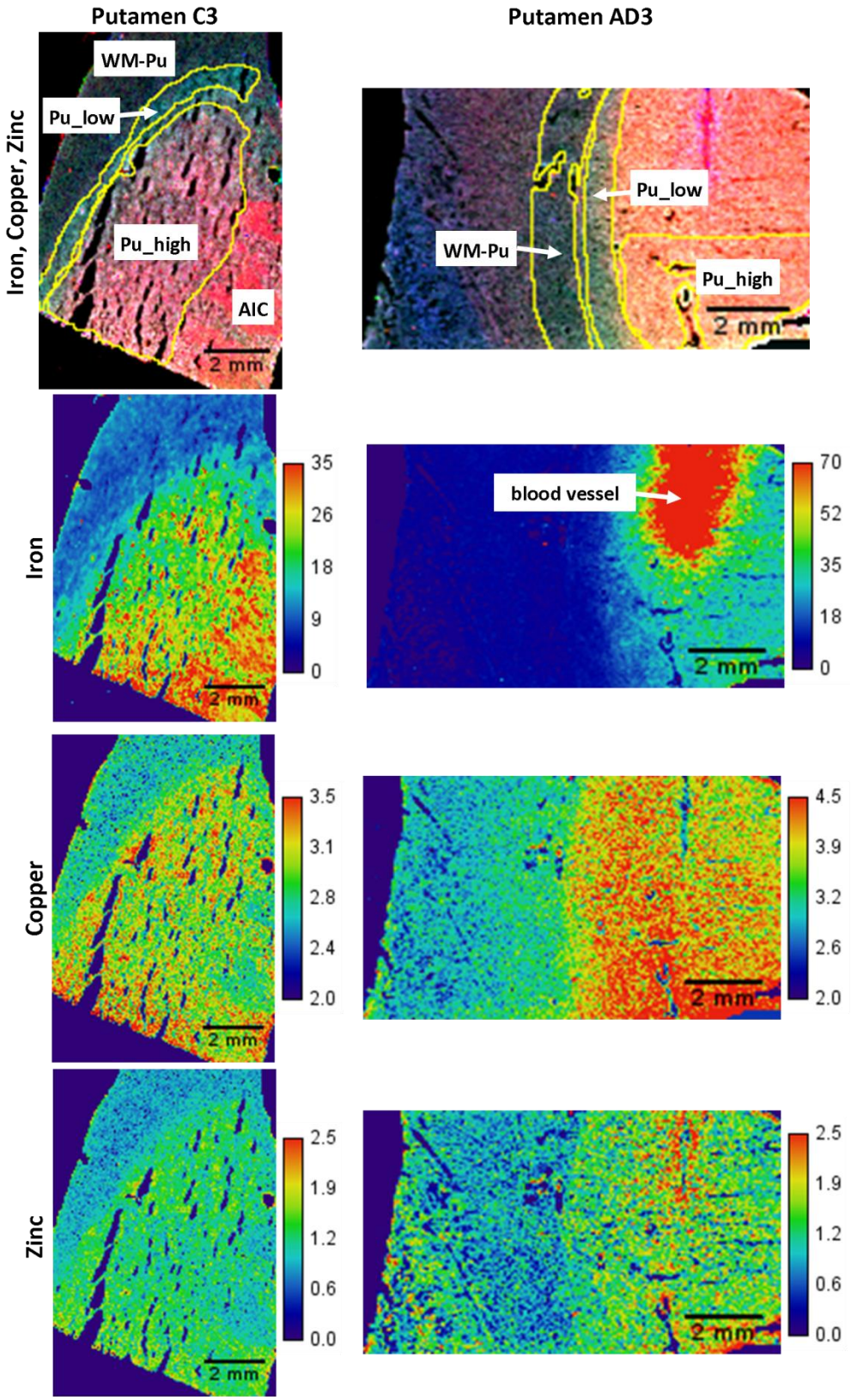

Figure 6.14: Iron, copper and zinc distribution in the putamen. The anatomical features present are the high and low iron regions of the putamen (Pu_high and Pu_low), the white matter lateral to the putamen (WM-Pu) and the anterior limb of the internal capsule (AIC, C3 map only). Individual metal maps are plotted using a temperature scale, where the calibration bars show the normalised SXRF signal intensity. Very high iron concentration is observed around a blood vessel in the AD sample. Copper concentration is elevated in the AD map. The distribution of copper and zinc is similar in the control and AD maps, but the concentration of copper is increased in the putamen.

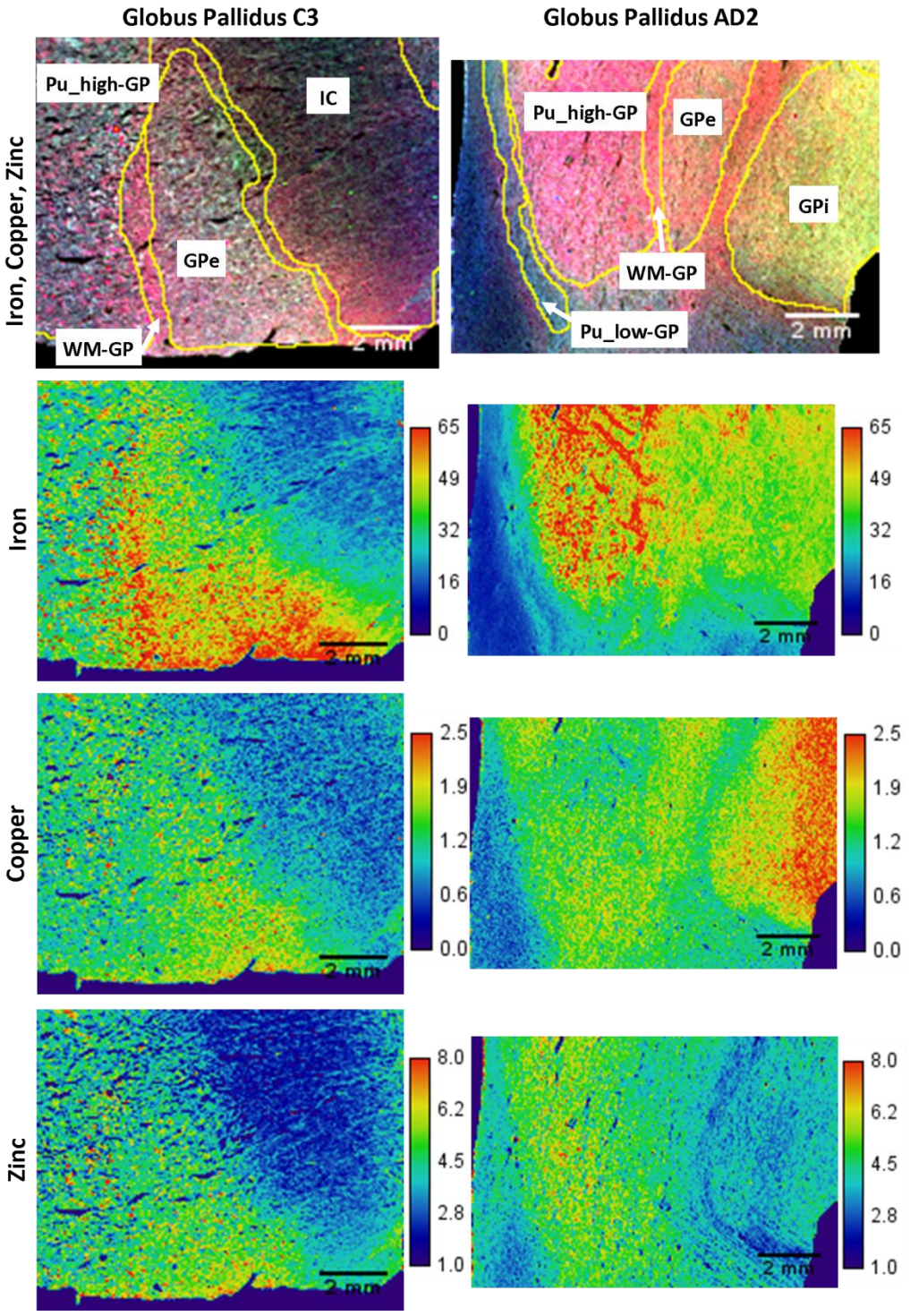

Figure 6.15: Iron, copper and zinc distribution in the globus pallidus. Individual metal maps are plotted using a temperature scale. The anatomical features present in the control map are: the high iron region of the putamen (Pu_high-GP), the internal globus pallidus (GPe), the lamina of white matter separating the putamen and GPe (WM-GP) and the internal capsule (IC). The AD map also includes: the internal globus pallidus (GPi) and the low iron region of the putamen (Pu_low-GP). The range of concentration of each metal is similar for control and AD and therefore the pairs of maps are plotted over the same range, where the calibration bars show the normalised SXRF signal intensity. Iron concentration is higher in the GPe of the control sample compared to the putamen, whereas in the AD sample iron is high in the putamen.

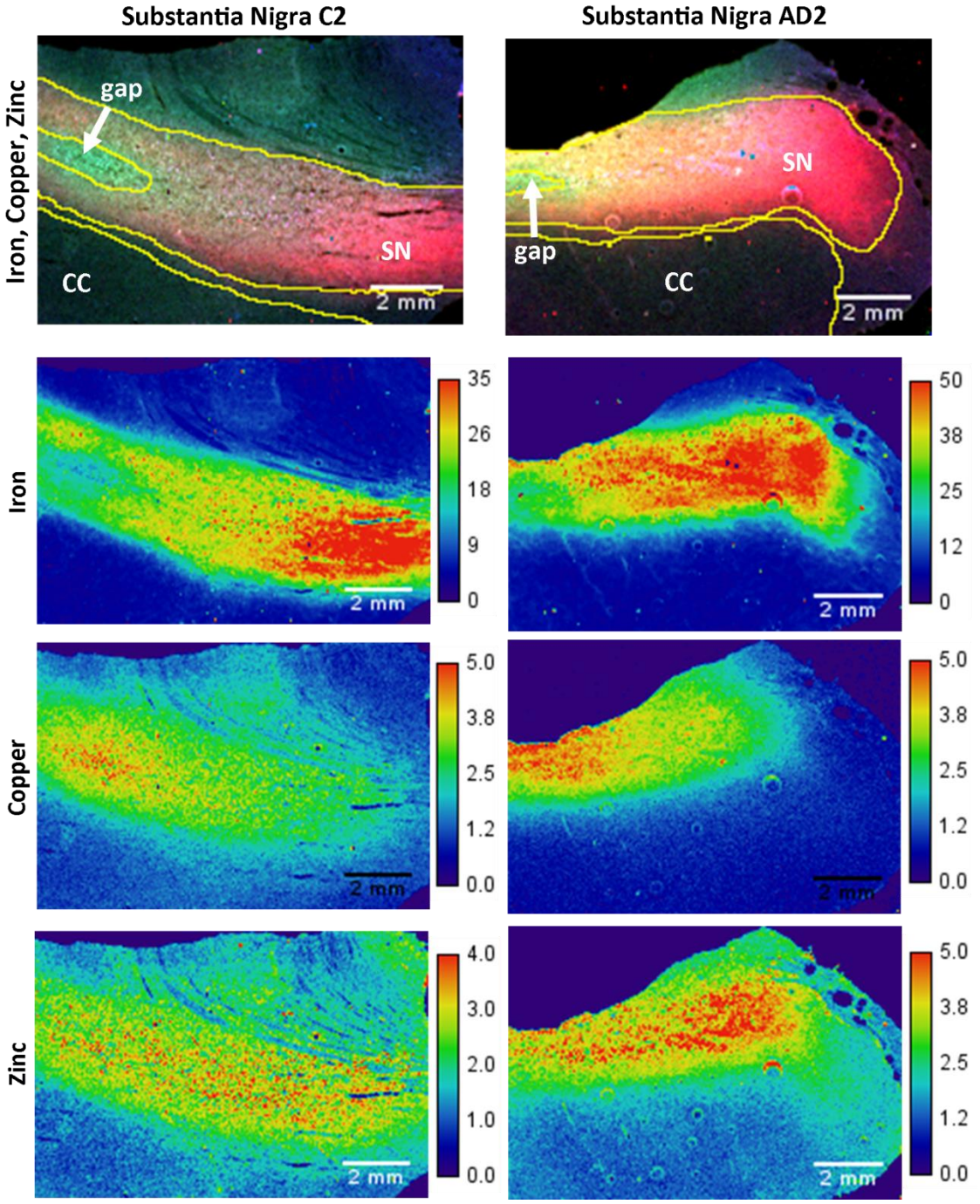

Figure 6.16: Iron, copper and zinc distribution in the substantia nigra. The anatomical features present are: the substantia nigra (SN), cerebral crus (CC) and a distinctive gap in the high iron signal of the SN (gap). Individual metal maps are plotted on a temperature scale, where the calibration bars show the normalised SXRF signal intensity. The concentrations of iron and zinc are higher in the SN of the AD sample compared to the control sample. The distribution of each metal shows a distinct pattern within the SN, with the same pattern seen in both the control and AD sample.

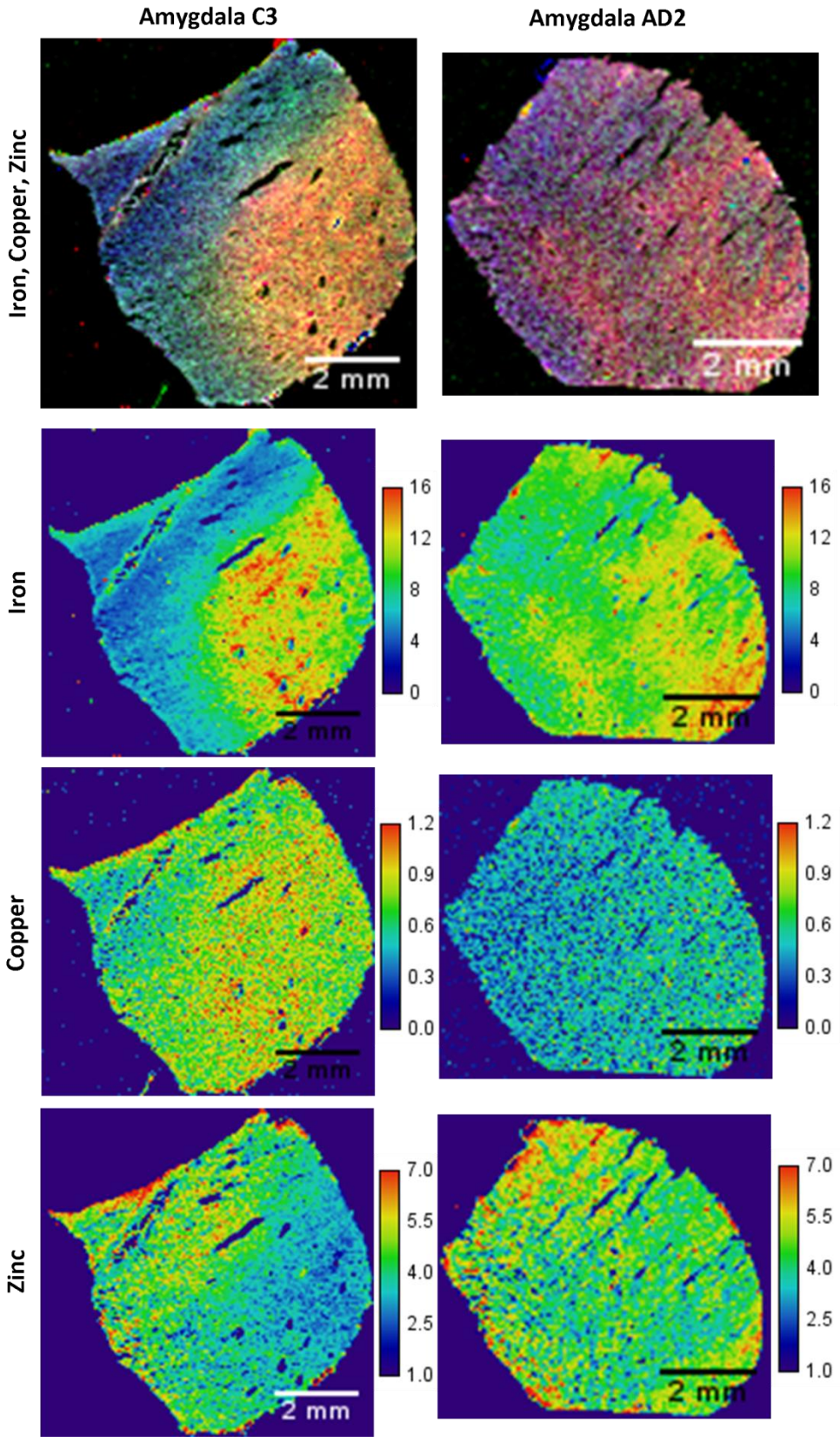

Figure 6.17: Iron, copper and zinc distribution in the amygdala. Individual metal maps show the relative concentration plotted on a temperature scale, where the calibration bars show the normalised SXRF signal intensity. The distribution of each metal is different in the control and AD example. This may be due to different sub-nuclei of the amygdala being included in each sample, but this could not be verified with the information available.

6.3.2 Quantitative analysis

Figure 6.18 shows the mean normalised SXRF signal intensity for the segmented regions of each map. The error bar shows the estimated measurement error of 5%. Iron concentration is increased above error in more than half (9 out of 14) of the regions, including the caudate nucleus, putamen and substantia nigra. On the other hand, iron is increased in the control data in two regions: WM-GP and WM-Pu.

Copper and zinc concentration are also increased in the AD data in a majority of the segmented regions, however an increase is not always observed for all three metals in the same region. For example, although the AD3 Pu map shows an increase in copper concentration compared to C3 across all segmented regions, there is little or no change in the concentration of zinc and iron in the same regions.

Across the different brain regions iron shows greater inhomogeneity than copper or zinc. Copper also varies significantly, whereas zinc concentration is more consistent. For example, the concentration of zinc in the amygdala is similar to the other regions, whereas the concentrations of copper and iron are lower compared to most other regions.

The putamen is mapped twice. Firstly at a level where it is lateral to the caudate nucleus and secondly where it is lateral to the globus pallidus. As was observed by visual comparison of the maps in Figures 6.14 and 6.15, the iron concentration in Pu in the samples lateral to the GP is much higher than where it is lateral to the CN (for both AD and control samples). The AD sample has a greater iron concentration in both cases.

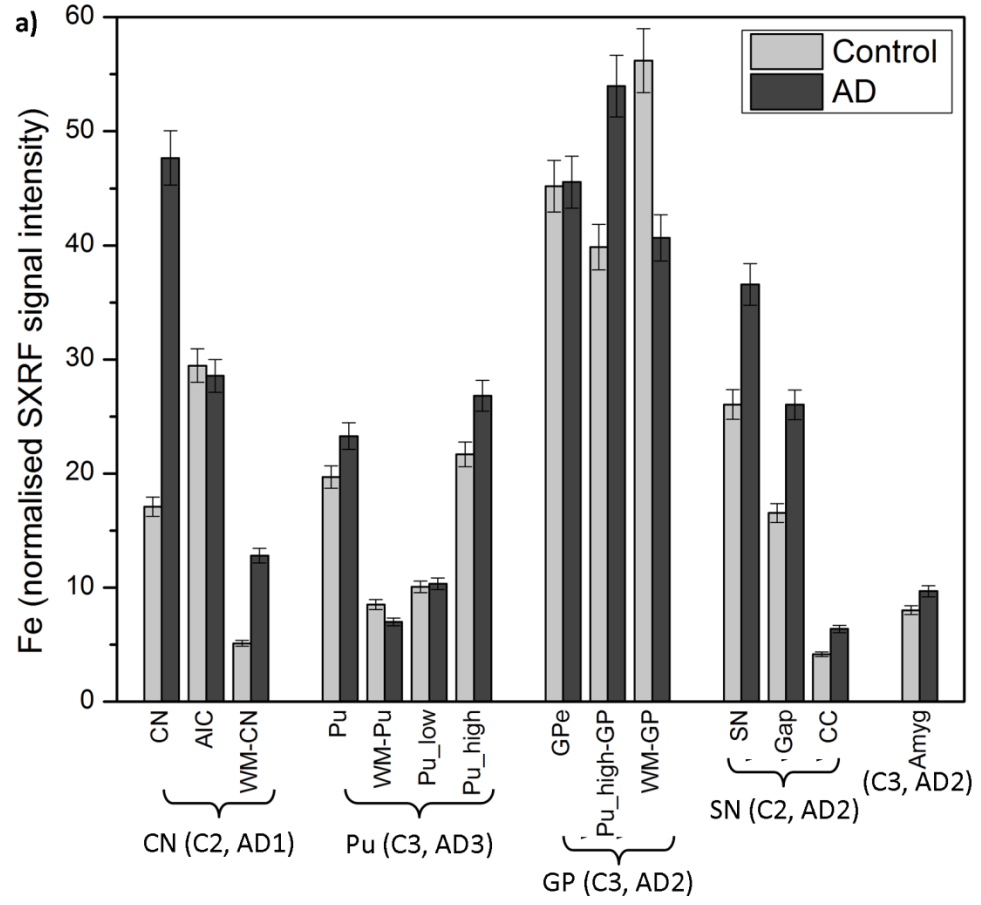
a)
Control
AD
Fe (normalised SXRF signal intensity)
0
10
20
30
40
50
60
CN
AIC
WM-CN
Pu
WM-Pu
Pu_low
Pu_high
GPe
Pu_high-GP
WM-GP
SN
Gap
CC
Amyg
CN (C2, AD1)
Pu (C3, AD3)
GP (C3, AD2)
SN (C2, AD2)
(C3, AD2)

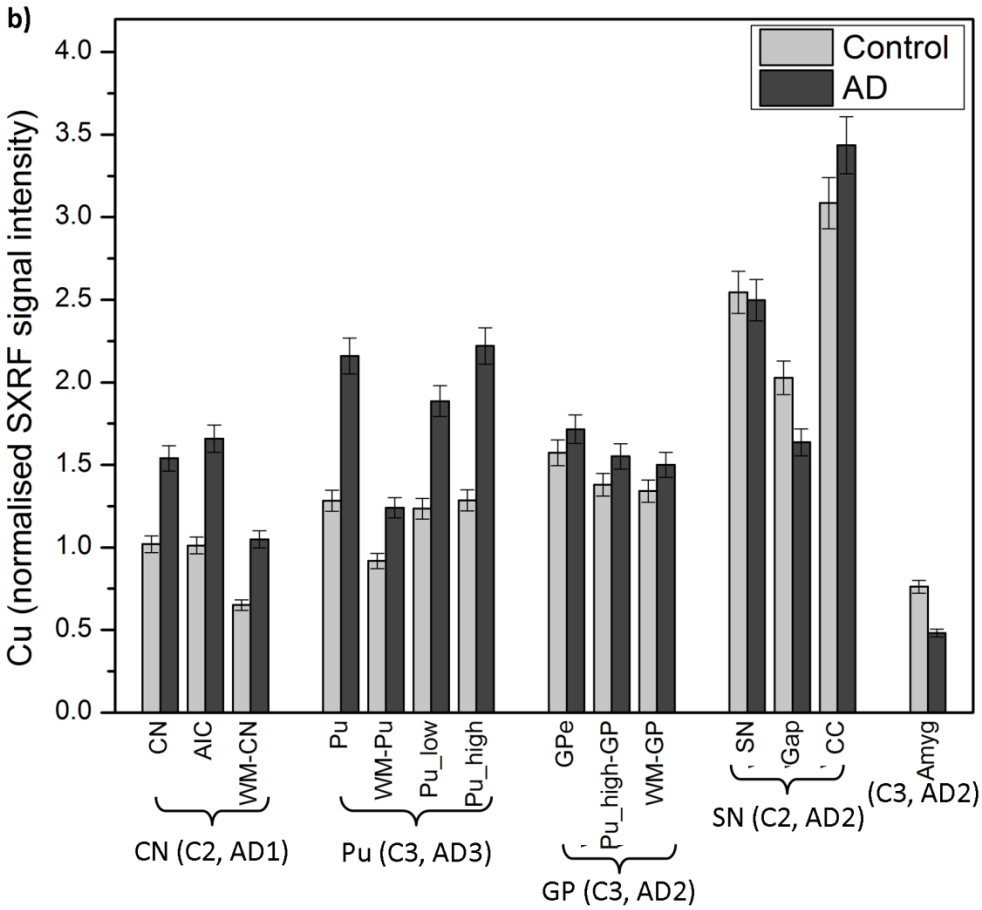
b)
Control
AD
Cu (normalised SXRF signal intensity)
0.0
0.5
1.0
1.5
2.0
2.5
3.0
3.5
4.0
CN
AIC
WM-CN
Pu
WM-Pu
Pu_low
Pu_high
GPe
Pu_high-GP
WM-GP
SN
Gap
CC
Amyg
CN (C2, AD1)
Pu (C3, AD3)
GP (C3, AD2)
SN (C2, AD2)
(C3, AD2)

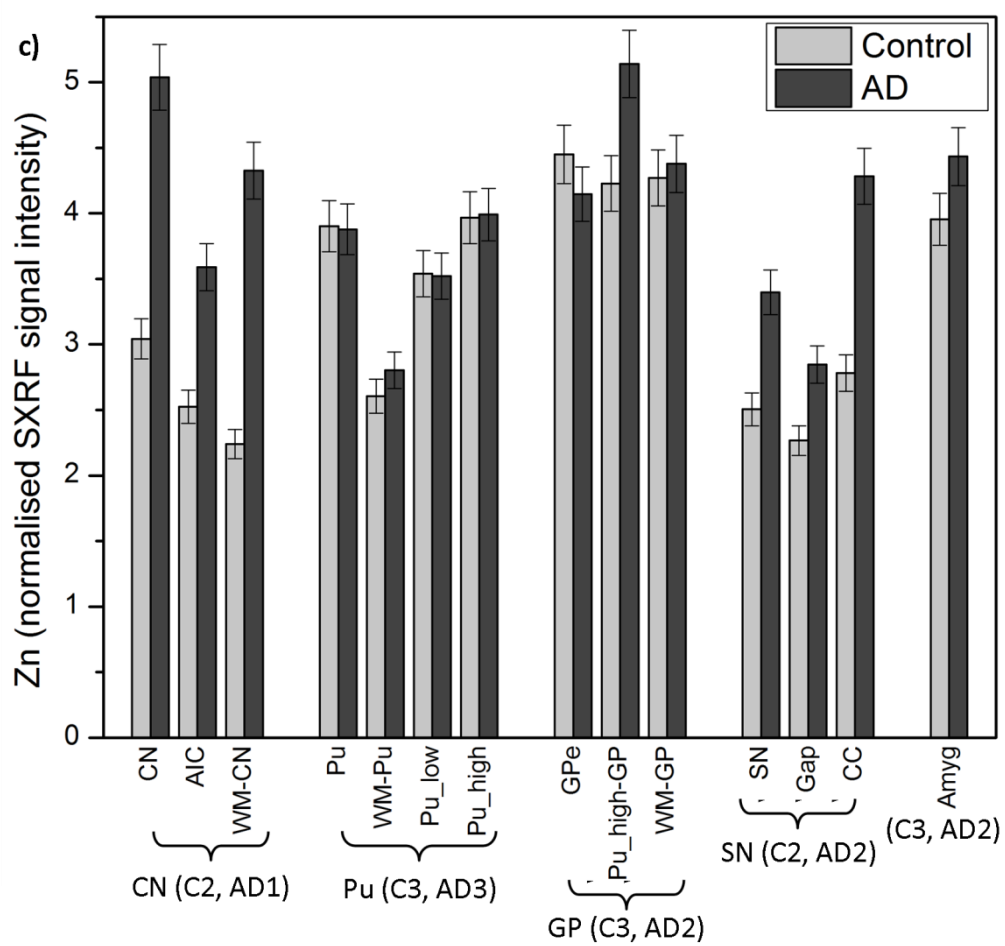

Figure 6.18: Mean relative iron, copper and zinc concentration in the segmented regions of SXRF maps from experiment DLS5. The mean normalised SXRF signal intensity for each metal for each tissue structure, which appeared in both the control and AD samples, is given. n=1 for each region. The error bars show the estimated 5% measurement error. The segmented regions are grouped according to which map they were segmented from. From the caudate nucleus maps: the caudate nucleus (CN), anterior limb of the internal capsule (AIC) and the white mater medial to the CN (WM-CN). From the putamen maps: the whole putamen (excluding the blood vessel in AD3) (Pu), the white matter lateral to the putamen (WM-Pu), the low iron part of the putamen (Pu_low) and the high iron part of the putamen (Pu_high). From the globus pallidus maps: the external globus pallidus (GPe) and the high iron part of the putamen (Pu_high). From the substantia nigra: the whole substantia nigra (SN), the gap in the iron signal of the SN (gap) and the cerebral crus (CC). The mean signal was taken from the whole of each amygdala map (Amyg). a) Relative mean iron concentration in the segmented brain regions. The iron concentration varies across the different regions more than copper or zinc does. Nine out of fourteen regions show an increase in iron, greater than the 5% measurement error, in the AD sample compared to control. In particular iron is increased in the CN, WM-CN, Pu_high-GP and SN. Iron is only increased in control compared to AD in the WM-Pu and WM-GP. b) Relative mean copper concentration in the segmented brain regions. Copper is increased in AD in the segmented regions of the caudate nucleus and putamen and to a lesser extent in the globus pallidus. Copper concentration is only increased in control tissue in the amygdala and the 'gap' region of the SN. c) Overall, zinc has the least variation in concentration between brain regions. Zinc is increased with AD in the segmented regions of the caudate nucleus and substantia nigra maps, in the amygdala and in the Pu_high-GP.

6.3.3 Standard deviation of pixel intensity in each region

Figure 6.18 shows the mean metal concentration of the pixels within each segmented region of the SXRF maps, but does not include any information about the variation in pixel intensities within each ROI. Therefore the standard deviation (σ) within each segmented area is shown in Figure 6.19. Standard deviation is equal to the square root of the variance and large variance indicates inhomogeneity of iron distribution (at 60 µm resolution).

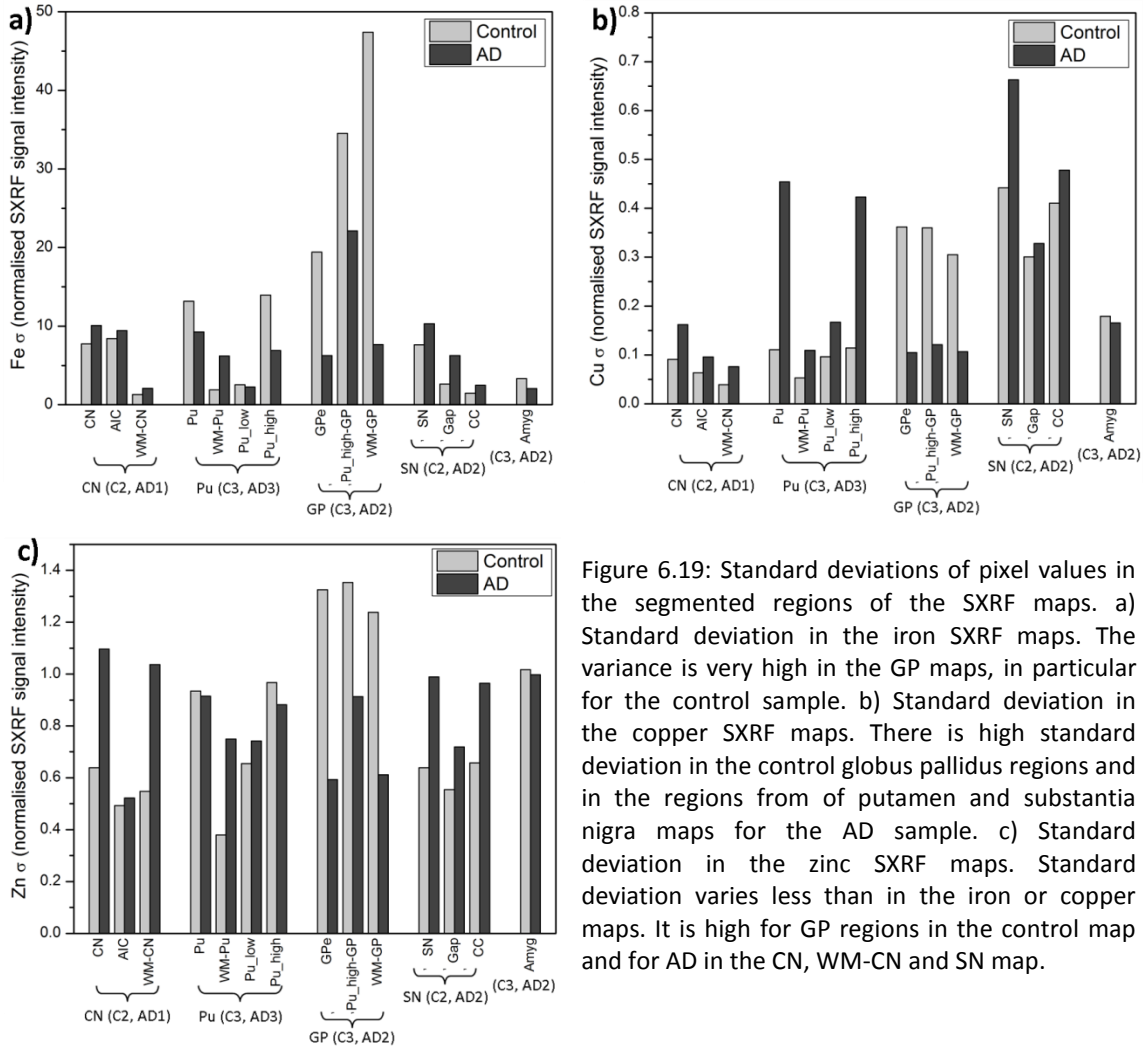

Figure 6.19: Standard deviations of pixel values in the segmented regions of the SXRF maps. a) Standard deviation in the iron SXRF maps. The variance is very high in the GP maps, in particular for the control sample. b) Standard deviation in the copper SXRF maps. There is high standard deviation in the control globus pallidus regions and in the regions from of putamen and substantia nigra maps for the AD sample. c) Standard deviation in the zinc SXRF maps. Standard deviation varies less than in the iron or copper maps. It is high for GP regions in the control map and for AD in the CN, WM-CN and SN map.

There is no overall trend to suggest that larger variance is seen in AD tissue compared to control. In half of the 14 regions the AD samples have the higher variance, whereas in the other half it is higher for the control samples. The largest variance in iron is seen in the segmented regions of the GP map. In these regions the control samples show the greater variation. However, this pair of samples is the least well anatomically matched of all the brain

regions (see Figures 6.7 and 6.8) and this may account for the large difference in variance within the segmented regions. Similarly to variation between means, the variance of zinc concentration at a 60 μm resolution is more consistent across the regions of the brain than the variance of iron or copper.

6.4 Using bulk tissue iron concentration to calibrate SXRF signal intensity

No suitable standards for calibrating the metal concentrations in the SXRF maps were available at beamline I18. Hence, in past publications and in this chapter the data have been described as a relative concentration. However, the iron concentration of adjacent tissue from a number of the samples has also been measured and this can be used to approximately calibrate the SXRF signal intensity. The calibration allows estimation of tissue iron content of regions not measured by ICP-MS or GFAAS.

6.4.1 Comparing SXRF and bulk tissue iron measurements

Measurements of iron concentration made by bulk tissue iron quantification and SXRF mapping are over a significantly different scale. For the bulk tissue measurements iron concentration in approximately 0.5 g of fresh-frozen tissue is quantified, whereas for SXRF mapping the relative iron concentration is examined over around 1 cm^2 of a 30 μm slice of tissue, which equates to approximately 0.003 g (assuming that tissue density is approximately the same as water). Additionally, the tissue in the two different measurements is from adjacent blocks within the region at a distance of around 10 mm. The comparison will therefore be affected by any changes in iron concentration throughout the region.

In order to estimate how well these two measurements compare, the ratio of the AD to control iron concentration (ACR) was found for: i) the relative mean iron concentration measured by SXRF mapping and ii) for the bulk tissue iron quantification. The ARC ratios are given in Table 6.2. The substantia nigra was bisected for bulk tissue analysis in the same plane

as the SXRF map. Therefore, the whole map is most closely representative of the tissue that was dissolved for iron quantification in Chapter 4. For the other regions, the mean SXRF signal from within the segmented regions is used. The SXRF comparison for the putamen excludes the very high iron region in the AD sample, which surrounds a blood vessel, as there is no reason to assume that a similar blood vessel would be found in the adjacent tissue taken for ICP-MS.

	ARC ICP-MS/GFAAS	ARC SXRF
Caudate Nucleus	3.04	2.80
Putamen	1.28	1.24
Substantia Nigra (whole map)	1.50	1.41

Table 6.2: Ratio of AD to control iron concentration (ARC), measured by bulk tissue analysis (ICP-MS: inductively coupled mass spectrometry or GFAAS: graphite furnace atomic absorption spectrometry) and SXRF mapping. The agreement between techniques is good for all regions.

Overall the ratios are in good agreement. In the putamen the results differ by only 0.04 and for the SN the difference is 0.09. The largest difference is in the CN data which disagrees by 0.24, however by both techniques this is the region which showed the largest increase in iron in AD compared to control.

6.4.2 Calibrating the SXRF data

The good agreement between the SXRF and ICP-MS/GFAAS measurements in Table 6.2 led to the hypothesis that the bulk tissue measurements could be used to calibrate the normalised SXRF iron data. This calibration assumes that the volume of tissue measured by ICP-MS or GFAAS and the area tissue mapped by SXRF have an equal concentration of iron. It has already been established that careful normalising of the SXRF maps from experiment DLS5 means that the SXRF signal intensity is comparable between maps and therefore the data from the

different samples can be pooled. The segmented ROI is used, rather than the average across the whole map, as the bulk tissue samples were carefully cut from the surrounding structures.

The iron concentration represented by 1 unit of normalised SXRF signal intensity was calculated for the control and AD sample from the SN, CN and Pu and then the mean result found and the standard deviation calculated. The result, shown in Table 6.3, gives an average iron concentration of 7.3 ± 12% μg/g of iron for every unit of normalised SXRF intensity.

	CONTROL			AD		
Region	Mean iron SXRF	Bulk iron concentration (μg/g)	Concentration of iron per SXRF unit (μg/g)	Mean iron SXRF	Bulk iron concentration (μg/g)	Concentration of iron per SXRF unit (μg/g)
SN	14.08	109.33	7.76	19.90	164	8.24
CN	17.03	124.36	7.30	47.66	378.26	7.94
Pu	21.70	133.49	6.15	26.90	171.13	6.36
			SXRF (μg/g)	σ	σ (%)	
		Average (all)	7.3	0.86	12	

Table 6.3: Estimation of iron concentration per unit of normalised iron SXRF intensity. The bulk tissue iron concentration is divided by the mean normalised SXRF signal intensity for each control and AD sample. The average iron concentration per unit of normalised SXRF signal intensity is calculated from all AD and control samples. The standard deviation (σ) is calculated to give an approximate error in the estimation of 12%.

6.4.3 Estimating iron concentration using calibrated SXRF

The amygdala and globus pallidus were mapped during experiment DLS5, but did not have an adjacent sample taken for bulk analysis. The calibrated SXRF signal intensity was used to make an estimation of the iron concentration in the control and AD iron maps. The estimated iron concentration in the control and AD amygdala and globus pallidus are shown in Table 6.4, alongside the values for those regions reported in the literature. The amygdala data compare extremely well with the iron concentration measurements made by Samudralwar *et al.* [16], where a concentration of 50.8 ± 3.7 μg/g was measured for control amygdala and 70.8 ± 4 μg/g for AD. The estimated concentration in the globus pallidus is much higher than the values for control (132.7 μg/g) and AD (160 ± 49.4 μg/g) published by House *et al.* [26], where the

concentration was measured by GFAAS. However, it is not more than the maximum concentration reported in the GP, which is 370.8 4 µg/g published by *Griffiths and Crossman* [106].

		Iron concentration (µg/g of fresh tissue)			
		Amygdala		Globus pallidus	
		Control	AD	Control	AD
Estimated iron from SXRF map		58.0 ± 7.0	70.5 ± 8.5	338.3±40.6	310.3±37
Reported in the literature	Studies of control and AD	48.3 ± 3.0 49 ± 4 <u>50.8 ± 3.7</u> 34	60.6 ± 4.9 64 ± 3 <u>70.8 ± 4</u> 40	102	131
	Just control data	49.0; 48.6; 48.9		213; 175.3; 182.0; 300.6; <u>370.8</u>	

Table 6.4: Estimated iron concentrations in the control and AD amygdala and globus pallidus and the values reported in the literature. The estimated values are most comparable with the higher values given in the literature. The estimated amygdala data agree particularly well with the values reported by Samudralwar *et al*. [16] (underlined). The globus pallidus estimation is higher than most published data, but less than that published by Griffiths and Crossman [106] (underlined).

6.5 The pons

The 60 µm resolution pons maps were made over three experimental visits to the DLS (Table 4.5) and the normalisation of these samples proved particularly difficult. The slide signal for the low resolution pons maps is shown in Figure 6.20 a), with the experiment number for each map indicated on the graph. The data varies more considerably than for the other samples, with the largest variation being between the samples AD2 and PD1. This is unexpected as these samples were measured during the same experiment. This is most likely due to varying detector position as during this experiment the detector was moved in and out when the sample was changed and the gauge to mark detector position had not yet been introduced.

Figure 6.20 b) shows the iron SXRF signal for the quartz slide for control, AD, PD and MSA pons maps at 3 µm resolution taken during experiment DLS4. There is very little variation between the different samples as the detector was not moved during this experiment. Table 6.5 shows

the percentage change of the iron signal of the quartz slide for each sample compared to control. The slide background is subtracted from the 60 μm and 3 μm resolution maps and then used to normalise the data.

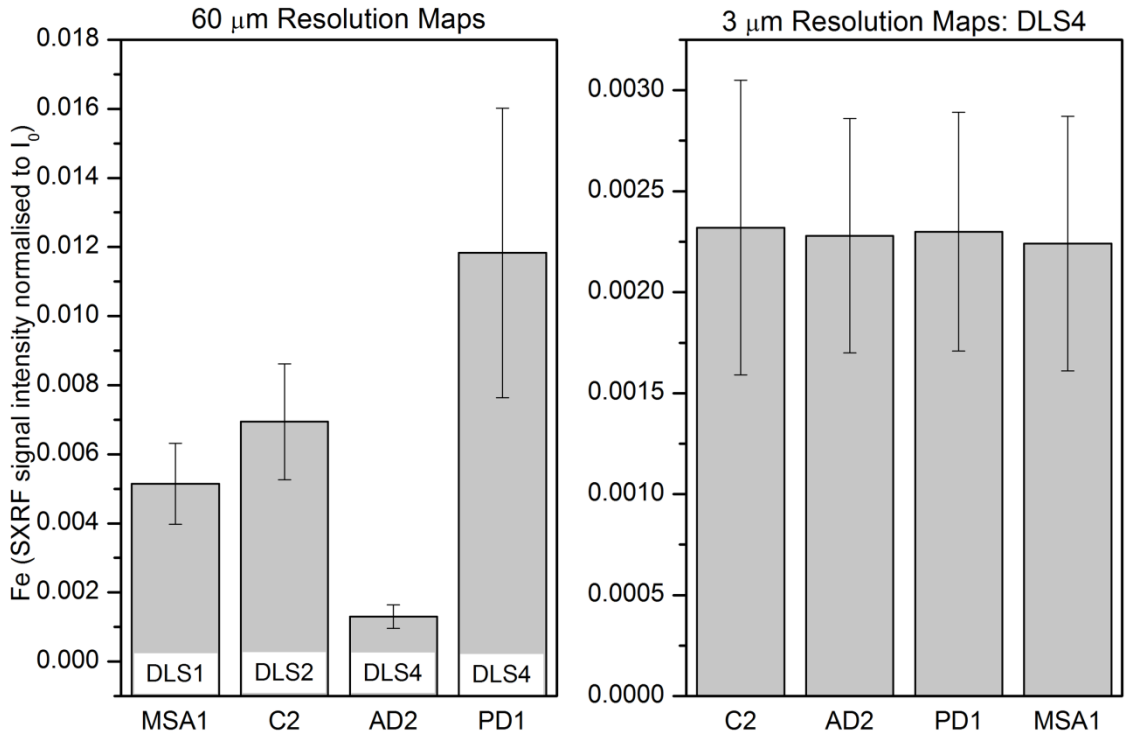

Figure 6.20: Iron SXRF signal intensity for the quartz slide background for the pons samples. a) 60 μm maps in experiments DLS1, DLS2 and DLS3 and b) 3 μm resolution maps in experiment DLS4. Fluorescence intensity has been normalised to I_0. Error bars indicate the standard deviation of signal in the area of quartz slide selected for the background. Pons samples were mapped from control, AD, PD (Parkinson's Disease) and MSA (Multiple System Atrophy) cases.

Map resolution	Disease	Difference in slide Fe signal in disease compared to control pons maps
60 μm (DLS1, DLS2, DLS3)	AD	-81.3%
	PD	-70.5%
	MSA	-25.9%
3 μm (DLS 4)	AD	-1.7%
	PD	-0.8%
	MSA	-3.4%

Table 6.5: Percentage difference of the measured iron fluorescence intensity of the quartz slides for disease samples compared to control. The difference between slide background for each disease is compared to the control sample for low and high resolution maps of the pons.

Table 6.6 shows the ratio of the mean normalised iron SXRF signal between the different samples and the equivalent ratio for bulk tissue iron quantification of the same samples. None

of the ratios agree as well as those shown for the samples measured in DLS5. The best agreement is for the ratio of the AD to Parkinson's Disease (PD) samples. These samples were measured during the same experiment so there is no reason to distrust the normalisation of these maps and as the bulk tissue iron measurements were made of adjacent samples, it is not unreasonable to expect some disagreement.

	GFAAS	SXRF
AD : control	2.4	6.08
PD : control	0.84	2.55
MSA : control	1.99	2.83
AD : PD	2.87	2.28

Table 6.6: Iron concentration ratio between disease groups in the pons. For tissue iron concentration by GFAAS (graphite furnace atomic absorption spectrometry) and SXRF mapping. The best agreement is between the AD:PD ratios.

The Multiple System Atrophy (MSA) and control samples were measured over two different experimental visits to the DLS and as the set up at the beamline is often updated there may be a measurement error which is not being corrected for by the normalisation to slide background and I_0. As the ratios do not agree well, no quantitative comparisons using the control and MSA pons maps will be made.

6.5.1 Sixty micron resolution SXRF maps

6.5.1.1 Qualitative observations

The normalised SXRF metal maps for the control and MSA samples are shown in Figure 6.21 and for the AD and PD samples in Figure 6.22.

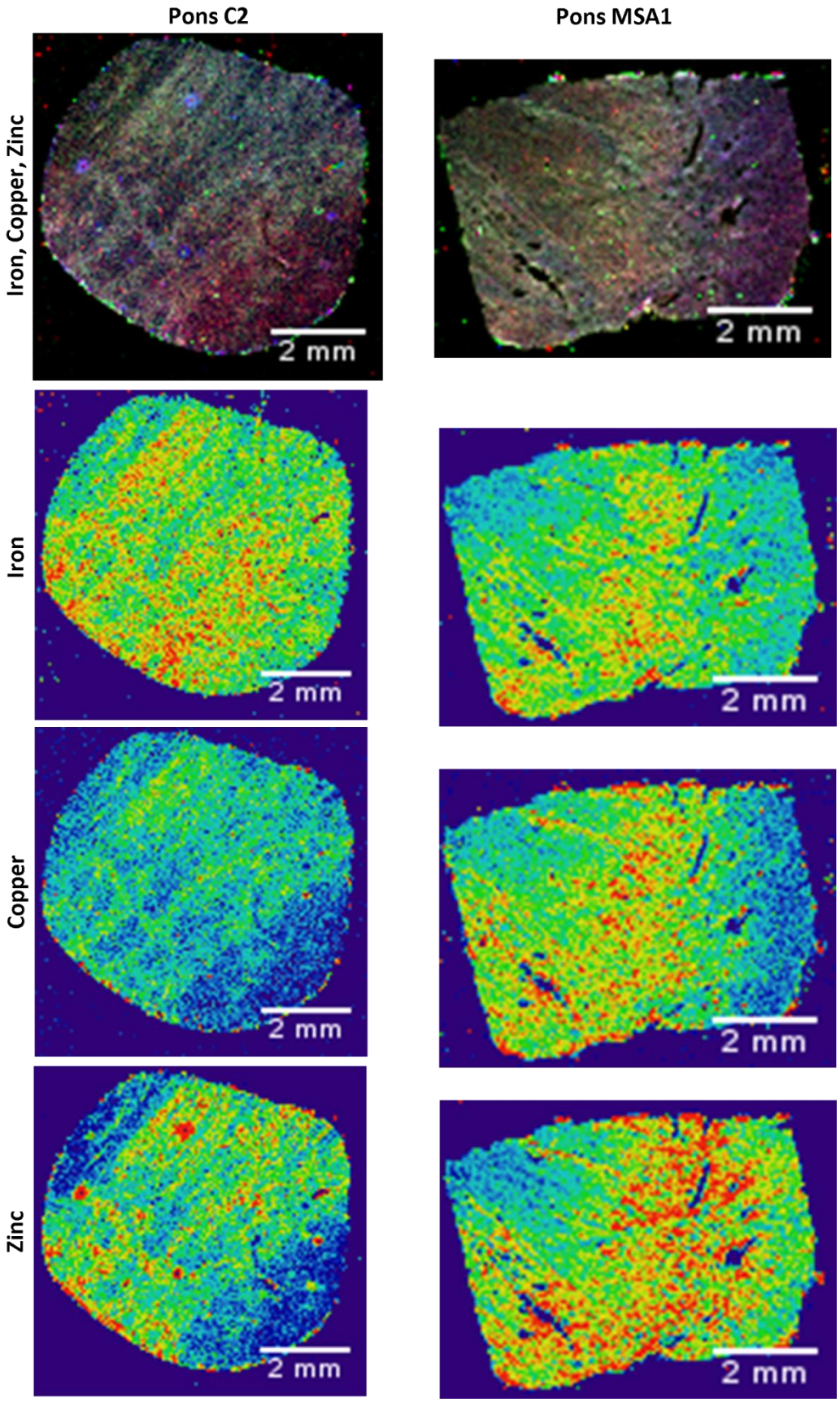

Figure 6.21: Metal distribution in the control and MSA pons. Individual metal maps show the relative concentration of iron, copper and zinc plotted on a temperature scale, however no calibration is given as the maps could not be normalised with confidence.

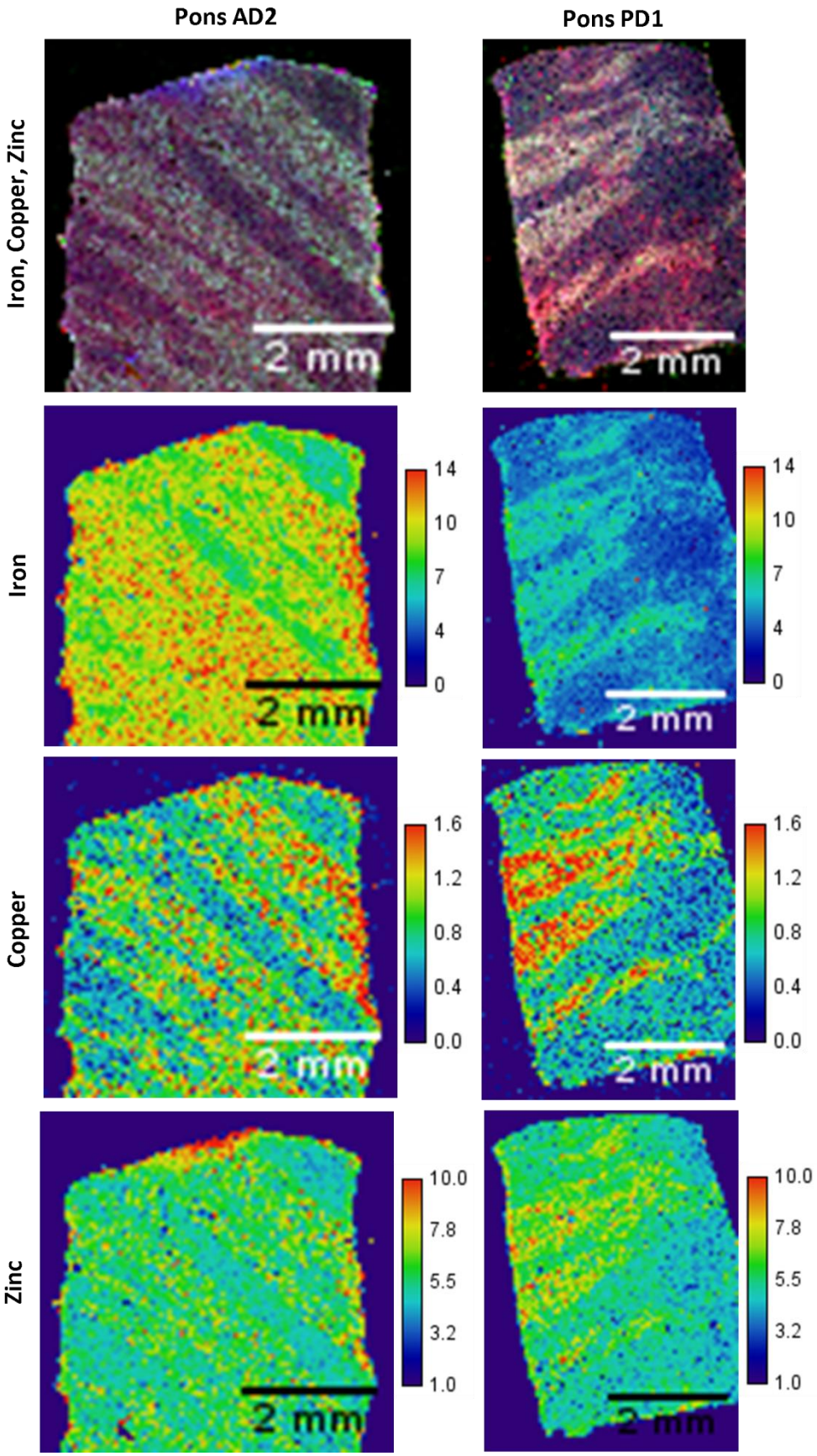

Figure 6.22: Metal distribution in the AD and PD pons. Individual metal maps show the relative concentration of iron, copper and zinc plotted on a temperature scale, where the calibration bar shows the normalised SXRF intensity. A similar distribution in the control and AD samples is observed for each metal, although the concentration of iron is higher in the AD sample.

As the normalisation of the control and MSA maps has been shown to be unsatisfactory, calibration bars are not included for these maps. Stripes of grey and white matter can be seen in each of the metal maps for the control, AD and PD samples, where higher metal concentration indicates grey matter. The MSA maps also show a fibrous structure, but at this resolution these are not clearly defined into grey and white matter. This indicates that this sample may have been cut from a slightly different region of the pons.

The AD and PD maps contain grey and white matter bands of similar widths and are anatomically well matched. The concentrations of zinc and copper show a very similar pattern and concentration across both sections, but the iron concentration is increased across the whole section in the AD sample.

6.5.1.2 Quantitative comparison between AD and PD maps

ImageJ was used to segment the grey and white matter tissue in the AD and PD maps of the pons as shown in Figures 6.23 and 6.24.

The mean and standard deviation of iron, copper and zinc relative SXRF signal intensity for the whole pons and for the segmented grey and white matter is shown in Figure 6.25. Iron is approximately doubled in both the grey and white matter of the AD pons compared to PD. There is a small increase in copper and zinc in the PD grey matter compared to AD. However, this is not observed in the white matter, or across the whole map. The fact that the copper and zinc comparisons give a different result than for iron adds confidence to the normalisation of these maps. If all metals were increased in the AD sample compared to control it might suggest that the data had not been normalised correctly.

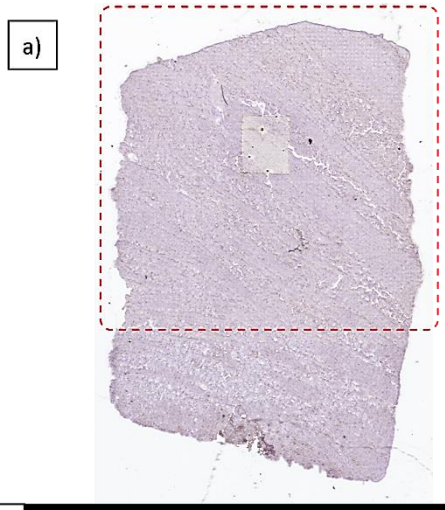

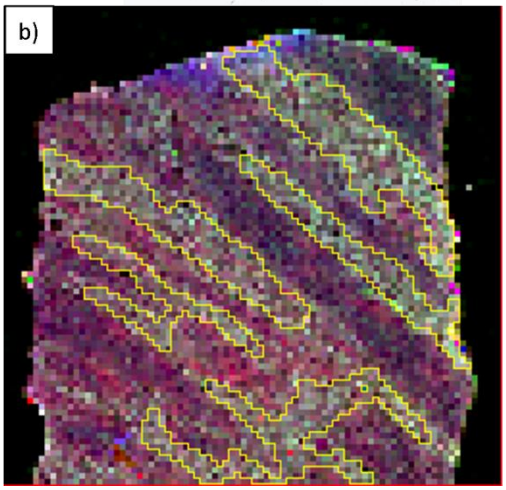

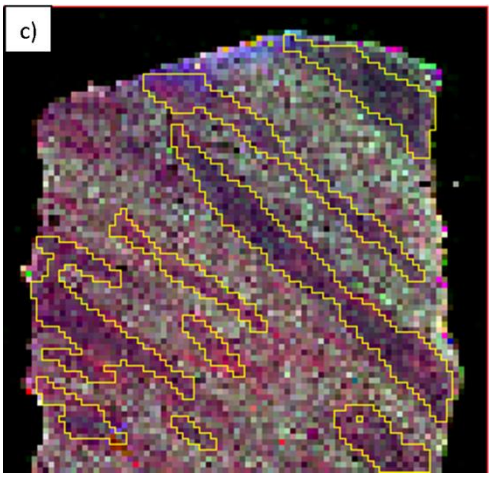

Figure 6.23 Segmentation of the SXRF map of pons sample AD2. a) The mapped section stained with haematoxylin, with the mapped area outlined in red. An area where a high resolution map was collected is also visible in the stained section. b) The grey matter segmentation in the SXRF map and c) the white matter segmentation.

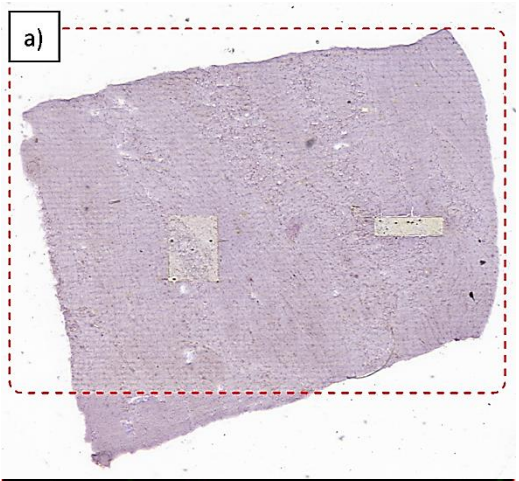

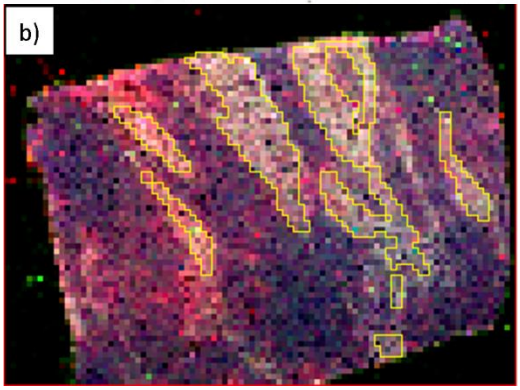

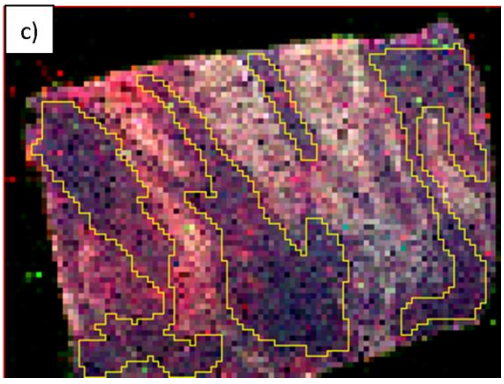

Figure 6.24: Segmentation of the SXRF map of pons sample PD1. a) The mapped section stained with haematoxylin, with the mapped area outlined in red. Two areas where high resolution maps were collected are also visible in the stained section. b) The grey matter segmentation in the SXRF map and c) the white matter segmentation.

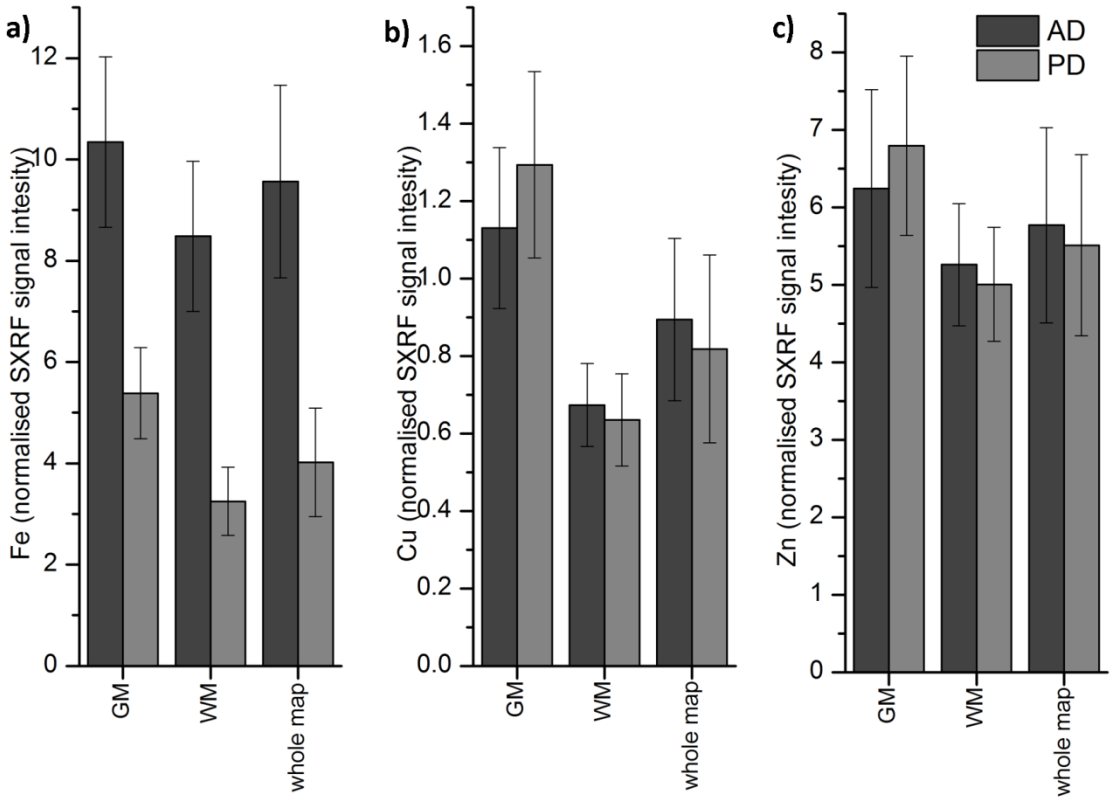

Figure 6.25: Relative metal concentrations in the segmented regions of the AD and PD pons maps. The mean and standard deviation of a) iron, b) copper and c) zinc SXRF signal intensity for the segmented grey and white matter tissue and for the whole map. Iron is increased in the AD map compared to PD. There is a small increase in copper and zinc in the GM of the PD samples.

6.5.2 High resolution SXRF mapping of the pons

6.5.2.1 Making 3 µm SXRF maps of the pons

To investigate the changes in pons iron concentration in greater detail, higher resolution SXRF maps were made of small areas of tissue. The location of each of these high resolution maps was chosen so as to include grey and white matter. First, the microscope and camera pointed at the slide were used to select a striped area of tissue and a small 30 µm resolution map was made. The contrast in iron concentration between the grey and white matter allowed the position of the high resolution (3x3 µm) map to be selected. Figure 6.26 shows this process for the AD sample. Due to the small spot size only a very small area could be mapped within the available time and therefore this careful region selection is extremely important. Inserts were

only made for the control, AD and PD samples as the MSA sample did not show the same stripes of grey and white matter.

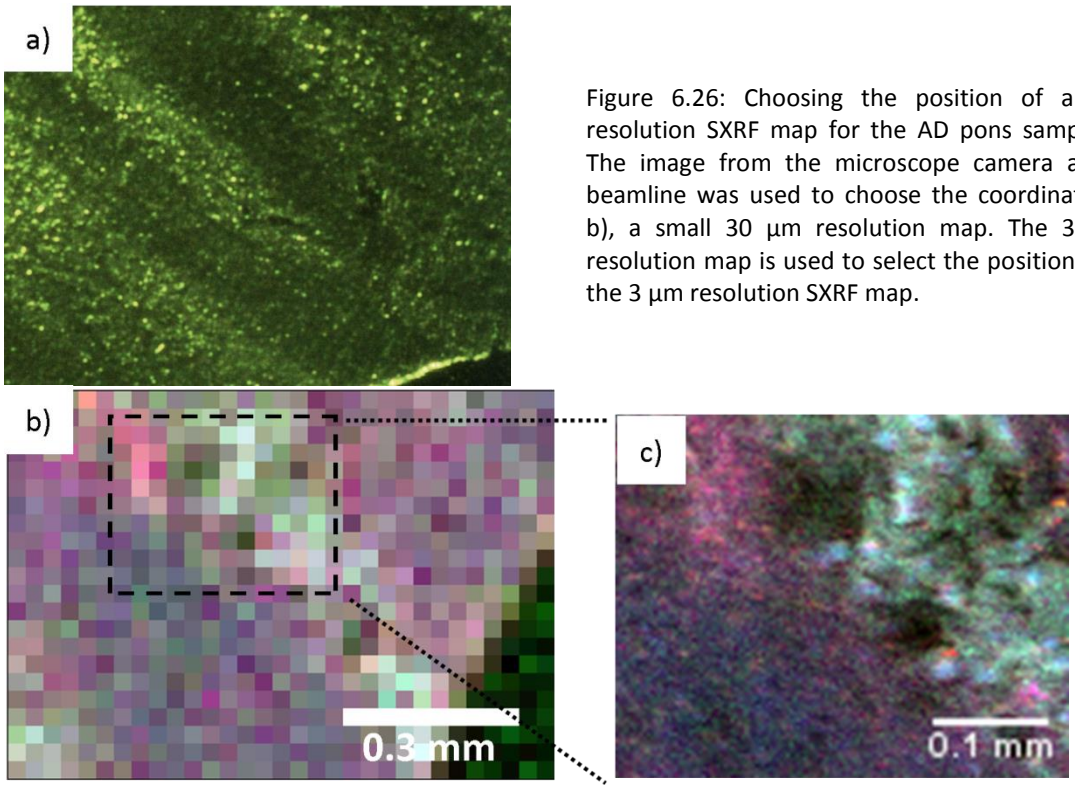

Figure 6.26: Choosing the position of a high resolution SXRF map for the AD pons sample. a) The image from the microscope camera at the beamline was used to choose the coordinates of b), a small 30 µm resolution map. The 30 µm resolution map is used to select the position of c), the 3 µm resolution SXRF map.

The 3µm maps were normalised to I_0 and to slide background, and the slide background was subtracted. The combined and individual iron, copper and zinc maps for the control, AD and PD samples are shown in Figure 6.27. The grey matter tissue has a higher iron, copper and zinc concentration (as was shown in the 60 µm resolution maps in Figures 6.23 and 6.24) than the white matter tissue. The 3 µm resolution maps show that within the grey matter all metals follow a similar distribution, with small, roughly oval shaped areas of increased concentration. In the white matter the copper signal is fairly low and even, whereas the zinc and, to a great extent, iron show a more mottled pattern.

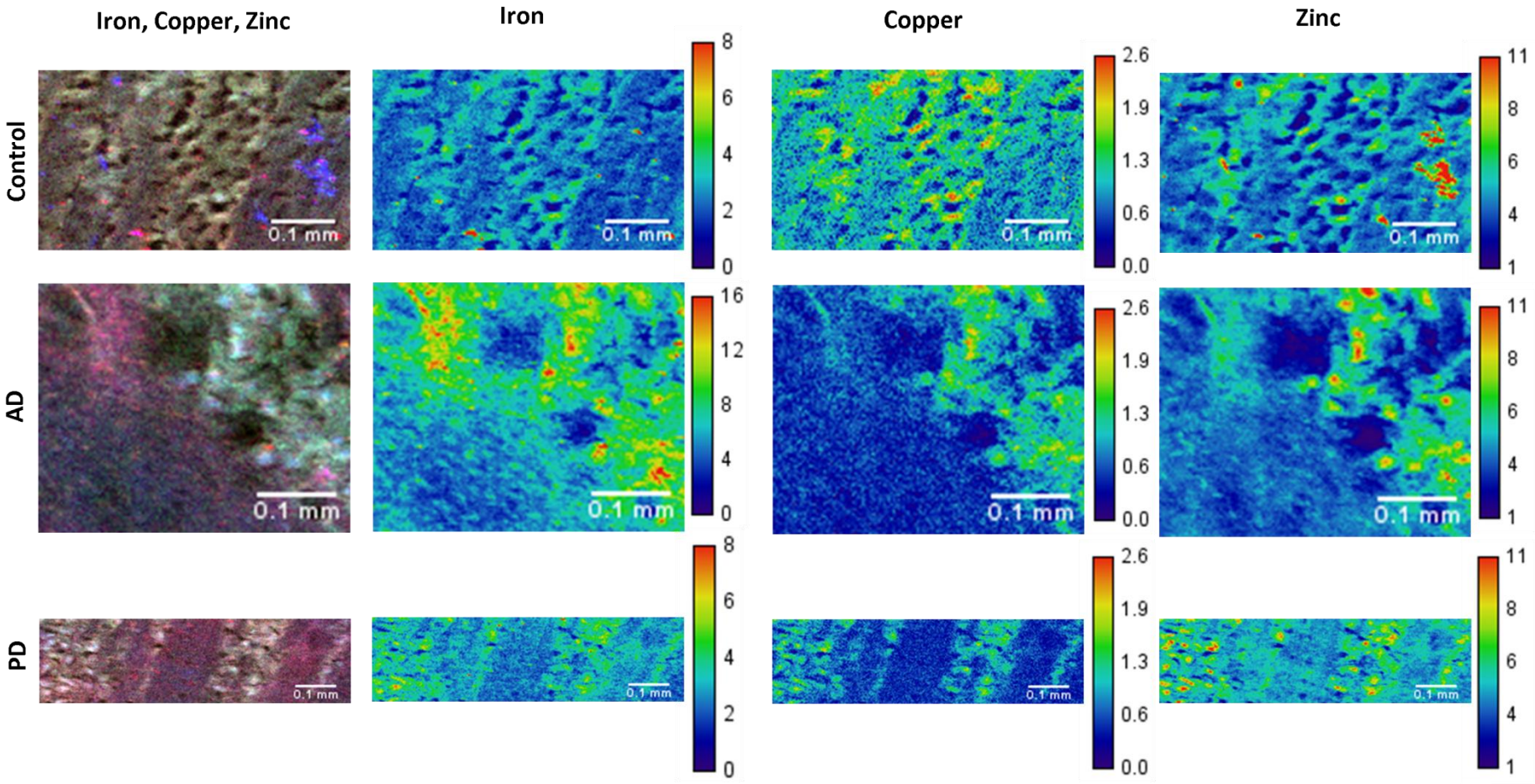

Figure 6.27: Three micron resolution SXRF metal distribution maps of the control, AD and PD pons. Each map contains a region of grey and white matter. The grey matter regions containsa higher concentration of each metal. Maps are plotted using temperature scale, where the calibration bar shows the normalised SXRF signal intensity.

6.5.2.2 Identifying neurons in the 3 µm maps

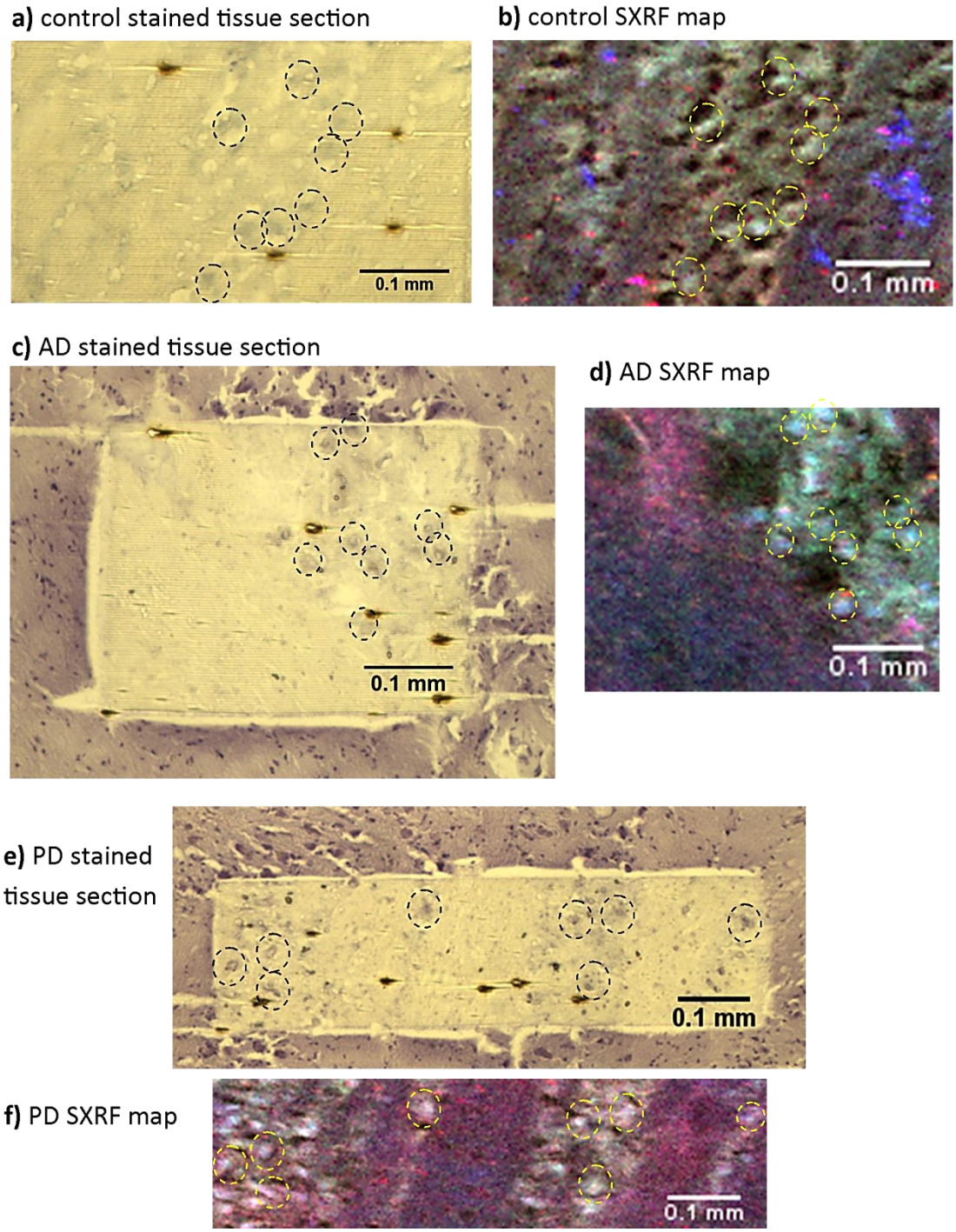

Figure 6.28: Identification of neurons in the 3 micron resolution SXRF maps. The SXRF maps and microscope images of the sections, which were stained with haematoxylin after mapping, were compared to identify neurons. Eight neurons are circled in black in the stained sections and in yellow in the SXRF maps. a) and b) show the neurons selected for the control sample, c) and d) show the neurons in the AD sample and e) and f) show the neurons selected in the PD sample.

The mapped pons sections were stained with haematoxylin using the post-SXRF staining protocol (Section 4.5.2). The areas of tissue mapped at 3 μm were particularly fragile due to the exposure to intense X-rays. This has the advantage of the precise area of the map being easily determined, but the disadvantage that the staining is not taken up as well and is not very clear. Despite the faint staining some neuronal bodies could be identified due to their staining, size (around 20-30 μm) and position (in the grey matter) within the section. These neurons are also visible in the SXRF maps as bright spots in the metal maps. They are particularly clear in the zinc maps.

A sample of eight neurons was identified in the stained mapped area for the control, AD and PD samples as shown in Figure 6.28. The neurons in the stained section were drawn around in ImageJ, which was then used to make a mask to select the same neurons in the SXRF map. The neurons can be seen as areas of increased metal concentration, appearing as near white in the combined metal maps. In order to compare the neurons to the surrounding tissue, the 3 μm maps were also segmented into grey (including neurons) and white matter.

6.5.2.3 Relative iron, copper and zinc concentration in the neurons of the control, AD and PD pons

Figure 6.29 shows the mean iron, copper and zinc concentration in the 8 neurons sampled for each case with the error bar representing the standard deviation. The mean relative metal concentration in the grey and white matter is also shown. As observed in the maps, the concentration of all metals is increased in the neurons compared to the surrounding tissue.

A statistical comparison of the mean metal concentrations of the neurons showed: a statistically significant increase in iron in AD compared to control and PD, a statistically significant decrease in copper for AD and PD compared to control and a statistically significant increase in zinc in the PD neurons compared to control. The data were normally distributed for each group as reported by the Shapiro-Wilk test ($p<0.05$). The copper and zinc data passed the

Levene's test of homogeneity of variance and therefore were assessed by one-way ANOVA and Tukey *post-hoc* analysis, whereas the iron data violated the test for homogeneity of variance and therefore Welch's ANOVA followed by Games-Howell *post-hoc* analysis were used. The results of the statistical analysis are indicated on the graph in Figure 6.29.

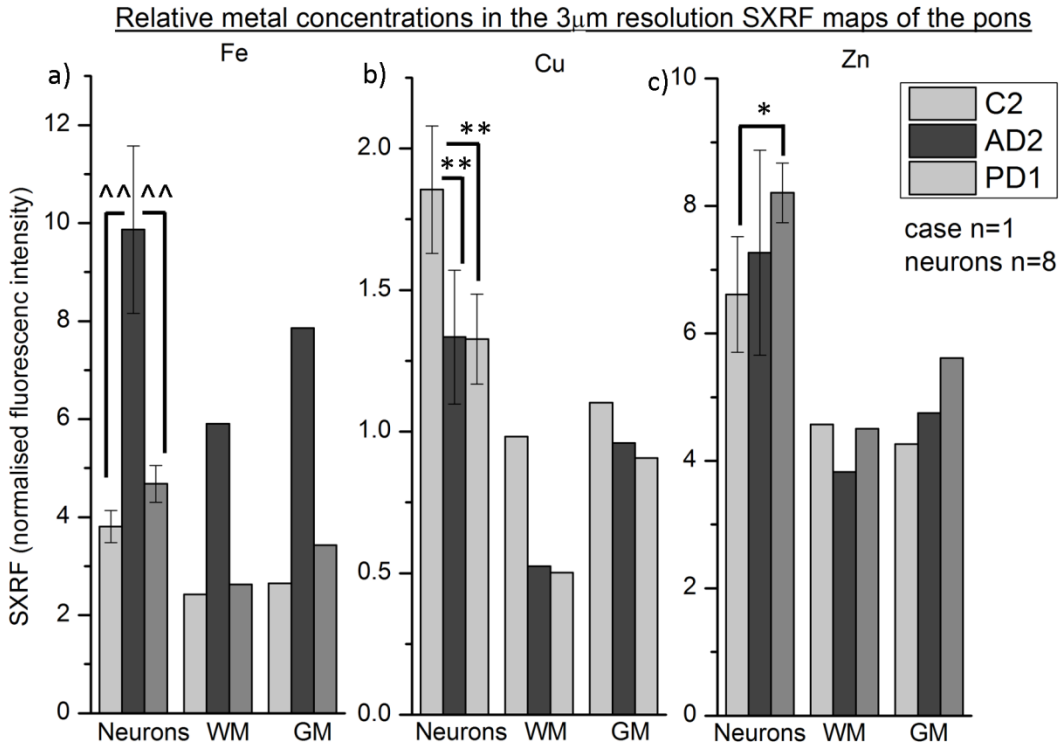

Figure 6.29: Relative metal concentrations in the neurons, grey matter and white matter of the pons. The mean and standard deviation of the eight neurons is shown in addition to the mean SXRF signal intensity in the white matter and grey matter. a) A statistically significant increase in iron in the AD neurons, compared to control and PD, is shown. b) A statistically significant decrease in copper was found in the AD and PD neurons. c) A statistically significant increase in zinc concentration is shown in the PD neurons, compared to control. * = $p<0.05$; **=$p<0.001$ by one-way ANOVA; ^^=$p<0.001$ by Welch's ANOVA.

However, Figure 6.29 also shows that there is a similar increase in each of the metals in the grey and white matter of the tissue. This indicates that the changes in metal concentrations observed in the regions of the map which have been identified as neurons may not be due to a change within the cell. The 30 μm thickness of the section means that the region containing the neuronal body will likely contain neuropil and/or glial cells (which are both also found in the grey matter). Table 6.7 shows the metal concentration for each region normalised to control. Iron concentration is more than doubled in both the grey and white matter of the AD

pons, however the largest increase is in the neurons and GM (which includes the neurons). Conversely, the table shows that for copper the greatest decrease is in the white matter. For the increase in zinc in PD the change is entirely in the GM (and neurons) with no change observed in the WM.

		Normalised to control		
		Neurons	GM	WM
Iron	Control	1.00	1.00	1.00
	AD	2.59	2.97	2.43
	PD	1.23	1.30	1.08
Copper	Control	1.00	1.00	1.00
	AD	0.72	0.87	0.53
	PD	0.72	0.82	0.51
Zinc	Control	1.00	1.00	1.00
	AD	1.10	1.11	0.84
	PD	1.24	1.32	0.99

Table 6.7: Metal concentration in the neurons, grey matter and white matter of the pons for AD and PD tissue normalised to control.

Ideally the concentration of metals in the neuronal bodies would be measured separately from the surrounding tissue in the grey matter, however with the staining quality of the post-SXRF mapped sections this could not be achieved. Therefore, despite the fact that individual neuronal bodies can be observed in the SXRF maps, it cannot be stated with confidence to what extent the metal concentration in the neurons of the pons is changed with disease.

6.6 Iron and amyloid deposition

Tissue sections adjacent to those mapped with synchrotron radiation were captured on glass and stained with Congo red and haematoxylin. These were examined under a microscope with and without cross-polarisers to look for evidence of amyloid deposition. Only the AD amygdala samples showed evidence of amyloid deposition. This is as expected as this is the only region being studied here that is widely reported to show AD pathology. The limited experimental time meant that high resolution mapping of the amygdala to look for changes in metal concentration in the region of amyloid plaques was not carried out. However, this could be an

interesting region to use in future to examine the relationship between iron, copper and zinc distribution and amyloid plaques.

6.7 Discussion

6.7.1 Comparison of bulk tissue and SXRF data

There was good agreement between bulk tissue and SXRF measurements, as investigated by comparing the ratio of iron content between AD and control samples (Table 6.2). This suggests that changes in iron concentration are relatively consistent throughout the two samples, where the bulk tissue sample was cut from tissue adjacent to the SXRF map, in a coronal tissue block (Figures 3.7 to 3.9). However, although the ratios agree well, this does not guarantee that the absolute concentration is constant throughout the regions. In fact there is evidence to show that this is not the case and this is discussed below.

6.7.2 Inhomogeneity of metal distribution

A significant observation made from examination of the SXRF maps is the inhomogeneity of metal distribution. Inhomogeneity is seen in the variation between mean concentrations in the segmented maps (Figure 6.18) and within anatomical structures (Figures 6.13 to 6.17). The distribution of iron is particularly inhomogeneous, which can be seen by the large standard deviations in mean iron concentration of segmented tissue structures (Figure 6.19).

The putamen was mapped at two different levels: where it is lateral to the caudate nucleus and where it is lateral to the globus pallidus. The control example at each level is from case C3 and therefore these maps can demonstrate how iron concentration within the putamen varies at these two positions, which are at a distance of approximately 2 cm. Figure 6.18 shows that the mean iron concentration in the map of the putamen lateral to the globus pallidus is 1.8 times greater than in the map lateral to the caudate nucleus. This demonstrates a substantial inhomogeneity in iron concentration within a brain structure, at a distance that would be resolvable at the resolution of clinical MRI.

It is common for the *post mortem* specimens to be sliced in 1-2 cm thick blocks (as was the case in this project) and therefore for large nuclei to be divided amongst several blocks. In the literature the size of samples taken for digestion varies from a small sample from within a region [27] to the whole region [19]. The data from the putamen highlight the importance of anatomically matching the position of samples taken. One consequence of this finding is that when comparing MRI relaxometry data to iron concentration values reported in other studies (as is often done [134]) the precise anatomical position of the tissue samples should always be considered. Unfortunately this is not always made clear in publications.

In the literature there is a wide variation in reported iron concentrations for the same brain region. This can be seen in a review by Haacke *et al.* [107] and in Table 3.2, which reproduces some of these data. It is possible that there is some inconsistency in the dissection of samples between studies and that consequently the spatial variation in iron concentration within a structure causes some of the spread in the data.

6.7.3 The potential of cellular resolution SXRF mapping

The development of a staining protocol for post-SXRF mapped tissue sections allowed the examination of metal concentrations within individual neurons in 3 μm resolution SXRF maps. However, the tissue is left very fragile and difficult to stain and therefore the identification of cells is difficult. It may be possible to reduce the damage to the tissue by using a slightly reduced X-ray intensity, which can easily be achieved at the beamline by insertion of attenuators. This would require some trial and error to find the optimum beam intensity to allow above background signal detection, but minimise tissue damage.

Although individual neurons could be resolved in the SXRF maps, changes in metal concentration within the neurons could not be fully separated from changes in the surrounding tissue. The development of a new beamline at the Diamond Light Source which is capable of creating beam sizes at nanometre resolution may help to enable this in the future.

At higher resolution it would be possible to more carefully define neurons and to compare their metal concentration to the rest of the grey matter.

6.7.4 Novelty of these measurements

SXRF mapping of metal distribution in biological samples is a fairly new technique. Other groups carrying out SXRF mapping have used thick (1 mm or more) sections of fixed tissue [89, 90, 136]. The thick tissue increased signal intensity and reduced mapping time, however variation in X-ray penetration and escape depth for X-rays of different energies means that different depths are being sampled for each metal.

The mapping of thin, unfixed sections mounted on spectroscopically clean slides is a technique developed by our group [113, 190] in parallel with a small number of other groups world-wide. It allows penetration of the X-rays through the whole section and avoids the need for fixatives, which can leach metal from tissue. The number of samples mapped using this technique is small and this is the first study of these regions of the basal ganglia.

The use of thin sections provides high depth resolution (30 µm in this case), in addition to high in-plane resolution. Therefore, very highly detailed maps of relative distributions of iron, copper and zinc were produced. This revealed features such as the low iron band at the lateral edge of the putamen and the distinct distributions of iron, copper and zinc in the substantia nigra. These patterns of metal distribution are not easily discerned from the thick sample mapping as can be seen in a study of the basal ganglia by Popescu *et al.* [89].

6.8 Summary

I. Sixty micron resolution maps of the relative iron, copper and zinc distribution in a control and AD sample from the caudate nucleus, putamen, globus pallidus, substantia nigra and amygdala were made. These maps revealed the distinct distribution of each metal across the brain regions.

II. The iron concentration measured in neighbouring tissue samples was used to calibrate the SXRF iron signal intensity, allowing estimation of iron concentration of tissue structures within the SXRF maps.

III. The inhomogeneity of iron was shown within brain nuclei, highlighting the importance of careful spatial matching when comparing between samples.

IV. High resolution SXRF mapping, followed by the new post-mapping haematoxylin staining protocol, demonstrated the potential for investigation of metal concentration within individual neurons.

Chapter 7:
MRI relaxometry

MRI relaxometry has been proposed as a method of detecting changes in brain iron concentration in Alzheimer's Disease and other neurodegenerative diseases [26]. Increased iron concentration (in particular particulate iron in the form of ferritin-encapsulated ferrihydrite and magnetite) causes increased R_2 and R_2*. At high field the effect of iron is increased [120] and due to the increased MRI signal higher imaging resolution can be achieved.

Region	Cases	Imaging field
Caudate nucleus	C1, C2, C3 AD1, AD2, AD3	400 MHz
Putamen	C1, C2, C3 AD1, AD2, AD3	400 MHz
Globus pallidus	C1, C2, C3 AD1, AD2, AD3	400 MHz
Substantia nigra	C1, C2, AD1, AD2 PD1, PD4	400 MHz
Amygdala	C1, C2, C3 AD1, AD2, AD3	600 MHz
Pons	C1, C2, C3 AD1, AD2, AD3 PD1, PD2, PD4 MSA1, MSA2	600 MHz

Table 7.1: List of samples measured with MRI relaxometry. Samples were imaged at 400 MHz (9.4 T) or 600 MHz (14.1 T). The details for each case are given in Table 3.4.

MRI mapping was carried out on control and AD samples from all of the regions chosen for investigation based on the literature review (Section 3.2). The protocol described in Section 4.3 was used to map R_2 and R_2* in the caudate nucleus (CN), putamen (Pu), globus pallidus (GP) and substantia nigra (SN) at 400 MHz, and the amygdala and pons at 600 MHz. Table 7.1 lists the samples mapped for each region at each field. Pons and substantia nigra tissue was also

measured for Parkinson's Disease (PD) and Multiple System Atrophy (MSA) cases, as indicated in the table.

In Chapter 5 the total and particulate iron concentration of samples from the pons, substantia nigra, putamen and caudate nucleus was examined. The results showed that although statistically significant differences between control and AD samples were not observed, discriminant analysis using data from multiple regions enabled 100% correct differentiation between AD and control samples. The same analysis was applied to the R_2 and R_2* data: the group means were compared first, followed by discriminant analysis.

Tissue iron content is just one factor affecting the MRI relaxation in each pixel within the segmented region of an SXRF map. Other factors include water and fat content. Increased water concentration has the opposite effect to increased iron concentration and decreases R_2 and R_2*. In a study by Schenck and colleagues an increase in pixels with both short and long transverse relaxation rates was observed within structures in the AD brain [191]. It was hypothesised that this is due to effects of both increased iron (causing pixels with rapid decay) and increased water (causing pixels with slow decay) within the AD tissue structures. The standard deviation within the regions is compared to examine this effect.

7.1 Segmentation of the R_2 and R_2* maps

In most cases, the mapped volume of tissue contained surrounding structures in addition to the target region. In order to include these structures in the analysis the maps were segmented into several regions of interest (ROIs). Segmentation was carried out manually using the open-source software ImageJ. Sections cut from the imaging block at 30 µm thickness, and stained with haematoxylin, were used to aid identification of anatomical structures. As far as possible the sections were cut in the same plane as the MRI imaging to provide the best reference. However, a certain amount of tissue compression/deformation can be expected due to the density of the Fluorinert in which the tissue was suspended during MRI

and some tissue features are more prominent in the MRI than in the stained sections and *vice versa*.

A selection of reference materials for these brain regions were used to aid segmentation [167, 170, 171]. These contained anatomical drawings or images of stained or fixed tissue but not MRI images, as there is little MRI imaging at such a high resolution of these regions of the human brain. Finally, advice was sought from pathologist Dr Lili-Naz Hazrati who also provided guidance on anatomy throughout the sample dissection process.

7.1.1 400 MHz maps

The caudate nucleus, putamen, globus pallidus and substantia nigra were mapped using the 400 MHz probe at the University of Warwick. Two stacks of seven interleaving maps with a resolution of 86 x 86 µm and a slice thickness of 150 µm (total imaged volume 1.05 mm) were produced. The main anatomical regions of interest were segmented in each high resolution slice in which they appeared. Other anatomical features common to all, or most, of the samples for that region were also segmented. These were only segmented in a subset of slices as segmentation is a labour intensive process. Where possible the data were taken from slices 1, 4, 7, 10 and 13, so as to include data from both interleaving stacks. For each ROI the mean R_2 and R_2* for each slice was measured using ImageJ and then the mean of these values calculated to give a final mean for the volume mapped. The mean and standard deviation of the standard deviation from each slice were also calculated.

Figures 7.1 to 7.7 show an example of the segmentation of one slice from an R_2 and R_2* map for one sample from each region. In addition to the segmented maps a stained section from the sample and the approximate anatomical position, as compared to the coronal sections from the Atlas of the Human Brain [167], is shown. Appendix E shows the segmentation of all of the remaining samples.

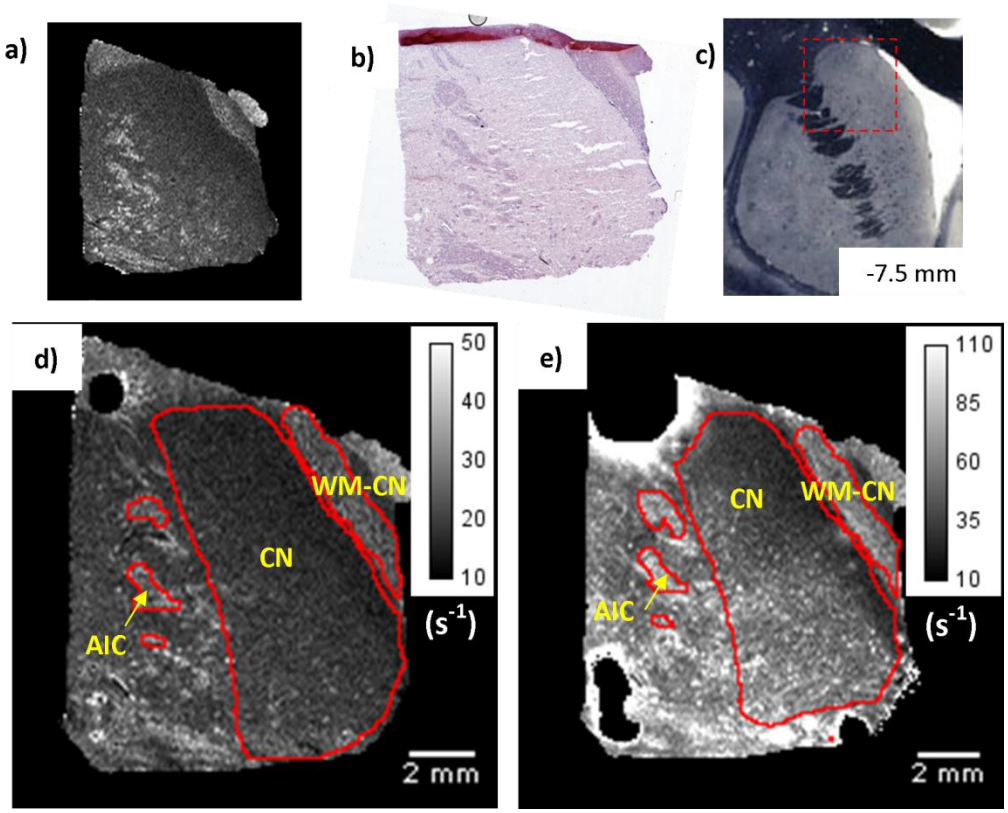

Figure 7.1 Segmentation of the MRI maps of caudate nucleus sample C1. a) The R_2 map, before segmentation; b) a stained tissue section cut from the imaged block; c) the approximate anatomical position of the tissue; d) the segmented R_2 and e) R_2* maps, showing the caudate nucleus (CN), anterior limb of the internal capsule (AIC) and the white matter medial to the caudate nucleus (WM-CN). Artefacts caused by bubbles were present in the R_2* map. These were excluded from the segmented regions.

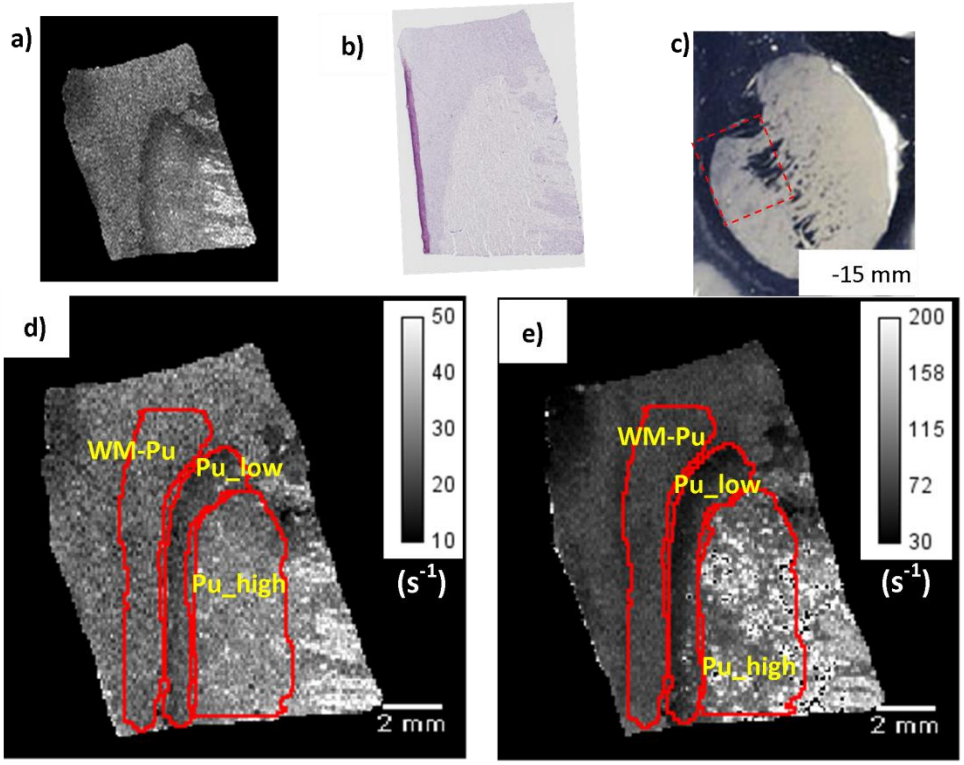

Figure 7.2: Segmentation of the MRI maps of putamen sample C3. a) The R_2 map, before segmentation; b) a stained tissue section cut from MRI block; c) the approximate anatomical position of the tissue; d) the segmented R_2 and e) R_2* maps, showing the putamen divided into the bright and dark region (Pu_high and Pu_low) and the white matter lateral to the putamen (WM-Pu). A small number of pixels in the R_2* map could not be fitted in ImageJ and can be seen as black pixels within the Pu_high region.

Caudate Nucleus

In addition to the caudate nucleus (CN), the maps are segmented in to the white matter medial to the caudate nucleus (WM-CN) and the anterior limb of the internal capsule (AIC) as shown in Figure 7.1 for sample C1. In this example the AIC is small and is only segmented where it can be clearly defined.

Putamen

The images were segmented into the entire putamen (Pu) and the white matter lateral to the putamen (WM-Pu). The putamen was further divided into areas named here as 'Pu_high' and 'Pu_low' as shown in Figure 7.2 for sample C3. 'Pu_high' makes up the majority of the putamen and has a relatively high R_2. 'Pu_low' forms a band of lower R_2 tissue along the lateral edge of the putamen and corresponds to the region of decreased iron that was observed in the SXRF maps in Chapter 6. In many cases the boundary of the 'Pu_high' region could be mistaken as the edge of the structure, but confirmation of the true edge was made by comparison to stained sections. The boundary of 'Pu_high' may appear to be the boundary of the putamen at typical clinical resolution, where less detail is captured. As the proportion of Pu_high compared to Pu_low included in each map varies depending on exactly how the sample was cut, Pu_high is used for a more consistent comparison between samples.

Globus Pallidus

The globus pallidus samples were segmented into the internal and external globus pallidus (GPi and GPe) and the high R_2 region of the putamen lateral to the globus pallidus (Pu_high-GP). The putamen in these maps is approximately 10 to 20 mm posterior to the putamen lateral to the caudate nucleus (shown in Figure 7.2). Figure 7.3 shows the segmentation of the GP for sample AD2, for which all ROIs were present. Cutting well matched samples for this region of the brain proved particularly challenging and the GPi was not present in many cases. Figure 7.4 shows the sample from case C2 which was excluded from analysis due to the uncertainty about its anatomy.

In some GP samples a proportion of pixels in the R_2* maps could not be fitted due to extremely rapid signal decay. These pixels were removed from the maps using the ImageJ threshold tool or by manual deletion.

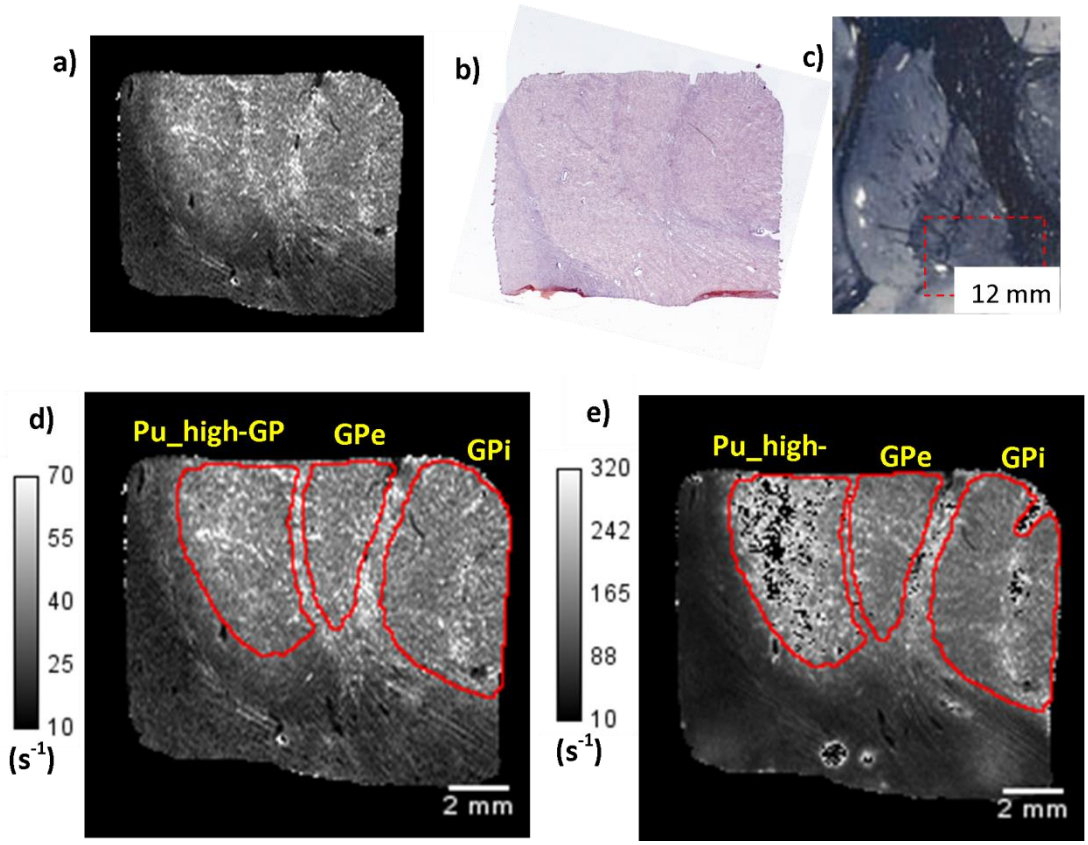

Figure 7.3: Segmentation of the MRI maps of globus pallidus sample AD2. a) The R_2 map, before segmentation; b) a stained tissue section cut from the imaged block; c) the approximate anatomical position of the tissue; d) the segmented R_2 and e) R_2* maps, showing the external globus pallidus (GPe), internal globus pallidus (GPi) and putamen (Pu_high-GP). The gap between each segmented region is the location of a thin lamina of white matter separating the nuclei. The R_2* map contains a number of pixels which could not be fitted in ImageJ and appear as black pixels.

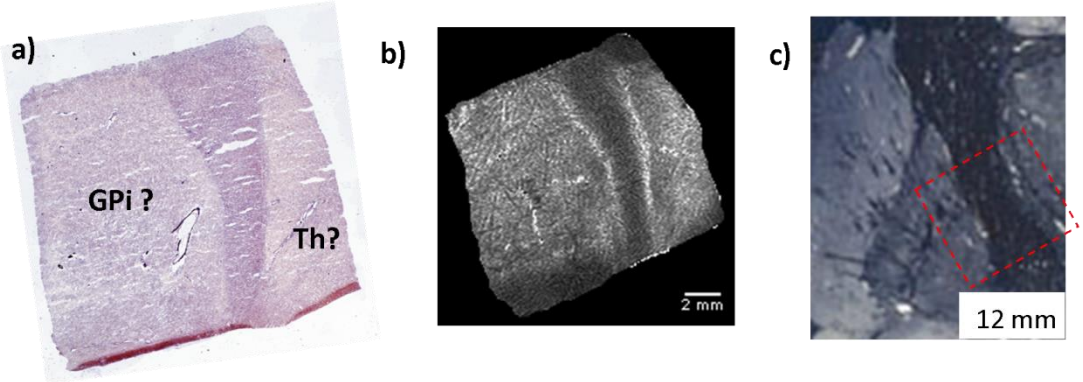

Figure 7.4: MRI of globus pallidus sample C2. The anatomy of this sample is hard to define. It may contain the internal globus pallidus (GPi) and thalamus (Th) as indicated on the stained section a). b) One slice of the R_2 map of the sample and c) the best approximation of the anatomical position. This sample was excluded from the analysis due to the uncertainty about its anatomy.

Substantia Nigra

The cerebral crus (CC) and the substantia nigra (SN) were segmented from the tissue as shown for sample C2 in Figure 7.5. The SN was defined as the bright band of tissue in the R_2 and R_2* maps, as is standard practice in clinical MRI [122]. Due to the thin pieces of tissue available for MRI, extra care had to be taken to avoid any imaging artefacts caused by bubbles next to the tissue. As bulk tissue measurements were prioritised for the substantia nigra there were only two control two AD samples for MRI. 2 PD samples were also mapped.

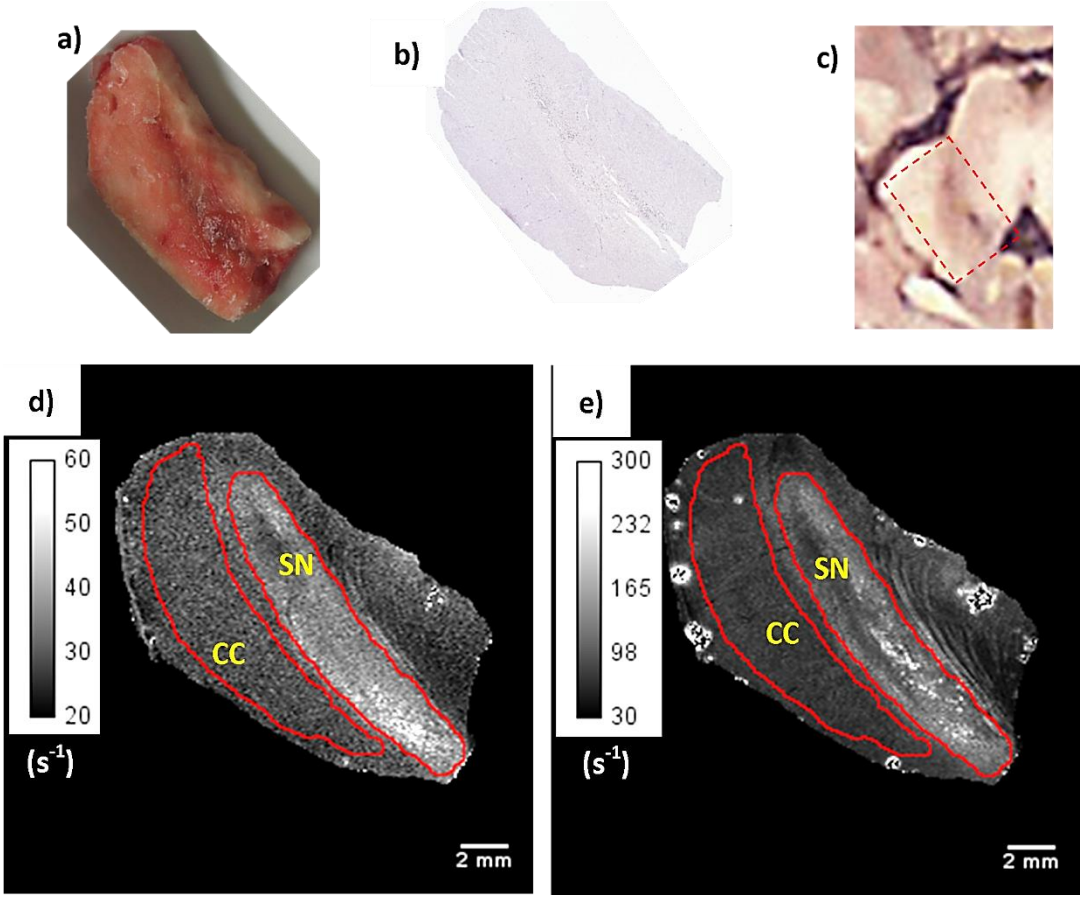

Figure 7.5: Segmentation of the MRI maps of substantia nigra sample C2. a) A photograph of the tissue before MRI; b) a stained tissue section cut from the imaged block; c) the approximate anatomical position of the tissue; d) the segmented R_2 and e) R_2* maps, showing the substantia nigra (SN) and cerebral crus (CC). The R_2* map contains some artefacts due to bubbles. However, these are around the edge of the sample are not included in the segmented regions.

7.1.2 600 MHz maps

The amygdala and pons tissues were imaged at 600 MHz at the University of Florida, producing maps with an in-plane resolution of 62 x 62 µm and a slice thickness of 80 µm. After imaging it

was discovered that the R_2 maps were unreliable due to variation in relaxation rate across the tissue volume, due to a parameter in the scan set-up (Section 4.3.3.1). Therefore only the R_2* maps are analysed.

Amygdala

The amygdala contains a number of different nuclei and as far as was possible tissue was cut from a similar area for each case. No distinct structures can be identified in the MRI maps and advice from neuropathologist Dr Lili-Naz Hazrati is that all tissue was cut from within the amygdala. No segmentation was carried out other than to exclude any artefacts and the mean was found from each high resolution slice. A representative slice from each amygdala sample is shown in Figure 7.6.

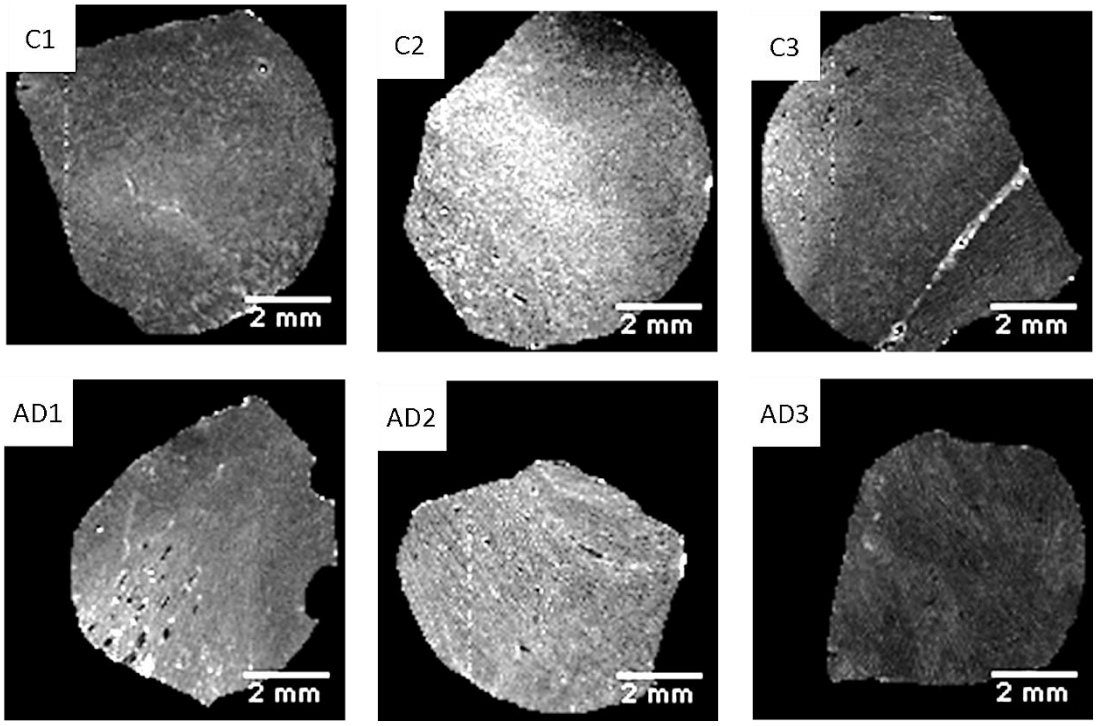

Figure 7.6: A representative slice from each of the R_2* MRI maps of the control and AD amygdala. The contrast gradient for each map was chosen to best display the features in each sample and is not the same for each case.

Pons

In addition to finding the average signal of the whole tissue volume, the stripy tissue of the pons was segmented into grey and white matter. The stained sections from the pons were

particularly useful in identifying the grey and white matter, where the MRI map contrast was ambiguous. Figure 7.7 shows the segmentation of the pons into grey and white matter for sample PD4.

In addition to the three control and AD cases, three PD and 2 MSA pons cases were imaged. For one of each of the control, AD and PD cases two samples were imaged. For the control and AD samples one of the duplicates provided a better example of the grey and white matter stripes than the other and the data from this case was used. For the PD case, both samples showed the typical grey and white matter stripes of the pons and therefore the data from both samples was averaged before finding the total average for the group. One R_2* slice from each pons sample is shown in Appendix F.

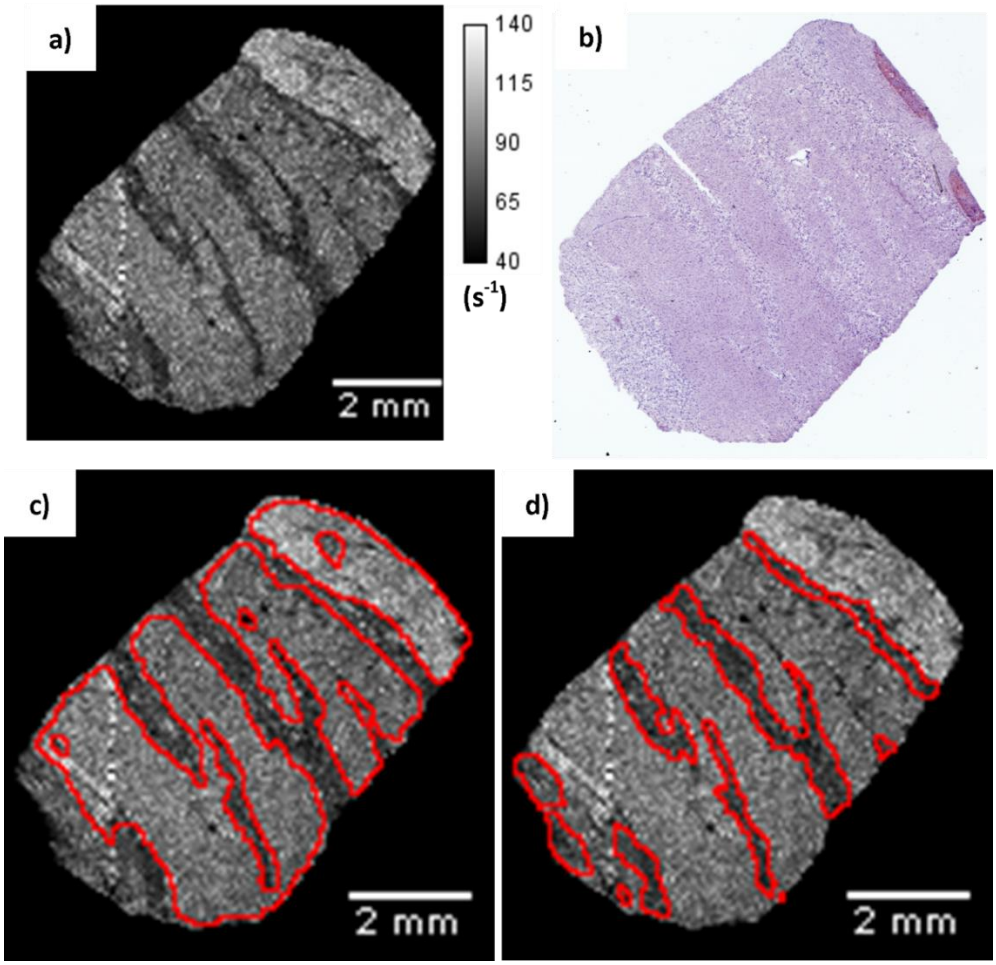

Figure 7.7: Segmentation of the R_2* map of pons sample PD4. a) The R_2* map before segmentation; b) a haematoxylin stained section from approximately the same level; c) the white matter segmentation of the R_2* map and d) the grey matter segmentation of the same map.

7.2 Comparison of means

Once the mean R_2 and R_2* for each segmented region in each sample was measured, the means for the AD and control samples were calculated. This was followed by discriminant analysis, which has already been used to create a model to differentiate between disease and control using the bulk tissue measurement in Chapter 5.

7.2.1 Control and AD samples

Figure 7.8 shows the mean R_2 and R_2* for the tissue structures segmented in the MRI maps of the AD and control samples. Figure 7.9 shows the data from the pons and substantia nigra maps, for which additional disease groups were imaged. The number of samples for each region is indicated on the graph. For regions where n=3 for each disease group, the statistical software SSPS was used to look for statistical differences between groups. Data were normally distributed as reported by the Shapiro-Wilk test ($p<0.05$) and were therefore examined using parametric statistics. No statistically significant differences were observed between group means. Where n=2 no statistical comparisons were made, due to the small group size.

R_2 is higher with AD in 6 out of the 10 brain regions mapped at 400 MHz (control is higher in 3 of 10, in the CC there is no change) and for the mean R_2* data this is reduced to 5 of 10 (control is higher in 4 of 10. Again in the CC there is no change).

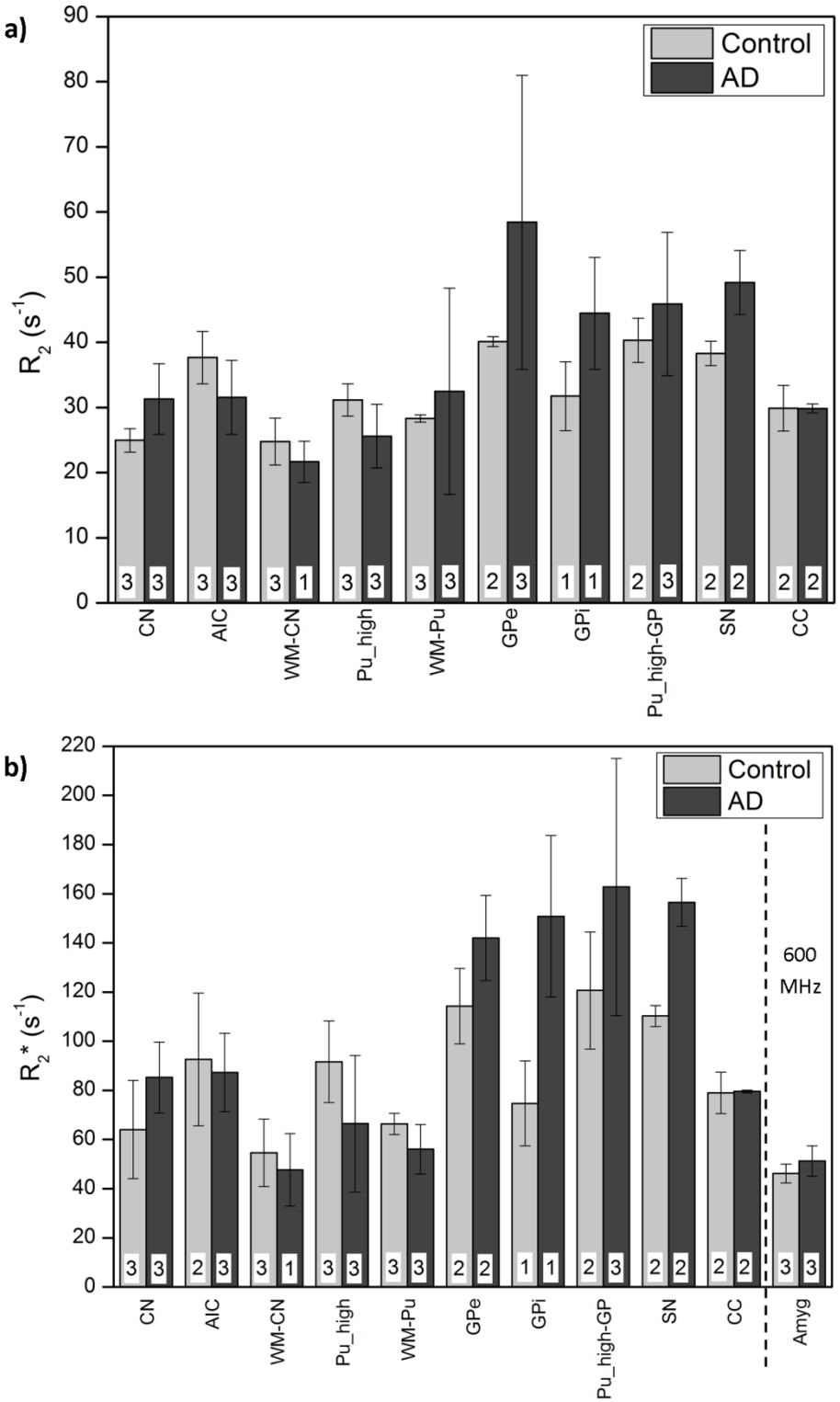

Figure 7.8: Mean R_2 and R_2* values in the segmented regions of MRI maps of the control and AD samples. The number of cases is indicated on the bar for each data set. a) Data from the R_2 maps of samples imaged at 400 MHz. b) Data from the R_2* maps, where all samples were imaged at 400 MHz, apart from the amygdala which was imaged at 600 MHz. One-way ANOVA revealed no statistically significant differences between control and AD for any region. CN=caudate nucleus; AIC=anterior limb of the internal capsule; WM-CN=white matter medial to the CN; Pu=putamen; WM-Pu=white matter lateral to the Pu; GPe= external globus pallidus; GPi=internal globus pallidus; Pu-GP=Pu lateral to the globus pallidus; SN=substantia nigra; CC=cerebral crus; Amyg=amygdala.

7.2.2 AD, PD and MSA samples

Figure 7.9 a) shows the mean R_2 and R_2* in the substantia nigra and cerebral crus of the control, AD and PD samples. The mean values for the CC are very similar between the disease groups, whereas R_2 and R_2* in the SN are increased in AD and PD samples compared to control. As only two samples were measured for each disease, statistical comparisons were not made.

Figure 7.9 b) shows the mean R_2* values for the grey and white matter of the control, AD, PD and MSA pons. The average for the whole volume of the pons is also included. No statistically significant differences were observed between group means, although there is a trend of increased R_2* in disease samples compared to control.

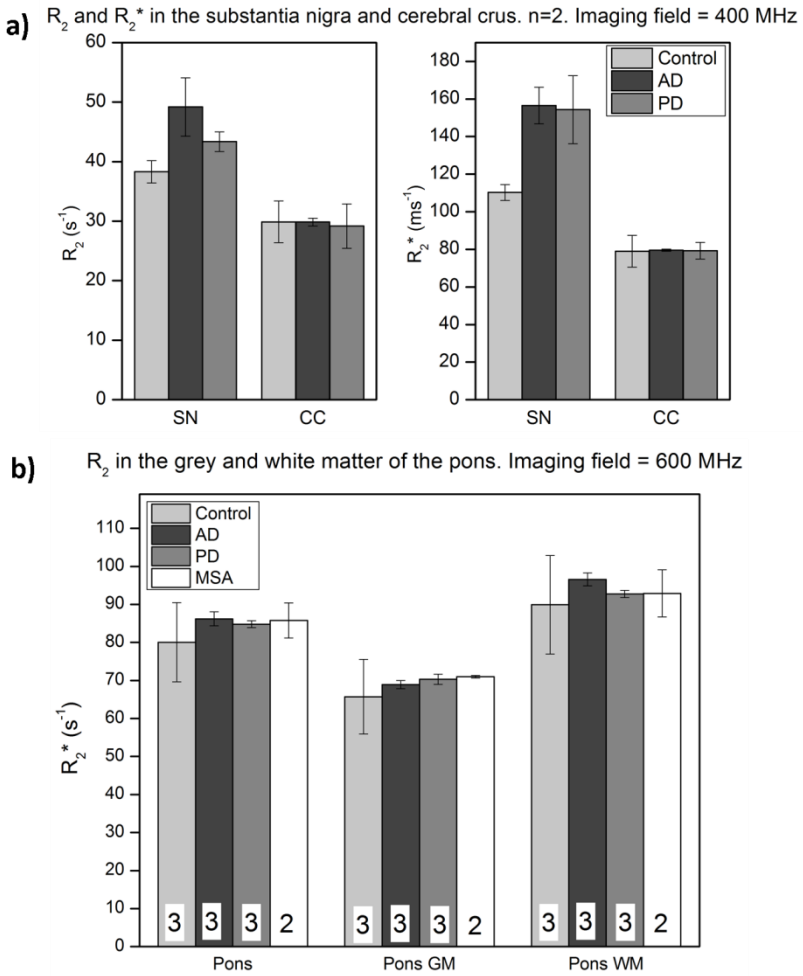

Figure 7.9: Data from MRI maps of control, AD, PD and MSA tissue. a) Mean R_2 and R_2* in the substantia nigra (SN) and cerebral crus (CC) imaged at 400 MHz. Both R_2 and R_2* are increased in AD and PD tissue compared to control, but as n=2 no statistical comparisons were made. b) R_2* of the grey matter, white matter and the whole pons imaged at 600 MHz. In each case the control shows a lower R_2* than the diseased tissue, but one-way ANOVA showed no statistically significant differences between groups.

7.2.3 Discriminant analysis of data from multiple regions

Although one-way ANOVA identifies no statistically significant differences between group means, analysis of total iron concentration in Chapter 5 showed that creating a model using discriminant analysis can increase the ability to distinguish between disease and control samples. This hypothesis was tested using the R_2 and R_2* data from the 400 MHz imaging and the R_2* data from the 600 MHz imaging. Only the regions for which n=3 for AD and control are included, as discriminant analysis requires a full data set for each case.

7.2.3.1 400 MHz measurements

100% correct classification of samples was achieved using R_2 data from the CN, Pu, AIC and WM-Pu regions (Table 7.2 a). Only 50% of the samples were classified correctly (no better than guessing) with cross-classification. Cross-classification involves removing a sample from the data set, creating a model with the remaining data and then using this model to classify the excluded sample. This is carried out (automatically, in the software SSPS) for each sample. It is not unexpected that poor cross-classification would be achieved with such a small number of samples as there is a limited amount of data to create the model.

Tables 7.2 b) and c) can be examined to see which variables are most important in the model. A larger absolute function coefficient in 7.2 b) indicates greater contribution to the model, whereas a small Wilks' Lambda and significance value in Table 7.2 c) indicate greater contribution. The data in both tables show that the CN data contributed the most to the model and that the white matter lateral to the putamen (WM-Pu) contributed the least. However, there is a disagreement as to whether the Pu or AIC contributes more to the model. Therefore discriminant analysis was carried out with different regional combinations which include the CN, but not the WM-Pu.

The results of this analysis are shown in Table 7.3. 100% correct classification was achieved with the data from just two regions: the CN and AIC. When cross-validation is considered this

actually produced a better result than combining data from all regions. Looking back at Figure 7.8 shows that the mean R_2 in the CN was increased in the AD samples compared to control, whereas the mean R_2 in the AIC was decreased in AD.

a) Classification Results

Brain regions	Original Group		Predicted Group Membership		Total proportion correct
			Control	AD	
All R_2: CN, Pu, AIC, WM-Pu	Count	Control	3	0	
		AD	0	3	100%
	Cross-validation	Control	2	1	
		AD	2	1	50.0%

b) Standardized Canonical Discriminant Function Coefficients

	Function 1
CN	-2.383
Pu	1.197
AIC	1.728
WM-Pu	1.090

c) Tests of Equality of Group Means

	Wilks' Lambda	F	df1	df2	Sig.
CN	.518	3.718	1	4	.126
Pu	.563	3.107	1	4	.153
AIC	.634	2.308	1	4	.203
WM –Pu	.950	.209	1	4	.671

Tables 7.2: Results of discriminant analysis of R_2 data collected at 400 MHz. a) The model has grouped all samples into the correct disease group, but only 50% with cross-validation. b) The standardised canonical discriminant function coefficients suggest that the order of importance of the regions to the model is CN, AIC, Pu and then WM-Pu. c) The equality of group means suggests that the order of importance is CN, Pu, AIC and then WM-Pu.

Brain regions	Original Group		Predicted Group Membership		Total proportion correct
			Control	AD	
CN	Model	Control	3	0	
		AD	1	2	83.3%
	Cross-validation	Control	3	0	
		AD	1	2	83.3%
CN & Pu	Model	Control	3	0	
		AD	1	2	83.3%
	Cross-validation	Control	3	0	
		AD	2	1	66.7%
CN & AIC	Model	Control	3	0	
		AD	0	3	100%
	Cross-validation	Control	3	0	
		AD	1	2	83.3%
CN, Pu & AIC	Model	Control	3	0	
		AD	0	3	100%
	Cross-validation	Control	3	0	
		AD	1	2	83.3%

Table 7.3: The results of discriminant analysis using combinations of R_2 data from different brain regions. 100% accurate classification (83.3% with cross-validation) was achieved by using R_2 of the CN and AIC.

Similar analysis was carried out with the R_2* data from the regions measured at 400 MHz (Tables 7.4 and 7.5). Although the WM-Pu was least important to the R_2 model it contributes the most to the R_2* model. When cross-validation is considered the best model is produced using data from the CN and WM-Pu. As with the R_2 model, the direction of change between mean R_2* of control and AD is different for these two regions: mean R_2* is increased in the Alzheimer's disease CN, but decreased in the WM-Pu compared to control.

a) Classification Results

Brain regions	Original Group		Predicted Group Membership		Total proportion correct
			Control	AD	
All R_2*: CN, Pu, WM-Pu	Count	Control	3	0	
		AD	0	3	100%
	Cross-validation	Control	2	1	
		AD	2	1	50.0%

b) Standardized Canonical Discriminant Function Coefficients

	Function 1
CN	-0.980
Pu	0.056
WM-Pu	0.981

c) Tests of Equality of Group Means

	Wilks' Lambda	F	df1	df2	Sig.
CN	.648	2.176	1	4	.214
Pu	.688	1.816	1	4	.249
WM-Pu	.601	2.654	1	4	.179

Tables 7.4: Results of discriminant analysis of R_2* data collected at 400 MHz. a) The model has grouped all samples into the correct disease group. b) The standardised canonical discriminant function coefficients suggest that the order of importance of regions to the model is WM-Pu, CN and then the Pu. c) The equality of group means suggests that the order of importance is WM-Pu, CN and then Pu.

Brain regions	Original Group		Predicted Group Membership		Total proportion correct
			Control	AD	
CN & WM-Pu	Model	Control	3	0	
		AD	0	3	100%
	Cross-validation	Control	2	1	
		AD	1	2	66.7%
CN & Pu	Model	Control	3	0	
		AD	0	3	100%
	Cross-validation	Control	2	1	
		AD	2	1	50.0%
Pu & WM-Pu	Model	Control	3	0	
		AD	1	2	83.3%
	Cross-validation	Control	1	2	
		AD	1	2	50.0%

Table 7.5: The result of discriminant analysis using combinations of R_2* data. The minimum number of regions needed to achieve 100% correct classification is two: using data from the CN and Pu or data from the CN and white matter lateral to the putamen (WM-Pu).

7.2.3.2 600 MHz data

The result of discriminant analysis of the data from the pons and amygdala samples is shown in Tables 7.6 and 7.7. 100% correct classification was achieved for a combination of data from the amygdala, pons white matter and pons grey matter, however this dropped to 50% with cross-validation. The information in Tables 7.7 b) and c) suggests that the pons white matter contributed the most to the model, but it is not clear which region contributed least. When cross-validation is considered, the best combination of regions for differentiating between AD and control was the amygdala and the grey matter of the pons (Table 7.7).

Discriminant analysis was carried out on control, AD and PD pons samples, where the R_2* measurements of the pons GM and WM were used as predictors. This only achieved 44% correct classification (not shown). The similarity in the mean R_2* of the AD and PD samples in this region (shown in Figure 7.9) does not provide the information required to differentiate between the disease groups.

a) Classification Results

Brain regions	Original Group		Predicted Group Membership		Total proportion correct
			Control	AD	
Amydala, Pons GM, Pons WM	Count	Control	3	0	
		AD	0	3	100%
	Cross-validation	Control	1	2	
		AD	1	2	50.0%

b) **Standardized Canonical Discriminant Function Coefficients**

	Function
	1
Amygdala	1.152
Pons GM	-1.972
Pons WM	2.688

c) **Tests of Equality of Group Means**

	Wilks' Lambda	F	df1	df2	Sig.
Amygdala	.648	1.415	1	4	.300
Pons GM	.688	.140	1	4	.728
Pons WM	.601	.440	1	4	.544

Tables 7.6: Results of discriminant analysis of R_2* data collected at 600 MHz. a) The model has grouped all samples into the correct disease group. b) The standardised canonical discriminant function coefficients suggest that order of importance of regions to the model is Pons WM, Pons GM and then the amygdala. c) The equality of group means suggests that the order of importance is the pons WM, amygdala and then pons GM.

Brain regions	Original Group		Predicted Group Membership		Total proportion correct
			Control	AD	
Amygdala, whole pons	Model	Control	3	0	
		AD	1	2	83.3%
	Cross-validation	Control	1	2	
		AD	1	2	50.0%
Pons GM, amygdala	Model	Control	3	0	
		AD	1	2	83.3%
	Cross-validation	Control	2	1	
		AD	1	2	66.7%
Pons WM, amygdala	Model	Control	3	0	
		AD	1	2	83.3%
	Cross-validation	Control	1	2	
		AD	1	2	50.0%
Pons GM, pons WM	Model	Control	2	1	
		AD	1	2	66.7%
	Cross-validation	Control	1	2	
		AD	2	1	33.3%

Table 7.7: The results of discriminant analysis using combinations of R_2* data collected at 600 MHz. 100% classification was not achieved. However, the pons GM and amygdala achieved 83.3% correct classification and 66.7% with cross-validation.

7.2.4 Further comparisons

The results of discriminant analysis of R_2 data in Table 7.4 showed that 100% classification could be achieved using data from the CN and AIC regions. Revisiting the data shown in Figure 7.8 reveals that the mean R_2 in the CN is higher in AD tissue, whereas the mean R_2 in the AIC is lower in AD tissue. This suggests that there is an increase in contrast between these neighbouring tissue structures. The mean CN:AIC ratio for control and AD tissue is shown in Figure 7.10. A strong statistically significant increase ($p<0.01$ by one-way ANOVA) in the ratio was observed for the AD samples.

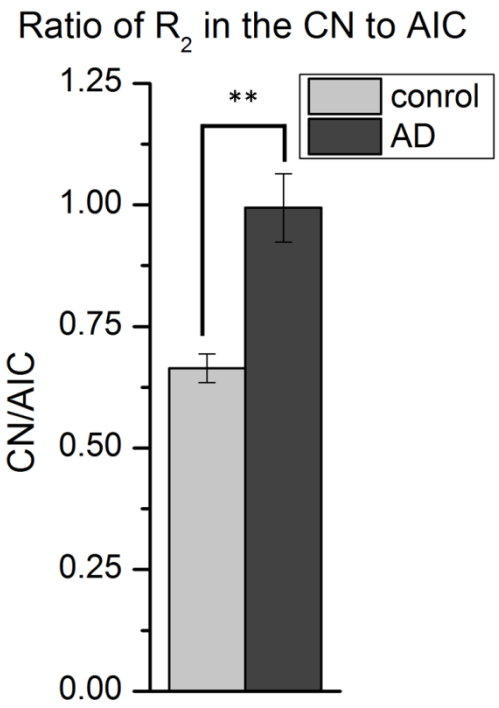

Figure 7.10: Mean ratio of R_2 in the caudate nucleus (CN) to R_2 in the anterior limb of the internal capsule (AIC). A statistically significant increase in the ratio was observed for the AD data (**p<0.01).

7.3 Comparison of standard deviations

Increased tissue water content decreases R_2 and R_2*, whereas they are increased by elevated iron concentration. Schenck and colleagues have shown that within some regions of the AD brain there is both an increase in the number of rapid and slow R_2 pixels [191]. This was examined here by comparing the standard deviation (the square root of variance) of the control and AD samples.

When mean R_2 and R_2* values were calculated from multiple slices, the variance within each segmented region was preserved by calculating the mean of the standard deviations from each slice. Figure 7.11 shows the mean R_2 and R_2* standard deviation for the control and AD samples, with the error bars indicating the standard deviation (of the standard deviations for each sample). Figure 7.12 shows the same for the whole pons and the segmented grey and white matter tissue for the control, AD, PD and MSA samples. Statistical comparisons for the cases where n=3, showed no statistically significant differences between AD and control samples.

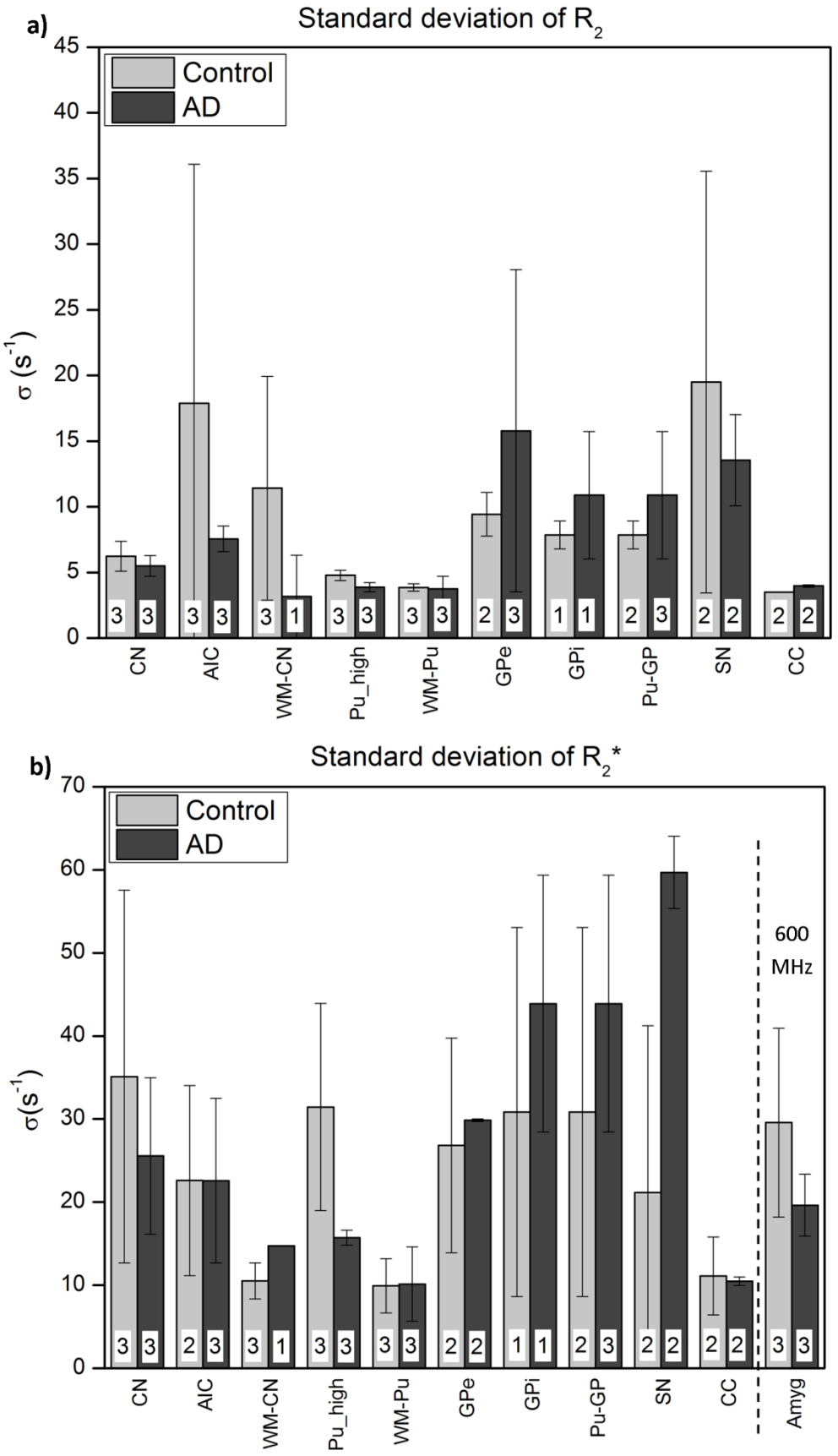

Figure 7.11: Mean standard deviation of R_2 and R_2*. Error bars represent the standard deviation of the standard deviations. No statistically significant differences were observed between means.

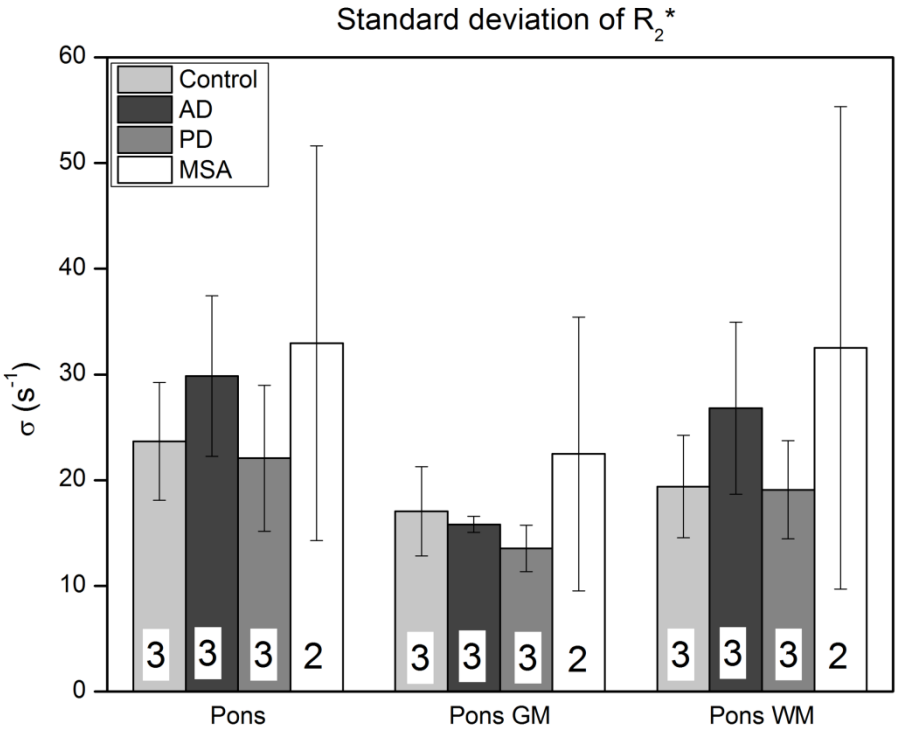

Figure 7.12: Mean standard deviation of R_2* in the pons. Error bars represent the standard deviation of the standard deviations. No statistically significant differences between disease groups were observed.

7.4 Discussion

7.4.1 R_2 and R_2* data can be used to differentiate between AD and control cases

The discriminant analysis of the R_2 and R_2* data has shown that by combining data from multiple regions 100% correct classification of control and AD cases can be achieved, even when there is no statistically significant difference between group means. This is in agreement with the analysis of the bulk tissue iron measurements and supports the hypothesis that MRI relaxometry could be used to differentiate between control and AD cases.

7.4.2 Contrast between the caudate nucleus and anterior limb of the internal capsule is increased in AD

A statistically significant increase was observed in the ratio of R_2 in the caudate nucleus to R_2 in the anterior limb of the internal capsule, for AD compared to control samples. The fact that

the statistically significant difference is observed in a ratio, and not in absolute R_2 values, is an advantage as it could be less sensitive to variations that exist between different imaging systems and scan sequences.

7.4.3 No difference in pixel variance was observed

No statistically significant difference was found between the standard deviation of pixel values of the control and AD tissues. This does not agree with previously published results which have reported a greater variance of R_2 in AD tissue in some regions [132, 191]. However, these findings were mostly limited to brain regions associated with significant AD pathology (such as the hippocampus), which may also be contributing to the variance in R_2 and R_2*.

The small bore sizes of the high resolution imaging systems used in this study meant that whole brain structures could not be imaged and small samples were taken from within these relatively large structures. Although the samples were cut carefully to provide as close matching as possible, there was some variation of the anatomical position of each sample. Therefore variance measured for each sample may not accurately reflect the variance of the whole structure

7.5 Summary

I. No statistically significant differences were found between R_2 or R_2* measurements of control and AD tissue.
II. As predicted in Chapter 5, discriminant analysis achieved differentiation between control and AD samples using data from multiple regions.
III. The ratio of R_2 in the caudate nucleus compared to the anterior limb of the internal capsule was statistically significantly increased in AD samples compared to control.
IV. Considering the MRI relaxation values in multiple brain regions may be more clinically useful than looking for a difference between individual regions.

Chapter 8:
The relationship between iron and MRI

The iron content of control and AD brain tissue was examined in bulk tissue samples by SQUID magnetometry and iron quantification in Chapter 5. The distribution of iron within regions was examined using high resolution SXRF mapping in Chapter 6 and in Chapter 7 high resolution MRI relaxometry was used to create R_2 and R_2* maps of the same set of cases. In this chapter the MRI and iron data will be compared in order to examine the relationship between iron concentration and R_2 and R_2*.

Tissue iron has been shown to increase the relaxation rates R_2 and R_2*, with the effect of iron increasing with field strength. This has been well studied at fields of up to 4.7 T [25, 26], with some additional studies at 7 T [27], however it is understudied at even higher fields. Here the relationship between tissue iron content and R_2 and R_2* at 9.4 T (400 MHz) and 14.1 T (600 MHz) is investigated.

8.1 Comparing SXRF and MRI relaxometry maps

SXRF maps were made of tissue from a sub-set of MRI imaged samples. Table 8.1 gives the SXRF experiment number and MRI field for each sample. The data for each SXRF map have been presented in Chapter 6 and the MRI data from all samples were investigated in Chapter 7.

The SXRF mapped sections were cut from the region of the MRI tissue block which was mapped at high resolution and in approximately the same plane as imaging. This protocol was described in more detail in Section 3.3.3.1 and was designed to allow good spatial matching between the SXRF section and one of the high resolution MRI slices. In this chapter the spatially matched data are used to investigate the relationship between iron concentration and the transverse relaxation rate, R_2, and the susceptibility related parameter R_2*.

Brain Region	Case number	SXRF experiment	MRI frequency
Caudate nucleus	C2	DLS5	400 MHz
	AD1	DLS5	400 MHz
Putamen	C3	DLS5	400 MHz
	AD3	DLS5	400 MHz
Globus pallidus	C3	DLS5	400 MHz
	AD2	DLS5	400 MHz
Substantia nigra	C2	DLS5	400 MHz
	AD2	DLS5	400 MHz
Amygdala	C3	DLS5	600 MHz
	AD2	DLS5	600 MHz
Pons	C2	DLS2	600 MHz
	AD2	DLS3	600 MHz
	PD1	DLS3	600 MHz
	MSA1	DLS1	600 MHz

Table 8.1: SXRF experiment number and the MRI spectrometer frequency for ^{1}H imaging used to image each sample. The majority of samples were mapped during experiment DLS5 and imaged at 400 MHz. The amygdala samples also had SXRF data collected during experiment DLS5, but were mapped at 600 MHz. The pons samples were also mapped at 600 MHz and the SXRF data were collected over a number of different experiments. The details of each case are given in Table 3.4.

Tissue sections, including those for SXRF mapping, were cut at 30 µm, whereas MRI slice thickness for the samples mapped at 400 MHz was 150 µm and at 600 MHz was 80 µm. Therefore the sections represent only around 20% and 38% of the volume being imaged. Additionally, perfect matching across the whole tissue section and MRI slice is not possible, in particular due the difficulty in matching sectioning and imaging plane. However, overall very close matching was achieved (as will be shown below) and therefore the iron (and copper and zinc) concentration of the SXRF matched section can be considered a very good representation of the iron concentration of the matched MRI slice.

In Chapter 6, Section 6.4 the normalised SXRF signal intensity for iron was calibrated using the iron quantification measurements made in Chapter 5. This calibration is carried into this

chapter and the iron concentration in the SXRF maps is reported as micrograms of iron per gram of tissue. The calibration had an approximate error of ± 12%, which must be taken into account when considering absolute iron concentrations. However, this does not affect the relative concentration of iron measured by normalised SXRF signal intensity, which has an estimated measurement error of ± 5%.

8.1.1 400 MHz data

8.1.1.1 Matching SXRF and MRI maps

Figure 8.1 shows the selection of the MRI slice which is most closely matched to the SXRF map for the caudate nucleus, case C2. Appendix G contains an equivalent figure for each sample and the final result of matching for each sample is shown in Figures 8.2 to 8.11.

Matching was carried out manually in ImageJ by comparing anatomical features in the SXRF map, MRI maps, the stained and unstained SXRF section and adjacent stained tissue sections. Firstly, the best matched slice for the high resolution MRI stack was chosen and then it was rotated into the same orientation as the SXRF map. The map was then trimmed to match the area of the SXRF map. Rotation and trimming were carried out using ImageJ. In addition to visual matching, the dimensions of the SXRF map (pixel size = 60 x 60 μm) were used to determine what the size the trimmed MRI map (pixel size = 86 x 86 μm) should be.

In Figure 8.1 matching is shown for the T_2 map, but was also carried out in parallel for the T_2* map. Finally R_2 and R_2* maps were generated, using the formulae $R_2=1/T_2$ and $R_2^*=1/T_2^*$.

Section 72, on glass, stained with haematoxylin

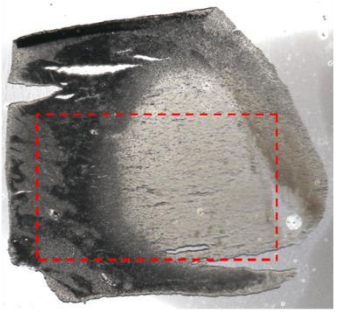

Section 73, on quartz, before drying and mapping.

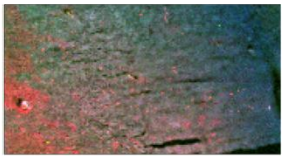

Combined metal SXRF map. red = iron; green = copper; blue = zinc.

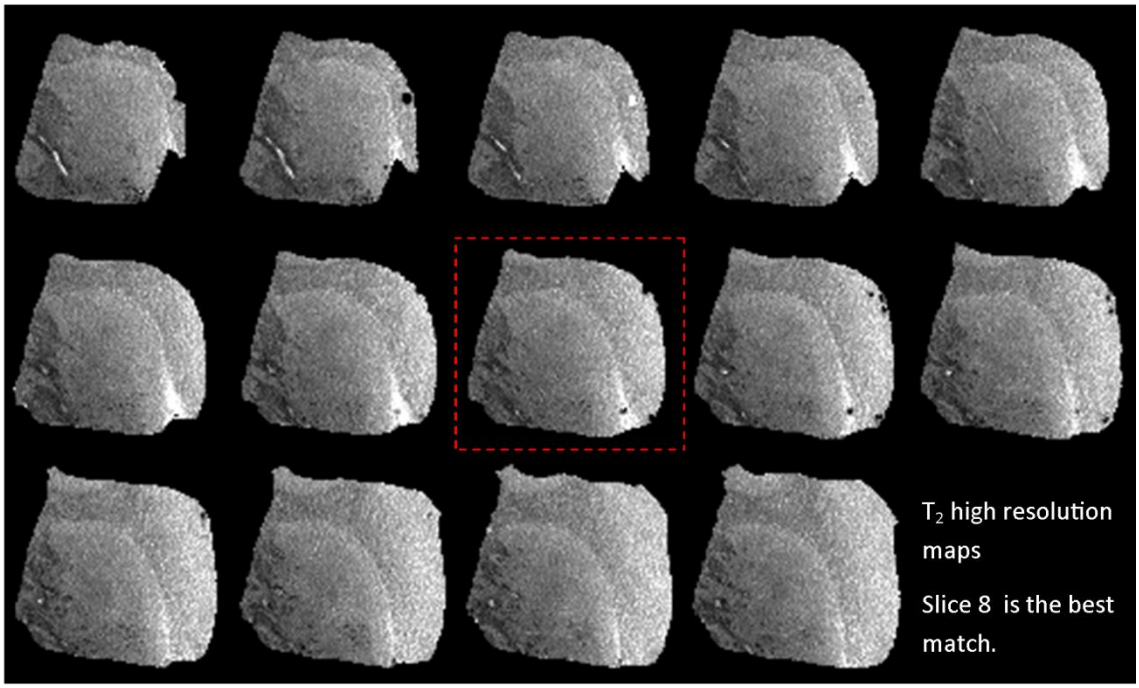

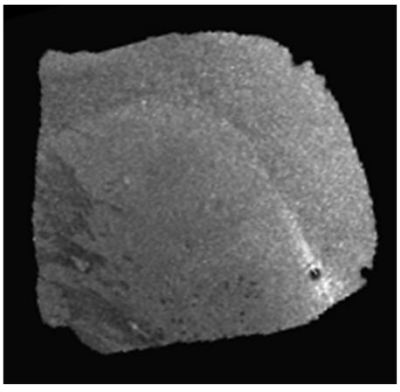

Slice 8 T_2 map is rotated into the same orientation as the SXRF map.

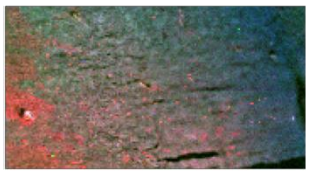

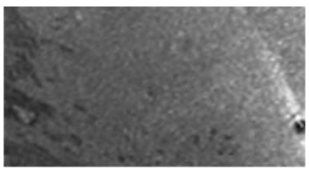

T_2 map is trimmed to the same dimensions as the XRF map.

Final R_2 map

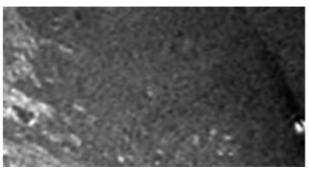

Finally the reciprocal of the matched, rotated and trimmed map is calculated to produce the R_2 map.

Figure 8.1: Matching the SXRF and MRI maps of the caudate nucleus for case C2. The anatomical structures visible in the SXRF map, adjacent stained section and unstained SXRF sample are compared to the high resolution T_2 maps in order to find the best matched slice. This is then rotated into the orientation of the SXRF map, before being trimmed to leave just the area matching the SXRF map. Finally, the reciprocal of the T_2 map is taken to produce an R_2 map. There is good matching of the detailed structure of the AIC at the left hand side of the map, but at the right hand side of the map there is slightly more white matter in the MRI map than in the SXRF map.

In general good matching was achieved. Where matching is not perfect this may be due to not sectioning in precisely the same plane as imaging, slight deformation of the tissue under pressure in the Fluorinert during MRI or mapped sections taken from slightly outside the high resolution MRI region. In addition cracks, tears or folding of the tissue section occasionally occurred during sectioning, due to the fragile un-fixed, un-embedded tissue.

For the control GP sample the accurate matching between the SXRF map and the high resolution MRI maps could not be achieved. This was due to the SXRF section being cut from outside the high resolution region and a better match was achieved with low resolution data. The matching process is shown in Appendix G and the final result in Figure 8.6. For comparison, a low resolution match to GP sample AD2 is also found and this is shown in Figure 8.7.

8.1.1.2 Segmenting the matched MRI and SXRF maps

The segmentation of maps to create regions of interest (ROIs) surrounding different anatomical structures has been shown for SXRF maps in Chapter 6 and similarly for MRI maps in Chapter 7. The segmentation of the same structures was refined in the matched maps to ensure the ROIs are also spatially matched.

The ROIs that were drawn around structures in the SXRF maps in Chapter 6 were scaled to account for the different pixel size in the MRI maps. Where necessary, small adjustments were made to the shape of the ROIs to compensate for slight miss-matching of structures. Small and detailed structures more often required correction. Figures 8.2 to 8.9 show the segmentation of the matched maps for the control and AD example from each brain region.

In each figure the SXRF combined metal map shows iron in red, copper in green and zinc in blue. The segmented regions are labelled on the SXRF map, with the same regions drawn onto the MRI maps. For the CN, Pu and GP samples the approximate anatomical position of the map is shown in respect to the anatomical reference given in Appendix A.

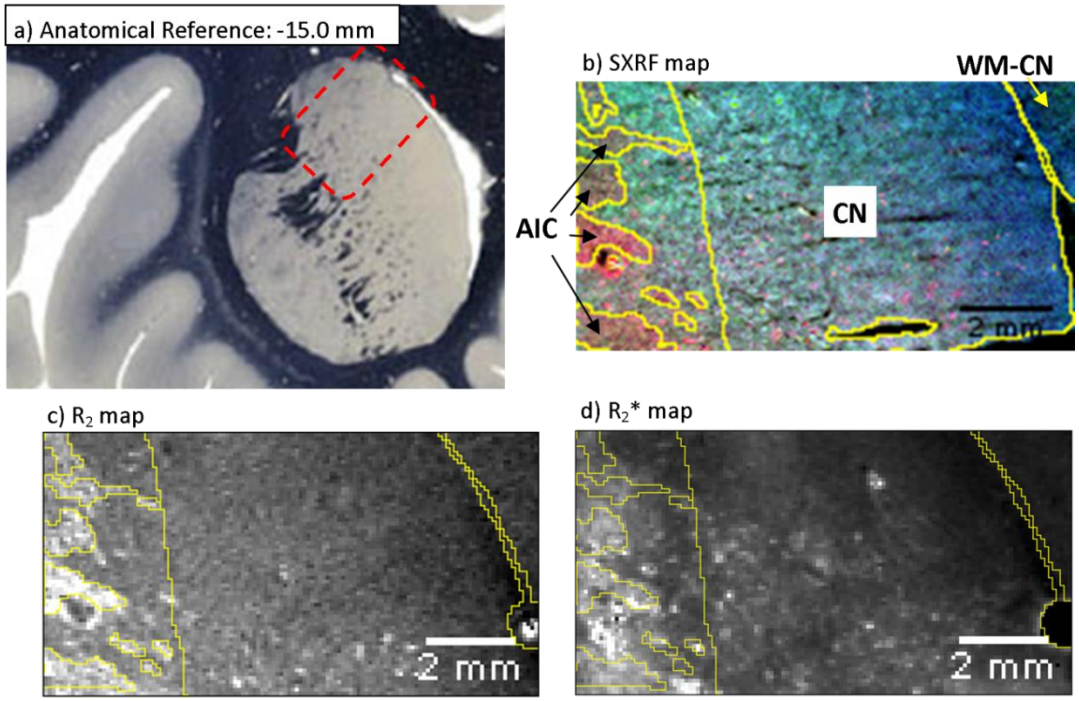

Figure 8.2: Segmentation of matched SXRF and MRI maps of caudate nucleus sample C2. a) Approximate position of the maps. b) The SXRF map and matched c) R_2 and d) R_2* maps are segmented into the caudate nucleus (CN), the anterior limb of the internal capsule (AIC) and the white matter medial to the caudate nucleus (WM-CN). Good matching of the detailed structure of the AIC was achieved. More WM-CN in is present in the MRI maps due to slight tearing of the WM from the CN during sectioning of the SXRF sample.

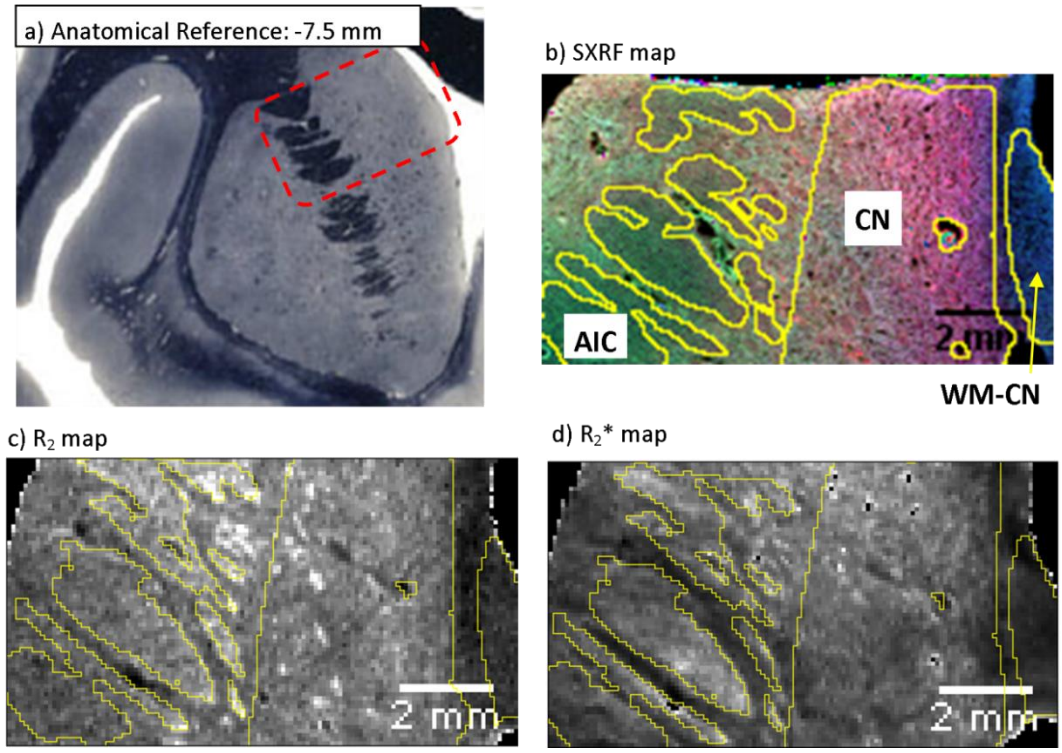

Figure 8.3: Segmentation of matched SXRF and MRI maps of caudate nucleus sample AD1. a) Approximate position of the maps. b) The SXRF map and matched c) R_2 and d) R_2* maps are segmented into the caudate nucleus (CN), the anterior limb of the internal capsule (AIC) and the white matter medial to the caudate nucleus (WM-CN). Good matching was achieved, only requiring a few adjustments to correct for slight variation in the detailed structure of the AIC.

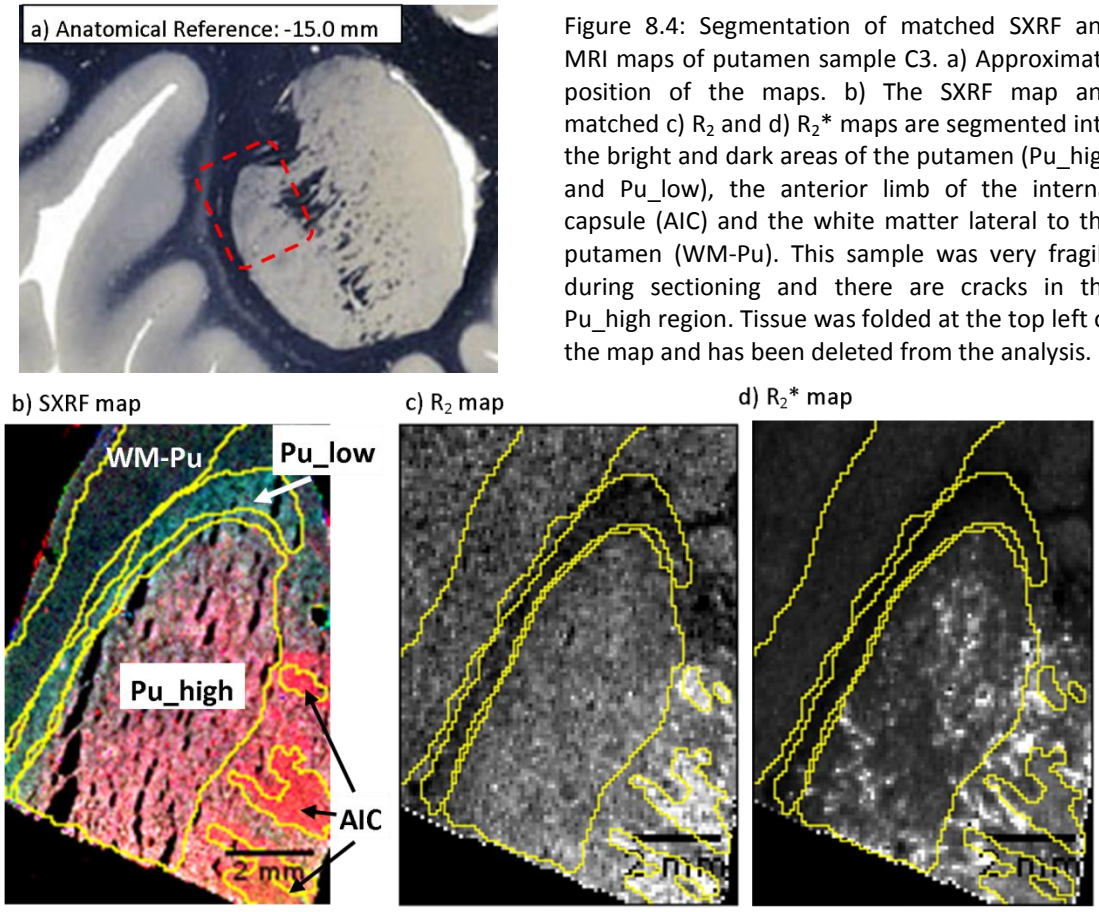

Figure 8.4: Segmentation of matched SXRF and MRI maps of putamen sample C3. a) Approximate position of the maps. b) The SXRF map and matched c) R_2 and d) R_2* maps are segmented into the bright and dark areas of the putamen (Pu_high and Pu_low), the anterior limb of the internal capsule (AIC) and the white matter lateral to the putamen (WM-Pu). This sample was very fragile during sectioning and there are cracks in the Pu_high region. Tissue was folded at the top left of the map and has been deleted from the analysis.

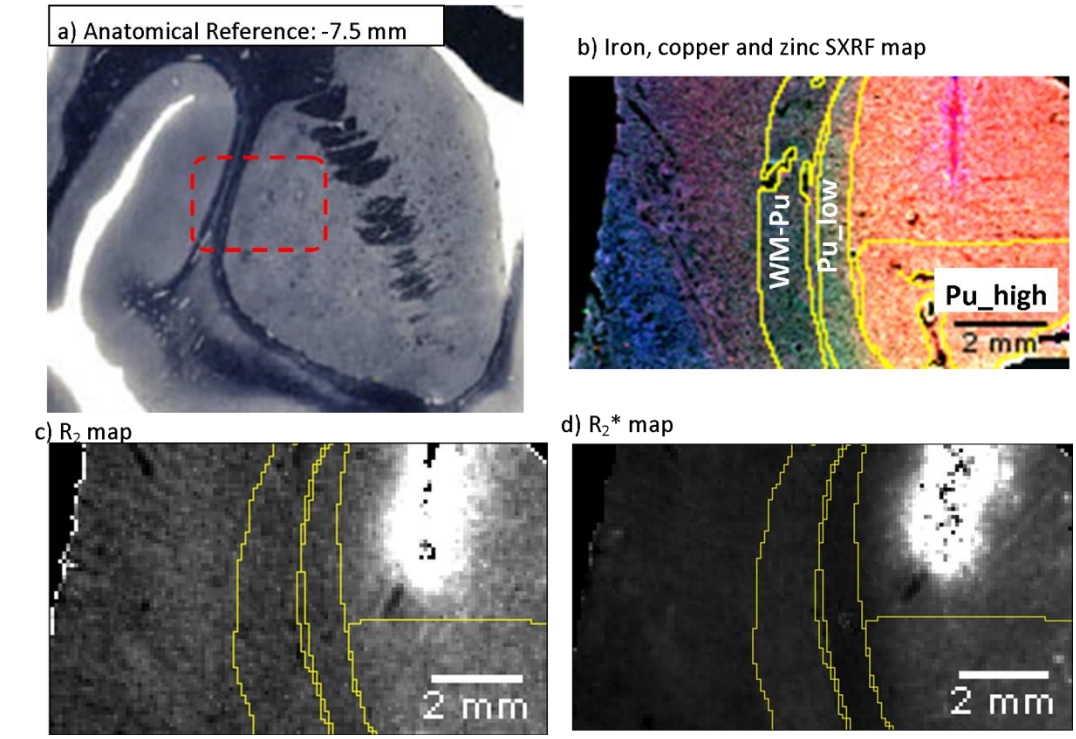

Figure 8.5: Segmentation of matched SXRF and MRI maps of putamen sample AD3. a) Approximate position of the maps. b) The SXRF map and matched c) R_2 and d) R_2* maps are segmented into the bright and dark areas of the putamen (Pu_high and Pu_low) and the white matter lateral to the putamen (WM-Pu). The very high iron region of the Pu is excluded from the analysis as this is due to a blood vessel. Good matching is achieved, although the WM-Pu structure is slightly wider in the MRI maps.

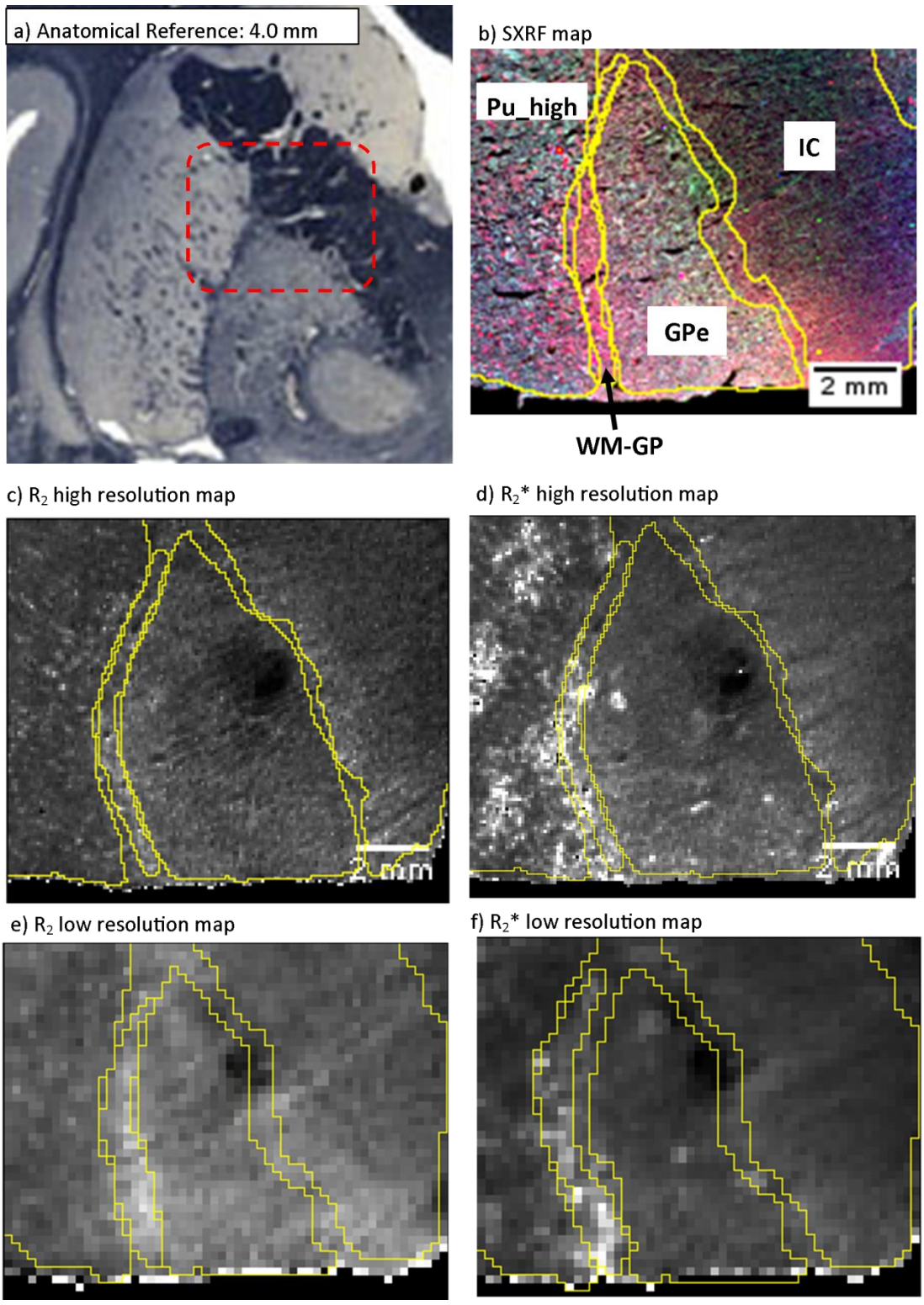

Figure 8.6: Segmentation of matched SXRF and MRI maps of globus pallidus sample C3. a) Approximate position of the maps. b) The SXRF map and matched c) high resolution R_2 map, d) high resolution R_2* map, d) low resolution R_2 map and e) low resolution R_2* map. The maps are segmented into the external globus pallidus (GPe), the bright part of the putamen (Pu_high), the internal capsule (IC) and the lamina of white matter separating the Pu and GPe (WM-GP). The tissue for the SXRF map was cut from outside the high resolution MRI region and better anatomical matching was achieved using a slice from the low resolution MRI data.

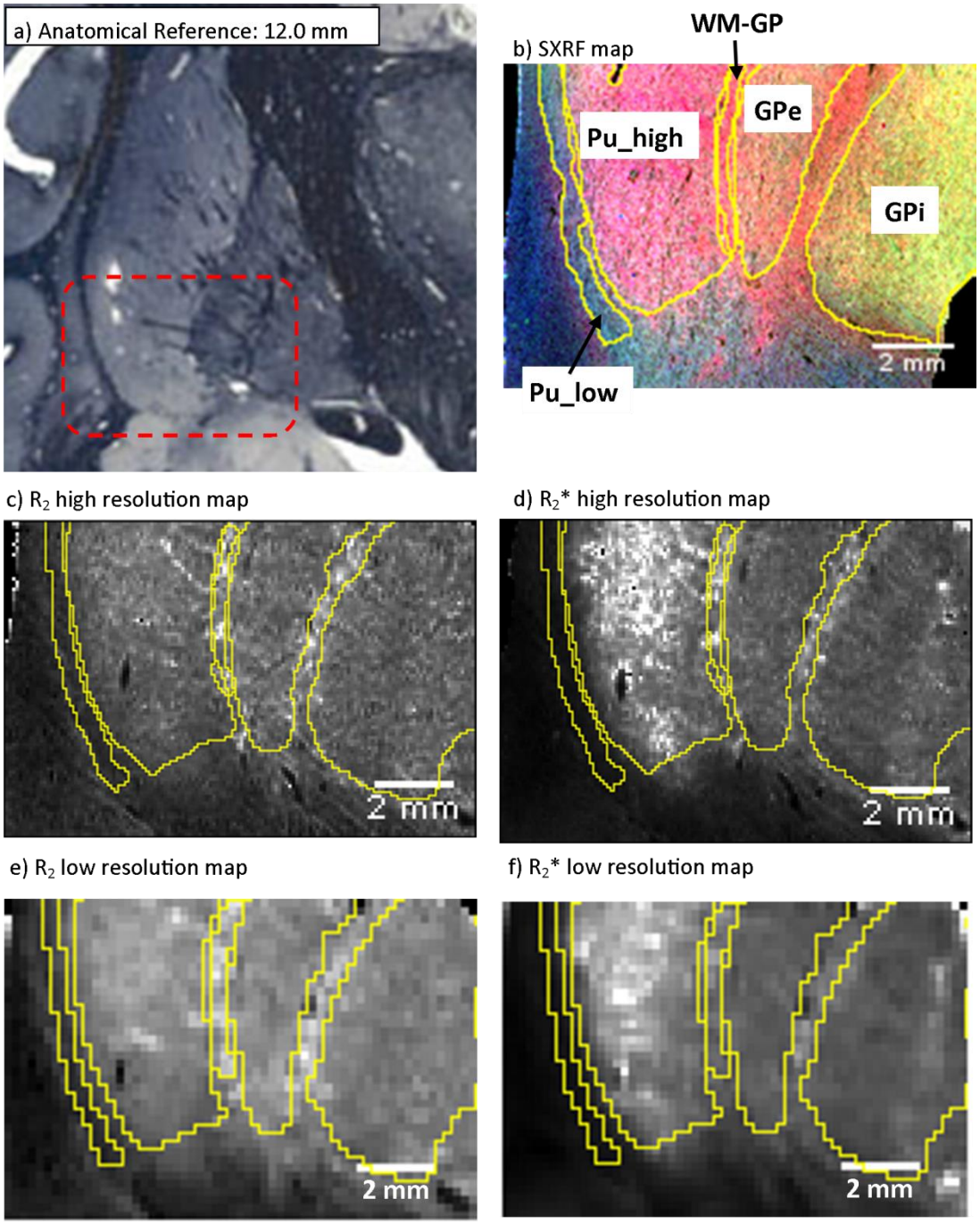

Figure 8.7: Segmentation of matched SXRF and MRI maps of globus pallidus sample AD2. a) Approximate position of the maps. b) The SXRF map and matched c) high resolution R_2 map, d) high resolution R_2* map, d) low resolution R_2 map and e) low resolution R_2* map. The matched maps are segmented into the external globus pallidus (GPe), the internal globus pallidus (GPi), the bright part of the putamen (Pu_high), the dark part of the putamen (Pu_low) and the lamina of white matter separating the Pu and GPe (WM-GP). Matching is good between the SXRF map and both the high and low resolution MRI maps.

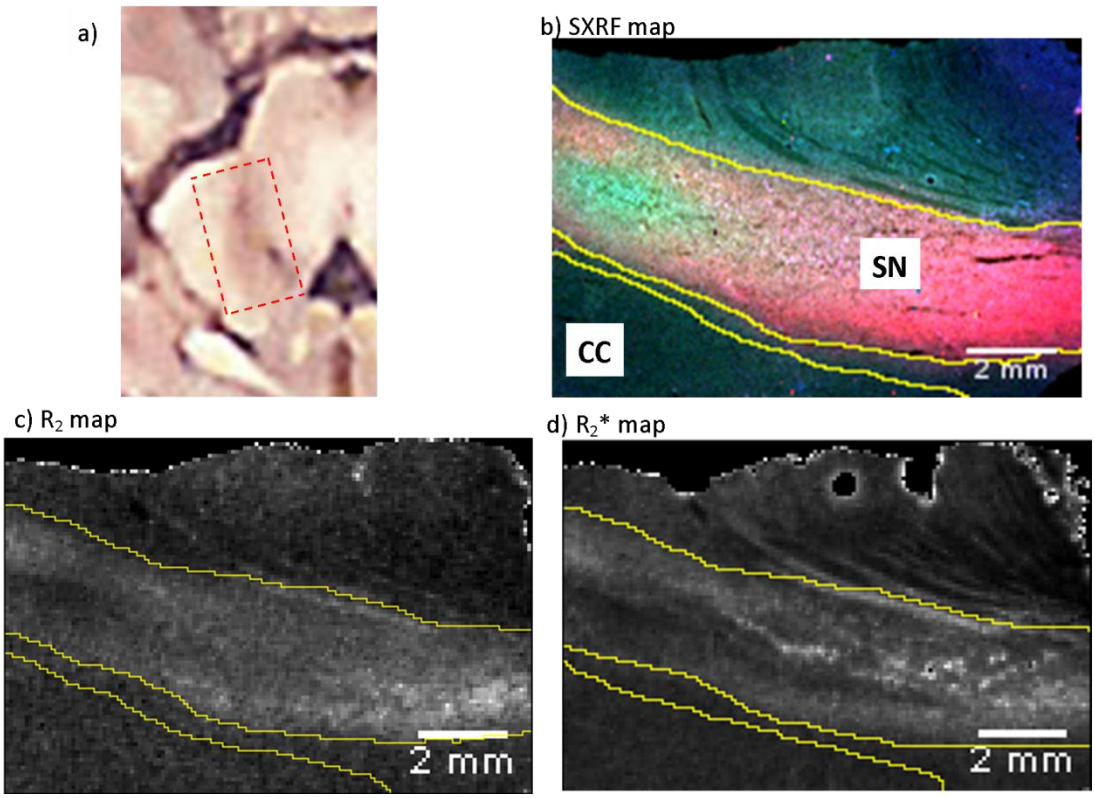

Figure 8.8: Segmentation of matched SXRF and MRI maps of substantia nigra sample C2. a) Approximate position of the maps. b) The SXRF map and matched c) R_2 and d) R_2* maps are segmented into the substantia nigra (SN) and cerebral crus (CC). Good matching was achieved.

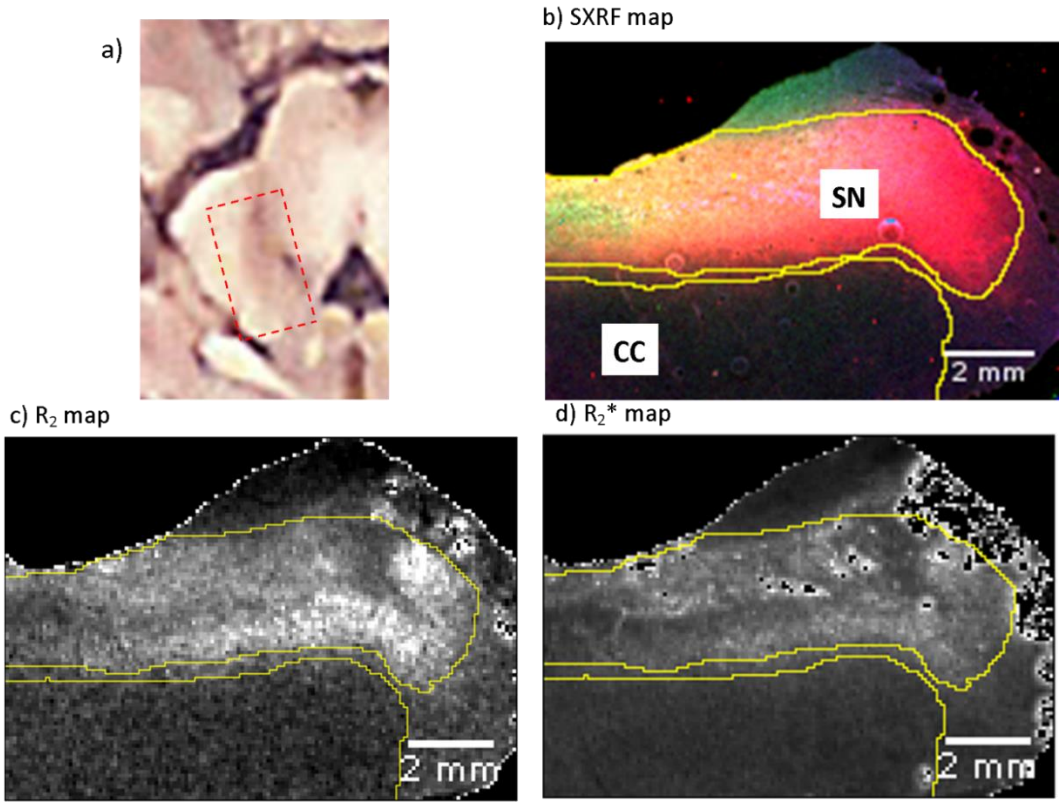

Figure 8.9: Segmentation of matched SXRF and MRI maps of substantia nigra sample AD2. a) Approximate position of the maps. b) The SXRF map and matched c) R_2 and d) R_2* maps are segmented into the substantia nigra (SN) and cerebral crus (CC). Good matching was achieved.

When the SXRF and MRI maps were processed in ImageJ the threshold tool was used to remove the background and main artefacts from the maps. Therefore the pixel value of the black background in the MRI and SXRF maps represents a value of 'NaN' meaning that these pixels will be discounted from any analysis (such as mean calculation) in ImageJ. This means that any cracks in the tissue included in the segmented regions do not need to be manually drawn around.

Caudate Nucleus

Figures 8.2 and 8.3 show the matching between the SXRF and MRI maps in the caudate nucleus samples C2 and AD1 respectively. The maps are segmented into the caudate nucleus (CN); the anterior limb of the internal capsule (AIC) and the white matter medial to the caudate nucleus (WM-CN).

Putamen

Segmentation and matching of SXRF and MRI maps are shown in Figure 8.4 for sample C3 and in Figure 8.5 for sample AD3. In these maps the putamen is segmented into 'Pu_high' and 'Pu_low' (as in Chapters 6 and 7), where Pu_high is the majority of the putamen which has a high iron concentration and R_2 or R_2* signal and Pu_low is the band of low iron concentration and R_2 or R_2* signal along the lateral edge of the structure. The white matter lateral to the Pu (Pu-WM) and the AIC are also segmented when present.

Globus Pallidus

The matched and segmented SXRF and high and low MRI maps for the globus pallidus samples are shown in Figure 8.6 for sample C3 and Figure 8.7 for sample AD2. The main segmented structures of the map are the high iron part of the putamen (Pu_high) and the external globus pallidus (GPe). Other regions which are segmented, when present, are the internal globus pallidus (GPi); the internal capsule (IC); the lamina of white matter separating the putamen and globus pallidus (WM-GP) and the low iron of the putamen (Pu_low).

Substantia Nigra

The segmentation of the matched SXRF and MRI maps of the substantia nigra samples is shown in Figure 8.8 for sample C2 and in Figure 8.9 for sample AD2. The tissue from the cerebral crus (CC) is segmented in addition to the approximate location of the substantia nigra (SN).

8.1.1.3 Mean iron concentration, R_2 and R_2* in the segmented regions

The mean iron concentration, R_2 and R_2* of segmented regions for each control and AD sample are shown in Figure 8.10. The main regions are the structures which were specifically chosen for investigation in this project. Also included are those which appeared in the maps of both the AD and control samples. The 'error bars' on the graph indicate the standard deviation of the pixel values within the segmented area.

Key: CN=caudate nucleus; AIC-CN=anterior limb of the internal capsule in CN map;
WM-CN= white matter medial to CN;
Pu=putamen; WM-Pu=white matter lateral to Pu;
Pu_low=dark region of the Pu;
Pu_high=bright region of the Pu;
GPe=external globus pallidus;
Pu_high-GP=bright Pu lateral to the GP;
WM-GP=white matter lamina separating Pu and GP;
SN=substantia nigra; CC=cerebral crus

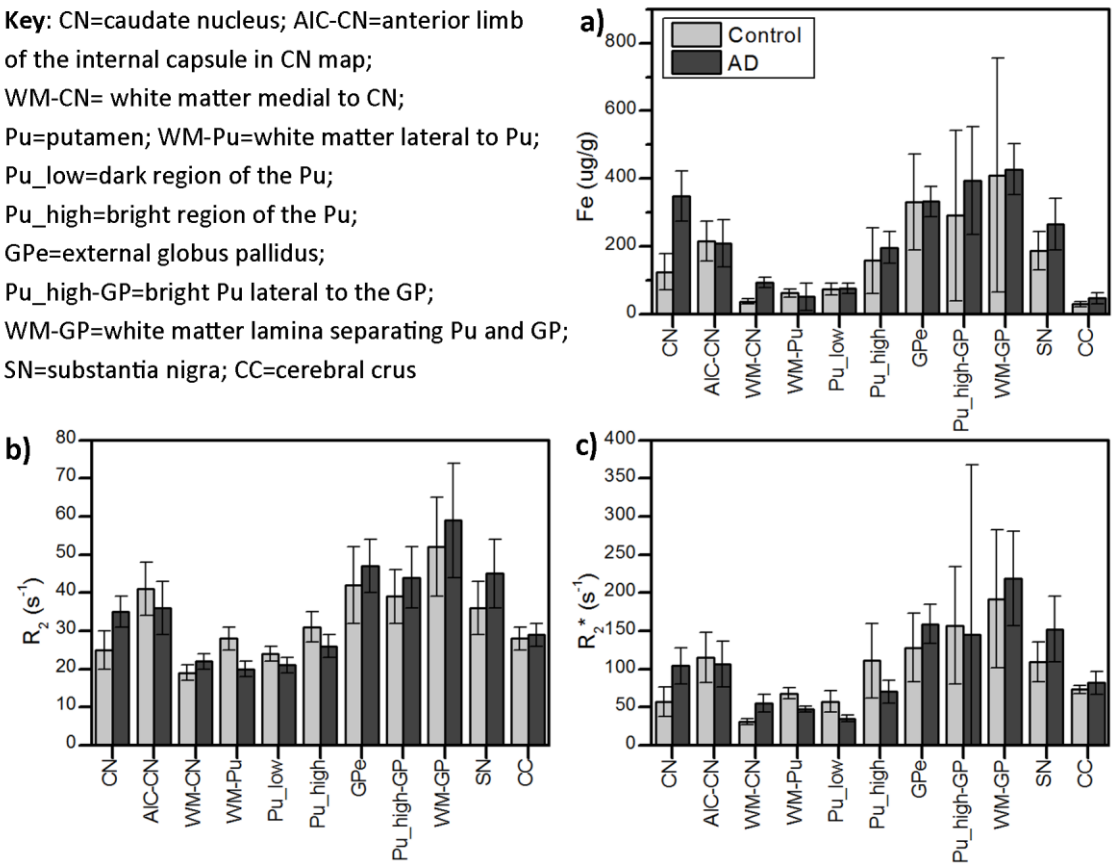

Figure: 8.10: Iron concentration, R_2 and R_2* in the matched SXRF and MRI maps. The mean and standard deviation of the pixels in each segmented area is given. a) The mean iron concentration in the segmented regions of the SXRF maps. b) Mean R_2 and c) mean R_2* in the segmented regions of the MRI maps after spatial matching with the SXRF map. The overall trend in iron concentration in the segmented regions is preserved in the R_2 and R_2* data.

Inspection of the bar charts indicates a similar trend in the iron concentration, R_2 and R_2* data. This agrees with the hypothesis that iron concentration has a significant effect on the value of R_2 and R_2*. This relationship is investigated using simple linear regression analysis in Section 8.1.1.5.

Another observation is the larger variation in the R_2* data compared to the R_2 data. This supports the hypothesis that effect of iron on R_2* is larger than on R_2. This is explored further in Section 8.1.1.6 by investigating the relationship between iron and R_2'.

The direction of change between AD and control seen in the iron data is generally conserved in the MRI data. For example, there is an increase in iron in the AD CN and a corresponding increase in R_2 and R_2*.

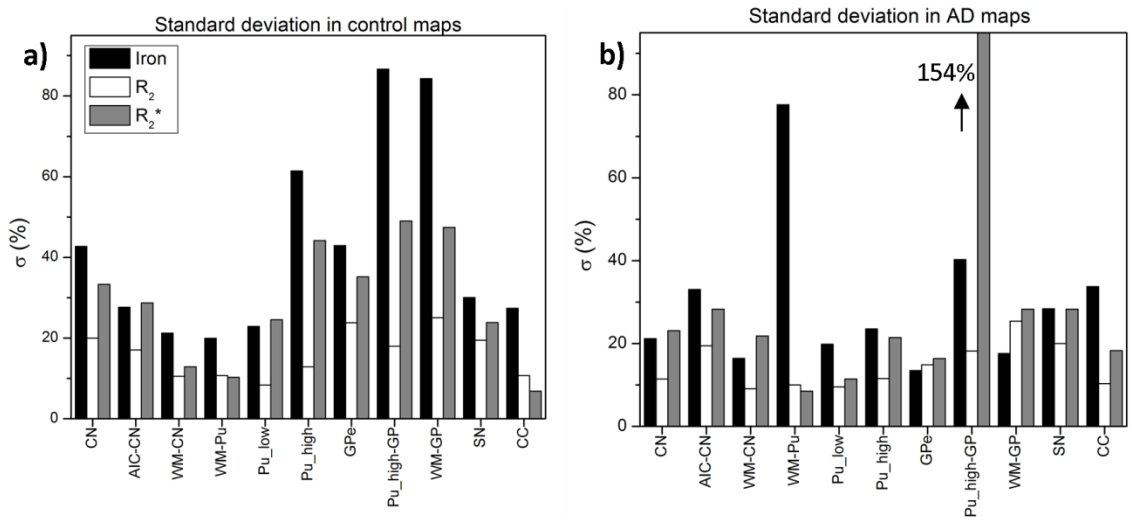

Figure 8.11: Relative standard deviation in control and AD SXRF and MRI maps. The standard deviation (σ) of the pixel values within each segmented region in the matched SXRF, R_2 and R_2* maps is given as a percentage of the mean for a) the control maps and b) the AD maps. The general trend is for the largest relative standard deviation to be shown by the iron maps, followed by the R_2* and the R_2 maps. Overall the control maps show a larger relative standard deviation than the AD maps. The relative standard deviation of the Pu_high-GP region in the AD R_2* map is extremely high (154%, the full height is not shown). However this is due to poor data quality in this region: very rapid decays could not be well fitted. The relative standard deviation in the WM-Pu AD iron map is high, however the absolution standard deviation is low as this is a region with low iron concentration (Figure 8.10).

The relative standard deviation of the pixel values within each segmented region of the control and AD SXRF, R_2 and R_2* maps is shown in Figure 8.11. In most cases the iron maps show the largest relative standard deviation, followed by the R_2* and R_2 map. This is in agreement with the hypothesis that R_2* maps are more sensitive to local field inhomogeneities caused by

tissue iron. Overall the control maps show a larger relative standard deviation that the AD maps. This is somewhat unexpected as some studies have shown greater variance with more outliers in the R_2 maps of AD tissue [132, 191].

There are couple of notable anomalies in the AD data in Figure 8.11. The relative standard deviation of the Pu_high-GP region in the AD R_2* maps is extremely high. However, as was previously described, the R_2* decays in this region were very fast and not well fitted by ImageJ. Although the relative standard deviation in the WM-Pu AD iron map is high, the absolute standard deviation is low as this is a low iron region (shown in Figure 8.10).

The approximate lower limit for T_2 and T_2* decays which could still be fitted reliably was examined in Section 4.3.3.3. The result of this was to be cautious of R_2 and R_2* values above 50 and 200 s^{-1} respectively. The mean values for the WM-GP region of the control and AD samples either approaches, or just exceeds this limit.

8.1.1.4 Effects of mismatching and of imaging resolution

Figure 8.12 shows the mean and standard deviation of R_2 and R_2* for the segmented regions of the high and low resolution maps of the globus pallidus (matched maps shown in Figures 8.6 and 8.7). Table 8.2 shows the percentage change in the low resolution compared to the high resolution data.

The control SXRF sample was better matched to the low resolution MRI maps. The biggest change in the control data is an increase of 11 % observed in the GPe R_2* data. However, a larger difference between the high and low resolution data is seen for the AD case, where both the high and low resolution MRI maps were from approximately the same position and both were matched to the SXRF map. Therefore this change cannot be attributed to the different position.

The largest change between high and low resolution MRI data is an increase of 33% in the high iron region of the putamen (High_Pu-GP) for the AD sample. The high resolution map of this

region contained some pixels with particularly high R_2* values, as shown by the large standard deviation. Many of the pixels have an R_2* much greater than the estimated limit of reliable fitting (200 s^{-1}) and some could not be fitted at all by ImageJ. When the low resolution data are considered the mean R_2* has increased, but the standard deviation has reduced.

This highlights both an advantage and disadvantage of imaging at a lower resolution. At the lower resolution each voxel is sampling a larger area (both in-plane and slice thickness) and the effects of the high iron concentration are averaged with the surrounding tissue to produce a decay which can be more easily measured. However, some detail of the iron distribution is lost as can easily be observed by inspection of the high and low resolution maps in Figure 8.7.

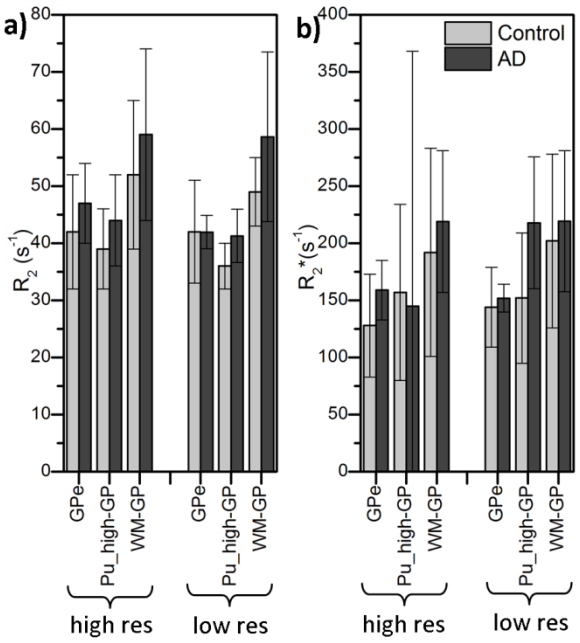

Figure 8.12: R_2 and R_2* of high and low resolution maps of the globus pallidus. a) The mean R_2 value of each segmented region. The most notable difference is a reduction in R_2 in the AD GPe at low resolution. b) The mean R_2* values in each segmented region. The biggest change is an increase in R_2* in the Pu_high-GP region in the low resolution AD data.

Disease	Region	Change in R_2	Change in R_2*
Control	GPe	0.0 %	11 %
	Pu_high-GP	-8.3 %	-3.2 %
	WM-GP	-6.1 %	5.0 %
AD	GPe	-12.0%	-4.6%
	Pu_high-GP	-6.6%	33.4%
	WM-GP	0.63%	0.15%

Table 8.2: Percentage difference in R_2 and R_2* in low compared to high resolution maps of the globus pallidus. The largest discrepancy between high and low resolution data is in the AD Pu_high-GP region.

8.1.1.5 The linear relationship between iron concentration, R_2 and R_2*

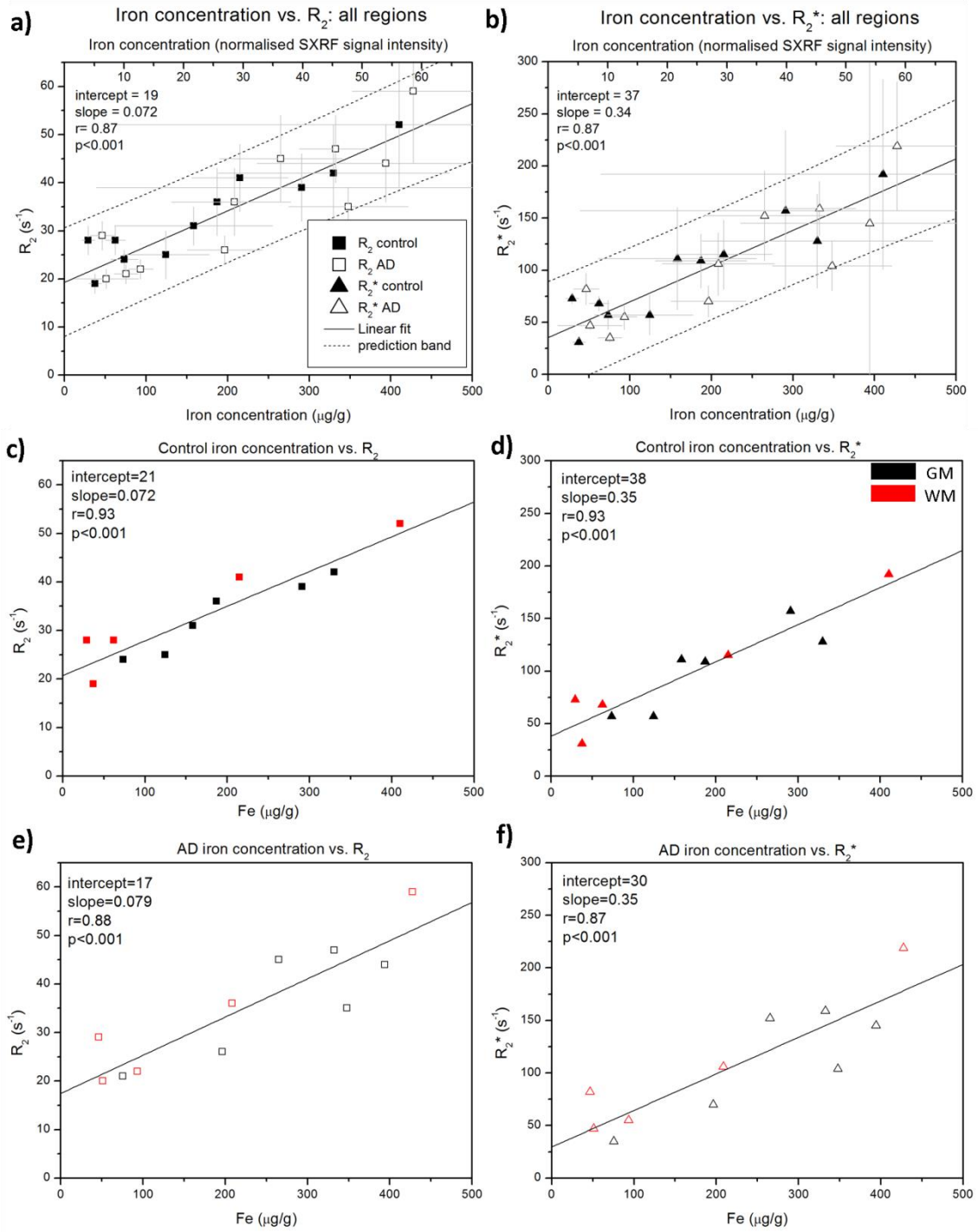

Figure 8.13: Iron concentration versus R_2 and R_2* at 9.4 T. Graphs a) and b) shows the linear relationship between iron and MRI (R_2 and R_2* respectively) for the pooled control and AD data. The light grey error bars represent the standard deviation within the segmented region. The x-axis at the top of each graph shows the normalised iron SXRF signal intensity and the lower x-axis shows the calibrated iron concentration (with an estimated error of ±12%). A straight line was fitted to the data using simple linear regression analysis. The prediction bands show the region in which 95% of any new measurements would be predicted to fall. Graphs c) and d) show the relationship between iron and R_2 and R_2* respectively for control samples and graphs c) and d) show the relationship between iron and R_2 and R_2* respectively, for AD samples. All linear fits to the data show a strong relationship (r=0.87 or greater) and high statistical significance. The liner fit is made to the combined grey matter and white matter data points (shown as black and red respectively).

a) Iron vs. R_2

Tissue regions	Disease	n	Slope (s^{-1}/(μg/g))	Intercept (s^{-1})	r	r^2	p
All	pooled	28	0.072 ± 0.008	20 ± 2	0.87	0.75	***
	Control	14	0.074 ± 0.010	21 ± 2	0.91	0.83	***
	AD	14	0.076 ± 0.013	17 ± 4	0.86	0.73	***
Paired	pooled	22	0.072 ± 0.008	19 ± 2	0.87	0.75	***
	Control	11	0.072 ± 0.009	21 ± 2	0.93	0.87	***
	AD	11	0.079 ± 0.012	17 ± 4	0.88	0.77	***
Paired GM	Control	6	0.072 ± 0.011	19 ± 2	0.96	0.92	**
	AD	6	0.076 ± 0.027	16 ± 8	0.82	0.67	*
Paired WM	Control	5	0.076 ± 0.013	22 ± 3	0.96	0.91	*
	AD	5	0.094 ± 0.016	18 ± 3	0.96	0.92	**

b) Iron vs. R_2*

Tissue regions	Disease	n	Slope (s^{-1}/(μg/g))	Intercept (s^{-1})	r	r^2	p
All	pooled	28	0.34 ± 0.04	37 ± 9	0.87	0.75	***
	Control	14	0.36 ± 0.05	41 ± 10	0.91	0.83	***
	AD	14	0.35 ± 0.06	26 ± 16	0.86	0.74	***
Paired	pooled	22	0.34 ± 0.04	37 ± 9	0.87	0.75	***
	Control	11	0.35 ± 0.05	38 ± 10	0.93	0.87	***
	AD	11	0.35 ± 0.07	30 ± 17	0.87	0.75	***
Paired GM	Control	6	0.35 ± 0.10	35 ± 21	0.87	0.76	*
	AD	6	0.35 ± 0.12	16 ± 35	0.82	0.70	*
Paired WM	Control	5	0.36 ± 0.06	41 ± 120	0.97	0.93	**
	AD	5	0.42 ± 0.07	33 ± 150	0.96	0.92	**

Table 8.3: Results of linear regression analysis of iron versus R_2 or R_2*. a) The linear relationship between iron and R_2. b) The linear relationship between iron and R_2*. The relationship is examined for the control and AD data separately and with both sets of data pooled. Data from grey and white matter regions is also examined separately. In all cases there a statically significant, strong linear relationship. The r-squared values show that at least 67% of the variation in the data is explained by the linear relationship. All R_2 models show a slope and intercept which agree within error. The same is true for all of the fits to the R_2* data. *p<0.05; **p<0.01; ***p<0.001

Figure 8.13 shows the mean iron concentration versus R_2 and R_2* for the segmented regions of the control and AD matched SXRF and MRI maps. Table 8.3 shows the results of simple linear

regression analysis of the relationship between iron concentration and R_2 or R_2* with different sets of data.

In Figure 8.12 data are only included from the 'paired' segmented regions: those which were measured in both the control and AD samples, whereas Table 8.3 also shows the fit to all segmented regions (including those only measured for either control or AD). In Figure 8.12 a) and b) the top x-axis shows the normalised iron SXRF signal intensity and the lower axis shows the calibrated iron concentration. Recall that the absolute iron concentration has an estimated error of ±12% arising from the calibration. The prediction bands show the range within which 95% of any new measurements would be expected to fall. Figure 8.13 c) and d) show the relationship of iron concentration in control samples to R_2 and R_2* respectively and the relationship for AD samples is shown in e) and f).

The results of simple linear regression in Figure 8.13 and Table 8.3 show a strong, statistically significant relationship for all data, regardless of whether it is broken down by disease group. Furthermore, the slope and intercept of the fitted lines agree within error for each model for both R_2 and R_2*. The r-squared values show that at least 67% (minimum for AD, GM regions in R_2 model) of the variation in the data is explained by the linear fit.

The mean R_2 and R_2* values for one control and AD data point approach or slightly exceed the maximum reliable values of 50 and 200 s^{-1} respectively (as defined in Section 4.3.3.3). However, these data points do not appear as outliers in Figure 8.13 and therefore do not need to be excluded from the analysis.

The grey and white matter structures were also fitted separately (Table 8.3). These also show strong linear relationships with gradients and intercepts that agree within error for both the R_2 and R_2* data. In clinical MRI imaging the different relaxation rates of grey and white matter tissues provide contrast in the image and this is attributed to their differing fat and water content in addition to iron. However, the agreement of the linear relationship between iron

and R_2 and R_2* for both grey and white matter, suggests that at this field (400 MHz) iron is the most significant factor in determining change in R_2 and R_2*.

Although all fits agree within error, the r-squared values of the AD data are slightly lower in each case (apart from for the fit to R_2 for only WM regions). This suggests that there may be another factor, such as water content, which is affecting R_2 and R_2* slightly more for AD samples than for control samples.

8.1.1.6 Iron and R_2'

The susceptibility related relaxation rate R_2* represents the combination of the transverse relaxation rate R_2 and the field inhomogeneity induced R_2'. It is reported in the literature that R_2* is more sensitive to changes in tissue iron concentration than R_2 [123] and this has been shown here in Figure 8.13 and Table 8.3. The hypothesis is that the increased sensitivity of R_2* to iron is due to increased tissue iron content causing increased local field inhomogeneities within the tissue.

Approximate mean R_2' was calculated for each segmented region, using the formula (from Equation 2.6):

$$R_2' = R_2^* - R_2$$

and is plotted against iron concentration in Figure 8.14. The result of linear regression analysis for the combined and separated control and AD data is given in Table 8.4. A strong, statistically significant relationship is shown for all three models with slopes and intercepts which agree within error.

Disease	n	Slope (s^{-1}/(μg/g))	Intercept (s^{-1})	r	r^2	P
pooled	22	0.27 ± 0.03	16 ± 7	0.88	0.77	***
Control	11	0.28 ± 0.04	18 ± 9	0.92	0.84	***
AD	11	0.27 ± 0.05	12 ± 14	0.86	0.74	**

Table 8.4: Results of linear regression analysis of iron concentration and R_2'. The slope and the intercept of the fit agree within error for both the pooled and separated control and AD data. The majority of the variation in the data in each case is explained by the linear model. **p<0.01; ***p<0.001

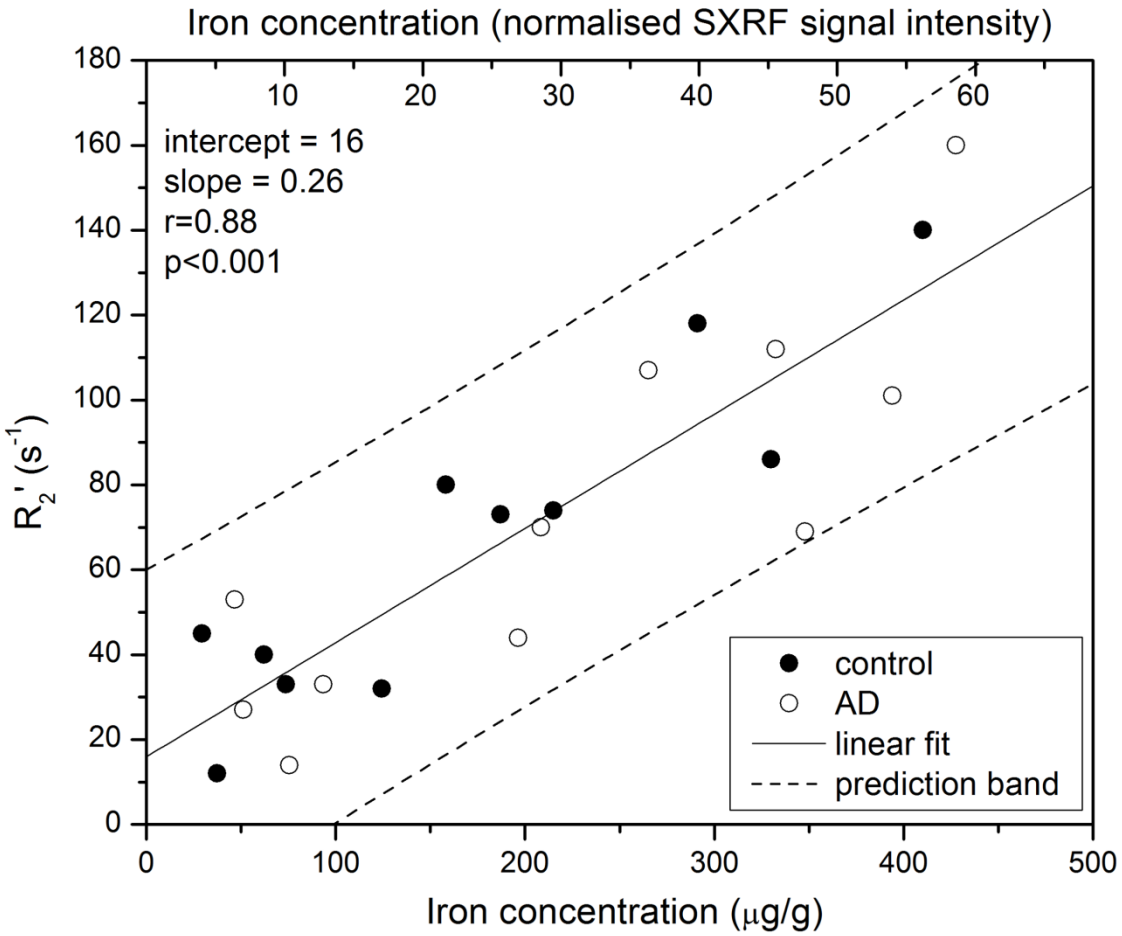

Figure 8.14: Iron concentration versus R_2'. The x-axis at the top of the graph shows the normalised iron SXRF signal intensity and the lower axis shows the calibrated iron concentration (with an estimated error of ±12%). A straight line was fitted to the data by simple linear regression analysis and shows a strong (r=0.88), statistically significant (p<0.001) linear relationship. The prediction bands show the region in which 95% of any new measurements would be predicted to fall.

8.1.1.7 Copper and zinc versus R_2 and R_2*

The SXRF metal maps presented in Chapter 6 showed that zinc and copper have a distribution distinct to that of iron and often also from one another. Figure 8.15 shows the copper and zinc plotted against R_2 and R_2* for all of the segmented regions in the control and AD maps. A simple linear regression analysis was carried out on the pooled control and AD data and separately on the data from each disease group (Table 8.5).

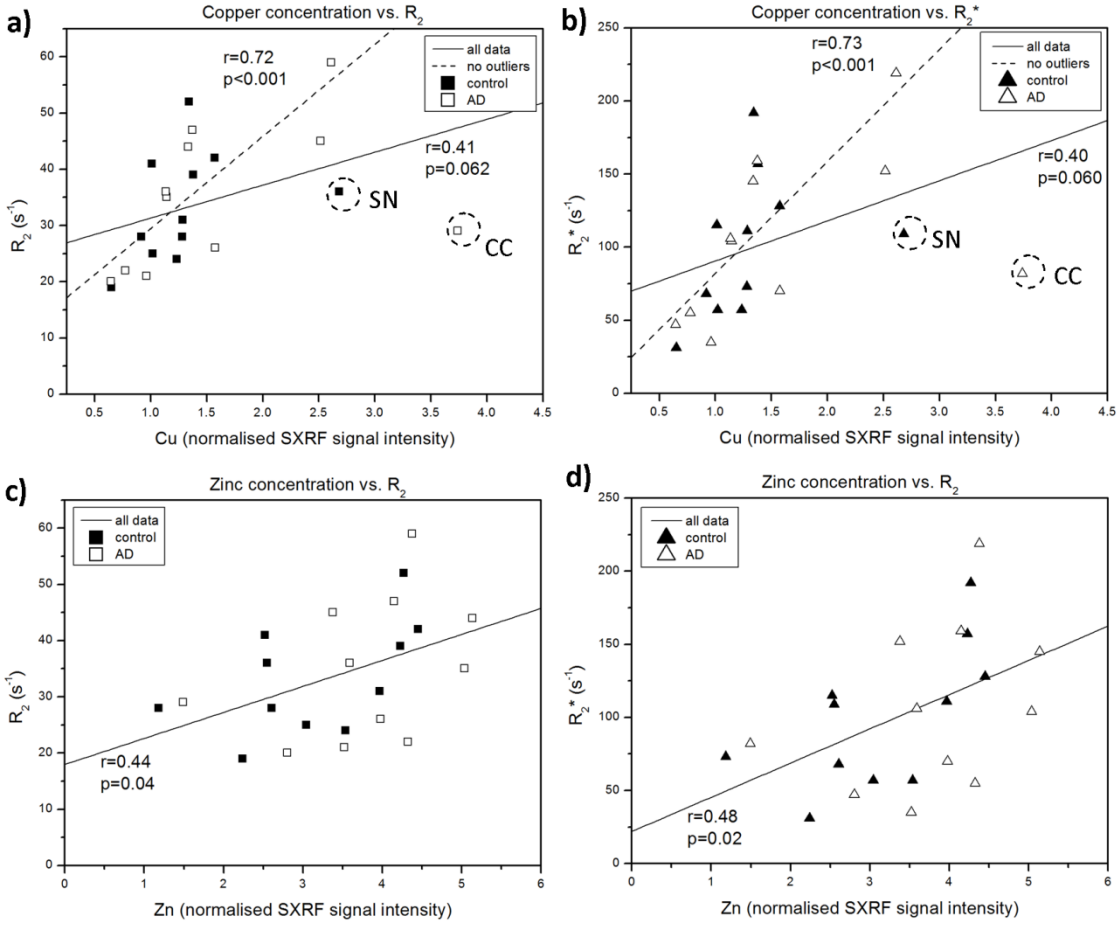

Figure 8.15: Copper and zinc concentration versus R_2 and R_2*. The copper and zinc concentrations in the segmented SXRF maps are plotted against the carefully matched regions in the R_2 and R_2* maps for the combined control and AD samples. Linear regression analysis showed no statistically significant linear relationship between copper and a) R_2 or b) R_2*. However, when the outliers (circled) are excluded a statistically significant relationship is observed. There is a statistically significant relationship ($p<0.05$) between zinc and c) R_2 and d) R_2*, however the correlation coefficients are low and show that the relationship is not very strong.

There was a statistically significant linear relationship ($p<0.05$) between zinc and R_2 and R_2* for the pooled control and AD data and also between zinc and R_2* for the control data only.

However, the r-squared values are small (0.2 and 0.24) and show that the zinc concentration data do not explain the majority of the variation in the data.

Copper did not show a statistically significant linear relationship with R_2 or R_2* when all of the data points were included. However, two regions with an elevated copper concentration appeared to be outliers from the rest of the data set. When these were excluded from the model a statistically significant linear relationship between copper and both R_2 and R_2* was observed.

Model	Disease	n	Slope (s^{-1}/ normalised SXRF intensity)	Intercept (s^{-1})	r	r^2	p
Copper vs. R_2 [excluding outliers]	Pooled	22 [20]	- [16 ± 7]	- [13 ± 5]	- [0.72]	- [0.53]	- [***]
	Control	11 [10]	- -	- -	- -	- -	- -
	AD	11 [10]	- [16 ± 5]	- [14 ± 7]	- [0.79]	- [0.63]	- [**]
Zinc vs. R_2	Pooled	22	4.6 ± 2.1	18 ± 8	0.44	0.20	*
	Control	11	-	-	-	-	-
	AD	11	-	-	-	-	-
Copper vs. R_2* [excluding outliers]	Pooled	22 [20]	- [77 ± 17]	- [5 ± 24]	- [0.73]	- [0.53]	- [***]
	Control	11 [10]	- [128 ± 49]	- [-50 ± 59]	- [0.68]	- [0.46]	- [*]
	AD	11 [10]	- [71 ± 19]	- [8 ± 29]	- [0.80]	- [0.64]	- [**]
Zinc vs. R_2*	Pooled	22	23 ± 9	22 ± 34	0.48	0.23	*
	Control	11	30 ± 12	7 ± 39	0.64	0.41	*
	AD	11	-	-	-	-	-

Table 8.5: Results of linear regression analysis of zinc and copper with R_2 and R_2* for segmented regions of control and AD tissue. Zinc concentration showed a statistically significant linear relationship with both R_2 and R_2* for the pooled data. When the outliers (shown in figure 8.14) are excluded from the copper model a statistically significant relationship is observed and the result is given in squared brackets. *p<0.05; **p<0.01.

The linear relationship between zinc and copper (excluding outliers) and MRI may be due to the metal distribution correlating with another property (such as iron concentration) of the tissue, which is influencing the relaxation rates. To investigate this, a multiple linear regression

analysis is carried out on the zinc, copper and iron data to test whether each metal contributes to the model.

Dependent	Independents	Disease	r	r^2	p
R_2	Fe***, Cu, Zn**	pooled	0.96	0.92	***
	Fe***, Cu, Zn*	Control	0.97	0.93	***
	Fe**, Cu, Zn	AD	0.96	0.92	***
R_2*	Fe***, Cu, Zn*	pooled	0.94	0.88	***
	Fe, Cu, Zn**	Control	0.94	0.83	**
	Fe**, Cu, Zn	AD	0.95	0.91	**
R_2	Fe**, Zn**	pooled	0.67	0.44	**
	Fe***, Zn*	Control	0.97	0.93	***
	Fe***, Zn**	AD	0.96	0.92	***
R_2*	Fe**, Zn**	pooled	0.70	0.49	**
	Fe**, Zn	Control	0.94	0.87	***
	Fe***, Zn**	AD	0.95	0.91	***

Table 8.6: Results of multiple linear regression analysis of iron, copper and zinc with R_2 and R_2* for control and AD tissue. The statistical significance of the coefficient for each metal in the model is given, in addition to the overall statistical significance of the model. *p<0.05; **p<0.01; ***p<0.001.

Table 8.6 shows that a multiple linear regression analysis of the iron, copper and zinc data achieves the best fit for the pooled control and AD data for both R_2 and R_2*. However, the additional fit information provided by the statistical analysis software SSPS suggests that copper does not contribute significantly to the models: it has a high p-value of 0.29 in the R_2 mode and 0.17 in the R_2* model. The multiple linear regression models using iron and zinc data show a higher correlation coefficient, r, for the separated control and AD samples, when compared to simple linear regression analysis of iron only (Table 8.3). Interestingly, the correlation coefficient of the Fe and Zn model is reduced for the pooled data, suggesting that there is a difference between the relationship for the control and AD samples. This was not observed with the iron or zinc data individually.

Zinc ions in solution have been shown to shorten T_2 [192] (and therefore increase R_2). However, it is also possible that zinc distribution is coinciding with another parameter that influences MRI, such as tissue water or fat content.

8.1.2 600 MHz data

MRI relaxometry of the pons and amygdala samples was carried out using the 600 MHz probe at the University of Florida. For reasons detailed in Section 4.3.3.1 only the R_2* data are considered reliable and analysed here. SXRF maps of the amygdala samples were collected during experiment DLS5 and therefore the estimated calibration of the iron concentration for the normalised SXRF signal applies.

The pons samples, which included control, AD, PD and MSA cases, were mapped over a number of different experiments. As described in Section 6.5, normalising the data between experiments produced unsatisfactory results. Therefore only the data from the AD and PD pons (both measured during experiment DLS3) are matched to MRI maps.

8.1.2.1 Amygdala

The bore size of the 600 MHz probe restricted the sample size to less than 8 mm in diameter and for the amygdala this contributed to difficulty in matching the SXRF and MRI maps. Each sample was taken from completely within the amygdala so there were no surrounding structures for reference and additionally there were limited distinguishing features within each map. The process of finding the best matched R_2* map to the SXRF map for the control and AD amygdala is shown in Appendix F and the final result of matching in Figure 8.16.

Matching for sample C3 is not perfect as some tissue from the top of the SXRF section was lost during sectioning and the outside edge of the sample was pressed into the shape of the NMR tube during MRI, which can be seen in the R_2* map. The matching was more straightforward for sample AD2, although the lack of distinctive structures within the MRI map meant the shape of the section was the only reference point.

As the amygdala sample contained no distinct regions for segmentation, the correlation between iron concentration and R_2* is examined across the whole map. ImageJ was used to create a series of square ROIs that effectively produce a grid overlay onto the matched SXRF and MRI maps (Figure 8.16).

The square ROIs are 5x5 pixels for both maps. However, the resolution of the MRI and SXRF maps are slightly different (64 x 64 µm and 60 x 60 µm respectively) and ImageJ can only divide the image into whole numbers of pixels. Therefore a 5x5 pixel ROI in the SXRF map is slightly smaller than in the MRI map. The remaining pixels are divided up as evenly as possible across the SXRF map and can be seen as rows and columns of 'skipped' pixels in Figure 8.16 a) and c).

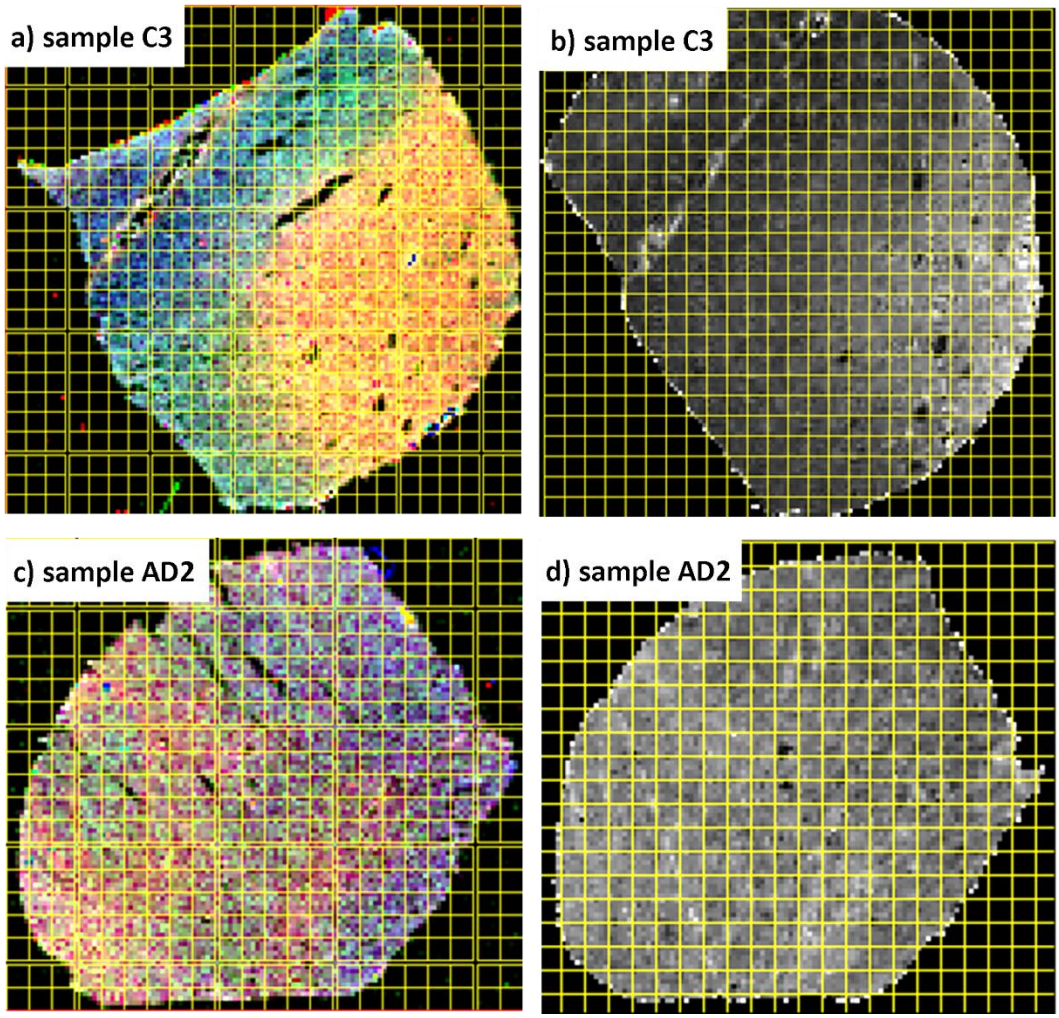

Figure 8.16: Matched SXRF and R_2* maps of the amygdala with a grid of square ROIs overlaid on each map. The matching for sample C3 is difficult as in the SXRF map, a), tissue from the top of the section was lost during sectioning and b) the R_2* map shows that the tissue was slightly deformed to the NMR tube during imaging. For sample AD2 matching between c) the SXRF map and d) R_2* map was more straight forward.

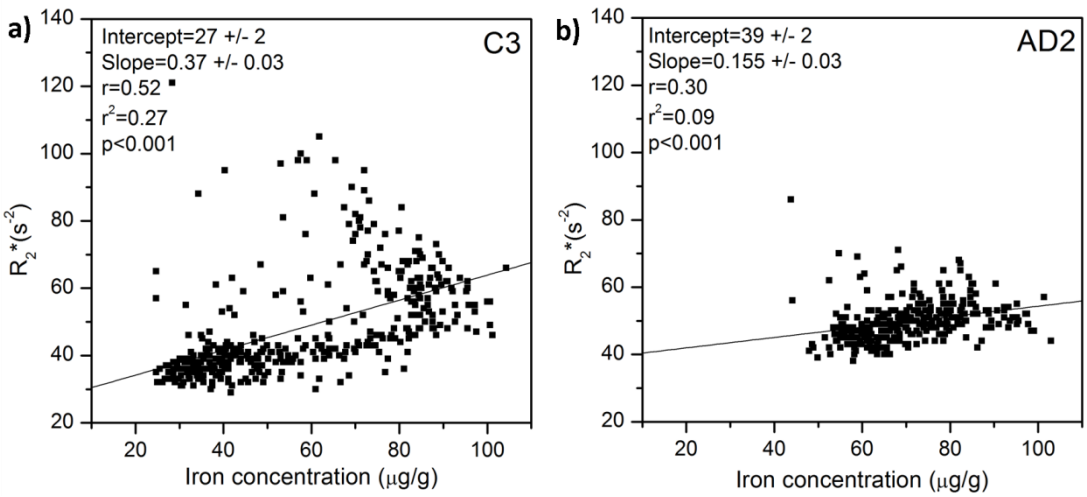

Figure 8.17: Iron concentration vs. R_2* in maps of the control and AD amygdala. There is a weak, but statistically significant linear relationship between iron concentration and R_2* for both a) sample C3 and b) sample AD2.

The ROI 'multi-measure' tool was used to sequentially measure the mean value of all of the square ROIs, so that ROI1 from the SXRF map corresponds spatially to ROI1 from the R_2* map. As the background pixels had been set to 'NaN' these were discounted when they fell within an ROI. When any ROI had a mean value of 'NaN' it, and its counterpart in the matched map, were deleted from the data set.

Figure 8.17 shows iron concentration versus R_2* for all of the ROIs, for sample C3 and AD2. Linear regression analysis shows that there is a highly statistically significant linear relationship between iron and R_2* for both samples. However, the r-squared values are very low: 0.27 for C3 and 0.09 for AD2. This shows that the linear regression model does not account for the majority of variation in the data.

The correlation coefficient for the relationship between iron and R_2* in the amygdala is much smaller than for the linear regression of maps from multiple brain regions (Table 8.3 and Figure 8.13). This may be due to the lower iron concentration, and smaller range of concentrations present in the amygdala map, compared to the magnitude and range of the segmented regions from multiple samples. If in Figure 8.13 only the data from regions with an iron concentration of below 50 μg/g are considered (comparable to the iron concentration in the

amygdala) a linear relationship is not clear; although the data points do not disagree with the overall trend, there is a large scatter about the fit.

8.1.2.2 Pons

The selection of the best matched MRI slice to the SXRF maps of the AD and PD pons is shown in Appendix G and the result of the matching in Figure 8.18. Good matching of the very fine stripes of grey and white matter was not achieved uniformly across the samples. Due to their small size, any difference between sectioning and imaging plane results in a miss-matching of structures and this appears to be what has happened in this case.

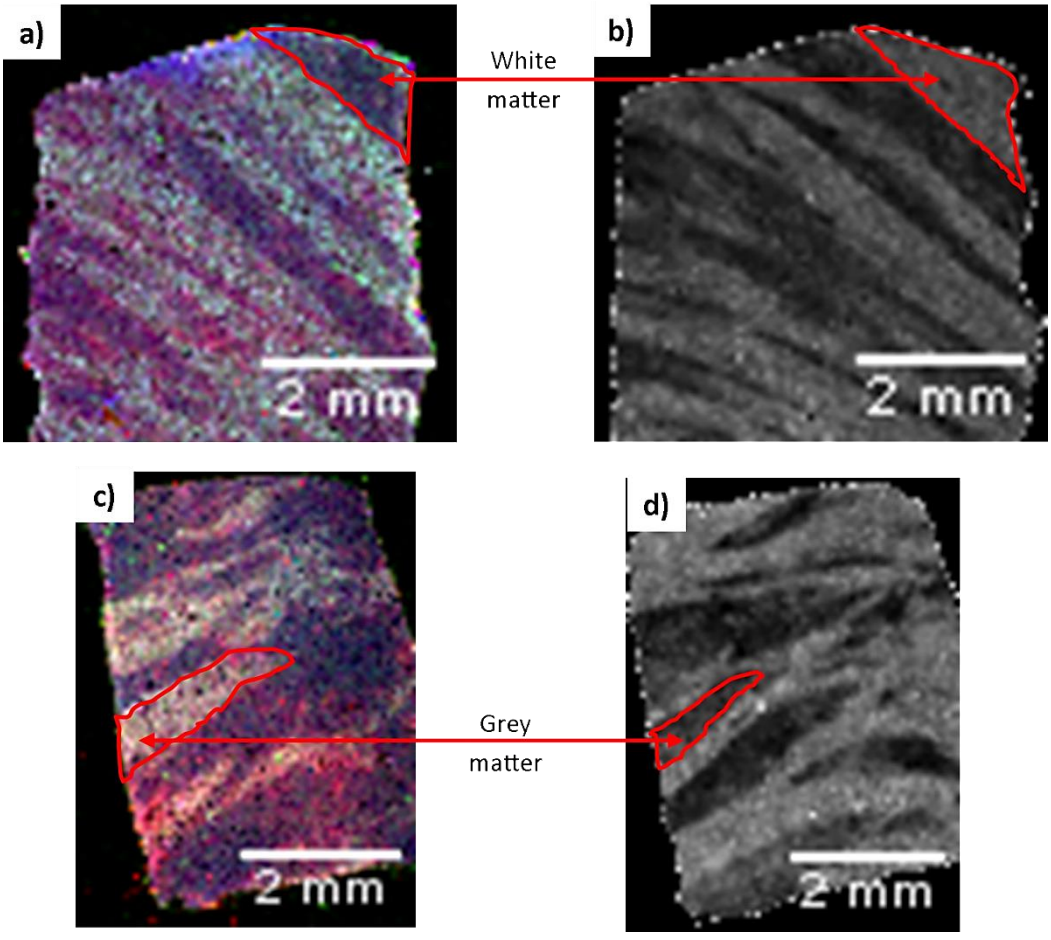

Figure 8.18: The result of matching the SXRF and R_2* maps of the AD and PD pons. Only partial matching is achieved between maps in both cases. In the a) SXRF and b) R_2* maps of sample AD2 a matched region of matched white matter is shown. In the c) SXRF and d) R_2* maps of sample PD1 an area of approximately matched grey matter is highlighted.

Although good matching was not achieved across the sample, it was sufficient to show that whereas iron concentration is highest in the grey matter of the pons, R_2* is higher in the white

matter. This can be seen by inspection of the matched maps in Figure 8.18 and also in Figure 8.19 which shows the mean iron concentration and R_2* in the grey and white matter of the samples, after the maps were segmented using ImageJ.

Comparison between the disease cases shows that iron is increased in the AD sample compared to PD and that this corresponds to a slightly increased R_2* in both the grey and white matter. However, despite the overall increase in iron in the grey matter the white matter has increased R_2*. This is not in agreement with the linear relationship between iron concentration and R_2* that was demonstrated in Section 8.1.1.5 for both grey and white matter tissue measured at 400 MHz.

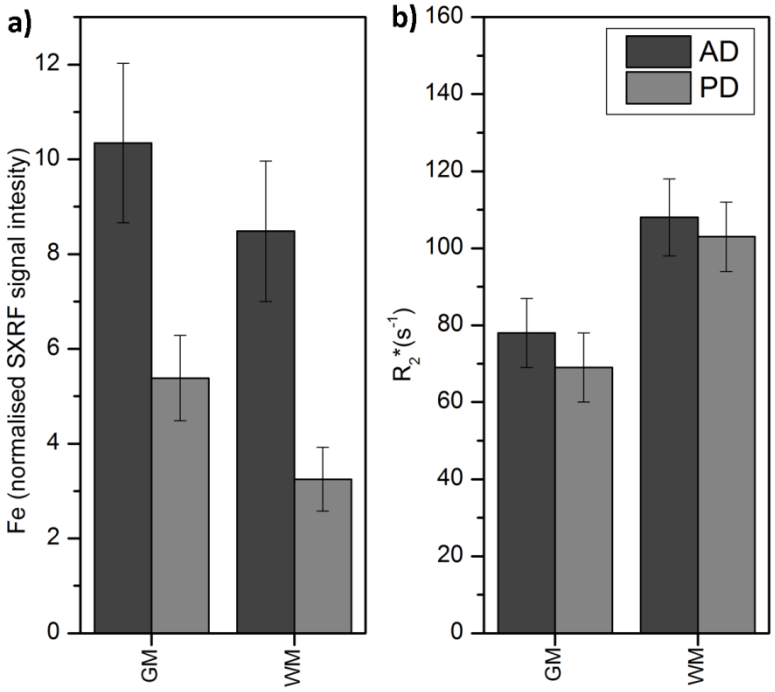

Figure 8.19: Relative iron concentration and R_2* in the grey and white matter of the AD and PD pons. The mean and standard deviation of the pixel values in the segmented regions of grey and white matter are given for a) the normalised iron SXRF maps and b) the R_2* maps. For both samples, iron concentration is higher in the grey matter, whereas R_2* is higher in the white matter.

Although the SXRF signal intensity of the pons maps was not calibrated, the bulk tissue iron concentration of adjacent tissue samples was measured and the results were given in Chapter 5. For case AD2 an iron concentration of 37.8 ± 1.1 µg/g was measured and for sample PD1 iron concentration was 13.2 ± 0.4 µg/g. As with the amygdala, the iron concentration is low. At this low concentration it may be that the difference in water content (concentration and

availability) between white and grey matter dominates the value of R_2*. However, when comparing the same type of tissue the increased iron concentration in the AD sample (compared to PD) corresponds to an increase in R_2*.

8.2 MRI versus bulk tissue iron concentration and SQUID measurements

In Chapter 5 SQUID magnetometry was used to examine the particulate iron content of the control and AD samples of tissue from the caudate nucleus (CN), putamen (Pu), substantia nigra (SN) and pons. The isothermal remanent magnetisation (IRM) of each sample was measured at 5 K, which gives an approximation of the relative ferritin concentration in the tissue. The iron concentration of each sample was then measured by GFAAS or ICP-MS.

In Chapter 7 R_2 and R_2* were calculated for adjacent blocks of tissue taken from within the same brain regions of the same cases. The CN, Pu and SN were imaged at 400 MHz, whereas the pons samples were imaged at 600 MHz.

8.2.1 Data summary

Figure 8.20 shows the average bulk tissue measurements: a) dry to wet mass ratio (DWR, a measure of tissue water content); b) iron concentration; c) IRM at 5 K (an approximate measurement of particulate iron) for the control and AD samples of each region measured in Chapter 5. The mean d) R_2 and e) R_2* from the corresponding cases is also given.

Only the R_2* data are included for the pons as the R_2 data collected at 600 MHz were not reliable (see Section 4.3.3.1). It is also important to note that R_2* is field dependent and therefore the pons data must be considered separately from brain regions measured at 400 MHz.

In Figure 8.20 there is no immediately obvious relationship between the bulk tissue and MRI measurements, as there was in figure 8.13. However, this is investigated further with linear regression analysis.

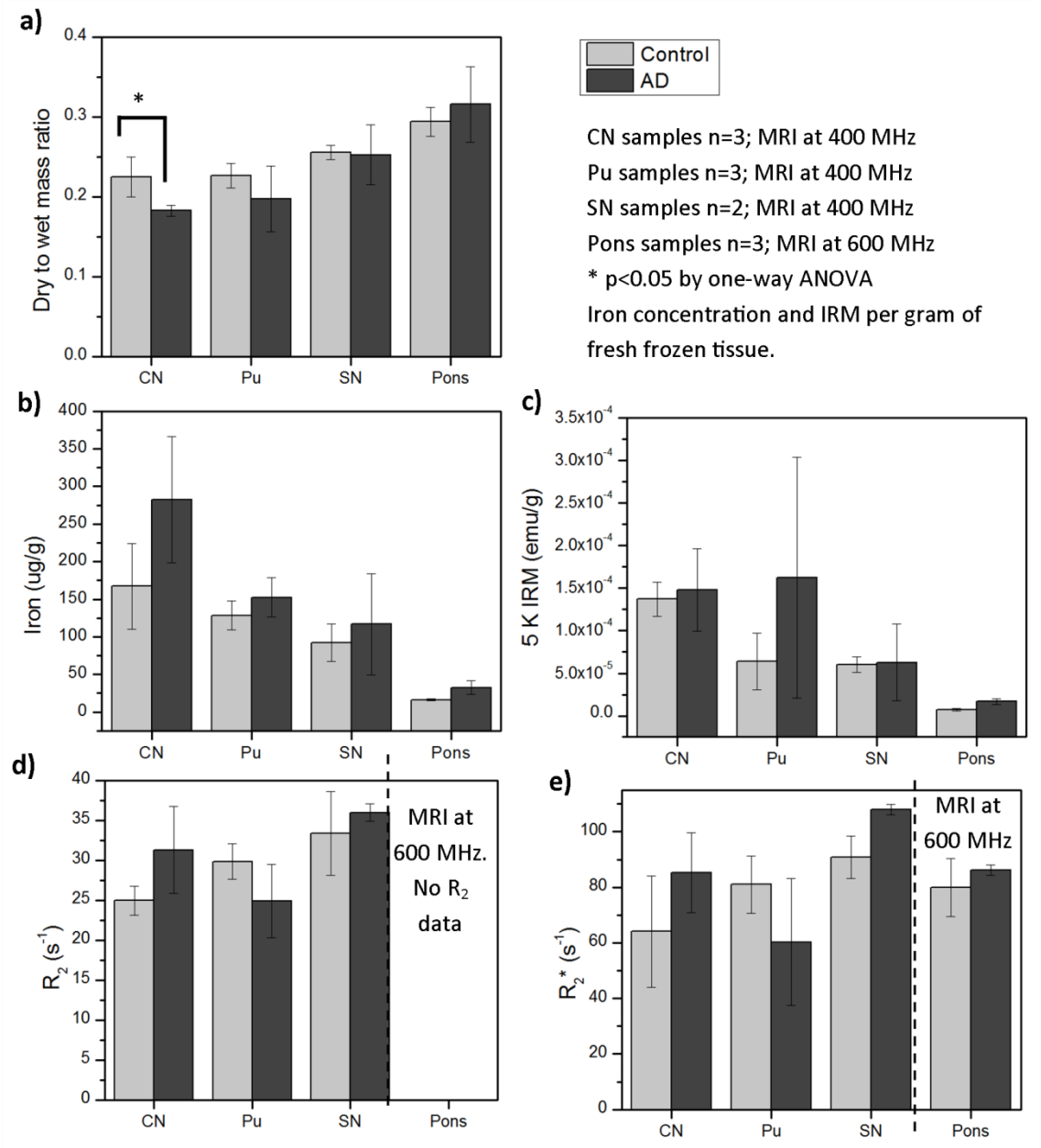

Figure 8.20: Summary of bulk tissue and MRI relaxometry measurements of tissue from the caudate nucleus, putamen, substantia nigra and pons. a) The dry to wet mass ratio showed a statistically significant increase in water content of the AD caudate nucleus. No statistically significant relationships were observed between control and AD in b) the mean iron concentration, c) the mean IRM at 5 K (an approximate measure of ferritin iron), d) the mean R_2 or e) the mean R_2*. Note that MRI relaxometry of the pons was carried out at 600 MHz, compared to 400 MHz for other samples.

8.2.2 Linear regression analysis

8.2.2.1 MRI at 400 MHz

Multiple linear regression analyses were carried out to investigate the relationship between bulk tissue iron and water content and the R_2 and R_2* measured in the adjacent blocks of tissue. Data from the different regions (CN, Pu and SN) were pooled, as a strong linear relationship between iron and MRI was shown across multiple regions for the matched MRI and SXRF maps (Figure 8.13).

Simple linear regression was carried using iron concentration, IRM at 5 K (which gives an approximate, relative concentration of ferritin) and DWR (dry to wet mass ratio) as the independent variables. Multiple linear regression analysis was then carried out using iron and DWR, and then IRM at 5 K and DWR, as pairs of independent variables. Data from control and AD samples were pooled and examined separately. The results are given in Table 8.7.

For most combinations of variables the model did not reach statistical significance and this was the case for all iron measurements. When statistical significance was shown, the direction of the relationship was negative: an increase in IRM at 5K resulted in a decrease in R_2 or R_2*. This does not agree either with the positive linear relationship observed between ferritin and R_2 that has been shown in the literature [120] or that shown between total iron and R_2 and R_2* using matched SXRF and MRI maps in Section 8.1. Additionally, the linear regression analysis between the matched maps showed a much stronger linear relationship with high regression coefficients (r) and r-squared values.

Dependent variable	Independent variables	n	Disease	r	r^2	Direction of slope	p
R_2	Fe	18	Pooled/control/AD				-
R_2*	Fe	18	Pooled/control/AD				-
R_2	IRM at 5 K	18	pooled	0.55	0.30	-ve	*
		9	Control	0.72	0.52	-ve	*
		9	AD	-	-	-	-
R_2*	IRM at 5 K	18	pooled	0.64	0.41	-ve	**
		9	Control	-	-	-	-
		9	AD	0.72	0.53	-ve	*
R_2	DWR	18	Pooled/control/AD				-
R_2*	DWR	18	Pooled/control/AD				-
R_2	Fe & DWR	18	Pooled/control/AD				-
R_2*	Fe & DWR	18	Pooled/control/AD				-
R_2	IRM at 5 K & DWR	18	Pooled/control/AD				-
R_2*	IRM at 5 K & DWR	18	pooled	0.67	0.44	-ve	*
		9	Control	-	-	-	-
		9	AD	-	-	-	-

Table 8.7: Results of linear regression analysis of bulk tissue and MRI data. Linear regression analysis was used to examine the relationship between the dependent variables R_2 or R_2* and the independent variables iron concentration, IRM at 5 K and DWR for tissue from the control and AD caudate nucleus, putamen and substantia nigra. Statistically significant linear relationships were only observed between IRM at 5 K and R_2 or R_2*. *p<0.05; **p<0.01; - p>0.05.

Figure 8.21 shows IRM at 5 K versus R_2 and R_2*, where it can be seen that one sample has a higher IRM at 5 K value than the others. This data point belongs to putamen sample AD1. Referring back to Figure 5.14 shows that this sample had a higher than expected IRM at 5 K, considering its iron content. If this data point is excluded from the analysis (shown by the dashed line in figure 8.12), there is no longer a statistically significant linear relationship between IRM at 5 K and R_2 or R_2*. Additionally, the statistical significance of the multiple linear regression analysis for IRM and DWR and R_2* is lost.

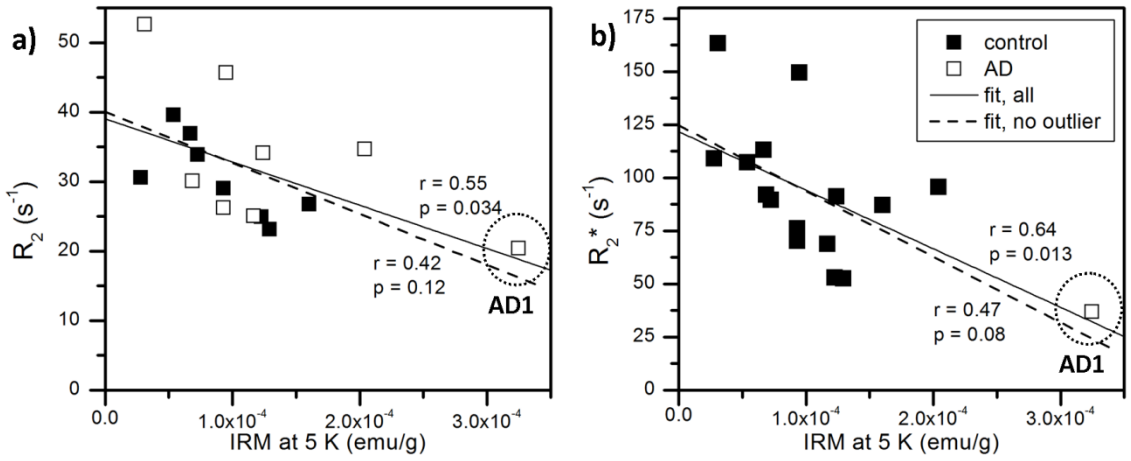

Figure 8.21: IRM at 5 K versus R_2 and R_2*. IRM measurements of bulk tissue samples are plotted against the mean a) R_2 and b) R_2* of the samples taken from adjacent tissue blocks. The measurement error for the IRM at 5 K and MRI is similar in size or smaller than the data markers. Linear regression analysis of all data points (solid line) showed a statistically significant negative relationship between IRM at 5 K and R_2 and R_2*. When putamen sample AD1 (circled) was excluded, the linear fit lost statistical significance.

The exclusion of putamen sample AD1, does not produce the expected positive linear relationship between bulk iron concentration or IRM with R_2 and R_2*. This disagreement is most likely due to the fact that the bulk tissue and MRI measurements were not made from the same blocks of tissue, but from adjacent blocks. Although these were cut from within the same structures, it is likely that the tissue did not display uniform properties.

8.2.2.2 MRI at 600 MHz

Similarly to the analysis of the 400 MHz data, linear regression analysis was carried using bulk tissue iron concentration, IRM at 5 K, DWR and R_2* measurements of the pons. No statistically significant model was found using any combination of variables by simple or multiple linear regression analysis. This is not unexpected considering the fact that no linear relationship was observed for the matched SXRF and R_2* maps.

8.3 Discussion

8.3.1 A very strong linear relationship was demonstrated between iron concentration and R_2, R_2* and R_2' at 9.4 T

The matching of SXRF and MRI maps of the caudate nucleus, putamen, globus pallidus and substantia nigra and their surrounding structures showed a very strong, statistically significant linear relationship between iron concentration and R_2, R_2* and R_2'. In each case, the gradient and intercept of the relationship agreed within error for control and AD tissue.

8.3.1.1 The linear relationship between iron and R_2 is shown in both grey and white matter

A number of studies have shown that the linear relationship between iron concentration and R_2 does not hold for white matter tissue. This includes studies by House *et al.* at 1.4 T [19] and 4.7 T [26]. Additionally Gelman *et al.* showed that the R_2 and iron data from the frontal white matter were not in line with data from grey matter regions [134].

Table 8.3 shows that in this study the data from both the grey and white matter regions show a statistically significant linear relationship between iron and R_2 (and R_2*), with gradients and intercepts which agree within error. However, this result is not directly comparable to the studies mentioned above as it does not include the same regions of the brain. In this thesis grey matter regions were the main focus and the white matter regions included are neighbouring structures which happened to be included in the MRI samples. Additionally, the white matter regions in this study have a wider range of iron concentrations than those included in the House *et al.* papers. This means that a linear relationship can more easily be observed above the scatter about the linear fit, which is seen in Figure 8.12 and in the literature.

The pons provided evidence that this relationship may not hold at lower iron concentrations. In this region, where total iron concentration is less than 50 μg/g, the white matter showed higher R_2* than grey matter, despite the fact that the grey matter had a higher iron concentration. However, increased iron lead to an increase in R_2* when the same tissue type (e.g. grey matter compared to grey matter) was compared. This suggests that although iron concentration is still contributing to R_2*, other factors such as the water concentration, are dominating the value of R_2*.

8.3.2 Predicting the concentration of iron from an MRI measurement

A strong statistically significant linear relationship between iron concentration and R_2 and R_2* was demonstrated in Figure 8.13 and Table 8.3. The linear equations which describe the relationship are:

$$\mathrm{R}_2 = 0.072 \times [\mathrm{Fe}] + 20 \qquad (8.1)$$

$$\mathrm{R}_2^* = 0.34 \times [\mathrm{Fe}] + 37 \qquad (8.2)$$

Where [Fe] is the concentration of iron in micrograms per gram of fresh-frozen tissue and R_2 and R_2* are measured in s^{-1}.

Equations 8.1 and 8.2 can be rearranged to estimate the concentration for iron from R_2 or R_2* measured at 2 °C, at 400 MHz:

$$[\mathrm{Fe}] = 13.9\ \mathrm{R}_2 - 278 \qquad (8.3)$$

$$[\mathrm{Fe}] = 2.94\ \mathrm{R}_2^* - 109 \qquad (8.4)$$

However, the 95% prediction bands in Figure 8.13 indicate a large uncertainty.

8.3.3 Iron concentrations below 50 μg/g did not dominate the value of R_2* at 14.1 T

A very strong linear relationship was demonstrated between iron concentration and R_2 and R_2* at 9.4 T. However, this was not successfully demonstrated at 14.1 T, using either data from the amygdala or the pons. A statistically significant relationship linear relationship was observed in the amygdala, however the gradient was low and the r-squared values small.

The number of samples measured at 14.1 T and also mapped by SXRF was small and this was exacerbated by the fact that the pons and amygdala data had to be handled separately due to their SXRF maps being collected during different experiments. This meant that less data were available to examine the relationship between iron and MRI at 14.1 T than for MRI at 9.4 T.

However, the most likely reason that a strong relationship was not shown is that the iron concentration in the pons and the amygdala is low compared to the other regions studied. Both regions have iron concentrations below 50 μg/g (iron concentration of the pons was measured in Chapter 5 and the iron concentration of the amygdala was estimated from SXRF measurements and is widely reported in the literature [107]). Even though a strong linear relationship between iron concentration and R_2* at 9.4 T is shown in Figure 8.13 b), if the data points from regions with an iron concentration below 100 μg/g are considered the relationship is not clear. Linear regression analysis of these 8 data points was carried out and revealed no statistically significant relationship. Therefore it is not unexpected that, even at a higher field, the linear relationship between iron concentration and R_2* is not observed in the pons or strongly in the amygdala. This is in agreement with the findings of House *et al.* who, in a 4.7 T study, predicted a threshold value of 55 μg/g above which iron will dominate R_2.

8.4 Summary

I. The SXRF metal maps were successfully matched to the MRI R_2 and R_2* maps.

II. The matched maps revealed a strong, statistically significant, positive linear relationship between iron concentration and R_2, R_2* and R_2' at 9.4 T, which was the same for control and AD samples and for grey and white matter tissue.

III. A corresponding strong linear relationship was not observed between iron concentration and R_2* at 14.1 T, however the most likely reason for this is that the iron concentration of the samples measured at this field was low, below 50 μg/g.

Chapter 9: Discussion and conclusions

9.1 The linear relationship between iron and MRI

A very strong linear relationship between iron concentration and transverse relaxation, R_2, and the susceptibility related parameter, R_2*, was demonstrated in Chapter 8. Linear regression analysis of data from matched ROIs in the matched iron SXRF and MRI relaxometry maps showed a statistically significant relationship ($p<0.001$), where the relationship accounted for around 75% of the variation in the data. Both grey and white matter regions were included in this fit. Contrast between these regions in clinical MRI is usually attributed to differences in the fat and water content of the tissue, however the linear regression analysis shows that iron concentration dominates at this field.

This is thought to be the first demonstration of the linear relationship between iron concentration and R_2 and R_2* in human brain tissue at 9.4 T and the first demonstration, with quantified iron values, above 7 T.

9.1.1 Comparison with the literature

The effect of iron on R_2 increases linearly with field strength, a property which has been utilised by Bartzokis *et al.* in their field dependent R_2 increase (FDRI) method of assessing brain iron concentration [125, 126, 133]. However, it has been suggested that the effect will saturate at high field due to the saturation of the magnetisation of ferritin iron [25]. Vymazal *et al.* measured the effect of iron concentration on R_2 at multiple field strengths (0.05 to 1.5 T) using fresh (never-frozen) brain tissue from a Rhesus monkey [135] at an imaging temperature of 37 °C. They produced an empirical equation to give the gradient of change in R_2 (in s^{-1}) with iron concentration (milligrams of iron per gram of fresh tissue) at an imaging field B:

$$slope = 14.1 + 6.2B \ \ s^{-1}/mg/g \qquad (9.1)$$

where B is the imaging field in tesla.

House *et al.* concluded that the relationship they observed between iron and R_2 at 4.7 T agreed with Vymazal's prediction, once certain experimental differences had been taken into account [26]. Yao *et al.* have also shown that R_2* displays a linear dependence on field strength up to 7 T [27], however they did not measure R_2.

9.1.1.1 R_2

To test whether any saturation effects are shown at 9.4 T, Equation 9.1 was solved for the imaging field of 9.4 T (400 MHz), which gives a slope of 0.0724 s^{-1}/μg/g. This compares extremely well with the gradient of the linear fit to the matched R_2 and SXRF iron maps in Figure 8.12 of 0.072 ± 0.008 s^{-1}/μg/g. Therefore there is no evidence of saturation of the field dependent R_2 increase at 9.4 T.

The degree of agreement is extraordinarily close considering a number of experimental conditions which varied between the Vymazal paper and the experiments conducted here. It is important to consider the impact of the differences in experimental protocol, although they appear to have combined here to give good agreement. Firstly, Vymazal shows that R_2 is increased by 13-22 % in tissue which has been frozen and defrosted, as these samples have been (but Vymazal's samples were not). This would result in a corresponding change to the gradient. Conversely, R_2 decreases with decreasing temperature [193] and therefore the low imaging temperature of our samples (2 °C) would result in a decreased gradient compared to that observed by Vymazal *et al.*

Another experimental difference is that in the Vymazal paper the interecho time, T_E, is 4 ms compared to 9.78 ms in this study. This is important as in the same paper Vymazal also described how increased interecho spacing increased the effect of iron content on R_2 [135]. From Figure 7 in the paper by Vymazal *et al.* an estimated 5-10% increase in the effect of iron on R_2 could be expected with T_E of 10 ms compared to 4 ms in MRI at 37 °C with a field of 1.5

T. The size of this effect may be field and temperature dependent. Exploring the relationship between T_E and R_2, with the MRI protocols used here, may be an interesting area of future work.

In summary an increase in the gradient of the relationship between R_2 and iron concentration is expected, due to the tissue having been frozen. In contrast the low temperature and longer T_E used in this study would be expected to decrease the gradient. A final source of error in the gradient of the fit in Figure 8.12 is calibration of the absolute iron concentration in the SXRF map. This has an estimated error of ± 12%.

9.1.1.2 R_2'

Tables 8.3 and 8.4 give the gradient of the linear relationship between iron concentration and R_2 and R_2' respectively. Comparing the data shows that the gradient for R_2' is 3.75 times larger than the gradient for R_2. In a study at 3 T by Gelman *et al.* [134], the magnitude of the gradients were shown to be approximately equal. Therefore, not only is there field dependent contribution to the gradient of R_2 with iron (as described by Vymazal *et al.* and shown above in Equation 9.1 [135]), but there is an additional field dependent contribution to the relationship of R_2' with iron concentration.

Assuming that this relationship is also linear, the 9.4 T data in this study can be combined with the 3 T data reported by Gelman *et al.* to produce an equation for the slope of R_2' with iron concentration at a particular imaging field B:

$$\text{slope} = -51.1 + 34.4\text{B} \ \text{s}^{-1}/\text{mg/g} \qquad (9.2)$$

Yao *et al.* [27] have shown that there is a linear relationship between the magnitude of the imaging field and R_2*, therefore it is reasonable to assume that the relationship is also linear for R_2'.

9.1.2 Measuring iron by MRI

The matched SXRF and MRI maps in Chapter 8 showed that at 9.4 T iron concentration dominates the value of R_2 and R_2*. Equations were produced to estimate the iron concentration of tissue from MRI relaxometry at 400 MHz. The prediction bands show that although the relationship is strong, the predicted R_2 or R_2* for a given iron concentration (or *vice versa*) covers a large range. This means that a large increase in iron would be required to ensure a significant change in R_2 or R_2*. In addition to this, bulk iron measurements in this study, and in the literature, show a large standard deviation. It is hard to say whether this is due to measurement error (which is suggested by the variation in means between different studies and further discussed in Section 9.3) or natural variation (which is supported by large standard deviations within studies). The combination of these two observations means that a very dramatic change in iron in one particular region would be required to differentiate with certainty between control and AD.

In this study the linear relationship between iron concentration and R_2 and R_2* was demonstrated with only n=2 for each region (one control and one AD example). Other tissue properties that vary between regions, such as fat and water content, will be contributing the value of R_2 and R_2* and therefore may be contributing to the spread about the fit in Figure 8.13. It is difficult to observe this effect with such a small number of samples. In a study by Langkammer *et al.* [123] there is some evidence of tissue samples from the same regions clustering together. Therefore comparing like-with-like tissue (i.e. from the same region) may reduce the size of the prediction bands, and therefore increase the sensitivity of MRI to changes in iron concentration.

9.2 Combining information from multiple brain regions enables the differentiation of control and AD tissue

Discriminant analysis has been used here to show that combining data from multiple regions increases the ability to distinguish between disease and control, even when no statistically

significant differences between AD and control for individual regions have been observed. This was demonstrated with total and particulate iron concentration in Chapter 5, and translated to R_2 and R_2* measurements in Chapter 7.

The literature review showed mixed results when comparing iron concentration (directly, or indirectly through MRI) between AD and control tissue, with some positive and negative findings reported for all regions. However, as has been shown in this data set, it is possible that discriminant analysis could be used to produce a model that is clinically useful in distinguishing between disease and control, without there being statistically significant differences between individual regions.

Measurement	Best combination of regions	Discriminant analysis result	Cross-validation result
Iron concentration	Pons, Pu Pons, Pu, CN SN, Pu, CN	100%	83.3%
IRM at 5 K	Pons Pons, SN Pons, Pu	100%	100%
R_2 at 400 MHz	CN, AIC CN, Pu, AIC	100%	83.3%
R_2* at 400 MHz	CN, WM-Pu	100%	66.7%
R_2* at 600 MHz	Pons GM, Amyg	83.3%	66.7%

Table 9.1: Summary of the best results from discriminant analysis of different measurements. The combination of brain regions which provided the most successful differentiation between control and AD is given for each measurement. In some cases more than one combination produced the same result. The percentage of the samples which were correctly grouped is given and the percentage correctly grouped with cross-validation. Pu = putamen; CN = caudate nucleus; SN = substantia nigra; AIC = anterior limb of the internal capsule; WM-Pu = white matter lateral to the putamen; GM = grey matter; Amyg = amygdala.

Table 9.1 shows the combinations of regions which provided the best differentiation between AD and control for each set of measurements. However, as not all regions were measured by all different methods, this cannot be considered a definitive guide to the best potential regions for further study. Other factors also need to be considered. For example, the pons provided good discrimination between diseases with iron concentration and IRM at 5 K data. However,

as this region has a low absolute iron concentration it may not be a good candidate for differentiation by MRI and in fact this was demonstrated in Chapter 8, Section 8.1.2.2.

9.2.1 Would 3 T MRI measurements give the same result?

The effect of iron on R_2 is field dependent, as is discussed in Section 9.1 above. Therefore, the sensitivity of R_2 to iron concentration is reduced at lower imaging fields. Routine clinical imaging systems currently do not have fields above 3 T (and are typically lower). Therefore it is important to consider whether the successful differentiation of AD and control samples, which was observed at 9.4 T, could in principle be achieved at 3 T. This was tested using R_2 data from the CN and AIC, which gave 100 % correct classification of samples using discriminant analysis (Table 9.1).

First, the linear relationship between iron and R_2 at 3 T was estimated. Equation 9.1 was used to predict the gradient of the relationship, giving a value of 0.0327 s^{-1}/μg/g. The empirical results from Langkammer *et al.* gave an intercept of 8.5 s^{-1} [123] and this value was used in the estimation. The final equation is

$$R_2 = 0.033 \times [\mathrm{Fe}] + 8.5 \qquad (9.3)$$

Equation 8.3, which predicts iron concentration from R_2 measured at 9.4 T, was then used to estimate iron concentration in each control and AD sample from the CN and AIC. These values were substituted into Equation 9.3 to estimate R_2 for each sample at 3 T.

		CN (mean ± σ)	AIC (mean ± σ)
Mean R_2, measured at 9.4 T (s^{-1})	Control	24.9 ± 1.8	37.7 ± 4.0
	AD	31.1 ± 5.4	31.6 ± 5.7
Mean iron concentration per unit mass of tissue, predicted from Equation 8.3 (μg/g)	Control	68.7 ± 25	245.5 ± 56.2
	AD	157.2 ± 75.4	160.7 ± 78.7
Mean R_2 predicted at 3 T (s^{-1})	Control	10.7 ± 0.8	16.4 ± 1.8
	AD	13.6 ± 2.4	13.8 ± 2.6

Table 9.2: The mean predicted R_2 of the caudate nucleus (CN) and anterior limb of the internal capsule (AIC) at 3 T. Also given are the mean R_2 measured at 9.4 T and the mean predicted iron concentration of the AD and control samples. σ = standard deviation.

Table 9.2 shows the mean R_2 for the control and AD tissue from the CN and AIC, as measured at 9.4 T. It also gives the mean predicted iron concentration for each region, and the mean predicted R_2 at 3 T. Discriminant analysis of the predicted R_2 values for the three control and AD cases achieved 100% correct classification, and 83.3% with cross-validation. This is the same result as shown for the 9.4 T data in Table 9.1. In conclusion, these data predict that discriminant analysis of R_2 data from multiple regions, collected at 3 T, may allow differentiation between AD and control tissue.

However, it is important to note that a limitation of this study is that all imaging was of *post mortem* tissue which has slightly different properties compared to living tissue. Therefore, an important future study would be to test this result with clinical imaging.

9.2.2 Other comments

Although iron is associated with AD pathology, increased iron concentration is not limited to regions of the brain in which AD pathology exists. This is shown in the literature review and further supported by the evidence in this thesis. These regions may provide a potential target for clinical MRI as the tissue is likely to have experienced less degeneration and the R_2 and R_2* decrease caused by increased water content may not be a problem.

A statistically significant difference between AD and control was observed in the ratio of R_2 in the caudate nucleus and the anterior limb of the internal capsule (Figure 7.10). As measurement of R_2* is machine dependent [149] and measurement of R_2 is sequence dependent [135], implementing consistent MRI relaxometry in a clinical setting may be difficult when a wide variety of scanners are used. Therefore an internal ratio between different brain regions may provide an interesting opportunity as it will, to some extent, correct for measurement errors. Looking at ratios between different regions of the brain may be an interesting future study.

9.3 The inhomogeneous distribution of iron within nuclei of the basal ganglia

SXRF mapping is a technique which provides high spatial resolution, and in Chapter 6 was used to demonstrate the inhomogeneity of iron distribution within brain structures. In particular this was demonstrated for the putamen from case C3, which was mapped twice. The two samples were approximately 2 cm apart and one sample had a mean iron concentration 80% higher than the other.

In Chapter 6, a comparison was made between the ratio of the AD to control iron concentration (ARC) for: i) the relative mean iron concentration measured by SXRF mapping and ii) for the measured bulk tissue iron concentration. The samples compared were from the caudate nucleus, putamen and substantia nigra and the tissue for each technique was cut adjacently, as shown in Figures 3.7 and 3.9. In general, the agreement for the ARC values was much better than described above, with a difference between the two techniques of 4% for the putamen, 9% for the substantia nigra and 24% for the caudate nucleus (Table 6.2). This suggests that either the concentration of the iron over these particular regions of tissue was relatively consistent, or that the relative change in iron concentration was proportionally the same throughout the sample, even if the absolute iron concentration varied.

As has been previously noted, the values of iron reported in the literature vary considerably between papers. This was shown in Tables 3.2 and 3.3 which summarised some of the data in the literature. Additionally, individual studies, such as the landmark study by Hallgren and Sourander [93], have large standard deviations which are comparable with the standard deviations of the samples measured here (Section 5.1.1). In this study, it is likely that small variation in the positions of the different samples cut from within the larger blocks has contributed to the variance in the data. This may well also be a factor in the values reported in the literature. For example, House *et al.* commented on the difficulty of precisely dissecting nuclei from the surrounding tissue [26].

In their paper *Imaging markers for Alzheimer disease: Which vs how*, Frisoni *et al.* compared a large number of imaging markers of AD, including volumetric MRI [53]. They concluded that the way in which an imaging marker is measured is at least as important to its success as the marker itself. The protocol for segmentation of MRI images was one of the parameters they considered. Due to the inhomogeneity of iron distribution within individual structures, demonstrated by SXRF mapping in Chapter 6, it is highly likely that carefully standardising the protocol for segmenting MRI relaxometry maps would be very important before any clinical application of this technique.

9.4 The form of iron in Alzheimer's disease tissue

In the literature review in Section 1.3 it was reported that some studies have shown an increase in magnetite in AD tissue from the superior temporal gyrus [110, 141]. This was not demonstrated in the regions studied in this thesis.

In Chapter 5 it was concluded that there was no evidence of a change in the form of iron in the AD tissue samples compared to control. Some individual samples showed evidence of increased magnetite concentration (Table 5.6), however there was no trend specific to AD (or Parkinson's disease or Multiple System Atrophy). This conclusion is supported by Figure 5.13, which shows the ratio of iron to IRM at 5 K (approximate, relative concentration of iron in ferritin) and IRM at 50 K (approximate, relative concentration of iron in magnetite), where no statistically significant differences were observed between disease groups. Additionally, Figure 5.14 shows a strong, statistically significant linear relationship between iron concentration and IRM at 5 K for samples from all disease groups.

The data in Figure 8.13 also support the conclusion that there is no significant difference between the particulate iron content of the control and AD samples. The SXRF maps represent the distribution of total iron, whereas MRI is most sensitive to particulate iron, with magnetite having a larger effect than ferrihydrite-like iron [158]. Therefore if there was a significant

difference in the proportion or form of particulate iron in the AD samples, the gradient of the linear relationship would be affected. This is not the case and the gradient of the fits to the control and AD data agree within error. However, it is possible that variations in the proportion of total iron as particulate iron in individual samples may be contributing to the scatter about the linear fit in Figure 8.13.

In this thesis particulate iron was evaluated in terms of ferrihydrite and magnetite, but not other iron oxide phases (such as those associated with neuromelanin and haemosiderin), as this was beyond the scope of this study. Additionally, the effect of clusters of ferritin on the magnetic properties of the tissue was not explored. In particular, it should be noted that significant intracellular accumulations of ferritin have been observed in MSA pons tissue, as reported in the study which ran parallel to this thesis [28]. This may have affected IRM values, but a full investigation of the effect was beyond the scope of the investigation.

9.5 Development and demonstration of techniques

In this project a unique set of complementary techniques was used to investigate changes in iron in the AD brain and the relationship between iron and high field MRI. The specific combination of techniques had certain advantages and disadvantages as described below.

9.5.1 Matching MRI and SXRF maps

A literature search has revealed that no other studies have used matched SXRF and MRI maps to show the relationship between iron concentration and R_2 and R_2*. Hopp *et al.* used SXRF maps of 1 mm slices of fixed tissue to calibrate susceptibility-weighted MRI images [90]. In a previous publication by our group SXRF and 14.1 T MRI maps of the hippocampus were matched, however as the iron maps had not been calibrated the relationship was not quantified in this preliminary study [132].

The use of the matched maps allowed the comparison between iron concentration and MRI to be made with high spatial accuracy. There are some limitations to this which reduce the

accuracy of matching, including: misaligned sectioning and imaging planes, differences between MRI and SXRF slice thicknesses and ambiguity about the boundaries of certain structures. However, this is still a more accurate technique than MRI followed by tissue dissection. Accurate dissection of specific brain nuclei is very challenging and particularly difficult when working with fresh-frozen tissue. The difficulty in dissecting structures without including adjacent tissue is commented on in the paper by House *et al.* [26] in which they suggest that this may be a cause of outlying data points.

9.5.2 Bulk iron analysis in adjacent blocks of tissue

In this study, adjacent blocks of tissue were cut from within tissue structure so as to allow a parallel investigation of bulk tissue iron and matching of MRI and SXRF maps in the same cases. Therefore the comparison of MRI and bulk tissue data is not a comparison between two measurements of exactly the same tissue sample. The result of this was that the expected positive linear relationship between iron concentration and R_2 and R_2* was not observed. However, this did serve to highlight the importance of spatial matching when comparing sub-regions of nuclei.

9.5.3 High field MRI

Although high field MRI relaxometry has the advantage of providing detailed structural information and increasing the sensitivity of R_2 and R_2* to iron concentration, it also has some limitations and some additional challenges. In particular, the small bore sizes of the high field spectrometers limited the maximum sample size, making anatomical matching and identification of samples very challenging.

The MRI of the amygdala at 14.1 T is a good example of this. The size of the sample was limited to fit inside the 8 mm diameter NMR tube and therefore no surrounding tissue structures were included in the sample, making confirmation of the anatomy extremely difficult. This is compounded by working with fresh rather than fixed tissue, which would have given clearer

contrast in the tissue blocks when they were initially cut. It is also difficult to guarantee anatomically matched samples when such a small block of tissue is cut. This was demonstrated in the globus pallidus data set, where some samples did not include all the targeted regions (Section 7.1.1).

One positive aspect of this study, is that imaging at this resolution provided an exceptional level of detail and may therefore be particularly useful in investigating smaller, highly complex structures: for example, for investigation of the substantia nigra (shown in this project) and the hippocampus, as already been demonstrated by our group [132].

9.5.4 Staining section post-SXRF mapping

The development of a staining protocol which allowed the staining of post-SXRF mapped tissue with haematoxylin, allowed the identification of individual neurons in the stained section and the SXRF map. This allowed comparison of the relative iron, copper and zinc concentration in AD and PD pons (Section 6.5.2).

9.6 Further work

9.6.1 The discriminant analysis model

The ability of discriminant analysis to differentiate between control and AD samples has been demonstrated repeatedly with this sample set. The next stage in using discriminant analysis would be to further validate the model by testing how well it classifies a set of samples that were not used in creating the model. This was not possible with the small number of samples available in this thesis.

Therefore, a suggestion for future work would be to test discriminant analysis on a larger data set. Using data from a whole brain (*post mortem* or *in vivo*) would have the advantage of allowing a large number of different regional combinations to be considered. However, the imaging field, and therefore sensitivity to differences in iron concentration would be reduced.

From the work in this thesis, and the data reported in the literature, regions of the basal ganglia remain an interesting target area for this purpose. Although no statistically significant differences between AD and control are reported here, the trend of increased iron in the putamen and caudate nucleus was observed.

9.6.2 T_1 data

As outlined in the methodology chapter, high resolution T_1 data were also collected for all of the samples measured by MRI. These data are available for analysis and would be expected to also show shortening with increased iron concentration, but to a lesser degree than was observed for T_2 [153]. It would also be interesting to compare T_1 to the relative zinc and copper concentrations measured by SXRF. Zinc ions in solution have been shown to shorten T_1 [192] and the paramagnetic properties of copper can also cause T_1 shortening [194].

9.7 Conclusions

Comparison of iron concentration, IRM at 5 K (an approximate indicator of ferritin-bound iron), R_2 and R_2* showed no statistically significant differences between control and AD tissue in the brain regions selected for this study. Despite this, discriminant analysis was used to demonstrate that the measurement of these properties can be used to differentiate between control and AD cases when data from multiple brain regions are combined. This shows that there is potential for iron changes in the brain in AD to provide a clinically useful marker of AD. A limitation of this study is that only *post mortem* samples were measured. Therefore it is now important to confirm that changes observed *post mortem* may also be observed in living persons.

A strong linear relationship between iron concentration and R_2, R_2* and R_2' was observed at 9.4 T, regardless of disease state or tissue type. The linear relationship between iron and R_2 agreed very well with the relationship predicted at 9.4 T using an empirical equation produced by Vymazal *et al.* [135], with no sign of saturation of the field dependent R_2 increase. However,

in brain regions with iron concentrations below 50 μg/g a strong linear relationship was not observed. This is in agreement with a prediction by House *et al.* [26] who gave a threshold concentration of 55 μg/g of iron, above which iron will dominate R_2.

References

[1] What is Alzheimer's disease? Alzheimer's Society, http://www.alzheimers.org.uk/site/scripts/documents_info.php?documentID=100, Accessed 30/10/13.

[2] Wimo A, Prince M (2010) Alzheimer's Disease International.

[3] Thomas P, Fenech M (2007) A review of genome mutation and Alzheimer's disease. *Mutagenesis* **22**, 15-33.

[4] Jack Jr CR, Knopman DS, Jagust WJ, Shaw LM, Aisen PS, Weiner MW, Petersen RC, Trojanowski JQ (2010) Hypothetical model of dynamic biomarkers of the Alzheimer's pathological cascade. *The Lancet Neurology* **9**, 119-128.

[5] Markesbery WR (1997) Oxidative stress hypothesis in Alzheimer's disease. *Free Radical Biology and Medicine* **23**, 134-147.

[6] Sutherland GT, Chami B, Youssef P, Witting PK (2013) Oxidative stress in Alzheimer's disease: Primary villain or physiological by-product? *Redox Report* **18**, 134-141.

[7] Quintana C, Gutierrez L (2010) Could a dysfunction of ferritin be a determinant factor in the aetiology of some neurodegenerative diseases? *Biochimica Et Biophysica Acta-General Subjects* **1800**, 770-782.

[8] Gerlach M, Benshachar D, Riederer P, Youdim MBH (1994) Altered Brain Metabolism of Iron as a Cause of Neurodegenerative Diseases. *Journal of Neurochemistry* **63**, 793-807.

[9] Noble M (2004) The possible role of myelin destruction as a precipitating event in Alzheimer's disease. *Neurobiology of Aging* **25**, 25-31.

[10] Bartzokis G (2004) Age-related myelin breakdown: a developmental model of cognitive decline and Alzheimer's disease. *Neurobiol Aging* **25**, 5-18; author reply 49-62.

[11] Dawbarn D, Allen SJ eds. (2007) *Neurobiology of Alzheimer's Disease*, Oxford University Press.

[12] McKhann G, Drachman D, Folstein M, Katzman R, Price D, Stadlan EM (1984) Clinical diagnosis of Alzheimer's disease: report of the NINCDS-ADRDA work group under the auspices of Department of Health and Human Services Task Force on Alzheimer's Disease. *Neurology* **34**, 939-944.

[13] Dubois B, Feldman HH, Jacova C, Cummings JL, DeKosky ST, Barberger-Gateau P, Delacourte A, Frisoni G, Fox NC, Galasko D, Gauthier S, Hampel H, Jicha GA, Meguro K, O'Brien J, Pasquier F, Robert P, Rossor M, Salloway S, Sarazin M, de Souza LC, Stern Y, Visser PJ, Scheltens P (2010) Revising the definition of Alzheimer's disease: a new lexicon. *The Lancet Neurology* **9**, 1118-1127.

[14] McKhann GM, Knopman DS, Chertkow H, Hyman BT, Jack CR, Jr., Kawas CH, Klunk WE, Koroshetz WJ, Manly JJ, Mayeux R, Mohs RC, Morris JC, Rossor MN, Scheltens P, Carrillo MC, Thies B, Weintraub S, Phelps CH (2011) The diagnosis of dementia due to Alzheimer's disease: Recommendations from the National Institute on Aging-Alzheimer's Association workgroups on diagnostic guidelines for Alzheimer's disease. *Alzheimers & Dementia* **7**, 263-269.

[15] Laakso MP, Partanen K, Lehtovirta M, Hallikainen M, Hanninen T, Vainio P, Riekkinen P, Soininen H (1995) MRI of amygdala fails to diagnose early Alzheimer's disease. *Neuroreport* **6**, 2414-2418.

[16] Samudralwar DL, Diprete CC, Ni BF, Ehmann WD, Markesbery WR (1995) Elemental imbalances in the olfactory pathway in Alzheimer's disease. *J Neurol Sci* **130**, 139-145.

[17] Cornett CR, Markesbery WR, Ehmann WD (1998) Imbalances of trace elements related to oxidative damage in Alzheimer's disease brain. *Neurotoxicology* **19**, 339-345.

[18] Loeffler DA, Connor JR, Juneau PL, Snyder BS, Kanaley L, Demaggio AJ, Nguyen H, Brickman CM, Lewitt PA (1995) Transferrin and Iron in Normal, Alzheimers-Disease, and Parkinsons-Disease Brain-Regions. *Journal of Neurochemistry* **65**, 710-716.

[19] House MJ, Pierre TGS, McLean C (2008) 1.4T study of proton magnetic relaxation rates, iron concentrations, and plaque burden in Alzheimer's disease and control postmortem brain tissue. *Magnetic Resonance in Medicine* **60**, 41-52.

[20] Thompson CM, Markesbery WR, Ehmann WD, Mao YX, Vance DE (1988) Regional Brain Trace-Element Studies in Alzheimers-Disease. *Neurotoxicology* **9**, 1-8.

[21] Dedman DJ, Treffry A, Candy JM, Taylor GAA, Morris CM, Bloxham CA, Perry RH, Edwardson JA, Harrison PM (1992) Iron and Aluminum in Relation to Brain Ferritin in Normal Individuals and Alzheimers-Disease and Chronic Renal-Dialysis Patients. *Biochemical Journal* **287**, 509-514.

[22] Connor JR, Snyder BS, Beard JL, Fine RE, Mufson EJ (1992) Regional Distribution of Iron and Iron-Regulatory Proteins in the Brain in Aging and Alzheimers-Disease. *Journal of Neuroscience Research* **31**, 327-335.

[23] Dexter DT, Carayon A, Javoy-Agid F, Agid Y, Wells FR, Daniel SE, Lees AJ, Jenner P, Marsden CD (1991) Alterations in the levels of iron, ferritin and other trace metals in Parkinson's disease and other neurodegenerative diseases affecting the basal ganglia. *Brain* **114 (Pt 4)**, 1953-1975.

[24] Schenck JF, Zimmerman EA (2004) High-field magnetic resonance imaging of brain iron: birth of a biomarker? *NMR Biomed* **17**, 433-445.

[25] Bizzi A, Brooks RA, Brunetti A, Hill JM, Alger JR, Miletich RS, Francavilla TL, Di Chiro G (1990) Role of iron and ferritin in MR imaging of the brain: a study in primates at different field strengths. *Radiology* **177**, 59-65.

[26] House MJ, St Pierre TG, Kowdley KV, Montine T, Connor J, Beard J, Berger J, Siddaiah N, Shankland E, Jin LW (2007) Correlation of proton transverse relaxation rates (R2) with iron concentrations in postmortem brain tissue from Alzheimer's disease patients. *Magnetic Resonance in Medicine* **57**, 172-180.

[27] Yao B, Li TQ, Gelderen P, Shmueli K, de Zwart JA, Duyn JH (2009) Susceptibility contrast in high field MRI of human brain as a function of tissue iron content. *Neuroimage* **44**, 1259-1266.

[28] Visanji NP, Collingwood JF, Finnegan ME, Tandon A, House E, Hazrati L-N (2013) Iron Deficiency in Parkinsonism: Region-Specific Iron Dysregulation in Parkinson's Disease and Multiple System Atrophy. *Journal of Parkinson's Disease*.

[29] Demography,Alzheimer's Society, http://www.alzheimers.org.uk/site/scripts/documents_info.php?documentID=412, Accessed 22/01/14.

[30] Molyneux GJ, McCarthy GM, McEniff S, Cryan M, Conroy RM (2008) Prevalence and predictors of carer burden and depression in carers of patients referred to an old age psychiatric service. *International Psychogeriatrics* **20**, 1193-1202.

[31] Masters CL, Simms G, Weinman NA, Multhaup G, McDonald BL, Beyreuther K (1985) Amyloid plaque core protein in Alzheimer disease and Down syndrome. *Proceedings of the National Academy of Sciences of the United States of America* **82**, 4245-4249.

[32] Grundkeiqbal I, Iqbal K, Tung YC, Quinlan M, Wisniewski HM, Binder LI (1986) Abnormal Phosphorylation of the Microtubule-Associated Protein-Tau (Tau) in Alzheimer Cytoskeletal Pathology. *Proceedings of the National Academy of Sciences of the United States of America* **83**, 4913-4917.

[33] Allen SJ (2001) Alzheimer's disease: past, present and future themes In *Neurobiology of Alzheimer's Disease*, Dawbarn D, Allen SJ, eds. Oxford University Press, pp. 1-32.

[34] Thompson PM, Hayashi KM, de Zubicaray G, Janke AL, Rose SE, Semple J, Herman D, Hong MS, Dittmer SS, Doddrell DM, Toga AW (2003) Dynamics of gray matter loss in Alzheimer's disease. *Journal of Neuroscience* **23**, 994-1005.

[35] Ke Y, Qian ZM (2003) Iron misregulation in the brain: a primary cause of neurodegenerative disorders. *Lancet Neurology* **2**, 246-253.
[36] Castellani RJ, Moreira PI, Liu G, Dobson J, Perry G, Smith MA, Zhu XW (2007) Iron: The redox-active center of oxidative stress in Alzheimer disease. *Neurochemical Research* **32**, 1640-1645.
[37] Smith MA, Harris PLR, Sayre LM, Perry G (1997) Iron accumulation in Alzheimer disease is a source of redox-generated free radicals. *Proceedings of the National Academy of Sciences of the United States of America* **94**, 9866-9868.
[38] Khan A, Dobson JP, Exley C (2006) Redox cycling of iron by Abeta42. *Free Radic Biol Med* **40**, 557-569.
[39] Deibel MA, Ehmann WD, Markesbery WR (1996) Copper, iron, and zinc imbalances in severely degenerated brain regions in Alzheimer's disease: Possible relation to oxidative stress. *Journal of the Neurological Sciences* **143**, 137-142.
[40] Magaki S, Raghavan R, Mueller C, Oberg KC, Vinters HV, Kirsch WM (2007) Iron, copper, and iron regulatory protein 2 in Alzheimer's disease and related dementias. *Neuroscience Letters* **418**, 72-76.
[41] Rivera-Mancia S, Perez-Neri I, Rios C, Tristan-Lopez L, Rivera-Espinosa L, Montes S (2010) The transition metals copper and iron in neurodegenerative diseases. *Chem Biol Interact* **186**, 184-199.
[42] Drayer BP (1988) Imaging of the aging brain - Part II. Pathologic Conditions. *Radiology*, 797-806.
[43] Zimny A, Bladowska J, Neska M, Petryszyn K, Guzinski M, Szewczyk P, Leszek J, Sasiadek M (2013) Quantitative MR evaluation of atrophy, as well as perfusion and diffusion alterations within hippocampi in patients with Alzheimer's disease and mild cognitive impairment. *Medical Science Monitor* **19**, 86-94.
[44] Korczyn AD (2008) The amyloid cascade hypothesis. *Alzheimer's & Dementia* **4**, 176-178.
[45] Hardy J, Selkoe DJ (2002) Medicine - The amyloid hypothesis of Alzheimer's disease: Progress and problems on the road to therapeutics. *Science* **297**, 353-356.
[46] Reitz C (2012) Alzheimer's disease and the amyloid cascade hypothesis: a critical review. *International journal of Alzheimer's disease* **2012**, 369808.
[47] Jeffries S, Burns A (2001) Clinical assessment of Alzheimer's disease In *Neurobiology of Alzheimer's DiseaseMolecular and Cellular Neurobiology Series*, Collingridge CL, Hunt SP, Rothwell NJ, eds. Oxford University Press, pp. 280-293.
[48] Dubois B, Feldman HH, Jacova C, Dekosky ST, Barberger-Gateau P, Cummings J, Delacourte A, Galasko D, Gauthier S, Jicha G, Meguro K, O'Brien J, Pasquier F, Robert P, Rossor M, Salloway S, Stern Y, Visser PJ, Scheltens P (2007) Research criteria for the diagnosis of Alzheimer's disease: revising the NINCDS-ADRDA criteria. *Lancet Neurology* **6**, 734-746.
[49] Clark CM, Xie S, Chittams J, Ewbank D, Peskind E, Galasko D, Morris JC, McKeel DW, Farlow M, Weitlauf SL, Quinn J, Kaye J, Knopman D, Arai H, Doody RS, DeCarli C, Leight S, Lee VMY, Trojanowski JQ (2003) Cerebrospinal fluid tau and beta-amyloid - How well do these biomarkers reflect autopsy-confirmed dementia diagnoses? *Archives of Neurology* **60**, 1696-1702.
[50] Morris JC, Roe CM, Grant EA, Head D, Storandt M, Goate AM, Fagan AM, Holtzman DM, Mintun MA (2009) Pittsburgh Compound B Imaging and Prediction of Progression From Cognitive Normality to Symptomatic Alzheimer Disease. *Archives of Neurology* **66**, 1469-1475.
[51] Patwardhan MB, McCrory DC, Matchar DB, Samsa GP, Rutschmann OT (2004) Alzheimer disease: Operating characteristics of PET - A meta-analysis. *Radiology* **231**, 73-80.

[52] Frisoni GB, Winblad B, O'Brien JT (2011) Revised NIA-AA criteria for the diagnosis of Alzheimer's disease: a step forward but not yet ready for widespread clinical use. *International Psychogeriatrics* **23**, 1191-1196.
[53] Frisoni GB, Bocchetta M, Chetelat G, Rabinovici GD, de Leon MJ, Kaye J, Reiman EM, Scheltens P, Barkhof F, Black SE, Brooks DJ, Carrillo MC, Fox NC, Herholz K, Nordberg A, Jack CR, Jr., Jagust WJ, Johnson KA, Rowe CC, Sperling RA, Thies W, Wahlund LO, Weiner MW, Pasqualetti P, Decarli C (2013) Imaging markers for Alzheimer disease: Which vs how. *Neurology* **81**, 487-500.
[54] Fox NC, Freeborough PA, Rossor MN (1996) Visualisation and quantification of rates of atrophy in Alzheimer's disease. *Lancet* **348**, 94-97.
[55] Fox NC, Warrington EK, Freeborough PA, Hartikainen P, Kennedy AM, Stevens JM, Rossor MN (1996) Presymptomatic hippocampal atrophy in Alzheimer's disease - A longitudinal MRI study. *Brain* **119**, 2001-2007.
[56] Bartzokis G, Cummings JL, Sultzer D, Henderson VW, Nuechterlein KH, Mintz J (2003) White matter structural integrity in healthy aging adults and patients with Alzheimer disease - A magnetic resonance imaging study. *Archives of Neurology* **60**, 393-398.
[57] Bartzokis G (2004) Age-related myelin breakdown: a developmental model of cognitive decline and Alzheimer's disease. *Neurobiology of Aging* **25**, 5-18.
[58] St Pierre TG, Clark PR, Chua-anusorn W (2004) Single spin-echo proton transverse relaxometry of iron-loaded liver. *Nmr in Biomedicine* **17**, 446-458.
[59] Nabuurs RJ, Hegeman I, Natte R, van Duinen SG, van Buchem MA, van der Weerd L, Webb AG (2010) High-field MRI of single histological slices using an inductively coupled, self-resonant microcoil: application to ex vivo samples of patients with Alzheimer's disease. *NMR Biomed*.
[60] Meadowcroft MD, Connor JR, Smith MB, Yang QX (2009) MRI and Histological Analysis of Beta-Amyloid Plaques in Both Human Alzheimer's Disease and APP/PS1 Transgenic Mice. *Journal of Magnetic Resonance Imaging* **29**, 997-1007.
[61] Vanhoutte G, Dewachter I, Borghgraef P, Van Leuven F, Van der Linden A (2005) Noninvasive in vivo MRI detection of neuritic plaques associated with iron in APP[V717I] transgenic mice, a model for Alzheimer's disease. *Magnetic Resonance in Medicine* **53**, 607-613.
[62] Sethi KD, Adams RJ, Loring DW, Elgammal T (1988) Hallervorden-Spatz Syndrome - Clinical and Magnetic-Resonance Imaging Correlations. *Annals of Neurology* **24**, 692-694.
[63] Salvador GA (2010) Iron in neuronal function and dysfunction. *Biofactors* **36**, 103-110.
[64] Bohic S, Ghersi-Egea JF, Gibon J, Paoletti P, Arnaud J, Hunot S, Boom A, Bouron A (2011) Biological roles of trace elements in the brain with special focus on Zn and Fe. *Revue Neurologique* **167**, 269-279.
[65] Curtis ARJ, Fey C, Morris CM, Bindoff LA, Ince PG, Chinnery PF, Coulthard A, Jackson MJ, Jackson AP, McHale DP, Hay D, Barker WA, Markham AF, Bates D, Curtis A, Burn J (2001) Mutation in the gene encoding ferritin light polypeptide causes dominant adult-onset basal ganglia disease. *Nature Genetics* **28**, 350-354.
[66] Harris ZL, Durley AP, Man TK, Gitlin JD (1999) Targeted gene disruption reveals an essential role for ceruloplasmin in cellular iron efflux. *Proceedings of the National Academy of Sciences* **96**, 10812-10817.
[67] Batista-Nascimento L, Pimentel C, Menezes RA, Rodrigues-Pousada C (2012) Iron and Neurodegeneration: From Cellular Homeostasis to Disease. *Oxidative Medicine and Cellular Longevity*.
[68] Johannesson P, Kristinsson J, Porsdottir G, Snaedal J (2012) Ceruloplasmin (Cp) and iron in connection with Parkinson's disease (PD) and Alzheimer's disease (AD). *Laeknabladid* **98**, 531-537.
[69] Loeffler DA, LeWitt PA, Juneau PL, Sima AAF, Nguyen HU, DeMaggio AJ, Brickman CM, Brewer GJ, Dick RD, Troyer MD, Kanaley L (1996) Increased regional brain

concentrations of ceruloplasmin in neurodegenerative disorders. *Brain Research* **738**, 265-274.
[70] Harrison PM, Arosio P (1996) Ferritins: Molecular properties, iron storage function and cellular regulation. *Biochimica Et Biophysica Acta-Bioenergetics* **1275**, 161-203.
[71] Jomova K, Baros S, Valko M (2012) Redox active metal-induced oxidative stress in biological systems. *Transition Metal Chemistry* **37**, 127-134.
[72] Fahn S, Cohen G (1992) The oxidant stress hypothesis in Parkinson's disease: evidence supporting it. *Annals of Neurology* **32**, 804-812.
[73] Jomova K, Vondrakova D, Lawson M, Valko M (2010) Metals, oxidative stress and neurodegenerative disorders. *Molecular and Cellular Biochemistry* **345**, 91-104.
[74] Morris CM, Candy JM, Keith AB, Oakley AE, Taylor GA, Pullen RGL, Bloxham CA, Gocht A, Edwardson JA (1992) BRAIN IRON HOMEOSTASIS. *Journal of Inorganic Biochemistry* **47**, 257-265.
[75] Collingwood JF, Dobson J (2008) Nanoscale Iron Compounds Related to Neurodegenerative Disorders In *Biomedical Nanostructures*, Gonsalves KE, Laurenein CL, Halberstadt CR, eds. John Wikey & Sons, Inc., pp. 455 - 484.
[76] Chasteen ND, Harrison PM (1999) Mineralization in ferritin: An efficient means of iron storage. *Journal of Structural Biology* **126**, 182-194.
[77] Quintana C, Cowley JM, Marhic C (2004) Electron nanodiffraction and high-resolution electron microscopy studies of the structure and composition of physiological and pathological ferritin. *Journal of Structural Biology* **147**, 166-178.
[78] Quintana C, Bellefqih S, Laval JY, Guerquin-Kern JL, Wu TD, Avila J, Ferrer I, Arranz R, Patino C (2006) Study of the localization of iron, ferritin, and hemosiderin in Alzheimer's disease hippocampus by analytical microscopy at the subcellular level. *Journal of Structural Biology* **153**, 42-54.
[79] Oconnell M, Halliwell B, Moorhouse CP, Aruoma OI, Baum H, Peters TJ (1986) Formation of hydroxyl radicals in the presence of ferritin and hemosiderin. Is hemosiderin formation a biological protective mechanism? *Biochemical Journal* **234**, 727-731.
[80] Kirschvink JL, Kobayashikirschvink A, Woodford BJ (1992) Magnetite Biomineralization in the Human Brain. *Proceedings of the National Academy of Sciences of the United States of America* **89**, 7683-7687.
[81] Schultheiss-Grassi PP, Wessiken R, Dobson J (1999) TEM investigations of biogenic magnetite extracted from the human hippocampus. *Biochimica Et Biophysica Acta-General Subjects* **1426**, 212-216.
[82] Collingwood JF, Mikhaylova A, Davidson M, C B, Steirt WJ, Terry J, Dobson J (2005) *In situ* characterisation and mapping of iron compounds in Alzheimer's disease tissue. *Jornal of Alzheimer's Disease* **7**, 267-272.
[83] Hautot D, Pankhurst QA, Morris CM, Curtis A, Burn J, Dobson J (2007) Preliminary observation of elevated levels of nanocrystalline iron oxide in the basal ganglia of neuroferritinopathy patients. *Biochimica Et Biophysica Acta-Molecular Basis of Disease* **1772**, 21-25.
[84] Dobson J (2002) Investigation of age-related variations in biogenic magnetite levels in the human hippocampus. *Experimental Brain Research* **144**, 122-126.
[85] Zecca L, Gallorini M, Schünemann V, Trautwein AX, Gerlach M, Riederer P, Vezzoni P, Tampellini D (2001) Iron, neuromelanin and ferritin content in the substantia nigra of normal subjects at different ages: consequences for iron storage and neurodegenerative processes. *Journal of Neurochemistry* **76**, 1766-1773.
[86] Gerlach M, Trautwein AX, Zecca L, Youdim MBH, Riederer P (1995) Mössbauer Spectroscopic Studies of Purified Human Neuromelanin Isolated from the Substantia Nigra. *Journal of Neurochemistry* **65**, 923-926.

[87] Gałązka-Friedman J, Bauminger ER, Friedman A, Barcikowska M, Hechel D, Nowik I (1996) Iron in parkinsonian and control substantia nigra—A mössbauer spectroscopy study. *Movement Disorders* **11**, 8-16.
[88] Bolzoni F, Giraudo S, Lopiano L, Bergamasco B, Fasano M, Crippa PR (2002) Magnetic investigations of human mesencephalic neuromelanin. *Biochimica et Biophysica Acta (BBA) - Molecular Basis of Disease* **1586**, 210-218.
[89] Popescu BFG, George MJ, Bergmann U, Garachtchenko AV, Kelly ME, McCrea RPE, Luning K, Devon RM, George GN, Hanson AD, Harder SM, Chapman LD, Pickering IJ, Nichol H (2009) Mapping metals in Parkinson's and normal brain using rapid-scanning x-ray fluorescence. *Physics in Medicine and Biology* **54**, 651-663.
[90] Hopp K, Popescu BF, McCrea RP, Harder SL, Robinson CA, Haacke ME, Rajput AH, Rajput A, Nichol H (2010) Brain iron detected by SWI high pass filtered phase calibrated with synchrotron X-ray fluorescence. *J Magn Reson Imaging* **31**, 1346-1354.
[91] Gellein K, Flaten TP, Erikson KM, Aschner M, Syversen T (2008) Leaching of trace elements from biological tissue by formalin fixation. *Biol Trace Elem Res* **121**, 221-225.
[92] Morris CM, Candy JM, Oakley AE, Bloxham CA, Edwardson JA (1992) Histochemical Distribution of Nonhaem Iron in the Human Brain. *Acta Anatomica* **144**, 235-257.
[93] Hallgren B, Sourander P (1958) The effect of age on the non-haemin iron in the human brain. *Journal of neurochemistry* **3**, 41-51.
[94] Bartzokis G, Tishler TA, Lu PH, Villablanca P, Altshuler LL, Carter M, Huang D, Edwards N, Mintz J (2007) Brain ferritin iron may influence age- and gender-related risks of neurodegeneration. *Neurobiology of Aging* **28**, 414-423.
[95] Goodman L (1953) Alzheimer's disease: A Clinico-pathologic Analysis of Twenty-three Cases with a Theory on Pathogenesis. *The Journal of Nervous and Mental Disease* **118**, 97-130.
[96] Connor JR, Menzies SL, Stmartin SM, Mufson EJ (1992) A Histochemical-Study of Iron, Transferrin, and Ferritin in Alzheimers Diseased Brains. *Journal of Neuroscience Research* **31**, 75-83.
[97] Hallgren B, Sourander P (1960) The non-haemin iron in the cerebral cortex in Alzheimer's disease. *J Neurochem* **5**, 307-310.
[98] Chamberlain R, Reyes D, Curran GL, Marjanska M, Wengenack TM, Poduslo JF, Garwood M, Jack CR (2009) Comparison of Amyloid Plaque Contrast Generated by T-2-Weighted, T-2(star)-Weighted, and Susceptibility-Weighted Imaging Methods in Transgenic Mouse Models of Alzheimer's Disease. *Magnetic Resonance in Medicine* **61**, 1158-1164.
[99] Kiernan JA (2008) *Histological and Histochemical Methods: Theory and Practice*, Scion Publishing Limited.
[100] Levine SM (1991) Oligodendrocytes and myelin sheaths in normal, quaking and shiverer brains are enriched in iron. *Journal of Neuroscience Research* **29**, 413-419.
[101] Connor JR, Menzies SL, Stmartin SM, Mufson EJ (1990) Cellular-Distribution of Transferrin, Ferritin, and Iron in Normal and Aged Human Brains. *Journal of Neuroscience Research* **27**, 595-611.
[102] Perl DP, Good PF (1992) Comparative Techniques for Determining Cellular Iron Distribution in Brain-Tissues. *Annals of Neurology* **32**, S76-S81.
[103] Lopes KO, Sparks DL, Streit WJ (2008) Microglial dystrophy in the aged and Alzheimer's disease brain is associated with ferritin immunoreactivity. *Glia* **56**, 1048-1060.
[104] Ha Y, Tsay OG, Churchill DG (2011) A tutorial and mini-review of the ICP-MS technique for determinations of transition metal ion and main group element concentration in the neurodegenerative and brain sciences. *Monatshefte Fur Chemie* **142**, 385-398.
[105] Chen JC, Hardy PA, Clauberg M, Joshi JG, Parravano J, Deck JH, Henkelman RM, Becker LE, Kucharczyk W (1989) T2 values in the human brain: comparison with quantitative assays of iron and ferritin. *Radiology* **173**, 521-526.

[106] Griffiths PD, Crossman AR (1993) Distribution of iron in the basal ganglia and neocortex in postmortem tissue in Parkinson's disease and Alzheimer's disease. *Dementia* **4**, 61-65.
[107] Haacke ME, Cheng NYC, House MJ, Liu Q, Neelavlli J, Ogg RJ, Khan A, Ayaz M, Kirsch W, Obernaus A (2005) Imaging iron stores in the brain using magnetic resonance imaging. *Magnetic Resonance Imaging* **23**, 1-25.
[108] Hautot D, Pankhurst QA, Dobson J (2005) Superconducting quantum interference device measurements of dilute magnetic materials in biological samples. *Review of Scientific Instruments* **76**.
[109] Dunn JR, Fuller M, Zoeger J, Dobson J, Heller F, Hammann J, Caine E, Moskowitz BM (1995) Magnetic material in the human hippocampus. *Brain Research Bulletin* **36**, 149-153.
[110] Pankhurst Q, Hautot D, Khan N, Dobson J (2008) Increased levels of magnetic iron compounds in Alzheimer's disease. *J Alzheimers Dis* **13**, 49-52.
[111] Ugarte M, Grime GW, Lord G, Geraki K, Collingwood JF, Finnegan ME, Farnfield H, Merchant M, Bailey MJ, Ward NI, Foster PJ, Bishop PN, Osborne NN (2012) Concentration of various trace elements in the rat retina and their distribution in different structures. *Metallomics* **4**, 1245-1254.
[112] Gallagher JJ, Finnegan ME, Grehan B, Dobson J, Collingwood JF, Lynch MA (2012) Modest Amyloid Deposition is Associated with Iron Dysregulation, Microglial Activation, and Oxidative Stress. *Journal of Alzheimers Disease* **28**, 147-161.
[113] Collingwood J, Dobson J (2006) Mapping and characterization of iron compounds in Alzheimer's tissue. *Journal of Alzheimers Disease* **10**, 215-222.
[114] Lovell MA, Robertson JD, Teesdale WJ, Campbell JL, Markesbery WR (1998) Copper, iron and zinc in Alzheimer's disease senile plaques. *Journal of the Neurological Sciences* **158**, 47-52.
[115] Collingwood JF, Chong RKK, Kasama T, Cervera-Gontard L, Dunin-Barkowski RE, Perry G, Posfai M, Siedlak SL, Simpson ET, Smith MA, Dobson J (2008) Three-Dimensional Tomographic Imaging and Charaterization of Iron Compounds within Alzheimer's Plaque Care Material. *Jornal of Alzheimer's Disease* **14**, 235-245.
[116] Quintana C, Lancin M, Marhic C, Perez M, Martin-Benito J, Avila J, Carrascosa JL (2000) Initial studies with high resolution TEM and electron energy loss spectroscopy studies of ferritin cores extracted from brains of patients with progressive supranuclear palsy and Alzheimer disease. *Cellular and Molecular Biology* **46**, 807-820.
[117] Bertsch PM, Hunter DB (2001) Applications of synchrotron-based X-ray microprobes. *Chemical Reviews* **101**, 1809-1842.
[118] Becker JS, Zoriy M, Becker JS, Dobrowolska J, Matusch A (2007) Laser ablation inductively coupled plasma mass spectrometry (LA-ICP-MS) in elemental imaging of biological tissues and in proteomics. *Journal of Analytical Atomic Spectrometry* **22**, 736-744.
[119] Becker JS, Zoriy M, Matusch A, Wu B, Salber D, Palm C, Becker JS (2010) Bioimaging of Metals by Laser Ablation Inductively Coupled Plasma Mass Spectrometry (La-Icp-Ms). *Mass Spectrometry Reviews* **29**, 156-175.
[120] Vymazal J, Brooks RA, Zak O, McRill C, Shen C, Dichiro G (1992) T1 and T2 of ferritin at different field strengths: effect on MRI. *Magnetic Resonance in Medicine* **27**, 368-374.
[121] Gossuin Y, Burtea C, Monseux A, Toubeau G, Roch A, Muller RN, Gillis P (2004) Ferritin-induced relaxation in tissues: an in vitro study. *J Magn Reson Imaging* **20**, 690-696.
[122] Manz C, Godau J, Berg D, Bender B, Ernemann U, Klose U (2010) The regional distribution of T2-relaxation times in MR images of the substantia nigra and crus cerebri. *Neuroradiology* **52**, 745-750.
[123] Langkammer C, Krebs N, Goessler W, Scheurer E, Ebner F, Yen K, Fazekas F, Ropele S (2010) Quantitative MR imaging of brain iron: a postmortem validation study. *Radiology* **257**, 455-462.

[124] Bartzokis G, Aravagiri M, Oldendorf WH, Mintz J, Marder SR (1993) Field-Dependent Transverse Relaxation Rate Increase May Be a Specific Measure of Tissue Iron Stores. *Magnetic Resonance in Medicine* **29**, 459-464.
[125] Bartzokis G, Sultzer D, Mintz J, Holt LE, Marx P, Phelan CK, Marder SR (1994) In vivo evaluation of brain iron in Alzheimer's disease and normal subjects using MRI. *Biol Psychiatry* **35**, 480-487.
[126] Bartzokis G, Tishler TA, Shin IS, Lu PH, Cummings JL (2004) Brain ferritin iron as a risk factor for age at onset in neurodegenerative diseases. *Redox-Active Metals in Neurological Disorders* **1012**, 224-236.
[127] Bartzokis G, Tishler TA (2000) MRI evaluation of basal ganglia ferritin iron and neurotoxicity in Alzheimer's and Huntingon's disease. *Cell Mol Biol (Noisy-le-grand)* **46**, 821-833.
[128] Bondareff W, Raval J, Colletti PM, Hauser DL (1988) Quantitative magnetic resonance imaging and the severity of dementia in Alzheimer's disease. *American Journal of Psychiatry* **145**, 853-856.
[129] Ordidge RJ, Gorell JM, Deniau JC, Knight RA, Helpern JA (1994) Assessment of relative brain iron concentrations using T2-weighted and T2*-weighted MRI at 3 Tesla. *Magnetic Resonance in Medicine* **32**, 335-341.
[130] Haacke EM, Xu YB, Cheng YCN, Reichenbach JR (2004) Susceptibility weighted imaging (SWI). *Magnetic Resonance in Medicine* **52**, 612-618.
[131] Manova ES, Habib CA, Boikov AS, Ayaz M, Khan A, Kirsch WM, Kido DK, Haacke EM (2009) Characterizing the mesencephalon using susceptibility-weighted imaging. *AJNR Am J Neuroradiol* **30**, 569-574.
[132] Antharam V, Collingwood JF, Bullivant JP, Davidson MR, Chandra S, Mikhaylova A, Finnegan ME, Batich C, Forder JR, Dobson J (2012) High field magnetic resonance microscopy of the human hippocampus in Alzheimer's disease: Quantitative imaging and correlation with iron. *Neuroimage* **59**, 1249-1260.
[133] Bartzokis G, Sultzer D, Cummings J, Holt LE, Hance DB, Henderson VW, Mintz J (2000) In Vivo Evaluation of Brain Iron in Alzheimer Disease Using Magnetic Resonance Imaging. *Achives of General Psychiatry* **57**, 47-53.
[134] Gelman N, Gorell JM, Barker PB, Savage RM, Spickler EM, Windham JP, Knight RA (1999) MR imaging of human brain at 3.0 T: preliminary report on transverse relaxation rates and relation to estimated iron content. *Radiology* **210**, 759-767.
[135] Vymazal J, Brooks RA, Baumgarner C, Tran V, Katz D, Bulte JWM, Bauminger ER, DiChiro G (1996) The relation between brain iron and NMR relaxation times: An in vitro study. *Magnetic Resonance in Medicine* **35**, 56-61.
[136] McCrea RPE, Harder SL, Martin M, Buist R, Nichol H (2008) A comparison of rapid-scanning X-ray fluorescence mapping and magnetic resonance imaging to localize brain iron distribution. *European Journal of Radiology* **68**, S109-S113.
[137] Ding B, Chen KM, Ling HW, Sun F, Li X, Wan T, Chai WM, Zhang H, Zhan Y, Guan YJ (2009) Correlation of Iron in the Hippocampus with MMSE in Patients with Alzheimer's Disease. *Journal of Magnetic Resonance Imaging* **29**, 793-798.
[138] Laakso MP, Partanen K, Soininen H, Lehtovirta M, Hallikainen M, Hanninen T, Helkala EL, Vainio P, Riekkinen PJ, Sr. (1996) MR T2 relaxometry in Alzheimer's disease and age-associated memory impairment. *Neurobiol Aging* **17**, 535-540.
[139] Zhu WZ, Zhong WD, Wang W, Zhan CJ, Wang CY, Qi JP, Wang JZ, Lei T (2009) Quantitative MR phase-corrected imaging to investigate increased brain iron deposition of patients with Alzheimer disease. *Radiology* **253**, 497-504.
[140] Akatsu H, Hori A, Yamamoto T, Yoshida M, Mimuro M, Hashizume Y, Tooyama I, Yezdimer EM (2012) Transition metal abnormalities in progressive dementias. *Biometals* **25**, 337-350.

[141] Hautot D, Pankhurst QA, Khan N, Dobson J (2003) Preliminary evaluation of nanoscale biogenic magnetite in Alzheimer's disease brain tissue. *Proceedings of the Royal Society B-Biological Sciences* **270**, S62-S64.
[142] House E, Collingwood JF, Khan A, Korchazkina O, Berthon G, Exley C (2004) Aluminium, iron, zinc and copper influence the *in vitro* formation of amyloid fibrils of $A\beta_{42}$ in a manner which may have consequences for metal chelation theropy in Alzheimer's disease. *Jornal of Alzheimer's Disease* **6**, 291-301.
[143] Huesgen CT, Burger PC, Crain BJ, Johnson GA (1993) In vitro MR microscopy of the hippocampus in Alzheimer's disease. *Neurology* **43**, 145-152.
[144] Brar S, Henderson D, Schenck J, Zimmerman EA (2009) Iron accumulation in the substantia nigra of patients with Alzheimer disease and parkinsonism. *Arch Neurol* **66**, 371-374.
[145] Antonini A, Leenders KL, Meier D, Oertel WH, Boesiger P, Anliker M (1993) T2 relaxation time in patients with Parkinson's disease. *Neurology* **43**, 697-700.
[146] Sofic E, Riederer P, Heinsen H, Beckmann H, Reynolds GP, Hebenstreit G, Youdim MBH (1988) Increased iron(III) and total iron content in post-mortem substantia nigra of Parkinsonian brain. *Journal of Neural Transmission* **74**, 199-205.
[147] Oakley AE, Collingwood JF, Dobson J, Love G, Perrott HR, Edwardson JA, Elstner M, Morris CM (2007) Individual dopaminergic neurons show raised iron levels in Parkinson disease. *Neurology* **68**, 1819-1826.
[148] Westbrook C, Kaut Roth C, Talbot J (1993) *MRI In Practice*, Blackwell Publishing.
[149] Haacke EM, Brown RW, Thompson MR, Venkatesan R (1999) *Magnetic Resonance Imaging: Physical Principles and Sequence Design*, Wiley.
[150] Bell SH, Weir MP, Dickson DPE, Gibson JF, Sharp GA, Peters TJ (1984) Mossbauer spectroscopic studies of human hemosiderin and ferritin. *Biochimica Et Biophysica Acta* **787**, 227-236.
[151] Schenck JF (1996) The role of magnetic susceptibility in magnetic resonance imaging: MRI magnetic compatibility of the first and second kinds. *Medical Physics* **23**, 815-850.
[152] Vollath D (2013) Wiley, Hoboken.
[153] Vymazal J, Brooks RA, Patronas N, Hajek M, Bulte JWM, DiChiro G (1995) Magnetic resonance imaging of brain iron in health and disease. *Journal of the Neurological Sciences* **134**, 19-26.
[154] Cho SB, Kim BJ, Suh BJ, Jang ZH (2004) Comparison of the magnetic properties of natural ferritin with those of aggregated magnetic core of ferritin. *Journal of the Korean Physical Society* **45**, 485-489.
[155] Schenck JF (2003) Magnetic resonance imaging of brain iron. *J Neurol Sci* **207**, 99-102.
[156] Schenck JF (1995) Imaging of brain iron by magnetic resonance: T2 relaxation at different field strengths. *J Neurol Sci* **134 Suppl**, 10-18.
[157] Vymazal J, Zak O, Bulte JWM, Aisen P, Brooks RA (1996) T-1 and T-2 of ferritin solutions: Effect of loading factor. *Magnetic Resonance in Medicine* **36**, 61-65.
[158] Na HB, Song IC, Hyeon T (2009) Inorganic Nanoparticles for MRI Contrast Agents. *Advanced Materials* **21**, 2133-2148.
[159] Gossuin Y, Hautot D, Muller RN, Pankhurst Q, Dobson J, Morris C, Gillis P, Collingwood J (2005) Looking for biogenic magnetite in brain ferritin using NMR relaxometry. *Nmr in Biomedicine* **18**, 469-472.
[160] Jernigan TL, Archibald SL, Berhow MT, Sowell ER, Foster DS, Hesselink JR (1991) Cerebral structure on MRI, Part I: Localization of age-related changes. *Biological Psychiatry* **29**, 55-67.
[161] Bartzokis G, Sultzer D, Lu PH, Neuchterlein KH, Mintz J, Cummings JL (2004) Heterogeneous age-related breakdown of white matter structural integrity: implications for cortical "disconnection" in aging and Alzheimer's diesase. *Neurobiology of Aging* **25**, 843-851.

[162] Lauffer RB (1987) Paramagnetic metal complexes as water proton relaxation agents for NMR imaging: theory and design. *Chemical Reviews* **87**, 901-927.
[163] Kamman RL, Go KG, Stomp GP, Hulstaert CE, Berendsen HJC (1985) Changes of relaxation times T1 and T2 in rat tissues after biopsy and fixation. *Magnetic Resonance Imaging* **3**, 245-250.
[164] Kamman RL, Go KG, Brouwer W, Berendsen HJC (1988) Nuclear Magnetic-Resonance Relaxation in Experimental Brain Edema - Effects of Water Concentration, Protein-Concentration, and Temperature. *Magnetic Resonance in Medicine* **6**, 265-274.
[165] Thompson A, Attwood D, Gullikson E, Howells M, Kim K-J, Kirz J, Kortright J, Lindau I, Liu Y, Pianetta P, Robinson A, Scofield J, Underwood J, Williams G (2009) *X-ray Data Booklet*, Lawrence Berkeley National Laboratory, University of California.
[166] Barrios FA, Baue C eds. (2013) *Basal Ganglia - An Integrative View*, InTech.
[167] Mai JK, Paxinos G, Voss T (2008) *Atlas of the human brain*, Academic Press.
[168] Leisman G, Melillo R, Carrick FR (2013) in *Basal Ganglia - An Integrative View* InTech.
[169] Seger CA, Cincotta CM (2005) The roles of the caudate nucleus in human classification learning. *Journal of Neuroscience* **25**, 2941-2951.
[170] Diamond MC, Scheibel AB, Elson LM (1985) *The Human Brain Coloring Book*, HarperPerennial.
[171] Haines DE (2011) *Neuroanatomy: An Atlas of Structures, Sections, and Systems*, Wolters Kluwer/ Lippincott Williams & Wilkins Health.
[172] Crossman AR (2008) Neuroanatomy In *Gray's Anatomy: The Anatomical Basis of Clinical Practice* Elsevier Health Sciences UK, pp. 289-290.
[173] Vargas JP, López JC, PortavellaKnafo M (2012) in *The Amygdala - A Discrete Multitasking Manager*, ed. Ferry DB InTech.
[174] Knafo S (2012) in *The Amygdala - A Discrete Multitasking Manager*, ed. Ferry DB InTech.
[175] Esiri MM (1996) The neuropathology of Alzheimer's disease In *Neurobiology of Alzheimer's disease*, Dawbarn D, Allen S, eds., pp. 157-158.
[176] Schmahmann JD, Ko R, MacMore J (2004) The human basis pontis: motor syndromes and topographic organization. *Brain* **127**, 1269-1291.
[177] Braak H, Braak E (1995) Staging of Alzheimer's disease-related neurofibrillary changes. *Neurobiol Aging* **16**, 271-278; discussion 278-284.
[178] Van Geet AL (1968) Calibration of the methanol and glycol nuclear magnetic resonance thermometers with a static thermistor probe. *Analytical Chemistry* **40**, 2227-2229.
[179] Collingwood JF, Chandra S, Davidson M, Mikhaylova A, Eksin T, Dobson J, Forder J, Batich C (2008) High-resolution magnetic resonance imaging to quantify relaxation parameters in Alzheimer's brain tissue. *Alzheimers & Dementia* **4**.
[180] Schneider CA, Rasband WS, Eliceiri KW (2012) NIH Image to ImageJ: 25 years of image analysis. *Nature Methods* **9**, 671-675.
[181] Manz B, Import Buker NMR Files, http://rsb.info.nih.gov/ij/plugins/bruker.html, Accessed 9th August.
[182] Prodanov D, MRI Processor, http://imagejdocu.tudor.lu/doku.php?id=plugin:filter:mri_processor:start, Accessed 9th August.
[183] Sole VA, Papillon E, Cotte M, Walter P, Susini J (2007) A multiplatform code for the analysis of energy-dispersive X-ray fluorescence spectra. *Spectrochimica Acta Part B-Atomic Spectroscopy* **62**, 63-68.
[184] IBM SPSS guides,Laerd Statistics, https://statistics.laerd.com/, Accessed 10/10/2013.
[185] One-way ANOVA in SPSS [Statistics website],Laerd Statistics, https://statistics.laerd.com/, Accessed 10/10/2013.
[186] Kilcoyne SH, Cywinski R (1995) Ferritin - a Model Superparamagnet. *Journal of Magnetism and Magnetic Materials* **140**, 1466-1467.

[187] Morales MP, Veintemillas-Verdaguer S, Montero MI, Serna CJ, Roig A, Casas L, Martinez B, Sandiumenge F (1999) Surface and internal spin canting in gamma-Fe2O3 nanoparticles. *Chemistry of Materials* **11**, 3058-3064.

[188] Damier P, Hirsch EC, Agid Y, Graybiel AM (1999) The substantia nigra of the human brain - II. Patterns of loss of dopamine-containing neurons in Parkinson's disease. *Brain* **122**, 1437-1448.

[189] Damier P, Hirsch EC, Agid Y, Graybiel AM (1999) The substantia nigra of the human brain - I. Nigrosomes and the nigral matrix, a compartmental organization based on calbindin D-28K immunohistochemistry. *Brain* **122**, 1421-1436.

[190] Mikhaylova A, Davidson M, Toastmann H, Channell JET, Guyodo Y, Batich C, Dobson J (2005) Detection, identification and mapping of iron anomalies in brain tissue using X-ray absorption spectroscopy. *Journal of the Royal Society Interface* **2**, 33-37.

[191] Schenck JF, Zimmerman EA, Li Z, Adak S, Saha A, Tandon R, Fish KM, Belden C, Gillen RW, Barba A, Henderson DL, Neil W, O'Keefe T (2006) High-field magnetic resonance imaging of brain iron in Alzheimer disease. *Top Magn Reson Imaging* **17**, 41-50.

[192] Davenport AJ, Forsyth M, Britton MM (2010) Visualisation of chemical processes during corrosion of zinc using magnetic resonance imaging. *Electrochemistry Communications* **12**, 44-47.

[193] Kamman RL, Go KG, Brouwer W, Berendsen HJC (1988) Nuclear magnetic resonance relaxation in experimental brain edema: Effects of water concentration, protein concentration, and temperature. *Magnetic Resonance in Medicine* **6**, 265-274.

[194] Warakaulle DR, Anslow P (2003) Differential Diagnosis of Intracranial Lesions with High Signal on T1 or Low Signal on T2-weighted MRI. *Clinical Radiology* **58**, 922-933.

Appendix A: Brain anatomy reference material

The following images of coronal sections of the brain were used to determine the approximate anatomical position of the caudate nucleus, putamen, globus pallidus and amygdala samples. Below is a summary of the set of continuous sections and the following pages show the anatomy of the target regions for this study in more detail. The images are reproduced from thehumanbrain.info.

-15 mm

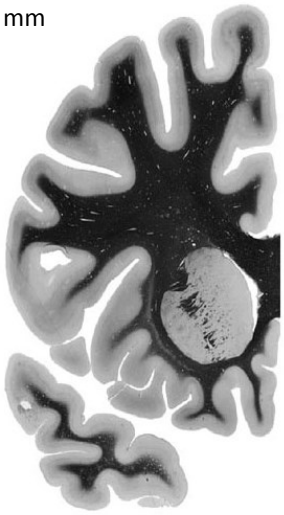

-7.5 mm

-1.3 mm

0.0 mm

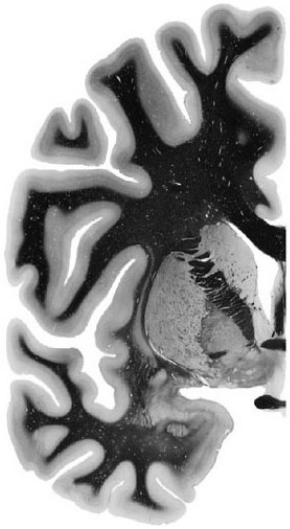

4.0 mm

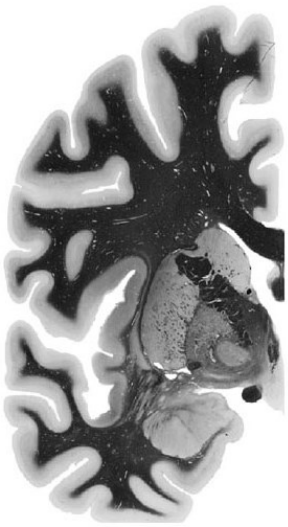

8.0 mm

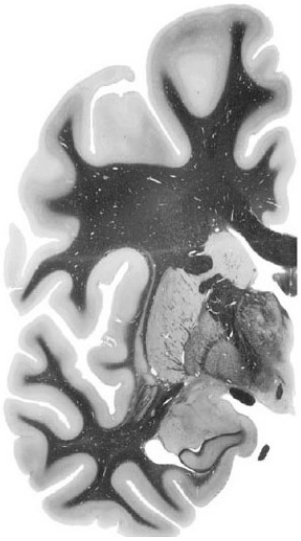

12.0 mm

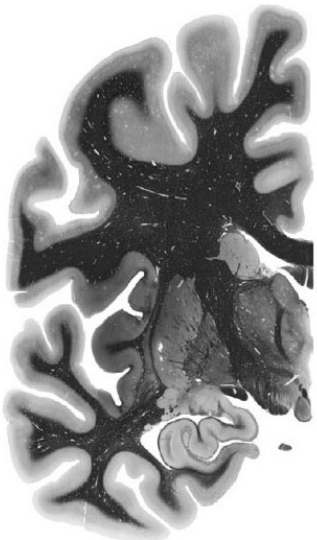

16.0 mm

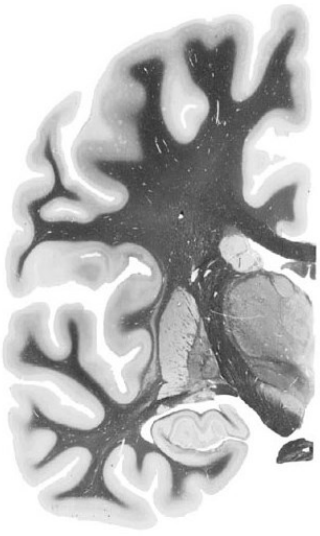

19.9mm

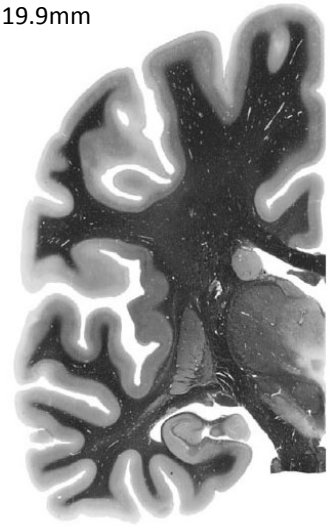

The caudate nucleus and putamen

-15.0 mm

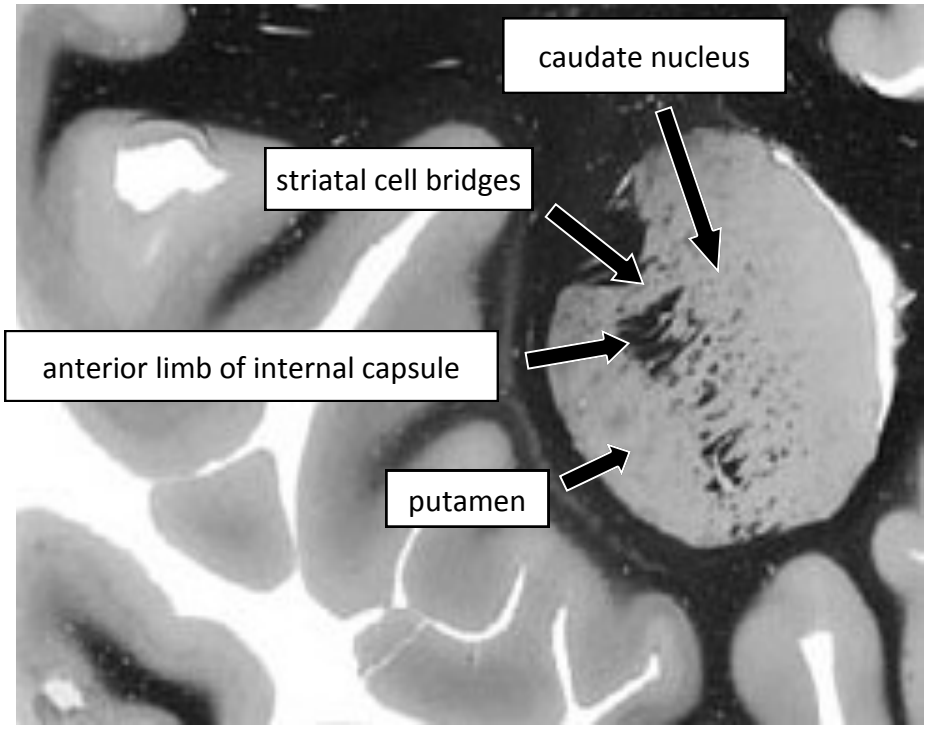

-7.5 mm

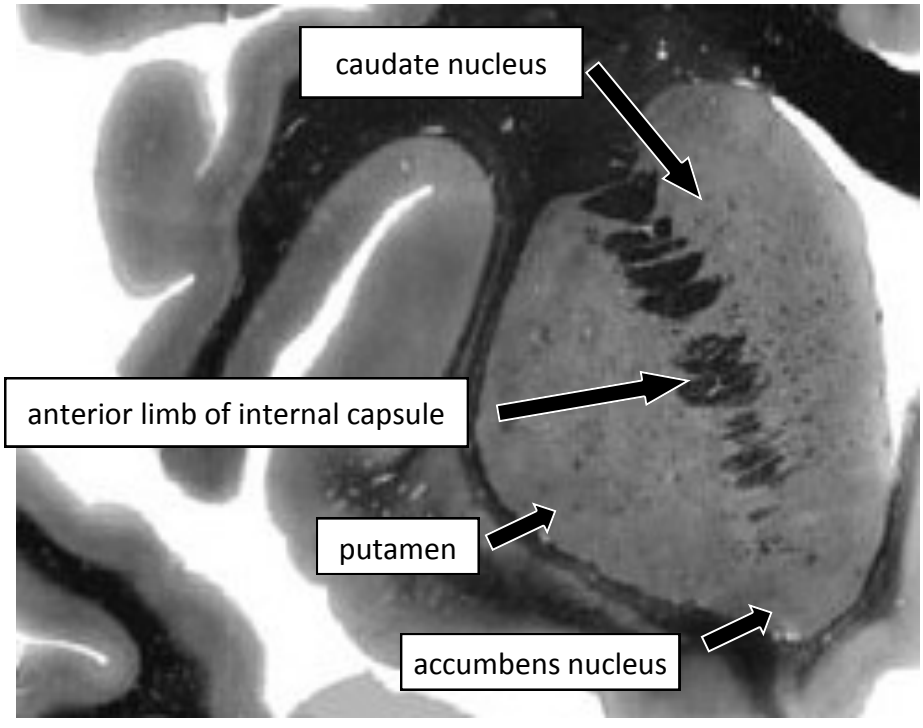

The globus pallidus

-1.3mm

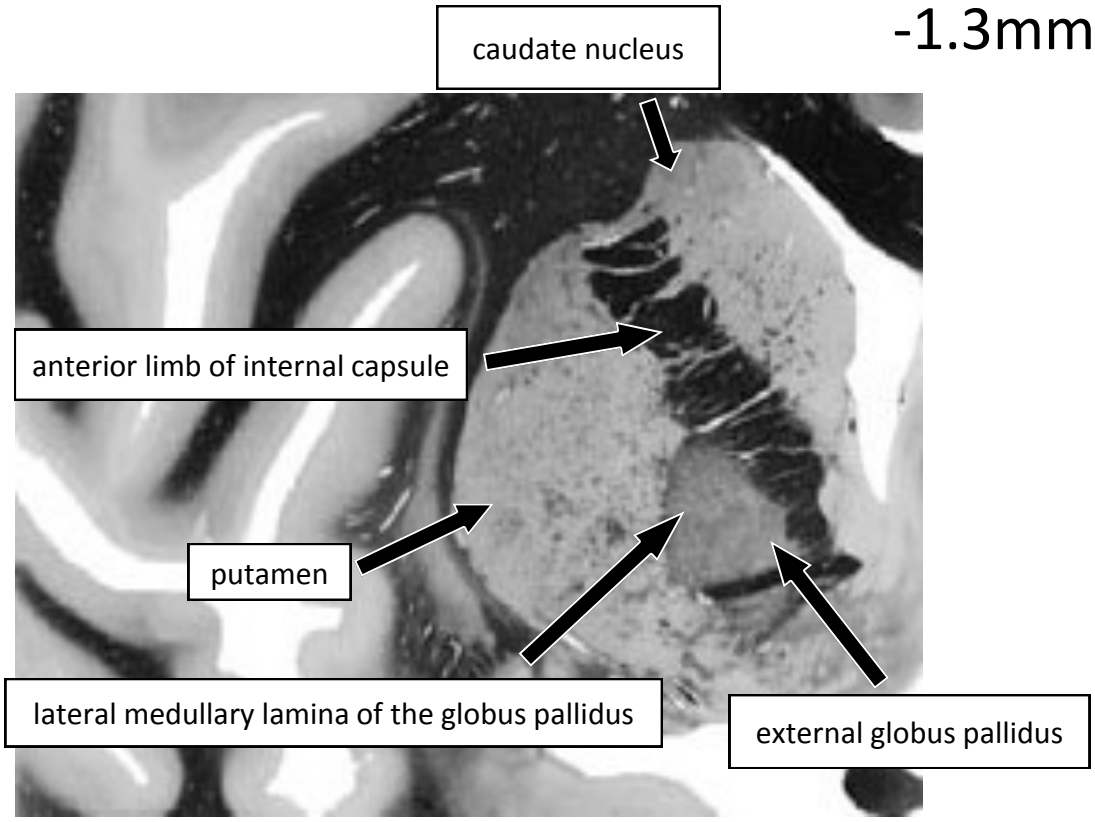

0.0 mm

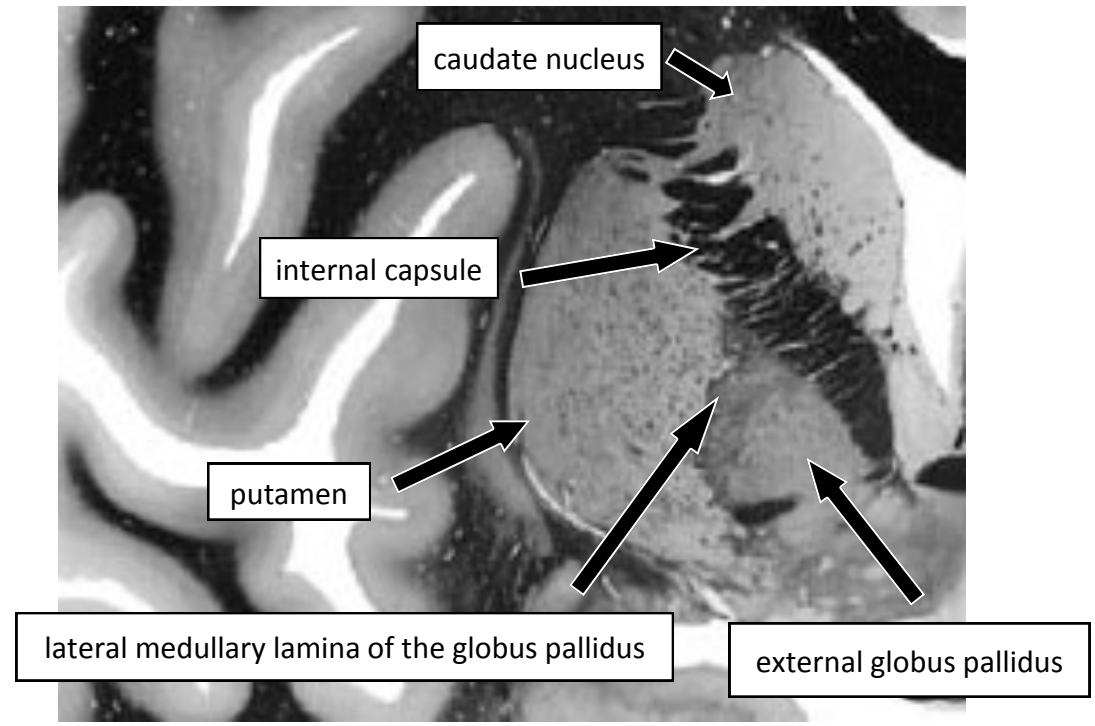

The globus pallidus

4.0mm

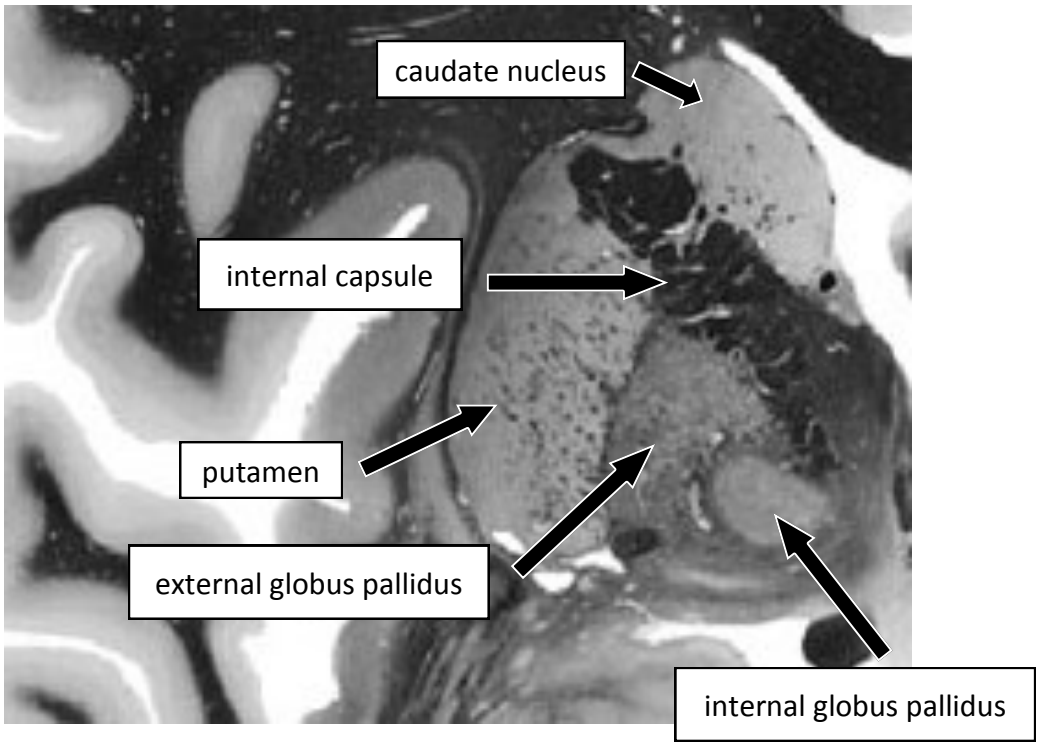

8.0mm

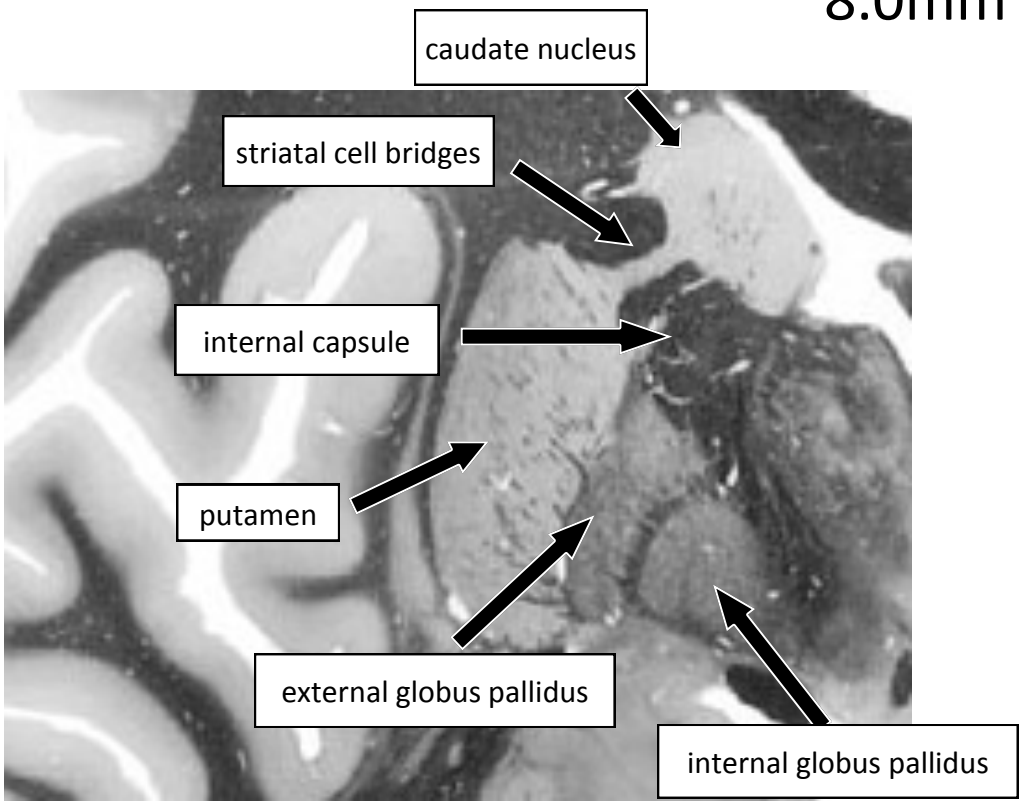

The globus pallidus

12.0mm

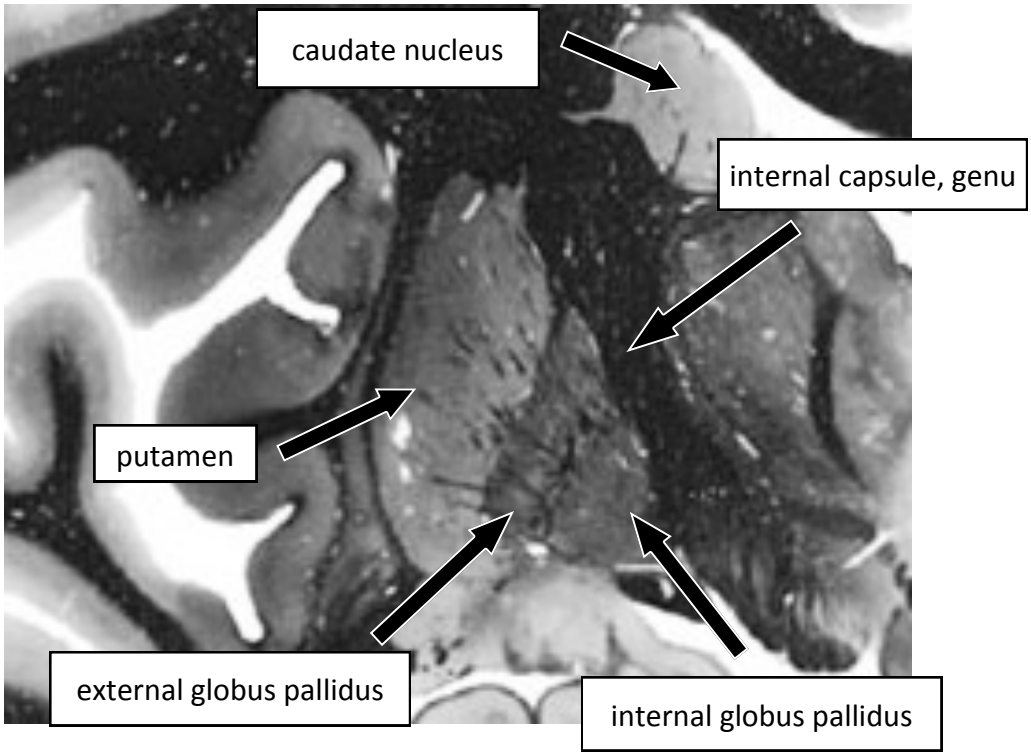

16.0mm

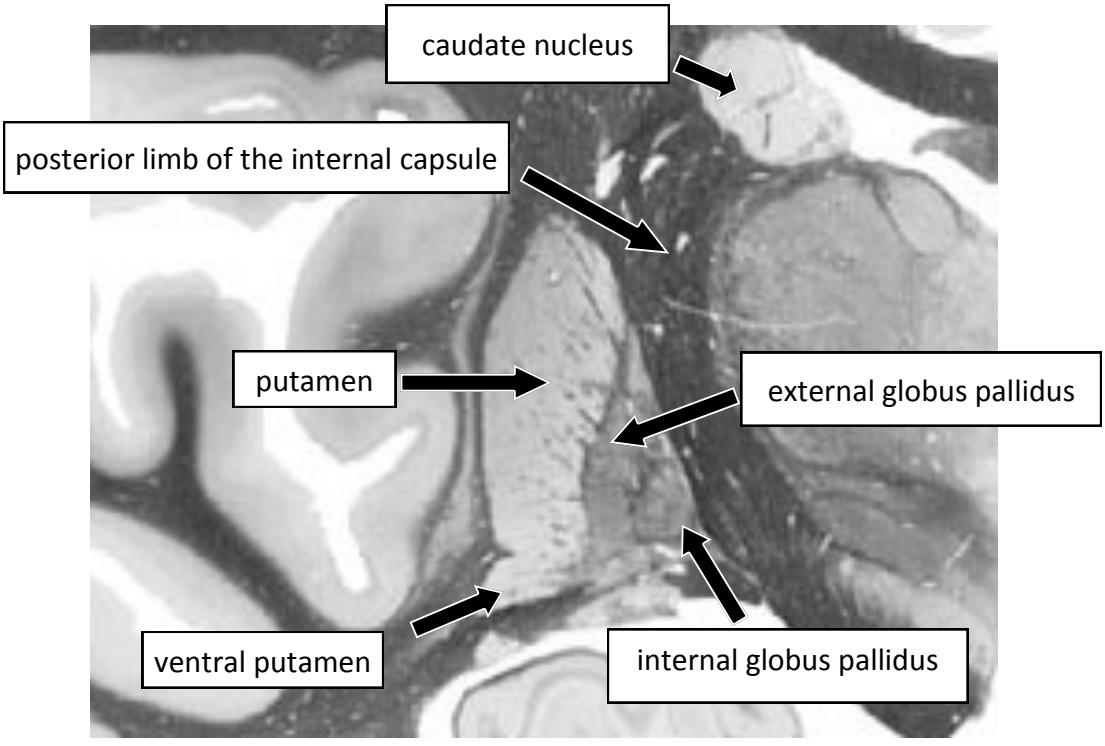

The amygdala

The amygdala is made up of a large number of nuclei, not all of which are labelled here.

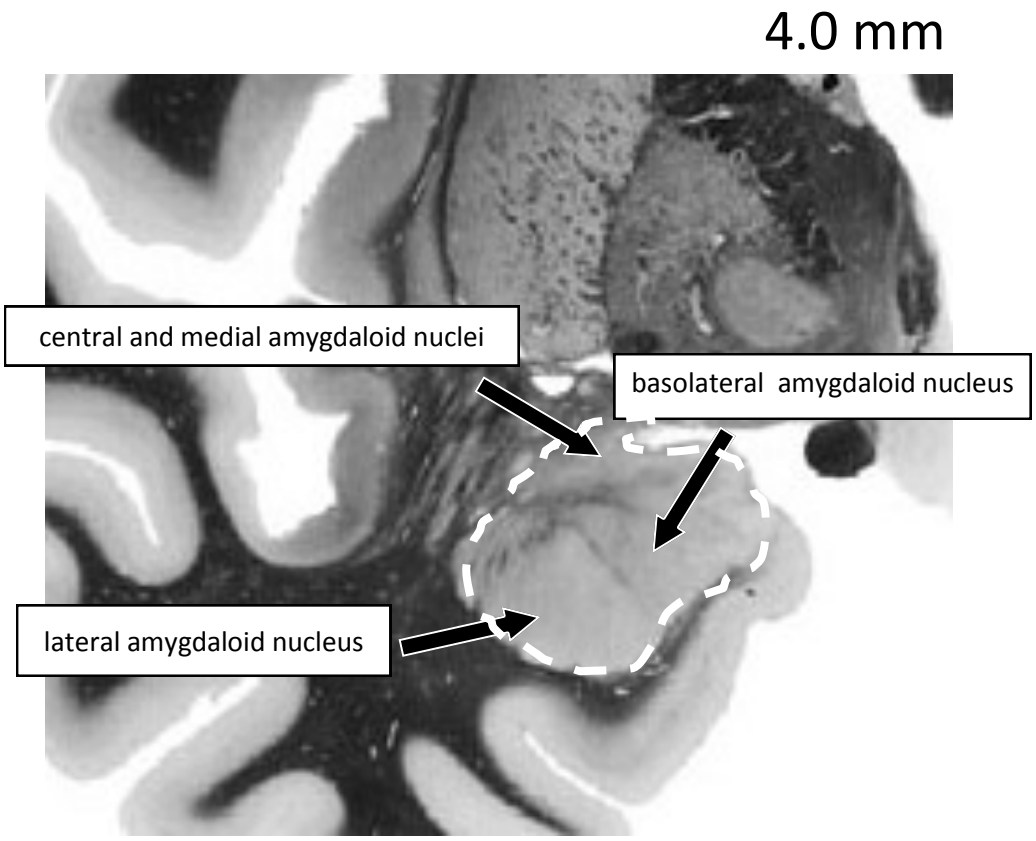

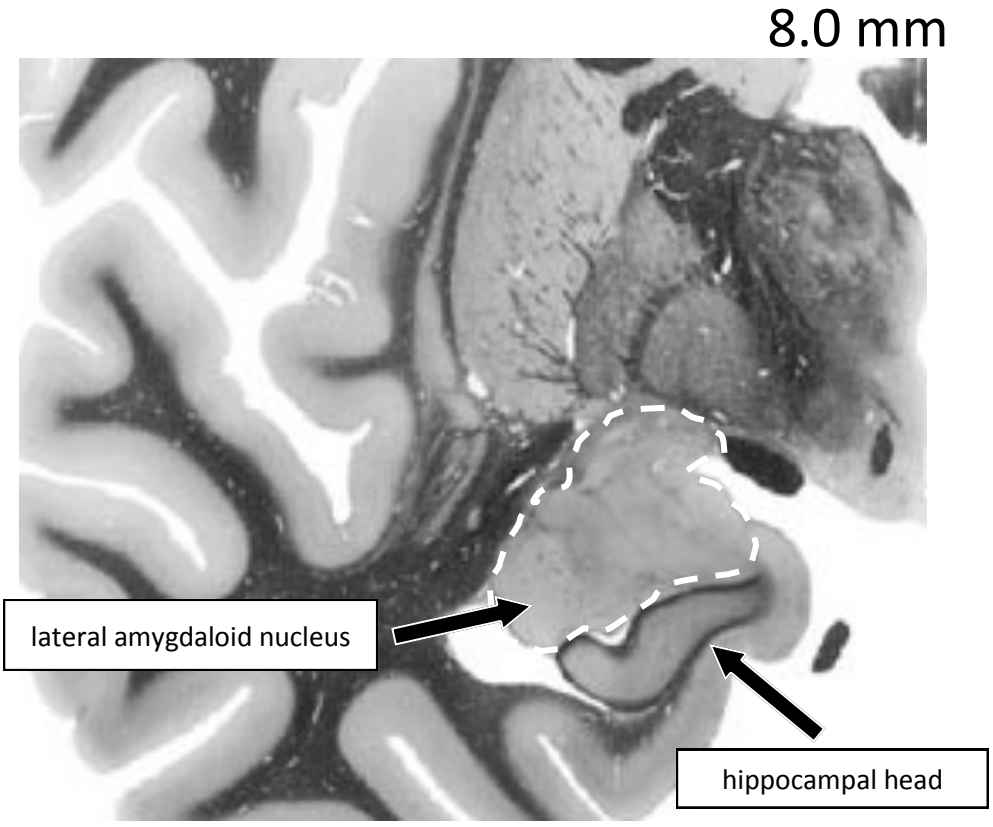

Appendix B:

Sample dissection for MRI and bulk tissue analysis

The following pages show how each sample was dissected from the tissue block received from the Canadian Brain Tissue Bank. Block A was cut for MRI and included the surrounding tissue structures. Block B was cut for bulk tissue analysis (SQUID magnetometry, followed by ICP-MS or GFAAS) and was cut carefully so as to include only tissue from the target region. Both A and B were not cut from every sample.

Appendix B-1: Caudate nucleus (CN) and putamen (Pu) samples

These samples were cut as described in Section 3.2.3.1 of the main text, with the cutting of sample C1 shown in Figure 3.7.

Case C2

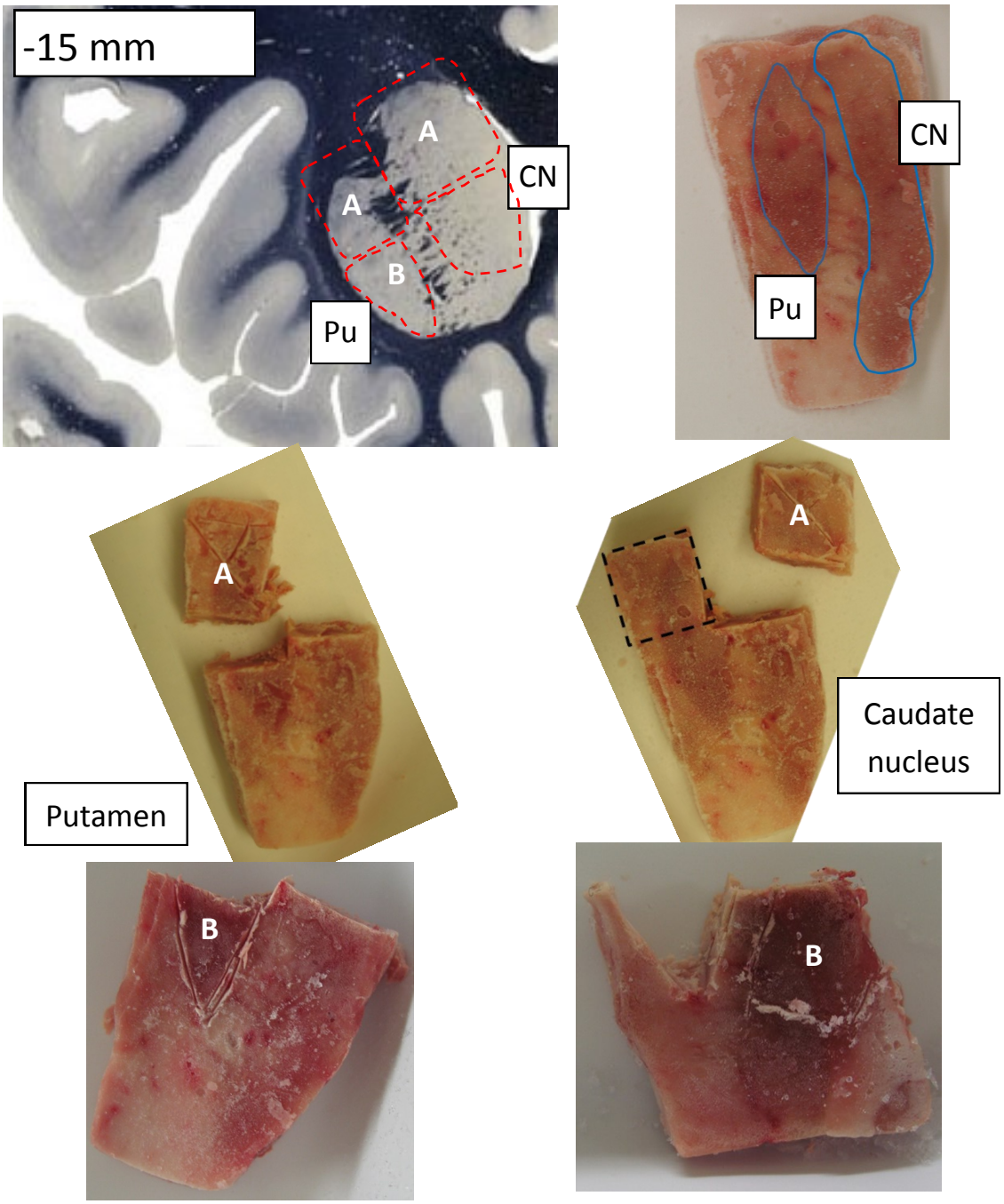

Case C3

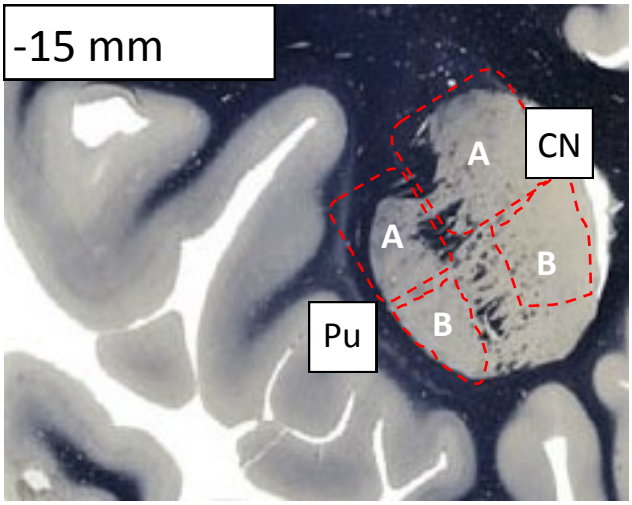

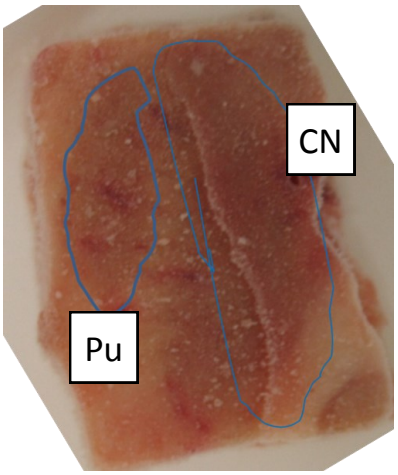

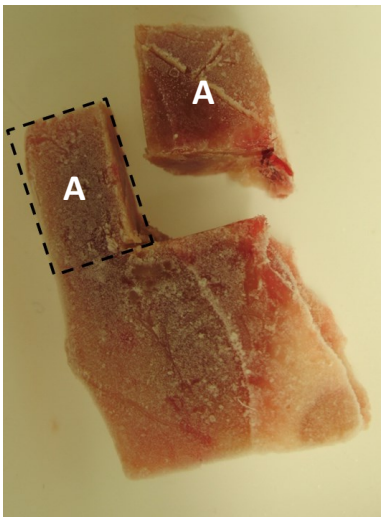

Putamen

Caudate nucleus

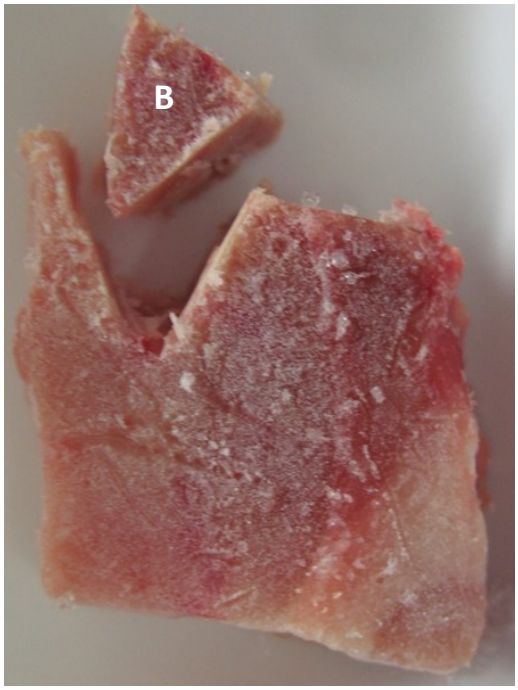

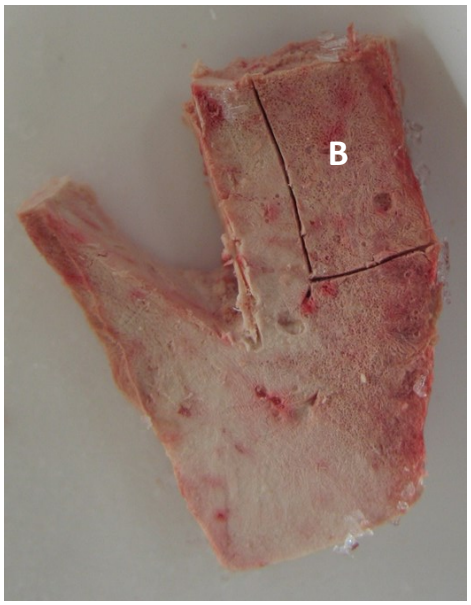

Case AD1:

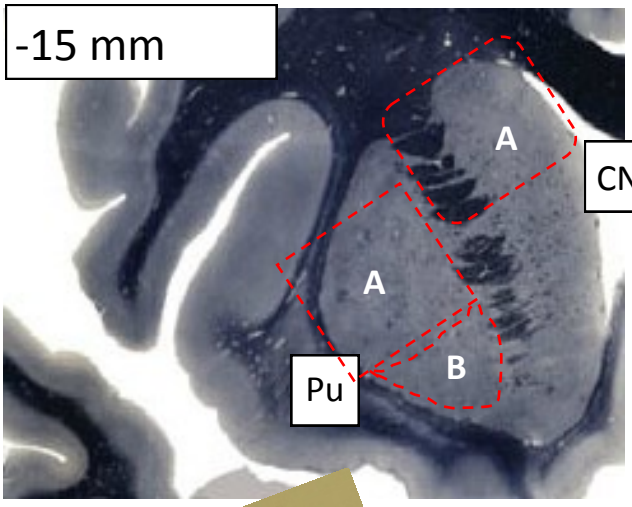

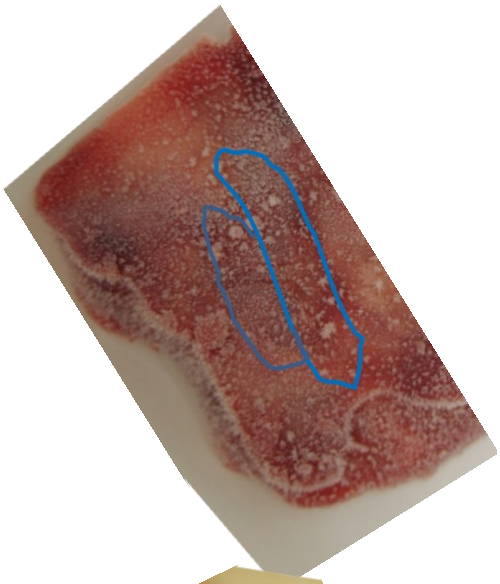

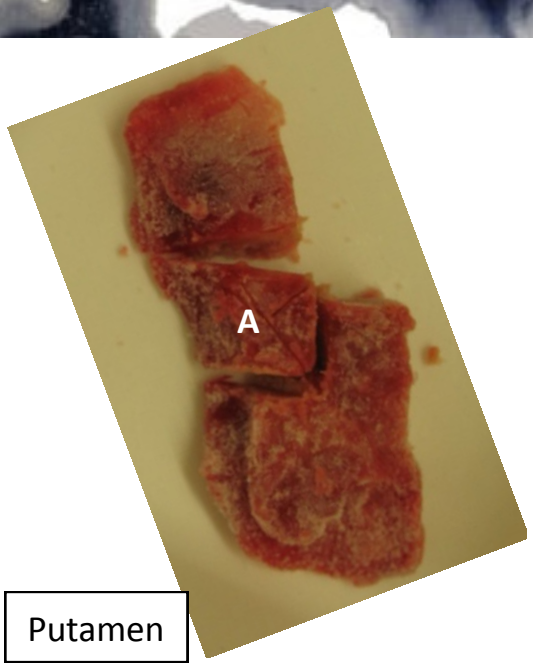

Putamen

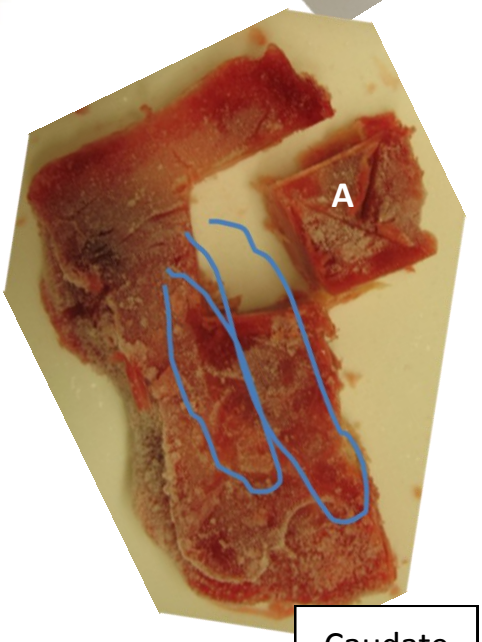

Caudate nucleus

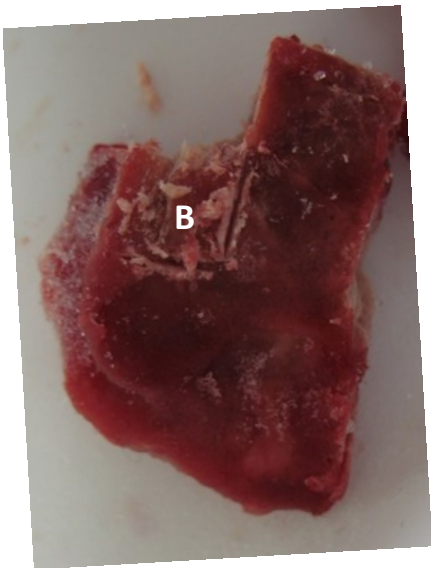

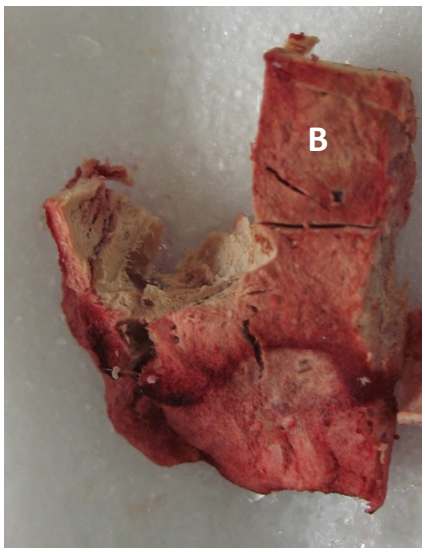

Case AD2:

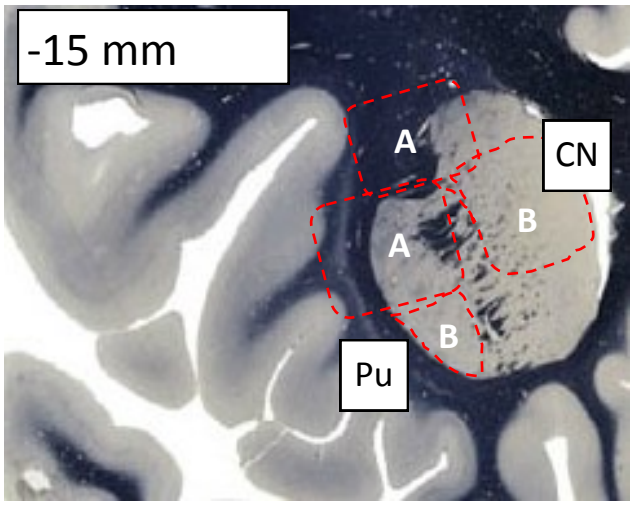

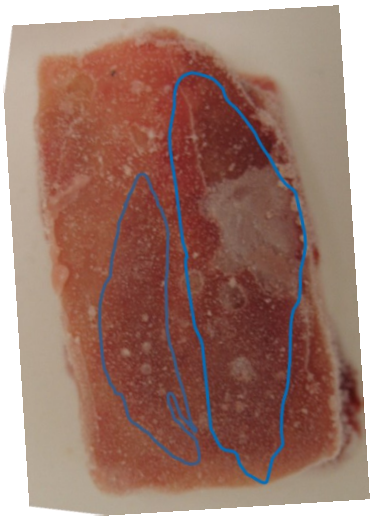

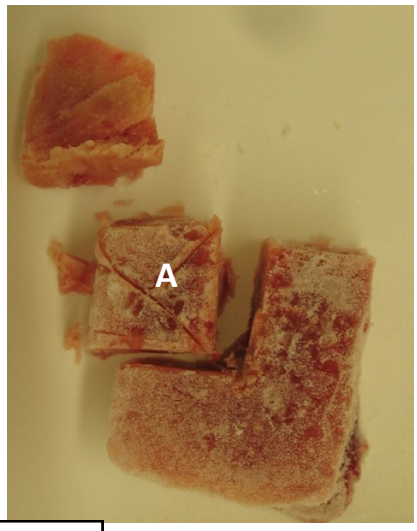

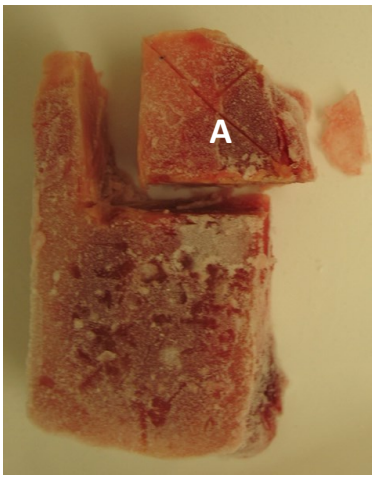

Putamen

Caudate nucleus

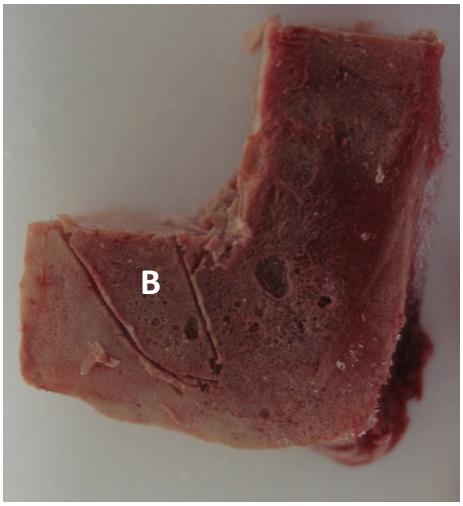

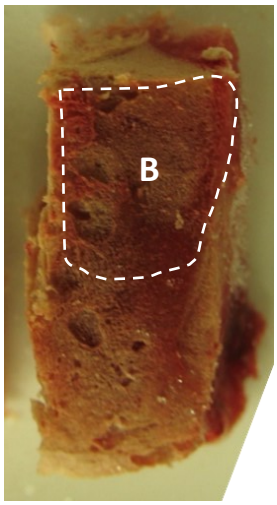

x

Case AD3:

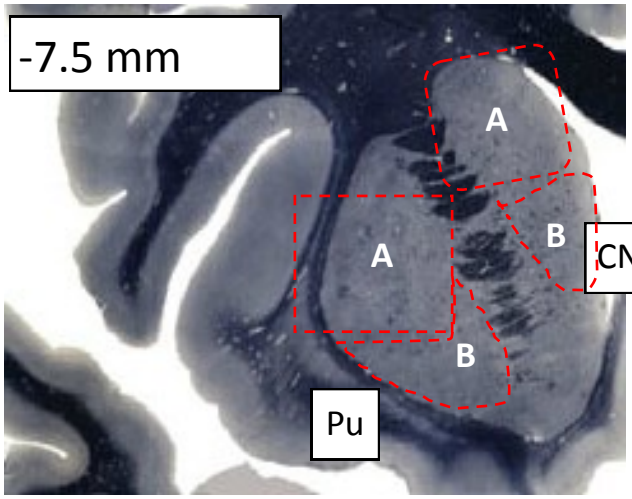

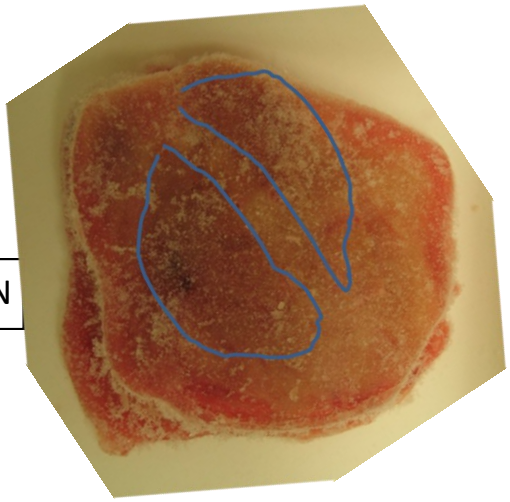

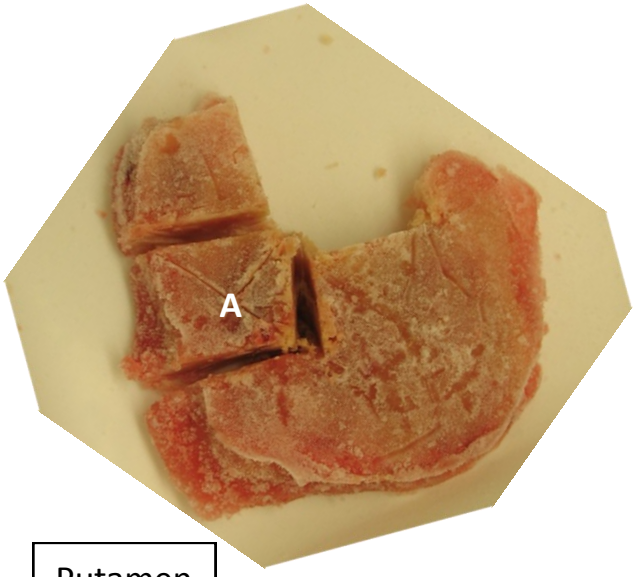

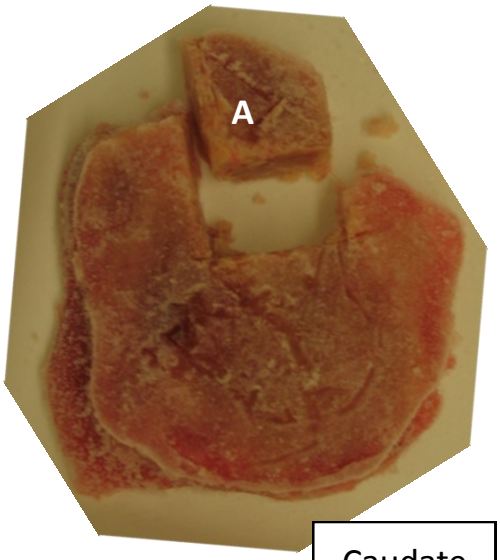

Putamen

Caudate nucleus

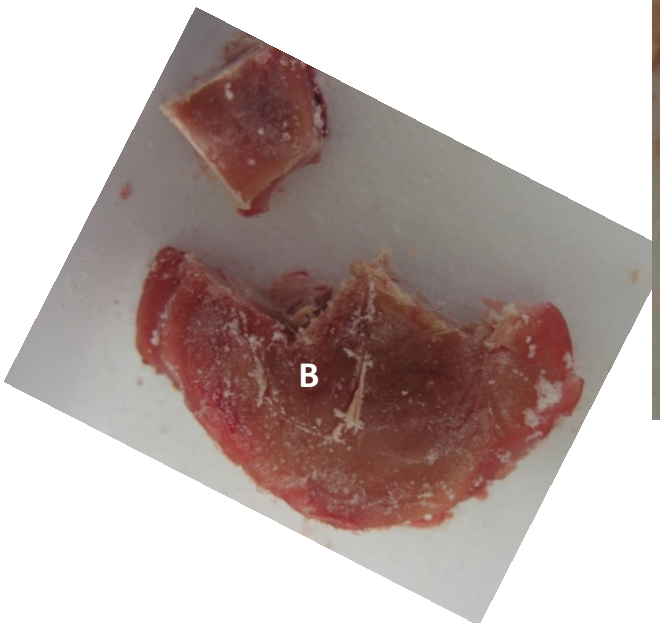

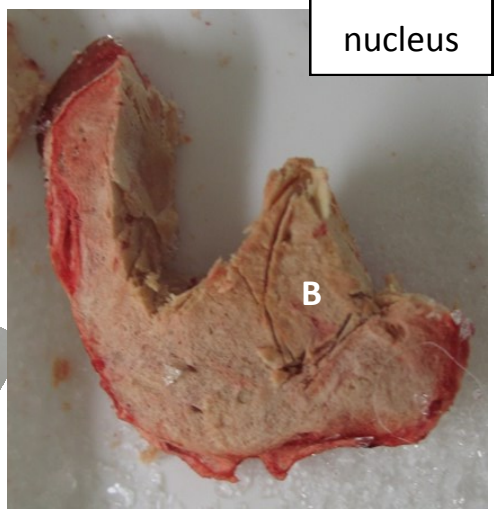

Additional putamen samples will also prepared from the 3 Parkinson's Disease and 3 Multiple System Atrophy cases. However, tissue was only cut for SQUID magnetometry and iron quantification (block B).

Case PD1:

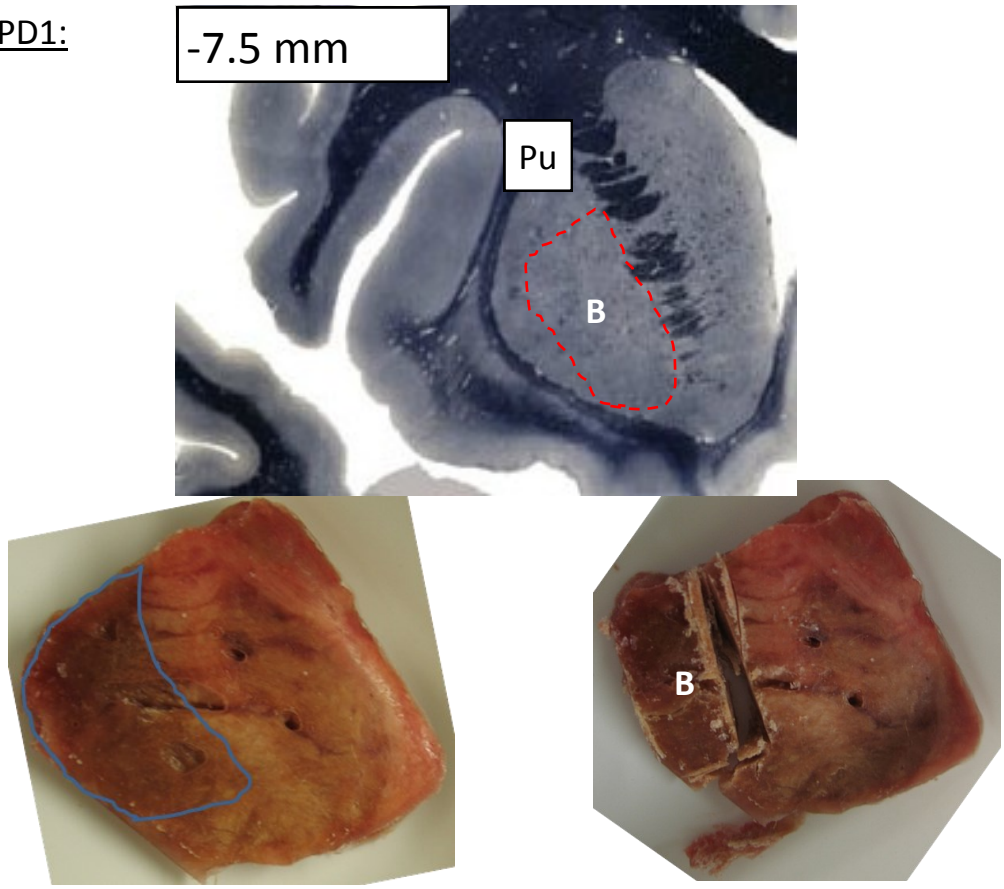

Case PD2:

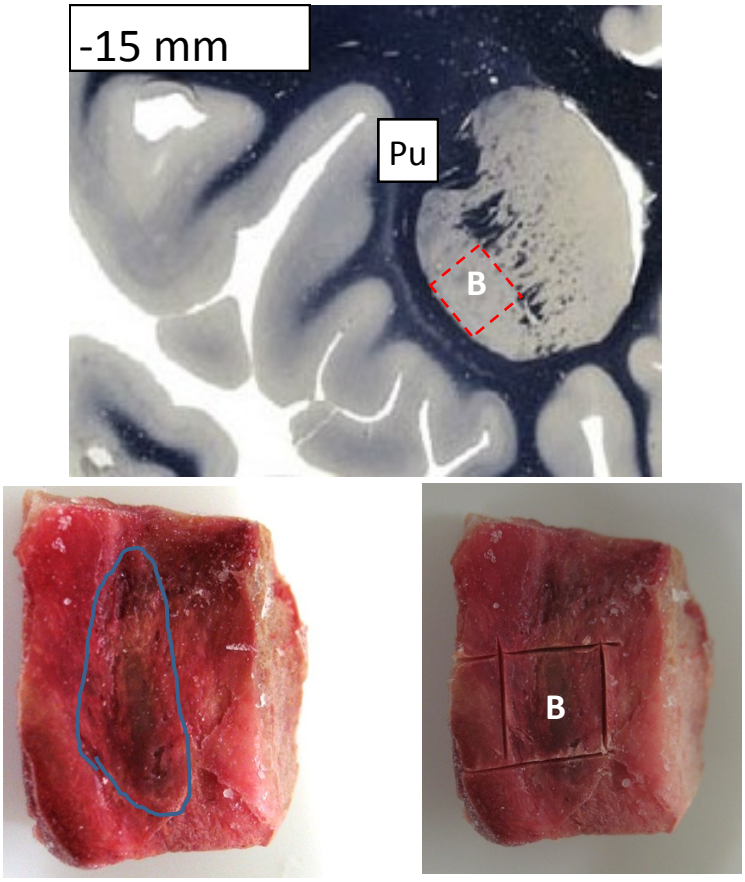

Case PD4:

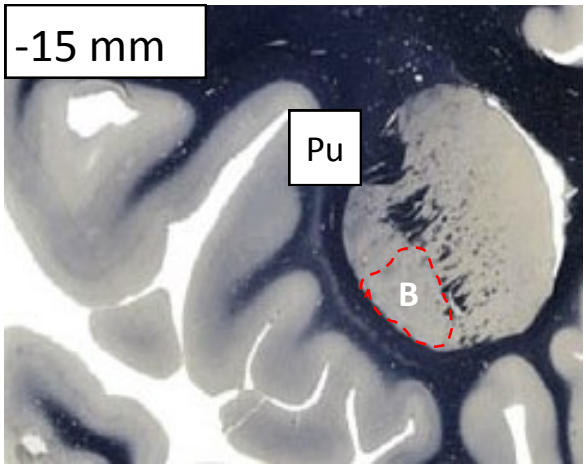

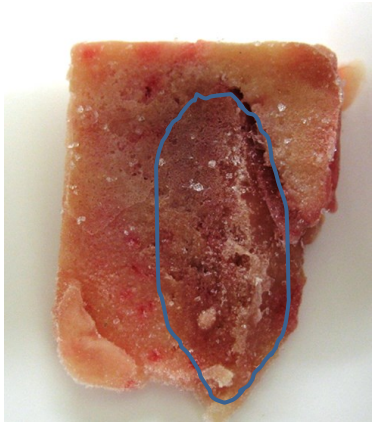

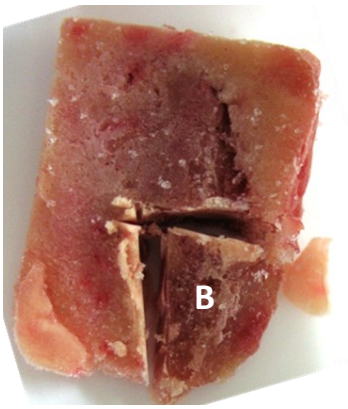

Case MSA1:

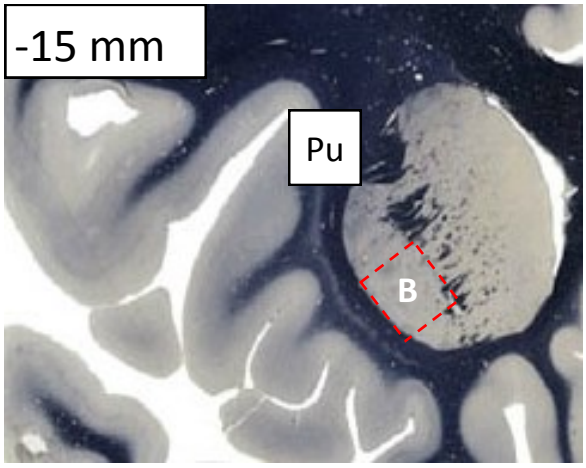

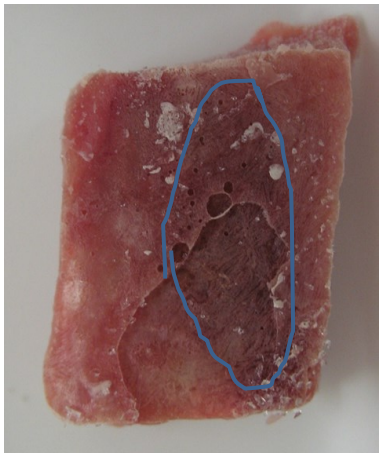

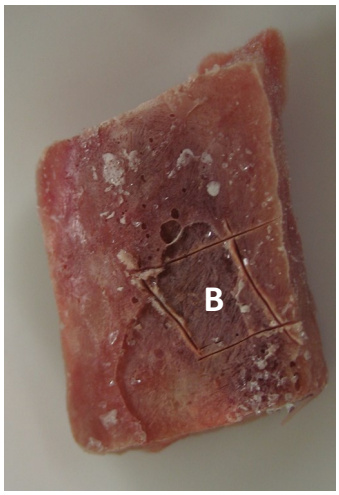

Case MSA2:

Anatomical identification of the putamen in this sample was difficult, however the tissue was cut based on advice from neuropathologist Dr Lili-Naz Hazrati.

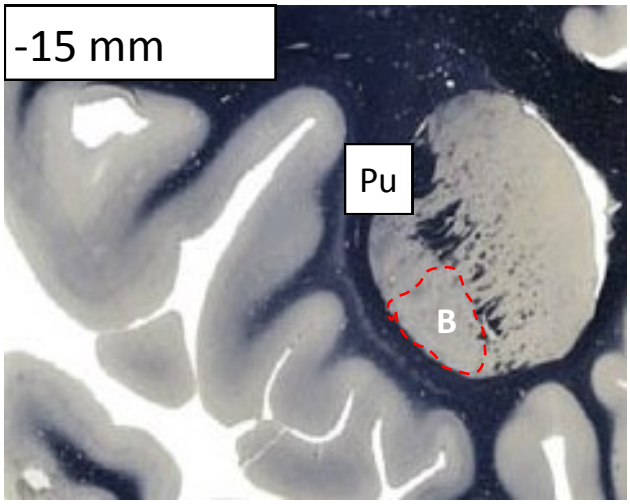

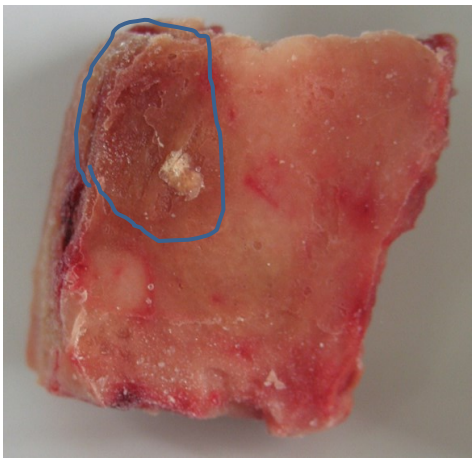

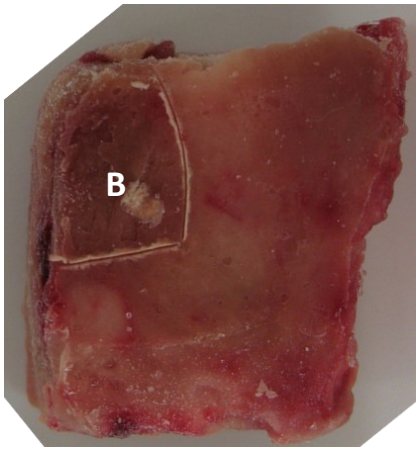

Case MSA3:

Anatomical identification of the putamen in this sample was difficult, however the tissue was cut based on advice from neuropathologist Dr Lili-Naz Hazrati.

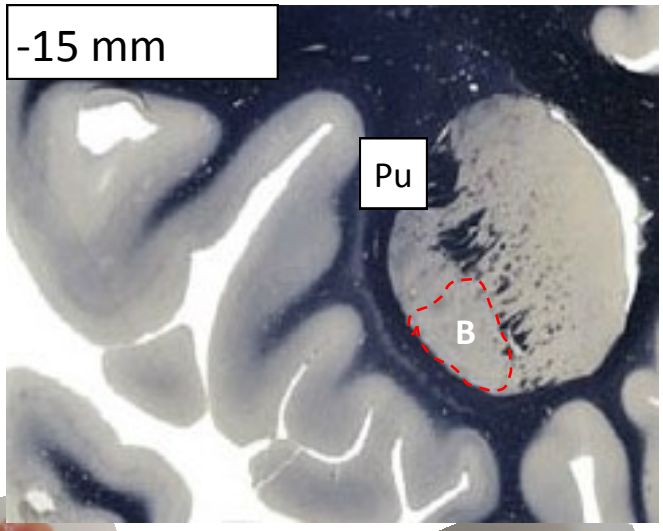

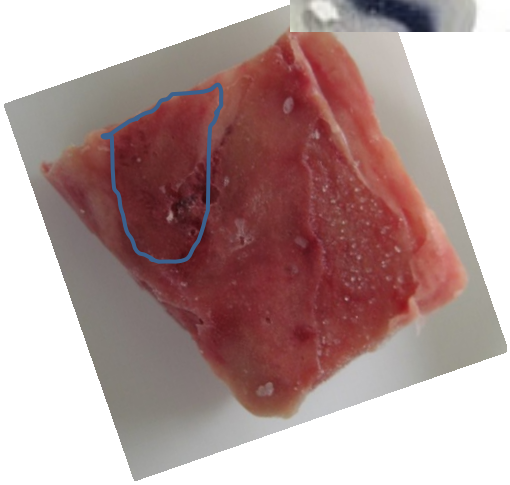

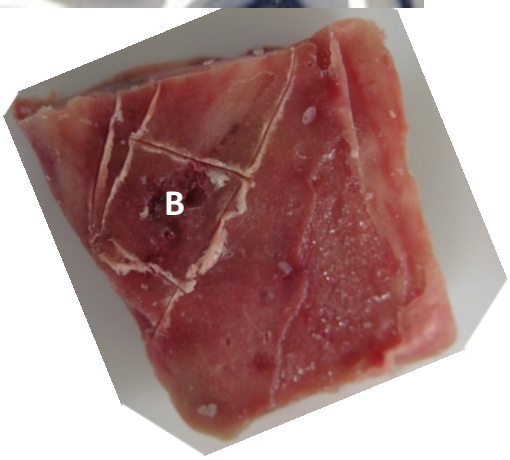

Appendix B-2: Globus Pallidus Samples

These samples were cut as described in Section 3.2.3.2 of the main text, with the cutting of sample C1 shown in Figure 3.8. The aim was to include tissue from the external and internal globus pallidus (GPi and GPe) and the putamen (Pu.) Only tissue for MRI (block A) was cut from the GP.

Case C2

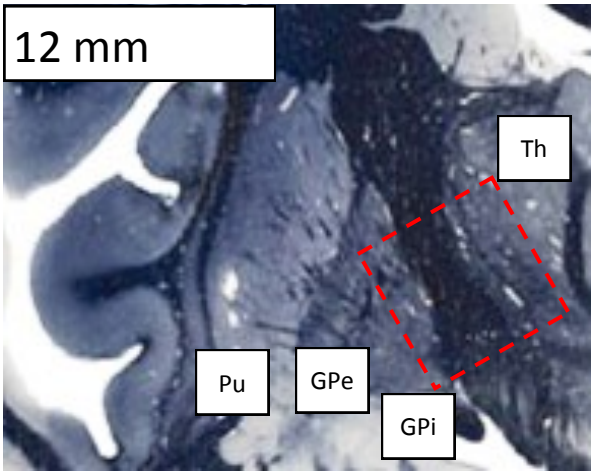

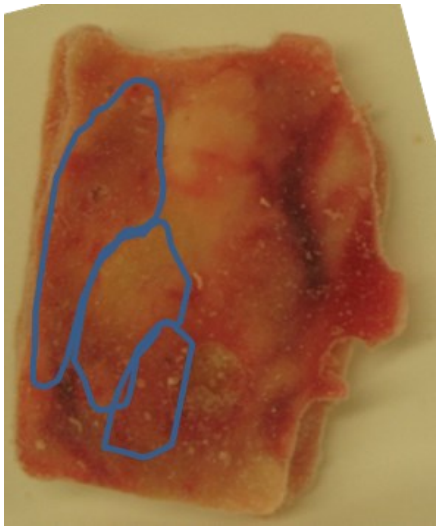

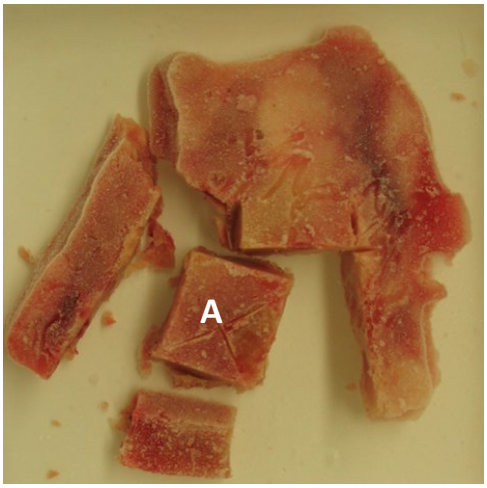

MRI and sectioning and staining of this sample (Figure 7.4), showed that it did not contain the target regions and its anatomy was difficult to identify. Advice from neuropathologist Dr Lili-Naz Hazrati was that may contain the internal globus pallidus and possibly the thalamus (Th), as indicated above.

Case C3:

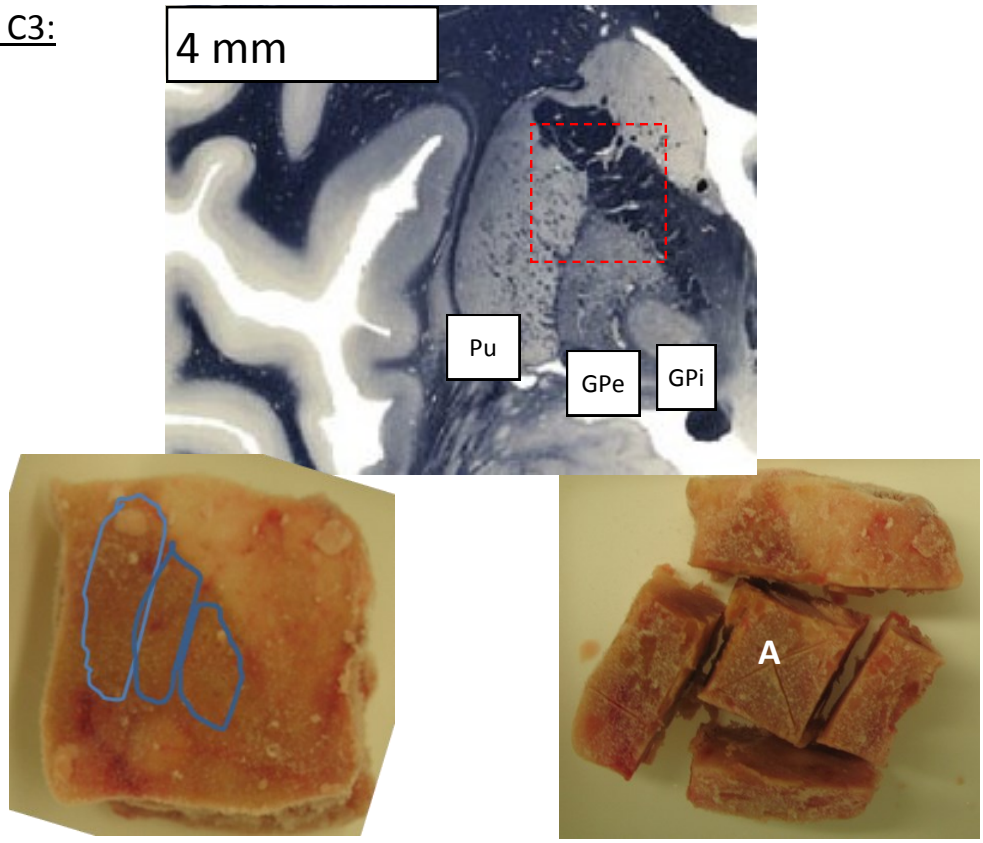

Case AD1

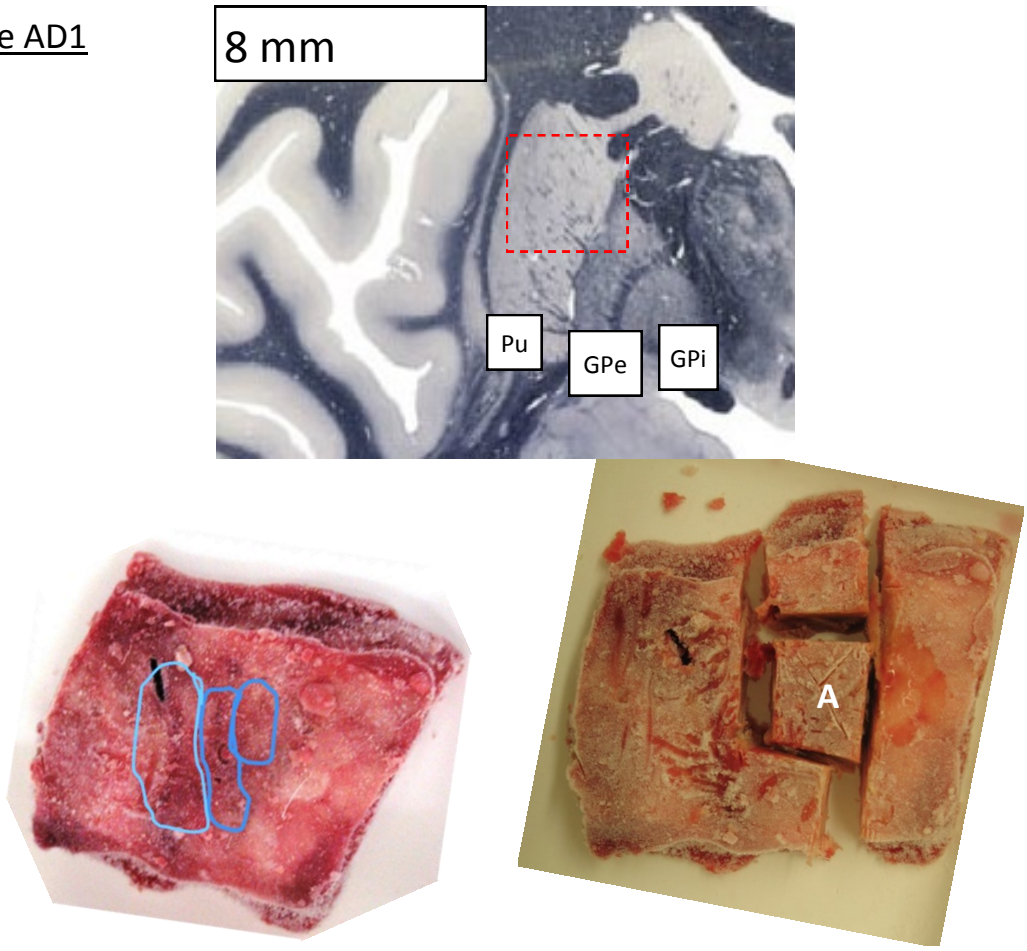

Case AD2

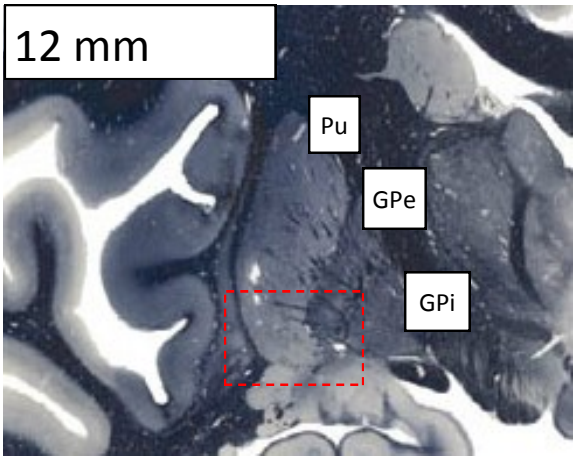

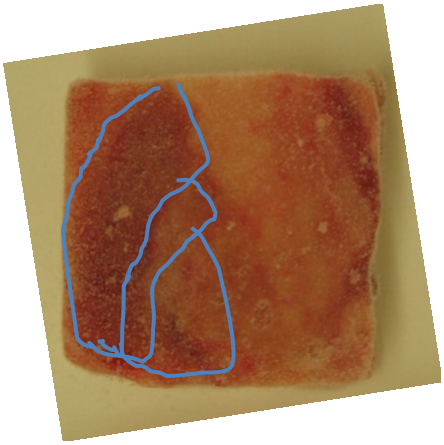

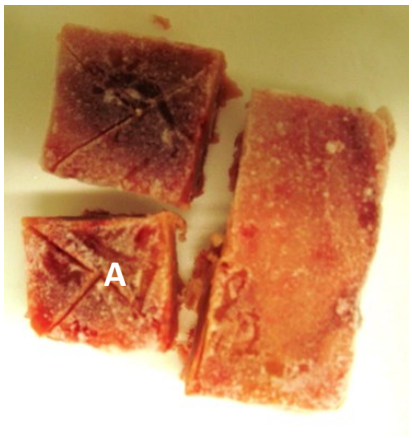

Case AD3:

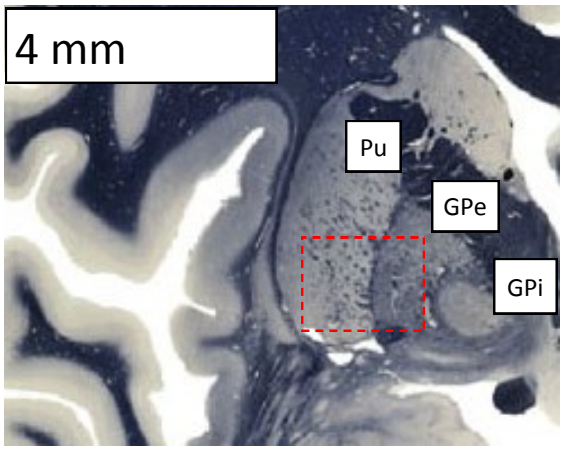

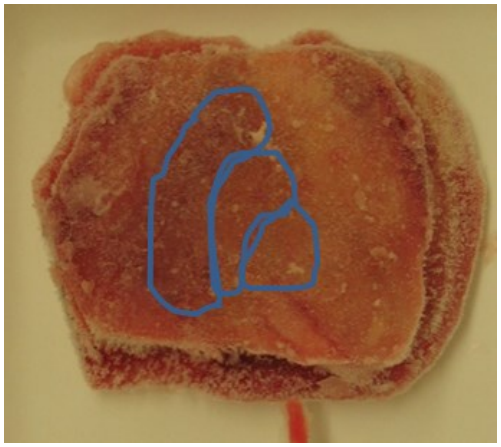

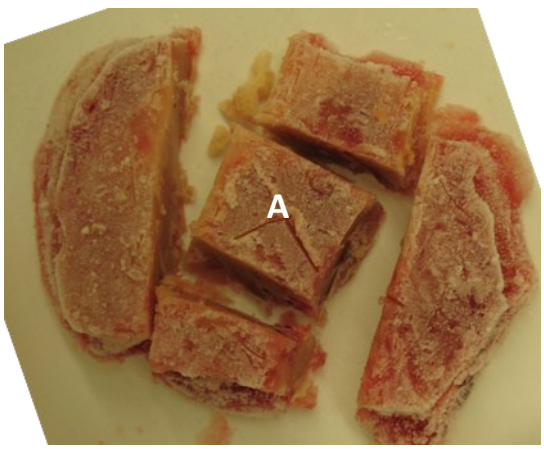

Appendix B-3: Substantia Nigra Samples

These samples were cut as described in Section 3.2.3.3 of the main text, with the cutting of sample C2 shown in Figure 3.9. Where possible, tissue was cut for both MRI (block A) and bulk analysis (block B), however when there was only a small volume of tissue present the bulk tissue analysis was prioritised.

Case C1

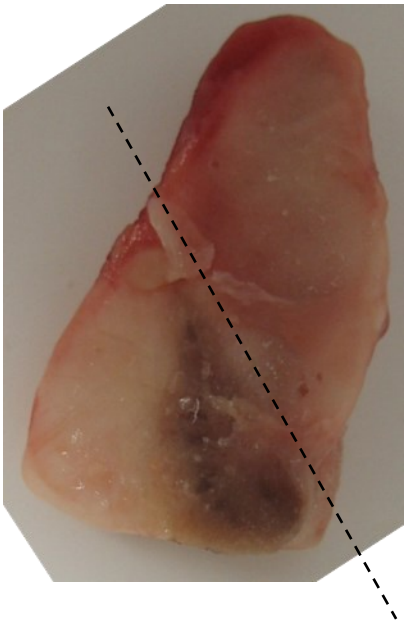

Substantia nigra cut from tissue block and bisected

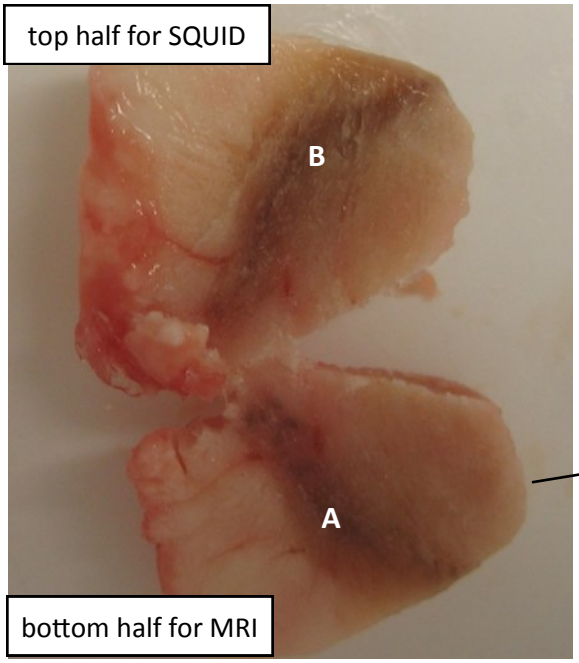

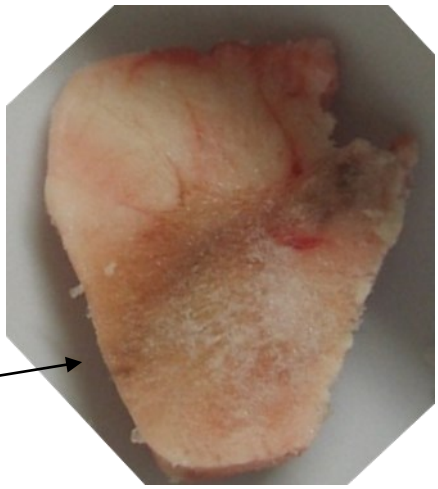

MRI sample

Case C3

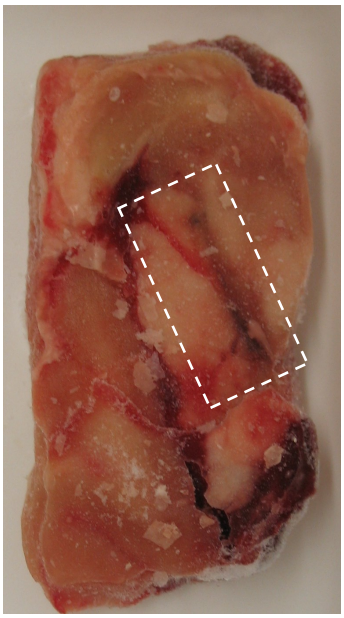

Due to the small sample size, both samples were taken for bulk tissue analysis

Case AD1

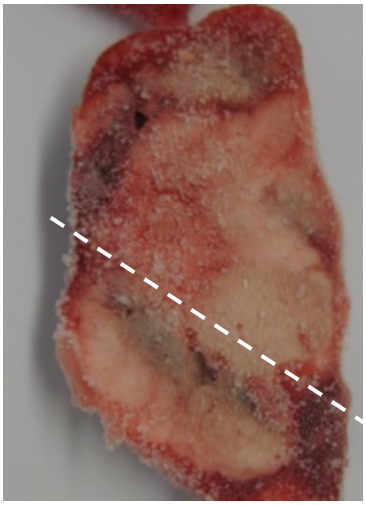

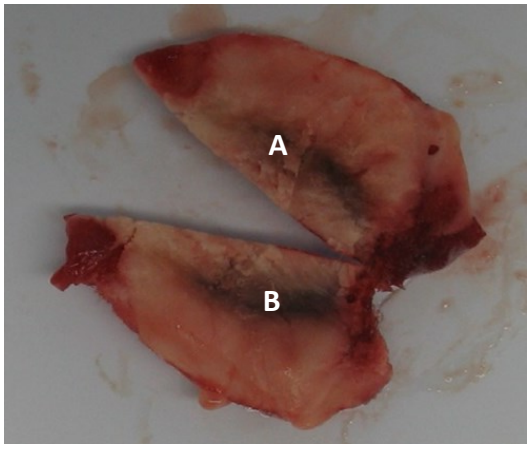

Case AD2

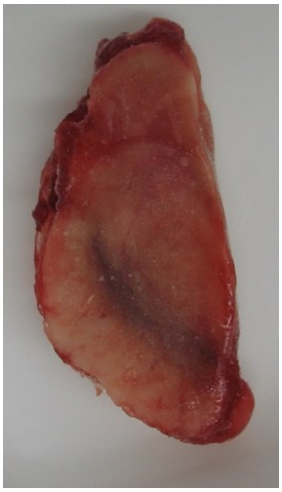

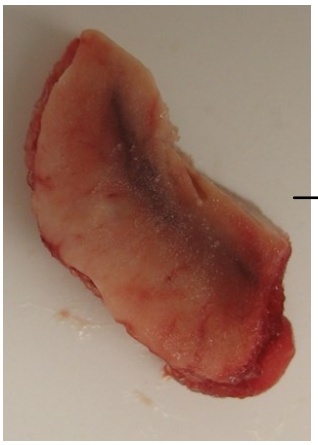

sample bisected

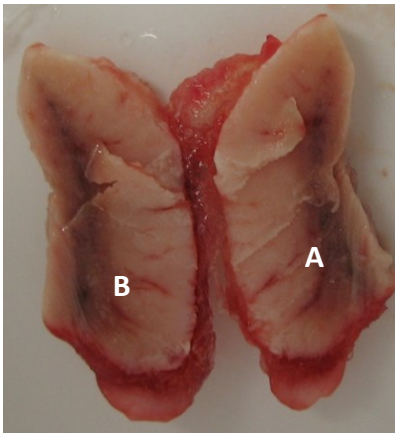

Case AD3

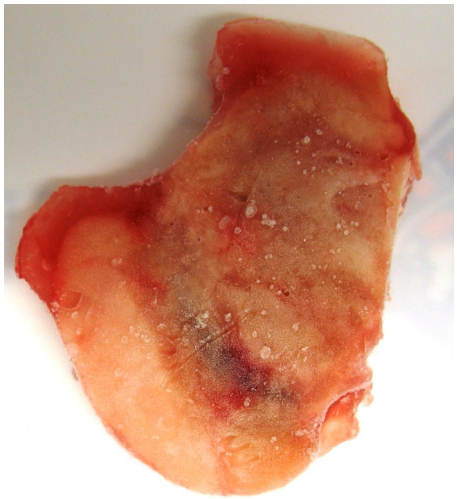

As this sample was very thin, it was not bisected and the whole nigra was taken for bulk tissue analysis

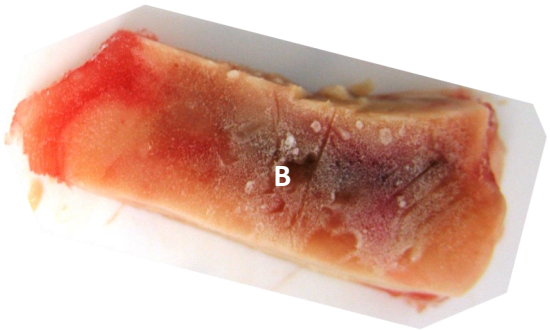

xx

Case PD1

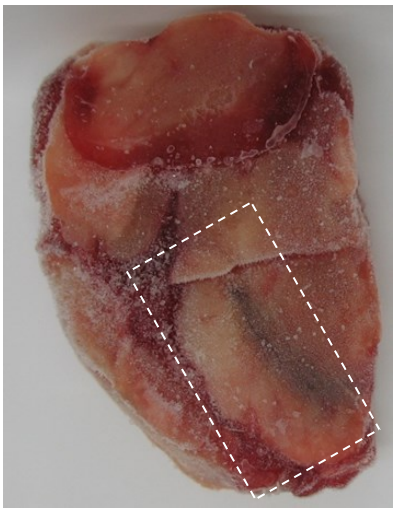

sample bisected →

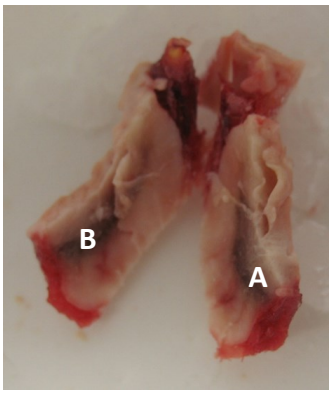

Case PD2

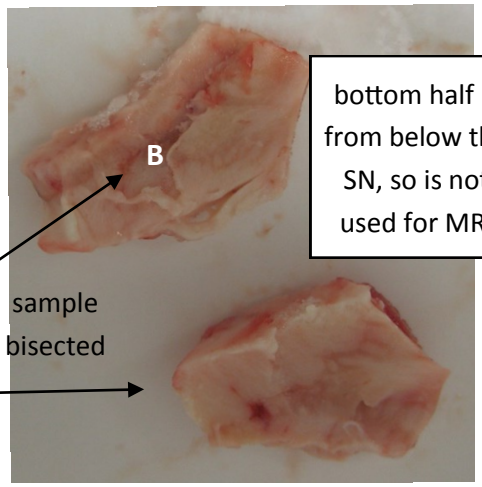

bottom half is from below the SN, so is not used for MRI

Case PD4

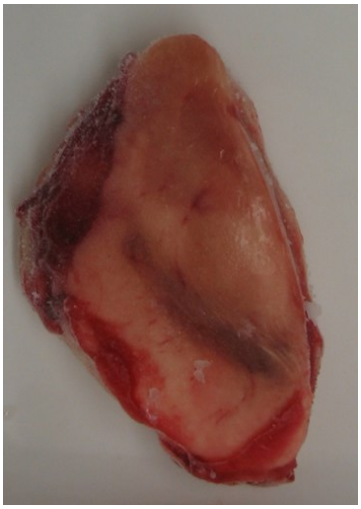

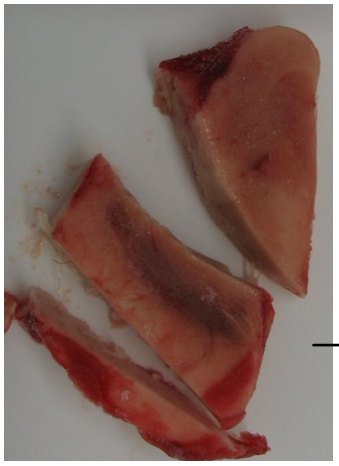

sample bisected

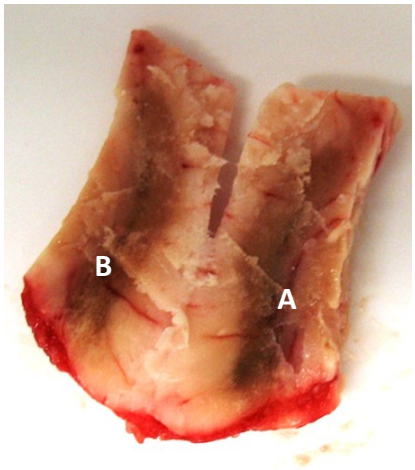

Case MSA1

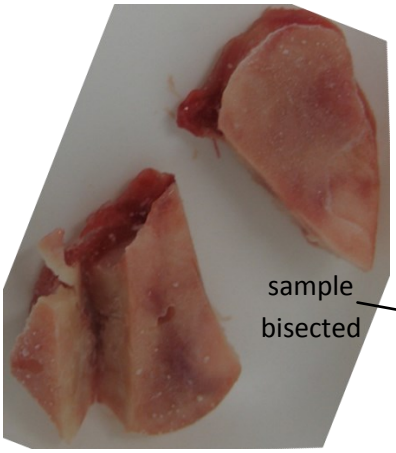

sample bisected

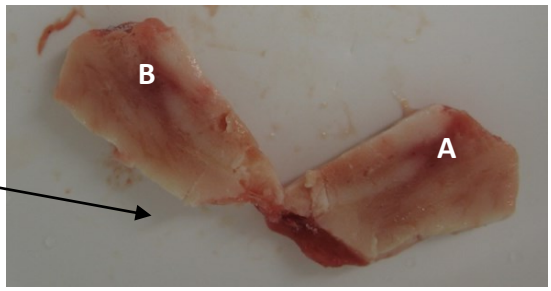

Case MSA2

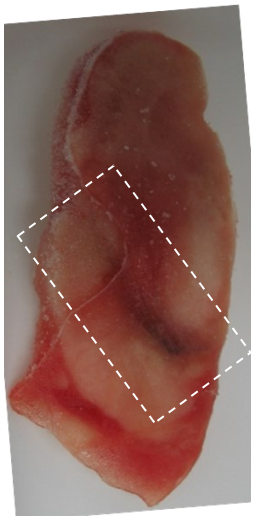

sample
bisected

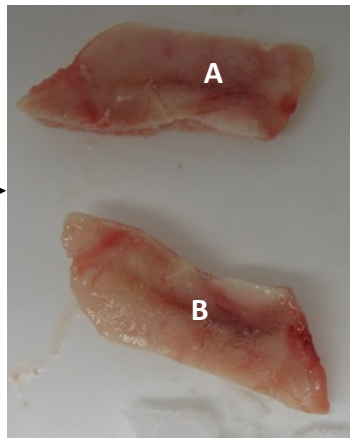

Case MSA3

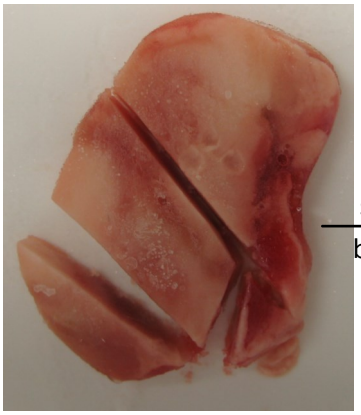

sample
bisected

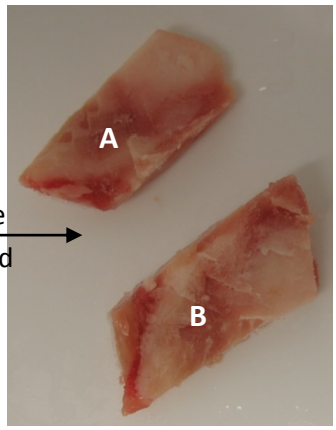

Appendix B-4: Amygdala Samples

These samples were cut as described in Section 3.2.3.4 of the main text, with the cutting of sample C3 shown in Figure 3.10. The anatomy of the amygdala was particularly difficult to identify and therefore neuropathologist Dr Lili-Naz Hazrati identified the area of tissue containing the amygdala with a blue oval. Tissue for MRI was cut from within this area (block A). No tissue was cut for bulk tissue analysis.

Case C1

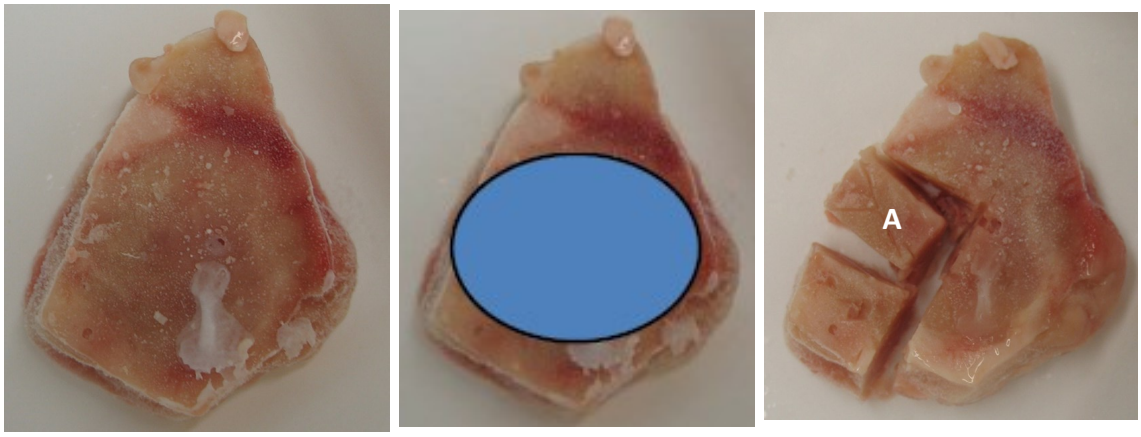

Case C2

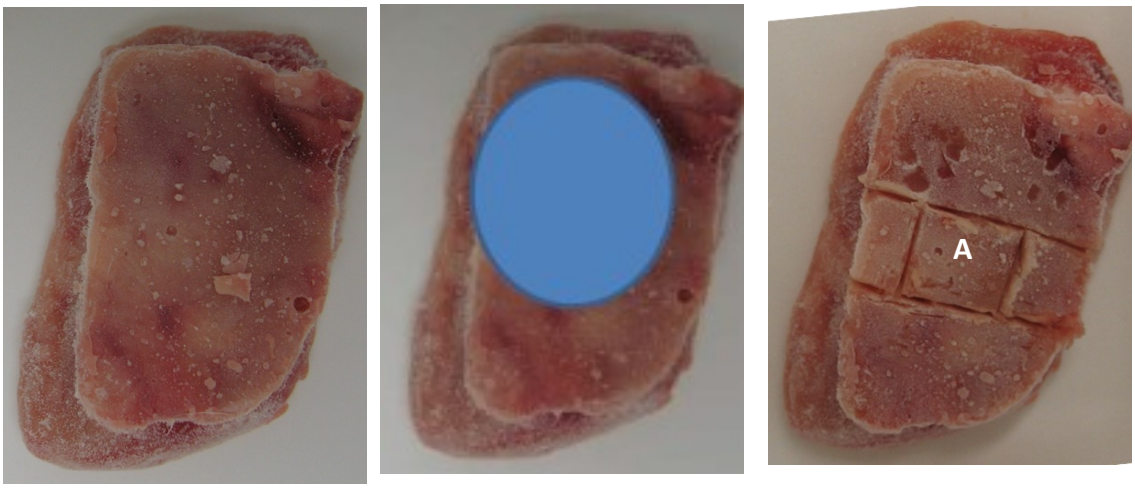

Case AD1

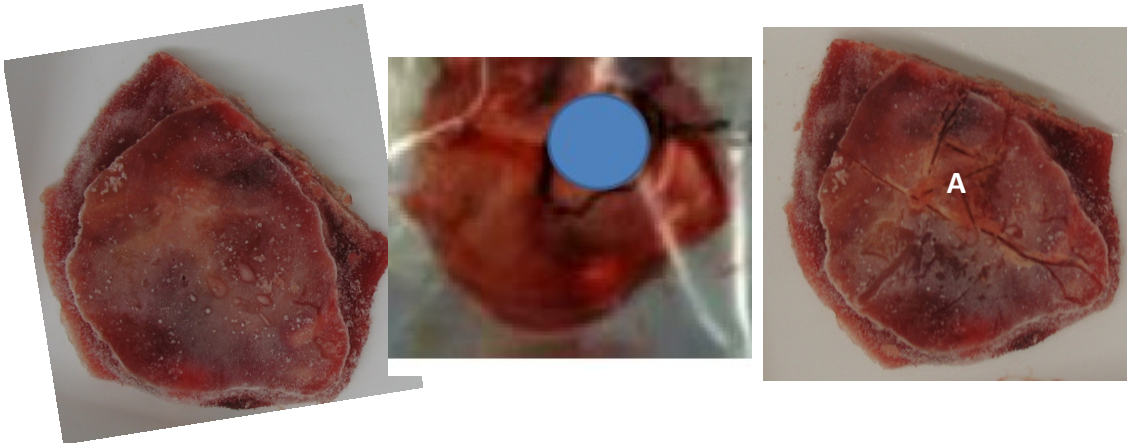

Case AD2

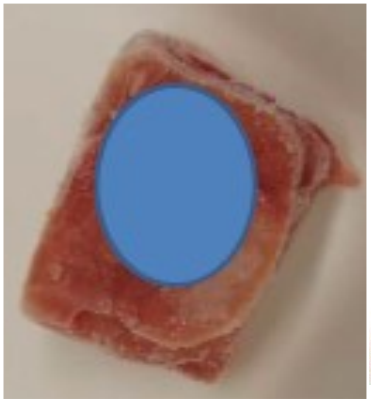

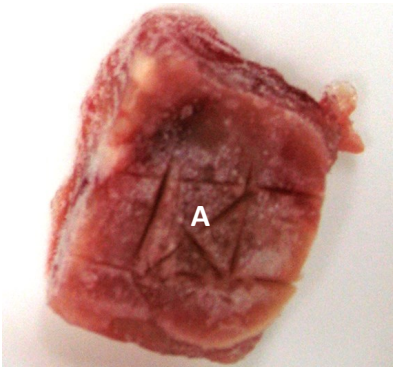

Case AD3

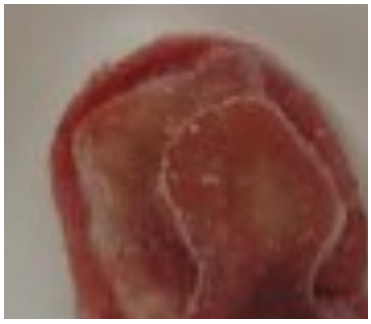

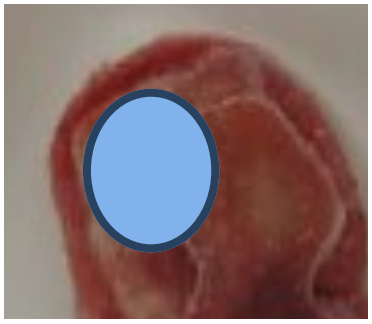

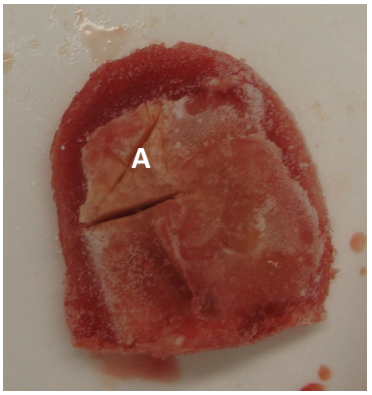

Appendix B-5: Pons Samples

These samples were cut as described in Section 3.2.3.5 of the main text, with the cutting of sample C1 shown in Figure 3.11. Tissue samples for bulk tissue analysis (bock B) were cut from an adjacent block of tissue, by Dr Joanna Collingwood, before the commencement of this PhD. This is not shown here, however tissue was cut using the same guide. Cutting of the samples for MRI (block A) is shown below.

Case C2

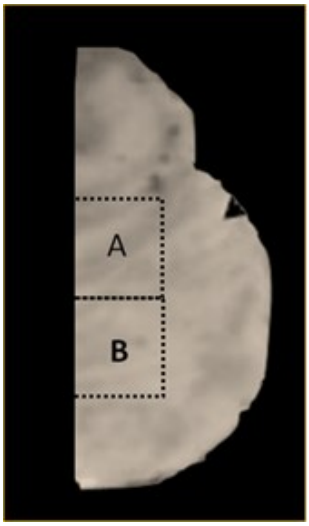

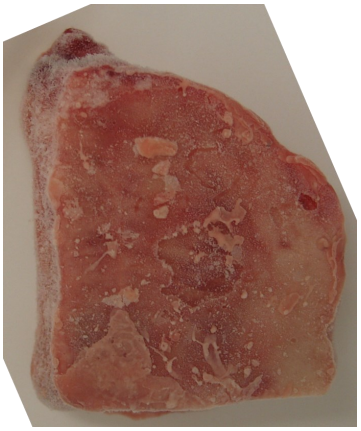

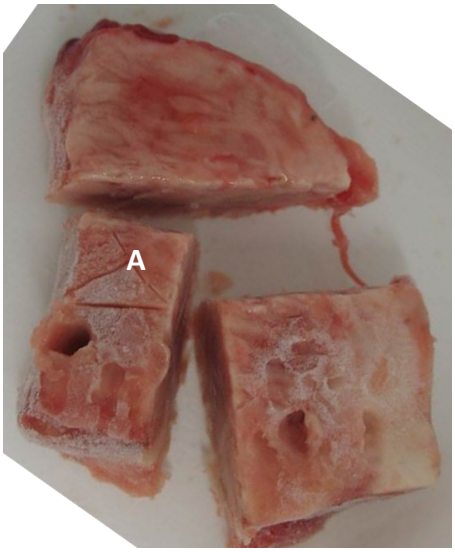

Case C3

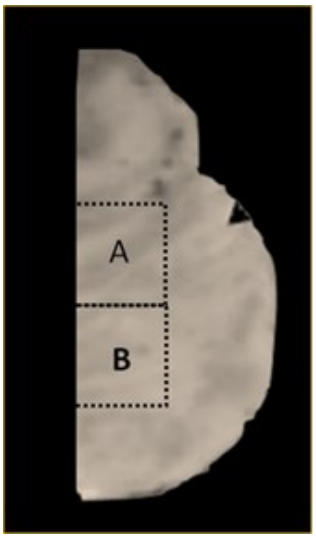

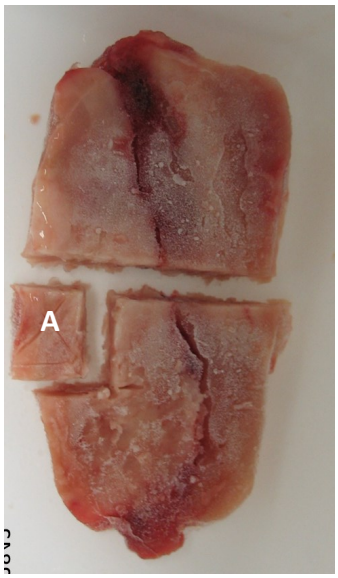

Case AD1

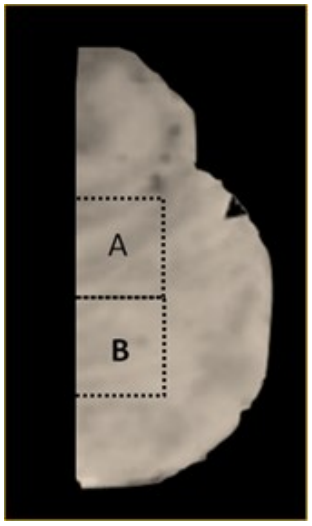

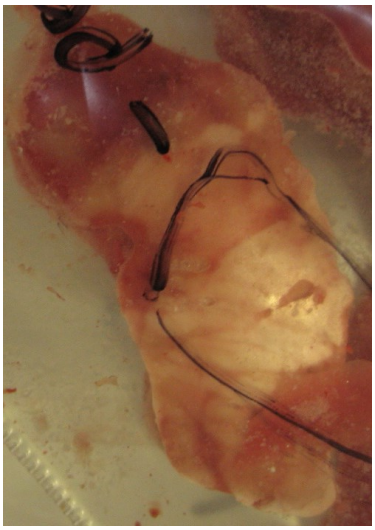

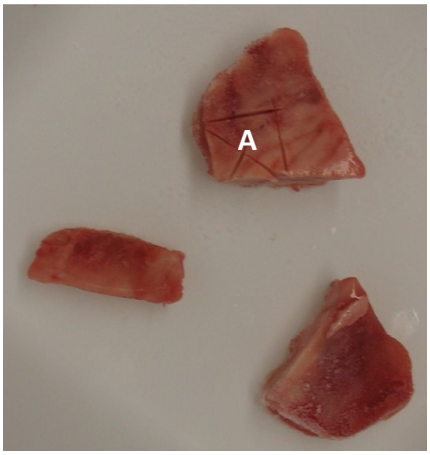

Case AD2

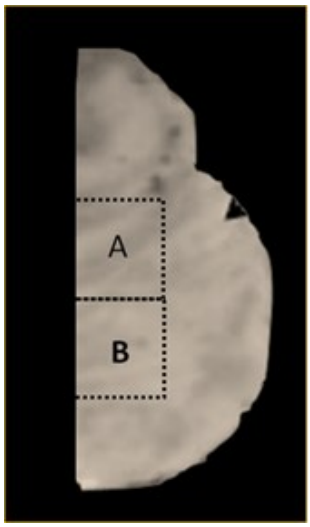

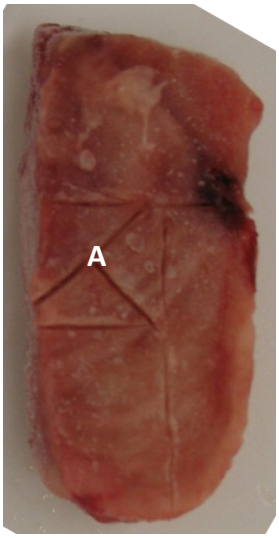

Case AD3

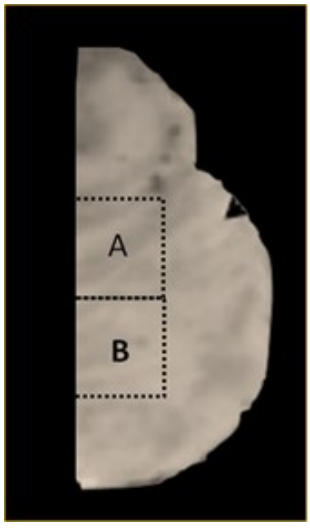

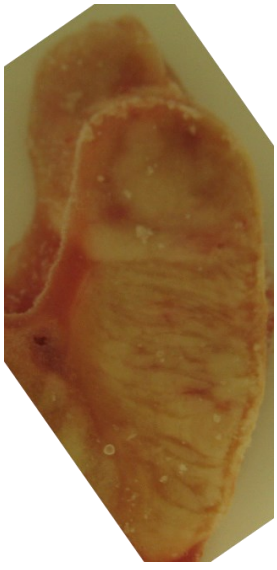

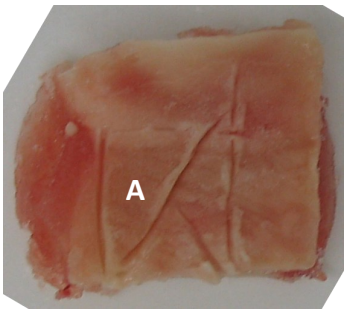

Case PD1

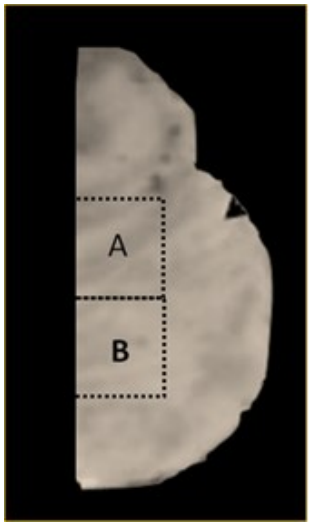

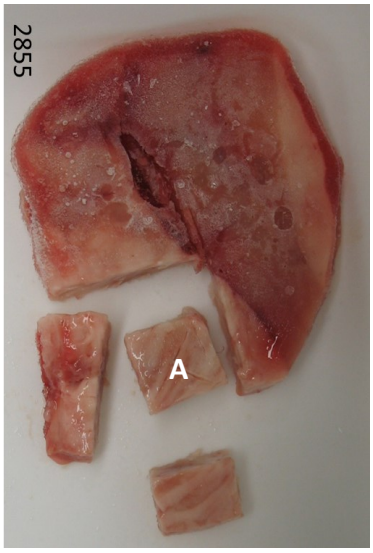

Case PD2

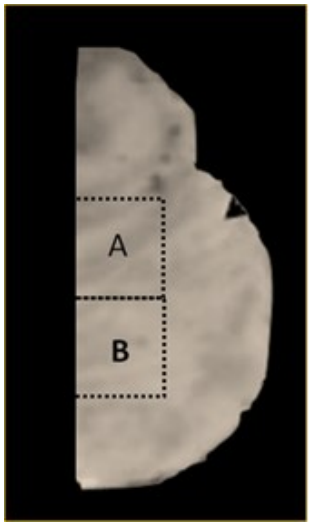

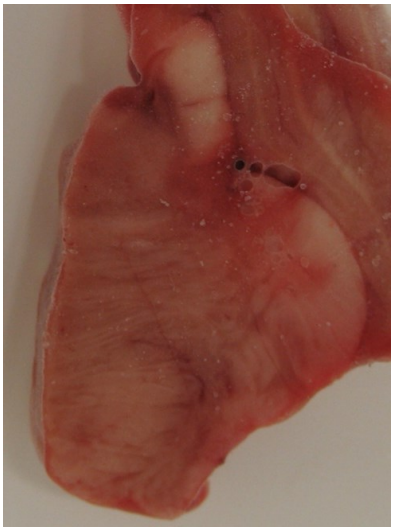

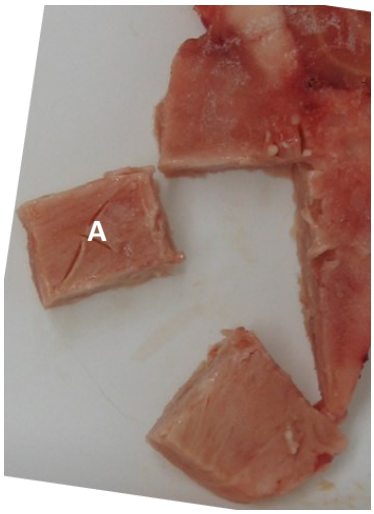

Case PD4

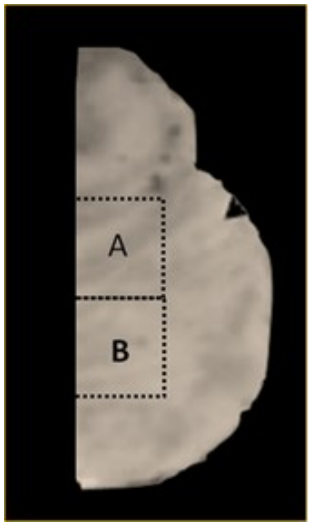

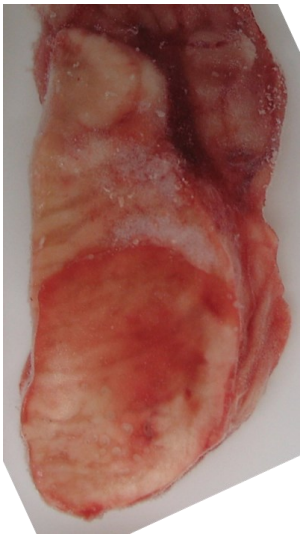

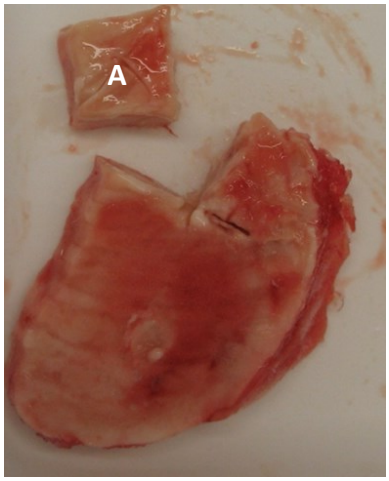

Case MSA1

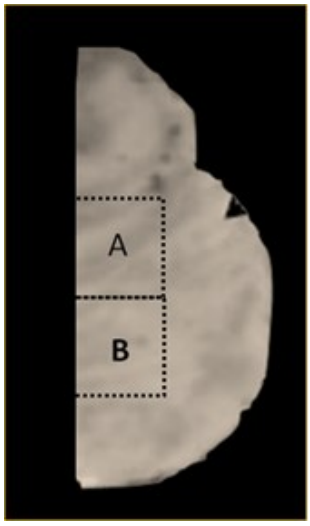

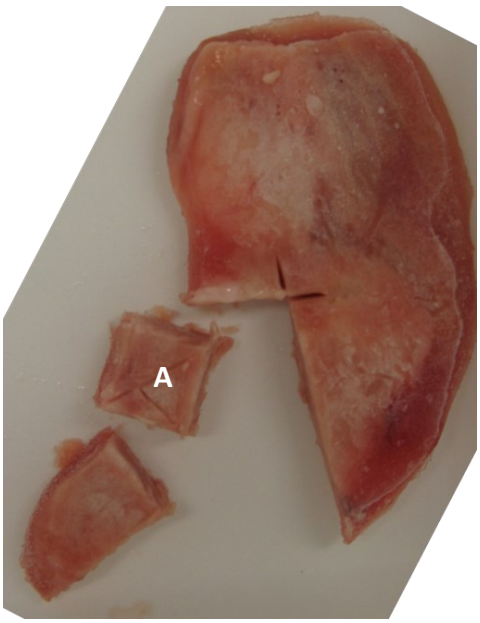

Case MSA2

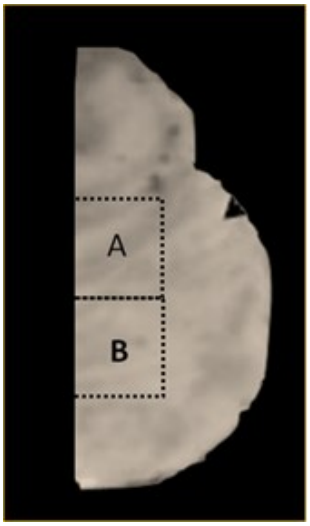

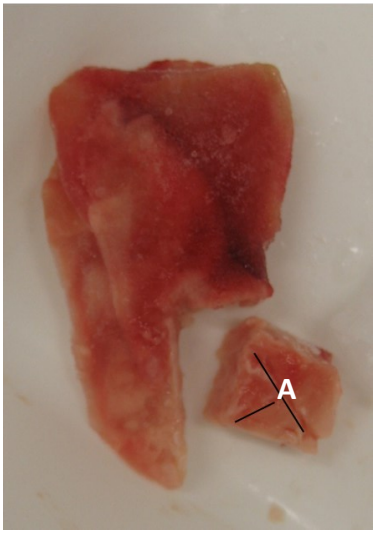

Case MSA1

No tissue was available for MRI from the pons sample from case MSA1.

Appendix C: SQUID Sequences

Appendix C-1: IRM Curves

The SQUID magnetometry sequence used to produce IRM curves at 5 and 50 K is given below. This is the sequence referred to in Section 4.1.2.1 of the main text.

The sample set up as follows:

i. The sample was inserted into the SQUID.

ii. The temperature was set to 300 K and the demagnetising sequence run.

iii. The temperature was returned to 5 K.

iv. A field of 250 Oe was applied.

v. A full direct current (DC) centring scan was run and the sample automatically centred.

Then the sequence was run:

1. Set field to 250 Oe (this should have already been done for centring).

2. Measure magnetic moment.

3. Reset magnet.

4. Measure the remanent magnetisation of the sample 8 times, where each measurement recorded by the SQUID is the average of 5 measurements.

5. Repeat steps 1 to 4, with the field set to 500, 750, 1000, 1500, 2000, 3000, 4000, 5000, 7500 and 10000 Oe.

6. Set the temperature to 300 K and wait for stability,

7. Run demagnetisation sequence,

8. Set temperature to 50 K,

9. Measure magnetic moment twice (this should be close to zero).

10. Apply 250 Oe.

11. DC centre automatically.

12. Repeat steps 1-5.

Appendix C-2: IRM at 300, 150, 50 and 5 K

The SQUID magnetometry sequence used to measure IRM at 300, 150, 50 and 5 K, from and applied field of 10 000 Oe, is given below. This is the sequence referred to in Section 4.1.2.2 of the main text.

Sample set up:

i. The sample was inserted into the SQUID, at 150 K.

ii. Once the temperature had stabilised a field of 1000 Oe was applied.

iii. A full DC scan was run and the sample centred based on this.

iv. After centring the field was switched off.

The following sequence was then run:

1. Temperature set to 300K.

2. Run demagnetising sequence.

3. Apply a field of 10000 Oe and wait for stable field.

4. Automatically DC centre.

5. Measure magnetic moment of the sample.

6. Reset magnet.

7. Measure the remanent magnetisation of the sample 8 times, where each measurement recorded by the SQUID is the average of 5 measurements.

8. Temperature set to 150 K and wait for stability.

9. Repeat steps 3-7.

10. Temperature set to 50 K and wait for stability.

11. Repeat steps 3-7.

12. Temperature set to 5 K and wait for stability.

13. Repeat steps 3-7.

Appendix D: Fitting SXRF spectra in PyMCA

This appendix provides a detailed protocol for fitting the SXRF spectra, which is described briefly in Section 4.4.2.2 of the main text. A selection of screen shots from this process is shown in Figure D. The EDF or NeXus data are opened using the 'ROI imaging tool', Figure D a). The average of all of the fluorescence spectra contained in the map is automatically shown in the PyMCA Main Window, Figure D b). The average spectrum for each map was used to create its configuration file, as this provided good signal to noise ratio and contained a contribution from all metals the present in the map.

The first step in the fitting process is to calibrate the energy of the detector channels to the energy of the fluoresced X-rays. In the main window select 'Calibrate' and then 'Compute'. A separate window opens showing the SXRF spectrum. Clicking the 'Peak' button highlights all of the peaks in the spectrum which can then be individually selected by clicking on them, Figure D c). In the fluorescence spectrum typical of a biological tissue a number of peaks can be easily identified by their relative heights and positions: typically the Fe, Cu, and Zn peaks are clearly visible above background. In Figure D c) the Fe peak has been selected by clicking on the line associated with its peak. Each easily identified peak is manually selected and then assigned to the correct elemental fluorescence peak. PyMCA uses this information to calibrate the energy of the entire spectrum. The energy calibration can be saved and loaded for subsequent maps, although it is good practice to recalibrate when looking at data from different visits to the DLS.

The next step is to begin fitting the spectrum by clicking 'Fit' in the main window and selecting 'Advanced' which opens the fitting window, Figure D e). Select configure to open the 'MCA Fit Parameters' window. This contains a number of tabs which are used to provide PyMCA with the information required to fit the spectrum.

Highlight the metals expected in the sample in the 'PEAK' tab, Figure D e). In addition to the metals expected to be present in the tissue (iron, copper and zinc), other transition metals which fluoresce in the same energy range (manganese, cobalt, chromium and nickel) should be selected. These metals may show up naturally or in contamination on the sample (for example from stainless steel) and therefore fitting these peaks is important to identify any false iron data due to contamination.

The 'FIT' tab, Figure D f), is used to set the range of the fit to just the energy range of the metals of interest. Check the box 'Limit fitting region to:' and choose the channel (and therefore energy) range.

After choosing the fitting parameters click 'OK' again, to display the fit to the spectrum in the 'McaAdvancedFit' window, Figure D d). In this window fit function, background function and the peak shapes can be adjusted to achieve the best fit to the data. This window also shows the breakdown of how each peak is fitted to a particular metal or combination of metals.

The fit includes the background, which is elevated towards the Zn peak end of the spectrum due to the scatter peak , from I_0 at 10 keV. It is important that this background is fitted well, as it is in the example here, because it will be subtracted from the spectrum before the area under each peak is calculated.

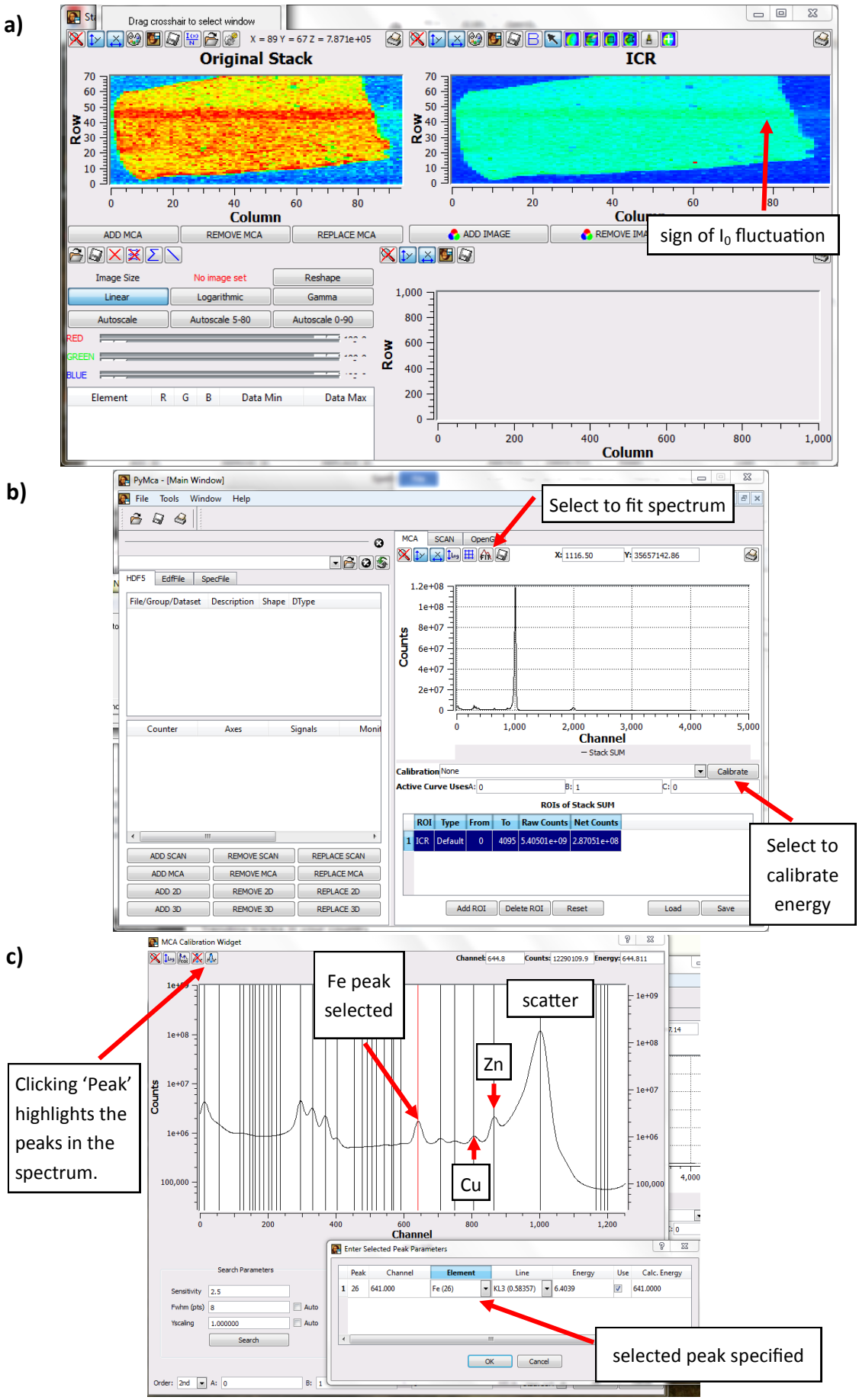

Figure D: Fitting a fluorescence spectrum in PyMCA. a) The ROI Imaging Tool window showing an SXRF map. b) The main PyMCA window showing the average SXRF spectrum for the map in a). The tool shown in c) is used to calibrate the energy of the detector channels.

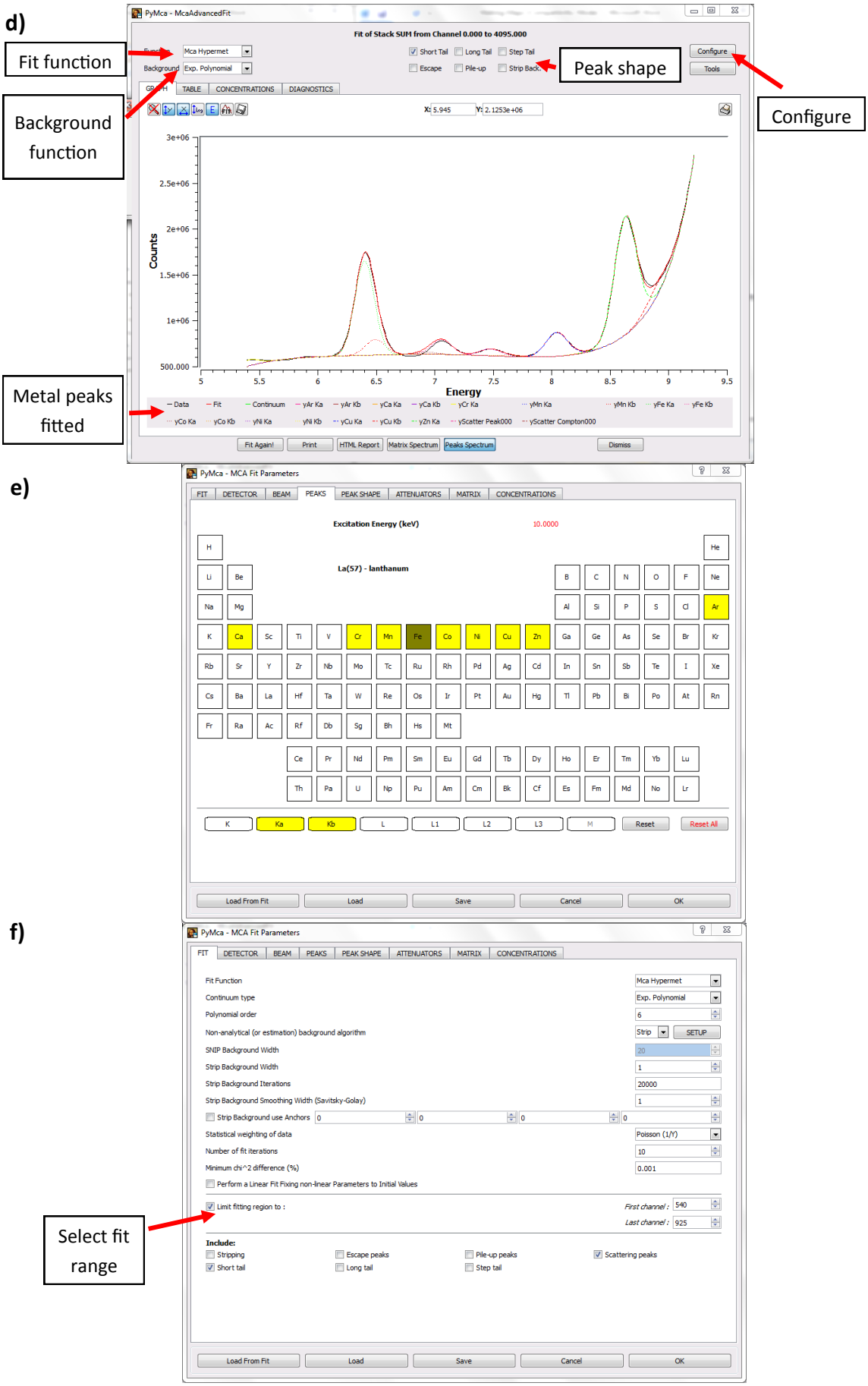

Figure D: Fitting fluorescence spectra in PyMCA continued. The Advance Fit tool is shown in d) displaying the fitted SXRF spectrum. The fit is achieved by choosing parameters such as the expected fluorescence peaks e) and by limiting the energy range of the fit f).

Appendix E : Segmentation of MRI maps made at 9.4 T

The following pages show the segmentation of a typical slice of an R_2 and R_2* map for all samples mapped at 9.4 T (and not already shown in Section 7.1.1 of the main text). Contrast in the maps was chosen to best reveal the structure and is not the same for each sample.

Caudate nucleus C2

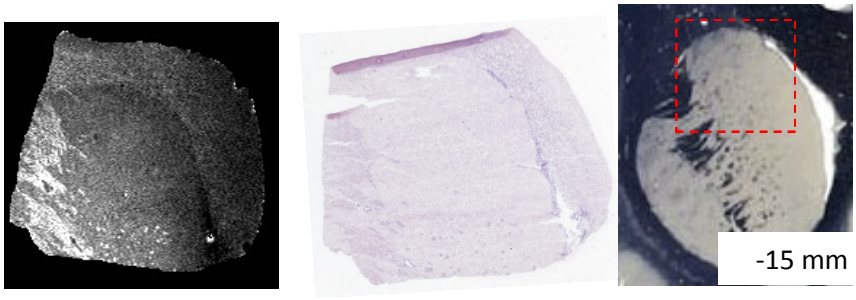

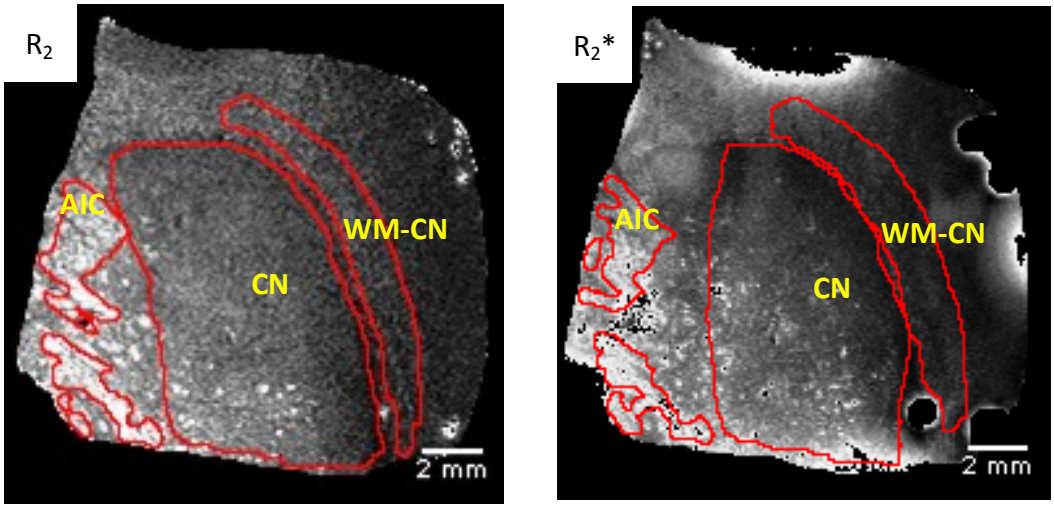

CN = caudate nucleus; AIC = anterior limb of the internal capsule;
WM-CN = the white matter medial to the caudate nucleus

Caudate nucleus C3

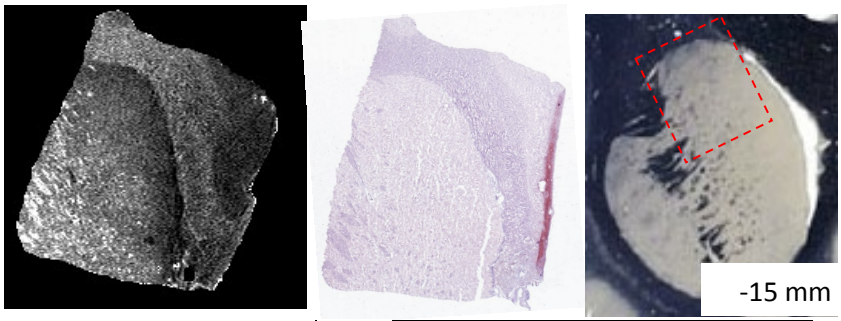

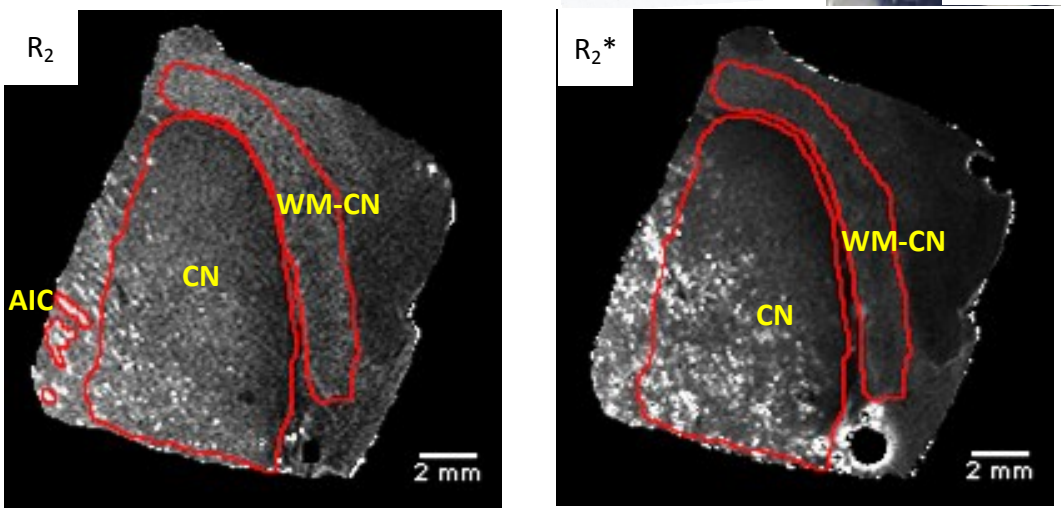

Caudate nucleus AD1

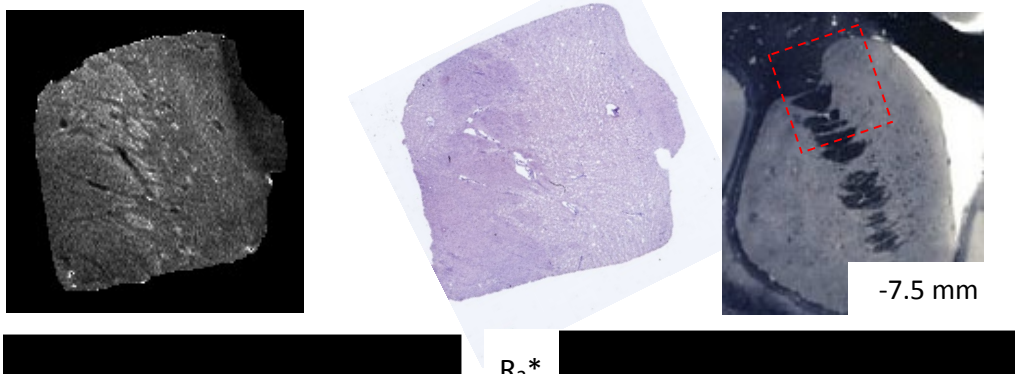

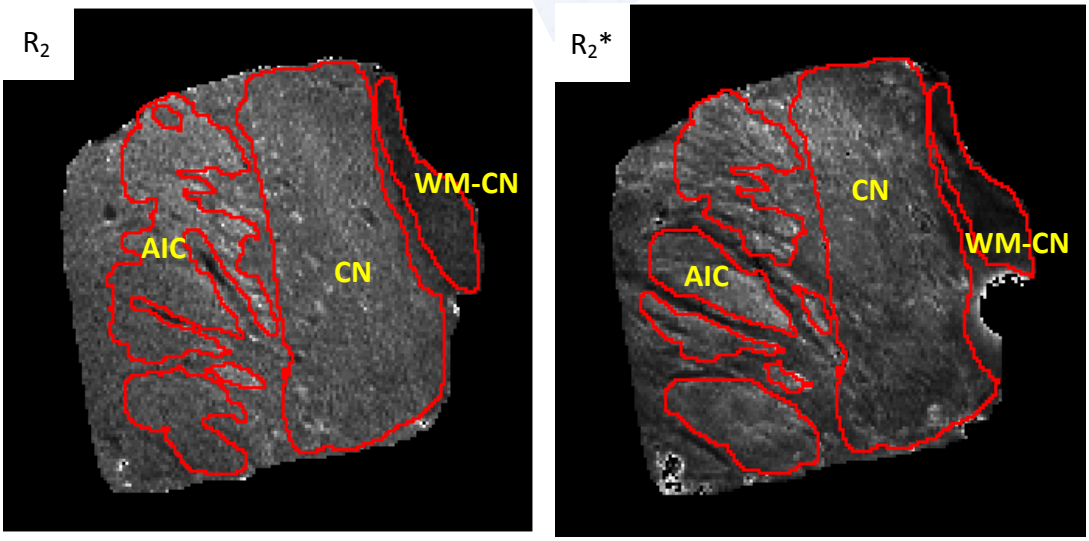

CN = caudate nucleus; AIC = anterior limb of the internal capsule;
WM-CN = the white matter medial to the caudate nucleus

Caudate nucleus AD2

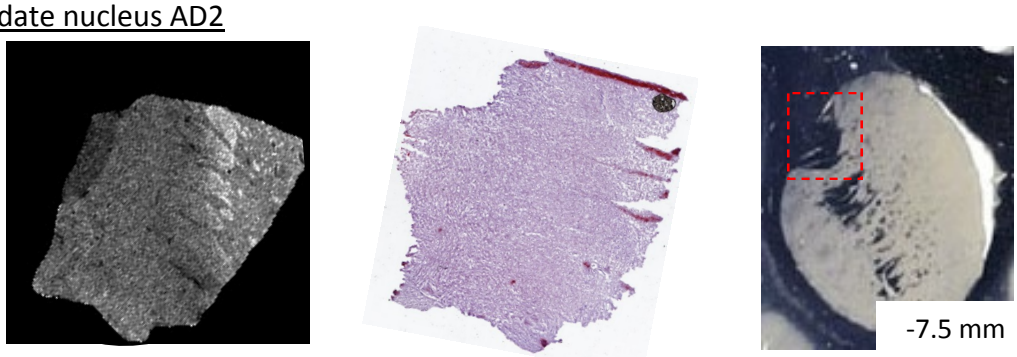

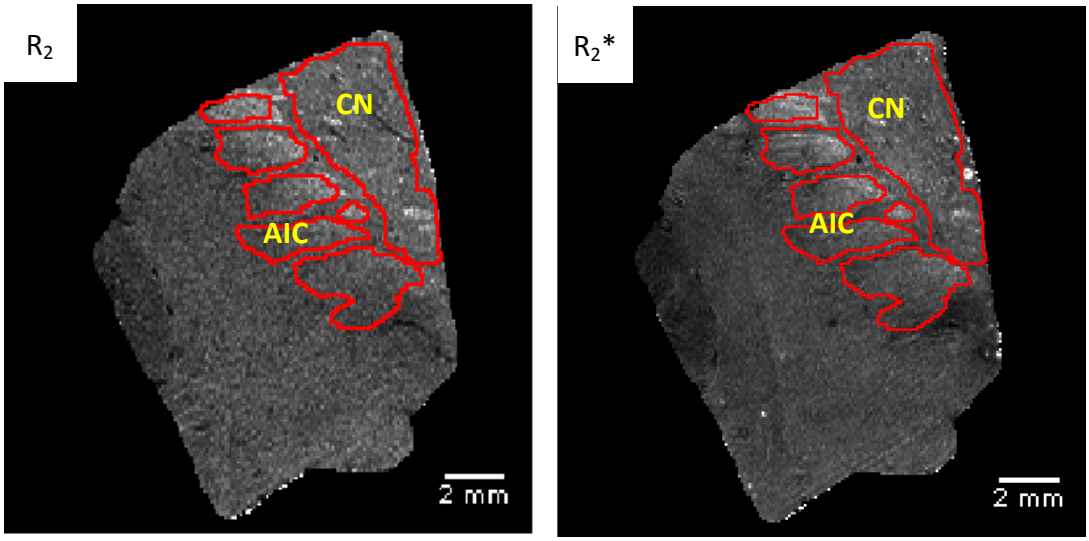

Caudate nucleus AD3

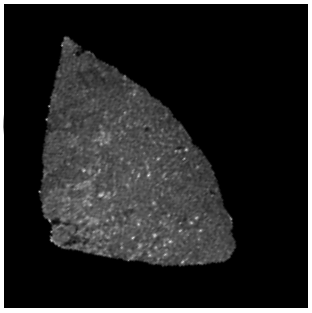
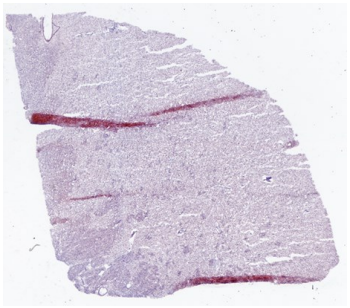
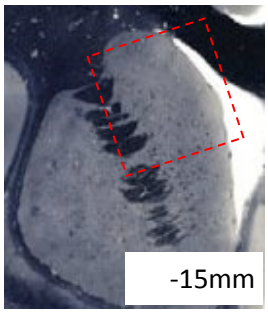

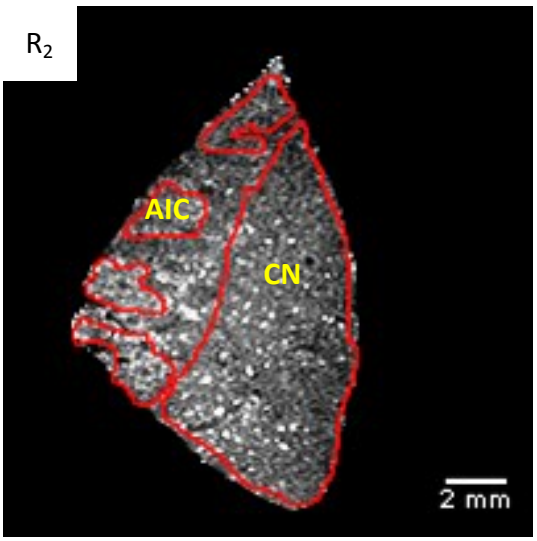

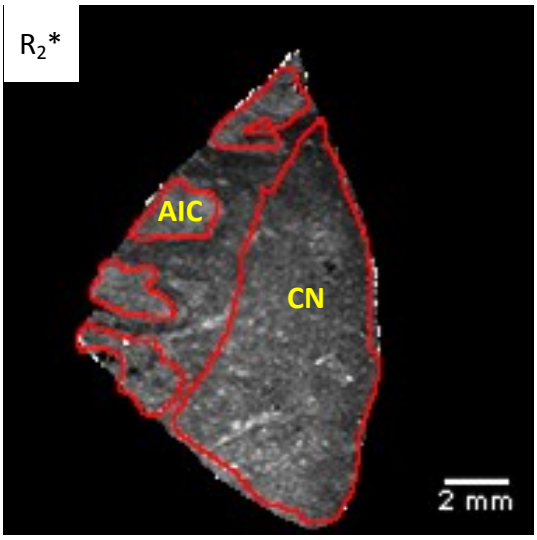

CN = caudate nucleus; AIC = anterior limb of the internal capsule;
WM-CN = the white matter medial to the caudate nucleus

Putamen C1

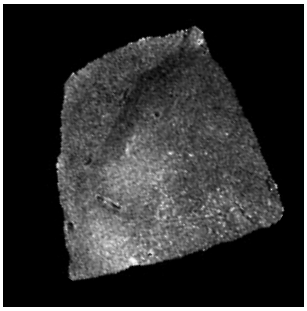
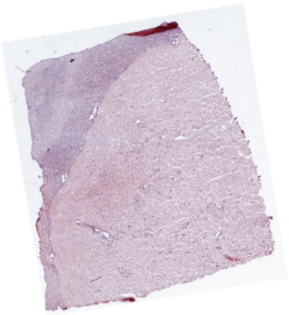
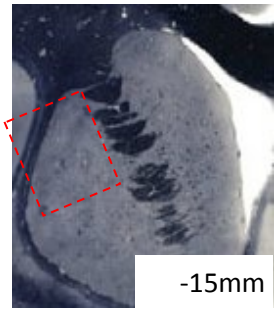

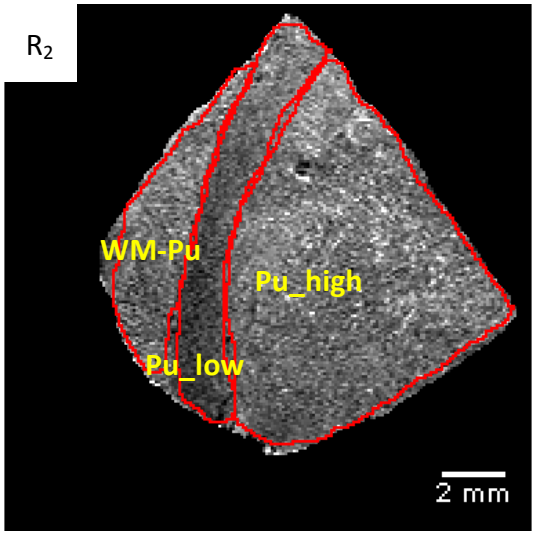

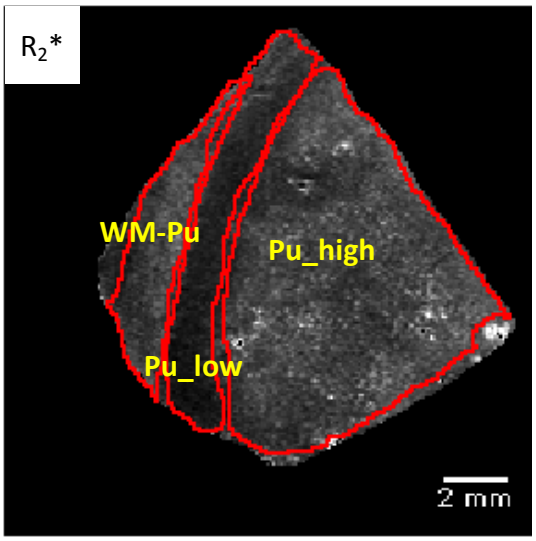

Pu_high = the bright area of the putamen; Pu_low = the dark band along the lateral edge of the putamen; Pu=WM = white matter lateral to the putamen

Putamen C2

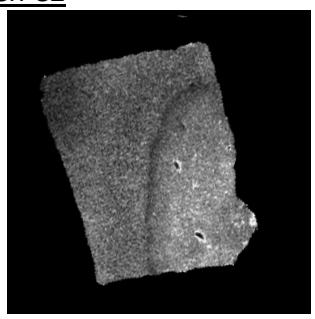

Sample was deformed between MRI mapping and sectioning.

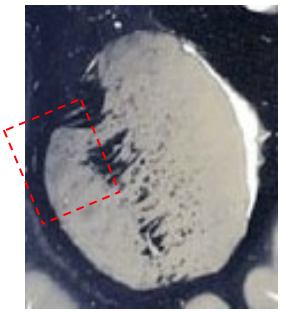

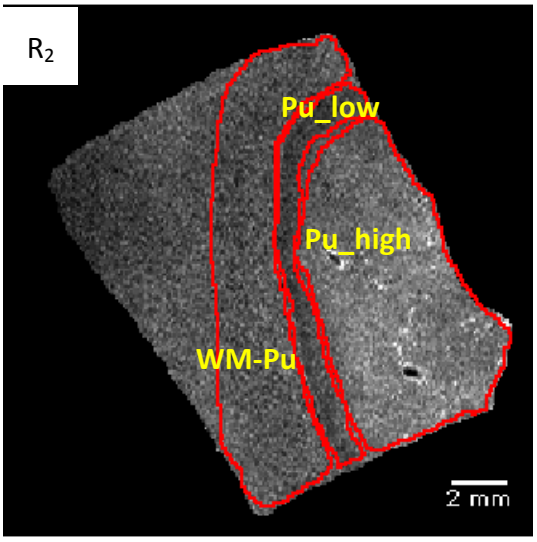

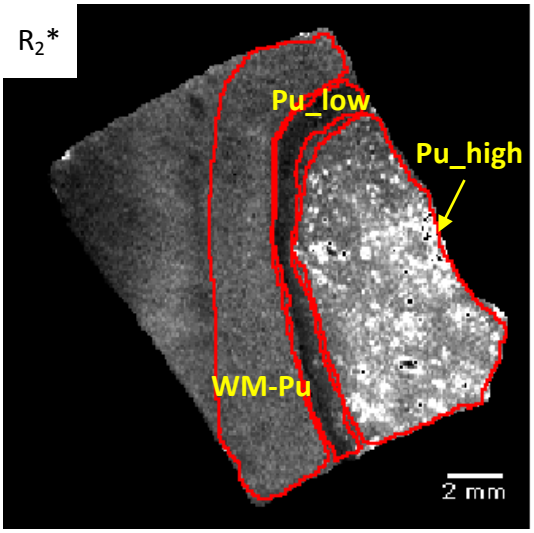

Pu_high = the bright area of the putamen; Pu_low = the dark band along the lateral edge of the putamen; Pu=WM = white matter lateral to the putamen

Putamen AD1

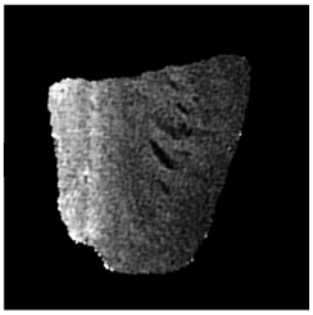

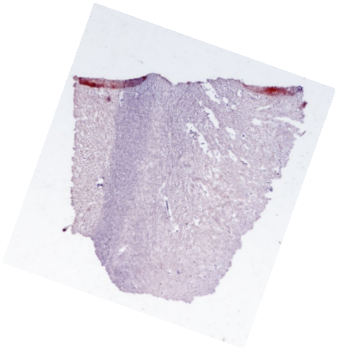

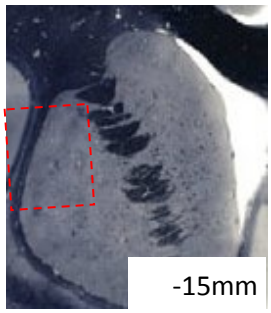

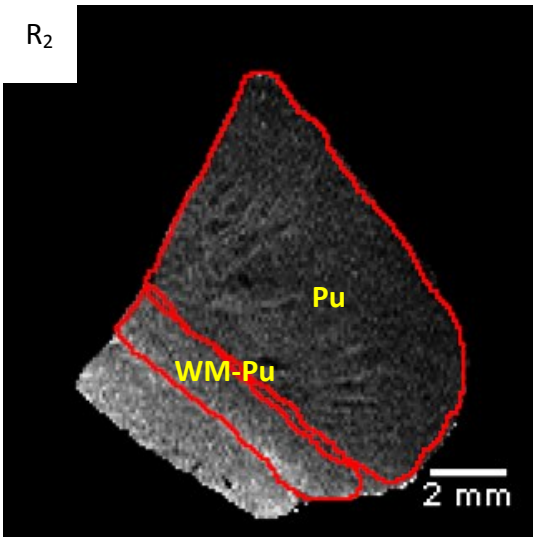

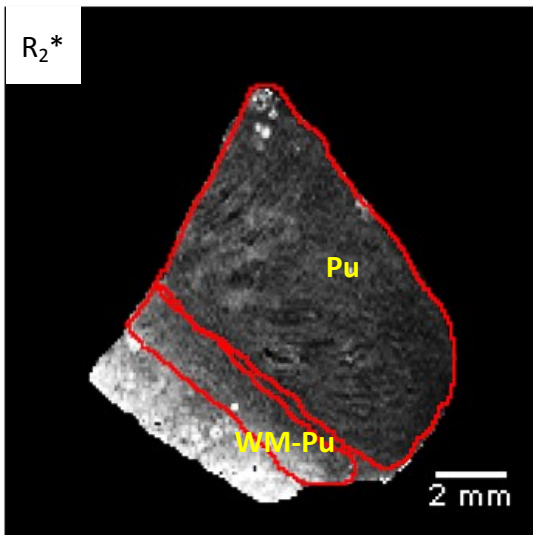

Putamen AD2

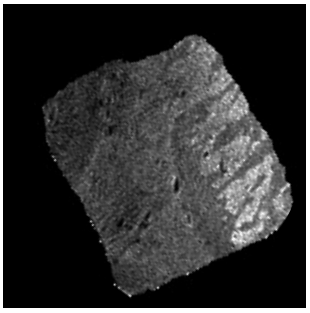
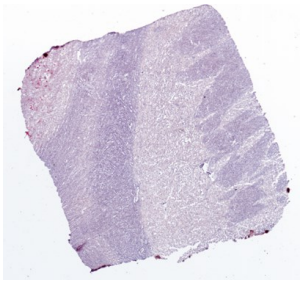
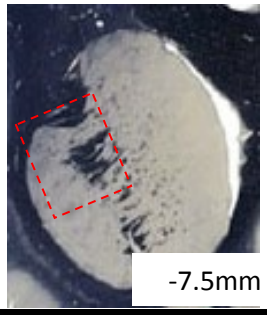

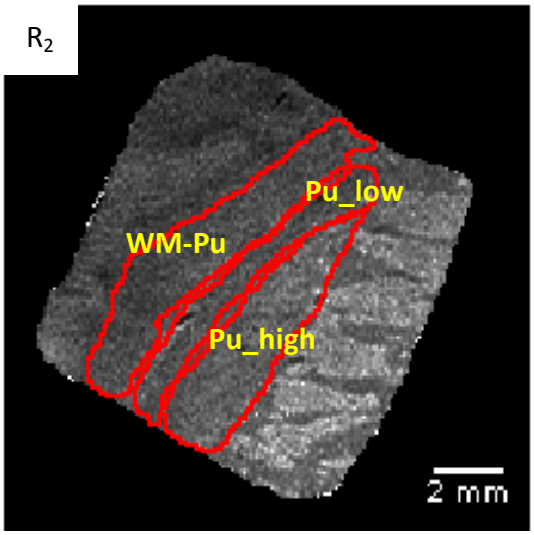

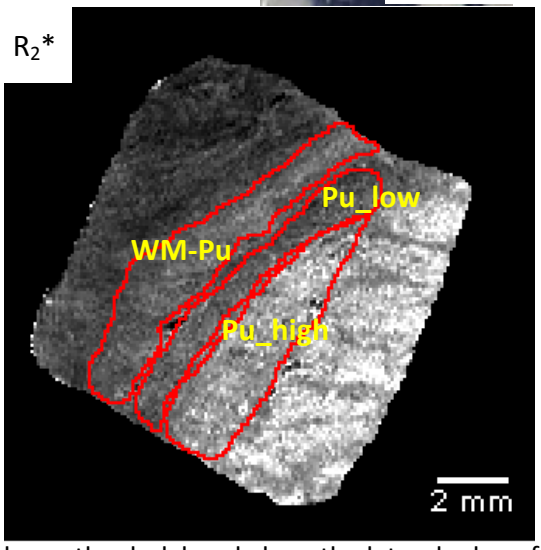

Pu_high = the bright area of the putamen; Pu_low = the dark band along the lateral edge of the putamen; Pu=WM = white matter lateral to the putamen

Putamen AD3

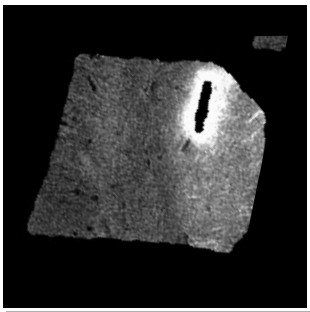
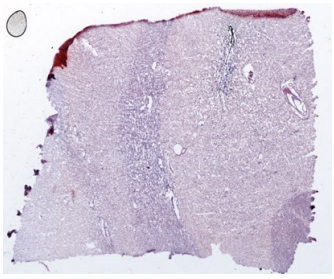
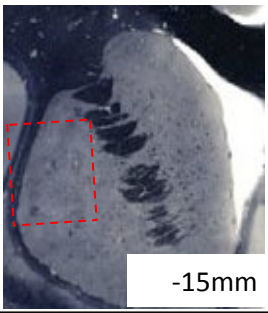

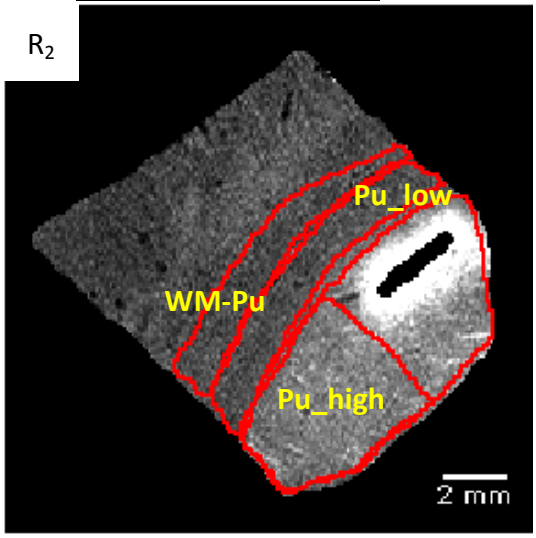

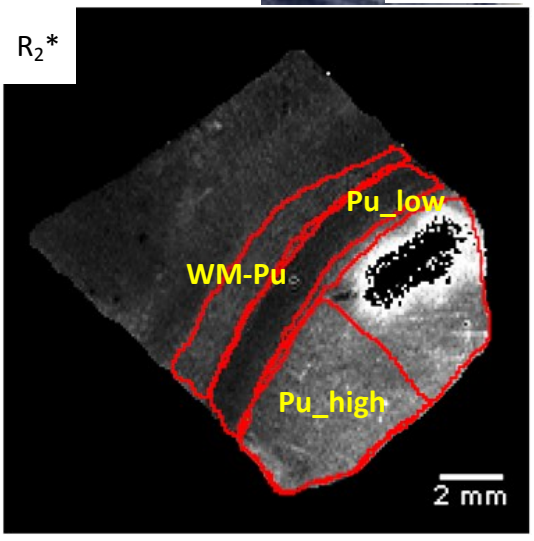

Note: the Pu_high region was selected to exclude the very bright region, which is caused by a blood vessel.

Globus pallidus C1

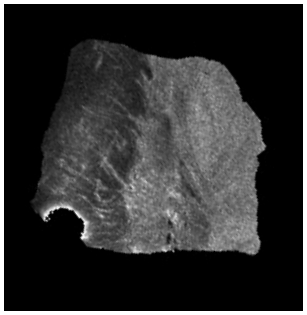

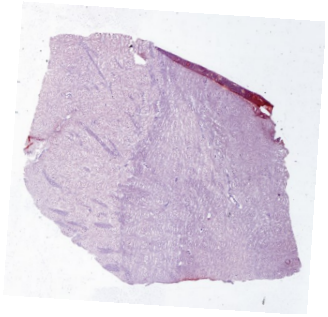

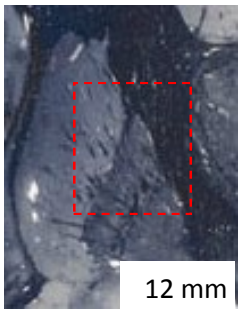

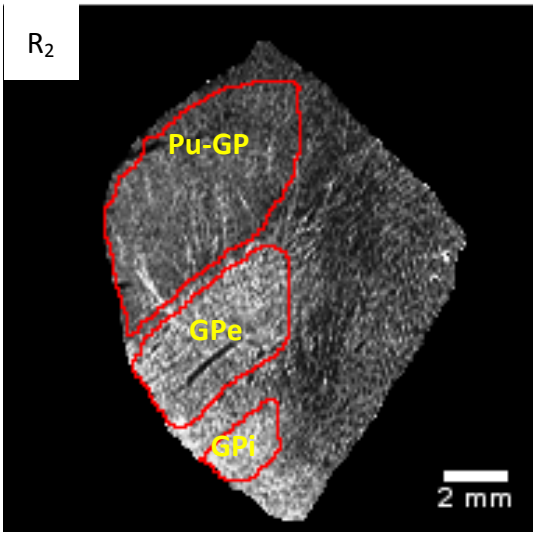

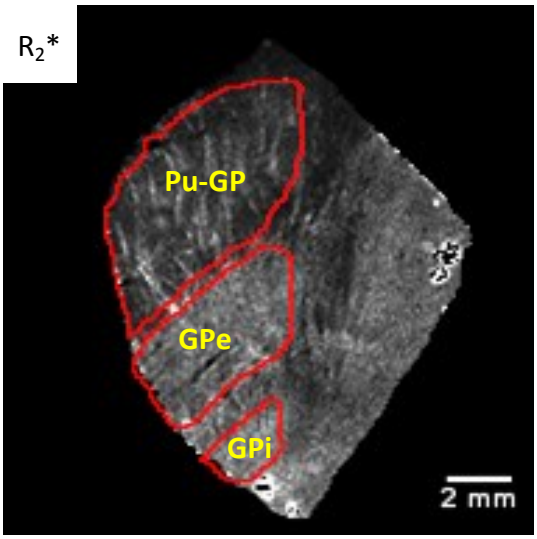

GPe = external globus pallidus; GPi = internal globus pallidus;

Pu-GP = putamen lateral to the globus pallidus

Globus pallidus C3

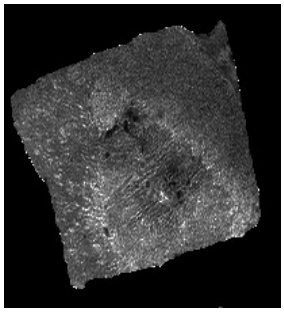

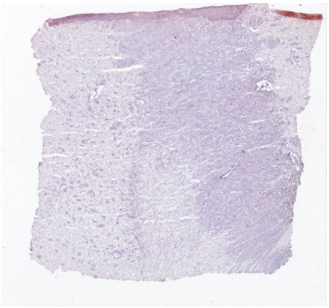

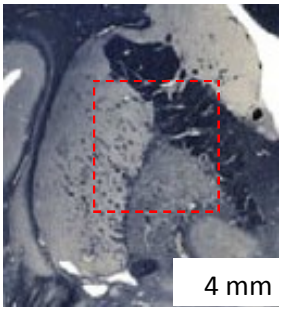

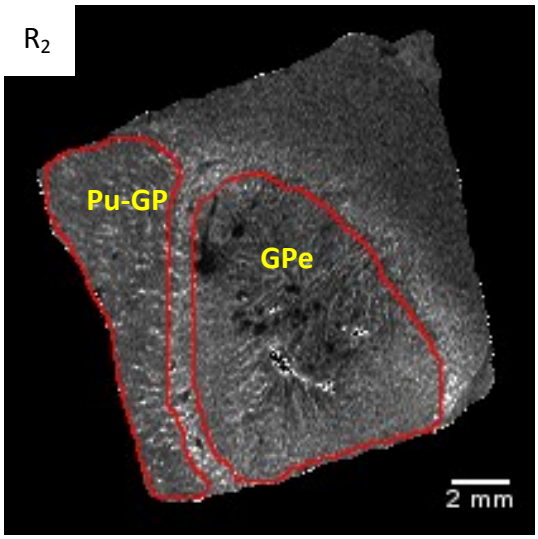

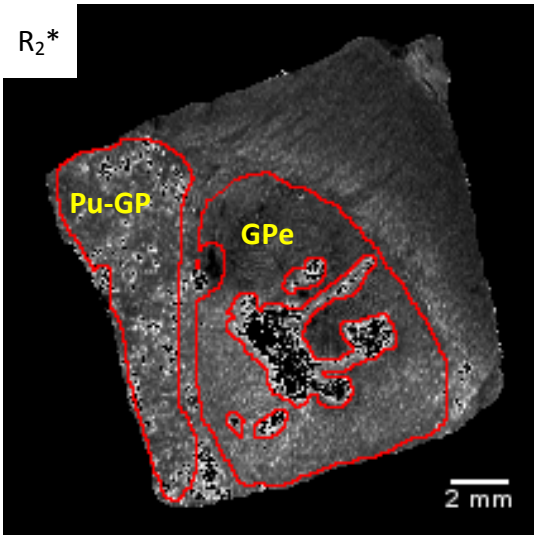

Globus pallidus AD1

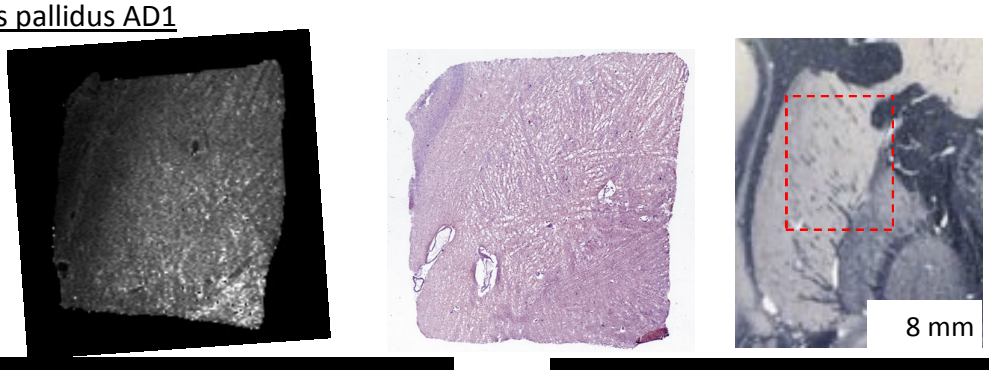

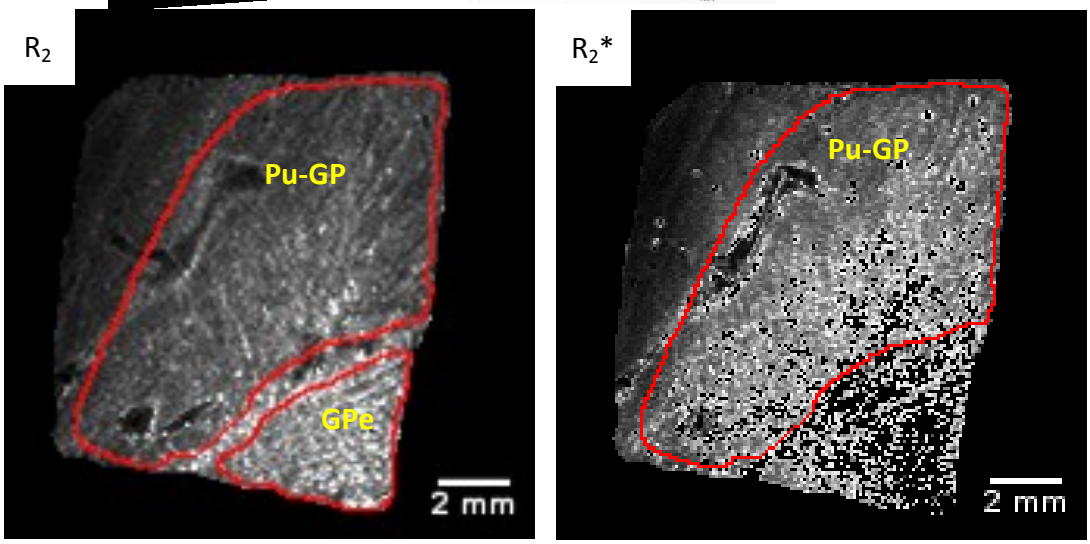

The GPe was not segmented in the R_2* as rapid decays prevented fitting of to a large number of pixels

GPe = external globus pallidus; GPi = internal globus pallidus;
Pu-GP = putamen lateral to the globus pallidus

Globus pallidus AD3

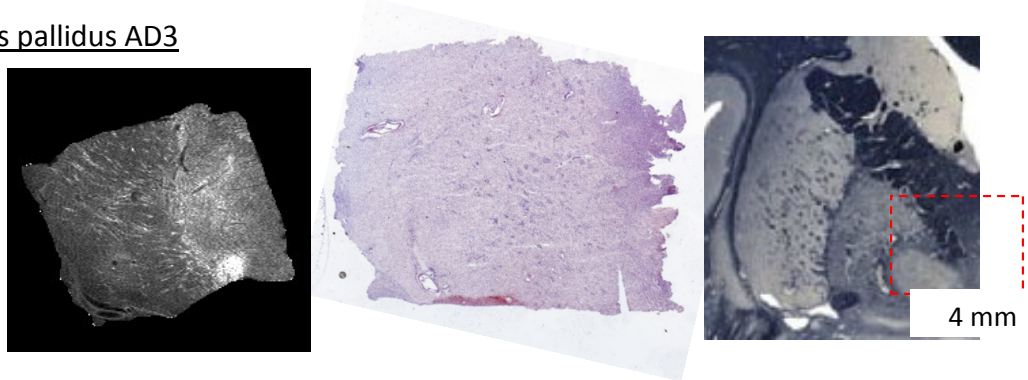

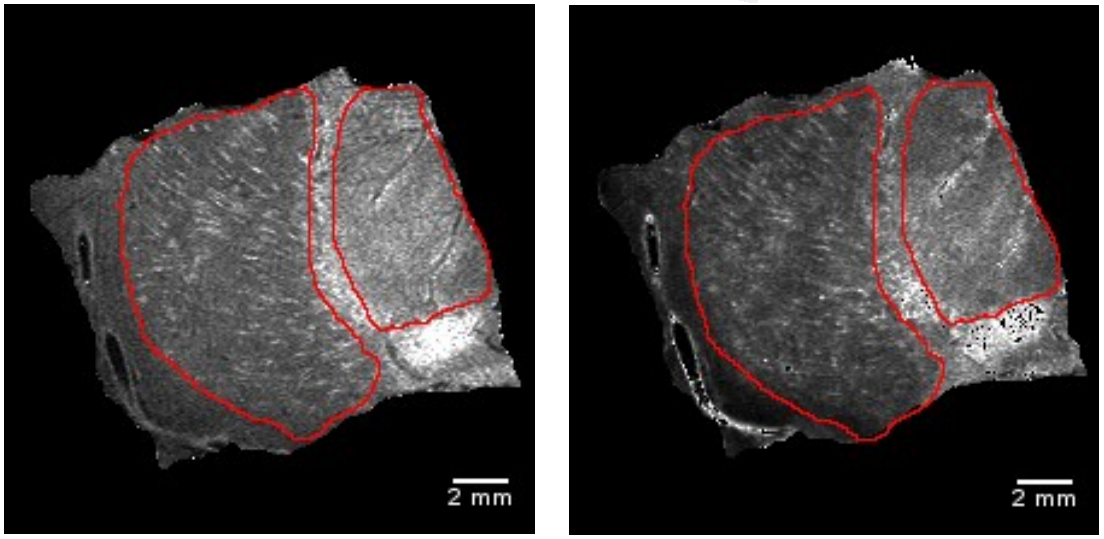

Substantia nigra C1

No stained section available

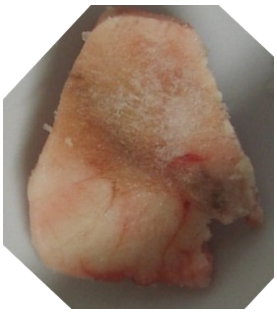

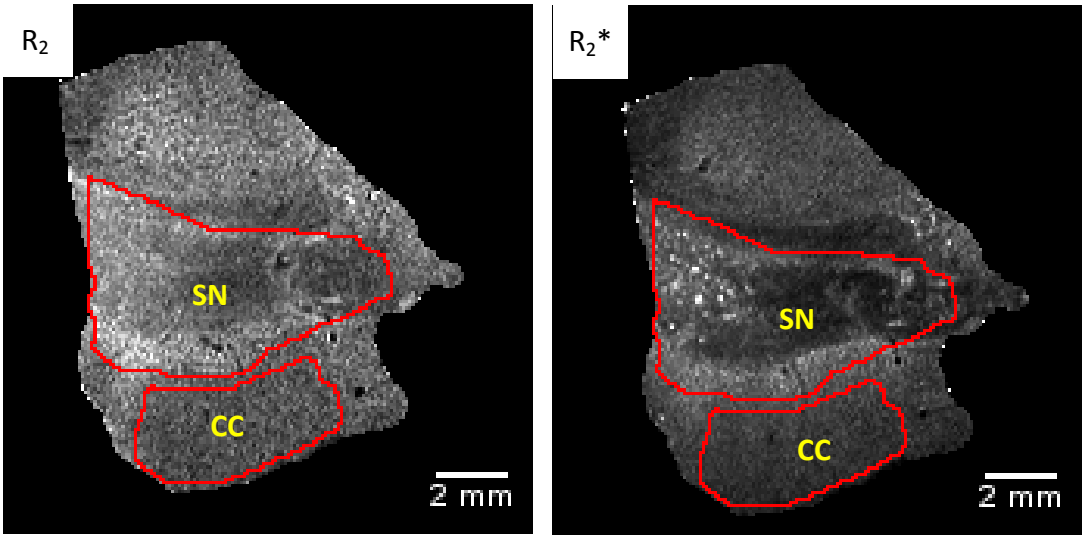

SN = substantia nigra; CC = cerebral crus

Substantia nigra AD1

No stained section available

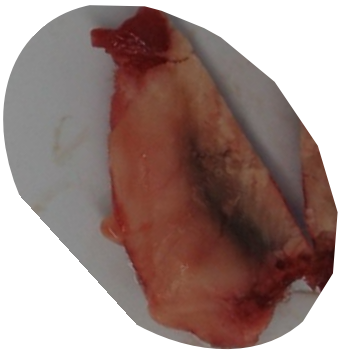

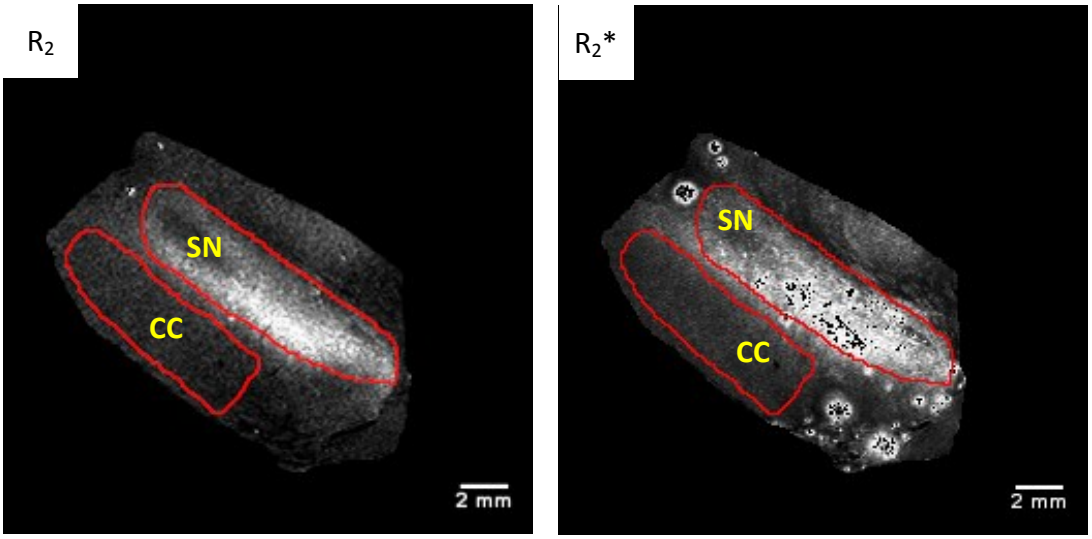

Substantia nigra AD2

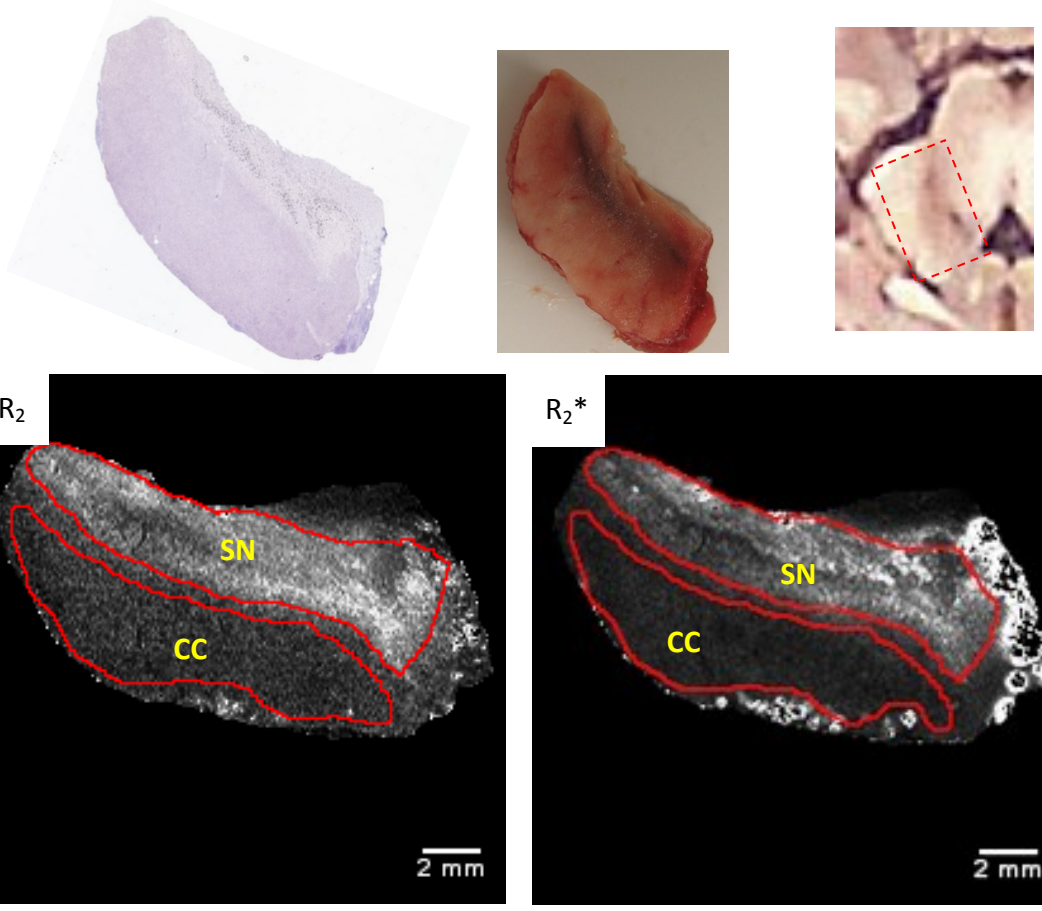

SN = substantia nigra; CC = cerebral crus

Substantia nigra PD1

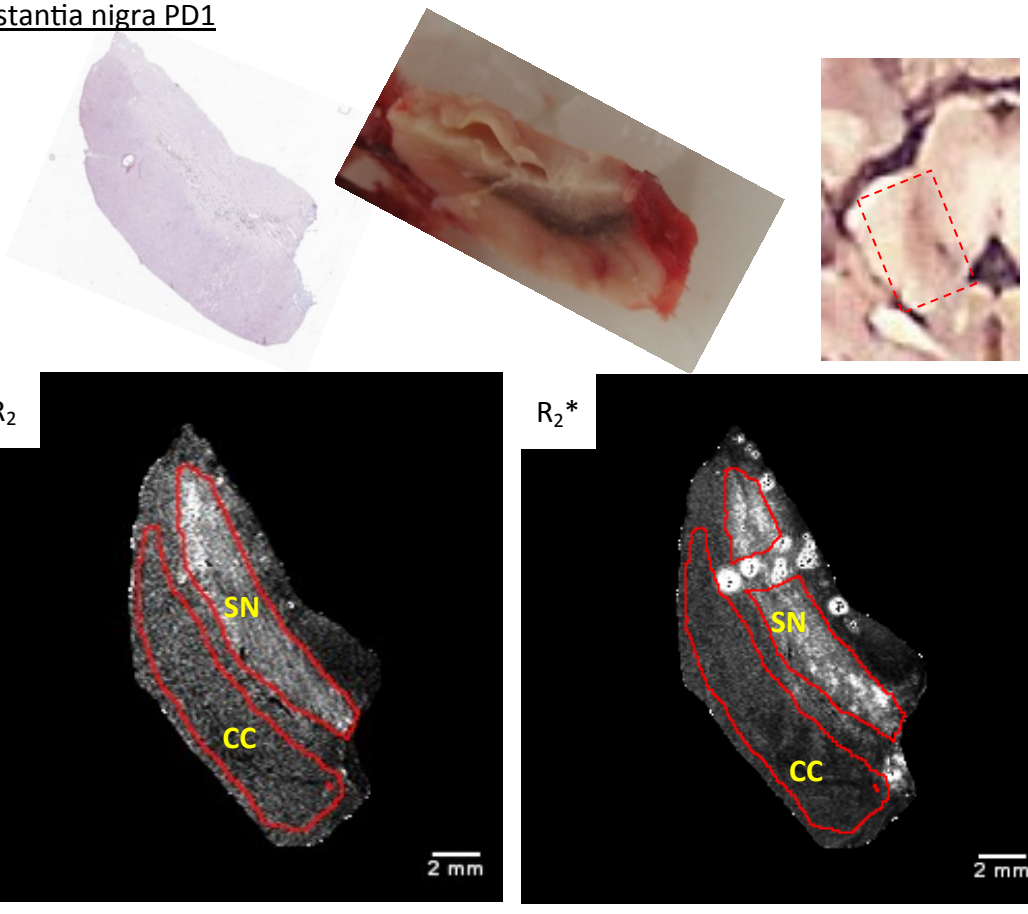

Substantia nigra PD4

No stained section available

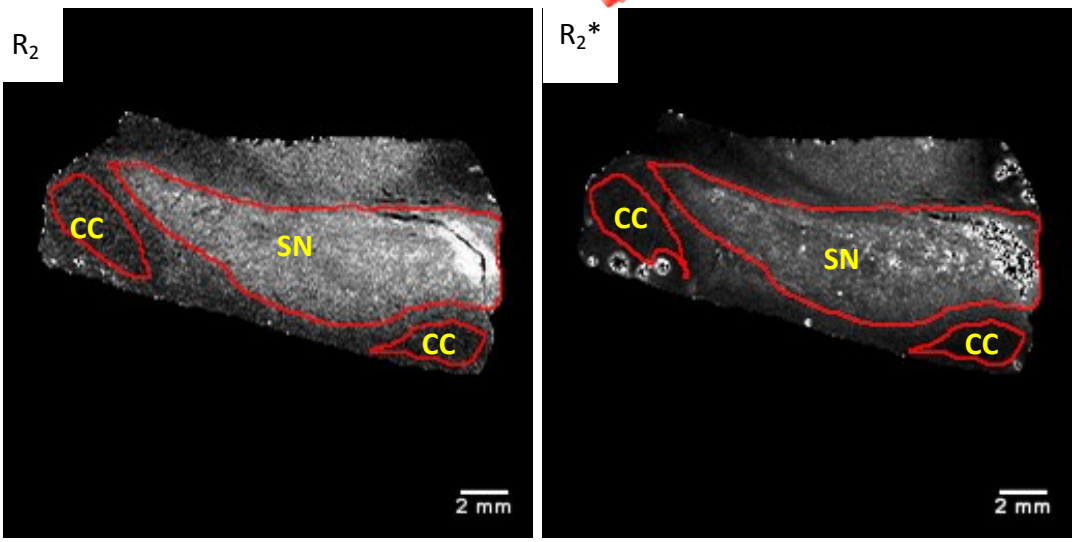

SN = substantia nigra; CC = cerebral crus

Appendix F : MRI maps of the pons at 14.1 T

The R_2* MRI maps of the pons, as discussed in Section 7.1.2 of the main text.

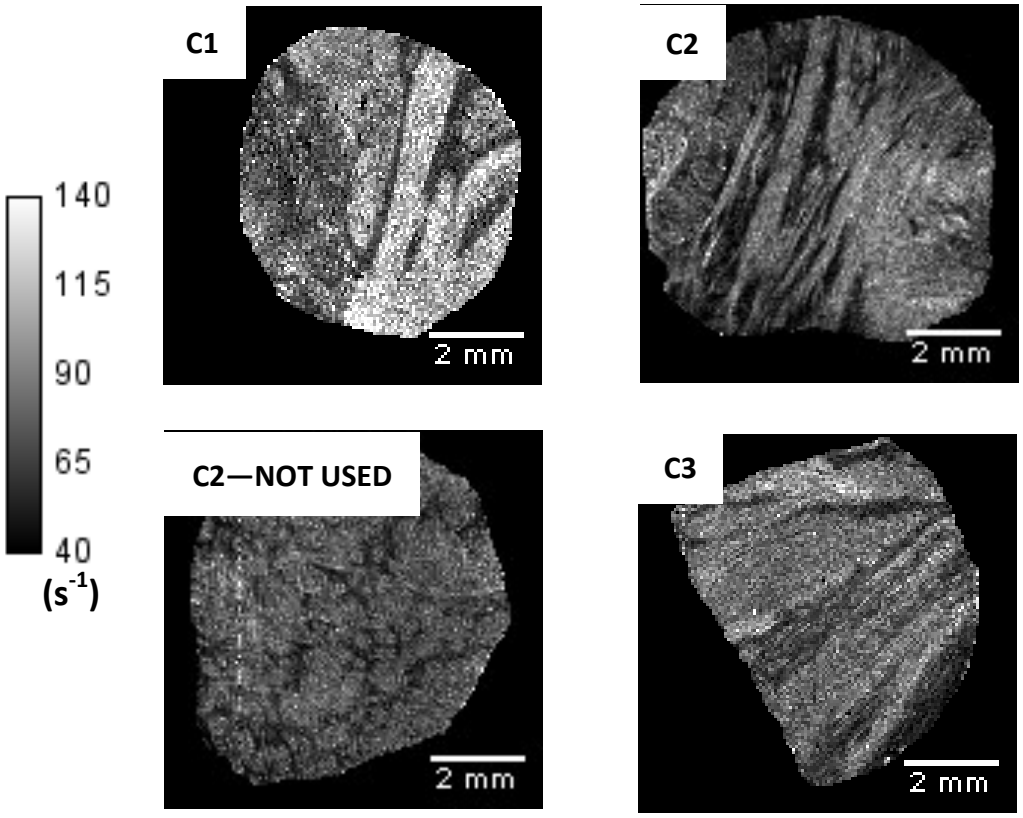

Control pons samples. The first C2 sample was used in the analysis.

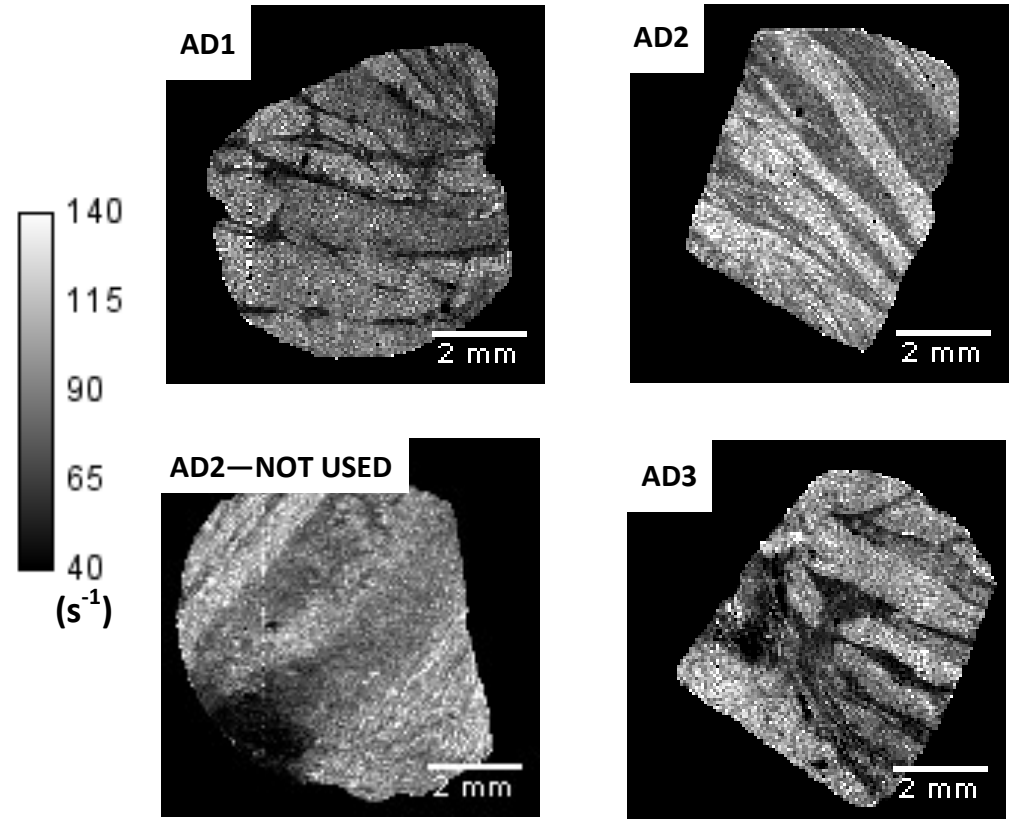

Alzheimer's disease pons samples. The first AD2 sample was used in the analysis.

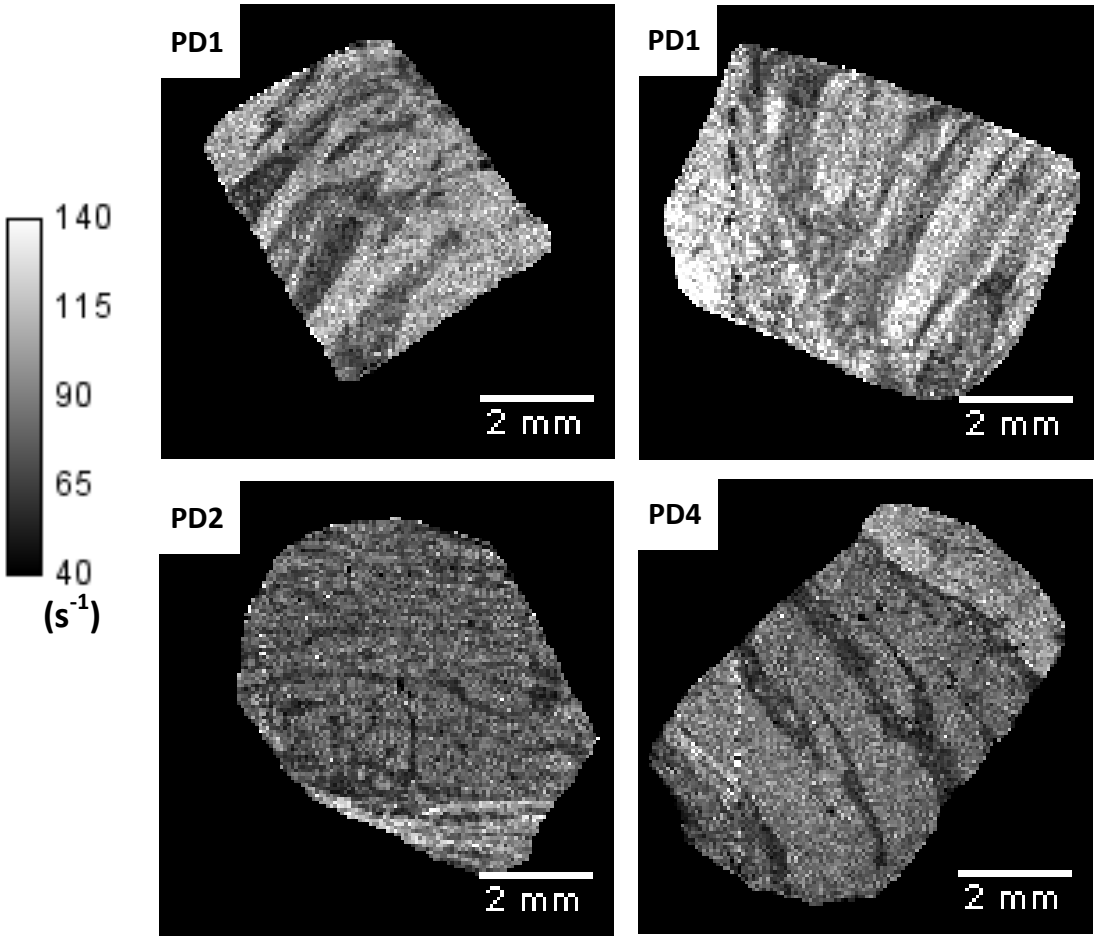

PD pons samples. The average R_2* from both PD1 samples was used.

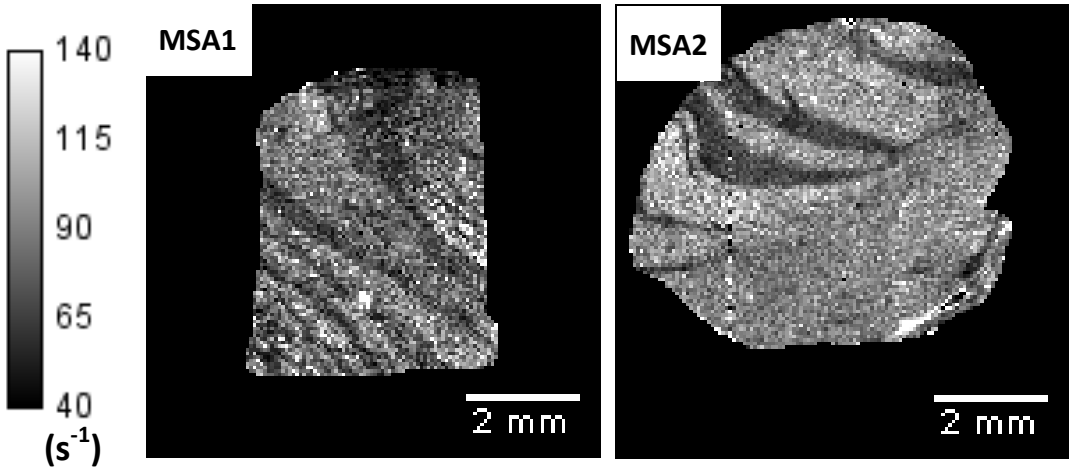

MSA pons samples.

Appendix G: Matching SXRF and MRI maps

The following pages shows how the MRI slice that best matches the SXRF map was chosen and trimmed. This process is described in Section 8.1.1.1 of the main text.

<u>Caudate Nucleus AD1</u>

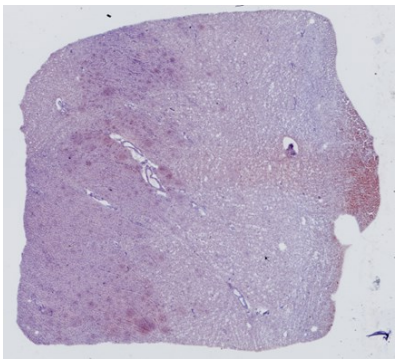

Section stained with haematoxylin, adjacent to mapped section

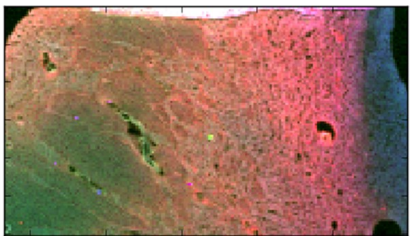

Combined metal SXRF map.
red = iron; green = copper;
blue = zinc.

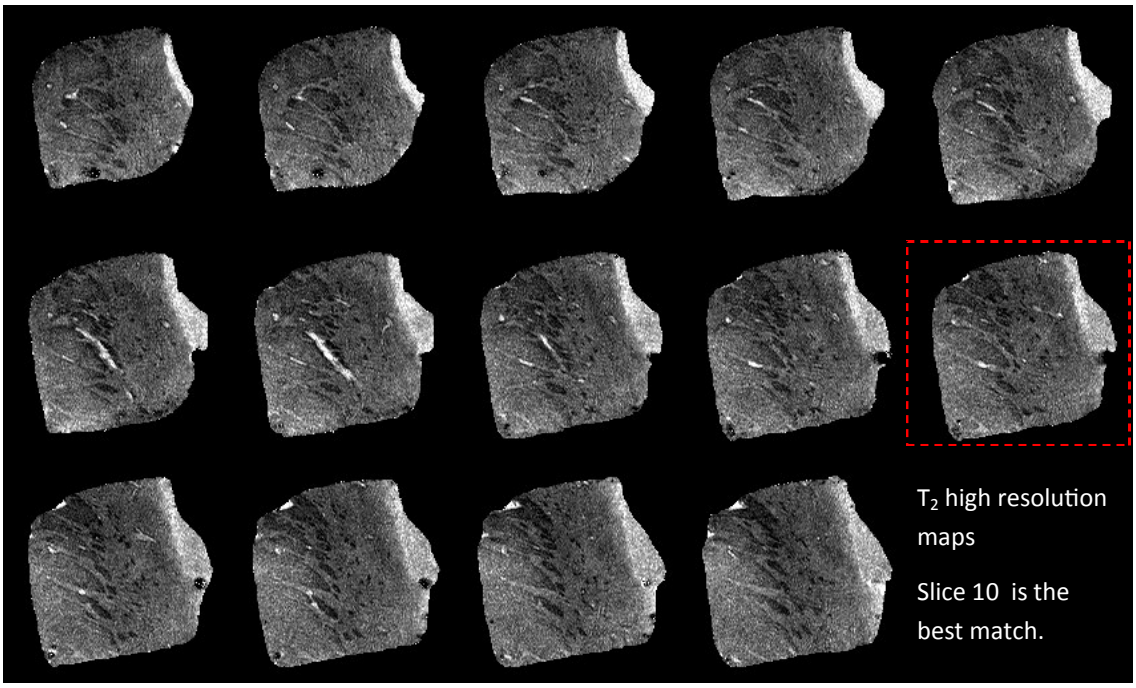

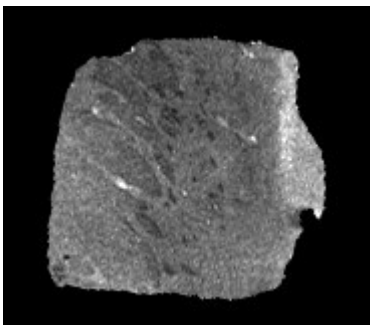

Slice 10 T_2 map is rotated into the same orientation as the SXRF map.

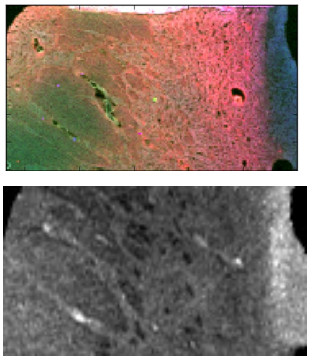

T_2 map is trimmed to the same dimensions as the SXRF map.

Final R_2 map

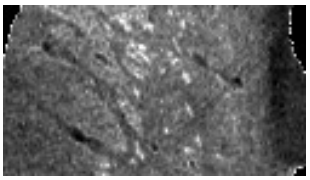

Finally the reciprocal of the matched, rotated & trimmed map is calculated to produce the R_2 map.

Putamen sample C3

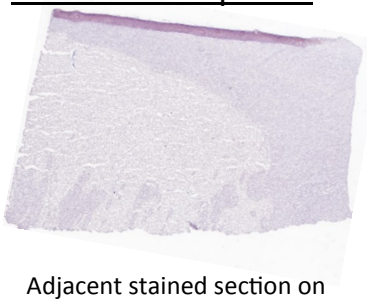

Adjacent stained section on glass

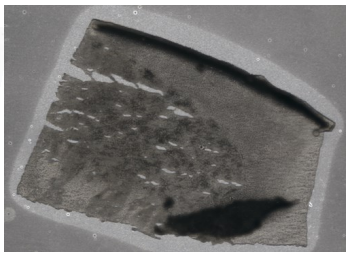

Unstained, mapped section on quartz.

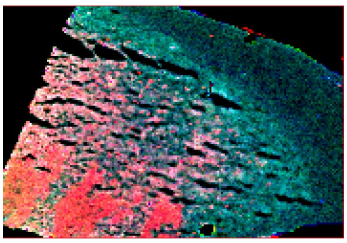

Combined metal SXRF map. red = iron; green = copper; blue = zinc.

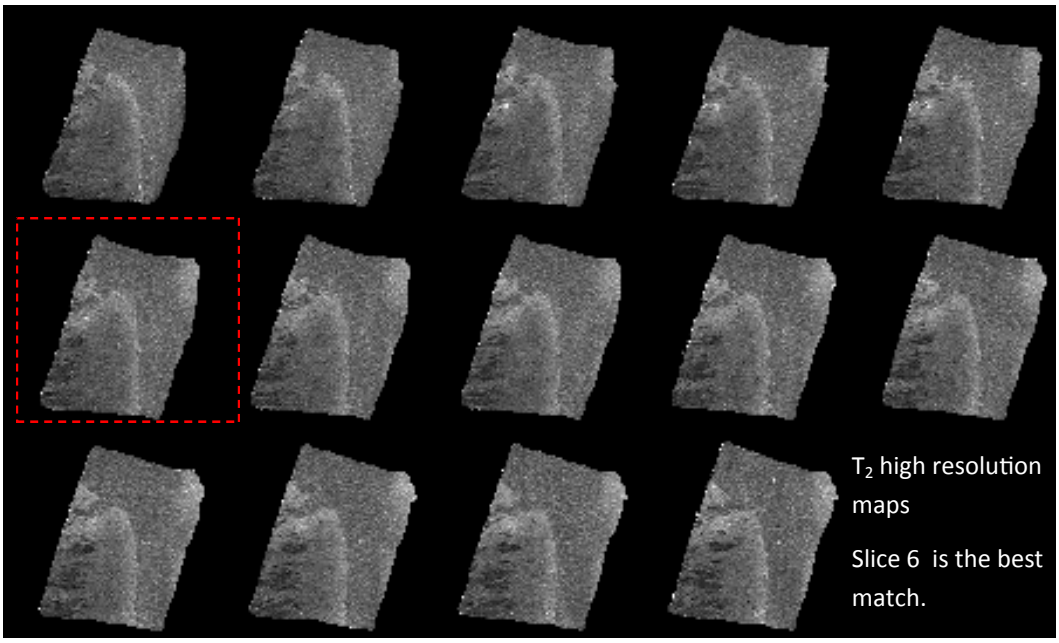

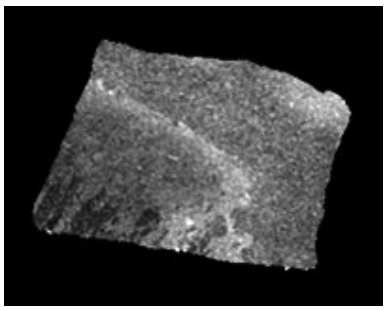

Slice 6 T_2 map is rotated into the same orientation as the SXRF map.

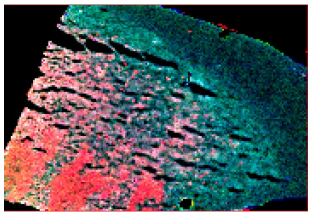

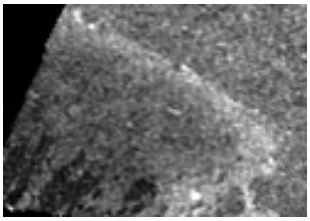

T_2 map is trimmed to the same dimensions as the SXRF map.

Final R_2 map

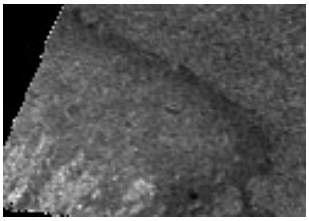

Finally the reciprocal of the matched, rotated & trimmed map is calculated to produce the R_2 map.

Putamen sample AD3

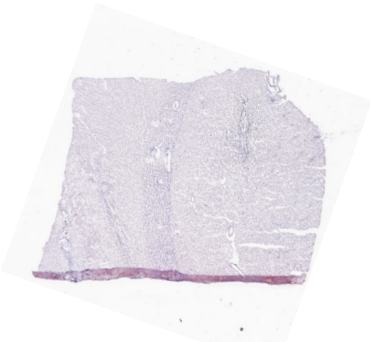

Adjacent stained section on glass

Unstained, mapped section on quartz.

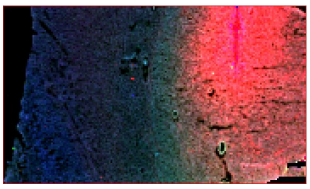

Combined metal SXRF map. red = iron; green = copper; blue = zinc.

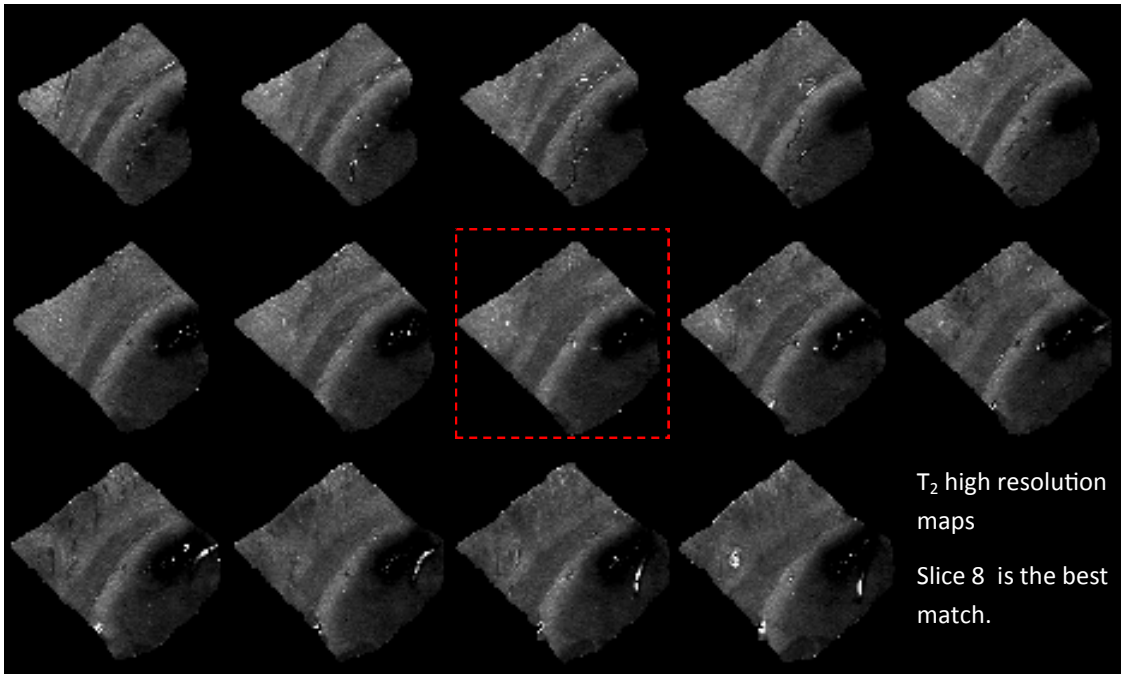

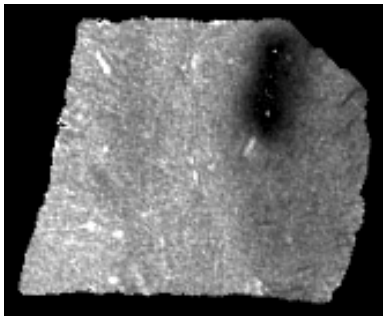

Slice 6 T_2 map is rotated into the same orientation as the SXRF map.

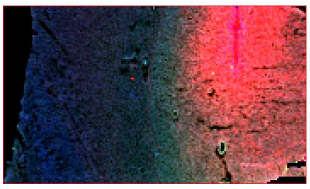

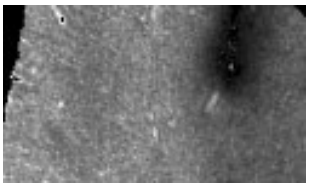

T_2 map is trimmed to the same dimensions as the SXRF map.

Final R_2 map

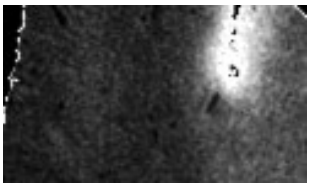

Finally the reciprocal of the matched, rotated & trimmed map is calculated to produce the R_2 map.

Globus pallidus sample C3

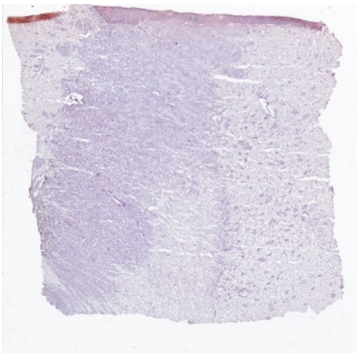

Adjacent stained section on glass

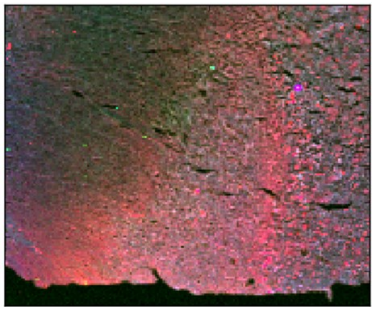

Combined metal SXRF map.
red = iron; green = copper;
blue = zinc.

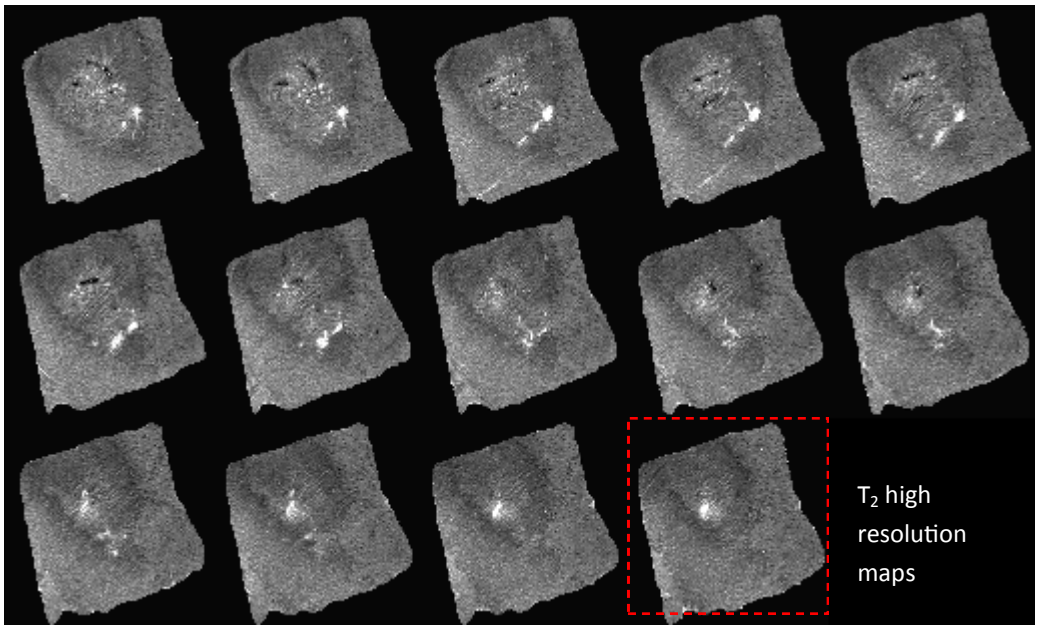

Slice 14 gives the best match in high resolution data, however a better match was achieved with the low resolution data (see below).

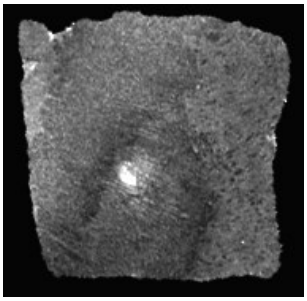

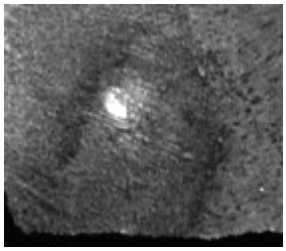

High resolution map (above) and low resolution map (below) are trimmed to the same dimensions as the SXRF map.

Final high resolution R_2 map

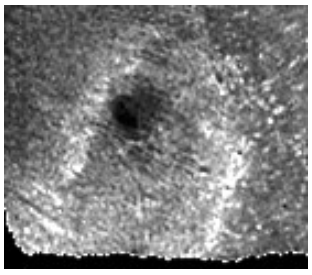

The reciprocal of the maps are taken to produce R_2 maps

Best matched high resolution (above) and low resolution (below) are rotated into the SXRF map orientation

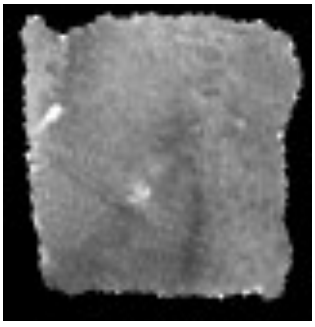

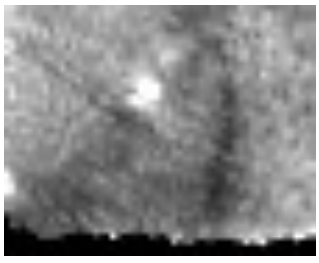

Final low resolution R_2 map

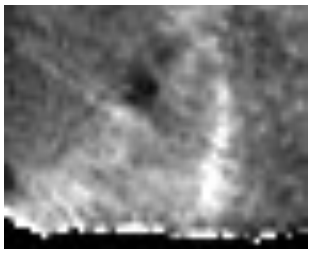

Globus pallidus sample AD2

Stained SXRF-mapped section

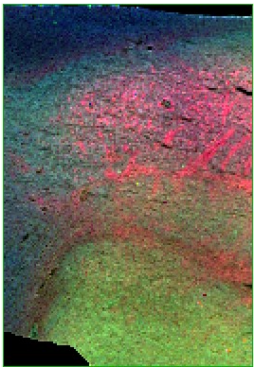

Combined metal SXRF map.
red = iron;
green = copper;
blue = zinc.

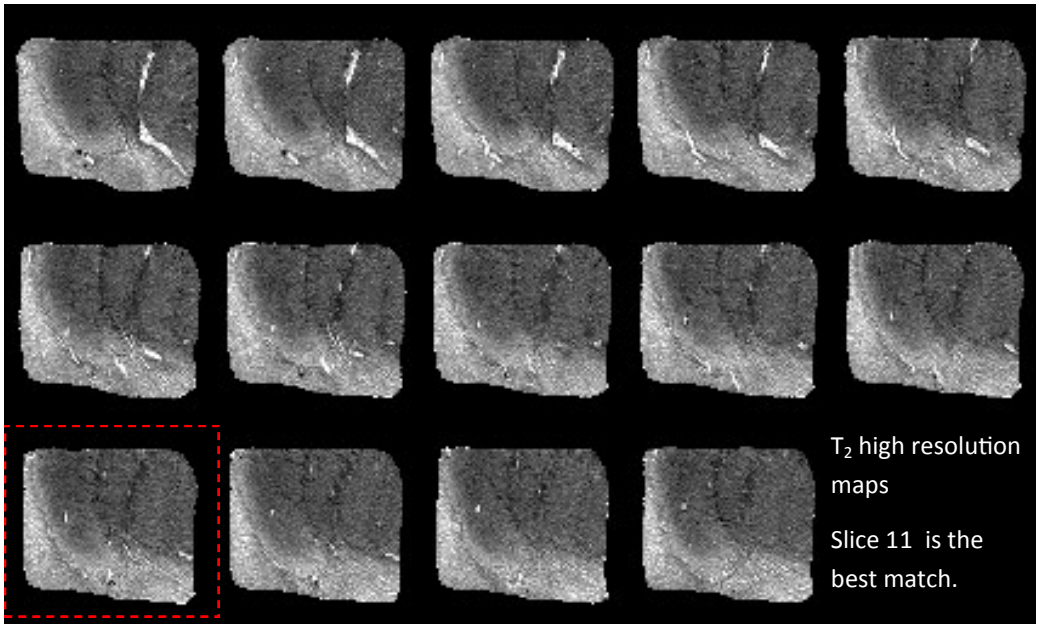

T_2 high resolution maps

Slice 11 is the best match.

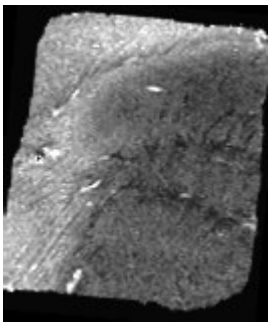

Slice 11 T_2 map is rotated into the same orientation as the SXRF map.

T_2 map is trimmed to the same dimensions as the SXRF map.

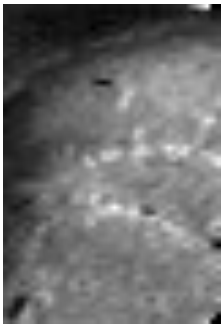

A matched low resolution MRI map is also produced to compare to the low resolution control GP map.

Final R_2 map

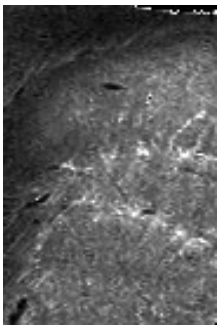

Finally the reciprocal of the matched, rotated and trimmed map is calculated to produce the R_2 map.

Substantia nigra sample C2

Unstained, mapped section on quartz.

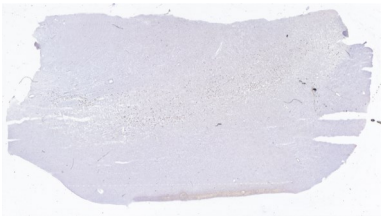

Stained section, after mapping

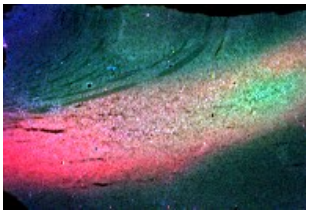

Combined metal SXRF map. red = iron; green = copper; blue = zinc.

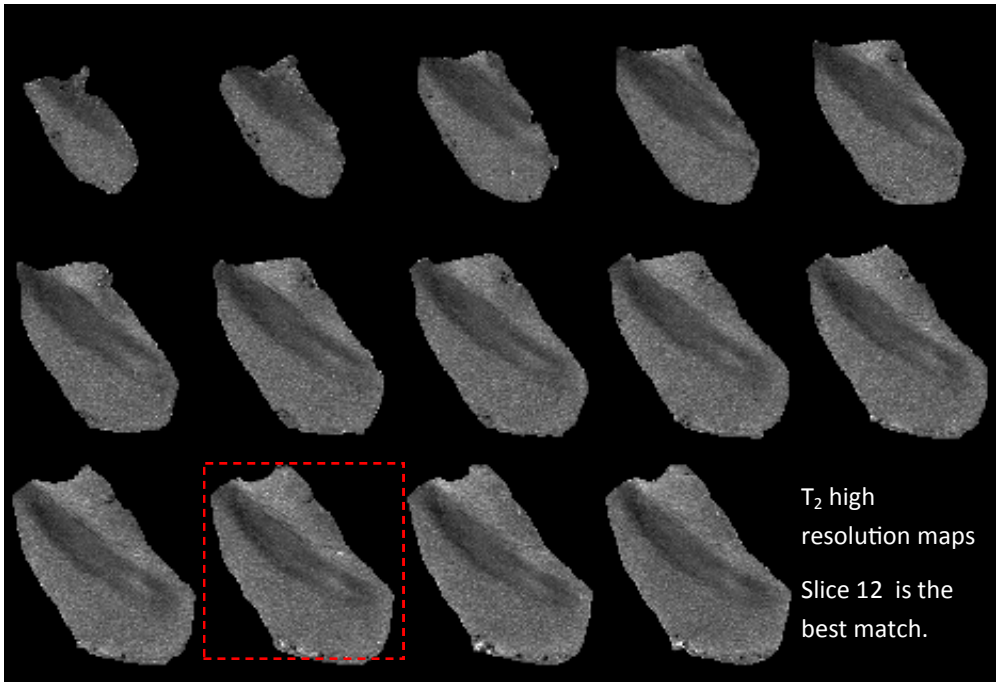

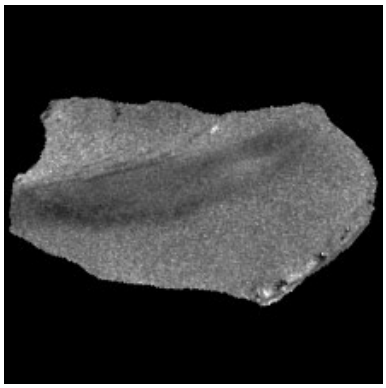

Slice 12 T_2 map is rotated into the same orientation as the XRF map.

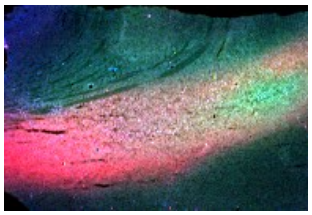

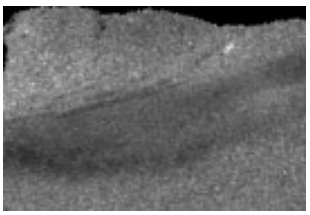

T_2 map is trimmed to the same dimensions as the SXRF map.

Final R_2 map

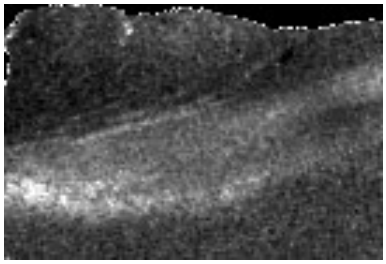

Finally the reciprocal of the matched, rotated & trimmed map is calculated to produce the R_2 map.

Substantia nigra sample C2

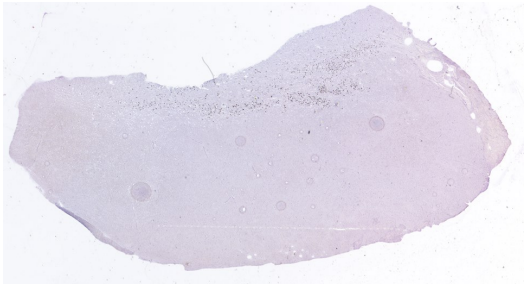

Stained section, after mapping

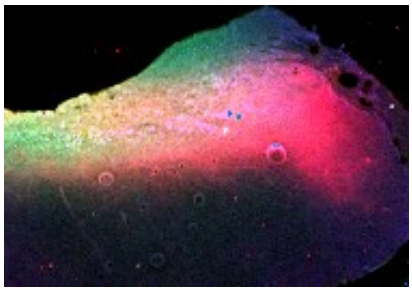

Combined metal SXRF map.
red = iron; green = copper;
blue = zinc.

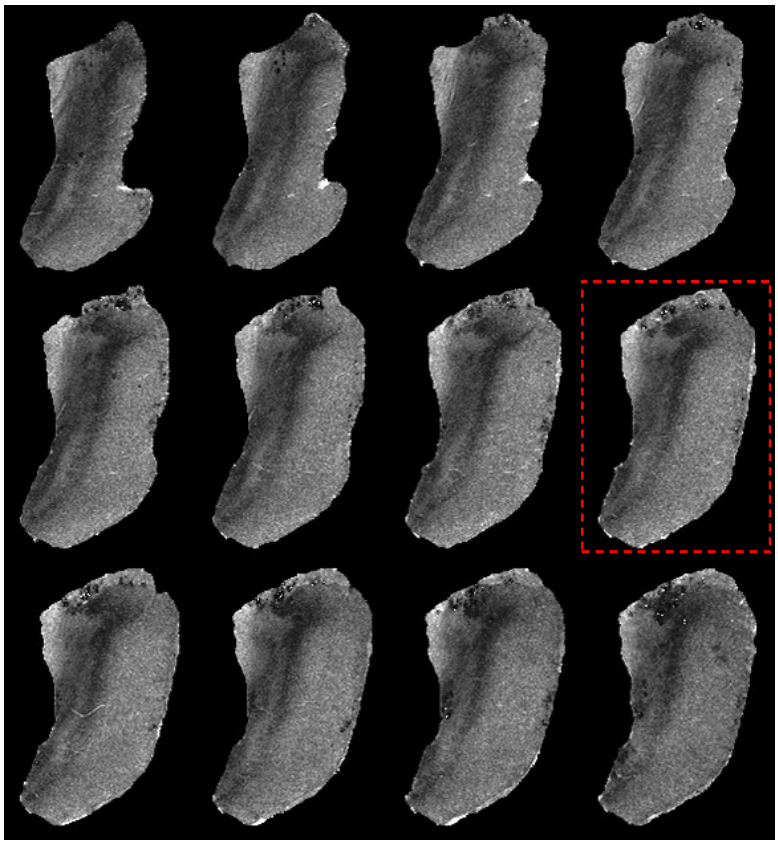

T_2 high resolution maps

Slice 8 is the best match.

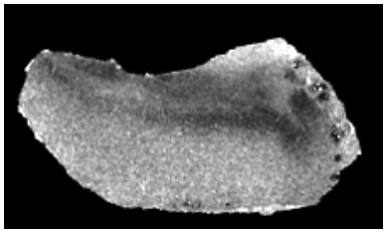

Slice 8 T_2 map is rotated into the same orientation as the SXRF map.

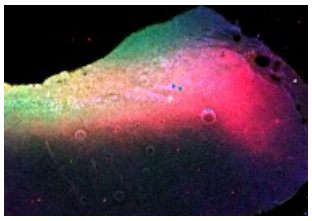

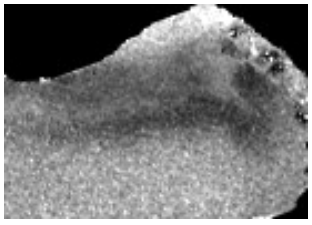

T_2 map is trimmed to the same dimensions as the SXRF map.

Final R_2 map

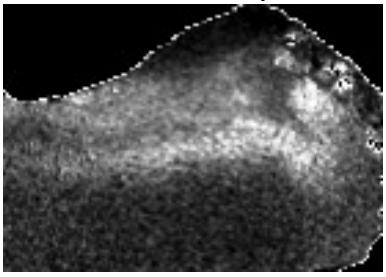

Finally the reciprocal of the matched, rotated & trimmed map is calculated to produce the R_2 map.

Amygdala sample C3

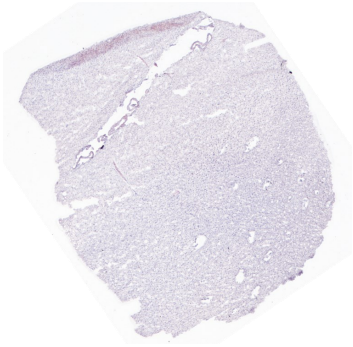

Neighbouring section stained on glass

Folded tissue deleted from map

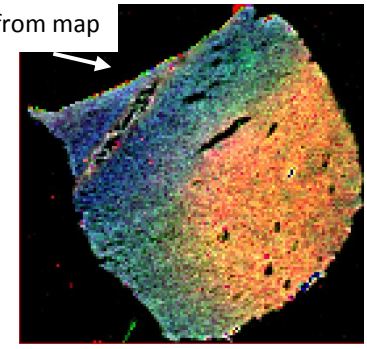

Combined metal SXRF map.
red = iron; green = copper; blue = zinc.

T_2* high resolution maps. Slice 15 is the best match.

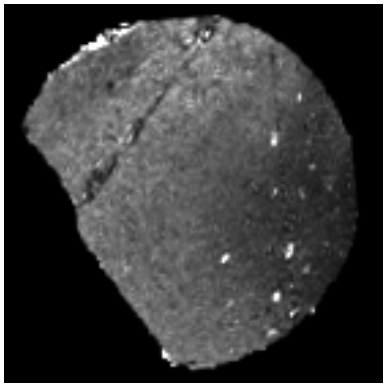

Slice 15 T_2* map is rotated into the same orientation as the SXRF map.

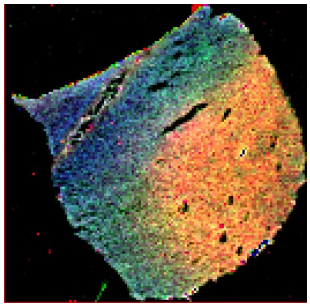

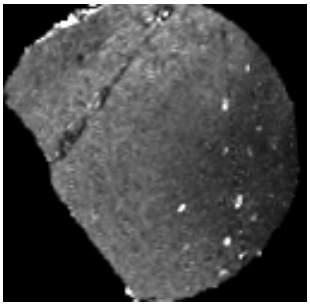

T_2* map is trimmed to the same dimensions as the SXRF map.

Final R_2* map

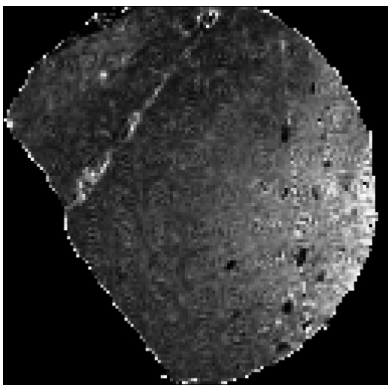

Finally the reciprocal of the matched, rotated and trimmed map is calculated to produce the R_2* map.

Amygdala sample AD2

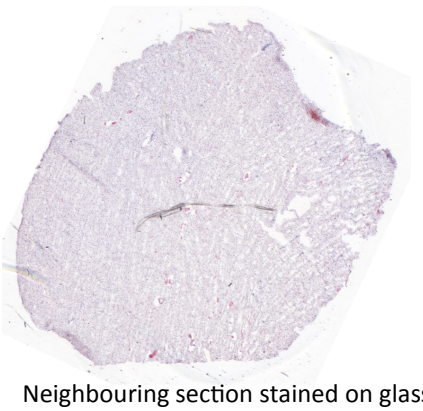

Neighbouring section stained on glass

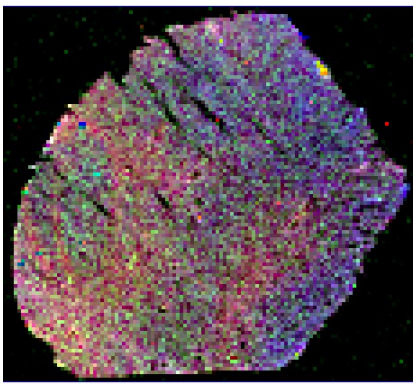

Combined metal SXRF map.
red = iron; green = copper; blue = zinc.

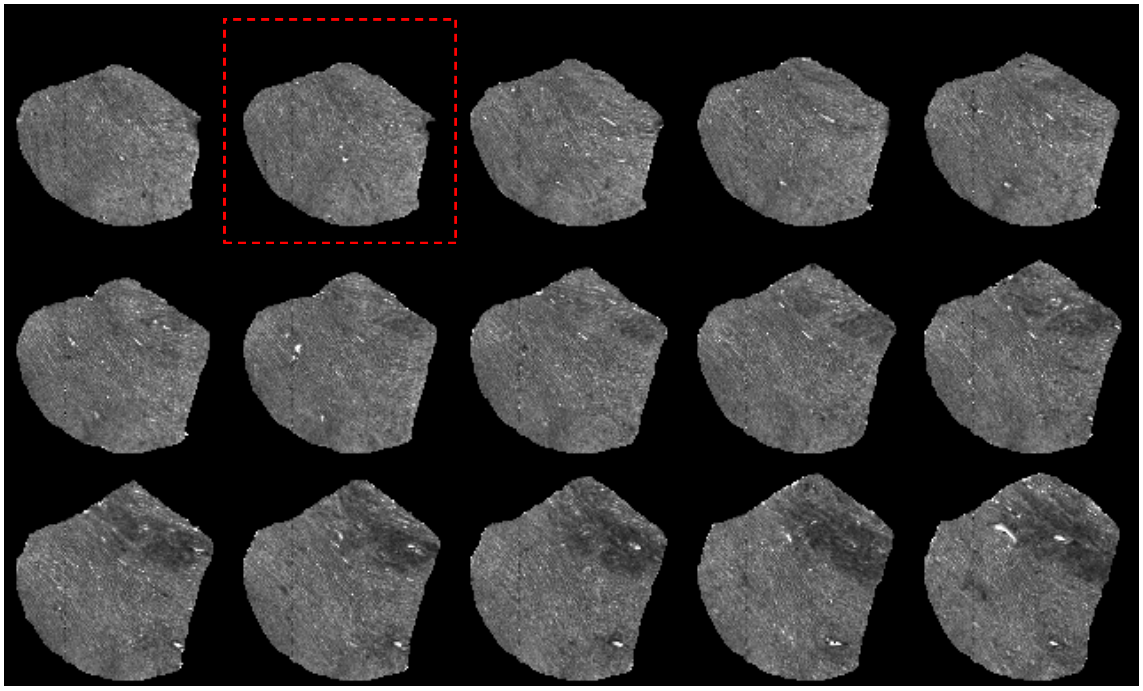

T_2* high resolution maps. Slice 2 is the best match.

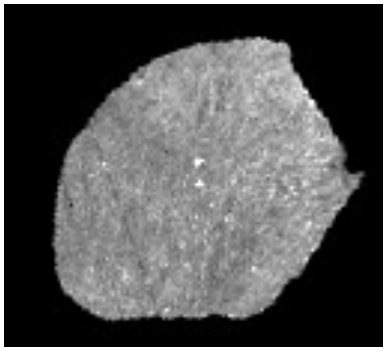

Slice 2 T_2* map is rotated into the same orientation as the SXRF map.

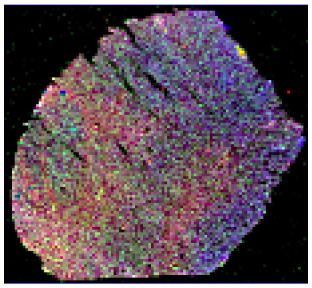

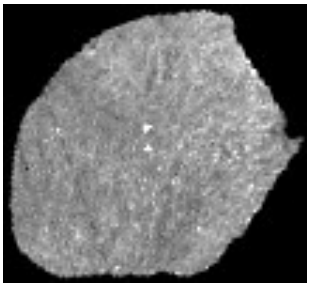

T_2* map is trimmed to the same dimensions as the SXRF map.

Final R_2* map

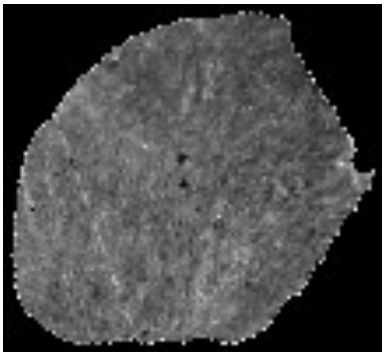

Finally the reciprocal of the matched, rotated and trimmed map is calculated to produce the R_2* map.

Amygdala sample AD2

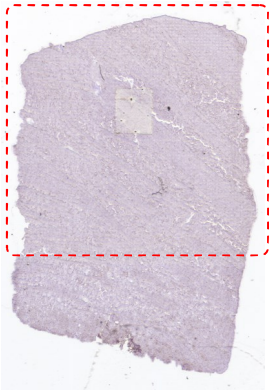

SXRF section, stained post-mapping

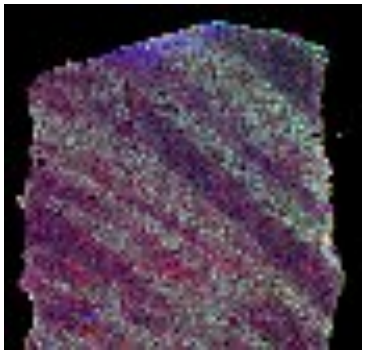

Combined metal SXRF map.
red = iron; green = copper; blue = zinc.

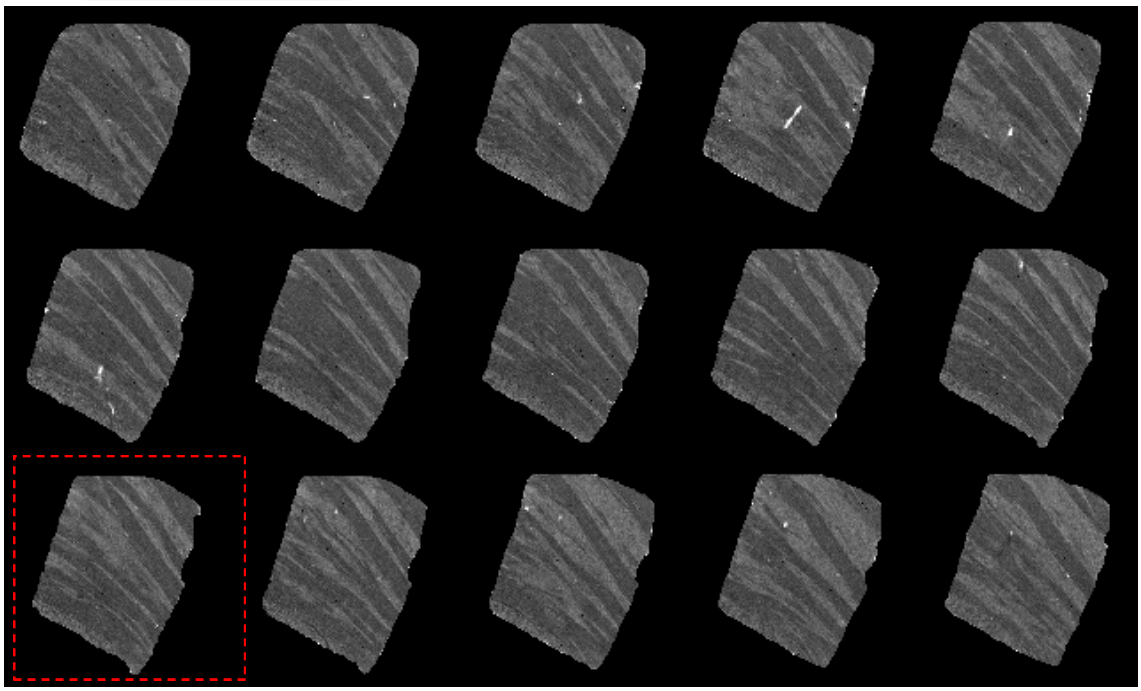

T_2* high resolution maps. Perfect matching is not achieved for any slice. Slice 11 is the best match.

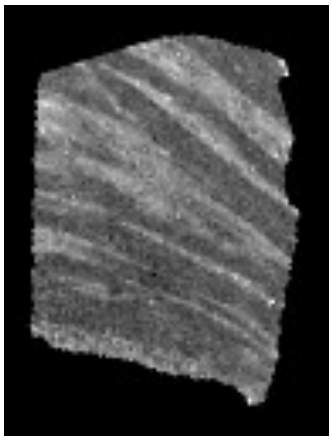

Slice 11 T_2* map is rotated into the same orientation as the SXRF map.

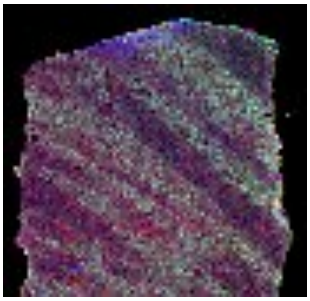

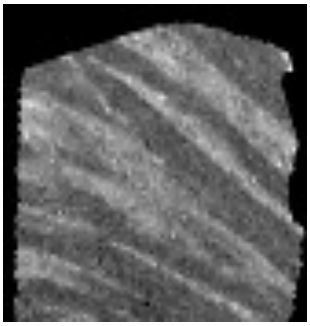

T_2* map is trimmed to the same dimensions as the SXRF map.

Final R_2* map

Finally the reciprocal of the matched, rotated and trimmed map is calculated to produce the R_2* map.

Amygdala sample AD2

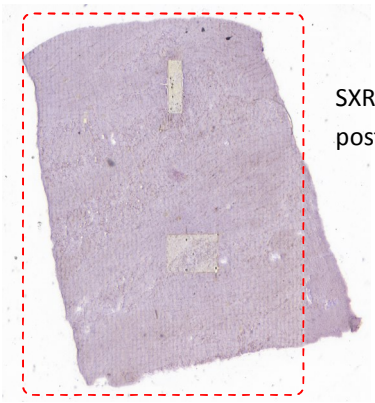

SXRF section, stained post-mapping

Combined metal SXRF map. red = iron; green = copper; blue = zinc.

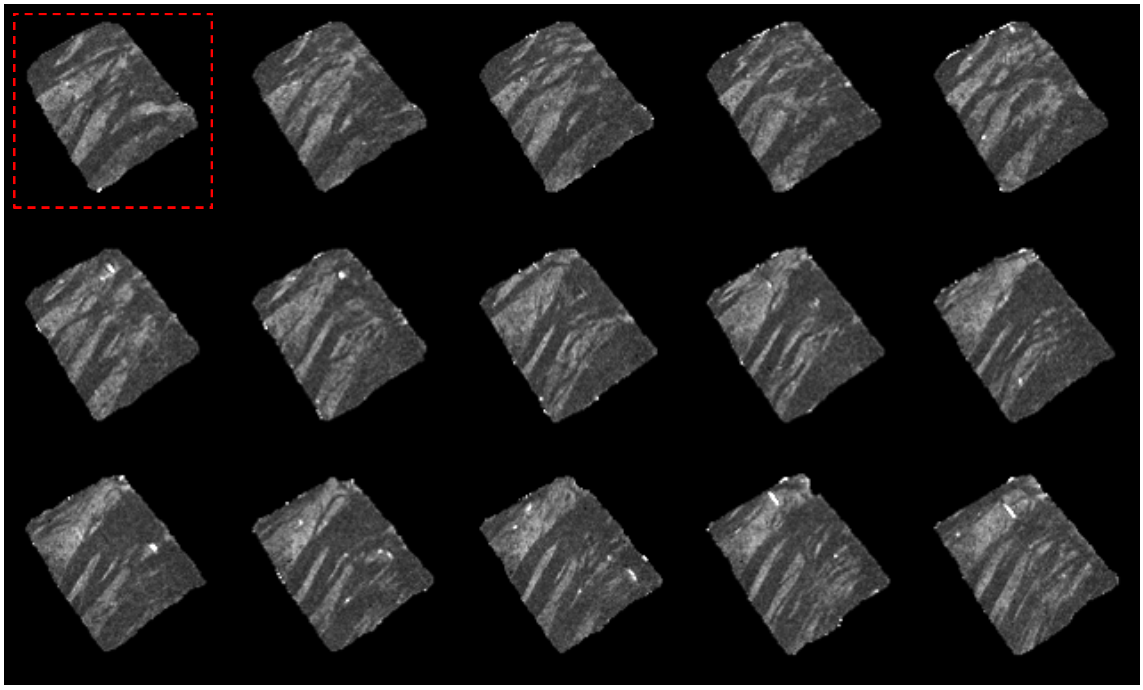

T_2* high resolution maps. Perfect matching is not achieved for any slice. Slice 1 is the best match.

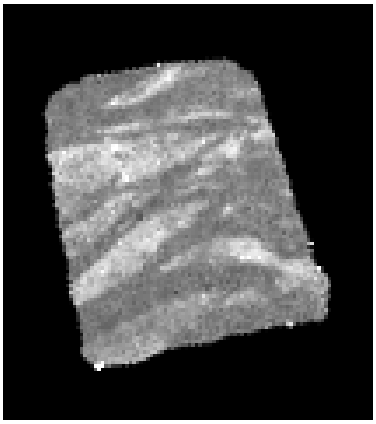

Slice 1 T_2* map is rotated into the same orientation as the SXRF map.

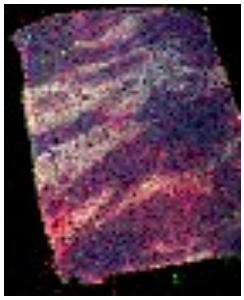

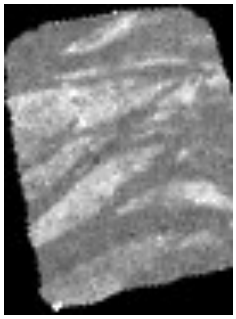

T_2* map is trimmed to the same dimensions as the SXRF map.

Final R_2* map

Finally the reciprocal of the matched, rotated and trimmed map is calculated to produce the R_2* map.

Journal of Parkinson's Disease 3 (2013) 523–537
DOI 10.3233/JPD-130197
IOS Press

Research Report

Iron Deficiency in Parkinsonism: Region-Specific Iron Dysregulation in Parkinson's Disease and Multiple System Atrophy

Naomi P. Visanji[a,*], Joanna F. Collingwood[b], Mary E. Finnegan[b], Anurag Tandon[c], Emily House[d] and Lili-Naz Hazrati[c]
[a]*Morton and Gloria Shulman Movement Disorders Centre, Toronto Western Hospital, Toronto, ON, Canada*
[b]*School of Engineering, University of Warwick, Coventry, UK*
[c]*Tanz Centre for Research in Neurodegenerative Disease, University of Toronto, ON, Canada*
[d]*The Birchall Centre, Keele University, Staffordshire, UK*

Abstract. Alpha synuclein pathology is widespread and found in diverse cell types in multiple system atrophy (MSA) as compared to Parkinson's disease (PD). The reason for this differential distribution is unknown. Regional differences in the distribution of iron are associated with neurodegenerative diseases, and here we characterize the relationship between iron homeostasis proteins and regional concentration, distribution and form of iron in MSA and PD.

In PD substantia nigra, tissue iron and expression of the iron export protein ferroportin increased, while the iron storage protein ferritin expression was unchanged. In the basis pontis of MSA cases, increased total iron concentration coupled with a disproportionate increase in ferritin in dysmorphic microglia and a reduction in ferroportin expression. This is supported by isothermal remanent magnetisation evidence consistent with elevated concentrations of ferritin-bound iron in MSA basis pontis.

Conventional opinion holds that excess iron is involved in neurodegeneration. Our data support that this may be the case in PD. While region-specific changes in iron are evident in both PD and MSA, the mechanisms of iron dysregulation appear quite distinct, with a failure to export iron from the MSA basis pontis coupling with significant intracellular accumulation of ferritin iron. This pattern also occurs, to a lesser extent, in the MSA putamen. Despite the excess tissue iron, the manner of iron dysregulation in MSA is reminiscent of changes in anemia of chronic disease, and our preliminary data, coupled with the widespread pathology and involvement of multiple cell types, may evidence a deficit in bioavailabile iron.

Keywords: Parkinson's disease, multiple system atrophy, iron, ferritin, inflammation, ferroportin

INTRODUCTION

Multiple system atrophy (MSA) and Parkinson's disease (PD) are both neurodegenerative disorders characterised by aggregation of intracellular alpha synuclein. However, a key difference between these two synucleinopathies is the distribution of the underlying pathology. In PD alpha synuclein-positive aggregates, termed Lewy bodies, are restricted to neurons and found in a limited number of structures including the substantia nigra (reviewed in [1]). However, in MSA, multiple regions and multiple cell types are affected, with insoluble deposits of alpha synuclein

*Correspondence to: Naomi Visanji, Morton and Gloria Shulman Movement Disorders Centre, Toronto Western Hospital, 399 Bathurst Street, Toronto, ON, M5T 2S8, Canada. Tel.: +1 416 603 6482; Fax: +1 416 603 5004; E-mail: naomi.visanji@uhnresearch.ca.

ISSN 1877-7171/13/$27.50

found in both neurons and glia accompanied by widespread neurodegeneration apparent in many brain regions (reviewed in [1]).

Disrupted iron homeostasis has long been associated with neurodegenerative diseases, yet the role of iron in neurodegeneration remains elusive. Within the brain, iron is vital to many different cell types for many processes, including oxidative phosphorylation, myelin synthesis, nitric oxide metabolism, neurotransmitter synthesis and oxygen transport. However, excess iron has been shown to lead to the production of reactive oxygen species which in turn can lead to cellular damage and degeneration (reviewed in [2]). The oxidation state of iron in the tissue is therefore particularly important, and tightly regulated processes involving many proteins ensure that bioavailable highly reactive Fe(II) is minimised, with the majority being bound as Fe(III) in the course of normal brain iron homeostasis. Iron demonstrably affects, and is affected by, the aberrant peptide aggregation observed in neurodegenerative disease, including alpha synuclein, and recent evidence indicates that alpha synuclein is a cellular ferrireductase [3], and as recently demonstrated in an alpha synuclein knockout mouse model, may play a significant role in regulation of iron homeostasis [4]. Changes in iron at the cellular and sub-cellular scale are reflected in detectable disease-related shifts in the regional distribution of iron in the brain [5]. It has been shown that high iron levels correlate with regions of neurodegeneration, with evidence of increased iron in the PD and MSA substantia nigra and in the MSA striatum, particularly in putamen [6, 7]. Within the brain, the majority of iron is sequestered within ferritin, a 450 kDa protein found in every cell type, each protein capable of storing up to 4500 iron ions [8, 9]. Ferritin levels are typically closely coupled to iron levels, such that increased iron leads to increased ferritin production. However, in PD substantia nigra there is evidence of a loss of this coupling such that iron is increased, but levels of ferritin are reportedly decreased [6, 7]. This may lead to an increase in free, reactive iron, although this remains to be elucidated.

Recent advances in the understanding of iron homeostasis and in the application of modern techniques able to probe the status of iron within the brain allow for a more detailed investigation of this complex relationship. We studied the relationship between iron homeostasis proteins and the levels, distribution and form of iron in control, MSA and PD brain with a view to investigating a potential role of iron in the differing pathology of these two related neurodegenerative diseases.

MATERIALS AND METHODS

Tissue

All human brain tissue was obtained from the Canadian Brain Tissue Bank. Each brain was bisected at the time of death with one side dissected rapidly and different regions of the brain frozen at -80°C and the other half immersed in 10% buffered formalin for subsequent blocking and embedding in paraffin. The median post mortem delay was 10 hours, with a range of 2–20 hours. Distributions of group size, sex, and mean age $\pm$ SEM were: control ($n = 3$; 2 male, 1 female; ages 47, 63 and 78 years); PD ($n = 3$; 2 male, 1 female; ages 56, 73 and 79 years); MSA ($n = 3$; 2 male, 1 female; ages 46, 66 and 76 years). For MSA the mean disease duration was 6 ± 1.1 years and all three cases presented clinically with MSA-P. The mean duration disease for PD cases was 21 ± 3.8 years and presented as akinetic-rigid. The diagnosis of all cases was confirmed neuropathologically. The brain areas used for western blotting, graphite furnace and Isothermal Remanent Magnetisation (IRM) analysis were from the frozen side whereas brain tissue used for immunohistochemistry was from the formalin fixed side of the brain. Different areas of interest included the substantia nigra (pars compacta), the basis pontis (pons) (both white and grey matter) and the lentiform nucleus (putamen, external/internal segments of the globus pallidus complex).

Western blotting

Frozen brain tissue was homogenised in 10x volume homogenisation buffer (100 mM NaCl, 50 mM Tris, 1 mM EDTA, 1% CHAPS, broad spectrum protease inhibitor cocktail (Sigma-Aldrich, St. Louis, MO). After 20 minutes of incubation at 4°C, homogenates were centrifuged at $20{,}000 \times g$ for 5 minutes. Protein concentration was determined by BCA assay (Thermo Scientific, Waltham, MA). Western blotting was carried out according to standard protocols. Briefly, samples were heated for 10 minutes at 70°C in 25% NuPage® LDS sample buffer (Invitrogen, Carlsbad, CA). Proteins were then separated on 4–12% Bis-Tris NuPage® Novex® Mini gels (Invitrogen, Carlsbad, CA) and transferred onto nitrocellulose membranes (Life Sciences, Frederick, CO). Blots were probed with antibodies to ferritin (SigmaAldrich), ferroportin (kind donation from Dr D Haile), transferrin receptor (GeneTex) and Glyceraldehyde 3-phosphate dehydrogenase (GAPDH, SigmaAldrich). Bound HRP-conjugated

anti-mouse or anti-rabbit IgG (Sigma-Aldrich, St. Louis, MO) were revealed by chemiluminescence using ECL Plus (GE Healthcare, UK) and detected with a Storm 860 fluorescent imager. Protein levels were quantified by densitometric analysis using ImageQuant software (GE Healthcare, UK). All proteins were expressed as percent of GAPDH to control for variability in volume loaded. For each protein measured by western blot, 1 sample per patient was run on each gel for a total of 3 control samples, 3 PD samples and 3 MSA samples. Analysis was performed on a single blot and expressed as the mean ± s.e.m of the 3 samples in a given group.

Immunohistochemistry

Formalin-fixed brain tissue was embedded in paraffin blocks, sectioned at 5μm and mounted on glass slides. Immunohistochemistry was performed according to standard protocols using antibodies for ferritin (SigmaAldrich), ferroportin (kind donation from Dr D Haile) and ionized calcium binding adaptor molecule 1 (iba1) (Abcam) and all tissue was counterstained with Mayer's Haematoxylin. Immunostained sections were scanned at 40x using a Scanscope digital slide scanner (Aperio Technologies, Inc., Vista, CA). Image files were viewed with ImageScope (Aperio Technologies, Inc., Vista, CA). Positive pixel analysis of iba1 stained tissue was carried out using a custom designed algorithm in ImageScope. The mean number of iba1 positive pixels in 3 equal sized regions of each sample was calculated.

Superconducting quantum interference device (SQuID) magnetometry

The fraction of brain iron that is contained in the iron storage protein ferritin (the ferritin core) is present as nanoscale iron oxide clusters, which typically have a ferrihydrite-like mineral structure. The magnetic properties of these ferritin cores are well-documented, and so magnetic analysis of tissue can be used to quantify the signal arising from the ferritin cores. If total iron concentration is measured subsequent to the magnetic analysis, the proportion of iron bound in ferritin may be estimated. In practice, a variety of iron biomineral phases are observed in ferritin cores, and the extent to which ferritin is clustered within tissue may vary; both factors can potentially affect the magnetic properties of the tissue. It should also be noted that other forms of bio-iron may contribute to IRM signal at 5 Kelvin (K), including neuromelanin-bound iron [10] and iron oxide deposits including magnetite which may be associated with pathologic features such as amyloid plaques [11, 12].

The parameter used to identify the signal from ferritin cores in the tissue was Isothermal Remanent Magnetisation (IRM). In this measurement, samples are exposed to a magnetic field. Biological material is primarily diamagnetic, which results in a negative linear magnetic response. This gives the 'background' signal, onto which the small but detectable positive response from the ferritin cores is superimposed. At body temperature, the positive response from the ferritin cores vanishes as soon as the applied magnetic field is removed. However, at very low temperatures (below approximately 20 K), the ferritin cores retain, for a temporary period, a magnetisation that can be detected and quantified using the sensitivity of a SQuID magnetometer. The signal from normal ferritin cores is almost absent at higher temperatures, making it possible to estimate their concentration in a known mass of tissue. This approach, to analyse biomineralized iron in human tissue, is now well established and described elsewhere [13].

Fresh-frozen samples were dissected to obtain the region of interest, and then prepared for SQuID measurement by freeze drying and compressing each sample into a dense pellet. Acid-washed ceramic blades and non-metallic piston rods were used for cutting and compression respectively, to avoid environmental contamination of the samples with iron-rich particulates.

A Quantum Design MPMS-5S SQuID was used to measure the isothermal remanent magnetisation (IRM) at 150 K, 50 K and 5 K. A demagnetising sequence was run prior to each IRM measurement to ensure that the initial condition for each sample was the same. IRM was obtained by applying a magnetic field of 1.0 Tesla, measuring the magnetic moment (the response from the tissue), and then removing the magnetic field. The IRM signal decays after the magnetic field is removed, so the remanent magnetisation is sampled eight times over approximately 10 minutes, and the final four readings (where the decay curve has stabilised) are averaged to obtain a measurement of the IRM; the error is the standard deviation for these four values. Only material capable of retaining a magnetic moment after application and removal of the 1.0 Tesla field can contribute to the IRM signal; this excludes the significant majority of biological material. The ferrihydrite-like iron oxide cores normally found in ferritin are assumed to be the primary contributor to the IRM signal at 5 K,

as tested by measurement of IRM saturation curves, and evidenced by loss of IRM signal at higher temperatures. All values were corrected for dry sample mass. Correction for finite sample length was applied using the method outlined by Hautot et al. [13].

Graphite furnace atomic absorption spectroscopy

Samples were digested using a Mars Xpress microwave (CEM Microwave Technology Ltd, UK) and analysed with an AAnalyst 600 atomic absorption spectrometer with a transversely heated graphite atomizer and longitudinal Zeeman-effect background corrector (Perkin Elmer, UK). The microwave digestion temperature program, GFAAS instrument parameters and calibration procedure were as described previously [14].

Freeze-dried tissue samples from the SQuID magnetometry analysis were dried to a constant weight (36–231 mg dry wt) in Teflon© vessels and microwave digested in 1 mL nitric acid (HNO_3 analytical reagent grade 15.8 M, Fischer Scientific, UK) and 1 mL hydrogen peroxide (H_2O_2, ARISTAR grade 30% w/v). After cooling, 3 mL ultrapure water (conductivity $\leq 6.8 \times 10^{-6}$ S m^{-1}) was added to each vessel, digest volumes were determined gravimetrically and ranged from 4.44 to 4.82 mL. Digests were yellow and clear with no precipitate or fatty residue visible. Iron concentration was determined in 800 and 200 fold dilutions of the digests (12.5 μL and 50 μL of digest diluted to 10 mL in 1% HNO_3, respectively). Vessels were cleaned by digesting with 1 mL HNO_3, rinsing with ultrapure water and storing in 5% HCl.

Samples were analysed in two batches. In each batch quality assurance (QA) samples included three method blanks, one reagent spike and two standard reference materials (NIST SRM 1566B oyster tissue and IAEA-407 fish homogenate). Two additional vessels containing spiked standard reference materials were included in the first batch. These QA were dried, digested and diluted, including the further 800 fold dilution, as for the tissue digests.

The mean of iron concentrations measured in 800 fold dilutions of the *ca* 5 mL method blank digests in batch one was 0.15 μg L^{-1} (S.D. 0.34 μg L^{-1}, $n = 3$) and 0.17 μg L^{-1} (S.D. 0.05 μg L^{-1}, $n = 3$) in batch two. Background contamination was corrected for by subtraction of the mean plus three standard deviations of the method blanks analysed in the same batch. This corresponded to 31.2 μg g^{-1} dry wt (S.D. 10.2 μg g^{-1}, $n = 9$ samples) in batch one and 23.3 μg g^{-1} dry wt (S.D. 7.1 μg g^{-1}, $n = 13$ samples) in batch two.

The reagent spike recoveries were 97.2% and 103.5%. The measured IAEA407 iron concentrations were 166.4 μg g^{-1} dry wt (S.D. 0.9 μg g^{-1} dry wt), and 147.2 μg g^{-1} dry wt (S.D. 1.0 μg g^{-1} dry wt), compared to a certified value of 146 μg g^{-1} (95 % CI 3 μg g^{-1}). The measured SRM1566B iron concentrations were 205.0 μg g^{-1} dry wt (S.D. 2.3 μg g^{-1}) and 173.6 μg g^{-1} dry wt (S.D. 0.9 μg g^{-1}) compared to the certified value of 205.8 ± 6.8 μg g^{-1}. Spike recoveries from SRM1566B and IAEA407 were 103.7% and 92.5% respectively.

The calibration curves had a correlation coefficient ≥ 0.998, and instrumental detection limits of 0.14 μg L^{-1} and 0.21 μg L^{-1}.The mean of characteristic masses derived from absorbance at each iron calibration standard for all calibrations was 13.3 pg per 0.0044 s (SD 0.9 pg per 0.0044 s $n = 16$), within ±20% of the 12.0 pg per 0.0044 s cited by the manufacturer. Initial and continuing calibration verification standards were analysed and were within 10% and 15% respectively of expected concentrations. A standard addition calibration was performed on one brain tissue digest. A *t*-test showed that the slope was not significantly different from that of the linear non-zero fit of the calibration performed in 1% HNO_3 at the $\alpha = 0.05$ level.

Statistical analysis

Data were analysed using one-way ANOVA, having passed the Shapiro-Wilk test for normality, and this was followed by Dunnett's *post-hoc* analysis or Linear regression where appropriate (GraphPad Prism 4.0, San Diego, CA). In all cases, $P < 0.05$ was taken as the level of significance. Linear Discriminant Analysis (Minitab) was used to assign the individual regional samples from each case into groups, based on data from multiple variables, and the proportion of samples correctly assigned to their true groups was reported for each parameter set considered.

RESULTS

Ferritin expression is selectively increased in MSA and unchanged in PD

In MSA basis pontis, there was an ∼2.5 fold increase in ferritin protein as compared to control levels ($P < 0.01$ *cf* control), with no change apparent in PD tissue (Fig. 1a and d). A similar pattern was seen in the putamen where ferritin levels in MSA tissue were significantly increased by ∼4.5 fold of control levels ($P < 0.05$ *cf* control, Fig. 1c and d). In addition there

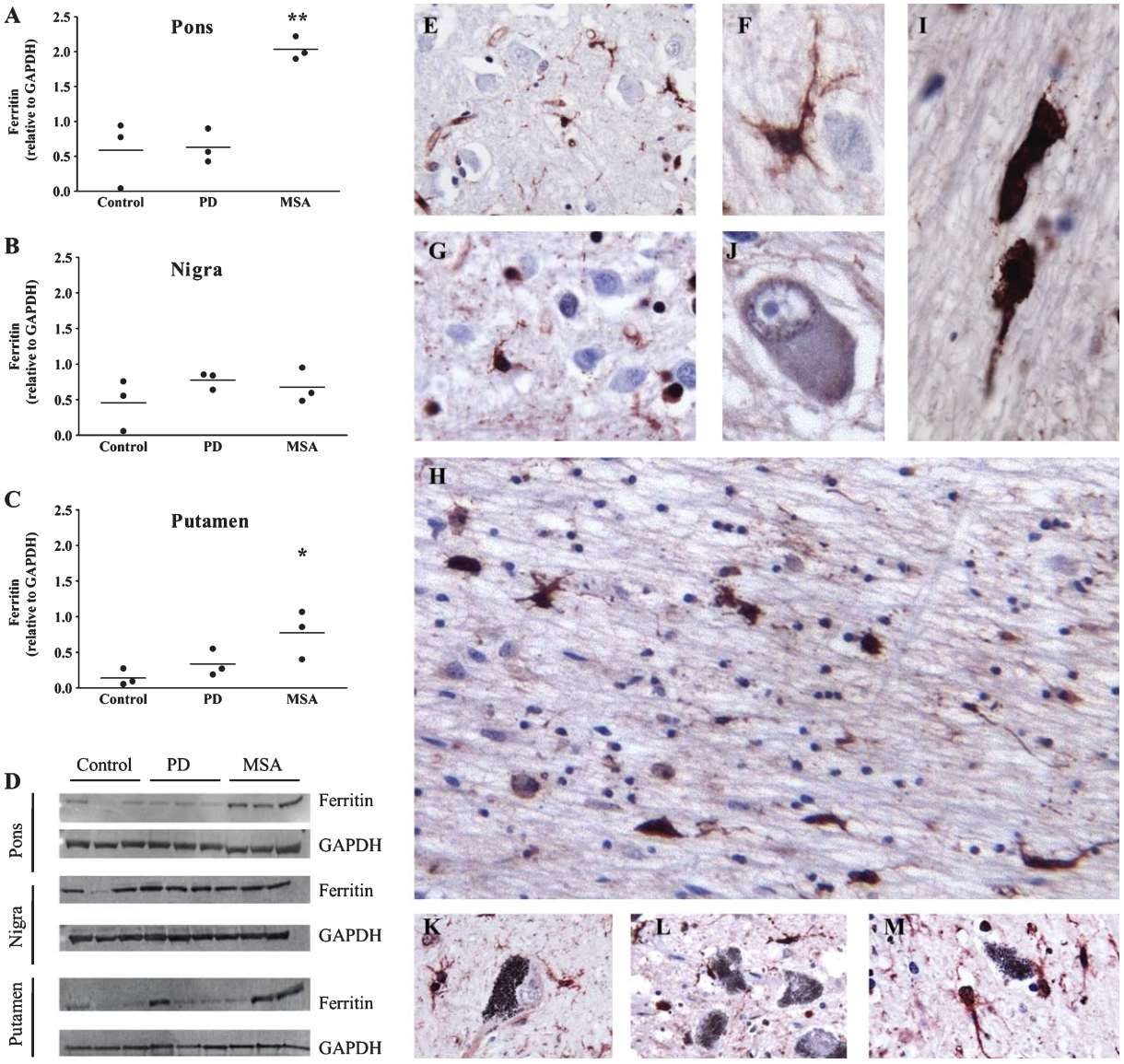

Fig. 1. Ferritin expression in control, PD and MSA brain. Ferritin signal relative to GAPDH was quantified by western blot in A) pons, B) substantia nigra and C) putamen. Individual values are shown, with the mean indicated by a black line. *represents significant difference from control levels, 1-way anova with Dunnett's *post hoc*, ($^{*}P<0.05$, $^{**}P<0.01$). Representative blots for each region are shown D). Ferritin immunostaining in control E, F) PD G) and MSA H–J) pons. Ferritin immunostaining in control K) PD L) and MSA M) nigra. Scale bar represents 40 μm in E, G, H & K–M, and 10 μm in F, J & I.

was an ∼1.4 fold increase in ferritin in PD putamen ($P<0.05$). In contrast, in the substantia nigra, ferritin levels remained unchanged in either PD or MSA as compared to control (both $P>0.05$, Fig. 1b and d).

Immunohistochemical analyses of basis pontis sections from human control, PD and MSA tissue further supported differences in the intensity of ferritin expression. In control pons, ferritin was localised to microglia with no apparent neuronal staining (Fig. 1E), and the microglia displayed the typical features of a resting state with a round dense nucleus without a visible cytoplasm surrounding it and long thin processes (Fig. 1F). Similarly in PD basis pontis, ferritin was also predominantly expressed in microglia with an apparent resting morphology (Fig. 1G). In MSA pons the gross level of ferritin immunostaining appeared increased compared to both control and PD pons, confirming the observed increase by western blot (Fig 1H). Furthermore, in MSA basis pontis intense ferritin staining was seen in microglia which had thicker branches and an

enlarged cytoplasm, a morphology associated with an activated state (Fig. 1I). There was no ferritin staining apparent in neurons in the pons of MSA cases (Fig. 1J). Immunohistochemical analysis of ferritin in the substantia nigra revealed the presence of microglia with an activated morphology clustered around the pigmented dopaminergic cells in both MSA and PD (Fig. 1K–M).

Iron concentration, and ferritin-bound iron, is altered in MSA and PD

In the basis pontis, total iron quantification with Graphite Furnace Atomic Absorption Spectroscopy (GFAAS) revealed an ~1 fold increase in iron in MSA as compared to control ($P < 0.01$), with levels in PD pons equivalent to control (Fig. 2a). The corresponding isothermal remanent magnetisation (IRM) measurements at temperatures of 5 K, 50 K, and 150 K revealed an ~1.6 fold increase in IRM at 5 K in MSA pons as compared to control pons ($P < 0.01$), with PD IRM again being unchanged (Fig. 2c). The observed increased IRM signal in MSA pons at 5 K is consistent with MSA pons containing a higher concentration of nanoscale iron oxide particles in the tissue than either the control or PD pons, where indications are that these are ferritin cores.

In the substantia nigra, the pattern of iron and IRM in MSA and PD was reversed. Thus on average there was approximately a 2-fold increase in iron in PD as compared to control (although this did not reach significance in this small group, testing at $p < 0.05$), with levels in MSA pons equivalent to control (Fig. 2b). The corresponding IRM signal from the same samples paralleled the trend indicated in the total iron data, revealing on average a 2-fold increase in IRM in PD nigra as compared to control nigra (approaching significance at $p = 0.06$), with MSA IRM from the nigra again equivalent to control (Fig. 2d). The evidence for increased IRM signal in PD nigra is consistent with a higher concentration of iron being present in nanoparticulate form in the tissue than in either control or MSA substantia nigra. There are various forms of iron that may contribute to IRM signal at 5 K, including ferritin iron oxide cores, and neuromelanin-bound iron, so it is not possible to differentiate the ferritin iron and neuromelanin iron fractions in the substantia nigra from these data alone [10]. However, lack of elevation in ferritin protein expression in the PD substantia nigra (Fig. 1B), and the increase in total iron and IRM in this same region, points towards an elevation of neuromelanin-bound iron (and a proportional, if not absolute, decrease in ferritin-bound iron) in the substantia nigra.

Increased iron is stored within ferritin in MSA pons

Linear regression analysis reveals a positive correlation between iron concentration and IRM at 5 K in tissue from both the pons ($r^2 = 0.95$, $P < 0.0001$) and substantia nigra ($r^2 = 0.97$, $P < 0.0001$) (Fig. 2e and f respectively). This indicates that the proportion of iron stored in the form of iron oxide clusters (as found in ferritin) increases in a linear fashion with total iron in the MSA pons (as opposed to an increase in the fraction of iron that is unbound or associated with low-molecular-weight species). There are no clear data in the literature showing accumulation of iron in the basis pontis, as most neuropathological data emphasise changes in the striatum in cases of MSA. Our own results show increased iron deposition in the pons in comparable density to observed changes in the striatum. A similar linear relationship between the IRM signal at 5 K and iron concentration in the substantia nigra is also observed.

Free iron may be decreased in MSA pons

Total tissue iron may be considered as that which is bound in ferritin, and that which is free or bound as individual ions to low molecular weight complexes such as transferrin (Tf). Notable exceptions include neuromelanin in the substantia nigra, which incorporates iron in ferritin-like oxyhydroxide clusters [15], and haemosiderin, reportedly a degradation product of ferritin, and which is more commonly observed in organs responsible for iron storage such as the liver. Tissue is primarily diamagnetic, and any magnetic signal from tissue at ultra-low temperatures, which is lost at higher temperatures, and follows ferritin-core-like magnetization saturation behaviour, would normally be attributable to the iron oxide cores in ferritin [13]. If we assume equivalent size distributions and biomineral properties of the ferritin cores in these pons tissue samples, then from inspection of the results shown in Fig. 2, it is evident that the proportion of non-ferritin-bound iron decreases in the MSA cases compared to controls, and to a greater extent than in PD. This indicates that in addition to an approximately 2-fold increase in iron concentration, the proportion of ferritin-bound iron also increases in the MSA pons. As shown previously, ferritin protein is elevated approximately 3-fold in this region of the brain (Fig. 1A).

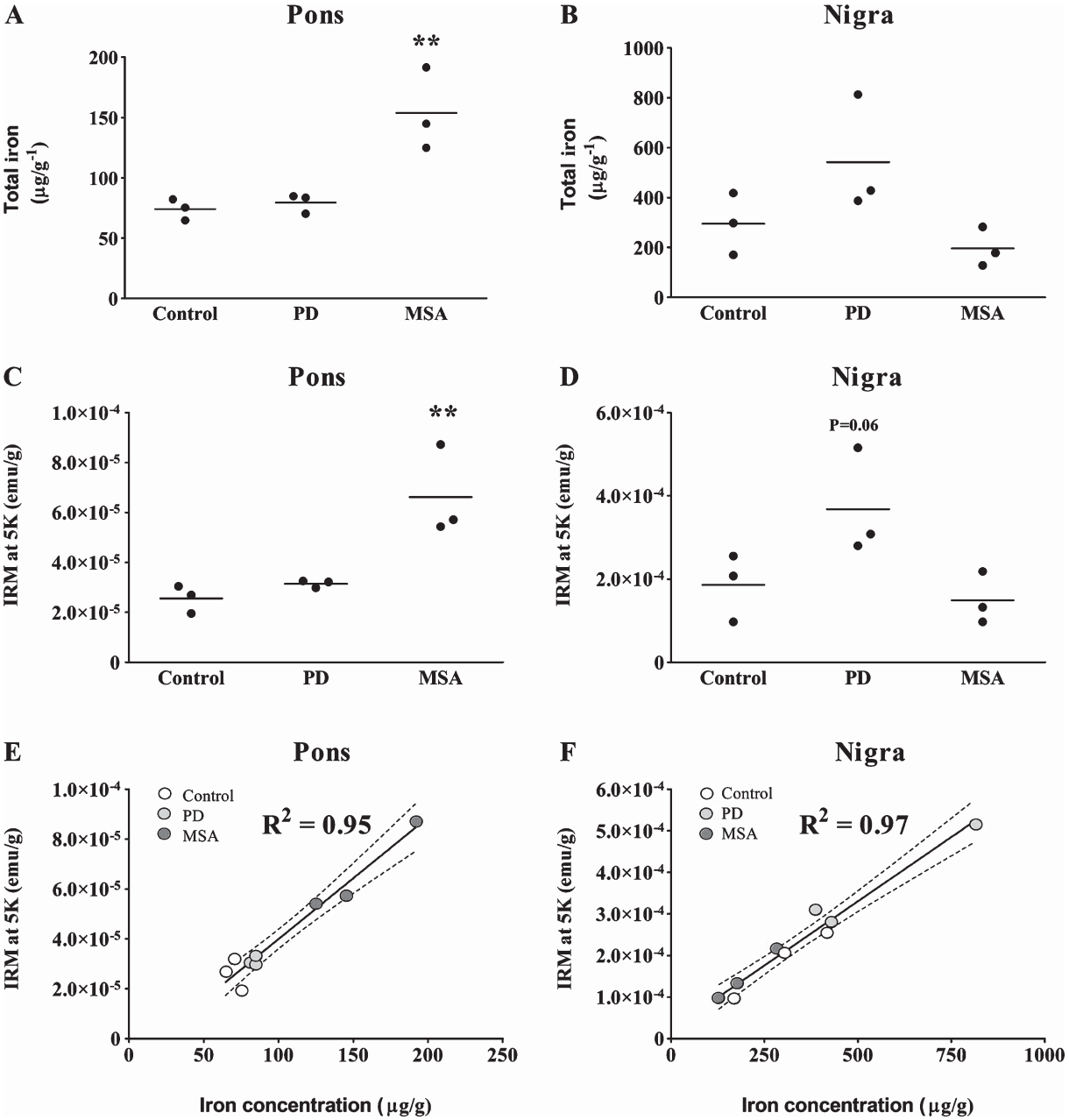

Fig. 2. Levels of iron and isothermal remanent megnetisation (IRM) in the pons and substantia nigra in control, PD and MSA brain. Total iron levels ($\mu g/g^{-1}$) are shown in A) pons and B) substantia nigra. IRM ($emu/\mu g^{-1}$) at 5 Kelvin in corresponding tissue is shown. Individual values are shown, with the mean indicated by a black line. *represents significant difference from control levels, 1-way anova with Dunnett's *post hoc*, (**$P < 0.01$). IRM ($emu/\mu g^{-1}$) at 5 Kelvin are plotted against total iron levels ($\mu g/g^{-1}$) in E) pons and F) substantia nigra. R^2 is shown. Line of best fit indicated by solid line, error by broken line.

Ferroportin and transferrin receptor expression is differentially altered in MSA and PD

In MSA pons, there was an ~0.75 fold decrease in ferroportin protein as compared to control levels ($P < 0.01$ *cf* control), with no change apparent in PD tissue (Fig. 3A). A similar pattern was seen in the putamen where ferroportin levels in MSA tissue were decreased by ~0.75 fold of control levels ($P < 0.05$ *cf* control, Fig. 3C) with no significant change in PD putamen. In contrast, in the PD substantia nigra, there was an ~1.4 fold increase in ferroportin pro-

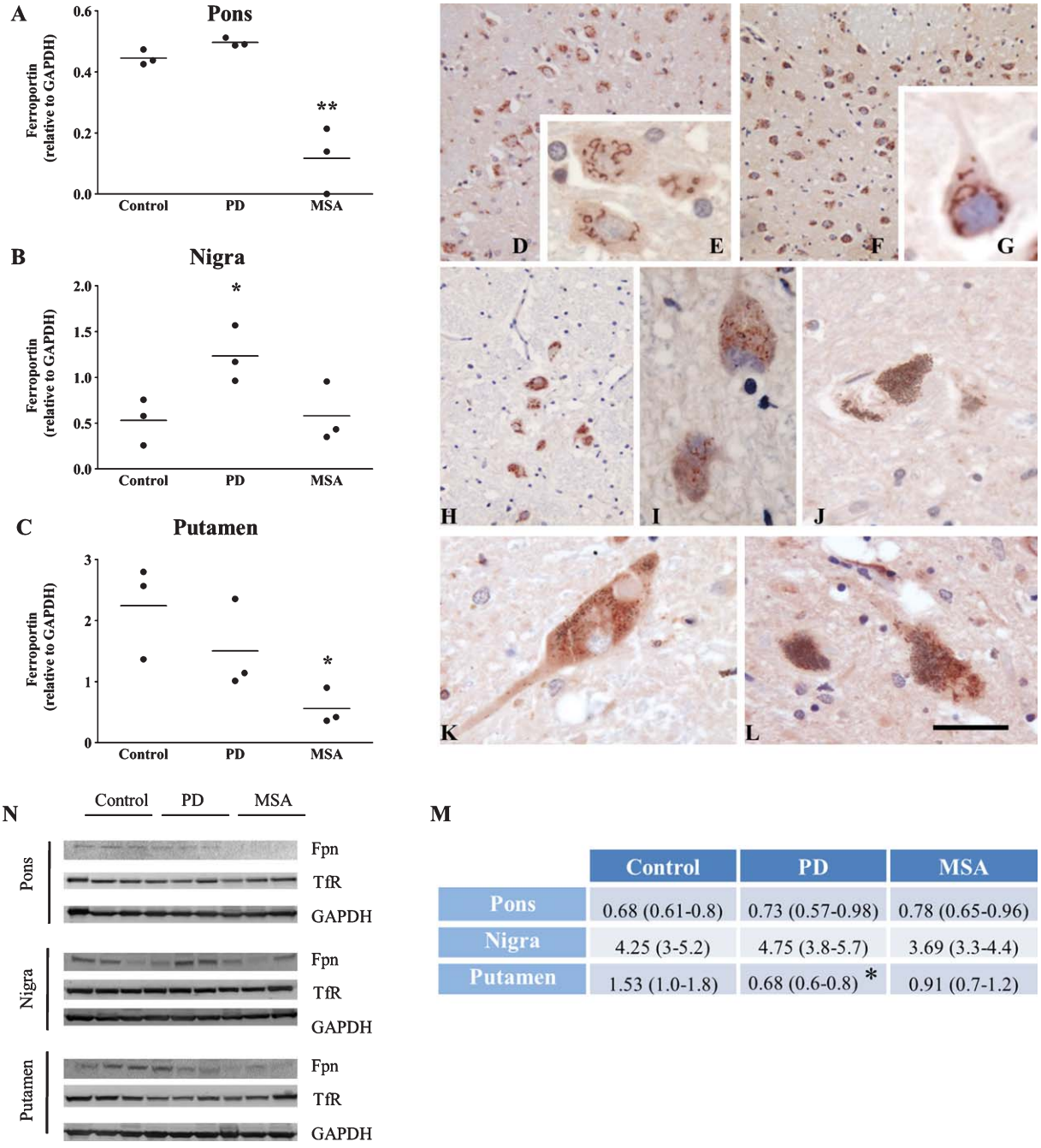

M

	Control	PD	MSA
Pons	0.68 (0.61-0.8)	0.73 (0.57-0.98)	0.78 (0.65-0.96)
Nigra	4.25 (3-5.2)	4.75 (3.8-5.7)	3.69 (3.3-4.4)
Putamen	1.53 (1.0-1.8)	0.68 (0.6-0.8) *	0.91 (0.7-1.2)

Fig. 3. Ferroportin (Fpn) and transferrin receptor (TfR) expression in control, PD and MSA brain. Ferroportin signal relative to GAPDH was quantified by western blot in A) pons, B) substantia nigra and C) putamen. Individual values are shown, with the mean indicated by a black line. *represents significant difference from control levels, 1-way anova with Dunnett's *post hoc*, (*$P < 0.05$, **$P < 0.01$). Ferroportin immunostaining in control D, E) PD F, G) and MSA FH, I pons and control J), PD K) and MSA L) substantia nigra neurons. Scale bar represents 200 μm in D, F, H and 20 μm in E, G, I–L. Transferrin receptor expression relative to GAPDH was quantified by western blot in pons, substantia nigra and putamen, mean and range are shown M) *represents significant difference from control levels, 1-way anova with Dunnett's *post hoc*, (*$P < 0.05$). Representative blots for each brain region are shown N).

tein as compared to control levels ($P < 0.05$ *cf* control), with no change apparent in MSA substantia nigra (Fig. 3B).

Immunohistochemical analyses of pons sections from human control, PD and MSA tissue revealed a selective neuronal expression of ferroportin and a

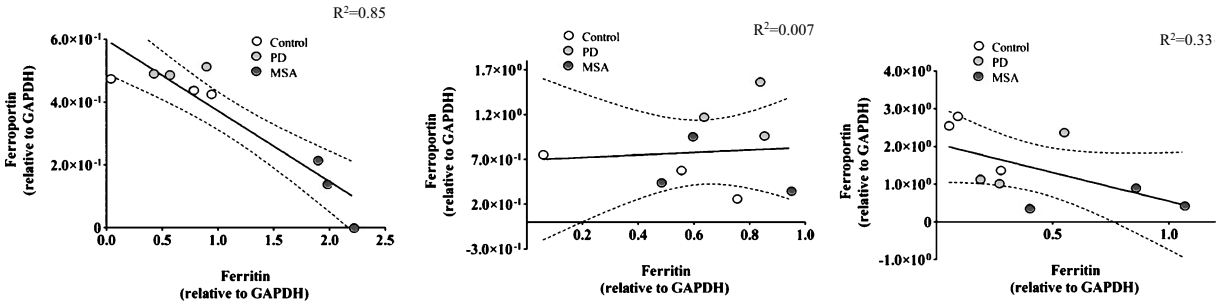

Fig. 4. Correlation between ferritin and ferroportin levels as measure by western blot in the pons, substantia nigra and putamen in control, PD and MSA brain. Ferritin and ferroportin signal relative to GAPDH was quantified by western blot in control, PD and MSA brain. Ferritin expression was plotted against ferroportin expression in A) pons, B) substantia nigra and c) putamen. R^2 is shown. Line of best fit indicated by solid line, error by broken line.

co-localization with the Golgi apparatus. In control pons, ferroportin staining was apparent in most neurons displaying a filiform perinuclear distribution (Fig. 3D and 3E). In PD pons the pattern of ferroportin staining was similar to control with an intact filiform appearance (Fig. 3F, G). In MSA pons, the ferroportin signal appeared weaker and more diffuse (Fig. 3H, I). Analyses of sections from human control, PD and MSA substantia nigra similarly revealed a selective neuronal expression of ferroportin. Indeed the signal for ferroportin was prevalent in all pigmented neurons. However, in the PD substantia nigra expression of ferroportin appeared diffuse and fragmented in comparison to control and MSA tissues (Figs. 3J–L).

Transferrin receptor expression was unaffected in all groups in the substantia nigra and pons (Fig. 3M). However, in the PD putamen, transferrin receptor expression was significantly lower than in the control putamen ($P < 0.05$). This contrasts with MSA, where transferrin receptor expression was unchanged as compared to control putamen.

Linear regression analysis reveals a strong negative correlation between ferritin levels and ferroportin levels in the pons ($R^2 = 0.85, P < 0.001$) (Fig. 4a). However, this strong negative correlation is not present in either the substantia nigra or putamen (Figs. 4b and c).

Microglia display activated morphology in MSA pons

Immunohistochemical analysis of the microglial membrane specific protein iba1 demonstrated that in MSA pons, microglia exhibit the morphology of an activated state: a large cell body with cytoplasmic hypertrophy and enlarged less defined nucleus and shorter thickened processes (Fig. 5c). This morphology was also apparent, albeit it to a lesser extent, in PD pons (Fig. 5b) but not in control pons (Fig. 5a). Positive pixel analysis of iba1 stained tissue revealed an ∼10 fold increase in iba1 positive pixels as compared to control levels ($P < 0.01$), and an ∼3.6 fold increase in PD pons ($P < 0.01$ *cf* control) (Fig. 5d).

Regional iron status differentiates MSA, PD, and healthy controls

A summary of the quantitative differences in measures of iron status is provided in Table 1. Although the cases are carefully matched in terms of age and gender, the sample size ($n = 3$ in each disease group) means that some relationships already well-established in the literature (such as elevated iron in the PD SN compared to healthy controls) do not reach significance in the present study at the 5% level using one-way ANOVA. Linear discriminant analysis (LDA) was used as a method appropriate to small groups to test whether individual samples are correctly assigned to their true disease groups on the basis of measured values of iron status in each brain region. As shown in Table 2a, the majority of samples were correctly assigned as controls, MSA, and PD when considered in terms of measured iron status values (ferritin, ferroportin, total iron, and IRM at 5 K) for each region in turn. For basis pontis and putamen, 8 out of the 9 individual samples were correctly assigned in each region, and 7 out of 9 in the substantia nigra. Assignment of the PD samples to the PD disease group on the basis of iron status was 100% correct (9/9) in all three brain regions. The results in Table 2a indicate a high degree of discrimination between disease groups, supporting the hypothesis that modes of iron dysregulation are disease-specific. An even higher degree of success was achieved when considering each measure of iron status in turn, and

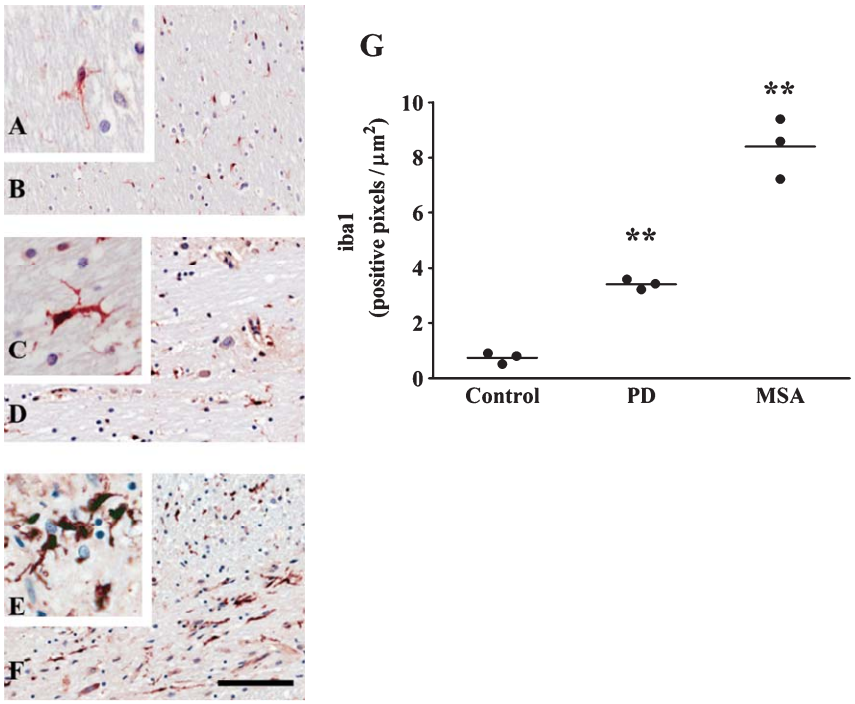

Fig. 5. Microglial morphology in control, PD and MSA pons. iba1 immunostaining in control A, B) PD C, D) and MSA E, F) pons. The number of iba1 positive pixels per μm^2 was calculated G). Individual values are shown, with the mean indicated by a black line. *represents significant difference from control levels, 1-way anova with Dunnett's *post hoc*, (**$P < 0.01$). Scale bar represents 30 μm in A, C & D and 75 μm in B, D & E.

Table 1
Summary of differences between MSA, PD, and control (C) groups ($n = 3$), for measures of iron status. Using one-way analysis of variance (ANOVA), statistically significant increases (↑) and decreases (↓) are indicated, with ⇧ and ⇩ used where values approach (but do not reach) significance at $P < 0.05$

	Basis pontis	Substantia nigra	Putamen
Total iron concentration	MSA ↑ c.f. C, PD $p < 0.005$	PD ⇧ vs. MSA $P = 0.09$	Unchanged
Particulate iron (IRM @ 5K)	MSA ↑ c.f. C, PD $p < 0.001$	PD ⇧ vs. MSA $P = 0.06$	MSA ↑ vs. C $p < 0.05$
Total vs. particulate iron [concentration vs. IRM @ 5K] (all cases)	Strong positive correlation, ($r^2 = 0.95$) $p < 0.0001$	Strong positive correlation, ($r^2 = 0.96$) $p < 0.0001$	–
Iron storage ferritin protein	MSA ↑ c.f. C, PD $p < 0.005$	Unchanged $p < 0.005$	MSA & PD ↑ vs. C
Iron export ferroportin protein	MSA ↓ c.f. C, PD $p < 0.005$	PD ↑ vs. C $p < 0.05$	MSA ↓ vs. C, $p < 0.005$
Storage vs. export [ferritin vs. ferroportin] (all cases)	Strong negative correlation, $p < 0.001$ ($r^2 = 0.85$)	No correlation ($r^2 = 0.01$)	Weak negative correlation ($r^2 = 0.33$)
Iron uptake transferrin protein	Unchanged	Unchanged	PD ↓ vs. C $p < 0.05$

assigning the individual samples on the basis of brain region (basis pontis, substantia nigra, putamen). These results are shown in Table 2b, where 100% of the samples were correctly assigned for ferritin, ferroportin, and IRM at 5 K, and all but one (a control assigned as PD) were correctly assigned for total iron. This supports the hypothesis that there are region-specific differences in iron as a function of disease, in addition to the disease-specific modes of iron dysregulation evidenced in Table 2a.

Table 2a
Linear Discriminant Analysis (LDA) of the individual cases, allocating each into disease groups (MSA, PD, control) on the basis of a) iron analyses performed for each region, and b) regional profile for a given analytical measure of iron. Correctly assigned samples are shown in bold font, incorrectly assigned are in brackets. a) LDA of the quantitative measures of iron status in each region, using ferritin, ferroportin, total iron, and particulate iron (IRM at 5 K) as the variables, gives a high degree of discrimination between disease groups, supporting the hypothesis that modes of iron dysregulation are disease-specific

	Allocated group	True group control	MSA	PD
Basis pontis	Control	**2**	0	0
89% success	MSA	0	**3**	0
	PD	(1)	0	**3**
Substantia nigra	Control	**2**	(1)	0
78% success	MSA	(1)	**2**	0
	PD	0	0	**3**
Putamen	Control	**2**	0	0
89% success	MSA	0	**3**	0
	PD	(1)	0	**3**

Table 2b
LDA of the samples by iron status, using the regions (basis pontis, substantia nigra, putamen) as variables, gives 100% success in assigning each sample to the correct disease group for three of the four independent measures of iron status. This supports the hypothesis that there are region-specific differences in iron as a function of disease. (Only 8 samples were included in this analysis; one matched PD SN sample was from another case.)

	Allocated group	True group control	MSA	PD
Ferritin	Control	**3**	0	0
100% success	MSA	0	**3**	0
	PD	0	0	**2**
Ferroportin	Control	**3**	0	0
100% success	MSA	0	**3**	0
	PD	0	0	**2**
Total iron	Control	**2**	0	0
88% success	MSA	0	**3**	0
	PD	(1)	0	**2**
Particulate iron (IRM @ 5K)	Control	3	0	0
100% success	MSA	0	**3**	0
	PD	0	0	**2**

DISCUSSION

Conventional opinion holds that excess redox-active iron is implicated in neurodegeneration via production of reactive oxygen species which cause lipid peroxidation, protein damage and finally precipitate aggregation (reviewed in [16]). Although there is some controversy in the literature regarding alterations in the level of iron the substantia nigra in PD (reviewed in [17]), our demonstration of an approximately two-fold increase in iron in PD substantia nigra compared to age-matched controls is consistent with similar increases demonstrated by several other groups using a range of techniques including X-ray fluorescence [18], spectrophotometry [19] and atomic absorption [20]. Furthermore, in a previous study of unfixed human tissue, using quantitative electron microprobe analysis, we demonstrated an approximately two-fold increase of cellular iron within individual nigral dopamine neurons in PD as compared to age-matched controls [21]. This approximate doubling of iron in the PD nigra, observed at cellular and whole tissue level, has thus been demonstrated to stand the test of time, and the demonstration of a strikingly similar level of increased iron by a range of techniques certainly adds validity to the GFAAS analysis employed in the present study. Here, we also demonstrate that the increased tissue iron and IRM signal is not accompanied by a statistically significant increase in the iron storage protein ferritin in the PD nigra, or a significant change in TfR expression. In isolation, the total tissue iron and ferritin expression data for the PD nigra support the findings of Dexter et al., who suggest that an decoupling of the relationship between iron and ferritin protein levels may lead to increased levels of redox active iron in the substantia nigra of PD [6]. We can extend this observation, as the IRM data, which parallel the increase in total tissue iron, indicate that the additional iron is coordinated in iron oxide clusters. Given the confirmed absence of ferritin elevation, this material that retains remanent magnetization at 5 K is most likely to be neuromelanin-bound iron [10]. The elevated IRM signal in MSA pons tissue may reasonably be attributed to an elevated concentration of ferritin iron oxide cores, indicating that the excess iron in this tissue is ferritin-bound. This is the most straightforward interpretation of these data; it is acknowledged that the SQuID measurements performed in this study cannot unambiguously prove that the IRM signal in the pons is directly and proportionately due to ferritin concentration, as the presence of other iron biomineral phases within the ferritin, clustering of ferritin, or the presence of other iron nanoparticle inclusions in the tissue could bias the IRM value. Detailed analysis of the biomineral cores in ferritin extracted from these cases will be undertaken in future work.

Interestingly, we find the level of tissue iron, IRM and ferritin protein to be unchanged in the MSA nigra. While others have noted an increase in both tissue iron and ferritin in this region [6], our data are consistent with prior studies which found no evidence for a decoupling of ferritin expression from tissue iron concentration in MSA nigra; this feature appears specific to PD. The extent to which this feature is specific to the

substantia nigra in PD remains to be confirmed. Other studies have shown an increase in iron in the putamen [22] and a decreased expression of transferrin receptors in the putamen in PD compared to age-matched controls [23]. We also note a decreased level of transferrin receptors in the putamen in PD, suggestive of increased levels of free iron in this region. Furthermore, we see a trend towards increased ferritin expression in the putamen in PD. It is interesting that the decoupling between iron and ferritin reported in the PD nigra is not apparent in MSA despite the loss of nigral dopamine cells and similarities in nigral pathology between MSA and PD.

We contrast these observations in the substantia nigra with the relationship between iron and ferritin in the basis pontis, a region heavily affected by neurodegeneration in MSA but spared in PD and devoid of neuromelanin. As expected we found levels of tissue iron, IRM and ferritin to be statistically unchanged in PD pons as compared to control, but we found a two-fold increase in total tissue iron concentration in the MSA pons mirroring the scale of the change observed by us and others in the PD nigra. Interestingly, in contrast to the PD nigra where ferritin expression was unchanged, we observed an approximately three-fold increase in the level of ferritin protein in the MSA pons. Thus, there is a distinct difference in the relationship between ferritin and total iron concentration in these two neurodegenerative diseases. We suggest that in MSA, although there is significantly elevated iron in the pons, this excess iron is sequestered by disproportionately elevated levels of the storage protein ferritin in reactive microglia, potentially leading to a net reduction in the levels of free iron. It remains unknown whether an initial increase in the number of activated microglia precedes an increase in ferritin, leading to an increased sequestration of iron, or an increased concentration of iron precipitates an increased production of ferritin and microglial activation. However, regardless of which is the initiating factor, the net result is a disproportionately high amount of ferritin protein (as determined by western blotting), as compared to the amount of iron, suggesting a deficit in bioavailable iron. As iron is vital to the function and survival of multiple cell types, we propose that a deficit in bioavailable iron may account for the involvement of multiple cell types in the pathology of MSA as compared to the more selective targeting of neurons in PD. As the presence of reactive microglia is well established in PD nigra, [24–27] the fact that we do not see a disproportionate increase in microglial ferritin in the PD nigra, as compared to in the MSA pons, is again indicative of a disease specific uncoupling of the relationship between ferritin and total iron concentration in MSA.

To further explore this hypothesis we investigated the neuronal iron export protein ferroportin. Iron homeostasis in the brain is performed by a variety proteins and a variety of cell types. Indeed, there are many mechanisms by which iron can be transferred between different cell types within the brain (reviewed in [28]). Given that synthesis of iron regulatory proteins is dependent on availability of iron for binding and that iron is readily transferred between cell types, it is important to examine relative levels of iron export and iron storage proteins at a system (whole tissue) level. Ferroportin expression typically parallels iron levels such that in times of iron excess more ferroportin is expressed (reviewed in [16]). As would be expected, we demonstrate a significant increase in ferroportin in the PD nigra as compared to control, with no change evident in MSA nigra, mirroring the changes we see in tissue iron concentration. The MSA pons is the exception, where despite a clear increase in tissue iron concentration, we observed a significant decrease in ferroportin expression. This decrease is accompanied by loss of the normal pattern of ferroportin distribution on the Golgi apparatus and implies possibly degradation of the iron exporter ferroportin and Golgi rearrangement [29]. This observation supports our hypothesis that the MSA pons may have a deficit in free cytosolic iron despite overall iron levels being increased, and that the cells' response to a perceived reduction in iron is a reduced expression of ferroportin. Consistent with previous reports, immunohistochemical analysis demonstrated the localisation of ferroportin to neurons in both the pons and substantia nigra, with some mild staining present in oligodendrocytes in the putamen [30]. There appeared to be two patterns of ferroportin subcellular signal. The most prevalent signal appeared to be bound to an intracellular cytoplasmic membrane and the other a more punctate signal suggestive of an endosomal localisation. Indeed it has been shown that ferroportin can be internalised and stored within endosomes prior to degradation [31]. Both patterns of expression were apparent in all positive neurons. Conventional opinion holds that ferroportin should be located on the extracellular membrane [28, 30]. Our findings, and those reported elsewhere, contradict this with an apparent lack of ferroportin signal on cell surface membranes [32]. Thus, although trafficking of ferroportin to the cell surface is likely regulated, this phenomenon certainly requires further investigation within the brain.

Another avenue that warrants further study is the potential role of ceruloplasmin (Cp) in MSA. Cp plays a critical role in cellular iron efflux; it is responsible for oxidation of the ferrous iron exported by ferroportin, and impaired function of Cp impacts ferroportin stability, leading to reduced ferroxidase activity and mislocalization in the endoplasmic reticulum [33]. Mutant Cp has been shown in cell culture to drive loss of Golgi morphology, and degradation of ferroportin [29]. Hypoceruloplasminemia and mutant Cp have also been reported in cases of MSA [34, 35]; further investigation is required to determine the extent to which impaired Cp function might affect ferroportin in MSA.

The gene sequences for both ferritin and ferroportin contain an upstream 5′ iron response element (IRE) allowing translation to be controlled by the relative affinity of iron response protein 1 and 2 (IRP 1 and 2 respectively) themselves regulated by iron levels (reviewed in [16]). As the expression of both ferritin and ferroportin are controlled by this same mechanism, our observation that ferritin is increased, and ferroportin decreased, in MSA pons suggests that in MSA the levels of these two key homeostatic proteins are influenced by more than just iron levels. Others have shown that during liver regeneration, an increased activation of IRP also led to divergent effects on ferritin and transferrin receptor expression, in spite of both proteins having the same 5′ IRE [36]. We found the levels of IRP1 to be unchanged in MSA pons (data not shown). An alternative explanation for the apparently paradoxical alterations in ferritin and ferroportin in MSA pons involves the hormone hepcidin. Systemic iron homeostasis is maintained by the hepcidin which is secreted by hepatocytes in response to increased iron and signals for the internalisation and subsequent degradation of ferroportin (reviewed in [16]). Hepcidin has been identified throughout the brain in areas known to contain ferroportin and has also been shown to be induced by the pro-inflammatory cytokine interleukin-6 (IL-6) [37, 38]. Interestingly, the presently observed alterations in levels of iron, ferritin and ferroportin are reminiscent of those underlying the anemia of chronic disease (ACD), a paradoxical condition mediated by pro-inflammatory cytokines whereby total body iron stores are elevated, but there is reduced bioavailable iron leading to an anemic condition [39]. We demonstrate that microglia in the MSA pons have a reactive profile with an enlarged irregular cell body and shorter thicker processes with little branching. Thus, we propose that a local inflammatory response, mediated by IL-6 secreted by activated microglia, may, via hepcidin, underlie the apparently paradoxical changes in ferroportin expression in MSA in the present study. Further, this situation may be more widespread than the pons, as there is much evidence of microglial activation throughout the MSA brain [40].

The link between iron levels and alpha synuclein is not well understood and any explanation would be speculative. However, recent evidence has demonstrated *in vitro* that alpha synuclein serves as a cellular ferrireductase, responsible for reducing iron (III) to bioavailable iron (II) [3]. As PD and MSA both involve aggregation of alpha synuclein, it is possible that the ferrireductase function of alpha synuclein is perturbed in these synucleiopathies. On the other hand, PD is associated with an increased expression of alpha synuclein which may lead to increased levels of bioavailable iron II. Indeed it is possible that both these mechanisms may contribute to different timepoints in the lengthy disease process. Accumulation of alpha synuclein, either as lewy bodies in PD or filamentous nuclear and cytoplasmic inclusions in neurons and glia in MSA, likely reflects an end-point stage reflective of stressed dying cells. The differences between the types of alpha synuclein aggregates in PD and MSA is poorly understood, but our findings suggest that Lewy bodies may form where there is excess iron and MSA aggregates where there are decreased levels of iron. The distribution of alpha synuclein pathology may be a reflection of differences in the regional susceptibility of some neurons and glia to changes in iron levels. Exploration of the specific role of alpha synuclein in iron dysregulation in all synucleinopathies clearly warrants further investigation.

In conclusion, while it is recognised that the low number of samples is a limitation of this study, our present findings raise the distinct possibility that despite an increase in total tissue iron concentration, there may a deficit in bioavailable iron in MSA. Future studies will determine the potential role of local inflammatory signalling in maintaining this paradoxical low bioavailable iron state. Furthermore, this deficit may account for the degeneration of multiple cell types in MSA pathology.

ACKNOWLEDGMENTS

We thank Prof J. Dobson and Dr M. Lees for advice concerning IRM measurement and analysis. NPV was supported by a Basic research fellowship from the Parkinson Society Canada. JFC acknowledges support for this study from EPSRC Postdoctoral Fellowship EP/D066654/1 and an RCUK Academic Fellowship.

MEF was supported by a PhD studentship grant from the Alzheimer's Society, UK. AT acknowledges support from the Canadian Institutes of Health Research (MOP 84501) and the Parkinson Society of Canada. All tissue samples used in this study were provided from the Canadian Brain tissue Bank and were studied under ethical approval from the relevant REC (UK) and University Health Network Research Ethics Board. The GFAAS analysis was performed with support from EPSRC. The SQuID magnetometer used in this research was obtained through the Science City Advanced Materials project: Creating and Characterising Next Generation Advanced Materials project, with support from Advantage West Midlands (AWM) and part funded by the European Regional Development Fund (ERDF).

REFERENCES

[1] Forno LS (1996) Neuropathology of Parkinson's disease. *J Neuropathol Exp Neurol*, **55**, 259-272.

[2] Crichton R & Ward RJ (2008) *Metal-based neurodegeneration – from molecular mechanisms to therapeutic strategies in Parkinson's disease*. John Wiley & Sons Ltd, 2006.

[3] Davies P, Moualla D & Brown DR (2011) Alpha-synuclein is a cellular ferrireductase. *PLoS One*, **6**, e15814.

[4] Ayton S, Lei P, Bush AI & Finkelstein DI (2013) Alpha synuclein is a major regulator of iron homeostasis, in 11th Annual Conference on Alzheimer's and Parkinson's diseases (AD/PD). *Florence*, 2013.

[5] Riederer P, Dirr A, Goetz M, Sofic E, Jellinger K & Youdim MB (1992) Distribution of iron in different brain regions and subcellular compartments in Parkinson's disease. *Ann Neurol*, **32** (Suppl) S101-s104.

[6] Dexter DT, Carayon A, Javoy-Agid F, Agid Y, Wells FR & Daniel SE, et al. (1991) Alterations in the levels of iron, ferritin and other trace metals in Parkinson's disease and other neurodegenerative diseases affecting the basal ganglia. *Brain*, **114**(Pt 4), 1953-1975.

[7] Dexter DT, Jenner P, Schapira AH & Marsden CD (1992) Alterations in levels of iron, ferritin, and other trace metals in neurodegenerative diseases affecting the basal ganglia. The Royal Kings and Queens Parkinson's Disease Research Group. *Ann Neurol*, **32**(Suppl), S94-S100.

[8] Friedman A, Arosio P, Finazzi D, Koziorowski D & Galazka-Friedman J (2011) Ferritin as an important player in neurodegeneration. *Parkinsonism Relat Disord*, **17**, 423-430.

[9] Arosio P & Levi S (2010) Cytosolic and mitochondrial ferritins in the regulation of cellular iron homeostasis and oxidative damage. *Biochim Biophys Acta*, **1800**, 783-792.

[10] Bolzoni F, Giraudo S, Lopiano L, Bergamasco B, Fasano M & Crippa PR (2002) Magnetic investigations of human mesencephalic neuromelanin. *Biochim Biophys Acta*, **1586**, 210-218.

[11] Hautot D, Pankhurst QA & Dobson J (2005) Superconducting quantum interference device measurements of dilute magnetic materials in biological samples. *Rev Sci Instrum*, **76**.

[12] Collingwood JF, Chong RK, Kasama T, Cervera-Gontard L, Dunin-Borkowski RE & Perry G, et al. (2008) Three-dimensional tomographic imaging and characterization of iron compounds within Alzheimer's plaque core material. *J Alzheimers Dis*, **14**, 235-245.

[13] Hautot D, Pankhurst QA & Dobson J (2005) Superconducting quantum interference device measurements of dilute magnetic materials in biological samples. *Rev Sci Instrum*, **76**.

[14] House E, Esiri M, Forster G, Ince PG & Exley C (2012) Aluminium, iron and copper in human brain tissues donated to the Medical Research Council's Cognitive Function and Ageing Study. *Metallomics*, **4**, 56-65.

[15] Zecca L, Gallorini M, Schunemann V, Trautwein AX, Gerlach M & Riederer P, et al. (2001) Iron, neuromelanin and ferritin content in the substantia nigra of normal subjects at different ages: Consequences for iron storage and neurodegenerative processes. *J Neurochem*, **76**, 1766-1773.

[16] Crichton RR, Dexter DT & Ward RJ (2011) Brain iron metabolism and its perturbation in neurological diseases. *J Neural Transm*, **118**, 301-314.

[17] Friedman A, Galazka-Friedman J & Koziorowski D (2009) Iron as a cause of Parkinson disease – a myth or a well established hypothesis? *Parkinsonism Relat Disord*, **15**(Suppl 3), S212-S214.

[18] Earle KM (1968) Studies on Parkinson's disease including x-ray fluorescent spectroscopy of formalin fixed brain tissue. *J Neuropathol Exp Neurol*, **27**, 1-14.

[19] Sofic E, Riederer P, Heinsen H, Beckmann H, Reynolds GP & Hebenstreit G, et al. (1988) Increased iron (III) and total iron content in post mortem substantia nigra of parkinsonian brain. *J Neural Transm*, **74**, 199-205.

[20] Griffiths PD & Crossman AR (1993) Distribution of iron in the basal ganglia and neocortex in postmortem tissue in Parkinson's disease and Alzheimer's disease. *Dementia*, **4**, 61-65.

[21] Oakley AE, Collingwood JF, Dobson J, Love G, Perrott HR & Edwardson JA, et al. (2007) Individual dopaminergic neurons show raised iron levels in Parkinson disease. *Neurology*, **68**, 1820-1825.

[22] De Volder AG, Francart J, Laterre C, Dooms G, Bol A & Michel C et al. (1989) Decreased glucose utilization in the striatum and frontal lobe in probable striatonigral degeneration. *Ann Neurol*, **26**, 239-247.

[23] Mash DC, Pablo J, Buck BE, Sanchez-Ramos J & Weiner WJ (1991) Distribution and number of transferrin receptors in Parkinson's disease and in MPTP-treated mice. *Exp Neurol*, **114**, 73-81.

[24] Block ML, Zecca L & Hong JS (2007) Microglia-mediated neurotoxicity: Uncovering the molecular mechanisms. *Nat Rev Neurosci*, **8**, 57-69.

[25] McGeer PL, Itagaki S, Boyes BE & McGeer EG (1988) Reactive microglia are positive for HLA-DR in the substantia nigra of Parkinson's and Alzheimer's disease brains. *Neurology*, **38**, 1285-1291.

[26] Langston JW, Forno LS, Tetrud J, Reeves AG, Kaplan JA & Karluk D (1999) Evidence of active nerve cell degeneration in the substantia nigra of humans years after 1-methyl-4-phenyl-1,2,3,6-tetrahydropyridine exposure. *Ann Neurol*, **46**, 598-605.

[27] Imamura K, Hishikawa N, Sawada M, Nagatsu T, Yoshida M & Hashizume Y (2003) Distribution of major histocompatibility complex class II-positive microglia and cytokine profile of Parkinson's disease brains. *Acta Neuropathol*, **106**, 518-526.

[28] Moos T, Rosengren Nielsen T, Skjorringe T & Morgan EH (2007) Iron trafficking inside the brain. *J Neurochem*, **103**, 1730-1740.

[29] Persichini T, De Francesco G, Capone C, Cutone A, di Patti MC & Colasanti M, et al. (2012) Reactive oxygen

species are involved in ferroportin degradation induced by ceruloplasmin mutant Arg701Trp. *Neurochem Int*, **60**, 360-364.

[30] Moos T & Rosengren Nielsen T (2006) Ferroportin in the postnatal rat brain: Implications for axonal transport and neuronal export of iron. *Semin Pediatr Neurol*, **13**, 149-157.

[31] De Domenico I, Ward DM, Langelier C, Vaughn MB, Nemeth E & Sundquist WI, et al. (2007) The molecular mechanism of hepcidin-mediated ferroportin down-regulation. *Mol Biol Cell*, **18**, 2569-2578.

[32] Rouault TA (2001) Systemic iron metabolism: A review and implications for brain iron metabolism. *Pediatr Neurol*, **25**, 130-137.

[33] Kono S, Yoshida K, Tomosugi N, Terada T, Hamaya Y & Kanaoka S, et al. (2010) Biological effects of mutant ceruloplasmin on hepcidin-mediated internalization of ferroportin. *Biochim Biophys Acta*, **1802**, 968-975.

[34] Yomono H, Kurisaki H, Murayama S, Hebisawa A, Miyajima H & Takahashi Y (2003) An autopsy case of multiple system atrophy with a heteroallelic ceruloplasmin gene mutation. *Rinsho Shinkeigaku*, **43**, 398-402.

[35] Kurisaki H, Yomono H, Murayama S & Hebisawa A (2002) Multiple system atrophy with a-/hypo-ceruloplasminemia: Distribution of iron in brains of 2 autopsy cases. *Rinsho Shinkeigaku*, **42**, 293-298.

[36] Cairo G, Tacchini L & Pietrangelo A (1998) Lack of coordinate control of ferritin and transferrin receptor expression during rat liver regeneration. *Hepatology*, **28**, 173-178.

[37] Zechel S, Huber-Wittmer K & von Bohlen und Halbach O (2006) Distribution of the iron-regulating protein hepcidin in the murine central nervous system. *J Neurosci Res*, **84**, 790-800.

[38] Nemeth E, Tuttle MS, Powelson J, Vaughn MB, Donovan A & Ward DM, et al. (2004) Hepcidin regulates cellular iron efflux by binding to ferroportin and inducing its internalization. *Science*, **306**, 2090-2093.

[39] Weiss G & Goodnough LT (2005) Anemia of chronic disease. *N Engl J Med*, **352**, 1011-1023.

[40] Ishizawa K, Komori T, Sasaki S, Arai N, Mizutani T & Hirose T (2004) Microglial activation parallels system degeneration in multiple system atrophy. *J Neuropathol Exp Neurol*, **63**, 43-52.